The Coupled Nonlinear Dynamics of Spacecraft with Fluids in Tanks of Arbitrary Geometry

by

MARTHINUS CORNELIUS VAN SCHOOR

Mech. Eng, Pretoria University, (1982)
SM, Massachusetts Institute of Technology, (1985)

SUBMITTED TO THE DEPARTMENT OF AERONAUTICS AND
ASTRONAUTICS IN PARTIAL FULFILLMENT OF THE REQUIREMENTS
FOR THE DEGREE OF

DOCTOR OF PHILOSOPHY

at the

MASSACHUSETTS INSTITUTE OF TECHNOLOGY

March, 1989

© Massachusetts Institute of Technology, 1989

Signature of Author _____
Department of Aeronautics and Astronautics
March 24, 1989

Certified by _____
Prof. Edward F. Crawley, Committee Chairman

Certified by _____
Prof. Triantaphyllos R. Akylas, Thesis Committee
(Department of Mechanical Engineering)

Certified by _____
Prof. John Dugundji, Thesis Committee

Certified by _____
Prof. R. John Hansman, Thesis Committee

Accepted by _____
Prof. Harold Y. Wachman
Chairman, Department Graduate Committee

The Coupled Nonlinear Dynamics of Spacecraft with Fluids in Tanks of Arbitrary Geometry

by

Marthinus C. van Schoor

Abstract

The nonlinear dynamics of a spacecraft coupled to a contained fluid with a free surface is studied both experimentally and analytically. A general finite degree-of-freedom, nonplanar model describing the dynamics of a spacecraft coupled to a fluid, contained in a tank of general geometry, is developed and verified by comparing analytical with experimental results.

The nonlinear model of the fluid/spacecraft system is accurate to third order in terms of the fluid motion amplitudes. A generalized coordinate description is obtained by satisfying the free surface boundary condition in an assumed mode approach. The kinematic boundary problem, posed as a variational problem, provides the relationship between the assumed free surface generalized coordinates and the fluid flow potential coordinates. Given the generalized coordinate description of the fluid, linear and nonlinear capillary forces, along with the standard energy terms, are included in the fluid Lagrangian. This method is valid for tanks with straight and parallel walls but results are presented which show that the method can be applied to tanks of more complex geometry if the geometry can be approximated with a straight/parallel wall assumption. In this research, the linear eigen-mode shapes as calculated with a finite difference routine, are used as assumed modes.

The nonlinear set of equations obtained by applying Lagrange's principle to the fluid Lagrangian, is solved for the forced response characteristics by numerical implementation of the Harmonic Balance method. The nonlinear time independent equations provided by this method are solved using an Inverse Iteration technique as well as a Newton-Raphson solver. The analytical model is used to investigate the nonlinear fluid slosh behavior in spherical, square, rectangular and cylindrical tanks.

Three scaled fluid tank models, namely; spherical, square and rectangular, were experimentally tested to determine the nonlinear characteristics of fluids contained in these types of tanks. The tanks are scaled to have Bond numbers representative of typical spacecraft fluid storage tanks. Both uncoupled (tank alone) and coupled forced excitation

2

tests are performed. In the coupled tests, the measured reaction slosh force is fed to an analog simulation of a spacecraft's modal dynamics, thus coupling spacecraft and fluid slosh dynamics. In these tests, the effects of system mass ratio, frequency ratio and damping ratio on the nonlinear coupled behavior are investigated.

The analytical and experimental results contributed to a general understanding of the complex behavior of fluid/spacecraft dynamic systems. In conclusion, tank vibrations exceeding 5% of the equivalent diameter show significant nonlinear effects, both in the fluid and spacecraft responses. The equivalent diameter is equal to four times the surface area divided by the circumference. For cylindrical tanks the equivalent diameter is equal to the tank diameter. At higher excitation levels (resonance amplitudes greater than 10-15% of the equivalent diameter), all the tanks exhibit jump phenomena and multi-valued oscillations. Convective (kinematic) fluid nonlinearities are important for all Bond numbers and capillary effects must be modeled for Bond numbers as high as 60.

Nonlinearities are the strongest for systems with low fluid mass fractions and for fluid-to-spacecraft frequency ratios between 0.8 and 1.0.

The experimentally observed amplitude dependent dissipation rates and shift in resonant frequencies (softening) are predicted by the analytical model. The model fails to predict the forced response characteristics when swirling motion occurs in the tanks which have repeated eigen-modes. If perturbed, to include a small coupling term between the spacecraft degree-of-freedom and the nonplanar slosh mode, the analytical model can predict the swirling motion. However a more detailed model of the nonplanar degree-of-freedom of the excitation system is required to correctly model the forced response characteristics when swirling occurs.

Thesis Supervisor: Prof. Edward F. Crawley
Title: Associate Professor of Aeronautics and Astronautics

Acknowledgements

I dedicate this thesis to my caring and loving wife, Marcelle and to my parents. Marcelle not only sacrificed her own studies to enable me to come to M.I.T. but she also constantly supported and encouraged me and made a major contribution to this document. My parents love and faith in me carried me through the difficult times.

I would like to express my appreciation and thanks to my advisor, Prof. Edward Crawley, for his guidance, insight and support over the last two years. Without him this would not have been possible. The contributions of my thesis committee, Prof. T. Akylas, Prof. John Dugundji and Prof. John Hansman are also appreciated. It was a privilege to have you on my committee. A special word of thanks to Prof. Andy von Flotow. He was always available to discuss new ideas or to suggest a new direction.

The support and friendship of so many people made our time at M.I.T. a great, fulfilling experience. The people in my laboratory always had time to help me and to join us on Friday evenings. A special word of thanks to two very special people; Javier and Dave. You two, along with Mindy and Jean, mean so much to us. I hope we will be friends for ever.

The rugby crowd, especially Leo Casey, Mike Murphy, Bruce Johnson, Jim Culliton and Joan Rice must also be mentioned. Hanging around them prevented me from becoming a complete workaholic. May there be many more tries and victory celebrations.

Vrystaaaat !!!!!!
(A cry of love and freedom)

Table of Contents

Nomenclature

a	Tank radius
(a_1, a_2, a_3)	Accelerations measured by the accelerometers mounted on the test model base
a_x	Planar tank acceleration component
a_y	Nonplanar tank acceleration component
a_{mn}	Nonlinear equivalent fluid slosh depth matrix
$a_{mn}^{(0)}$	Zero'th order equivalent fluid slosh depth matrix
$a_{mn}^{(1)}$	Linear correction to the nonlinear equivalent fluid slosh depth matrix
$a_{mn}^{(2)}$	Quadratic correction to the nonlinear equivalent fluid slosh depth matrix
Bo	Bond number
c	Damping constant for the spacecraft mode
c_{q_i}	Damping constant for the ith fluid mode
d_e	Equivalent diameter $= 4\dfrac{\text{Surface Area}}{\text{Surface Circumference}}$
d_{mn}	Nonlinear kinematic matrix
$d_{mn}^{(0)}$	Zero'th order kinematic matrix
$d_{mn}^{(1)}$	Linear correction to the nonlinear kinematic matrix
$d_{mn}^{(2)}$	Quadratic correction to the nonlinear kinematic matrix
d	Tank diameter
f	Free surface equilibrium position, dimensional
(F_1, F_2, F_3)	Forces measured by the force reaction balance force transducers
F_{ex}	Externally applied force (x-direction)

10

fo, f_0	Spacecraft mode natural frequency
fs	Primary planar fluid mode natural frequency
F_{xs}	Planar (x) reaction slosh force component
F_{ys}	Nonplanar (y) reaction slosh force component
F_x	Total planar force component measured
F_y	Total nonplanar force component measured
g	Apparent acceleration at a tank location
g_o	Earth normal gravity (9.81 m/s^2)
G	Linear system reactance matrix
G_ζ	Spacecraft mode feedback gain corresponding to damping ratio
G_ω	Spacecraft mode feedback gain corresponding to frequency
G_m	Spacecraft mode feedback gain corresponding to mass
h	Fluid depth
I	Kinematic integral which is minimized to satisfy fluid boundary conditions
I_{zD}	Total moment of inertia of the dry mass of the model tank and mounting hardware
k_{mn}	Nonlinear fluid wave number matrix
$k_{mn}^{(0)}$	Zero'th order fluid wave number matrix
$k_{mn}^{(1)}$	Linear correction to the fluid wave number matrix
$k_{mn}^{(2)}$	Quadratic correction to the fluid wave number matrix
k	Spacecraft mode spring rate
K	Stiffness matrix
K_a	Accelerometer sensitivity (mvolts/g)
K_x	Proximeter sensitivity (volts/inch)
K_f	Slosh force resolver sensitivity (volts/pound)

K_g	Normal accelerometer sensitivity (volts/g)
K_n	Equivalent mechanical slosh model spring rate
l_{mn}	Nonlinear fluid wavelength matrix
$l_{mn}^{(0)}$	Zero'th order fluid wavelength matrix
$l_{mn}^{(1)}$	Linear correction to the fluid wavelength matrix
$l_{mn}^{(2)}$	Quadratic correction to the fluid wavelength matrix
L	Lagrangian of the coupled fluid-spacecraft system
m	Spacecraft modal mass
m_D	Total dry mass inertia of the model tank and mounting hardware
m_F	Total fluid mass
m_p	Proof mass used in the force measurement calibration
m_r	Residual null-out dry mass in the force measurement calibration
m_{xq}, m_{yq}	Fluid-spacecraft inertial coupling coefficients
M_{zs}	Vertical slosh reaction moment component
M_z	Total vertical reaction moment component measured
N	Number of modes in the assumed modal decomposition of the fluid dynamics
N_{v_1}	Gravity scaled viscosity
N_{v_2}	Surface tension scaled viscosity
$\mathbf{n}$	Outward pointing normal to the fluid volume V on the surface S_F (including free surface and container walls)
q_n	Free surface modal coordinates
r	Radial coordinate, dimensional
R	Radial coordinate, units of tank radius
$\mathbf{R}$	Inertial coordinates of the tank frame origin

r_T	Radius of the force transducer center-lines on the slosh force reaction balance
r_a	Radius of the accelerometer center-lines on the slosh force reaction balance
r_h	Hydraulic radius
RC	Time constant of the spacecraft mode circuit
R_{cg}	Spacecraft orbital radius at the center of gravity
s	Laplace's variable
S_F	Fluid free surface
S_B	Tank cross section
t	Time
T_F	Total fluid kinetic energy
$T_{s/c}$	Spacecraft mode kinetic energy
u	Fluid potential velocity relative to coordinate system fixed in the tank
u,v	Curvilinear coordinate system defining the boundary of an enclosed fluid
u_1, u_2	Amplitudes of the complex eigen-mode coefficients, A_1 and A_2
u_{x_i}, u_{q_i}	Linear system eigen-mode coordinates
U_G	Free surface gravitational potential energy
$U_{s/c}$	Spacecraft mode potential energy
U_σ	Free surface capillary potential energy
V_{fex}	Input voltage of the compliant actuator spacecraft mode circuit
V_{fxs}	Planar slosh force measurement voltage
V_{fys}	Nonplanar slosh force measurement voltage
V_x	Proximeter displacement measurement voltage
V_{xc}	Output voltage of the compliant actuator spacecraft mode circuit
v	Kinematic viscosity of the fluid

x	Planar tank displacement (coordinate)
$\dot{x}$	Inertial velocity vector of a fluid particle
y	Nonplanar tank displacement (coordinate)
z	Vertical coordinate (parallel to gravity vector)
z_T	Tank displacement from spacecraft center of gravity

Greek:

α	Fluid-vapor-solid contact angle
α_i, α_{ijk}	Nonlinear convection (fluid modal inertia) coefficients
β_i, β_{ijk}	Nonlinear capillary coefficients
χ_n	Fluid flow field potential mode shapes
∇	Gradient operator (2 or 3 dimensions, depending on the function)
ε	Small parameter ($<<1$)
γ_{ijk}	Secondary fluid mode forced solution coefficients for the quadratic perturbation equation
Γ	Linear hysteresis constant
η	Free surface height parallel to g vector
λ	Linear fluid sloshing mass fraction
μ	Coupled system mass ratio (total fluid over spacecraft mode)
μ_{xq}, μ_{yq}	Linear fluid-spacecraft inertial coupling coefficients
μ_{33}, μ_{44}	Secondary fluid mode mass ratios
ν	Coupled system frequency ratio (slosh over spring frequencies)
ν_1, ν_2	Coupled system eigen-frequencies (units of spring-mass frequency)

ν_3, ν_4	Secondary fluid mode natural frequencies (units of spring-mass frequency)
Ω	Excitation frequency
ϕ	Fluid flow potential field
ϕ_n	Fluid flow potential field modal coordinates
Φ	Fluid flow spatial modal coordinate
σ	Surface tension
ω_s	Slosh circular frequency
ξ_n	Free surface mode shapes
Ξ_{ex}	Non-dimensional externally applied force
ζ	Spacecraft mode damping ratio
ζ_{q_i}	Fluid mode damping ratio

Derivatives:

$(\dot{\ })$	Total time derivative
$(\ )_x$	Partial derivative with respect to any variable x

Chapter 1

Introduction

This Chapter motivates the research on coupled spacecraft/fluid systems (Section 1.1), discusses the underlying assumptions on which the assumed mode analytical model is based (Section 1.2) and explain how this analytical model was modified in this research to be valid for tanks of more complex geometry (Section 1.3). The chapter concludes with an outline of this document.

1.1   Research Motivation

The precise operating requirements of modern spacecraft demand a detailed model of all the on board dynamic components. Nonlinearities that were ignored in the past, must be modeled and understood in order to satisfy stringent operating requirements. For example; the resolution of orbiting optical systems can be significantly degraded by imperfections of 10^{-5} radians. Furthermore, attitude errors during transfer orbit insertion can result in a fuel mass penalty for the spacecraft. Since unmodeled dynamics during the design phase can result in sub-standard system performance and lead to instabilities, the modeled spacecraft dynamics must reflect the design requirements. For very tight tolerances, this will invariably lead to a very complex model. Effects, that may have to be modeled are; nonlinear geometric and material properties and multi-body dynamic effects.

Another potentially important nonlinear effect is fluid slosh. Nonlinear fluid/spacecraft motion caused by finite amplitude fluid slosh will depart significantly from motion predicted by linear theory. Liquid propellants are more efficient than solid propellants and more spacecraft designs rely on liquid propellants than ever before. Communication satellites carry as much as 50% of their total mass as liquid, both for orbital transfer and for attitude control. Liquid-fueled upper stages and orbital transfer vehicles can have mass fractions as high as 120%. These large mass fractions, spacecraft dry mass versus propellant mass, indicate that the dynamics associated with the fuel slosh is of paramount importance. The

longitudinal vibrations, also known as the pogo phenomena, observed in rockets and launch vehicles (for example; Thor-Agena and Titan II) [Kana in Abramson, 1966] and the fluid induced roll oscillations encountered in the Saturn I rocket program [Abramson, 1966] emphasize the need to accurately model the fluid slosh dynamics. Since it may be impossible to completely avoid interactions between the spacecraft motion and the contained fluid, this research is an attempt to develop a rational approach to the modeling of the coupled dynamics associated with spacecraft carrying contained fluids.

In the past many researchers have published work on this topic, namely; Reynolds and Satterlee [1964, 1966], Luke [1967], Yeh [1967], Abramson [1963, 1966] and Ibrahim [1975a, 1975b] and in the recent past; Peterson [1987] on the coupled nonlinear dynamics of fluid/spacecraft systems with cylindrical tanks, Agrawal [1987] on the interaction between liquid propellant slosh modes and attitude control in a dual-spin spacecraft, Berry [1981] on modeling large amplitude propellant slosh, Kanan [1987] on modeling nonlinear rotary slosh in propellant tanks, Komatsu [1987] on the analysis of nonlinear sloshing of liquids in tanks with arbitrary geometries, Nakayama [1981] on using the boundary element method to analyze two-dimensional nonlinear sloshing problems and Yu [1987] on the nonlinear analysis of sloshing in circular cylindrical tanks using the perturbation method. This list, far from a complete one, illustrates the considerable importance the engineering community has attached to the nonlinear fluid slosh problem. Studying the literature on the subject, one can conclude that there are many innovative ways to approach and solve the problem. It is not clear, however, how to generalize most of these methods to tanks of arbitrary geometry while keeping the model simple. Some of the approaches yield unwieldy equations, require significant algebraic manipulation and are not computationally cost effective.

The Rayleigh-Ritz assumed mode approach, developed by Miles [1984a and 1984b] and modified by Peterson [1987] for low Bond numbers, was selected, in this research as a method that could best be extended to tanks of arbitrary geometry. The following section is devoted to the underlying assumptions and simplifications associated with the assumed mode approach, while the next section of this chapter explains how this method was modified for this research.

17

1.2 Assumed Mode Approach

This section discusses and outlines the assumed mode approach developed by Miles [1984a and 1984b] and Limarchenko [1978a, 1978b and 1980]. This method was modified by Peterson [1987] to be valid for low Bond numbers. The method starts out by assuming separate sets of generalized coordinates for the free surface motion and for the internal potential flow function. The kinematic boundary condition at the fluid free surface is then used to relate the fluid flow potential generalized coordinates to the free surface motion generalized coordinates. Given a unique, independent set of generalized coordinates, the fluid kinetic and potential energies are expressed in terms of the free surface generalized coordinates and combined to form the system Lagragian. The next few paragraphs outline the underlying assumptions of the assumed mode model and identifies the important parameters.

Sources of Nonlinearities: The relationship between the fluid flow potential function generalized coordinates and the free surface generalized coordinates is nonlinear and is one of the major sources of nonlinearity in the fluid slosh behavior. Consider the action of the convection forces at the fluid free surface of the fluid. The potential flow (ϕ) and the free surface motion (η) must satisfy the kinematic boundary condition (Fig. 1.1):

$$\frac{\partial \eta}{\partial t} + \nabla\phi \cdot \nabla\eta \Big|_{z=\eta} = \frac{\partial \phi}{\partial z}\Big|_{z=\eta} \qquad (1.1)$$

This equation is an analytical expression of the Dirichlet and Neumann problems and constitutes a nonlinear relation between the fluid flow potential (ϕ) and the free surface motion (η). Eq. 1.1 is a mathematical expression for the requirement that the fluid at the free surface boundary must follow the motion of the free surface.

Another source of nonlinearity is the potential energy stored in the capillary viscous forces [Limarchenko, 1981], given by:

$$U_\sigma = \sigma \int\!\!\int_S \sqrt{1 + \nabla\eta \cdot \nabla\eta} \; dS \qquad (1.2)$$

The potential energy of the free surface is a function of the total dynamic free surface area. The free surface area is a complex nonlinear function of

18
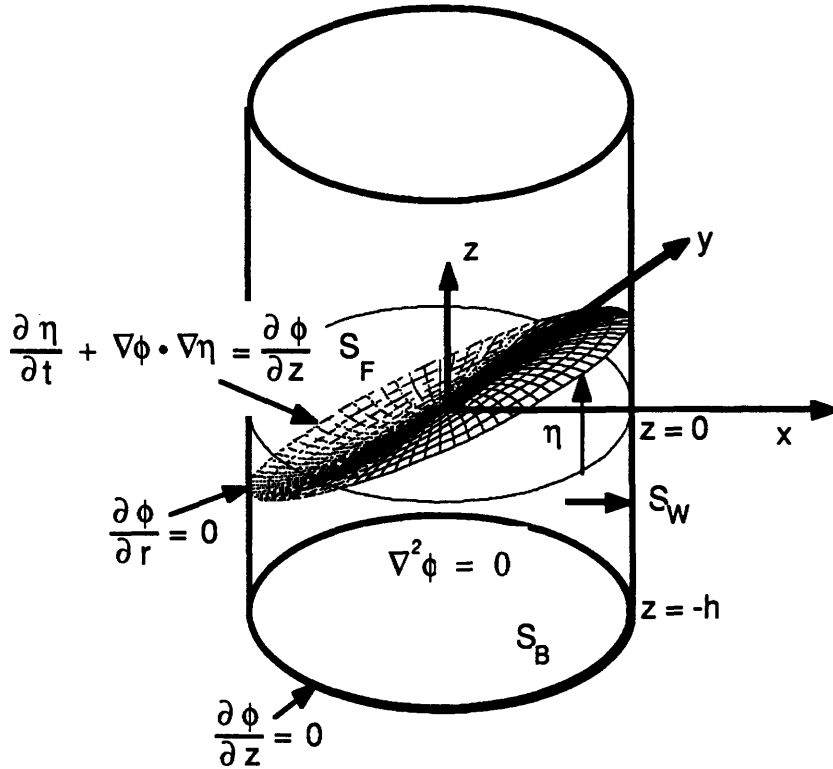
Figure 1.1 **Inviscid Fluid Flow Boundary Conditions for a Cylindrical Tank.**

Fluid is constrained to flow parallel to the solid walls. The free surface boundary condition leads to nonlinear inertia effects in the fluid equations of motion.

the free surface shape (η). Peterson [1987] extended the work of Miles [1984a] by expressing the free surface shape as a sum of the equilibrium or static free surface and the dynamic motion of the free surface. The capillary energy is then a function of the equilibrium free surface or Bond number (Bo). The Bond number is a non-dimensional measure of the relative importance of gravity versus capillary forces (eq. 1.3).

$$Bo = \frac{\rho g a^2}{\sigma} \tag{1.3}$$

In this equation (ρ) is the fluid density, (g) is the mean apparent gravity level, (a) is some fluid tank size scale factor and (σ) is the surface tension. Fig. 1.2 depicts the Bond numbers for Hydrazine, Liquid Oxygen and Liquid Hydrogen due to gravity gradient, expressed as the tank displacement from the spacecraft's center of gravity, in a 3 m diameter cylindrical tank.
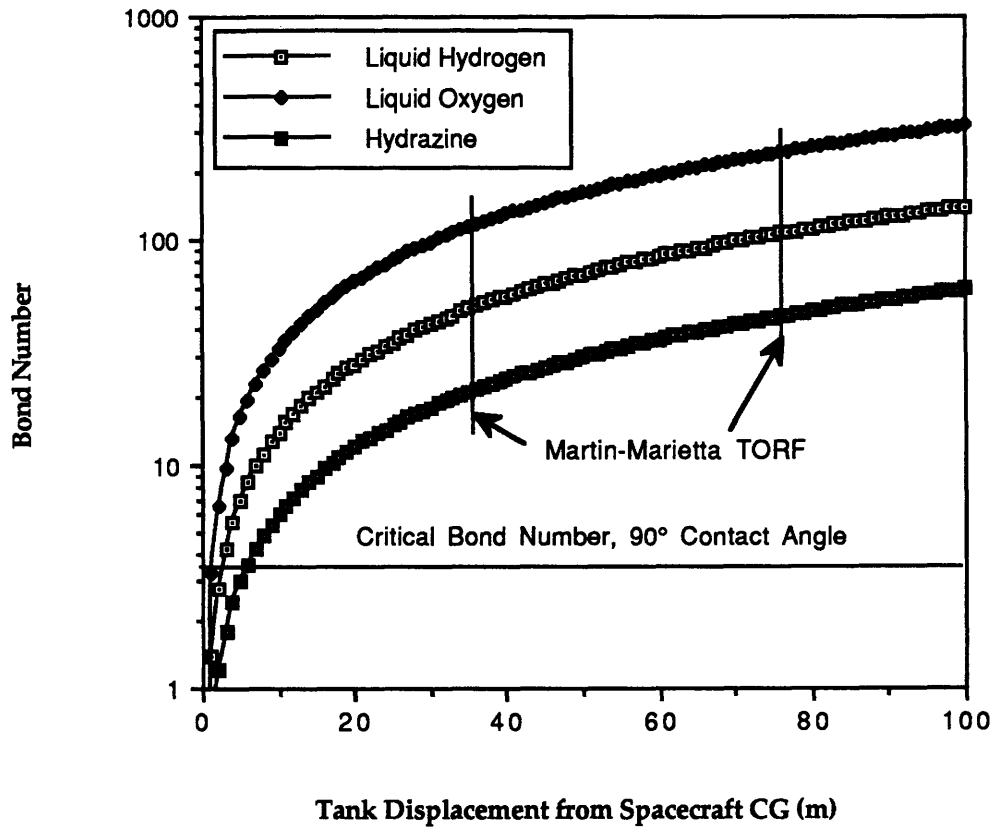
Figure 1.2   Typical Bond numbers

In terms of the equilibrium free surface, gravity tends to minimize the free surface height and the capillary forces tend to minimize the free surface area. Many researchers [Satterlee and Reynolds, 1964; Myshkis, et al, 1987] have showed that at very low Bond numbers, the fluid can assume many stable configurations. Each equilibrium configuration of the fluid and vapor corresponds to a local minimum in the capillary-gravity potential energy expression. Large enough motions of the fluid container can re-orientate the fluid into another stable configuration. For Bond numbers above 200, gravity dominates and the fluid gathers in the bottom of the tank with a flat free surface. For moderate Bond numbers (below 100 and above a critical value), however, the capillary and gravity forces are comparable and the fluid has a curved free surface. Below a critical Bond number, the fluid equilibrium free surface is no longer stable and multiple configurations can exist. Each configuration is associated with a local minimum in the

20

capillary-gravity potential energy. A large enough perturbation of the tank will cause the fluid to re-orientate from one stable configuration to another. If the gravity vector reverses direction, there is critical Bond number at which the vibration frequency goes to zero. This corresponds to a static instability of the fluid, and is the critical re-orientation Bond number. The critical Bond number is a function of the contact angle (α) of the fluid at the tank wall and thus on the fluid type. For example, for a cylindrical tank the critical Bond number is given by:

$$Bo \Big|_{Critical} = -3.40 + 2.57 \cos \alpha \qquad (1.4)$$

Low contact angle fluids are therefore less stable than high contact angle fluids. In this research however it is assumed that the Bond number is above the critical value (See Peterson [1987]) and that an equilibrium free surface exists.

Contact Angle Hysteresis Effects: Another effect that must be included to correctly model the dynamics of the fluid, is the contact angle hysteresis effect. Satterlee and Reynolds [1964] showed that this effect can be linearized and included in the fluid description as an additional boundary condition at the fluid free surface contact contour with the container wall (eq. 1.5).

$$\left[\frac{\partial \eta}{\partial n} = \frac{\Gamma}{a} \eta \right]_{on\ contact\ surface} \qquad (1.5)$$

In this equation, Γ is the contact angle hysteresis constant which is a function of the fluid type and the tank wall surface and n is the normal to the tank wall at the free surface contact contour.

Fluid Flow Field Assumptions: The fluids considered in this research as well as typical spacecraft propellants, can be considered as viscous and incompressible. Model simplifications can be justified based on the knowledge of the dominant physical behavior. Potential flow can be assumed if fluid viscous effects are restricted to the Stokes layer near the wall of the container. This condition is satisfied if the surface tension scaling parameter $N_{v_2} << 1$ (see eq. 1.7). In this research, given the model tanks and fluids used, N_{v_2} ranges from 0.001 to 0.0014, justifying the potential flow assumption.

21

The viscous effects are included in the model as linear non-conservative damping forces. Predicting the fluid slosh damping can often only be done experimentally [Abramson, 1966], but analytical scaling analysis and estimation is possible [Miles, 1967]. For high Bond numbers, the fluid slosh damping scales with gravity and viscosity. The appropriate scaling parameter is:

$$N_{v_1} = \frac{v}{\sqrt{ga^3}}$$

(1.6)

where (v) is the kinematic viscosity of the fluid. For low Bond numbers, eq. 1.6 must be multiplied with the Bond number (which is equivalent to scaling the Navier-Stokes equation using surface tension instead of gravity as the reference force), yielding an alternative scaling parameter:

$$N_{v_2} = v\sqrt{\frac{\rho}{\sigma a}}$$

(1.7)

These scaling parameters have been experimentally verified by Salzman and Masica [1969], who showed that the damping ratio at low Bond number is approximately six times higher than the high Bond number value. Salzman and Masica suggested that this is due to the free surface curvature effects on the flow profile. Important to note is that baffles and propellant management devices can enhance the fluid damping. This, however, only produces a finite amount of damping and if the baffles are partially submerged, they tend to break up and separate the fluid oscillation modes which, incidentally, produces a very nonlinear geometric effect [Abramson, 1966].

The analytical method of this research completely ignores all geometric nonlinear effects. Some of these effects are; partially submerged baffles that cause fluid flow impact, drainage and complex container walls that cannot be aligned with a curvilinear grid.

Container: The analytical model assumes a rigid container which considerably simplifies the problem. This assumption is valid for containers that have structural frequencies spectrally separated from the dominant fluid slosh and control modes. The boundary condition at the tank walls, for a rigid tank, is simply that there is no flow normal to the tank wall. The previous paragraphs summarized the fluid flow assumptions and the rest of

this section will concentrate on the assumed coupled characteristics of the fluid/spacecraft system.

Recent studies of the coupled fluid/spacecraft problem have concluded that any proper model must be nonlinear in order to correctly model the coupling between the fluid and container motion. The problem of a water tower on flexible supports was analytically and experimentally studied by Ibrahim and Barr [1975a and 1975b] (Also see Ibrahim and Heinrich [1987]). Their analytical model did not include capillary effects, nor secondary fluid modal interactions. Peterson [1987], on the other hand, included these effects in his model to study a fluid/spacecraft configuration similar to the one considered in this research.

In order for the results to be applicable to a wide range of spacecraft, this research concentrated on coupled nonlinear dynamics of the system depicted in Fig. 1.3. In this figure, a fluid container (not necessarily a cylindrical container) is attached to a one degree-of-freedom spacecraft mode. The motion of the container, but not the fluid, is restricted to be in one direction (the x-direction or planar direction) only. The spacecraft degree-of-freedom can be either an attitude control mode or one of the support structure's modes. The stiffness, mass and damping of this mode may be tuned to study the coupling effects on the fluid/spacecraft dynamic behavior. The response of the coupled system will be dependent on the relative tuning between the primary fluid slosh mode and the spacecraft mode. The relevant non-dimensional parameters are therefore the mass ratio, the ratio of total fluid mass to total dry mass of the tank

$$\mu = \frac{m_F}{m}$$

(1.8)

and the frequency ratio, the ratio between the fundamental fluid slosh frequency and the frequency of the spacecraft mode

$$\nu = \frac{f_s}{f_o}$$

(1.9)

23
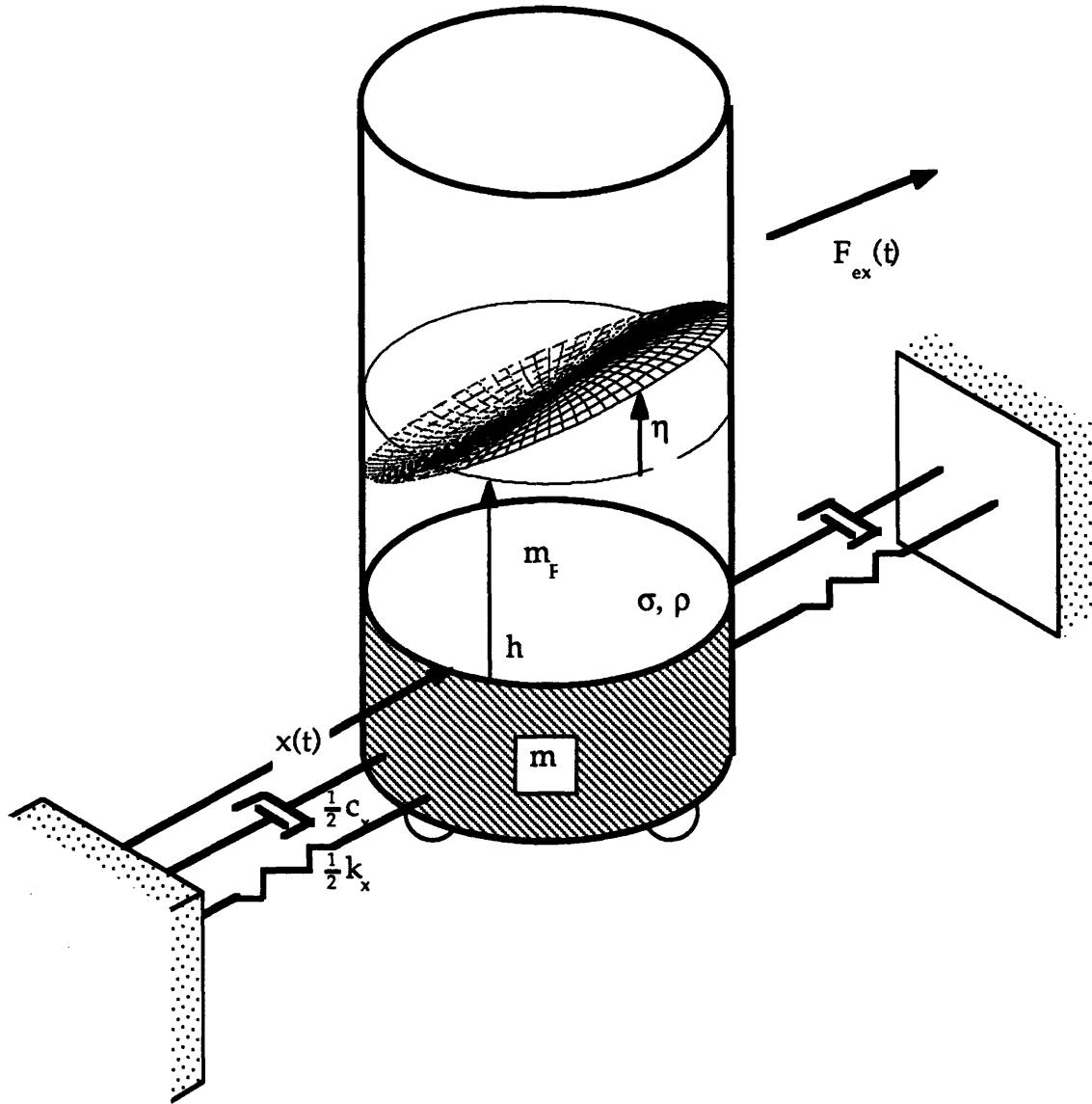
Figure 1.3   Research Fluid/Spacecraft Study Model

One other non-dimensional parameter remains that will influence the fluid/spacecraft system response, namely the applied force:

$$\Xi_{ex} = \frac{F_{ex}}{k\,d}$$

(1.10)

where (k) is the stiffness of the spacecraft mode and (d) some scale length. Since the response will scale with Ξ_{ex}, given an absolute force level F_{ex}, a more compliant (softer k) spacecraft will result in a more nonlinear response.

In practice, spacecraft have six degrees-of-freedom. Therefore the assumption that the nonplanar degree-of-freedom is infinitely stiff, that is;

$v_{s/c}$ in eq. 1.11 is assumed to be infinite, is only valid for the experimental setup of this research. Incidentally, it was found that this assumption was one of the major limitations of the analytical model used in this research.

$$v_{s/c} = \sqrt{\frac{k_y}{k_x}}$$

(1.11)

1.3 Research Approach and Outline

This section outlines how the analytical method of Miles [1984a and 1984b] and Peterson [1987] was modified to be valid for tanks of arbitrary geometry, and describes the solution procedure used to determine the nonlinear characteristics of the fluid/spacecraft system along with the experimental studies that were performed to validate the analytical model.

In order to apply the assumed mode model developed by Peterson, the Taylor series expansion of the kinematic integrals [Peterson, 1987] had to be modified to be valid for a numerical grid curvilinear system. The method also had to be adapted for numerically derived eigen-modes. This allowed the nonlinear formulation to be valid for almost any tank geometry and also for tanks with baffles, as long as the baffles remain submerged during fluid oscillations. The method derived, however, is only valid for tanks with side-walls aligned with one of the curvilinear coordinates.

Although many standard computer packages exist on the market that can calculate the linear eigen-modes of the fluid in the container, a finite difference program was developed for flexibility, cost and data management reasons. The finite difference method used shape functions to implement the boundary conditions that are misaligned with the finite difference mesh. The effect of contact angle hysteresis was included to yield the experimentally observed linear eigen-frequencies.

In order to correctly model Bond number effects (the effect of the nonlinear capillary forces), the equilibrium free surface shape was calculated and added to the finite difference mesh of the linear eigen-routine. The capillary and acceleration potential energies were posed in a variational integral.

Test 410-1. Non-dimensional Tank Displacement (x/d).
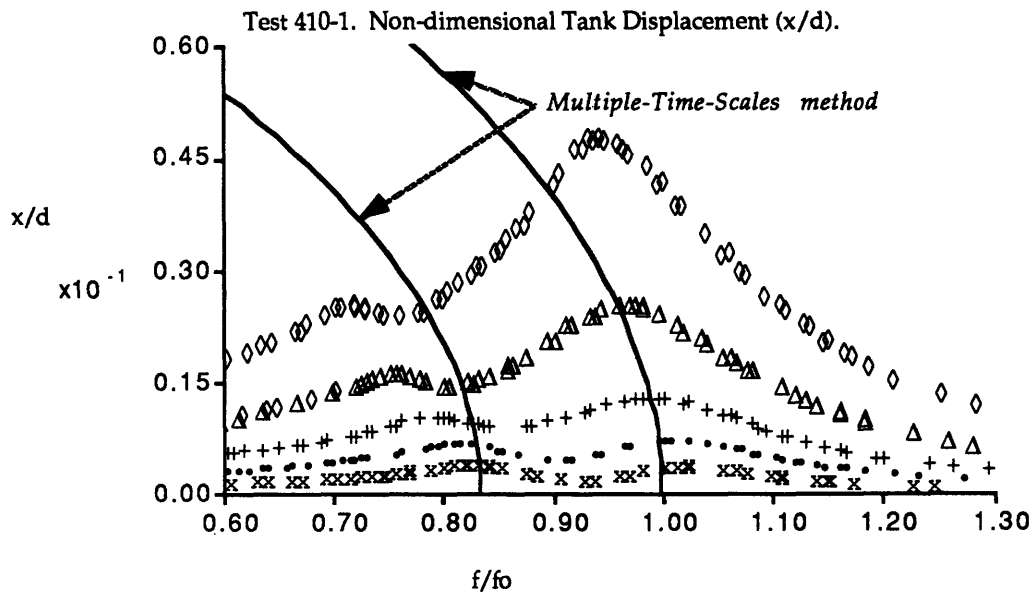
Figure 1.4 **An example of the Amplitude Dependent Dissipation Rates observed by Peterson [1987].**

Euler's equation, which satisfies the requirement that the variational integral remains stationary with respect to independent variations, was used to solve for the Bond number-dependent equilibrium free surface. This was achieved by discretizing the free surface in a finite difference mesh and solving the resultant non-linear equations with an Inverse Iteration scheme. This approach is one of the major contributions of this research and it can be applied to tanks of arbitrary geometries.

Peterson [1987] used the Multiple-Time-Scales method to solve for the nonlinear forced response characteristics of the fluid/spacecraft system. This method can only predict the shift in resonant frequencies and failed to predict the amplitude dependent dissipation rates observed in the coupled system resonances (See Fig. 1.4). In this research, the Harmonic Balance Method is used to predict the coupled nonlinear forced response characteristics, using a full nonplanar model of the fluid/spacecraft system. The nonlinear time independent equations provided by this method are solved using both an Inverse Iteration Scheme and a Newton-Raphson solver with an adaptive under-relaxation scheme.

The objective of the experiments was to verify the analytical model and to extend the database on the dynamic behavior of coupled

26

fluid/spacecraft configurations. The experimental setup was essentially the same as the one used by Peterson. In this research, however, a personal computer was used to control the experiment, collect data and perform pre-data analysis. A spherical, square and rectangular tank were used as study models. The results obtained with these tanks, combined with the cylindrical tank results obtained by Peterson, were considered adequate to verify the analytical method.

1.4 Report Outline

Chapter 2 develops the nonplanar, nonlinear analytical model based on the assumed mode approach. The fluid flow potential generalized coordinates are related to the free surface generalized coordinates through the application of the kinematic free surface boundary conditions. The nonlinear relationship between these coordinates are formulated to facilitate the use of numerically determined eigen-modes. The finite difference method used to determine the linear eigen-modes is outlined as well as the determination of the equilibrium free surface shape. This chapter concludes with the fluid energy Lagragian.

Chapter 3 describes the Harmonic Balance method and how the method was numerically implemented. This chapter also discusses solution techniques other than the Harmonic Balance method and ways to solve systems of nonlinear equations.

Chapter 4 describes the experimental setup, and the test and calibration procedures. Chapter 5 presents the experimental uncoupled and coupled results obtained with the three study models.

Chapter 6 compares the analytical results obtained with the model developed in Chapter 2 with the experimental results of Chapter 5. In addition to the three study models, the analytical model was also used to predict the nonlinear coupled forced characteristics of fluids contained in cylindrical tanks. These results are compared with the results obtained by Peterson [1987].

Chapter 7 concludes with a short review of the research and conclusions that can be drawn from the experimental and analytical results.

This chapter also identifies the implications for future research and discusses the application of the results to practical systems.

Appendix A derives the nonplanar model from the system Lagragian obtained in Chapter 2. Appendix B presents simplified planar and nonplanar models based on the results of Appendix A. These models are simplified in the sense that zero terms are omitted and that the models are expressed in matrix form.

Chapter 2

General Nonlinear Fluid Model

This chapter develops and derives the equations of motion describing the nonlinear coupled dynamics of the fluid-spacecraft system. The analytical model developed is valid for tanks of arbitrary geometry.

The goal of the analytical formulation is a description of the fluid-spacecraft motion in terms of a finite set of system degrees of freedom. This description will be in the form of a coupled system Lagrangian and a set of coupled nonlinear differential equations derived from this Lagrangian.

The formulation of such a coupled system Lagrangian requires generalized coordinates for the motion of the spacecraft and the motion of the fluid. For the spacecraft in the study model, the generalized coordinates will be the physical displacement coordinates of the fluid tank in the horizontal plane (x and y). For the fluid, however, the choice of generalized coordinates is far more complicated.

The first part of this chapter will concentrate on the derivation of such a generalized coordinate description of the fluid motion. The kinematics (boundary conditions) are solved approximately with nonlinear and Bond number effects included. An expression for the kinetic and potential energy of the fluid system is formulated with nonlinear surface motion and nonlinear capillary effects included.

This chapter also outlines the approach that was used to calculate the linear fluid eigen-characteristics and the fluid free surface shape. In the final section, the generalized coordinate description of the fluid is used to formulate the coupled fluid-spacecraft Lagrangian.

2.1 Kinematic Description of the Fluid Dynamics

In this section, using existing methods, the kinematic description of the fluid is developed in terms of assumed modal series for the flow potential and the free surface motion. The flow potential generalized coordinates are expressed as nonlinear functions of the free surface

29
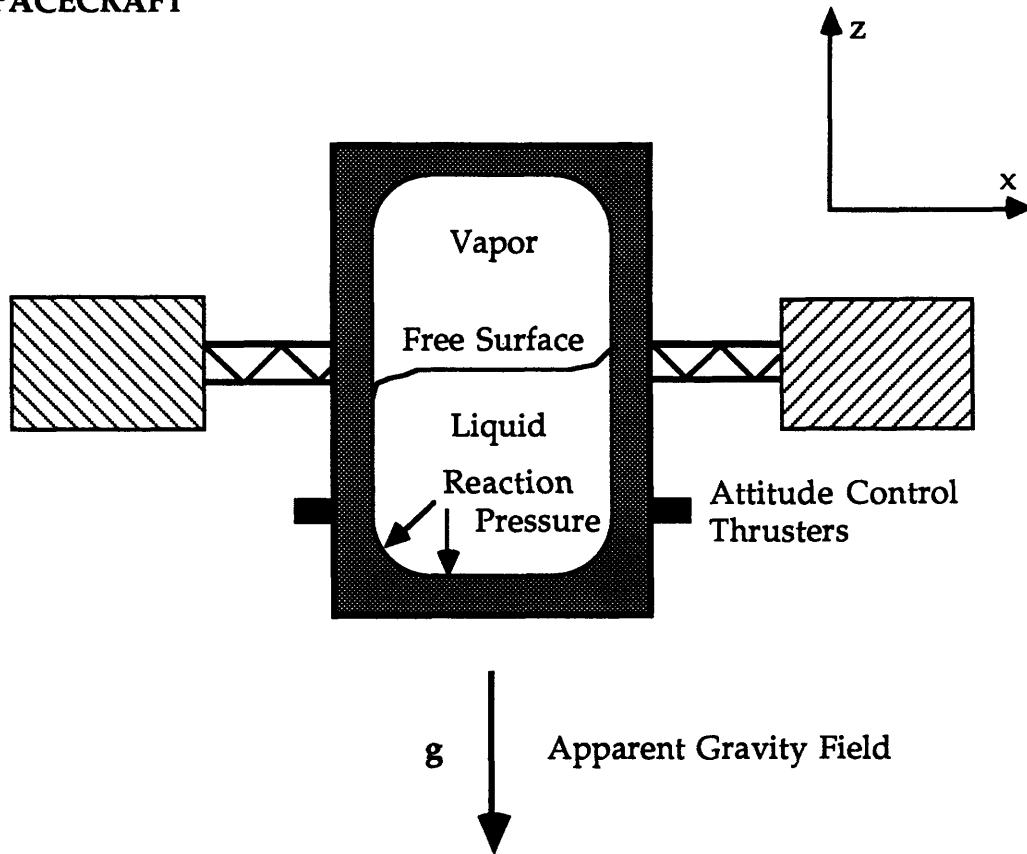
SPACECRAFT

Figure 2.1   **General Fluid-Spacecraft System.**

Fluid with a free surface is vibrating inside a spacecraft mounted fuel tank. Attitude control dynamics and structural modes may interact with fluid dynamics.

generalized coordinates through the application of a particular free surface boundary condition.

2.1.1 Problem Statement

Consider the general fluid-spacecraft system diagrammed in Fig. 2.1. A fluid tank, partially filled with a liquid, is supported by the spacecraft structure. The spacecraft motion is forced by attitude control thrusting, gravity gradient, or the action of any other external forces. When the mean gravity level produces a Bond number above the critical value, the fluid will collect into a single mass at the end of the tank aligned with the mean gravity vector, with a free surface at the other end. External excitation of the
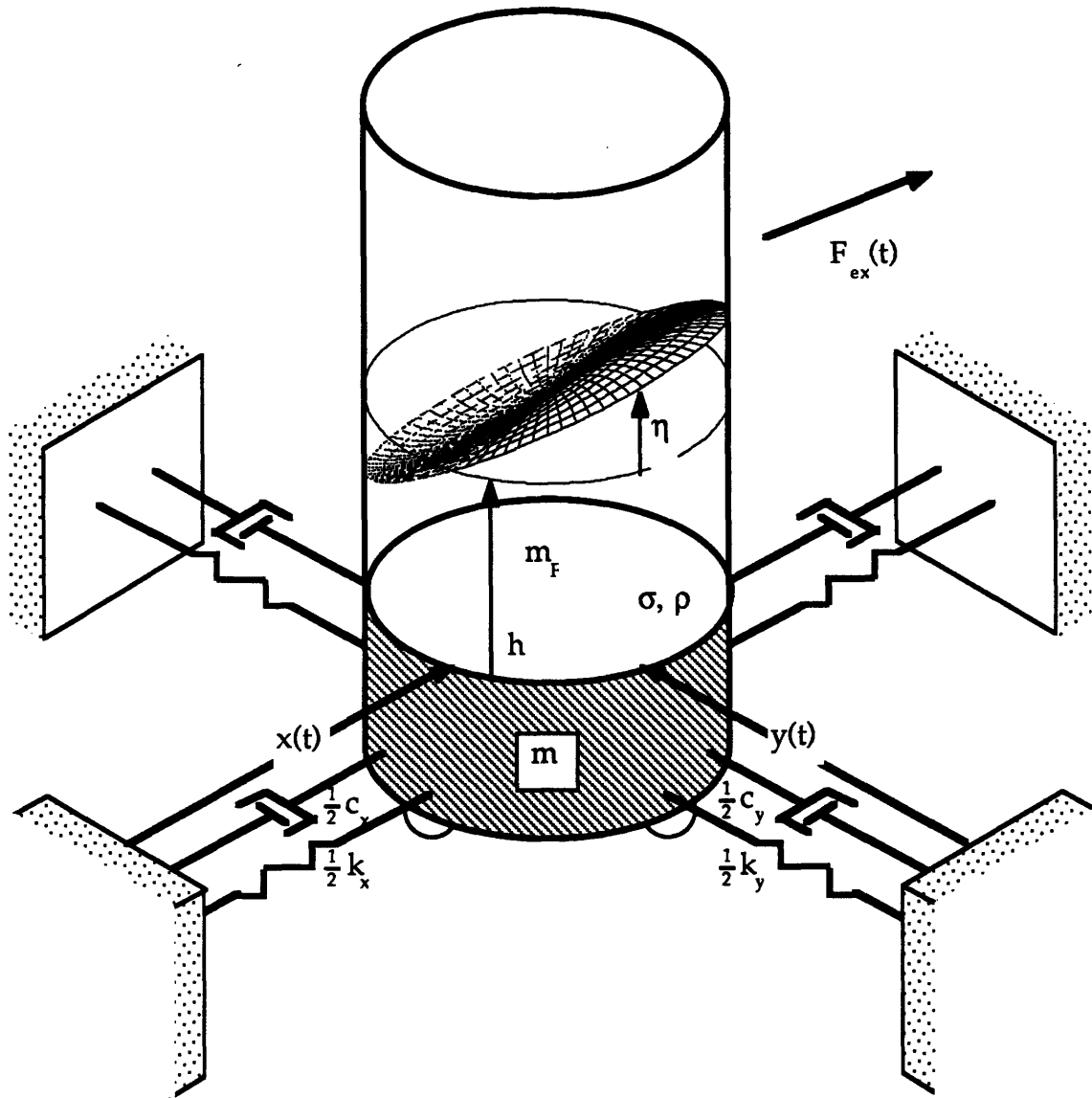
Figure 2.2: **Study Nonplanar Model.**

The planar (x) direction is in line with the excitation force; the
nonplanar (y) direction is perpendicular to the excitation force.

fluid tank will result in fluid vibratory response about this equilibrium
shape.

The resultant vibratory response of the fluid inside the tank creates a
fluid pressure field against the tank walls, which will have three
dimensional force and moment fields. These reaction slosh loads will
appear in the equations of motion for the dry dynamics of the spacecraft as
motion-dependent forcing terms. In this manner, the fluid and the
spacecraft motion are coupled.

Consider the generic fluid-spacecraft system (Fig. 2.2). The equation of motion for the spacecraft in the direction of excitation (planar direction) is

$$m\ddot{x} + c\dot{x} + kx = F_{ex} + F_{xs} \qquad (2.1a)$$

and in the nonplanar direction:

$$m\ddot{y} + c\dot{y} + ky = F_{ys} \qquad (2.1b)$$

Where x is the x-direction degree of freedom of the tank, y the y-direction degree of freedom, F_{ex} the external modal load component evaluated at the tank, F_{xs} and F_{ys} the net reaction slosh forces acting against the tank in the x and y directions.

The net reaction slosh force F_{xs} is the integration of the pressure field created by the fluid motion within the tank, and will therefore be a function of the fluid generalized coordinates, q_n. The equations for these (as yet unspecified) fluid generalized coordinates can be symbolically expressed by a nonlinear equation:

$$N\left(q_1, q_1^2, ..., q_2, q_2^2, ..., \dot{q}_1 \dot{q}_1^2, ..., \dot{q}_2, \dot{q}_2^2, ..., \ddot{q}_1, ...\right) = N = 0 \qquad (2.2)$$

These equations, along with (2.1) form the coupled equations of motion of the fluid-spacecraft.

2.1.2 Modeling

Instead of evaluating and integrating the flow pressure field, which can be very complicated even for the simplest of tank geometries [Abramson, 1966], a variational energy method will be used which does not explicitly require the evaluation of the pressure field. This approach has been successfully used before [Peterson, 1987, Limarchenko, 1978a; 1981; 1983]. In the variational method, the virtual work done by the pressure field against the tank wall will be part of the total fluid kinetic energy, provided the flow boundary conditions have been satisfied by the choice of generalized coordinates.

The next step in modeling the fluid motion is to find a Lagrangian description of the fluid-spacecraft dynamics. Although the derivations for the spacecraft part of the Lagrangian are trivial, those of the fluid dynamics

are much more complicated. In particular, a generalized coordinate description of the fluid must be found which also satisfies the boundary conditions of the flow.

The modeling of the fluid-spacecraft dynamics can thus be separated into three distinct modeling steps.

- Model of the fluid motion consistent with the fluid boundary conditions (the *Kinematic description of the fluid*),
- Express the kinetic and potential energy of the fluid in terms of generalized coordinates, as derived in the first step, and
- Formulate the coupled system Lagrangian

Each of these steps will be discussed in the subsequent paragraphs.

2.1.3 Boundary Conditions

Some approaches in the past, such as Luke (1967), included the fluid boundary conditions as constraints in the Lagrangian. This will not be necessary if all the flow boundary conditions have been satisfied by the generalized coordinate flow fields. Choosing such generalized coordinates for the fluid is the 'kinematic problem' for the flow. Limarchenko (1978) solved this problem using the boundary condition differential equations in a Galerkin-type procedure. Miles (1976) provided a more general approach which uses a 'kinematic variational' to solve this problem. The approach used in this analysis is the approach used by Peterson, which is an adaptation of Miles's 'kinematic variational' method.

The main procedures and assumptions used in finding a generalized coordinate description of the fluid, are:

- Assume inviscid, incompressible flow.
- Postulate assumed modes for the free surface motion and the flow potential.
- Relate the flow potential generalized (modal) coordinates to the free surface generalized (modal) coordinates through a variational procedure.

Each of these procedures (and assumptions) will be discussed in the next sections.

2.1.3.1 Assumptions on the Fluid Flow Field and Boundary Conditions

In general, the fluid is a viscous, compressible continuum, and has a very complicated slosh behavior. Assumptions and simplifications, however, can be justified based on the knowledge of the dominant physical behavior.

Most of the following sections will assume a general curvilinear coordinate system (e_1, e_2, e_3). The actual coordinate system used for the four study models considered in this research is:

- **Cylindrical tanks**   Cylindrical Coordinate system (r, θ, z)
                             Velocity Components: (u_r, u_θ, u_z)
- **Spherical tanks**   Cartesian Coordinate System (x, y, z)
                             Velocity Components: (u_x, u_y, u_z)
- **Rectangular tanks**   Cartesian Coordinate System (x, y, z)
  (of which **Square tanks** Velocity Components: (u_x, u_y, u_z)
  are a subset)

A cartesian coordinate system, instead of a spherical coordinate system, was used for the spherical model tanks since the equilibrium free surface is not aligned with one of the spherical coordinates. If the fluid viscous effects are restricted in a Stokes layer near the wall of the tank $(N_{v_2} = v\sqrt{\dfrac{\rho}{\sigma a}} \ll 1)$, the fluid flow velocity u relative to the tank reference frame can be completely described by an irrotational, three dimensional potential field ϕ. (See eq. 4.1b for a definition of the surface tension parameter N_{v_2}). In this research, given the model tanks and the modeling fluids used, the capillary viscous parameter $\left(N_{v_2}\right)$ range from 0.001 to 0.0014. :

$$u = \nabla\phi \tag{2.3}$$

Since the fluid is incompressible, the divergence of the velocity field must vanish throughout the fluid volume:

$$\nabla \cdot \mathbf{u} = 0 \qquad (2.4)$$

The resulting partial differential equation describing the flow potential is the Laplace equation:

$$\nabla^2 \phi = 0 \qquad (2.5)$$

If ϕ is continuous inside the fluid volume V, it will be completely and uniquely specified by its value and the value of its normal derivative

$$\nabla \phi \cdot \mathbf{n} = \frac{\partial \phi}{\partial \mathbf{n}} \qquad (2.6)$$

at the boundary of the fluid (Hildebrand, 1976).

For the 'Dirichlet Problem', in which the value of ϕ is prescribed at the fluid boundary, the solution to (2.5) will be *unique* in V. For the 'Neumann Problem', in which the value of $\partial \phi / \partial \mathbf{n}$ is prescribed at the fluid boundary, the solution to (2.5) will be *unique within an additive constant* in V. For the case of fluid flow in a closed container, only the velocity of the fluid at the boundary is specified, and so the fluid description is a Neumann Problem. Solution of Equation (2.5) will then lead to a unique value of $\nabla \phi$ in V, which will uniquely define the flow velocity field, $\mathbf{u}$. What this means physically is that if the free surface motion is known, the fluid flow velocity profile will be completely specified.

Fig. 2.3 to 2.5 depicts the boundary conditions of the flow potential for the four study tanks considered in this research. For the cylindrical tank (Fig. 2.3) a cylindrical coordinate system (r, θ, z, t) is used. Three separate surfaces bound the fluid volume. The bottom of the cylinder is designated S_B, the walls of the cylinder are designated S_W, and the free surface is designated S_F. The free surface is defined by the surface η(r, θ, z, t) with η aligned with the z-axis. The following boundary conditions apply at each of these surfaces:

$$\frac{\partial \phi}{\partial z} = 0 \quad \text{on } S_B \qquad (2.7a)$$

$$\frac{\partial \phi}{\partial r} = 0 \quad \text{on } S_W \qquad (2.8a)$$

$$\frac{\partial \eta}{\partial t} + \nabla \phi \cdot \nabla \eta \bigg|_{z=\eta} = \frac{\partial \phi}{\partial z} \bigg|_{z=\eta} \quad \text{on } S_F \qquad (2.9a)$$
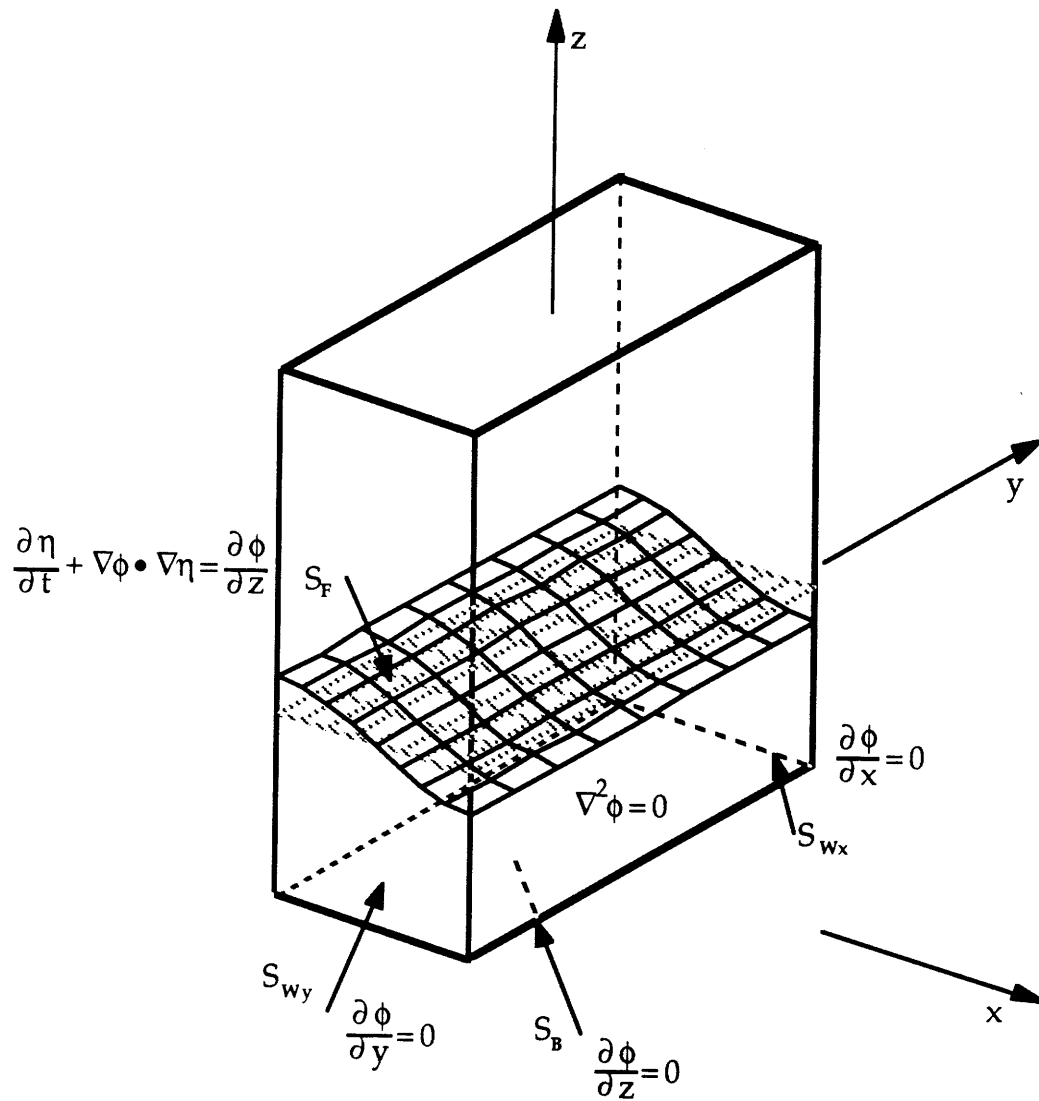
The first two boundary conditions analytically state that the fluid does not penetrate the solid walls of the container. The third boundary condition, however, is a mathematical expression for the requirement that the fluid at the free surface (S_F) must follow the motion of the free surface. This 'convective boundary condition' on the flow drives the dynamics of the fluid motion within the fluid volume V. It is also the principal source of the fluid slosh nonlinearity.
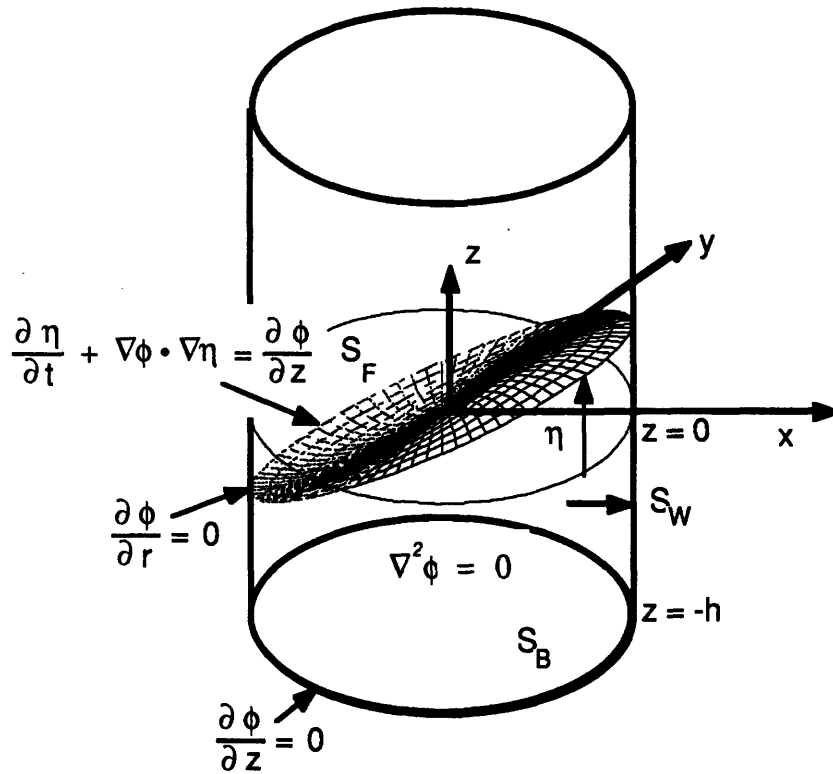
Figure 2.3 Inviscid Fluid Flow Boundary Conditions for a Cylindrical Tank. (Repeat of Figure 1.1)

Figure 2.4   **Inviscid Fluid Flow Boundary Conditions for a Spherical Tank.**

For spherical, rectangular and square tanks it is convenient to use a cartesian coordinate system. The free surface is defined by the surface $\eta(x, y, z, t)$ with η aligned with the velocity component u_z. The boundary conditions, for the spherical tank, (Fig. 2.4), are:

$$\frac{\partial \phi}{\partial r} = 0 \quad \text{on } S_W \tag{2.7b}$$

$$\frac{\partial \eta}{\partial t} + \nabla \phi \cdot \nabla \eta \bigg|_{z=\eta} = \frac{\partial \phi}{\partial z} \bigg|_{z=\eta} \quad \text{on } S_F \tag{2.9b}$$

where S_W is the spherical surface of the tank.

Figure 2.5 **Inviscid Fluid Flow Boundary Conditions for a Rectangular and Square Tank.**

The boundary conditions for rectangular tanks (Fig. 2.5) (of which square tanks are a subset), are:

$$\frac{\partial \phi}{\partial z} = 0 \quad \text{on } S_B \tag{2.7c}$$

$$\frac{\partial \phi}{\partial x} = 0 \quad \text{on } S_{Wx}$$

$$\frac{\partial \phi}{\partial y} = 0 \quad \text{on } S_{Wy} \tag{2.8c}$$

38

$$\frac{\partial \eta}{\partial t} + \nabla\phi \cdot \nabla\eta \Big|_{z=\eta} = \frac{\partial \phi}{\partial z}\Big|_{z=\eta} \quad \text{on } S_F \qquad (2.9c)$$

S_{Wx} and S_{Wy} being the tank walls in the x- and y-directions respectively.

2.1.4 Variational Solution of the Neumann Kinematic Problem

While no general solution to the above nonlinear potential flow boundary value problem is known, approximate solutions can be found which are valid for finite motion of the free surface. The approach followed here assumes modal behavior for both the free surface and the flow potential. The generalized coordinates describing the flow potential are then related to the generalized coordinates describing the free surface motion using a variational expression for the Neumann problem.

Luke (1967) and Miles (1976) extended earlier work of Clebsch (1859) and Hargreaves (1908) to show that the general Neumann problem for fluid flow in containers can be satisfied by requiring that the integral of eq. 2.10 remains stationary with respect to arbitrary variations of the function ϕ. Application of this integral to specific container geometries can be found in the literature, for example; Miles (1976) and Peterson (1987) - cylindrical tanks and Moiseev and Petrov (1966) - spherical tanks.

$$SI = \frac{1}{2}\iiint_V (\nabla\phi \cdot \nabla\phi)\, dV - \iint_{S_F} \phi\Big|_{z=\eta} dS_F \qquad (2.10)$$

in which η is the function describing the dynamic free surface, S the equilibrium free surface area (as projected on the plane perpendicular to z-coordinate) and S_F the dynamic free surface area. The requirement that the integral remains stationary for arbitrary fluid motion ($\delta\phi$) yields Laplace's Equation (2.6) and the flow boundary conditions of eq.'s (2.7), (2.8), and (2.9).

This integral will be minimized by the exact nonlinear solution to the kinematic problem but in the absence of a known exact solution, an approximate solution to the kinematic problem can be found using assumed potential flow behavior and assumed free surface motion. The assumed motions are not independent and their relationship can be found by substituting the assumed motions into eq. 2.10 and requiring the result to be

stationary. This will result in a *'least squares'* solution to the nonlinear boundary value problem. No mathematical preconditions are set on the assumed functions except that they be continuous in V.

This variational principle can be applied to any (single-valued) equilibrium free surface shape. In this research it will be applied to a moderate-to-low Bond number equilibrium curved free surface shape.

At this point it is assumed that the free surface and the fluid potential can be described by the superposition of finite modal sets. Ignoring geometric nonlinearities, that is assuming that the in-plane motion of the fluid can be neglected, the free surface motion η is described in terms of the departure from the equilibrium free surface shape f (Fig. 2.6) as:

$$\eta(e_1, e_2, t) = f(e_1, e_2) + \sum_{n=1}^{N} \xi_n(e_1, e_2) q_n(t)$$

(2.11)

or

$$\eta(e_1, e_2, t) = f(e_1, e_2) + \eta_d(e_1, e_2, t)$$

(2.11a)
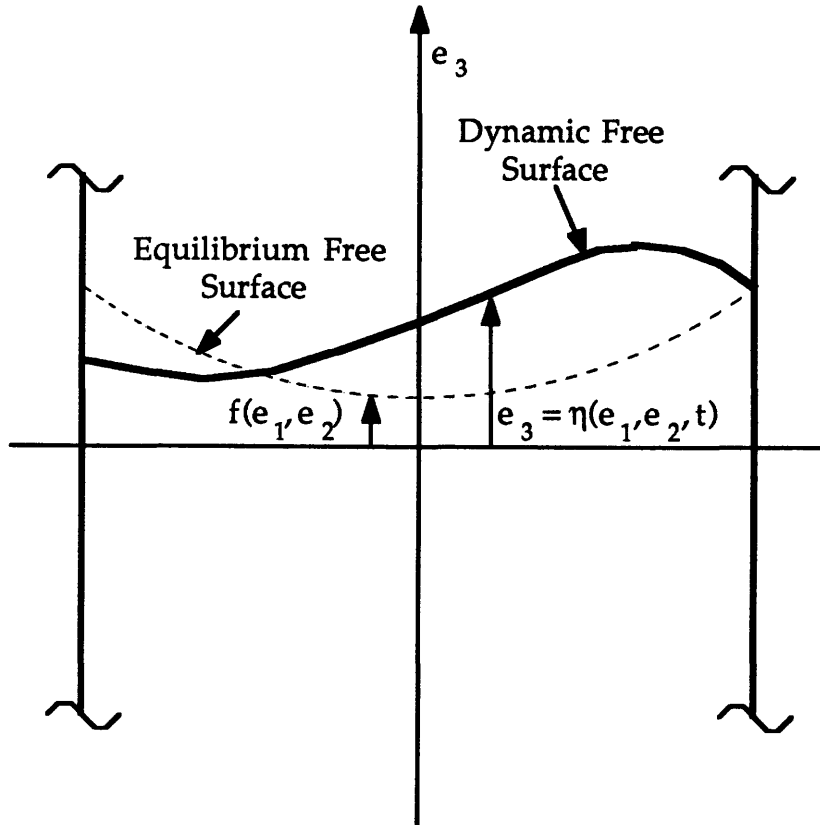
Figure 2.6   Coordinate System for Dynamic Free Surface and Equilibrium Free Surface Shape.

in which q_n are the generalized coordinates for the free surface motion. Implied in eq. 2.11 is that η is the coordinate defining the free surface shape. In this research, η is the vertical coordinate (e_3 or z) of the free surface height. For the cylindrical and rectangular tanks η completely describes the free surface, but for spherical tanks η will define the free surface for moderate amplitudes of free surface motion. Thus for a grid defined on the e_1-e_2 plane $f(e_1, e_2)$ is the displacement, along the e_3-axis, from the grid-plane to the equilibrium free surface and $\eta_d(e_1, e_2, t)$ is the displacement, along the e_3-axis, of the dynamic free surface from the equilibrium free surface. In order to obtain a correct definition of the free surface, a coordinate transformation will be required that will align surface motion with one of the axis. An arbitrary orthogonal coordinate system (e_1, e_2, e_3) is used for generality.

The fluid potential field $\phi(e_1, e_2, e_3, t)$ is assumed to be of the form:

$$\phi(e_1, e_2, e_3, t) = \sum_{m=1}^{N} \chi_m(e_1, e_2, e_3) p_m(t) \tag{2.12}$$

in which the p_m are the generalized coordinates for the flow potential.

The number of modes describing the flow potential (M) and the free surface motion (N) are set equal to ensure that the problem is completely determined and that no additional least squares match is required. The number of modes N (N=M) to be used in the analysis will be kept arbitrarily large but will be truncated later to include only those which significantly contributes to the fluid vibratory motion.

The two sets of generalized coordinates q_n and p_m are related by the nonlinear free surface boundary condition (2.9), and are therefore not independent. Selecting the free surface generalized coordinates q_n to be the independent fluid generalized coordinates, the flow potential coordinates (p_m) can be expressed as nonlinear functions of the free surface generalized coordinates q_n.

$$p_m = P(q_n) \tag{2.13}$$

Substituting the assumed modal behavior into the kinematic integral of eq. 2.10, yields:

$$SI = \frac{1}{2} \sum_{m=1}^{N} \sum_{n=1}^{N} \phi_m k_{mn} \phi_n - \sum_{m=1}^{N} \sum_{n=1}^{N} \dot{q}_m d_{mn} \phi_n \qquad (2.14)$$

in which the kinematic matrices are:

$$k_{mn} = \iiint_V (\nabla \chi_m \cdot \nabla \chi_n) dV \qquad (2.15)$$

$$d_{mn} = \iint_{S_F} \left(\xi_m \chi_n \big|_{z=\eta} \right) dS_F \qquad (2.16)$$

The matrix k_{mn} is the generalized symmetric wavenumber matrix of the fluid motion, having units of inverse length The matrix d_{mn} is both unsymmetrical and unitless. Both of these matrices are nonlinear functions of the free surface modal vector q_n because the volume V depends on η and the function χ_n is evaluated on the free surface.

In matrix notation, (2.14) is the same as

$$SI = \frac{1}{2} \{p_m\}^T [k_{mn}]\{p_n\} - \{p_n\}^T [d_{mn}]^T \{\dot{q}_m\} \qquad (2.17)$$

Now requiring that the kinematic integral remains stationary with respect to p_{ij} results in:

$$\frac{\partial(SI)}{\partial p_j} = [k_{jn}]\{p_n\} - [d_{jm}]^T \{\dot{q}_m\} \equiv 0 \qquad (2.18)$$

by which the flow potential generalized coordinates p_m can be related to the free surface generalized coordinates q_n by

$$p_m = \sum_{n=1}^{N} \sum_{r=1}^{N} [k_{mr}]^{-1} d_{nr} \dot{q}_n \qquad (2.19)$$

which is the same as

$$p_m = \sum_{n=1}^{N} l_{mn} \dot{q}_n \qquad (2.20)$$

in which the matrix l_{mn} is given by

$$l_{mn} = \sum_{r=1}^{N} [\, k_{mn} \,]^{-1} d_{nr}$$

(2.21)

The matrix l_{mn} is the generalized nonlinear wavelength matrix, and is a nonlinear function of the modal vector q_n. Equation (2.20) is the desired functional relation which expresses the potential generalized coordinates (p_m) in terms of the free surface generalized coordinates (q_n).

Based on the experimental results cubic and higher order terms in l_{mn} of the generalized free surface coordinates will be considered as small. This truncation will yield a fluid flow description valid to cubic order in the amplitude of the motion.

2.1.5 Note on the Assumed Mode Shapes

The number and choice of the mode shape functions χ_m and ξ_n will determine the ultimate accuracy of the above kinematic solution. Selection of these mode shapes must be based on experience, previous research or experimental results. In practice it may be required to progressively increase the number of assumed modes while keeping track of the relative change in the predicted fluid motion. Intuition also suggests that more accuracy will result from those assumed mode shapes that satisfy most of the kinematic conditions exactly. The linear eigen-modes of the slosh, which satisfy the linearized kinematic conditions, is an obvious choice, since the kinematic integral (I) would contain only error terms due to the nonlinear correction of the kinematic conditions. In Chapter 6 both theoretical mode shapes and numerically determined mode shapes are used to predict moderate-to-low Bond number fluid motion in cylindrical tanks. In predicting the fluid motion in spherical, rectangular and square tanks (Chapter 6) only numerically determined mode shapes were used.

An additional presumption is made about the two dimensional components of the assumed mode shapes. The assumed mode shapes must

43

be orthogonal and normalized as follows:

$$\iint_S \xi_m \xi_n dS = \iint_S \chi_m \chi_n dS = \delta_{mn} S \tag{2.22}$$

where S is the equilibrium free surface area.

In this research, the mode shapes assumed for the free surface motion, ξ_n is equal to the surface component of flow potential mode shapes at the free surface; namely: $\xi_n(e_1, e_2) = \chi_n(e_1, e_2, e_3 = f)$.

2.1.6 Formulation of the Generalized Wavenumber Matrix

The calculation of the wavenumber matrix l_{mn} involves an integration over the dynamic fluid volume. The volume integral can be written as:

$$k_{mn} = \iint_{S_F(e_1, e_2)} \left\{ \int_{h(e_1, e_2)}^{\eta(e_1, e_2, t)} \nabla \chi_m \cdot \nabla \chi_n de_3 \right\} dS_F \tag{2.23}$$

where e_3 is the coordinate that defines the free surface, namely z for the model tanks considered in this research and $h(e_1, e_2)$ is the surface describing the bottom surface of the tank. Implicit in this statement is that the free surface area, S_F, is independent of the fluid height or that the tank has straight and parallel walls. This assumption is clearly violated in the spherical tank case but for certain spherical fluid volumes, the error introduced by assuming a constant projected surface area (projected on the (e_1, e_2) plane) will be small for a large range of fluid motions. This error will also be discussed in Chapter 6, the chapter that discusses the analytical results. In this statement, k_{mn} is a nonlinear matrix with respect to the generalized coordinates q_n in that the inner integration must be performed from the bottom surface to the dynamic (non-stationary) free surface. The free surface, defined by $\eta(e_1, e_2, t)$ is assumed to be a sum of modal terms (eq. 2.11) and also a function of time. The inner integral can be split into two parts, one over the equilibrium fluid volume and the other over the perturbation of the equilibrium free surface.

44

$$k_{mn} = \underbrace{\iint_{S(e_1, e_2)} \left\{ \int_{h(e_1, e_2)}^{f(e_1, e_2)} \nabla \chi_m \cdot \nabla \chi_n \, de_3 \right\} dS}_{k_{mn}^e} +$$

$$\underbrace{\iint_{S(e_1, e_2)} \left\{ \int_{f(e_1, e_2)}^{\eta^d(e_1, e_2, t)} \nabla \chi_m \cdot \nabla \chi_n \, de_3 \right\} dS}_{k_{mn}^d} \qquad (2.24)$$

where η^d is defined in eq. 2.11a and k_{mn}^e is the contribution to k_{mn} due to the volume integral of eq. 2.23 over the equilibrium fluid shape and k_{mn}^d the contribution to k_{mn} due to the dynamic motion of the free surface. Note that k_{mn}^e is not dependent on the generalized coordinates q_n. The integrand of the inner integral of k_{mn}^d can be approximated by a Taylor expansion about a free surface $e_3 = f$, as:

$$\{\nabla \chi_m \cdot \nabla \chi_n\} = \{\nabla \chi_m \cdot \nabla \chi_n\}_{e_3=f} + (e_3 - f)\frac{\partial}{\partial e_3}\{\nabla \chi_m \cdot \nabla \chi_n\}_{e_3=f} +$$

$$\frac{1}{2}(e_3 - f)^2 \frac{\partial^2}{\partial^2 e_3}\{\nabla \chi_m \cdot \nabla \chi_n\}_{e_3=f} + \ldots \qquad (2.25)$$

Substituting eq. 2.25 into the second integral of eq. 2.24 and integrating with respect to $(e_3 - f)$, yields:

$$k_{mn}^d = \iint_{S(e_1, e_2)} \left\{ \eta^d (\nabla \chi_m \cdot \nabla \chi_n)_{e_3=f(e_1, e_2)} \right\} dS +$$

$$\iint_{S(e_1, e_2)} \left\{ \frac{1}{2}(\eta^d)^2 \frac{\partial}{\partial e_3}(\nabla \chi_m \cdot \nabla \chi_n)_{e_3=f(e_1, e_2)} \right\} dS + \ldots \qquad (2.26)$$

where S is the fluid equilibrium free surface.

The Taylor expansion of the integrand and the subsequent integration with respect to e_3, transformed the volume integral to a sum of two surface integrals. The first term in eq. 2.24 is independent of the fluid motion but is a function of the equilibrium free surface shape and therefor a function of the Bond number. The second term, however, is a nonlinear function of the free surface degrees of freedom (q_n) and leads to a nonlinear series expansion for k_{mn}^d of the form:

$$k_{mn}^d = \sum_{r=1}^{N} k_{mnr}^{(1)} q_r + \sum_{r=1}^{N} \sum_{s=1}^{N} k_{mnrs}^{(2)} q_r q_s + \dots \qquad (2.27)$$

These terms express progressive corrections to the flow wavenumber as a function of the wave motion amplitude.

Equations 2.24 and 2.26 yield a convenient form to evaluate the wavenumber matrix numerically. The evaluation, however, requires the numeric evaluation of the first order derivatives ($\partial/\partial e_1$, $\partial/\partial e_2$, $\partial/\partial e_3$) and the following second order derivatives; $\partial^2/\partial e_1 \partial e_3$, $\partial^2/\partial e_2 \partial e_3$ and $\partial^2/\partial e_3^2$. The accuracy of a numerically evaluated k_{mn} matrix will thus depend on the "*smoothness*" of the χ functions.

At this point the series for the wavenumber matrix will be truncated to include only the linear and quadratic terms in q_n. The truncation errors will only appear in the evaluation of the k_{mn}^d matrices, since k_{mn}^e is independent of q_n. This will result in a cubic expression relating the potential field degrees of freedom with the free surface degrees of freedom (eq. 2.21), that is; l_{mn} will be cubic in q_n.

In conclusion, k_{mn} depends on the assumed free surface modes $\xi_n(e_1, e_2)$, the assumed potential field profiles $\chi_m(e_1, e_2, e_3)$, the equilibrium free surface shape $f(e_1, e_2)$ and the fluid depth $h(e_1, e_2)$. The dependence on the equilibrium free surface implies a Bond number dependence.

46

2.1.7 Formulation of the "d" Kinematic Matrix

The d_{mn} matrix was defined as:

$$d_{mn} = \iint\limits_{S_F} \left(\xi_m \chi_n\big|_{z=\eta}\right) dS_F \qquad (2.16)$$

This matrix is also a nonlinear function of the free surface degrees of freedom q_n and again a Taylor expansion about the equilibrium free surface, $f(e_1, e_2)$, can be used to transform the integral so that it can be evaluated numerically as a series of terms. Let:

$$\chi_n = \chi_n\bigg|_{e_3=f} + (e_3 - f)\frac{\partial}{\partial e_3}\chi_n\bigg|_{e_3=f} + \frac{1}{2}(e_3 - f)^2\frac{\partial^2}{\partial^2 e_3}\chi_n\bigg|_{e_3=f} + \dots \qquad (2.28)$$

then if eq. 2.28 is truncated after the second order term, eq. 2.16 can be written as:

$$d_{mn} = \iint\limits_{S(e_1,e_2)} \left[\xi_m\left\{\chi_n\bigg|_{e_3=f} + \eta^d\left[\frac{\partial\chi_n}{\partial e_3}\right]_{e_3=f} + \right.\right.$$

$$\left.\left. \frac{1}{2}(\eta^d)^2\left[\frac{\partial^2\chi_n}{\partial^2 e_3}\right]_{e_3=f} + \dots\right\}\right]dS \qquad (2.29)$$

so that d_{mn} is given by:

$$d_{mn} = d_{mn}^{(0)} + \sum_{r=1}^{N} d_{mnr}^{(1)} q_r + \sum_{r=1}^{N}\sum_{s=1}^{N} d_{mnrs}^{(2)} q_r q_s + \dots \qquad (2.30)$$

The coefficients of the Taylor series expansion again express progressive corrections to the kinematic matrix (d_{mn}). Eq. 2.29 is less complex than the equivalent expressions for the wavenumber matrix (k_{mn}) and can be evaluated numerically for continuous or discretely defined mode shapes. Again the matrix depends on the assumed modes, the equilibrium

47

free surface (therefor the Bond number) and, although not explicitly, also on the fluid depth. The dependence on the fluid depth is hidden in the assumed mode shapes.

2.1.8 Formulation of the Generalized Wavelength Matrix

The wavelength matrix was defined in eq. 2.21 as:

$$l_{mn} = \sum_{r=1}^{N} [k_{mr}]^{-1} d_{nr} \qquad (2.21)$$

or

$$d_{mn} = \sum_{r=1}^{N} k_{mr} l_{rn} \qquad (2.31)$$

The inversion of the wavenumber matrix is not simple and again a Taylor expansion must be used to find an approximate expression for the wavelength matrix. Substituting for k_{mn} and d_{mn} into the eq. 2.31, yields:

$$\sum_{i=1}^{N} k_{mi}^{(0)} l_{in}^{(0)} +$$

$$\sum_{r=1}^{N} \left\{ \sum_{i=1}^{N} \left[k_{mi}^{(0)} l_{inr}^{(1)} + k_{mir}^{(1)} l_{in}^{(0)} \right] \right\} q_r +$$

$$\sum_{r=1}^{N} \left\{ \sum_{s=1}^{N} \left\{ \sum_{i=1}^{N} \left[k_{mi}^{(0)} l_{inrs}^{(2)} + k_{mirs}^{(2)} l_{in}^{(0)} + k_{mir}^{(1)} l_{ins}^{(1)} \right] \right\} \right\} q_r q_s$$

$$= d_{mn}^{(0)} + \sum_{r=1}^{N} d_{nmr}^{(1)} q_r + \sum_{r=1}^{N} \sum_{s=1}^{N} d_{nmrs}^{(2)} q_r q_s \qquad (3.32)$$

This equation must be true for each order of the expansion in q_n. Therefore, a recursion sequence for the l_{mn} expansion coefficients can be generated, which yields that in the limit of no fluid motion, the wavelength matrix is

given by:

$$l^{(0)}_{mn} = \sum_{r=1}^{N} k^{(0)^{-1}}_{mr} d^{(0)}_{nr} \tag{2.33}$$

with the linear correction to the wavelength matrix, due to fluid motion, given by:

$$l^{(1)}_{mnr} = \sum_{i=1}^{N} k^{(0)^{-1}}_{mi} \left[d^{(1)}_{nir} - \sum_{j=1}^{N}\sum_{k=1}^{N} k^{(1)}_{ijr} k^{(0)^{-1}}_{jk} d^{(0)}_{nk} \right] \tag{2.34}$$

and the quadratic correction:

$$l^{(2)}_{mnrs} = \sum_{i=1}^{N} k^{(0)^{-1}}_{mi} \left[d^{(2)}_{nirs} - \sum_{j=1}^{N}\sum_{k=1}^{N} k^{(2)}_{ijrs} k^{(0)^{-1}}_{jk} d^{(0)}_{nk} \right] -$$
$$\sum_{i=1}^{N}\sum_{j=1}^{N}\sum_{k=1}^{N} k^{(0)^{-1}}_{mi} k^{(1)}_{ijr} k^{(0)^{-1}}_{jk} \left[d^{(1)}_{nks} - \sum_{l=1}^{N}\sum_{t=1}^{N} k^{(1)}_{kls} k^{(0)^{-1}}_{lt} d^{(0)}_{nt} \right] \tag{2.35}$$

These definitions can now be substituted into equation eq. 2.19:

$$P_m = \sum_{n=1}^{N} l^{(0)}_{mn} \dot{q}_n + \sum_{n=1}^{N}\sum_{r=1}^{N} l^{(1)}_{mnr} \dot{q}_n q_r + \sum_{n=1}^{N}\sum_{r=1}^{N}\sum_{s=1}^{N} l^{(2)}_{mnrs} \dot{q}_n q_r q_s \tag{2.36}$$

expressing the potential flow degrees of freedom, p_m, as nonlinear functions of the free surface degrees of freedom, q_n, to third order accuracy.

This completes the derivation of the kinematic description of the fluid and although almost identical to the results of Peterson [1987], this description is valid for any tank geometry, for which an equilibrium free surface is defined and is in a convenient form for numerical evaluation.

2.2 Fluid Energy Description

In the preceding sections a nonlinear functional description was derived, relating the flow potential and the free surface generalized coordinates. In the following sections, the kinetic and potential energy of the fluid system will be expressed in terms of both the flow potential and free surface generalized coordinates.

2.2.1 Kinetic Energy

In order to retain generality, an expression for the fluid kinetic energy will be given which includes translational and rotational motion. This expression will then be truncated to the horizontal translational case, which is applicable to the four study models used in this research.

2.2.1.1   Arbitrary Tank Motion

The kinetic energy of the fluid flow is the volume integral of the squared magnitude of the fluid velocity referenced to an inertial frame (Fig. 2.7):

$$T_F = \frac{1}{2} \iiint_V \rho\, (\mathbf{u} \cdot \mathbf{u})\, dV$$

(2.37)
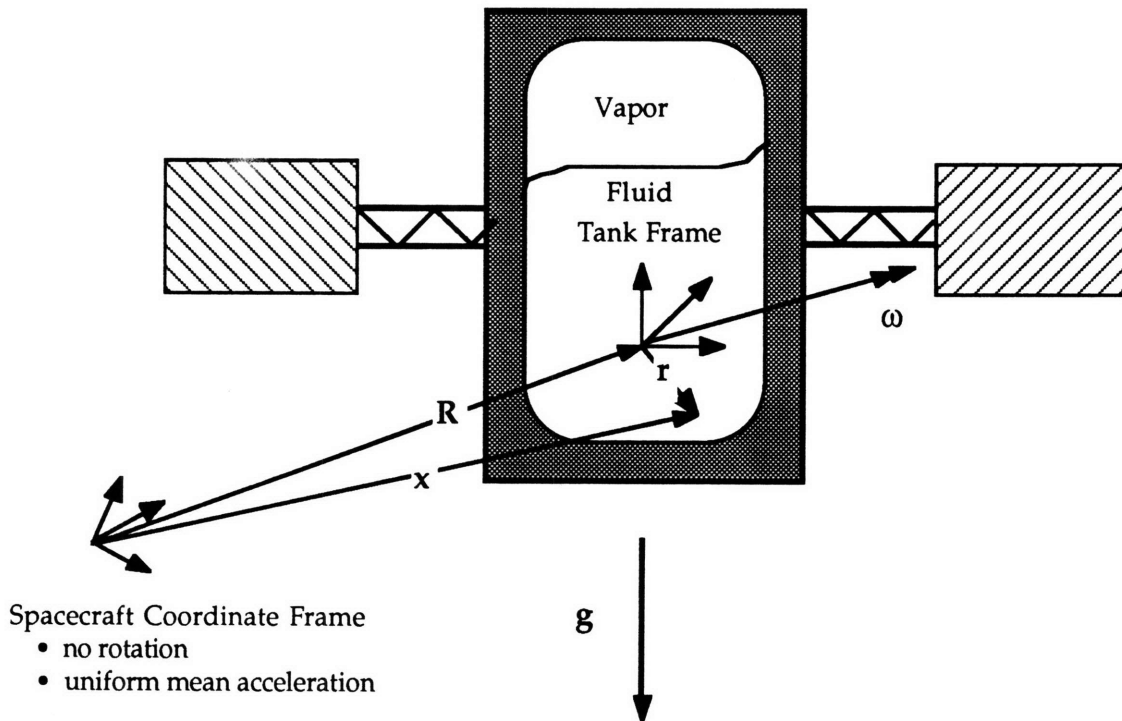
Figure 2.7   **Motion of a Fluid Particle for Arbitrary Rotation and Translation of the Tank.**

The total velocity of a fluid particle has components of both the fluid velocity (potential) field and the motion of the tank.

The flow velocity, u relative to the inertial frame is the resultant of three components:

- Velocity due to tank translation
- Velocity due to tank rotation
- Fluid flow velocity

so that:

$$u = \dot{R} + \omega x r + \nabla\phi \tag{2.38}$$

Substituting eq. 2.38 into eq. 2.37, applying Green's Theorem [Hildebrand, 1976], an expression for the kinetic energy of the fluid is obtained:

$$T_F = \underbrace{\frac{1}{2}m_F \dot{R}\cdot\dot{R}}_{(i)} + \underbrace{\frac{1}{2}\omega\cdot I_F\omega}_{(ii)} + \underbrace{\frac{\rho}{2}\iint_{S_F} \phi n\cdot\nabla\phi\, dS_F}_{(iii)} +$$

$$\underbrace{\rho\iiint_V \dot{R}\cdot\nabla\phi\, dV}_{(iv)} + \underbrace{\rho\iiint_V (\omega x r)\cdot\nabla\phi\, dV}_{(v)} + \underbrace{\dot{R}\cdot\omega x r_o}_{(vi)} \tag{2.39}$$

Each term has a physical meaning, with:

Term	Physical Meaning
(i)	The translational kinetic energy of the fluid if stationary m_F = Total mass of fluid.
(ii)	The rotational kinetic energy of the fluid if stationary I_F = Instantaneous moment of the fluid with:

$$\omega\cdot I_F\,\omega = \iiint_V \rho(\omega x r)\cdot(\omega x r)\, dV \tag{2.40}$$

Evaluation of the integral will depend on the dynamic motion of the free surface, rendering this component to be a nonlinear function of the free surface generalized coordinates.

51

(iii)   The contribution to the kinetic energy due to the motion of the free surface relative to the tank.

(iv)   Inertial coupling between the fluid flow potential and the translation of the tank.

(v)   Inertial coupling between the fluid flow potential and the rotation of the tank.

(vi)   The kinetic energy correction for the offset between the origin of the spacecraft reference frame and the fluid center of mass.

2.2.1.2   Horizontal Translational Kinetic Energy

Deleting terms other than those resulting from tank horizontal translation, yields the following expression for the fluid kinetic energy, which is valid for all four the study models considered in this research.

$$T_F = \frac{1}{2} m_F \dot{R} \cdot \dot{R} + \frac{1}{2} \rho \iint_V \phi \frac{\partial \phi}{\partial n} dS_F + \rho \iiint_V \dot{R} \cdot \nabla \phi \, dV \qquad (2.41)$$

The first term is equal to:

$$\frac{1}{2} m_F \left(\dot{x}^2 + \dot{y}^2 \right) \qquad (2.42)$$

and since:

$$\frac{\partial \phi}{\partial n} = \nabla \phi \cdot n = \left(\frac{\partial \phi}{\partial z} - \nabla \phi \cdot \nabla \eta \right) \qquad (2.43)$$

with

$$\frac{\partial \eta}{\partial t} + \nabla \phi \cdot \nabla \eta \Big|_{e_3 = \eta} = \frac{\partial \phi}{\partial z} \Big|_{e_3 = \eta} \quad \text{on } e_3 = \eta \qquad (2.44)$$

or:

$$\frac{\partial \eta}{\partial n} = \frac{\partial \eta}{\partial t} \quad \text{on } e_3 = \eta \qquad (2.45)$$

the second integral can be written as:

$$\frac{1}{2}\rho \int\int_{S_F} \phi\Big|_{e_3=\eta} \eta_t \, dS_F$$

(2.46)

Using the results obtained in the previous section, this integral can be expanded to:

$$\sum_{m=1}^{N}\sum_{n=1}^{N} \dot{q}_m a_{mn} \dot{q}_n$$

(2.47)

where a_{mn}, the slosh depth matrix, is defined by:

$$a_{mn} = \sum_{i=1}^{N} d_{mi}\, l_{in}$$

(2.48)

using the expressions for d_{mn} and l_{mn}, a_{mn} can be written as:

$$a_{mn} = a_{mn}^{(0)} + \sum_{r=1}^{N} a_{mnr}^{(1)} q_r + \sum_{r=1}^{N}\sum_{s=1}^{N} a_{mnrs}^{(2)} q_r q_s$$

(2.49)

with, in the limit of no fluid motion:

$$a_{mn}^{(0)} = \sum_{i=1}^{N} d_{mi}^{(0)}\, l_{in}^{(0)}$$

(2.50)

The linear correction to the slosh depth matrix is given by:

$$a_{mnr}^{(1)} = \sum_{i=1}^{N}\left(d_{mir}^{(1)}\, l_{in}^{(0)} + d_{mi}^{(0)} l_{inr}^{(1)} \right)$$

(2.51)

and the quadratic correction by:

$$a_{mnrs}^{(2)} = \sum_{i=1}^{N}\left(d_{mir}^{(1)}\, l_{ins}^{(1)} + d_{mirs}^{(2)}\, l_{in}^{(0)} + d_{mi}^{(0)} l_{inrs}^{(2)} \right)$$

(2.52)

Note that a_{mn}, the slosh depth matrix, has the dimension of length and if an inertia is associated with each surface degree of freedom (q_n), then the elements of this matrix represents the depth of fluid having a mass equal to the associated free surface modal inertia. The inertia of each slosh mode will appear to change with the amplitude of the slosh motion.

Using Green's Theorem, the third term of eq. 2.41 can be written as:

$$\int_{S_F}\int (x\ddot{x} + y\ddot{y})\, \eta_t\, dS_F$$

(2.53)

and after substituting the modal series expansion for the free surface motion eq. 2.53 becomes:

$$\iiint_V \dot{R}\cdot\nabla\phi\, dV = \int_{S_F}\int (x\ddot{x} + y\ddot{y})\eta_t\, dS_F$$

(2.54)

by using Green's Theorem and substituting the assumed series expansion for (η) (see eq. 2.11), this integral can be written as:

$$\dot{x}\left[\sum_{n=1}^{N}\dot{q}_n\int_S\int \xi_n x\, dS\right] + \dot{y}\left[\sum_{n=1}^{N}\dot{q}_n\int_S\int \xi_n y\, dS\right]$$

(2.55)

Combining eq.'s. 2.42, 2.46 and 2.55, the expression for the kinetic energy of the fluid (eq. 2.41) becomes:

$$T_F = \frac{1}{2}m_F\left(\dot{x}^2 + \dot{y}^2\right) +$$

$$\frac{\rho}{2}\sum_{m=1}^{N}\sum_{n=1}^{N}\left[\left\{a_{mn}^{(0)} + \sum_{r=1}^{N}a_{mnr}^{(1)}\, q_r + \sum_{r=1}^{N}\sum_{s=1}^{N}a_{mnrs}^{(2)}\, q_r q_s\right\}q_m q_n\right] +$$

$$\rho\dot{x}\left[\sum_{n=1}^{N}\dot{q}_n\int_S\int \xi_n x\, dS\right] + \rho\dot{y}\left[\sum_{n=1}^{N}\dot{q}_n\int_S\int \xi_n y\, dS\right]$$

(2.56)

2.2.2 Potential Energy

This section formulates the expression for the fluid potential energy. The fluid potential energy is the sum of the virtual work done on the fluid by external conservative forces. Two types of potential energies are important in this derivation: acceleration potential energy and capillary potential energy. The acceleration potential energy is the virtual work done by the slosh motion against the mean spacecraft acceleration field; it acts on the volume of the fluid. The capillary potential energy is the virtual work

54

done by the slosh motion against the surface tension of the fluid-vapor interface; it acts on the free surface of the fluid.

2.2.2.1 Fluid Acceleration Potential Energy for a Uniform Acceleration Field

Each differential mass element of the fluid has potential energy equal to the work done against the uniform acceleration field in moving the fluid element, in the direction of the acceleration field, from some reference position to its instantaneous position. For a constant acceleration field strength, a (aligned with the e_3 axis), the potential energy due to this motion is:

$$dU_a = \rho a e_3 dV \tag{2.57}$$

The total fluid acceleration potential energy is the integral of dU_a over the entire fluid volume. As before, the integral can be written as a sum of integrals (see equations 2.23 and 2.24):

$$U_a = \underbrace{\int\int_S \int_{f(e_1,e_2)}^{\eta^d(e_1,e_2,t)} \rho a e_3 de_3 dS}_{U_a^d} + \underbrace{\int\int_S \int_{h(e_1,e_2)}^{f(e_1,e_2)} \rho a e_3 de_3 dS}_{U_a^e} \tag{2.58}$$

where U_a^e is the contribution of the acceleration potential energy from the motion of the fluid over the equilibrium volume and U_a^d is the contribution due to the motion of the free surface about the equilibrium free surface position. For an incompressible fluid in an uniform gravity acceleration field (a = g), this becomes

$$U_g = \frac{\rho g}{2} \left[\sum_{m=1}^{N} \sum_{n=1}^{N} \int\int_S \left[\eta^d(e_1,e_2,t) - f^2(e_1,e_2) \right] dS \right] +$$

$$\frac{\rho g}{2} \int\int_S \left[h^2(e_1,e_2) - f^2(e_1,e_2) \right] dS \tag{2.59}$$

The first term is time dependent but the second not. Using the modal series expansion for η (eq. 2.11), eq. 2.59 can be written as:

$$U_g = \frac{\rho g}{2}\left\{\left[\sum_{m=1}^{N}\sum_{n=1}^{N}\iint_S [\xi_m\xi_n q_m q_n - f^2]dS\right] + \iint_S [h^2 - f^2]dS\right\}$$ (2.60)

Note that eq. 2.60 can be simplified if the orthogonality of the assumed mode shapes are used; that is:

$$\iint_S \xi_m\xi_n dS = S\delta_{mn}$$ (2.61)

The first group in eq. 2.60 is a constant independent of the free surface motion and it reflects the static equilibrium of the free surface shape for a given uniform acceleration field. When added to a similar term for the capillary potential energy, this leads to a variational expression for the free surface equilibrium shape, $f(e_1, e_2)$. The second term in eq. 2.60 is the primary quadratic acceleration potential energy which leads to a linear restoring force term in the final equations of motion.

2.2.2.2   Fluid Capillary Potential Energy

Each differential surface element at the free surface S_F has a potential energy equal to the area times the local surface tension of the interface:

$$dU_\sigma = \sigma dS_F$$ (2.62)

When it is assumed that the surface tension is uniform over the entire free surface, the total capillary potential energy is (from Peterson [1987]):

$$U_\sigma = \sigma \iint_{S_F} dS_F$$ (2.63)

Projecting the fluid surface onto the plane (e_1, e_2) perpendicular to the coordinate describing the fluid surface (e_3) see Fig. 2.6 , the capillary potential

energy can be expressed as:

$$U_\sigma = \sigma \int \int_S \sqrt{1 + \nabla\eta \cdot \nabla\eta} \; dS$$

(2.64)

From this expression it is clear that the capillary energy will be a nonlinear function of the free surface degrees of freedom (q_n). Following the work of Peterson [1987], the square root is expanded in a binomial series of η. The resultant expression for the capillary potential energy is:

$$U_\sigma = \sigma S^{(0)} + \sigma \sum_{m=1}^{N} S_m^{(1)} q_m + \sigma \sum_{m=1}^{N} \sum_{n=1}^{N} S_{mn}^{(2)} q_m q_n +$$

$$\sigma \sum_{m=1}^{N} \sum_{n=1}^{N} \sum_{r=1}^{N} S_{mnr}^{(3)} q_m q_n q_r + \sigma \sum_{m=1}^{N} \sum_{n=1}^{N} \sum_{r=1}^{N} \sum_{s=1}^{N} S_{mnrs}^{(4)} q_m q_n q_r q_s$$

(2.65)

In which the series is truncated after the fourth order term in order to retain cubic order terms in the final equations of motion. The nonlinear surface area coefficients, $S^{(i)}$, are progressive corrections to the free surface area due to the deformation of the free surface. In absence of free surface motion, the area of the equilibrium free surface is given by:

$$S^{(0)} = \int \int_S \sqrt{1 + \nabla f \cdot \nabla f} \; dS$$

(2.66)

The linear correction coefficient is:

$$S_m^{(1)} = \int \int_S \frac{\nabla f \cdot \nabla \xi_m}{\sqrt{1 + \nabla f \cdot \nabla f}} \; dS$$

(2.67)

The quadratic correction coefficient is:

$$S_{mn}^{(2)} = \frac{1}{2} \int \int_S \sqrt{1 + \nabla f \cdot \nabla f} \left\{ \frac{\nabla \xi_m \cdot \nabla \xi_n}{(1 + \nabla f \cdot \nabla f)} - \frac{(\nabla f \cdot \nabla \xi_m)(\nabla f \cdot \nabla \xi_n)}{(1 + \nabla f \cdot \nabla f)^2} \right\} dS$$

(2.68)

57

The cubic correction coefficient is:

$$S^{(3)}_{mnr} = \frac{1}{2} \int\int_S \sqrt{1 + \nabla f \cdot \nabla f} \left\{ \frac{(\nabla f \cdot \nabla \xi_m)(\nabla f \cdot \nabla \xi_n)(\nabla f \cdot \nabla \xi_r)}{(1 + \nabla f \cdot \nabla f)^3} - \frac{(\nabla f \cdot \nabla \xi_m)(\nabla \xi_n \cdot \nabla \xi_r)}{(1 + \nabla f \cdot \nabla f)^2} \right\} dS \tag{2.69}$$

and the quartic correction coefficient is:

$$S^{(4)}_{mnrs} = \int\int_S \sqrt{1 + \nabla f \cdot \nabla f} \left\{ -\frac{1}{8} \left[\frac{(\nabla \xi_m \cdot \nabla \xi_n)(\nabla \xi_r \cdot \nabla \xi_s)}{(1 + \nabla f \cdot \nabla f)^2} \right] + \right.$$
$$\frac{3}{4} \left[\frac{(\nabla f \cdot \nabla \xi_m)(\nabla f \cdot \nabla \xi_n)(\nabla \xi_r \cdot \nabla \xi_s)}{(1 + \nabla f \cdot \nabla f)^3} \right] -$$
$$\left. \frac{5}{8} \left[\frac{(\nabla f \cdot \nabla \xi_m)(\nabla f \cdot \nabla \xi_n)(\nabla f \cdot \nabla \xi_r)(\nabla f \cdot \nabla \xi_s)}{(1 + \nabla f \cdot \nabla f)^4} \right] \right\} dS \tag{2.70}$$

The surface correction coefficients depend on both the free surface mode shapes and the shape of the equilibrium free surface, and therefore on the Bond number. The relative influence of the capillary potential energy on the fluid dynamics will thus be a function of the Bond number. The physical role of these terms are follows:

- $S^{(0)}$ is the equilibrium free surface area. Together with the constant terms if the acceleration potential energy, U_a, it defines the equilibrium free surface shape, $f(e_1, e_2)$.

- $S^{(1)}_m$ will appear as an inhomogeneous term in the final equations of motion.

- $S^{(2)}_{mn}$ multiply the linear surface tension restoring forces in the fluid modal equations of motion. This terms weakens as the free surface curvature increases.

- $S_{mnr}^{(3)}$ multiply the quadratic surface tension nonlinear forces in the fluid modal equations of motion and are zero for a flat free surface.

- $S_{mnrs}^{(4)}$ multiply the cubic surface tension nonlinear forces in the fluid modal equations of motion. These terms are negative, resulting in a cubic softening of the fluid dynamics as a function of amplitude.

2.2.3 Fluid/Spacecraft Lagragian

The Lagragian for the fluid/spacecraft system is given by the sum of the total kinetic (eq. 2.56) and the total potential energy. The spacecraft kinetic and potential energy, eq. 2.71, must be added to the fluid energy terms.

$$T_{sc} = \frac{1}{2}m\dot{x}^2 + \frac{1}{2}m\dot{y}^2$$
(2.71a)

$$U_{sc} = \frac{1}{2}k_x x^2 + \frac{1}{2}k_y y^2$$
(2.71b)

The Lagrangian of the fluid/spacecraft system is the total kinetic energy minus the total potential energy (T - V). Instead of writing out the unwieldily equation, the fluid/spacecraft Lagragian is stated to be the sum of eq.'s 2.56 and 2.71a minus the sum of eq.'s 2.58, 2.65 and 2.71b.

2.3   Fluid Equilibrium Free Surface Shape and Linear Fluid Eigen-Characteristics

In order to calculate the coefficients in the energy expression, a selected set of assumed shape functions is required for the surface motion and the velocity potential function. As discussed in section 2.2.5, the linear eigen-modes of the fluid system is an obvious choice. The next sections will formulate a finite difference scheme for calculating the linear eigen-modes of the fluid system. The fluid equilibrium free surface will be calculated and

included in the fluid geometry to improve the accuracy of the linear eigen-modes and to correctly Bond number effects. The linear effect of contact-angle-hysteresis will be included via a special boundary condition at the fluid contact surface.

2.3.1 Fluid Equilibrium Free Surface

As indicated in the previous section, two terms in the fluid energy expression determine the fluid equilibrium free surface. When the dynamic terms in the fluid energy expression are set to zero and constant terms are ignored, a variational integral is obtained for the fluid equilibrium free surface equation, $f(e_1, e_2)$, namely:

$$I = \int \int_S \left(\sqrt{1 + \nabla f \cdot \nabla f} + \frac{1}{2} Bo \ f^2 \right) dS$$

(2.72)

where Bo is the Bond number based on some characteristic length a and $f = f/a$. Let F be the integrand of eq. 2.72, then Euler's equation that will satisfy the requirement that the integral remains stationary with respect to independent variations, is:

$$\frac{\partial}{\partial e_1} \left(\frac{\partial F}{\partial f_{e_1}} \right) + \frac{\partial}{\partial e_2} \left(\frac{\partial F}{\partial f_{e_2}} \right) - \frac{\partial F}{\partial f} = 0$$

(2.73)

The subscript e_1 and e_2 indicates partial derivatives with respect to the coordinates e_1 and e_2 respectively. After evaluation eq. 2.73 yields the following nonlinear equation for the fluid equilibrium free surface.

$$\left(1 + f_{e_2}^2 \right) f_{e_1 e_1} - 2 f_{e_1} f_{e_2} f_{e_1 e_2} + \left(1 + f_{e_1}^2 \right) f_{e_2 e_2} - $$

$$Bo \left(1 + f_{e_1}^2 + f_{e_2}^2 \right)^{3/2} = 0$$

(2.74)

The nonlinear problem of minimal surfaces is known as Plateau's problem [Simmons, 1972] and finding an exact solution is extremely difficult. In general, the boundary conditions that must be satisfied are; the prescribed contact angle at the tank walls, the fluid height at the center of the tank (as defined by the fluid volume) and for symmetric tank geometries (as

are the four study models considered in this research) the zero slope requirement at the symmetry axis (axes).

Several numeric solution techniques are found in the literature, for example; the method of local variations and the method of optimal discretization discussed in Myshkin [Myshkin, et al, 1987] and a shooting technique described by Peterson [Peterson, 1987]. Also see Satterlee [Satterlee and Reynolds, 1964]. The shooting technique used by Peterson works well for axi-symmetric problems, where the problem is one dimensional but this technique is considered too complex to be implemented for two-dimensional problems.

The approach used in this research is based on a finite difference approximation of eq. 2.74 and the inverse iteration method discussed in Chapter 3. The domain over which the fluid surface is defined (S) can be discretized, with the fluid surface $f(e_1, e_2)$ only defined at a finite number of discrete points $(e_{i,j})$. The derivatives of the free surface shape can be approximated with a second order accurate central finite difference approximation. For example:

$$f_{e_k}(e_i, e_j) = \frac{f^{i,j+1} - f^{i,j-1}}{e_k^{i,j+1} - e_k^{i,j-1}} + O(\Delta e_k^2)$$

(2.75)

$$f_{e_k e_k}(e_i, e_j) = \frac{f^{i,j+1} - 2f^{i,j} + f^{i,j-1}}{\left(e_k^{i,j+1} - e_k^{i,j-1}\right)^2} + O(\Delta e_k^2)$$

and

(2.76)

Using these finite difference expressions eq. 2.74 can be written as a nonlinear set of equations:

$$A\left(f_{e_1}^{2^{n-1}}, f_{e_2}^{2^{n-1}}, f_{e_1 e_2}^{n-1}, Bo\right) f_{i,j}^n = B\left(f_{e_1}^{2^{n-1}}, f_{e_2}^{2^{n-1}}, f_{e_1 e_2}^{n-1}, Bo\right)$$

(2.77)

The equilibrium free surface shape is iteratively solved by:

- Calculate **A** and **B**, as a function of f^{n-1}, where f^{n-1} is the solution for the the free surface shape at the previous iteration (n-1).
- Solve for the free surface shape by inverting **A**. (Inverse Iteration).
- Repeat until convergence.

The convergence criteria is:

$$\sum_{i=1}^{m} \sum_{j=1}^{l} \left| \left(f_{i,j}^{n} - f_{i,j}^{n-1} \right) \right| \leq \epsilon$$

(2.78)

That is, if the left-hand-side of eq. 2.78 is less than the convergence limit ϵ, the solution has converged. In practice a zero initial guess for the free surface shape worked well and convergence was significantly improved by decreasing the discretization grid spacing near the tank walls (See Figures 2.8a to 2.8d). Intuitively the decrease in grid spacing at the tank walls is an obvious requirement, since the sharp changes in fluid slope at the tank walls require a fine grid mesh for a good finite difference approximation of the slope. The grid spacing can be increased near the symmetry axis (axes) where the slope changes are more gradual. Figures 2.8a to 2.8d compares the results obtained with this inverse iteration method with those obtained by the shooting technique used by Peterson [1987]. The results are presented for the equilibrium free surface of a cylindrical tank of radius (r). The Bond number is based on the tank diameter (d) and the acceleration vector aligned with the symmetry axis. The equilibrium free surface shapes for the study models of this analysis will be discussed in later chapters.

As can be seen from Figures 2.8a to 2.8d, the results obtained with the inverse iteration method match the results obtained with the shooting technique.

Bo = 66, Contact Angle = 1°
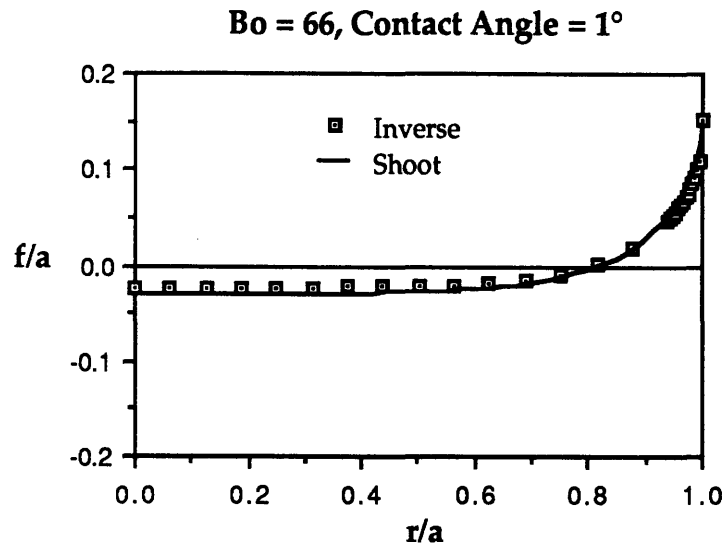
Figure 2.8a   Comparison of Inverse Iteration and Shooting Technique Results.

Bo = 58, Contact Angle = 60°
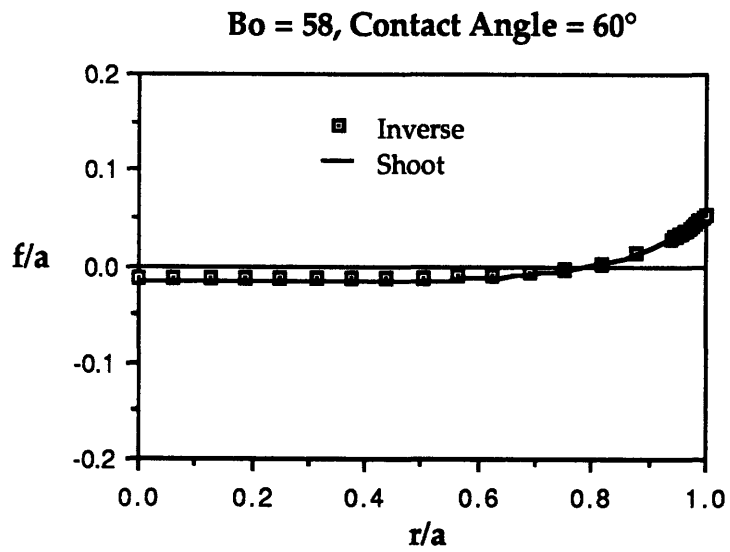
Figure 2.8b   Comparison Continued.

Bo = 33, Contact Angle = 60°
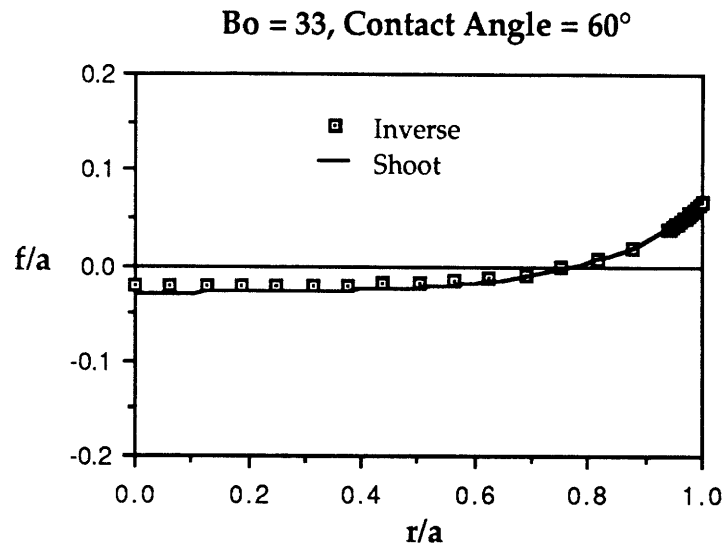
Figure 2.8c   Comparison Continued.

Bo = 0, Contact Angle = 60°
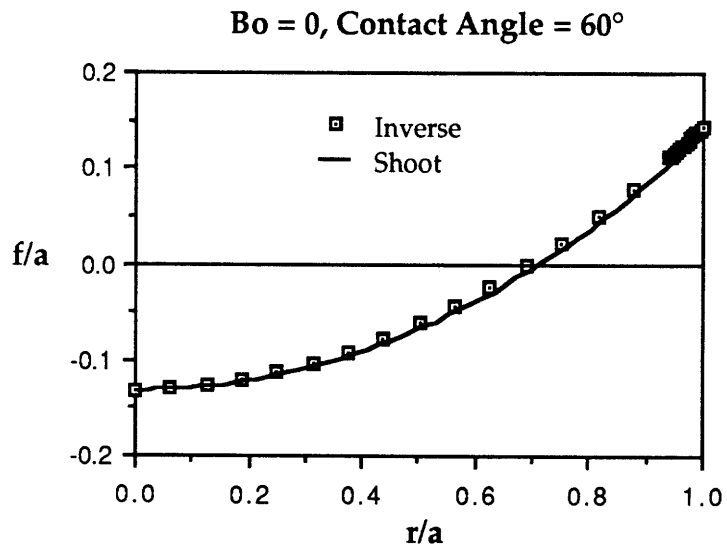
Figure 2.8d   Comparison Continued.

2.3.2 Fluid Linear Eigen-Characteristics

Although exact solutions exist for many containers of simple geometry [Moiseev and Petrov, 1966], numerical methods will be required to calculate the eigen-characteristics of tanks of arbitrary geometry. Several numerical methods exist for the calculation of these eigen-characteristics, i.e.; finite element methods, virtual mass methods, fluid ring element method (See [Stavrindis, 1985]), boundary element methods [Nkayama and Washizu, 1981] and finite difference methods. No attempt will be made to evaluate the pros and cons of these methods but it is important to note that in calculating some of the coefficients, spatial derivatives are required, indicating that methods which yield mode shapes with continuous first order spatial derivatives will be superior to those that did not.

The simple tank geometries considered in this research favored a finite difference scheme. The governing differential equations for the linear (small amplitude oscillations) fluid slosh problem is (refer to Fig.'s 2.4 to 2.5):

$$\nabla^2 \phi = 0 \quad \text{inside the fluid volume} \tag{2.79}$$

$$\frac{\partial \phi}{\partial n} = 0 \quad \text{on the tank walls} \tag{2.80}$$

$$\frac{\partial \phi}{\partial n} = \frac{\partial \eta}{\partial t} \quad \text{and} \tag{2.81}$$

$$\frac{\partial \phi}{\partial t} + g\eta = 0 \quad \text{on the fluid surface} \tag{2.82}$$

Differentiating eq. 2.82 with respect to time and substituting eq. 2.81 in the result, yields the following boundary condition at the fluid surface:

$$\frac{\partial^2 \phi}{\partial t^2} + g\frac{\partial \phi}{\partial n} = 0 \tag{2.83}$$

Assuming sinusoidal behavior for the potential function ϕ, that is, let:

$$\phi = \Phi e^{j\lambda t} \tag{2.84}$$

eq. 2.83 can be written as:

$$\frac{\partial \Phi}{\partial n} = \frac{\lambda^2}{g}\Phi \qquad \text{on the fluid surface} \qquad (2.85)$$

Equation 2.79 is the governing differential equation with eq.'s 2.80 and the 2.85 the boundary conditions. Note that eq. 2.85 is a time dependent boundary condition which will eventually determine the eigen-characteristics of the fluid. Using a second order accurate central finite difference scheme, based on a cartesian coordinate system and uniformly spaced grid (mesh), eq. 2.79 can be approximated as:

$$\nabla^2 \Phi\left(e_1 = e_1^i, e_2 = e_2^j, e_2 = e_2^k\right) = \left\{\frac{\partial^2 \Phi}{\partial e_1^2} + \frac{\partial^2 \Phi}{\partial e_2^2} + \frac{\partial^2 \Phi}{\partial e_3^2}\right\}^{i,j,k} =$$

$$\frac{\left\{\dfrac{\Phi^{i+1} - \Phi^i}{e_1^{i+1} - e_1^i} - \dfrac{\Phi^i - \Phi^{i-1}}{e_1^i - e_1^{i-1}}\right\}}{\frac{1}{2}\left(e_1^{i+1} + e_1^{i-1}\right)} + \frac{\left\{\dfrac{\Phi^{j+1} - \Phi^j}{e_2^{j+1} - e_2^j} - \dfrac{\Phi^j - \Phi^{j-1}}{e_2^j - e_2^{j-1}}\right\}}{\frac{1}{2}\left(e_2^{j+1} + e_2^{j-1}\right)} +$$

$$\frac{\left\{\dfrac{\Phi^{k+1} - \Phi^k}{e_3^{k+1} - e_3^k} - \dfrac{\Phi^k - \Phi^{k-1}}{e_3^k - e_3^{k-1}}\right\}}{\frac{1}{2}\left(e_3^{k+1} + e_3^{k-1}\right)} + O\left(\Delta e_1^2, \Delta e_2^2, \Delta e_3^2\right)$$

$$(2.86)$$

Where:

$$\nabla e_1 = \frac{e_1^{i+1} - e_1^{i-1}}{2}, \quad \nabla e_2 = \frac{e_2^{j+1} - e_2^{j-1}}{2}, \quad \nabla e_3 = \frac{e_3^{k+1} - e_3^{k-1}}{2} \qquad (2.87)$$

Eq. 2.86 is also valid for non-uniformly spaced grids except that the error term becomes first order [Lapidus and Pinder, 1982]. In this research a uniformly spaced curvilinear grid will be used for the rectangular (square) and cylindrical tanks. A uniformly spaced cartesian grid will be used for the spherical tank with a quadratic interpolation scheme at the boundary nodes to account for boundaries that are not aligned with the mesh. The non-curvilinear mesh for the spherical tank was used since the fluid free surface in a spherical tank is not aligned with a spherical coordinate system. The use of a cartesian grid for a non-rectangular tank will also illustrate the general application of the finite difference technique. The boundary

66

conditions, again using a second order accurate finite difference approximation can be expressed as:

(a)   For boundaries aligned with the grid mesh (See Fig. 2.9):

$$\frac{\partial^2 \Phi}{\partial e_1^2} = 2\frac{\left(\Phi^B - \Phi^I\right)}{\left(e_1^B - e_1^I\right)} + O\left(\Delta e_1^2\right) \qquad \text{on the tank walls} \qquad (2.88)$$

$$\frac{\partial^2 \Phi}{\partial e_3^2} = 2\frac{\left(\Phi^B - \Phi^I\right)}{\left(e_3^B - e_3^I\right)^2} + \frac{\lambda^2}{g}\frac{2\Phi^B}{\left(e_3^B - e_3^I\right)}O\left(\Delta e_3^2\right) \qquad \text{on the surface} \quad (2.89)$$

(b)   For skew boundaries, a quadratic interpolation scheme can be used to eliminate the external nodes. Using the specific nodal numbering in Fig. 2.9, the interpolation scheme can be expressed as:

$$\Phi\left(\bar{e}_1, \bar{e}_2, \bar{e}_3\right) = \sum_i^7 N_i\left(\bar{e}_1, \bar{e}_2, \bar{e}_3\right)\Phi_i \qquad (2.90)$$

67

Boundary Aligned with Grid

Skew Boundary
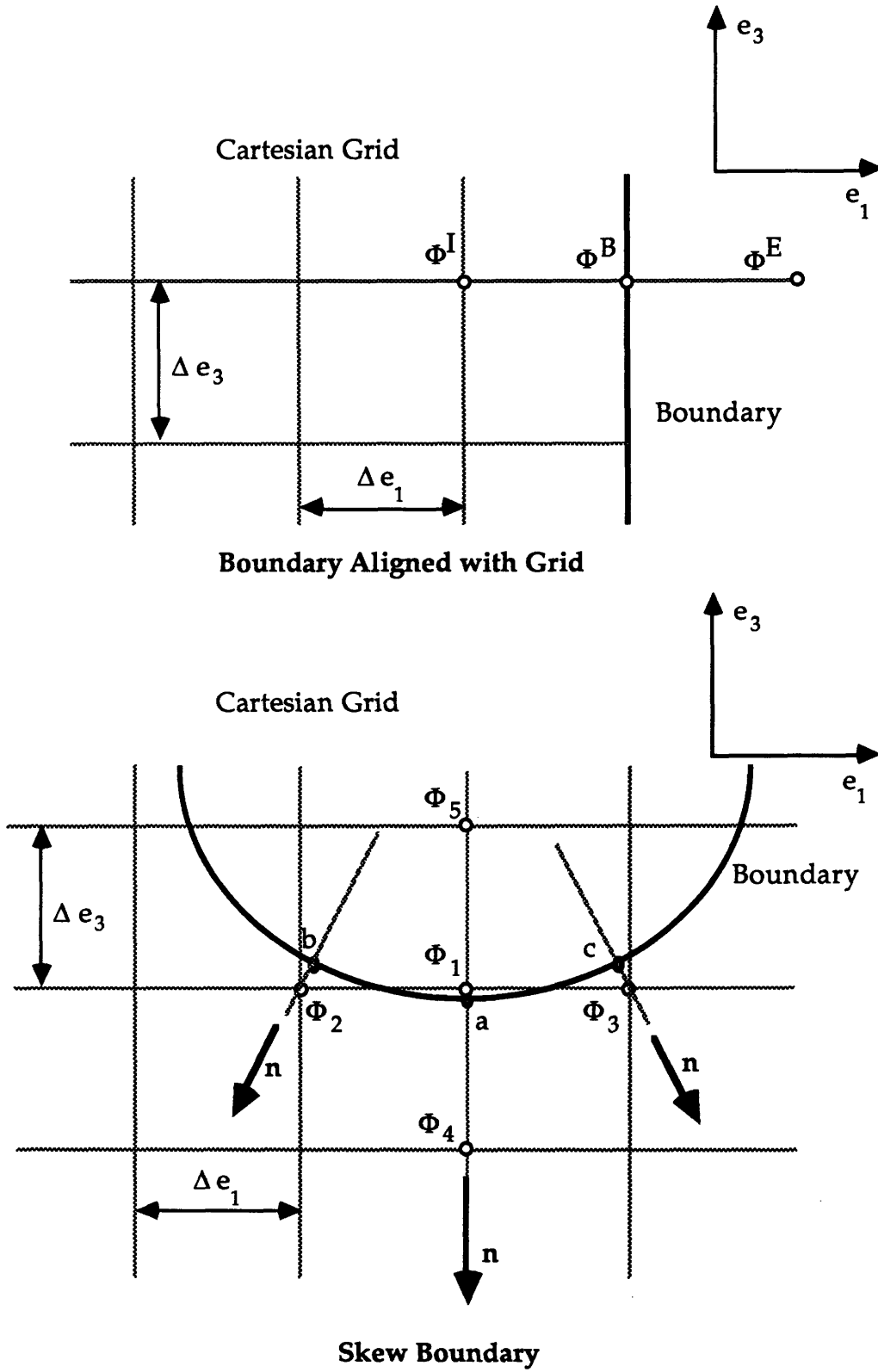
Figure 2.9   **Boundary Conditions for Finite Difference Scheme.**

n is the vector normal to the boundary.

This expression is valid for the seven node finite difference model of 2.86 and the bars on the coordinates indicating that the coordinate system is a local non-dimensional coordinate system. The shape functions N_i, in terms of the non-dimensional coordinates, are:

$$N_1 = 1 - \bar{e}_1^2 - \bar{e}_2^2 - \bar{e}_3^2, \quad N_2 = \frac{(\bar{e}_1 - 1)\bar{e}_1}{2}$$

$$N_3 = \frac{(\bar{e}_1 + 1)\bar{e}_1}{2}, \quad N_4 = \frac{(\bar{e}_2 - 1)\bar{e}_2}{2}$$

$$N_5 = \frac{(\bar{e}_2 + 1)\bar{e}_2}{2}, \quad N_6 = \frac{(\bar{e}_3 - 1)\bar{e}_3}{2}$$

$$N_7 = \frac{(\bar{e}_3 + 1)\bar{e}_3}{2}$$

(2.91)

As an example, the potential function at the boundary nodes in the two-dimensional problem of Fig. 2.9 (Bottom), namely Φ_2, Φ_3, and Φ_4, can be eliminated from Laplace's equation by using the boundary condition that the normal derivative of the potential function must be zero on the tank wall. Thus:

$$\Phi_2 = \Phi_b, \quad \Phi_3 = \Phi_c, \quad \Phi_4 = \Phi_a$$

(2.92)

Plugging the coordinates of the auxiliary nodes a, b and c into eq. 2.90, yields a linear set of equations that express the potential function at the external boundary nodes in terms of the internal boundary nodes. That is:

$$\Phi_b = \Phi_2 = \sum_i^7 N_i^b \Phi_i, \quad \Phi_c = \Phi_3 = \sum_i^7 N_i^c \Phi_i, \quad \Phi_a = \Phi_4 = \sum_i^7 N_i^a \Phi_i$$

(2.93)

The superscripts on the shape functions (N_i) indicating that the shape functions are evaluated at the location of the superscript nodes. Re-organizing and writing in matrix form, yields:

$$\begin{pmatrix} \Phi_2 \\ \Phi_3 \\ \Phi_4 \end{pmatrix} = A \begin{pmatrix} \Phi_1 \\ \Phi_5 \\ \cdots \\ \cdots \end{pmatrix}$$

(2.94)

Using eq. 2.94, the potential function at the external nodes can be eliminated from the finite difference approximation of Laplace's equation

(eq. 2.86). This interpolation scheme can be used for other higher order finite difference approximations and allows the use of a non-curvilinear coordinate system to solve for the linear eigen-characteristics of a fluid system.

The process of determining the eigen-characteristics can be simplified, by solving for the internal degrees of freedom in terms of the surface degrees of freedom. The finite difference equations can be written in block matrix form, as:

$$
\begin{bmatrix}
[A_{1,1}] & [A_{1,2}] & [0] & [0] & \cdot & \cdot & \cdot \\
[A_{2,1}] & [A_{2,2}] & [A_{2,3}] & [0] & \cdot & \cdot & \cdot \\
[0] & [A_{3,2}] & [A_{3,3}] & [A_{3,4}] & \cdot & \cdot & \cdot \\
\cdot & \cdot & \cdot & \cdot & \ddots & \cdot & \cdot \\
\cdot & \cdot & \cdot & \cdot & \cdot & \ddots & \cdot \\
\cdot & \cdot & \cdot & \cdot & \cdot & \cdot & \ddots \\
\cdot & \cdot & \cdot & \cdot & [0] & [A_{m,m-1}] & [A_{m,m}]
\end{bmatrix}
\begin{Bmatrix}
\Phi_1 \\ \Phi_2 \\ \Phi_3 \\ \cdot \\ \cdot \\ \cdot \\ \Phi_m
\end{Bmatrix} =
$$

$$
\begin{Bmatrix}
[B_1(\lambda)] \\ [0] \\ [0] \\ \cdot \\ \cdot \\ \cdot \\ [0]
\end{Bmatrix}
\tag{2.95}
$$

Where [0] is the block zero matrix, m the number of mesh levels in the e_3 direction, Φ_1 is the vector containing the surface degrees of freedom, Φ_2 vector of the nodes one level below the surface level and Φ_m the vector of tank bottom nodes (See Fig. 2.10). This formulation is only valid for the seven point finite difference approximation of Laplace's equation. The value of the potential function, Φ, at any one of the nodes on a given mesh level is only dependent on the nodal values of the potential function at one level above and one level below the given mesh level.

Figure 2.10   Nodal Numbering Scheme.

Eq. 2.95 is in tri-diagonal block matrix form and the internal degrees of freedom can be solved for as follows:

$$\Phi_m = -\left[A_{m,m}\right]^{-1}\left[A_{m,m-1}\right]\Phi_{m-1}$$
and
$$\left[A_{m-1,m-1}\right]\Phi_{m-1} + \left[A_{m-1,m}\right]\Phi_m = -\left[A_{m-1,m-2}\right]\Phi_{m-2} \qquad (2.96)$$

$$\Phi_{m-1} = -\left[\left[A_{m-1,m-1}\right] - \left[A_{m-1,m}\right]\left[A_{m,m}\right]^{-1}\left[A_{m,m-1}\right]\right]\left[A_{m-1,m-2}\right]\Phi_{m-2}$$
$$(2.97)$$

71

The internal degrees of freedom of the potential can thus be eliminated from the problem and the result is a standard characteristic equation in terms of the surface potential function degrees of freedom:

$$\left| I \Lambda^2 - B_1^{-1} A^r \right| \Phi_{surface} = 0 \tag{2.98}$$

where I is the identity matrix, B_1 a diagonal matrix and a function of λ and A^r the matrix obtained by the repeated application of eq.'s 2.97. The solution of eq. 2.98 yields the eigen-values Λ, from which λ can be calculated along with the eigen-vectors or linear mode shapes. The shape of the modes at the internal nodes can be found by back-substitution of the shapes at the surface nodes into eq.'s 2.97.

2.3.2.1 Note on Contact Hysteresis Angle

In this research the model fluid, water/photoflo solution, has a contact angle near zero and a zero hysteresis contact angle constant (Γ). Experimental results for the non-linear slosh characteristics of water in cylindrical tanks were available [Peterson, 1987] and in order to analytically predict these results, the linearized effect of contact angle hysteresis were included in the eigen-analysis by introducing the following inhomogenous boundary condition [Satterlee and Reynolds, 1964]:

$$\left[\frac{\partial \eta}{\partial n} = \frac{\Gamma}{a} \eta \right]_{on\ contact\ surface} \tag{2.99}$$

where n is the normal to the contact surface and d is the cylindrical radius. Eq. 2.99 is only valid for cylindrical tanks and must be modified for tanks of other geometry. This boundary condition can be transformed to be a boundary condition for the fluid potential (Φ).

$$\frac{\partial}{\partial n_{cs}} \left(\frac{\partial \Phi}{\partial n_{fs}} \right) = \frac{\Gamma \lambda^2}{gd} \Phi \Big|_{on\ contact\ surface} \tag{2.100}$$

Here n_{cs} is the normal to the tank wall at the fluid/tank wall contact contour and n_{fs} is the normal on the fluid equilibrium free surface. Eq. 2.100 is a modification of the boundary condition in eq. 2.85 at the fluid/tank wall

contact contour. Eq. 2.85 is still valid for the rest of the fluid free surface. Eq. 2.100 can easily be incorporated in the finite difference approximation of fluid governing differential equations and the accompanying boundary conditions.

2.4 Derivation of the Nonlinear Fluid-Spacecraft Equations of Motion

Given the fluid Lagragian, namely the sum of eq.'s 2.56, 2.58, 2.65 and 2.71, Lagrange's principle;

$$\frac{d}{dt}\left(\frac{\partial L}{\partial \dot{q}_i}\right) - \frac{\partial L}{\partial q_i} = 0$$

(2.101)

can be applied to find the nonlinear coupled fluid/spacecraft differential equations. Appendix A presents these equations both in dimensional and non-dimensional form. Appendix A also address the question of model truncation and simplification. The nonlinear matrices for a planar model and a nonplanar model are presented in Appendix B.

2.5 Summary

This chapter derived the nonlinear governing differential equations of motion, describing the dynamic fluid behavior of fluids contained in tanks of arbitrary geometry. This chapter also presented a finite difference model for the calculation of the linear fluid eigen-characteristics and the nonlinear equilibrium fluid surface shape. The fluid dynamic model developed in this chapter will be used in Chapter 6 to predict the fluid behavior in the study models considered in this research.

Chapter 3

Prediction of the Dynamic Characteristics of Coupled Non-linear Systems

In this chapter the available analytical and numerical methods for determining the dynamic characteristics of coupled non-linear equations will be discussed. The discussion will be general but with specific emphasis on the type of non-linear coupled equations that are associated with the fluid slosh problem discussed in chapter 2.

The first section will be an overview of some of the known solution techniques for nonlinear time dependent differential equations, while in the ensuing section (Section 3.2) the harmonic balance method will be discussed in more detail. Section 3.3 discusses the solution of time independent nonlinear equations and the chapter concludes (Section 3.4) with a discussion of an alternative method to the Harmonic Balance method, namely; the least squares fitting technique.

3.1 Introduction and Discussion of Available Solution Methods

There are many approaches to the solution of time dependent nonlinear differential equations. The approaches can be divided into two broad categories, namely; time domain and frequency domain techniques. The following paragraphs weigh the pros and cons of these two methods and serve as a motivation for the approach used in this research.

3.1.1 Time Domain versus Frequency Domain Solution Techniques

Given that many solution techniques exist for non-linear equations, one must look at the form in which the solution is preferred. In general the characteristics of coupled dynamic systems are defined in terms of the natural frequencies and damping ratios. This is best illustrated by the one degree-of-freedom spring/mass problem. Let:

$$m\ddot{x}(t) + d\dot{x}(t) + kx(t) = F_o \cos(\Omega t) \qquad (3.1)$$

be the governing differential equation describing the motion of a spring/mass system. The natural frequency is given by:

$$\omega_n = \sqrt{\frac{k}{m}} \qquad (3.2)$$

and the damping ratio by:

$$\zeta = \frac{d}{2}\sqrt{\frac{1}{mk}} \qquad (3.3)$$

The maximum amplification for sinusoidal excitation, is given by:

$$\frac{A_{Dynamic}}{A_{Static}} = \frac{1}{2\zeta} \qquad (3.4)$$

and this maximum occurs when the excitation frequency (Ω) is equal to the natural frequency (ω_n). The dynamic characteristics can also be defined by the amplitude versus excitation frequency solution. Eq. 3.5 states the amplitude of vibration as a function of the excitation frequency (Ω).

$$\frac{A_{Dynamic}}{A_{Static}} = \frac{1}{\left[\left(1 - \left(\frac{\Omega}{\omega_n}\right)^2\right)^2 + \left(2\zeta\frac{\Omega}{\omega_n}\right)^2\right]^{\frac{1}{2}}} \qquad (3.5)$$

where
$$A_{Static} = \frac{F_o}{k} \qquad (3.6)$$

This solution form is well known to control engineers and structural dynamists. For non-linear systems, in general, the natural frequencies and damping ratios are a function of the excitation amplitude (F_o). The forced amplitude of vibration solution (eq. 3.5) is thus also a function of the excitation amplitude. For a single degree-of-freedom system we can state that:

$$\omega_n = \omega_n(F_o)$$
$$\zeta = \zeta(F_o) \qquad (3.7)$$

and that $\dfrac{A_{Dynamic}}{A_{Static}}$ is not only a function of the natural frequency (ω_n) and damping ratio (ζ) but also a non-linear function of the excitation amplitude (F_o). From a control engineering point of view one can consider the limits of the frequency and damping ratio dependence as tolerances on the control plant parameters. The structural dynamist, similarly, could consider these as limits for dynamic analyses. Given the information contained in this solution form, one may conclude that control engineers and structural dynamists should prefer that the results of an acceptable non-linear solution technique be in a similar form.

Such a preference would exclude time integration techniques since these methods result in time domain solutions. The main drawback of these methods are that they lack the insight provided by frequency domain techniques, that their results are very dependent on the initial conditions, and that they are computationally expensive. One must note that some frequency domain insight can be obtained by transforming the time domain results into the frequency domain (Fourier transforms) but that these methods do not generally provide the researcher with the dependence of the natural frequencies and damping ratios on excitation amplitude. Time integration methods would therefore fail to provide the control engineers and structural dynamists with tolerance limits. The rest of this chapter will concentrate on frequency domain solution methods for non-linear dynamic systems.

3.1.2 Frequency Domain Solution Techniques

Many different approaches exist to solve non-linear equations [Nayfey, 1981] and a list (albeit an incomplete one) is:

- Straightforward Expansion
- Averaging Technique
- Describing Function Method
- Multiple Time Scales
- Harmonic Balance
- Lindstedt-Poincare
- Fitting Techniques

Each of these methods have advantages and disadvantages over the others. The major disadvantage of Straightforward expansion, Lindstedt-Poincare and Multiple Time Scales methods are the complexity involved when multiple degree-of-freedom systems are considered. Peterson [1987] solved the non-linear planar fluid slosh problem with the Multiple Time Scales (MTS) method The simplified algebra, for this four degree-of-freedom problem, spanned more than thirty pages. Extending the problem to include the non-planar degrees-of-freedom would yield an algebraic problem too complex to solve. Not only is the expansion of the non-linear equations into the perturbation equations error prone, but the solution of the resultant perturbation equations for the amplitude dependence of the frequencies, would require MACSYMA or an equivalent mathematical manipulation program. A further drawback of these methods is that they fail to yield the dependence of the damping ratio on the excitation amplitude. With the MTS-method Peterson [1987] was able to predict the experimentally observed frequencies shifts as a function of excitation amplitude but failed to predict the amplitude dependence of the magnification factor on the excitation amplitude.

Given the complexity involved when multiple degree-of-freedom systems are considered, techniques that solve the non-linear problem without algebraic manipulation have a considerable advantage over those

that do not. At present, the previously mentioned methods require algebraic manipulation, but the averaging, describing function and fitting methods can be numerically implemented to solve the non-linear equations without algebraic manipulation of the non-linear governing differential equations.

By comparing the harmonic balance method with the describing function method, without going into detail, one can conclude that they are equivalent if, in the describing function method, only the first frequency term in the Fourier expansion of the non-linear function is retained.

The averaging technique, for a one degree of freedom system, yields the frequencies and damping ratios as averaged over one cycle. However, with multiple degree-of-freedom systems, it is unclear over which averaging period the frequencies and damping ratios must be averaged. Van Schoor [1988] showed that the frequencies and damping ratios converge as the period over which the non-linear functions are averaged is increased. An increased averaging period is accompanied with increased computational effort, making this method less attractive. The least squares fitting technique, discussed in the last section of this chapter, also requires a long time period for an assumed solution to be fitted to the non-linear response. The ability to find the higher harmonic terms however, makes this method an alternative to the harmonic balance method.

In conclusion one must emphasize, given the infinite number of non-linear systems, that none of these methods can be discarded. A suitable solution technique will depend largely on the nature and complexity of the non-linear problem. Also, that solutions obtained with numerical techniques do not provide the researcher with a closed form solution. Except for finding trends by perturbing the coefficients, relative importance of terms in the non-linear governing differential equation can not be determined.

3.2 Harmonic Balance Method

In this research, the harmonic balance method was selected to determine forced response characteristics from the nonlinear analytical model developed in Chapter 2. This section will discuss the harmonic

balance method and numerical implementation of this method. The first step will be to approximate the nonlinear equations with a describing function. The describing function is obtained by expanding the nonlinear equations in a Fourier series. In the next step the describing function is truncated to retain only the harmonic term. In doing so, the force associated with the component of the response oscillating at the excitation frequency is matched with the external forcing, hence the name; harmonic balance.

A periodic function f(t) can be expressed as a series of sine and cosine terms [Arfken, 1970]. Let eq. 3.8 be a set of coupled non-linear, time dependent, differential equations, similar to the equations presented in Appendix B.

$$N\left(q_1, q_1^2, ..., q_2, q_2^2, ..., \dot{q}_1 \dot{q}_1^2, ..., \dot{q}_2, \dot{q}_2^2, ..., \ddot{q}_1, ...\right) = N = 0 \tag{3.8}$$

Where the q_i's are the modal degrees of freedom. Assuming a sinusoidal solution for the modal degrees-of-freedom, q_i's, that is:

$$q_i(t) = A_i^o + \sum_{n=1}^{\infty}\left[A_i^n e^{j\omega t} + \bar{A}_i^n e^{-j\omega t}\right]$$

where: $A = \text{Complex} = a + jb$; $j = \sqrt{-1}$

and $\bar{A} = \text{Complex conjugate of } A$ \qquad (3.9)

Plugging these assumed solutions into equation 3.8 and also expanding N into a Fourier series, yields:

$$N = N_o^a\left(A_j^o, A_j^{o^2}, ..., \bar{A}_j^o, \bar{A}_j^{o^2}, ..., A_j^1, ...\right)$$

$$+ \sum_{n=1}^{\infty}\left[N_n^a\left(A_j^o, A_j^{o^2}, ..., \bar{A}_j^o, \bar{A}_j^{o^2}, ...\right)\cos(n\omega t)\right]$$

$$+ \sum_{n=1}^{\infty}\left[N_n^b\left(A_j^o, A_j^{o^2}, ..., \bar{A}_j^o, \bar{A}_j^{o^2}, ...\right)\sin(n\omega t)\right] \tag{3.10}$$

The first term is the so called DC term. The matrices N_n^a and N_n^b are non-linear and time independent matrices. These matrices are known as the Fourier coefficient matrices and can be determined as:

$$N_n^a = \frac{1}{\pi} \int_0^{2\pi} N \cos(n\varpi t) d(\varpi t)$$

$$\text{and} \quad N_n^b = \frac{1}{\pi} \int_0^{2\pi} N \sin(n\varpi t) d(\varpi t) \tag{3.11}$$

At this point it must be noted under which conditions such an expansion is valid. The Sturm theorem [Arfken, 1970] guarantees the validity of the expansion for functions that satisfy the Dirichlet conditions. The Dirichlet conditions are [Arfken]:

- The function has a finite number of finite discontinuities,
- and the function has a finite number of extreme (maxima or minima) values.

Functions that satisfy these conditions are called piecewise regular. In this research, N is a non-linear function of linear, quadratic, cubic, etc powers of the degrees-of-freedom (q_i) and their time derivatives. N is thus a continuous function of time, satisfying the first Dirichlet condition. Given that N is a function of the powers of the degrees-of-freedom it can be shown that N has a finite number of extreme values, satisfying the second Dirichlet condition. However, note that contrary to linear systems, where the response to an infinite number of sinusoids completely defines the response to all inputs, this is not the case for non-linear systems. In this research, the excitation is harmonic (single frequency) and the results obtained will not be valid for excitations other than harmonic.

Up to this point the derivation is in essence the describing function method. When a Fourier series is used to approximate a periodic function, the choice of ϖ is obvious; namely the frequency of oscillation which is the inverse of the oscillation period. Given that for most nonlinear systems, at least the one considered in this research, the dominant response (after the homogeneous terms have died away) to harmonic excitation would be at the frequency of excitation, the best choice for ϖ is the frequency of excitation (Ω). The problem however is that higher harmonic terms ($n\varpi$ or $n\Omega$) may or may not coincide with the other components in the non-linear response. Clearly the expansion of eq. 3.9 would fail to predict the sub-harmonic resonances observed in a single degree-of-freedom system with a non-linear cubic stiffness. The use of non-integer multiples of ϖ comes to mind but it

must be noted that in doing so the orthogonality conditions in eq. 3.11, are violated.

Section 3.4 will address the problem of sub- and super-harmonics but at this point it will be assumed that $\varpi = \Omega$ and the Fourier expansion of N is truncated to retain only the first harmonic. That is, let:

$$N = N_1^a \left(A_j^1, A_j^{1^2}, ..., \bar{A}_j^1, \bar{A}_j^{1^2}, ... \right) \cos(\Omega t) +$$
$$N_1^b \left(A_j^1, A_j^{1^2}, ..., \bar{A}_j^1, \bar{A}_j^{1^2}, ... \right) \sin(\Omega t) \tag{3.12}$$

The requirement that eq. 3.8 must be satisfied for all time (t), yields two non-linear sets of equations which can be solved to yield the modal amplitudes $(A = a + jb)$. Let $A = \{A_1, A_2, ...\}^T$ and dropping the subscript denoting the first harmonic term, these two equations are:

$$N^a \left(A, A^2, ..., \bar{A}, \bar{A}^2, ... \right) = 0$$
and
$$N^b \left(A, A^2, ..., \bar{A}, \bar{A}^2, ... \right) = 0 \tag{3.13}$$

In the next paragraph, it will be shown how these equations can be manipulated to solve for the coefficients (A) numerically.

3.2.1 Numerical Implementation of the Harmonic Balance Method.

The governing differential equations obtained with the analytical model developed in Chapter 2, can be written in a structural dynamic equivalent form as:

$$M(q,\dot{q},\ddot{q})\ddot{q} + D(q,\dot{q},\ddot{q})\dot{q} + K(q,\dot{q},\ddot{q})q - F\cos(\Omega t) = 0 \tag{3.14a}$$

with M, the nonlinear mass matrix, D the nonlinear damping matrix and K the nonlinear stiffness matrix. F is the forcing vector. The origin of the terms decides the matrix placing. If a term of the form, $\ddot{q}q$, originated from the kinetic energy expression, the term will be included as a mass term. If the term originated from the potential energy expression, the term will be

included as a stiffness term. Terms of the from, $\dot{q}\dot{q}$, will be included as damping terms.

Comparing eq. 3.14a to 3.8, the non-linear matrix N is :

$$N = M(q,\dot{q},\ddot{q})\ddot{q} + D(q,\dot{q},\ddot{q})\dot{q} + K(q,\dot{q},\ddot{q})q - F\cos(\Omega t) \quad (3.14b)$$

In the harmonic balance method, the assumed solution for a modal degree-of-freedom (q_i) is of the form:

$$q_i = A_i e^{j\Omega t} + \bar{A}_i e^{-j\Omega t} \quad (3.15)$$

and using eq.'s 3.13, the problem can be formulated as:

$$N_A^a\left(A,A^2,...,\bar{A},\bar{A}^2,...\right)A +$$

$$N_{\bar{A}}^a\left(A,A^2,...,\bar{A},\bar{A}^2,...\right)\bar{A} = F^a \quad (3.16a)$$

and

$$N_A^b\left(A,A^2,...,\bar{A},\bar{A}^2,...\right)A +$$

$$N_{\bar{A}}^b\left(A,A^2,...,\bar{A},\bar{A}^2,...\right)\bar{A} = 0 \quad (3.16b)$$

The matrices are the Fourier coefficient matrices, with:

$$N_A^a = \frac{1}{\pi}\int_0^{2\pi} \left[K - \Omega^2 M + j\Omega D\right] e^{j\Omega t}\cos(\Omega t)d(\Omega t) \quad (3.17a)$$

$$N_{\bar{A}}^a = \frac{1}{\pi}\int_0^{2\pi} \left[K - \Omega^2 M + j\Omega D\right] e^{-j\Omega t}\cos(\Omega t)d(\Omega t) \quad (3.17b)$$

$$N_A^b = \frac{1}{\pi}\int_0^{2\pi} \left[K - \Omega^2 M + j\Omega D\right] e^{j\Omega t}\sin(\Omega t)d(\Omega t) \quad (3.17c)$$

$$N_{\bar{A}}^b = \frac{1}{\pi}\int_0^{2\pi} \left[K - \Omega^2 M + j\Omega D\right] e^{-j\Omega t}\sin(\Omega t)d(\Omega t) \quad (3.17d)$$

$$F^a = \frac{1}{\pi} \int_0^{2\pi} F \cos(\Omega t) \cos(\Omega t) \, d(\Omega t)$$

(3.17e)

Eq. 3.16b can be used to express $\overline{A}$ in terms of A:

$$\overline{A} = \left[-N_{\overline{A}}^b \right]^{-1} N_A^b A$$

(3.18)

Placing this result in eq. 3.16a, yields:

$$A = \left[N_A^a - N_{\overline{A}}^b N_A^{b-1} N_{\overline{A}}^a \right]^{-1} F^a$$

(3.19)

Note that the matrices (N) are functions of both A and the complex conjugate of A. This formulation is slightly different from the formulation used by Bowden [1988]. In this form, if m is the number of modal degrees-of-freedom, the amplitudes (A) can be determined by two matrix inversions. Given that the number of calculations required to invert a matrix of order m is m^3, the required number of calculations to solve for the modal amplitudes, A, in this formulation is $2m^3$. If the formulation of Bowden [1988] was used, the number of calculations would have been $(2m)^3$. The formulation used in this research, since $(2m)^3 > 2m^3$, significantly reduced the computational effort required to solve for the modal amplitude vector (A).

3.3 Numerical Solution of Time Independent Non-linear Equations

Eq. 3.19 of the previous section is a non-linear equation in terms of the modal amplitudes (A). The solution of nonlinear equations is not trivial as illustrated by the following quote from "Numerical Recipes" [Press, et al, 1987], *"There are no good, general methods for solving systems of more than one non-linear equation"*. In this research an inverse iteration scheme and a Newton-Raphson scheme were used to solve for the modal amplitudes (A) from eq. 3.19. An alternative method, although not used in this research, will also be outlined. The method, known as the Continuation Method, requires undesirable algebraic manipulation of the

governing differential equations. However, based on the limiting results obtained with the other two methods, future researchers may be inspired to implement this method. The next paragraphs will outline the three methods; the inverse solution technique (3.3.1), the Newton-Raphson method (3.3.2) and the continuation method (3.3.3).

3.3.1 Inverse Solution Technique

In the inverse solution technique, the matrices in eq.'s 3.19 are calculated using the solution for the modal amplitude at the previous iteration step. If n denotes the iteration step number, the process is:

- For iteration n, calculate the matrices N_A^a, N_A^a, N_A^b and N_A^b using eq.'s 3.17 and the solution for A^{n-1} at the previous iteration step.
- Solve for A^n using eq.'s 3.16a and 3.16b.
- Repeat the procedure until convergence.

As in all non-linear solution methods, it was found in practice that the method performed well if the initial guess for A was close to the final solution. This method yielded good results for moderate forcing levels but failed to converge for high force excitation levels, especially when jump phenomena occurred. Convergence was improved by implementing an adaptive under-relaxation solution technique. The modal amplitude of mode (i) at the next iteration was calculated as follows:

$$A_i^n = A_i^{n-1} + \frac{\delta A_i^{n-1}}{\left[1 + \dfrac{\sum\limits_{i=1}^{M} \delta A_i^{n-1}}{M}\right]^p}$$

where $\delta A_i^{n-1} = A_i^* - A_i^{n-1}$ and

$A_i^* = $ Solution from eq. 3.16

(3.20)

The power (p) was adjusted to yield the fastest convergence and the value used in this research was p = 2. This approach yielded better results than the

84

standard under-relaxation method. In the results presented in Chapter 6, the forced response characteristics were predicted by calculating the modal amplitudes for various forcing frequencies and amplitudes. The linear solution for **A**, with all the non-linear terms set to zero, was used as an initial guess at the lowest excitation frequency (if the forcing frequency was increased) or the highest excitation frequency (if the forcing frequency was decreased). At forcing frequencies other than these frequencies, the solution at the previous excitation frequency was used as an initial guess.

3.3.2 Newton-Raphson Method

An alternative solution approach to the inverse solution technique, is the Newton-Raphson method. For the Newton-Raphson method, eq. 3.19 can be written as:

$$
\mathbf{N}^f(\mathbf{A}) = \mathbf{A} - \left\{ \mathbf{N}_A^a - \mathbf{N}_A^b \mathbf{N}_A^{b^{-1}} \mathbf{N}_A^a \right\}^{-1} \mathbf{F}^a = 0
\tag{3.21}
$$

$\mathbf{N}^f$ can be expanded into a Taylor series, namely:

$$
\mathbf{N}_i^f(\mathbf{A} + \delta\mathbf{A}) = \mathbf{N}_i^f(\mathbf{A}) + \sum_{k=1}^{m} \left\{ \frac{\partial \mathbf{N}_i^f}{\partial A_k} \delta A_k \right\} + O(\delta\mathbf{A}^2)
\tag{3.22}
$$

where $\mathbf{N}_i^f$ is the i'th equation of $\mathbf{N}^f$. By neglecting terms of $\delta\mathbf{A}^2$ and higher, eq. 3.22 yields a linear set of equations for the corrections ($\delta\mathbf{A}$) that simultaneously move each function (i) closer to the zero , namely:

$$
\sum_{k=1}^{m} \left\{ \frac{\partial \mathbf{N}_i^f}{\partial A_k} \delta A_k \right\} = - \mathbf{N}_i^f
\tag{3.23}
$$

The Jacobian $\mathbf{J} = \sum_{k=1}^{m} \left\{ \frac{\partial \mathbf{N}^f}{\partial A_k} \right\}$ was calculated numerically using $\delta\mathbf{A}$ of the previous iteration step. The same adaptive under-relaxation scheme used in the inverse iteration scheme was used in this method to improve the convergence. The Newton-Raphson method yielded better results than the inverse iteration scheme and converged for almost all combinations of excitation amplitudes and frequencies that were used.

The solution process is:

- Starting out with the linear solution, calculate the Jacobian (J).
- Find the correction term (δA) from eq. 3.23.
- Calculate the updated modal amplitude vector (A) using eq. 3.20.
- Repeat with updated solution until convergence is reached.

3.3.3 Continuation Method

The continuation method [Ricther and DeCarlo, 1983] arises from branches in mathematics not widely studied in engineering circles (Algebraic Topology and Differential Topology) and is best illustrated by a simple example. Let:

$$F(z) = z^2 + z + 1 \tag{3.24}$$

The objective is to find $F(z) = 0$. The solutions can easily be obtained as:

$$z_{1,2} = \frac{-1 \pm \sqrt{-3}}{2} \tag{3.25}$$

In the continuation method, $H(z,r)$ is defined as:

$$H(z,r) = z^2 + rz + 1 \tag{3.26}$$

with $r = [0,1]$. Note that at $r = 1$, $H(z,r) = F(z)$ and at $r = 0$, $H(z,r) = \pm\sqrt{-1}$. Differentiating H with respect to r, yields:

$$\frac{dH(z(r),r)}{dr} = 2z\frac{dz}{dr} + r\frac{dz}{dr} + z = 0 \tag{3.27}$$

which reduces to the following initial value problem for $z(r)$.

$$\frac{dz}{dr} = \frac{-z(r)}{2z(r) + r}$$

where

$$z(0) = \pm\sqrt{-1} \tag{3.28}$$

Solving the initial value problem, yields:

$$z(r) = \frac{-r \pm \sqrt{r^2 - 4}}{2}$$

(3.29)

Eq. 3.29 could also have been obtained from solving eq. 3.28 numerically. H is known as the Homotopy function. In other words this method is the integration of the derivative with respect to the variable (r) from the known linear solution (r=0) to the required nonlinear solution (r=1). This method can also be applied to systems of non-linear equations. The only problem is the algebraic manipulation required to obtain equation 3.27. This method however, presents the possibility of finding all the roots of a non-linear system of equations which may justify the additional effort required. The reader is referred to Keller [Keller and Rabinowitz, 1977] for a more detailed discussion.

3.3.4 Note on Numerical Integration

The non-linear solutions methods used in this research were iterative and required evaluation of the non-linear, amplitude dependent matrices (eq.'s 3.17) at each iteration step. Given that the time functions, in this research, are continuous, the integrations of eq.'s 3.17 could be performed outside the iteration loop. This not only speeded up the solution but also made it more accurate. The accuracy was improved by using many integration points over the integration integral. If the integration was inside the iteration loop, more integration points would have slowed down the solution method. For example, by defining:

$$I_r^c = \frac{1}{\pi} \int_0^{2\pi} \left[e^{jr\Omega t} \cos(\Omega t) \right] d(\Omega t)$$

(3.30a)

$$\bar{I}_r^c = \frac{1}{\pi} \int_0^{2\pi} \left[e^{-jr\Omega t} \cos(\Omega t) \right] d(\Omega t)$$

(3.30b)

$$I_r^s = \frac{1}{\pi} \int_0^{2\pi} \left[e^{jr\Omega t} \sin(\Omega t) \right] d(\Omega t)$$

(3.30c)

$$\bar{I}_r^s = \frac{1}{\pi} \int_0^{2\pi} \left[e^{-jr\Omega t} \sin(\Omega t) \right] d(\Omega t)$$

(3.30d)

a term in N_A^a of the form Cq_1, with C being a coefficient, could be evaluated as:

$$\frac{1}{\pi} \int_0^{2\pi} \left[C\, q_1 \right] e^{j\Omega t} \cos(\Omega t) d(\Omega t) = C \left[A_1 I_1^c + \bar{A}_1 \bar{I}_1^c \right]$$

(3.31)

or a term in N_A^b of the form $Cq_1\dot{q}_2$ as:

$$\frac{1}{\pi} \int_0^{2\pi} \left[C\, q_1 \dot{q}_2 \right] e^{j\Omega t} \sin(\Omega t) d(\Omega t) =$$

$$j\Omega C \left[A_1 A_2 I_3^s + \bar{A}_1 A_2 I_1^s + A_1 \bar{A}_2 I_1^s + \bar{A}_1 \bar{A}_2 \bar{I}_1^s \right]$$

(3.32)

The evaluation of the non-linear matrices (eq.'s 3.31) thus becomes a simple multiplication of the matrix coefficients, the modal amplitude(s) and the pre-evaluated integral expressions (I).

Although the integrals could have been evaluated by hand, numerical integration (Simpson's rule) was used. Using this method instead of doing the integrations inside the iteration loop, the time spend solving for the modal amplitudes was reduced by a factor of 8. This approach cannot be used for systems with discontinuous (or piecewise linear) elements (mass, damping or stiffness).

3.3.5 Presentation of Results

The output from the force response analysis was the excitation amplitude and frequency dependent amplitudes. The modal amplitudes could be linearly combined to yield the slosh force amplitudes and the tank displacement. Amplitude versus excitation frequency curves could be obtained, for force excitation amplitudes corresponding to experimental values. The magnitude of the modal amplitudes were calculated as follows:

from
$$A_i e^{j\Omega t} + \bar{A}_i e^{-j\Omega t} = 2a_i \cos(\Omega t) - 2b_i \sin(\Omega t) \qquad (3.33)$$

if
$$A_i = a_i + jb_i \qquad (3.34)$$

then
$$A_i e^{j\Omega t} + \bar{A}_i e^{-j\Omega t} = R_i \cos(\Omega t + \phi_i) \qquad (3.35)$$

if
$$R_i = 2\sqrt{a_i^2 + b_i^2} \qquad (3.36)$$

and
$$\phi_i = \tan^{-1}\left\{\frac{b_i}{a_i}\right\} \qquad (3.37)$$

The relative modal amplitudes could also be graphically presented by drawing the fluid free surface for various phase angles. Given a solution (A^s) for the modal amplitudes, the equivalent linear frequencies and damping ratios were calculated by plugging the solution into the homogeneous equivalent of eq. 3.15. That is, a solution of the form:

$$q^s = A^s e^{\lambda t} + \bar{A}^s e^{\lambda t} \qquad (3.38)$$

is assumed, where $(\bar{\lambda})$ is the complex conjugate of $\lambda = \zeta + j\omega$. Using this assumed solution, the homogeneous equation can be written as:

$$\left[\lambda^2 M\left(q^s, \dot{q}^s, \ddot{q}^s, \lambda\right) + \lambda D\left(q^s, \dot{q}^s, \ddot{q}^s, \lambda\right) + \right.$$
$$\left. K\left(q^s, \dot{q}^s, \ddot{q}^s, \lambda\right)\right] A^s e^{\lambda t} + \left[\bar{\lambda}^2 M\left(q^s, \dot{q}^s, \ddot{q}^s, \lambda\right) + \right.$$
$$\left. + \bar{\lambda} D\left(q^s, \dot{q}^s, \ddot{q}^s, \lambda\right) + K\left(q^s, \dot{q}^s, \ddot{q}^s, \lambda\right)\right] \bar{A}^s e^{\lambda t} = 0 \qquad (3.39)$$

It can be shown that eq. 3.39 is satisfied if:

$$f(\lambda) = \left[\lambda^2 M\left(q^s, \dot{q}^s, \ddot{q}^s, \lambda\right) + \lambda D\left(q^s, \dot{q}^s, \ddot{q}^s, \lambda\right) + \right.$$
$$\left. K\left(q^s, \dot{q}^s, \ddot{q}^s, \lambda\right)\right] A^s e^{\lambda t}$$
$$= 0 \qquad (3.40)$$

Eq. 3.40 is a nonlinear equation with time dependent coefficients. If the damping ratios (ζ) are small, that is: $\zeta \ll 1$, the equation can be

linearized by expanding $f(\lambda)$ as a Fourier series. Let $\lambda \approx j\omega t$ and retaining only the first term in the Fourier series, $f(\lambda)$ can be approximated as:

$$f(\lambda) = \left[a_1(\lambda) - jb_1(\lambda) \right] A^s e^{j\omega t}$$

(3.41)

where

$$a_1 = \frac{1}{2\pi} \int_0^{2\pi} f(\lambda) \cos(\omega t) \, d(\omega t)$$

(3.42a)

$$b_1 = \frac{1}{2\pi} \int_0^{2\pi} f(\lambda) \sin(\omega t) \, d(\omega t)$$

(3.42b)

The eigen-values are obtained by finding the roots of the determinant of the characteristic equation (eq. 3.43).

$$\left[a_1(\lambda) - jb_1(\lambda) \right] A^s = 0$$

(3.43)

In this research, the eigen-values were calculated using Muller's method [Press, et al, 1987]. The eigen-frequencies (ω) and the eigen-damping ratios (ζ) thus obtained can be compared with their linear values to quantify the effects introduced by the nonlinear terms.

3.4   Least Squares Method

Another way to approach the problem of predicting the dynamic characteristics of coupled nonlinear systems is to pose the problem as a standard curve fit problem. Consider the following set of nonlinear equations:

$$M(q,\dot{q},\ddot{q},t,\ldots)\ddot{q} + D(q,\dot{q},\ddot{q},t,\ldots)\dot{q} +$$
$$K(q,\dot{q},\ddot{q},t,\ldots)q = F \cos(\Omega t)$$

(3.44)

Eq. 3.44 can be conveniently written as:

$$M(q,\dot{q},\ddot{q},t,\ldots)\ddot{q} + D(q,\dot{q},\ddot{q},t,\ldots)\dot{q} + K(q,\dot{q},\ddot{q},t,\ldots)q -$$
$$F \cos(\Omega t) = E(q,\dot{q},\ddot{q},t,\ldots) = 0$$

(3.45)

A solution of the form:

$$q_i = A_1^i \cos(\omega_1^i t + \phi_1^i) + A_2^i \cos(\omega_2^i t + \phi_2^i) + \dots \qquad (3.46)$$

is assumed for each of the modal degrees-of-freedom (q_i). The error function is defined as:

$$\varepsilon(q,\dot{q},\ddot{q}) = \int_{T_l}^{T_u} [E(q,\dot{q},\ddot{q},t)]^T [E(q,\dot{q},\ddot{q},t] dt \qquad (3.47)$$

The integration limits (T_l and T_u) will be determined by the accuracy required and the period over which the assumed function must be valid.

The least squares solution for the unknown coefficients can be obtained defining the Norm (known as the the L^2 Norm or Least Squares Norm):

$$L^2 = \varepsilon(q,\dot{q},\ddot{q}) \qquad (3.48)$$

Posing the problem in this fashion allows for the unknown coefficients (A_j^i, ω_j^i and ϕ_j^i) to be determined with standard least squares numerical methods. The difference between this approach and the harmonic balance method discussed in the previous section is that the equivalent norm for the harmonic balance method would be:

$$\varepsilon(q,\dot{q},\ddot{q}) = \frac{1}{2\pi} \int_0^{2\pi} \{ E(q,\dot{q},\ddot{q},t) \} \cos(\Omega t) d(\Omega t) \qquad (3.49)$$

Note that the number of terms in the assumed solution of eq. 3.42 is arbitrary and that the frequencies are not fixed to be equal to the excitation frequency (Ω). More complex assumed solutions can also be assumed, for example: saw tooth, square wave, exponential functions, etc. This method, given the correct initial conditions and assumed solution functions, will yield the correct solution for time transient non-linear behavior. The method is best illustrated by applying it to the well known non-dimensional one-degree-of-freedom spring/mass oscillator with a cubic spring. The governing differential equation is:

$$\ddot{x} + \bar{d}\dot{x} + \bar{k}x + \bar{k}_3 x^3 = \bar{F}\cos(\Omega t) \qquad (3.50)$$

Assuming a solution of the form:

$$x = A_1 \cos\left(\omega_1 t + \phi_1\right) + A_2 \cos\left(3\omega_2 t + \phi_2\right) \tag{3.51}$$

and using the following values for the non-dimensional coefficients:

$$\bar{d} = 0.1$$
$$\bar{k} = 1.0$$
$$\bar{k}_3 = 0.15$$
$$\bar{F} = 1.0 \tag{3.52}$$

the least squares method was used to solve for the unknown coefficients in eq. 3.51. Fig. 3.1 plots the least squares obtained frequencies (ω_1 and ω_2) versus the least squares obtained amplitudes A_1 (curve 1) and A_2 (curve 2). A three term assumed solution was also used but yielded an insignificant increase in accuracy.
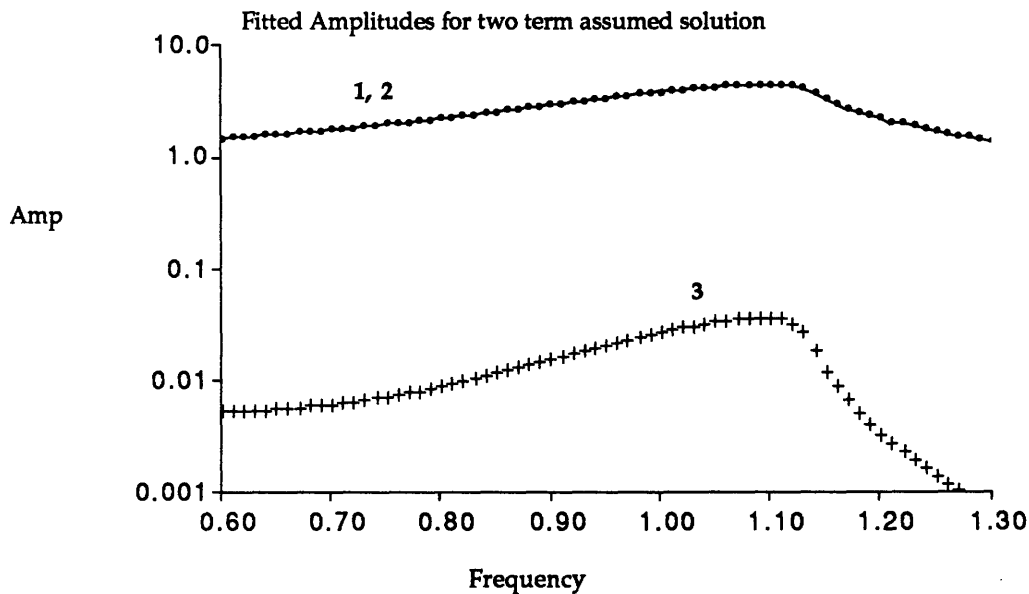
Figure 3.1   Amplitudes as Predicted with Least Squares and Harmonic Balance Methods.

Note: Curve 1 is the amplitude versus frequency curve obtained with the harmonic balance method and curve 2 the amplitude versus frequency of the first term in the least squares assumed solution. These two curves fall on top of each other. Curve 3 is the amplitude versus frequency for the second term in the least squares assumed solution.

Harmonic Balance versus Least Squares Fit

Amp

$$
\begin{array}{r}
5.00 - \\
3.75 - \\
2.50 - \\
1.25 - \\
0.00 -
\end{array}
$$

0.60 0.70 0.80 0.90 1.00 1.10 1.20 1.30

Frequency
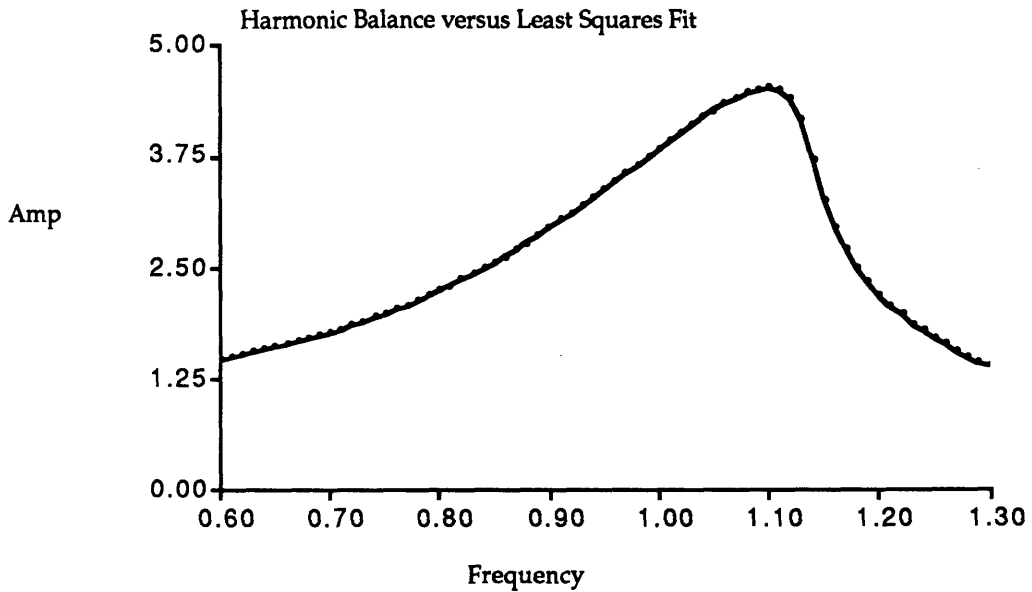
Figure 3.2   Harmonic Balance versus Least Squares Method.

Note: The Harmonic balance method solution is plotted as a line and the least squares method solution is plotted with the dots. Plotted on linear scale for clarity.

Residual Time Traces

Residual

$$
\begin{array}{r}
1.00 - \\
0.50 - \\
-0.00 - \\
-0.50 - \\
-1.00 -
\end{array}
$$

0.00 2.00 4.00 6.00 8.00 10.00 12.00 14.00
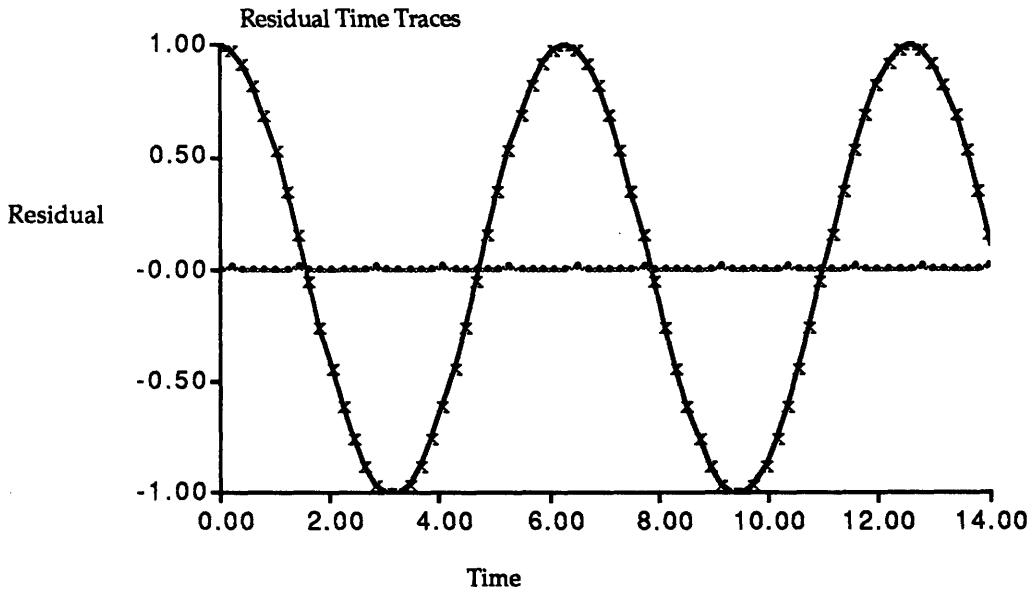
Time

Figure 3.3   Residual Time Traces.

Note: Trace 1 is the forcing signal and trace 2 is residual after the least squares solution is subtracted from the forcing signal

93

Fig. 3.2 compares the amplitude A_1 with the amplitude obtained with the harmonic balance method discussed in the previous section. The two curves are almost identical. Fig. 3.3 shows how well the least squares solution fits the forcing function. Curve 1 is the forcing function and curve 2 is a time plot of the error $E(q, \dot{q}, \ddot{q}, t)$.

At this point it is important to point out a peculiar feature of the least squares method. The accuracy of the least squares method depends on the assumed solution. For example; if only one term was used in the assumed solution, namely, let:

$$x = A_1 \cos(\omega_1 t + \phi_1)$$

(3.53)

the amplitude versus frequency curve obtained with the least squares method will not match the results obtained with harmonic balance method. Fig. 3.4 illustrates this behavior. Curve 1 is the amplitude (A_1) versus frequency (ω_1) as obtained with the least squares method and the assumed solution of eq. 3.51.
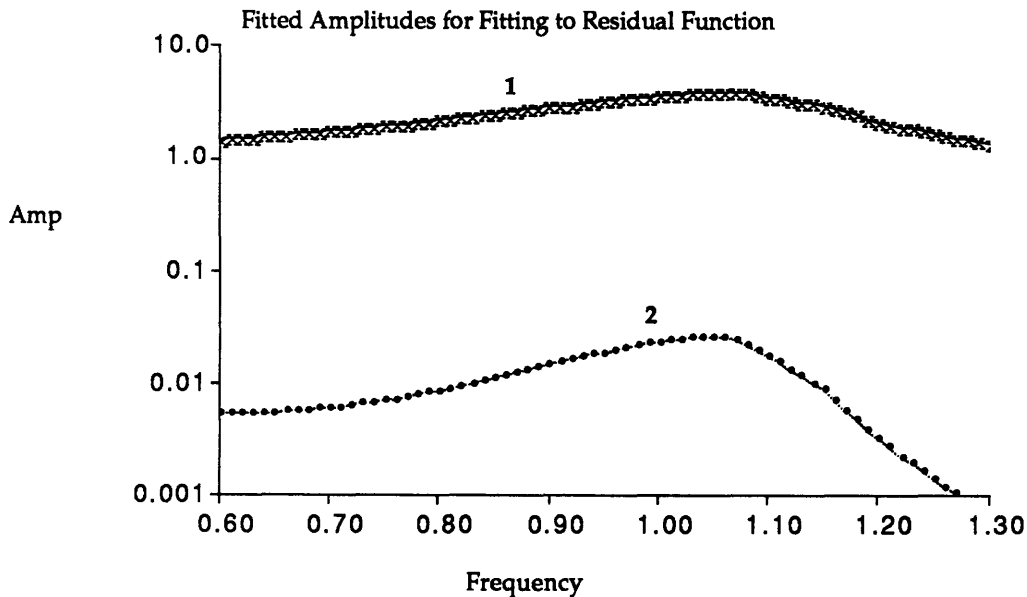
Figure 3.4   Amplitudes as obtained by Least Squares Method.

Note: Curve 1 is the predicted amplitude versus frequency obtained by fitting a single term assumed solution to the problem. Curve 2 is the amplitude predicted by the least squares method if another single term assumed solution is fitted to the residual of the first fit.

Residual Time Traces
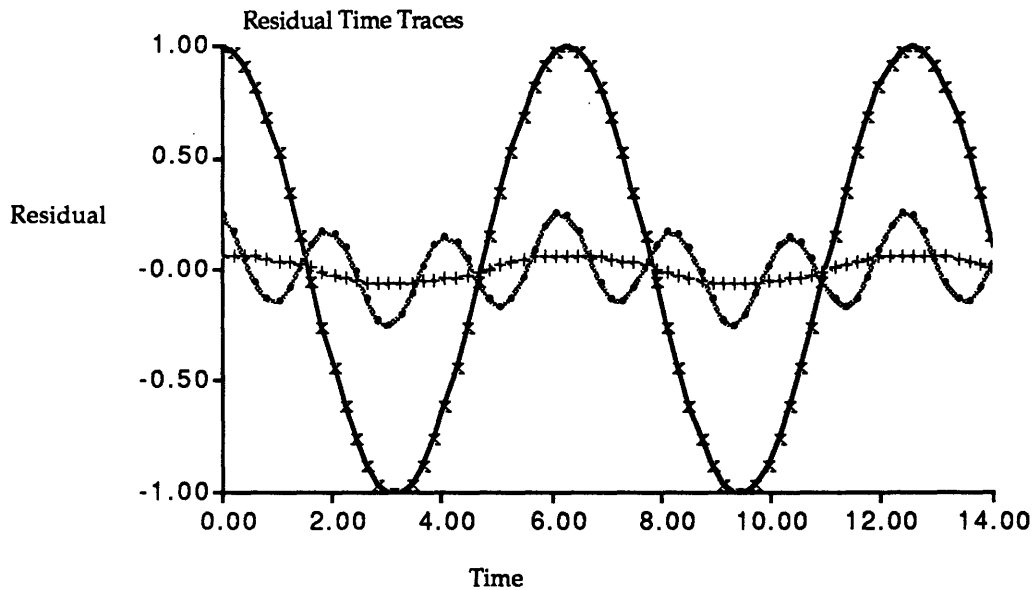
Figure 3.5 **Residual Time Traces for the Least Squares Solution of Fitting Sequentially to the Residual Functions.**

Note: Trace 1 is the forcing function, trace 2 the residual after the first least squares solution is subtracted from the forcing function and trace 3 after the second least squares solution is subtracted from trace 2.

This curve is different from the solution obtained with the two term solution of eq. 3.51 and the harmonic balance solution. This behavior can be explained by noting that as the least squares method increases the amplitude A_1 to minimize the error in the "harmonic" ($\omega_1 = \Omega$) term, the $\cos^2(3\omega_1 t)$ term increases.. Since the least squares method does not have a matching term in the assumed solution to cancel this term, the method tries to minimize the two terms and yields an amplitude A_1 smaller than the amplitude predicted by the harmonic balance method. This point is illustrated by fitting a second solution to the residual time function of the first least squares solution. Define the new error function as:

$$E_n(x,\dot{x},\ddot{x},t) = \bar{F}\cos(\Omega t) + \left[\omega_1^2 - \bar{k}\right]A_1\cos\left(\omega_1 t + \phi_1\right) -$$
$$\bar{d}A_1\sin(\omega_1 t + \phi_1) - \bar{k}_3 A_1^3\cos^3(\omega_1 t + \phi_1) \qquad (3.54)$$

and fit the following assumed solution to the resultant error function:

$$x' = A_2\cos\left(\omega_2 t + \phi_2\right) \qquad (3.55)$$

95

Curve 2 in Fig. 3.4 depicts the result of this step. Fig. 3.5 depicts the error time residual functions. Curve 1 being the original forcing function, curve 2 the residual time trace after subtracting the first solution (A_1 and ω_1) from the forcing term and curve 3 is the residual time trace after subtracting the second solution (A_2 and ω_2) from the first residual time trace. The presence of a component oscillating at the harmonic frequency is clear in curve 3, indicating that the first solution yielded an amplitude A_1 smaller than expected.

One more observation must be made as to the integration limits of eq. 3.47. The convergence and thus the accuracy of the least squares method was found to be sensitive to:

(a)   The number of oscillations in the integration time limits
(b)   and the number of points per cycle.

As a rule of thumb, it was found that at least 10 cycles were required to yield an accurate frequency estimates and at least 20 points per cycle for accurate amplitude estimates. The number of required cycles refers to the maximum frequency of interest which was in the cubic spring example, the super-harmonic term.

3.4.1 Summary of the Least Squares Method

The least squares method is an attractive method to predict the nonlinear behavior of coupled nonlinear systems. The advantages of this method over the harmonic method discussed in the previous section are:

- Determination of response amplitudes at frequencies other than the excitation frequency.
- Prediction of transient nonlinear behavior.
- Use of non-sinusoidal functions.
- Can be combined with the harmonic balance method to determine the location of the dominant sub- and super-harmonic terms.

The method has several disadvantages, namely:

- Requires time integration at each least squares iteration.
- Requires insight in order to select a "complete" assumed solution.
- Requires many cycles and points per cycle for accurate estimates of the frequencies and amplitudes.

The first and last points make this method unattractive for use in this research but future research may benefit by combining this method with the harmonic balance method to determine the sub- and super-harmonic terms or determining the impulse characteristics of non-linear systems.

3.5 Conclusion

In this chapter the methodology to solve for the dynamic characteristics of the non-linear fluid behavior has been discussed and outlined. In Chapter 6, the Harmonic balance method will be used to determine the non-linear dynamic fluid slosh behavior experimentally observed in the study models. Chapter 6 will also investigate the power of the Inverse solution and Newton-Raphson methods.

Chapter 4

Experimental Apparatus and Procedures

The experimental apparatus used to investigate the nonlinear dynamic characteristics of contained fluids is described in this chapter. The first section discusses the motivation behind the experimental design, the second describes the apparatus and the theory of operation, the third outlines the actual experimental procedure, while the final section gives the equipment calibration results.

4.1   Design Philosophy

Full scale testing of a fluid-spacecraft system is neither practical nor efficient for determining the nonlinear dynamic characteristics of fluid-spacecraft systems..   The cost associated with full scale testing and the question of the validity of extrapolating the full-scale results to other fluid (fluid tank)/spacecraft configurations, are the main drawbacks.   Sub-scale model testing is an attractive alternative.   Sub-scale model testing is not only cheaper but many configurations can be tested to model many fluid/spacecraft configurations.   The size and weight of sub-scale models are also suitable for testing on board the space shuttle.   Other arguments against full-scale testing is the hazard involved and the long turn around time between tests.

In order to determine whether sub-scale models can be used, the relevant scaling parameters must be determined.   Assuming a rigid-wall container, the relevant non-dimensional parameters governing the fluid-spacecraft motion are:

Non-dimensional Fluid Scaling Factors:

$$\text{Bond Number} = \text{Bo} = \frac{\rho g a^2}{\sigma} \tag{4.1a}$$

$$\text{Capillary Viscous Parameter} = N_{v_2} = v\sqrt{\frac{\rho}{\sigma a}} \qquad (4.1b)$$

$$\text{Contact Angle} = \theta \qquad (4.1c)$$

Non-dimensional Fluid-Spacecraft Coupling Parameters:

$$\text{Mass ratio} = \mu = \frac{m_{fluid}}{m_{spacecraft}} \qquad (4.2a)$$

$$\text{Frequency ratio} = v = \frac{f_{slosh}}{f_{spacecraft}} \qquad (4.2b)$$

Most spacecraft fluid tanks are large enough that these are the only parameters that must be matched in a sub-scale model.

4.1.1 Matching the Bond Number and Selecting a Model Fluid

Low full scale Bond numbers can be achieved by changing the model tank radius, a, the density of the fluid, ρ, the surface tension, σ, or by placing the test article in reduced gravity. Fig. 4.1 depicts the Bond number as a function of the tank displacement from the spacecraft center of gravity for three representative spacecraft propellants namely; hydrazine, liquid oxygen and liquid hydrogen in a 2 meter diameter tank. In studying this figure a typical Bond number range of 10 - 200 can be defined.

Past research [Peterson] has shown that impulse tests are unreliable in determining the nonlinear characteristics of a fluid system. The main reason is that the results of many impulse tests under the same g-level and initial conditions are required to obtain a reliable data base. Harmonic tests in which the test article is excited long enough for the homogeneous terms to decay, are considered the best way to determine the nonlinear behavior. The 0-g time of the KC135 Reduced Gravity Test Facility (approximately 40 - 50 seconds), is too short for harmonic tests but random initial conditions
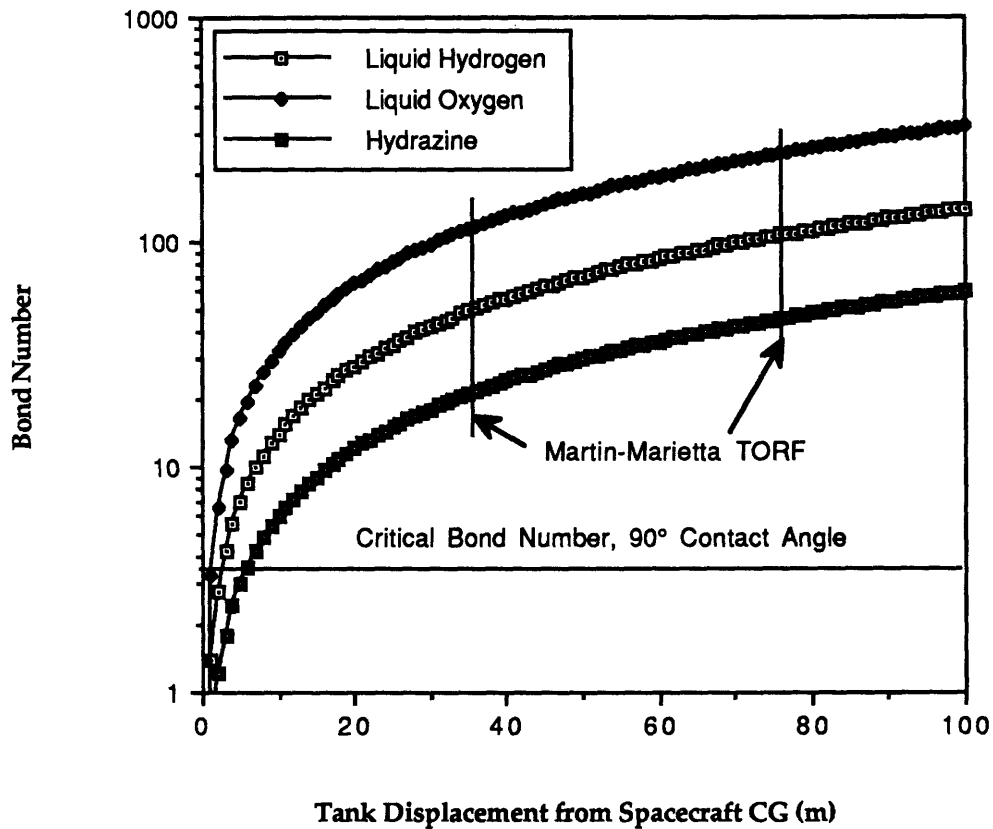
Figure 4.1   Typical Spacecraft Bond Numbers. (Repeat of Fig. 1.1).

and the varying g-level, during the 0-g period, yields scattered impulse test results. The other alternative is in-orbit testing but shuttle availability ruled this out as an option for this research. Thus, although g levels other than 1-g can be achieved, a 1-g test environment was decided on for this research. A follow-up experiment, designated the MODE experiment, has been scheduled to fly on the shuttle in the near future. The purpose of this experiment will be to validate the 1-g results obtained in this research. By properly choosing model fluids, the Bond number of actual systems can be matched in a 1-g test setup by scaling the tank geometry, (a), thus properly scaling the fluid vibration dynamics.

The scaled model tank radius is given by:

$$a_m = a_{fs} \sqrt{\frac{\rho_{fs} g_{fs} \sigma_m}{\rho_m g_m \sigma_{fs}}}$$

(4.3)

in which the subscript m denotes model and the subscript fs denotes full scale or actual tank. The size of the scaled model tank is determined by the specific surface tension σ/ρ, of the full scale propellant (or liquid) and the selected scale model fluid. In this research, model tanks with dimensions ranging from 1.5 cm to 2 cm were used that covered a Bond number range of 30 - 120. This Bond number range is typical for present fluid/spacecraft systems.

At this point something must be said about the selection of a scale model fluid. Water, with its high specific surface tension, (σ/ρ), and inert nature is a likely candidate. The high specific surface tension of water will yield the same Bond number for a much larger model tank than any other non-reactive fluid. Water also has been approved for in orbit use. The main drawback of water is that it has a high contact angle hysteresis in glass containers. The nonlinear effects of contact hysteresis angle makes the prediction of the linear fluid characteristics difficult [Dodge, 1967]. While no liquid vapor can be hysteresis free, it is usually very small for spacecraft propellants [Abramson, 1966]. In order to minimize the effects of contact angle hysteresis, a 2% photoflo-water solution was selected as a modeling fluid. Photoflo is a surfacant (wetting agent) used in photographic processing which reduces the surface tension of water by a factor of two and reduces the contact angle to near 0° (5° - 15° experimentally). Finally Table 4.1 is a summary of the properties of selected spacecraft propellants and possible model fluids.

The non-dimensional parameter, contact angle (eq. 4.1c), is the requirement that the contact angle of the model fluid must match the contact angle of the actual fluid. The contact angle of a 2% Photoflo-water solution approaches zero which matches the "wetting" contact angle found with most spacecraft propellants.

Table 4.1   Properties of Spacecraft Propellants and Model Fluids

Fluid	Density ρ (gm/cm^3)	Kinematic Viscosity v (cm^2/sec^2)	Surface Tension σ (dyne/cm)	Kinematic Surface Tension σ/ρ (cm^3/sec^2)
Typical Propellants:				
Liquid Hydrogen	0.07	0.0020	1.9	26.8
Liquid Qxygen	1.14	0.0017	13.2	11.6
Hydrazine	1.01	0.0097	63.2	62.7
Typical Modelling Fluids:				
Water	1.00	0.0101	72.8	72.9
Methanol	0.79	0.0075	22.6	28.5
2% Photoflo/ Water	1.00	0.0100	36.0	36.0

Given the properties of a 2% Photoflo-Water solution, the scaled Bond number is given by:

$$Bo_{Model} = 27\,778\,a^2g \tag{4.4a}$$

or for testing in a 1-g environment:

$$Bo_{Model} = 272\,500\,a^2 \tag{4.4b}$$

Equations 4.4 are valid for a in meter.

4.1.2   Matching the Capillary Viscous Parameter

In contrast with the Bond number that scales with a^2, the capillary viscous parameter scales with $a^{-1/2}$. Therefor, given a specific model fluid

(with a given kinematic viscosity), matching the Bond number will result in a mismatched capillary viscous parameter. The viscosity will increase as the tank size decreases and the relative strength of viscous forces to gravity and surface tension forces are inflated. As with wind tunnel testing, some mismatch in the viscosity scaling is acceptable. The primary effect of viscosity is to increase the fluid damping ratio. Peterson [1987] showed that if the fluid damping is small, its effects on the fluid vibration dynamics is at least the order of the nonlinearities. The expected increased fluid damping ratios (due to the viscous effects) in very small tanks, will alter the nonlinear behavior of the fluid. Thus very low Bond numbers cannot be investigated using 1-g Bond number scaled models. In general Bond numbers below 20 are considered to be too low to yield accurately scaled 1-g models. This conclusion restricted the use of the 1-g experimental apparatus discussed in this chapter to scale models with Bond numbers exceeding 20.

4.1.3 Matching the Mass and Frequency Ratios

In order to accurately simulate the coupled dynamics of the fluid/spacecraft in the sub-scale model, the fluid mass fraction, μ and frequency ratio, v, must be matched. A simple spring/mass model of the spacecraft mode is an obvious choice. However, mechanical friction, high model tank weight versus fluid weight, manufacturing tolerances and lack of flexibility, led the design to be a more sophisticated compliant actuator. With this device, the motion of the spacecraft mode (single degree-of-freedom) was simulated by using the measured fluid reaction slosh force as the excitation for an analog representation of the spacecraft dynamics. The dry mass inertia force was subtracted from the measured force signal to allow for higher mass ratios.

This device allowed for mass ratios as high as 0.4 and frequency ratios ranging from 0.5 to 1.5. With the analog simulation of the spacecraft mode, the modal damping could also be altered (in a range $\xi = 0.02$ to 0.12).

4.2 Experimental Apparatus

As outlined in the introduction, several model tanks were tested. The geometry and design of each of these model tanks will be discussed in Chapter 5. In general, the tanks were made of stock pyrex, the base and end cap of the tanks were made of black delrin. Delrin is easy to machine precisely, has a low density, and is chemically inert. The top plates were Lexan, 0.125" thick. The fluid mass in the test article was specified by the height above the bottom of the tank.

Fig. 4.2 is a schematic block diagram of the experimental apparatus. Fig. 4.3 is a video image of the primary test equipment. Each component in the block diagram performs a unique function. The slosh reaction balance and resolver measured and amplified the planar (x) and non-planar (y) reaction forces as well as the acceleration vector of the model tank. The dry mass compensator removed the dry mass inertia force component from the measured force and the spacecraft mode simulator is an analog computer which solved the differential equation of motion for the spacecraft one degree-of-freedom mode. The electro-mechanical shaker moved the tank as specified by the output of this simulator. The actual displacement of the tank base was measured with a non-contact proximeter probe. A personal computer, hooked to a CAMAC data acquisition crate, generated the external excitation signal and recorded the measured forces, accelerations and the tank displacement. The personal computer was also programmed to perform most of the experimental tests automatically.

The measurement of the fluid slosh reaction forces is only an indirect measurement of the fluid dynamics. The dynamic motion of the free surface was recorded, for selected cases, by a video camera with a macroscopic lense.

The subsequent paragraphs will describe each of the components in greater detail.
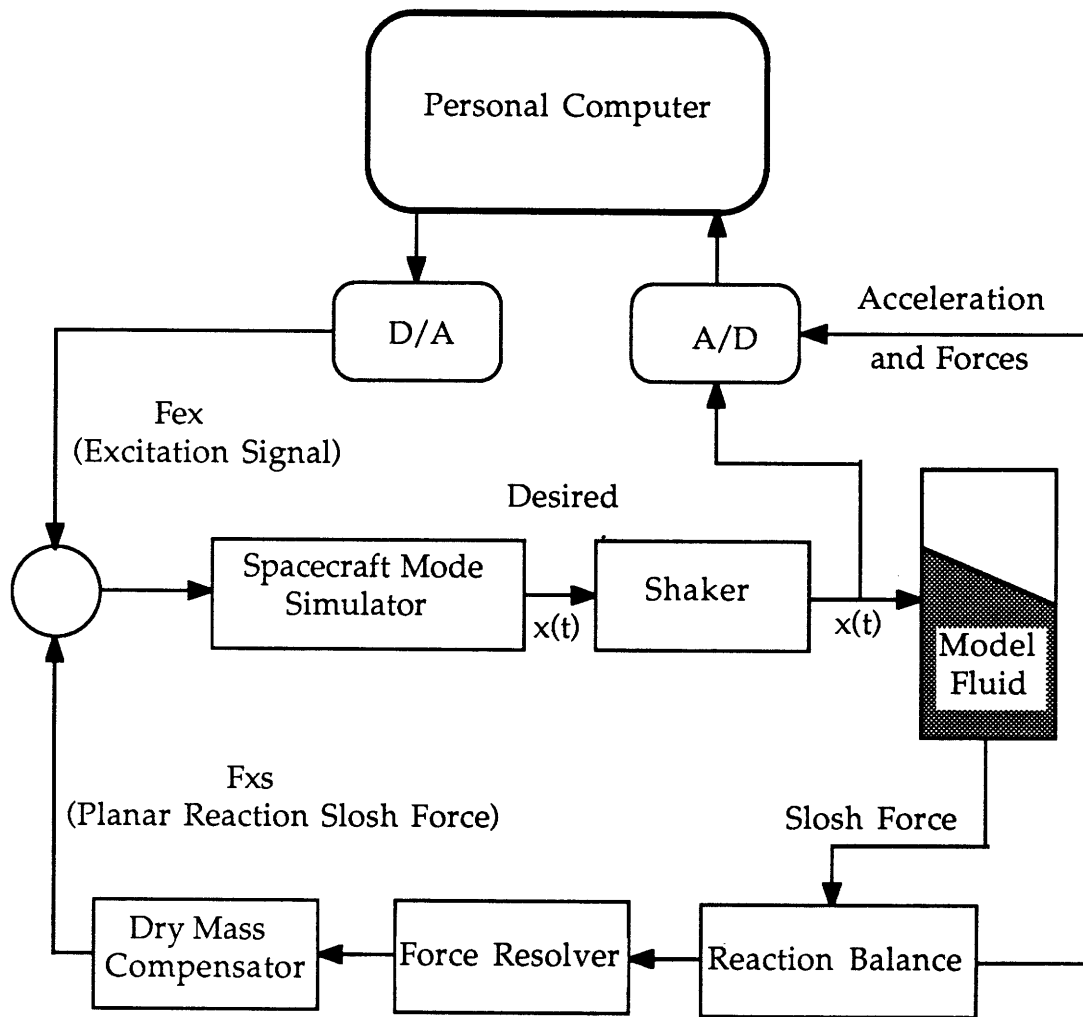
Figure 4.2   Experimental Apparatus Component Block Diagram.
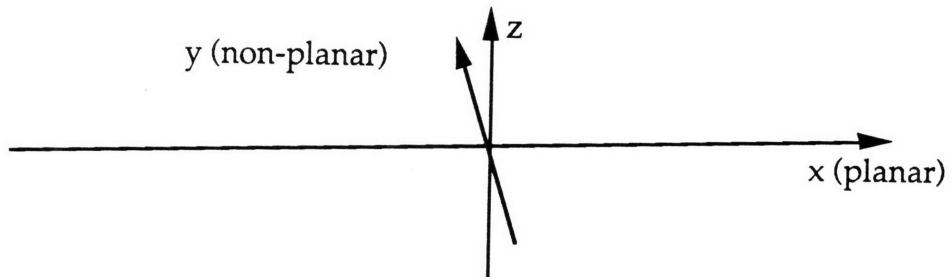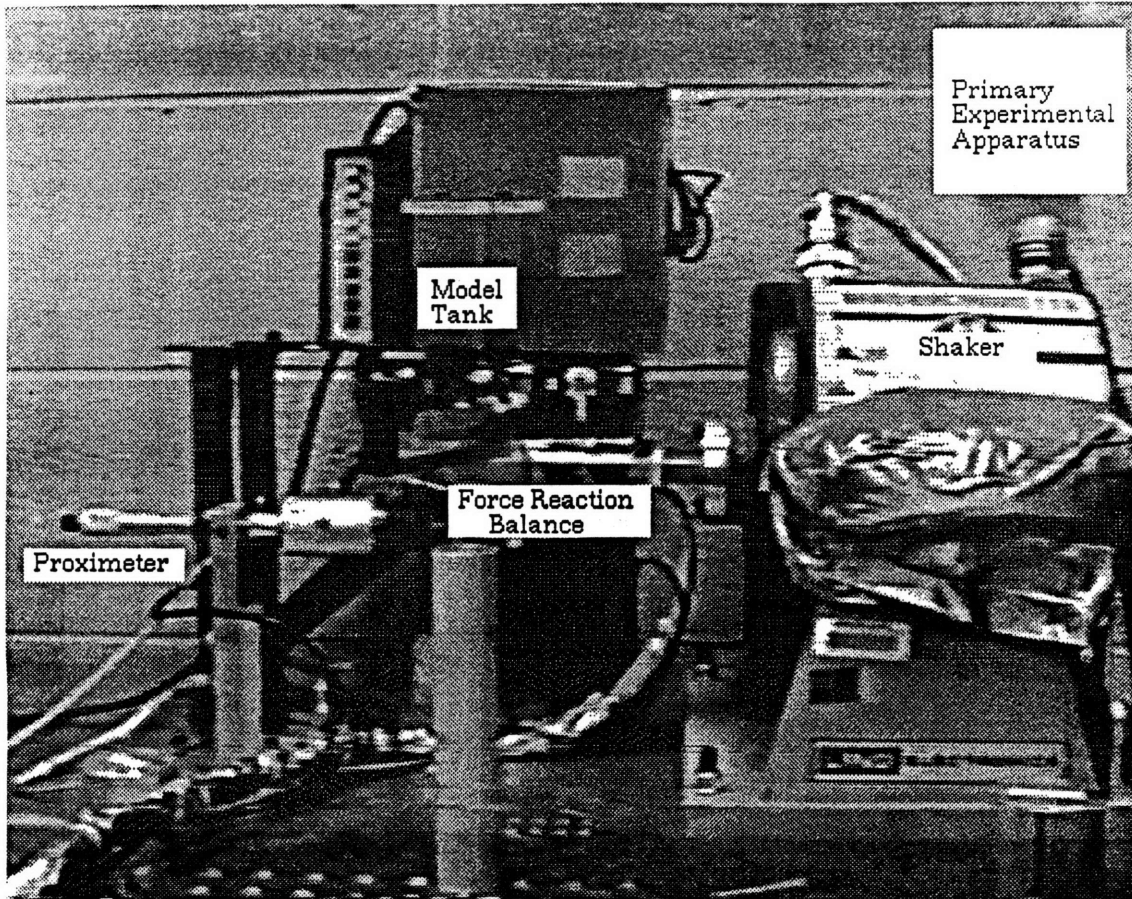
Figure 4.3   **A Video picture of a Part of the Experimental Setup.**

The Modal Tank, Reaction Balance, Shaker and Proximeter are visible.

4.2.1 Slosh Force Reaction Balance and Resolver

The reaction slosh forces produced by sub-scale model tanks are very small. Peterson [1987] showed that for tank sizes with characteristics dimensions of 25 - 50 mm, the expected reaction forces are in the 10^{-3} to 10^{-1} Newton. These forces are of the same magnitude as the dry mass inertial forces, and the external environmental forces, such as air currents [Dodge and Garza, 1970]. The force balance and resolver used in this experiment is the one developed by Peterson [1987]. The model tank was mounted on this balance, which measured horizontal components of the fluid slosh force against the tank walls. The reaction balance (Fig. 4.4) consisted of a triad of sensitive piezoelectric force transducers mounted on a statically determinant structure. The planar (F_{xs}), non-planar (F_{ys}) slosh forces and vertical reaction slosh moment (M_{zs}) could be obtained from the measured transducer signals by applying the reaction balance force and moment equilibrium equations [Peterson, 1987]. This linear transformation was performed by a signal conditioning circuit.

A similar triad of accelerometers, see Fig. 4.4, measured the acceleration of the reaction balance in the horizontal plane. The planar and non-planar acceleration components were resolved using a electronic circuit similar to that of the force resolver. Using the measured accelerations, the dry mass inertial force was subtracted electronically from the measured force signal. The remaining force signals are a direct measurement of the fluid reaction slosh forces.

The load path between the tank model and the transducers are provided by three stainless steel flexures, each 0.005" thick, 0.5" wide and 0.75" long. The bending stiffness of the flexures are considerably smaller than their axial stiffness. The thickness ratio, $t/l = 0.7\%$, was small enough for the flexures to be modeled as providing only axial stiffness, making the force balance system statically determinant. Eq. 4.5 gives the relationship between the measured forces and required forces.

Top View
Scale: 1" = 0.80"

Side View
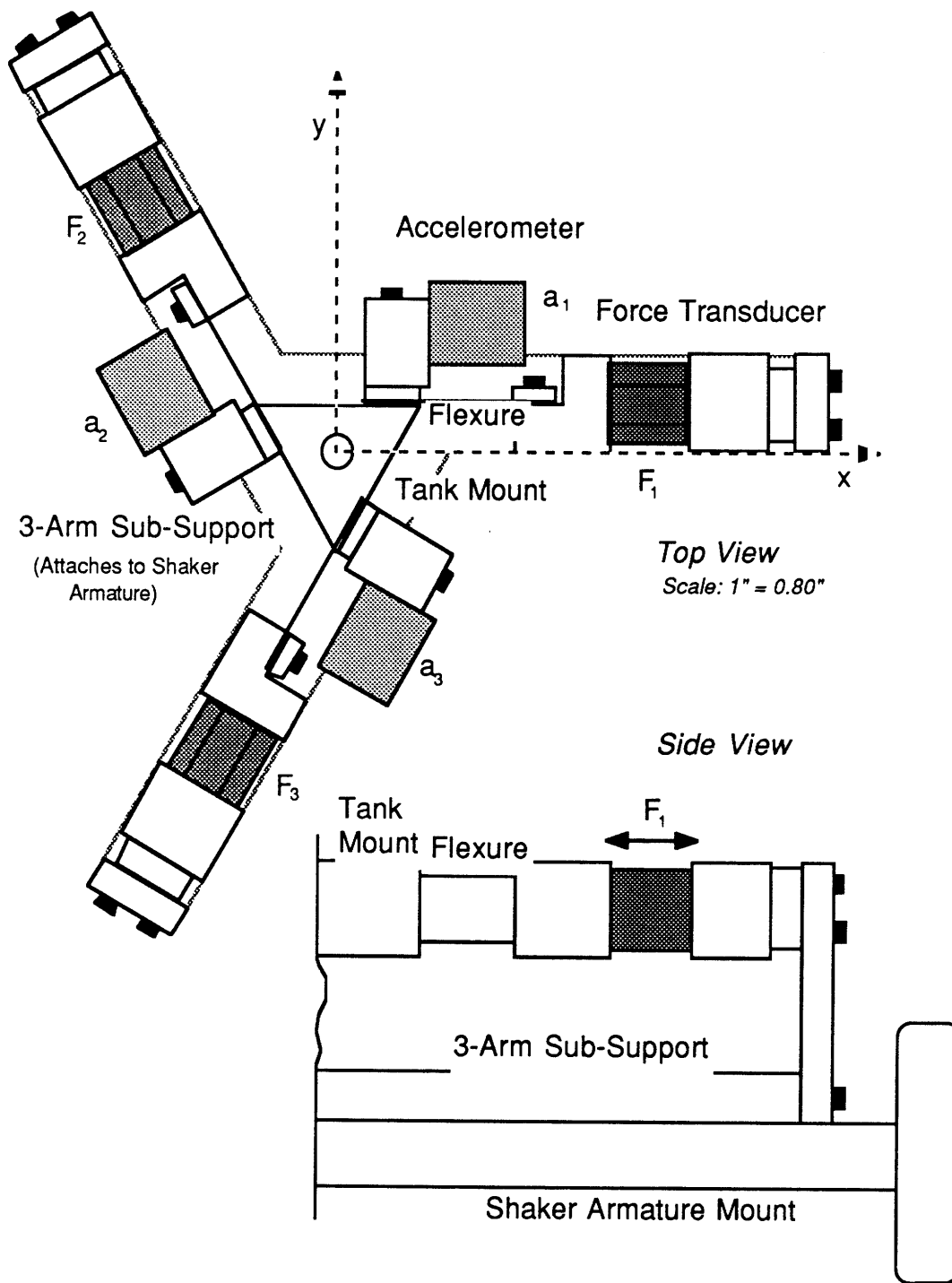
Figure 4.4   Slosh Force Reaction Balance.

$$\begin{Bmatrix} F_x \\ F_y \\ M_z \end{Bmatrix} = \begin{bmatrix} -1 & \dfrac{1}{2} & \dfrac{1}{2} \\ 0 & -\dfrac{\sqrt{3}}{2} & \dfrac{\sqrt{3}}{2} \\ r_t & r_t & r_t \end{bmatrix} \begin{Bmatrix} F_1 \\ F_2 \\ F_3 \end{Bmatrix} \qquad (4.5)$$

where F_1, F_2 and F_3 are the transducer outputs and rt is the offset radius of the transducers from the center of the force balance.

4.2.2 Dry Mass Compensator

The force applied to the reaction balance is the sum of the fluid slosh reaction forces and the D'Alembert force of the dry mass. The force is:

$$\begin{Bmatrix} F_x \\ F_y \\ M_z \end{Bmatrix}^{D'Alembert} = \begin{bmatrix} m_D & 0 & 0 \\ 0 & m_D & 0 \\ 0 & 0 & I_D^z \end{bmatrix} \begin{Bmatrix} a_x \\ a_y \\ \ddot{\theta} \end{Bmatrix} \qquad (4.6)$$

where m_D is the dry mass of the tank and support structure (between the tank and the load cells) and I_z the moment of inertia about the z-axis of the tank and support structure (between tank and load cells). The transformation for the measured accelerations to the desired components in eq. 4.6 is given by equation 4.7.

$$\begin{Bmatrix} a_x \\ a_y \\ \ddot{\theta} \end{Bmatrix} = \begin{bmatrix} \dfrac{2}{3} & -\dfrac{1}{3} & -\dfrac{1}{3} \\ 0 & -\dfrac{\sqrt{3}}{3} & \dfrac{\sqrt{3}}{3} \\ -\dfrac{1}{3r_a} & -\dfrac{1}{3r_a} & -\dfrac{1}{3r_a} \end{bmatrix} \begin{Bmatrix} a_1 \\ a_2 \\ a_3 \end{Bmatrix} \qquad (4.7)$$

r_a being the radial offset from the force balance center to the accelerometer position. Finally the desired slosh force components are given by:

$$\begin{Bmatrix} F_{xs} \\ F_{ys} \\ M_{zs} \end{Bmatrix} = \begin{Bmatrix} F_x \\ F_y \\ M_z \end{Bmatrix}^{D'Alembert} + \begin{Bmatrix} F_x \\ F_y \\ M_z \end{Bmatrix} \qquad (4.8)$$

4.2.3 Signal Conditioning

Fig. 4.5 is a schematic representation of the slosh force conditioning process. The force measurements (F_1, F_2, F_3) were provided as the output voltages of the transducer signal conditioning amplifiers with a nominal sensitivity of 112 mV/N. The acceleration measurements were the output from their transducer signal amplifiers with a nominal sensitivity of 100 mV/g. The next stage in the signal conditioning process was a differential amplifier input stage to remove any possible electrical ground loops which might otherwise corrupt the signals with noise. The output voltages from the transducer amplifiers were thereby referenced to the equipment rack power supply ground voltage. The gain of each signal was also adjusted to yield an equal gain for all the transducers. Three special electronic units transformed the amplified and equalized transducer signals to slosh force measurement signals (Eq. 4.8).
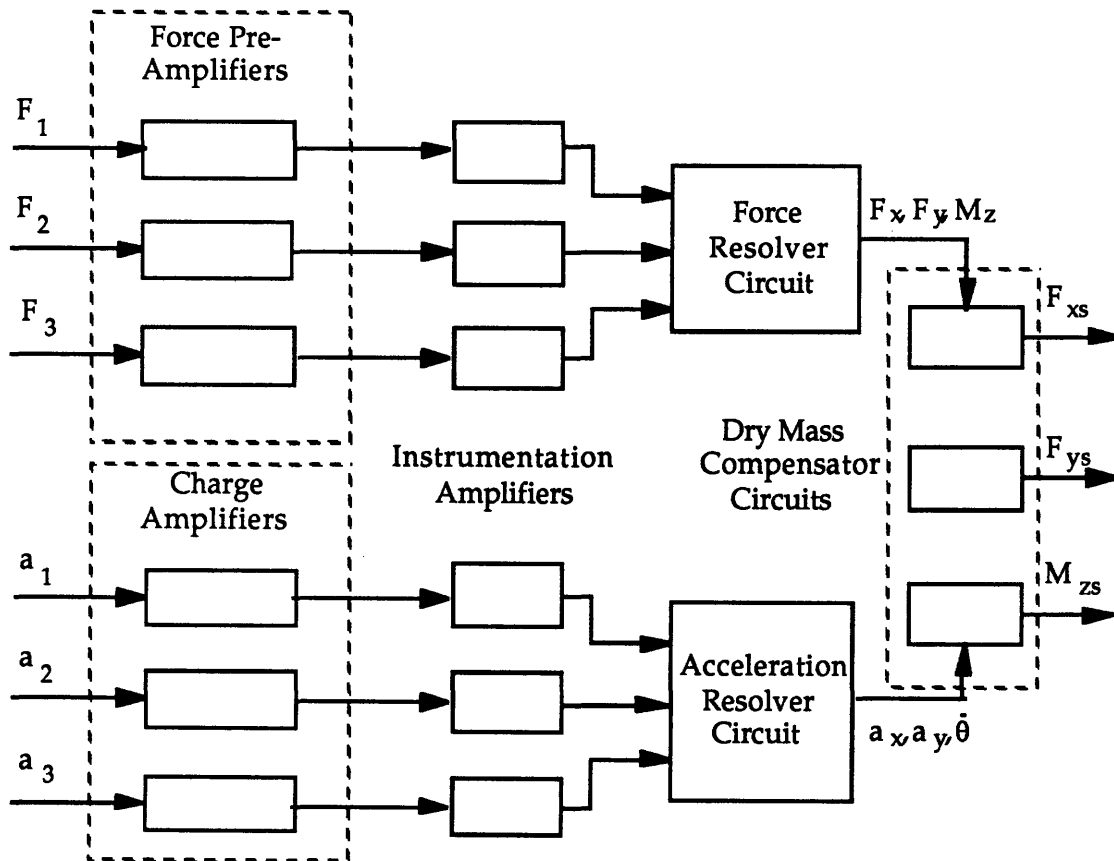
Figure 4.5   **Schematic of the Slosh Force Signal Conditioning Process.**

110

The first unit performed the matrix multiplications on the force and acceleration signals, the second compensated for the dry mass inertia, and the final stage amplified the resultant slosh force output signals.

4.2.4 Measuring the Tank Motion

The actual planar (x) displacement of the tank was measured with a non-contact Bentley-Nevada 25 mm proximeter probe (Fig. 4.6). This measurement provided the time history of the simulated spacecraft response.
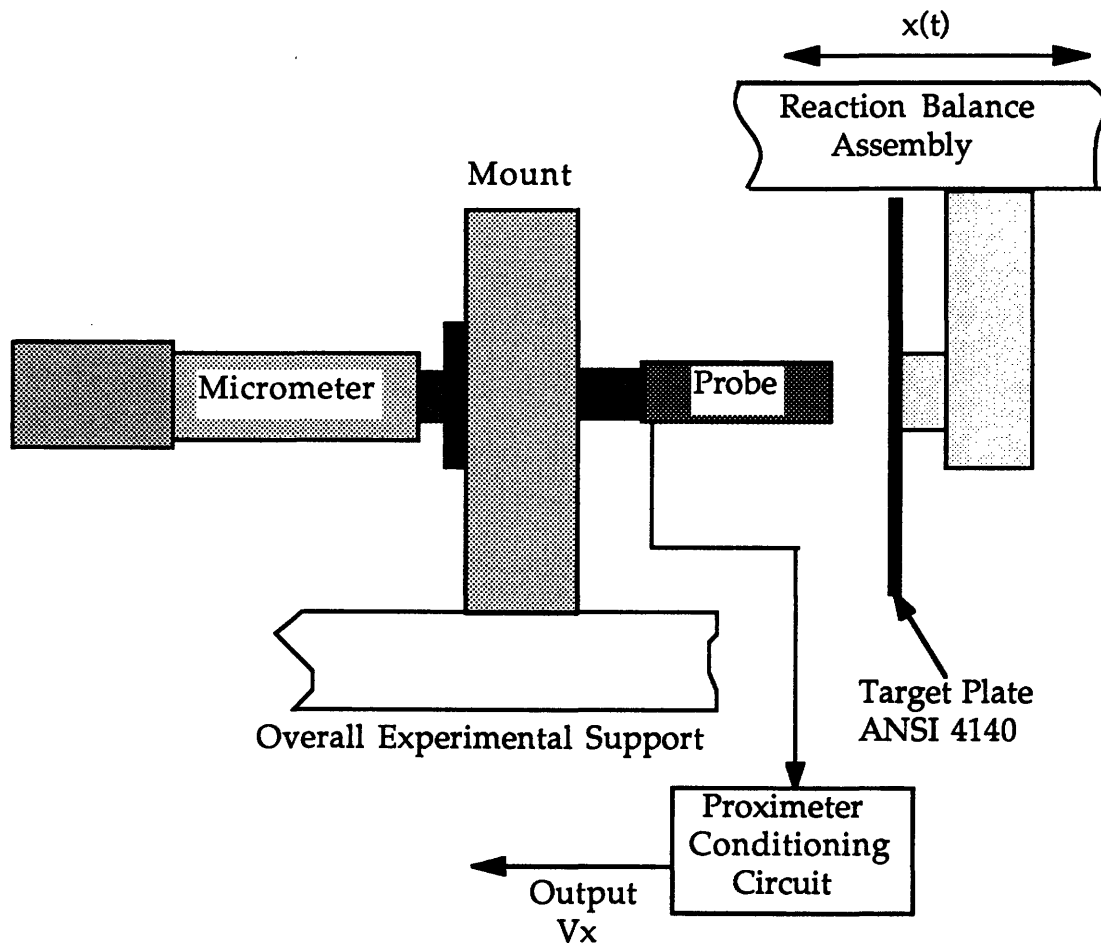
Figure 4.6   Proximeter Assembly.

The device was mounted on a separate support structure in line with the shaker axis and a target plate of ANSI 4101 turbine steel was attached to the reaction balance assembly. The proximeter measured the width of the gap between the target plate and the proximeter head. The nominal sensitivity was 0.79 V/mm and the proximeter, when used with the chosen target material and plate size, has a linear range of +/- 12 mm.

The proximeter was mounted with a non-rotating micrometer head to facilitate calibrations. The micrometer could measure the proximeter/target gap with an accuracy of 0.03 mm. The proximeter had its own power supply and was amplified via a AD521 differential instrumentation amplifier to reference the output voltage to the primary ground voltage used in the analog equipment rack.

4.2.5 Compliant Actuator

The compliant actuator calculated the tank displacement which would correspond to the motion of the two degree-of-freedom spacecraft mode, using the measured slosh forces and tank displacement. The simulation circuit is an analog computer circuit [Peterson, 1987] which computed the desired tank motion in real-time. The required motion was provided by a electromagnetic shaker. The second order differential equation that describes the motion of the tank is:

$$m\ddot{x} + c\dot{x} + kx = F_{ex} + F_{xs} \qquad (4.9)$$
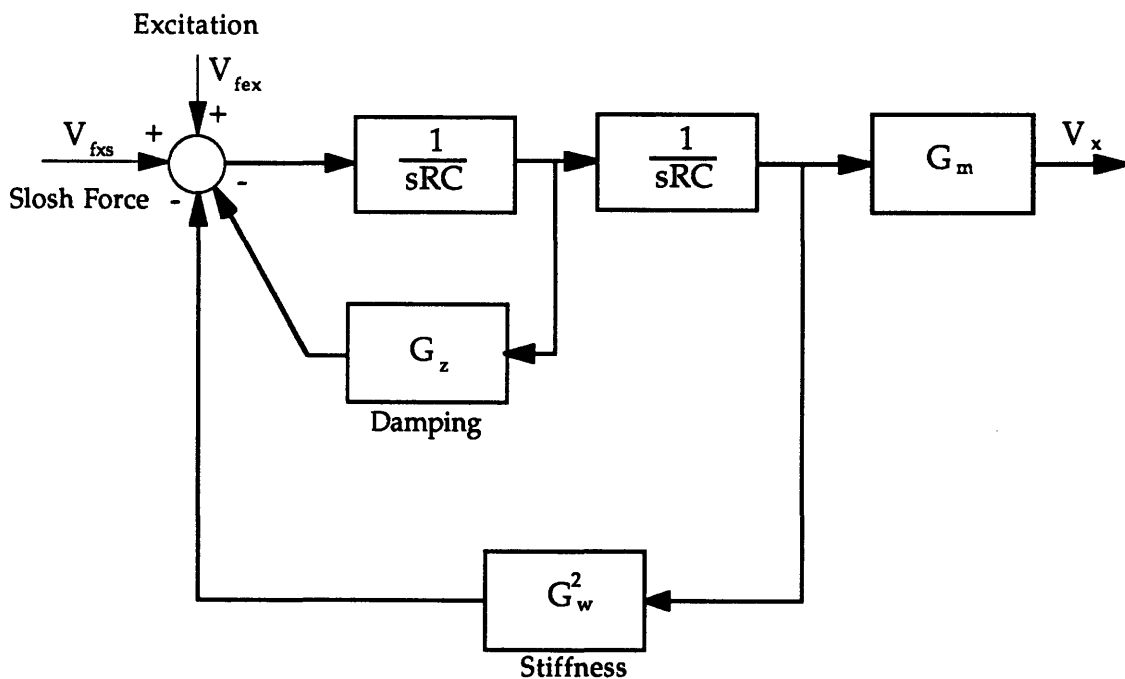
Table 4.7   Spacecraft Mode Simulator Block Diagram.

The commanded voltage to the shaker can be solved for since the fluid slosh force F_{xs} is a measured function of time. Fig. 4.7 is a block diagram of the analog model of the spacecraft mode. Let Kx, be the proximeter gain and Kf, the slosh force gain, then the equations for the mass, damping and stiffness of the simulator are:

113

$$m = \frac{(RC)^2 K_x}{G_m K_f}$$

$$(4.10a)$$

$$c = \frac{G_\zeta RC K_x}{G_m K_f}$$

$$(4.10b)$$

$$k = \frac{G_\omega^2 K_x}{G_m K_f}$$

$$(4.10c)$$

From elementary dynamics, the modal frequency and damping ratios are:

$$f = \frac{1}{2\pi}\sqrt{\frac{k}{m}} = \frac{G_\omega}{2\pi RC}$$

$$(4.11)$$

$$\zeta = \frac{c}{2m\omega} = \frac{G_\zeta}{2G_\omega}$$

$$(4.12)$$

The gains, G_m, G_ω and G_ζ, could be set via potentiometers. A Ling 420 electro-mechanical shaker, powered by an Altec amplifier, was used to move the force reaction balance and model tank assembly. In order to compensate for certain unwanted shaker dynamics, a close loop servo was used. The actual displacement of the shaker, as measured with the proximeter, was compared with the desired displacement to generate an error signal. The error signal was fed through a compensator to remove the unwanted dynamics. The net effect of the servo controller was to provide both position and rate feedback to the shaker motion.

4.2.6 Data Acquisition and Experimental Control

An IBM PC was used to control the experiment, as well as acquire and store the measured force, acceleration and displacement signals. The nonlinear characteristics of the fluid was determined by driving the model tank with a sinusoidal excitation signal of varying amplitude and frequency (harmonic excitation). Fig. 4.8 is a flow diagram of the control program.

A control program, written in FORTRAN, given the user selected frequency and amplitude ranges, generated the excitation signal . The user

114

also selected the number of excitation levels, but the number of frequency steps were determined by program. The frequency of the excitation signal was matched with the discrete frequencies possible with the Fast Fourier Transform (FFT) used to determine the amplitudes of the measured signals. Instead of calculating and storing the complete FFT's of each of the channels for each excitation frequency and amplitude, only the complex amplitude of the signals at the excitation frequency was calculated (using an FFT) and stored. This reduced the amount of data to be stored, facilitated data reduction and gave results matching the results obtained with the harmonic balance method used in the analysis (Chapter 3). The program could also store the time traces but this was only done in a few selected cases. The excitation frequency was matched with the discrete FFT frequency bin's center frequency to minimize spill-over errors.

```
┌─────────┐     ┌──────────────────────────────────┐
│ Program │     │ Type of Test: Sinusoidal or Impulse │
│   FST   │────▶│ Frequency Range: f-start to f-end   │◀──── User Input
└─────────┘     │ Number of Amplitude levels          │
                │ Amplitude Range: %'s of Maximum     │
                └──────────────────────────────────┘
```

```
┌──────────────────────────┐
│ Set A/D parameters (Frequency, │
│ # of Points, # of Channels)    │
└──────────────────────────┘
```

```
( Amplitude Loop )◀─────────┐
```

```
┌─────────────────┐
│ Generate and Load │
│ Excitation Signal │
└─────────────────┘
```

```
( Frequency Loop )
```

```
┌──────────────────────┐
│ Set D/A Output Frequency │
└──────────────────────┘
```

```
┌────────────────────┐
│ Trigger D/A to Output │
│ Excitation Signal     │
└────────────────────┘
```

```
┌──────────────────────────┐
│ Wait 5 seconds for Slosh Motion │
│ to Reach Steady State           │
└──────────────────────────┘
```

```
┌──────────────────────┐
│ Trigger A/D to Capture │
│ Measured Data          │
└──────────────────────┘
```

```
┌───────────────────────────┐
│ Store Time Traces if Required │
└───────────────────────────┘
```

```
┌──────────────────────────────┐
│ Perform FFT on Signals and Store │
└──────────────────────────────┘
```

```
                                                  Yes
        Yes    ╱ New ╲    No        ╱ New ╲    No
       ◀──────◀ Frequency ▶────────▶ Amplitude ▶────▶ ( Exit )
               ╲      ╱              ╲        ╱
```

Figure 4.8   **Control Program Flow Diagram.**

116

The frequency difference between points in an FFT is given by:

$$\Delta f = \frac{1}{T} = \frac{1}{N \Delta t}$$

(4.13)

where $1/\Delta t$ = sampling frequency at which the data was taken, N = number of data points in the time trace, and $T = N \Delta t$ = total time length of the data trace. The excitation frequency was set, by selecting the correct D/A output rate, to be a multiple of Δf.

The control program could also excite the fluid system with an impulse input of variable amplitude and time width. The program also programmed the CAMAC crate's A/D sampling parameters, namely; sampling rate, number of post trigger samples and number of active channels. A summary of the program sequence is:

- The program prompted the user for the number of amplitude levels, the range of amplitude levels (as a percentage of the maximum D/A voltage output of +/10 Volts), the type required(sinusoidal or impulse) and the excitation frequency range. Note that the level of excitation was determined by a series of gains (this included the gain of the D/A).

- The program then programmed the A/D for the number of required channels, the sampling rate and number of post-trigger samples,

- generated the excitation signal (the sinusoid was generated with a nominal frequency and the selected amplitude) and loaded this signal into the D/A's memory. The required frequency of excitation was achieved by altering the D/A's output frequency. The excitation signal had to be re-calculated for each new amplitude level.

- The program started the test by triggering the D/A to send out the excitation signal. The signal, filtered with a smoothing filter, was added to the spacecraft mode output (for coupled tests) to drive the electro-mechanical shaker.

117

- The A/D was triggered after a 5 second delay to store the incoming force, acceleration and displacement signals. The delay period ensured that the non-homogeneous terms, excited by the initial conditions, decayed before the data was taken.

- On completion of the data acquisition cycle, the program stored the data time traces on disk (if required) and performed FFT's on the data signals. Only the amplitudes corresponding to the excitation frequency were retained and stored on disk.

- The cycle was repeated for each of the excitation frequencies and amplitude levels.

- On completion of the test, the amplitude versus excitation frequency results were graphically checked before a different fluid system was tested.

Table 4.2 summarizes the relevant test parameters.

Table 4.2   Test Parameters

Parameter Description	Value	Units
D/A:		
Output Range:	+/- 10.0	Volts
Number of points describing excitation signal	8000	
A/D:		
Number of data points per channel	4096	
Number of active channels	4	
Sampling Frequency	200.0	Hz
Input Voltage Range	+/- 5.0	Volts
Time delay between start of excitation and start of data acquisition	5.0	seconds
Total time of data acquisition	25.5	seconds
Equivalent FFT frequency step (Δf)	0.4883	Hz

118
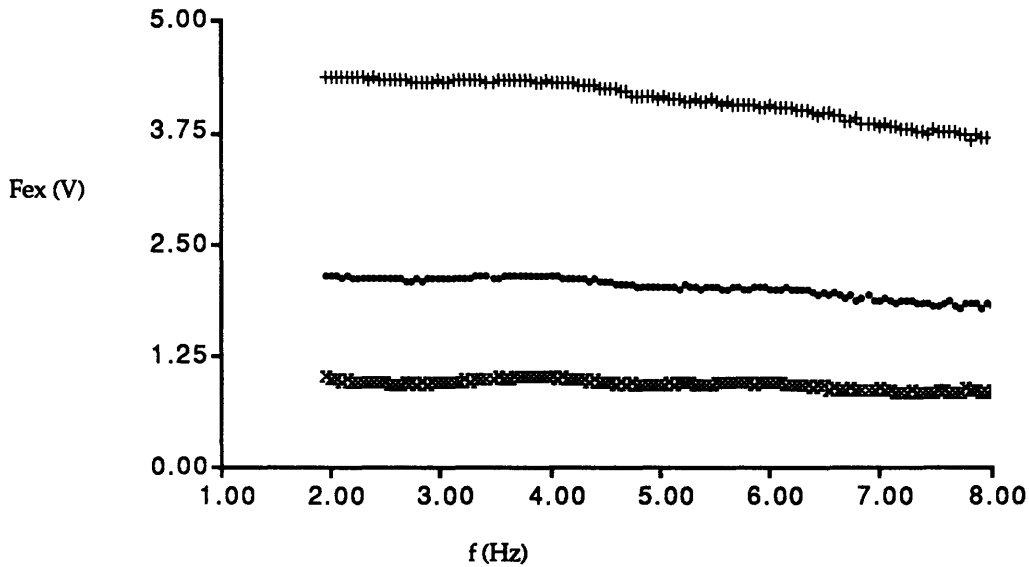
Figure 4.9   Effect of Smoothing Filter.

Output from D/A for three forcing excitation amplitudes (F_{ex}).

The smoothing filter (a low pass filter) between the D/A output and the shaker was used to remove the high frequency effect of the quantized signal. This filter had a corner frequency at 6 Hz which effectively made the excitation signal slightly frequency dependent (See Fig. 4.9). This frequency dependence was taken into account in the analysis.

4.3   Test Procedures

This section will describe the various test procedures followed in this research.

4.3.1 Pre-Test Procedure

The pre-test procedure was followed for both the uncoupled and coupled tests. In the uncoupled test, the spacecraft mode simulator was by-passed. The uncoupled tests were performed to identify the linear fluid eigen-characteristics and for comparison with coupled tests. The experimental

119

apparatus was calibrated before a new tank geometry was tested. The calibration procedures and results are described in the next section. The pre-test procedures were:

Model Tank Test Article Preparation:

The tanks were carefully washed before each test to ensure the glass surface free of airborne oils and dust particles. First the tanks were rinsed with distilled water, then reagent grade methanol was poured into the tank to wet the entire surface. The methanol was kept in the tank for approximately fifteen minutes. Afterwards, the tank was dried by turning it upside down on a glassware towel. The tank's dry mass was determined and recorded with a unique tank identification number. The next step was to add the correct amount of modeling fluid. This was done by placing the empty tank on a mass balance, zeroing the mass balance and adding the fluid until the correct fluid mass was reached. The mass balance could determine the mass to within 0.01 grams.

Determination of Dry Mass Null Gain (Coupled Tests only)

The dry mass null gain was determined by placing the clean, empty model tank on the force balance, shaking the balance with a known sinusoidal signal with a known frequency and amplitude, while the gain was adjusted until the observed slosh force, F_{fxs}, was zero. The residual dry mass was limited by system noise but a residual dry mass of less than 1 g could be inferred from the measured residual slosh force voltage.

4.3.2 Test Procedure

The only difference between the uncoupled tests and the coupled tests were that the spacecraft simulation circuit feedback path was removed from the loop. The output from the D/A was connected directly to the input port of the servo control circuit. This was the only difference between the uncoupled and coupled tests. The computer control program allowed for

both an impulse and a harmonic excitation signal but only a harmonic signal was used in this research. The test sequence was:

- Configure the spacecraft simulation circuit (only for the coupled tests).
- Supply power to all the test equipment, except the shaker amplifier.
- Run the control program (FST) on the personal computer.
  - Select the type of excitation (Harmonic or Impulse).
  - Set the excitation amplitude range
  - and the number of logarithmic amplitude increments.
  - Set the excitation frequency range.
  - Select whether the time traces must be stored or not.

At this point the program would calculate the excitation signal and download the signal to the D/A's memory. The program also provided the researcher with a digital voltmeter of the measured signals. The next step was to check the signals measured for the stationary tank:

- Check that the measured planar force voltage, V_{fxs}, was 0.0 V +/- 20 mV.
- Check that the measured non-planar force voltage, V_{fys}, was 0.0 V +/- 20 mV.
- Check that the measured tank displacement voltage, $V_x f$, was 3.5 V +/- 20 mV.
- Check that the measured planar acceleration voltage, V_{fys}, was 0.0 V +/- 20 mV.

These checks were required to ensure that none of the A/D's channels were saturated during the initialization process. The tank displacement proximeter was adjusted to yield a output voltage of 3.5 Volts for the stationary tank, to ensured that the measured voltage (during the harmonic tests) would not exceed the +/- 5 Volts input range of the A/D. At this point the computer program adjusted the D/A's output voltage to zero and notified the researcher that power could be supplied to the shaker amplifier. The researcher then initiated the test sequence, in which the fluid response

121

was recorded for a range of excitation frequencies and amplitudes. On completion of the test, the researcher was reminded to cut power to the shaker amplifier (to protect the experimental setup) and in which files the FFT results were stored.

4.3.3 Post-Test Procedure

On completion of a series of tests on a model tank geometry, the calibration of the experimental setup was verified before the next tank geometry was tested. The results of the experimental tests, in the form of an amplitude and phase file (or time traces of the measured results) was transferred from the IBM PC to a MicroVax (using the standard communications package: KERMIT) and from the MicroVax to a Mactintosh (again using KERMIT). The data was then scaled, according to the scaled calibration parameters (see next section), and graphically displayed with a graphics package developed specifically for this purpose.

4.4 Calibration

The different components of the experimental apparatus were individually calibrated before each test. The calibration procedure for each of these components are described in the next sections and the results are summarized in section 4.5.4.

$$f\,(Hz) = 0.065 + 2.77\,Gw, \quad R^{\wedge}2 = 1.000$$
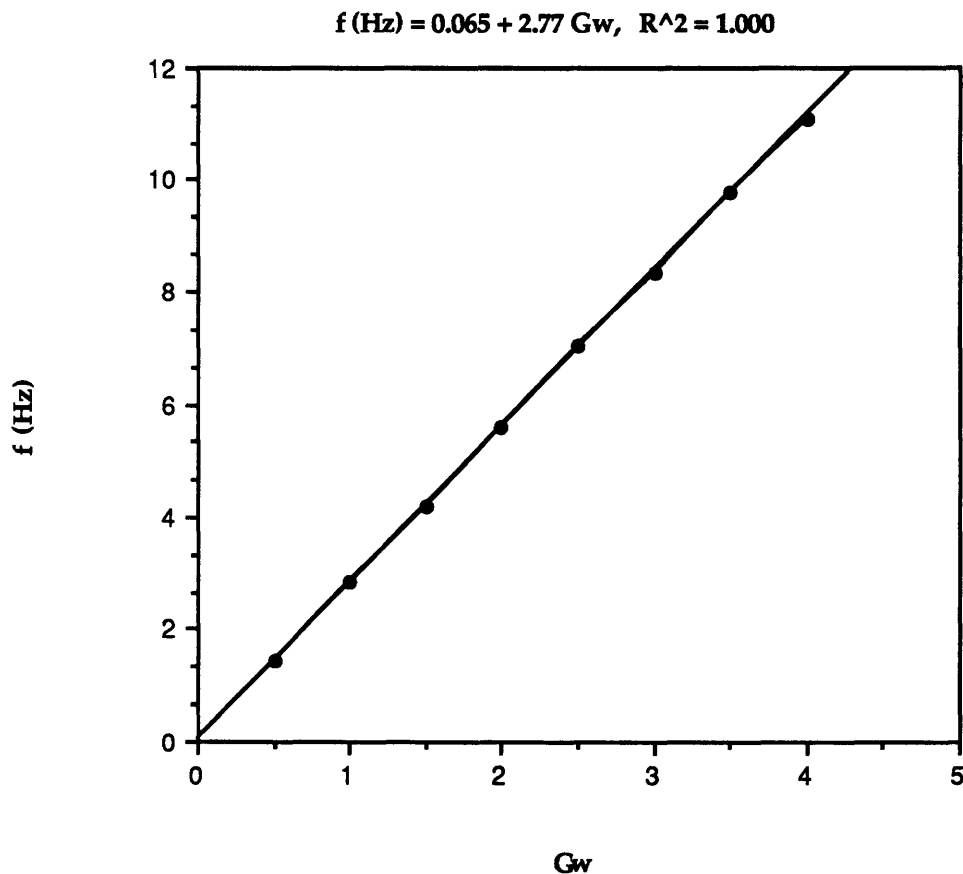
Figure 4.10   Determination of the Constant RC.

4.4.1 Calibration of the Compliant Actuator

The spacecraft mode simulator circuit was calibrated to determine the constant RC in eq.'s 4.10. The simulator was driven by a random signal from a spectrum analyzer (HP) and by recording the frequency of the

123

measured resonance. A range of gains, G_ω, were used to determine the value of RC in eq. 4.11. Fig. 4.10 depicts the results, while the results of a linear regression are summarized in Table 4.4. The linearity of the compliant actuator, with respect to excitation amplitude, is shown in Fig. 4.11.

$\zeta_{Measured} = 1.0\%$

$\zeta_{Selected} = 1.05\%$

$fo_{Measured} = 3.46\ Hz$

$fo_{Selected} = 3.46\ Hz$
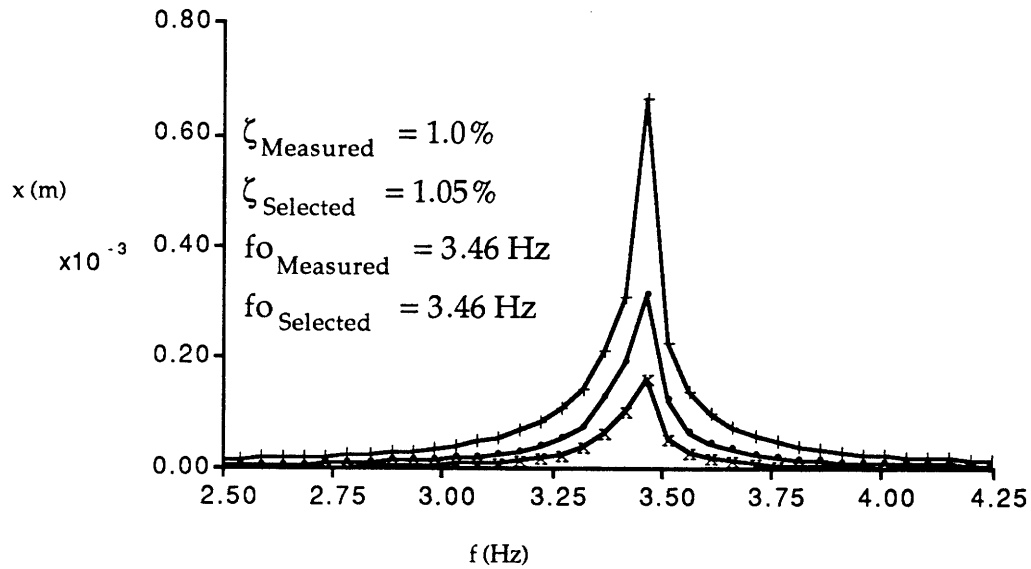
Figure 4.11   Verification of Compliant Actuator Dynamics.

4.4.2 Proximeter Calibration

The proximeter was calibrated by measuring the output voltage of the proximeter signal conditioning circuitry as the gap between the proximeter and the force balance target disc was varied. The results of one of the calibration tests are depicted in Fig. 4.12 and the linear regression results (of fitting a straight line through the experimental data) are summarized in Table 4.4.

x = 0.00037 + 0.00129 Volts,   R^2 = 0.999
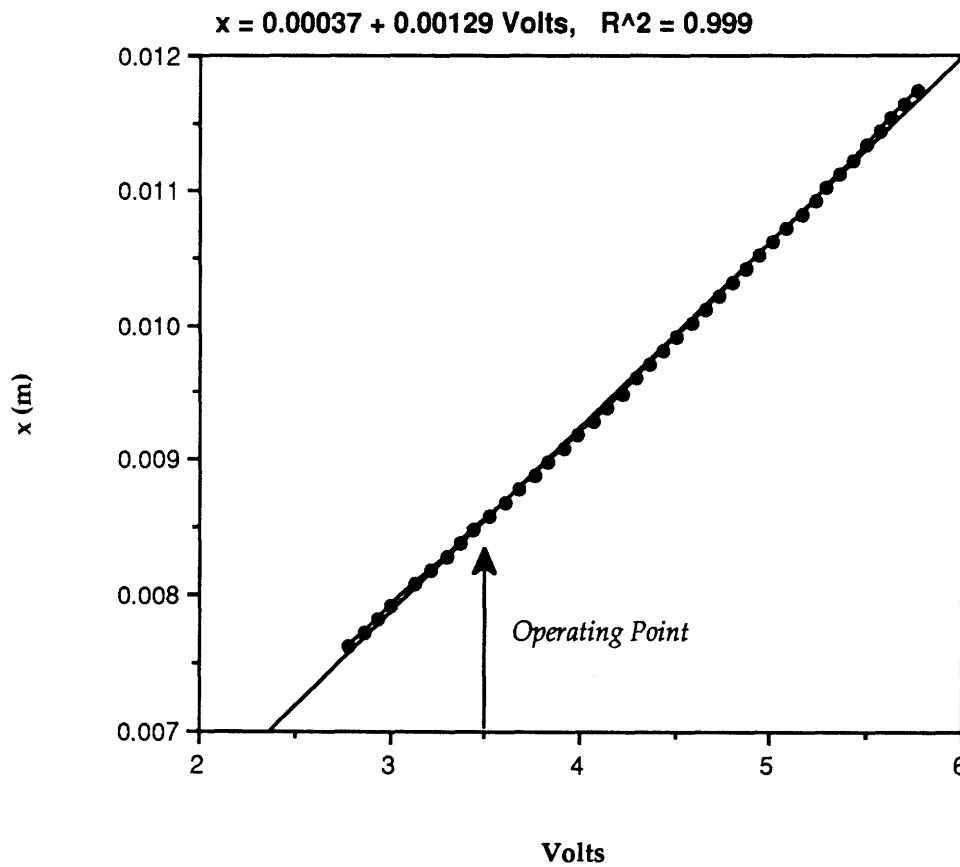
Figure 4.12   Proximeter Calibration.

4.4.3 Calibration of the Force Resolver Signal Conditioning Electronics

A careful calibration of the analog signal processing electronics was required to ensure accurate planar and non-planar force signals. The gains of this particular circuitry were seen to drift over several weeks and were adjusted before each new tank model geometry was tested. The calibration process consisted of four steps: offset adjustment, input amplifier stage gain adjustment, resolver stage gain adjustment and mass output gain adjustment. The electronics were allowed to settle down (about twenty minutes) before the offset nulls of each amplifier in the electronics were adjusted to yield a zero output for a zero input. Then a reference voltage, 1.000 Volt DC (measured by a VDC), was applied to the input stage of each channel. The gains of each input stage were adjusted to yield a net gain for each transducer signal (112.13 mV/kg {or 500 mV/lb} for the force transducer and 100 mV/g for the accelerometers). The individual gains were determined by individual calibration tests (Peterson [1987]) performed on the force transducers and accelerometers. Table 4.3 presents the channel gains for this calibration.

Table 4.3   Input Stage Amplifier Gains

Channel	Transducer Sensitivity	Ideal Gain
F_1	119.08 mV/N	0.94163
F_2	121.90 mV/N	0.91985
F_3	119.60 mV/N	0.93753
a_1	98.98 mV/g	1.01031
a_2	98.55 mV/g	1.01468
a_3	99.70 mV/g	1.00296

Next, the gains of the force and accelerometer stages were adjusted. The gain of each stage in the resolver circuit represented the entries in the transformation matrices of eq.'s 4.5 to 4.8. When two of the three transducer

voltage input channels were set to zero, the net gain of the resolver stage would equal the matrix element corresponding to the non-zero channel entry. Thus, when a known voltage (1.000 Volts DC) was applied to the non-zero input stage channel, the net gain of the resolver stage equaled the transducer sensitivity multiplied by the resolver gain for the element in the transformation matrix. The analog adjustment was performed for each resolver transformation element independently.

The final step in the analog circuitry calibration was the adjustment of the slosh force isolation and amplification stage. A 1.000 Volt (RMS) signal at 10 Hz was applied to the input stage for F_2, with the remaining channels zeroed (set to ground). Note that the F_2 signal appears in all three the resolver transformations. The output stage gain was then adjusted to achieve the desired force sensitivity.

4.4.4 Calibration of the Planar Slosh Force Measurement

As an overall calibration test, the planar slosh force was calibrated by mounting a known mass (a total of three different masses were used) on top of the force balance. A computer control program (FST) via the CAMAC's D/A provided the excitation signal for the shaker to oscillate the reaction balance. The measured planar force voltage V_{fxs} and the proximeter voltage corresponding to the excitation frequency were obtained from an FFT on the measured signals. These amplitudes were stored for the different excitation frequencies and amplitudes. The excitation frequencies ranged from 2 to 8 Hz and the excitation amplitudes from 10% to 90% of the maximum output voltage of the D/A. The equation relating the measured planar slosh force voltage to the calibration mass (m_c), the proximeter voltage (V_x), the residual mass (m_r) of the force reaction balance, the excitation frequency (f) and the planar slosh force gain (K_f), is:

$$F_{fxs} = K_f (m_c + m_r)(2\pi f)^2 \frac{V_x}{K_x}$$

(4.14)

where K_x is the proximeter calibration factor (See Table 4.4). This equation can be rearranged to yield an expression suitable for linear regression.

127

$$m_c = -m_r + \frac{1}{K_f}\left[\frac{V_{fxs}K_x}{V_x(2\pi f)^2}\right]$$

(4.15)

The linear regression results are summarized in Table 4.4.

4.4.5 Summary of the Calibration Results

Table 4.4 summarizes the calibration results. The value ρ, is the linear correlation coefficient and is a measure of how well the data is approximated by a linear curve.

Table 4.4   Calibration Sensitivities

Quantity	Measurement	Sensitivity	Units	Value	ρ
F_{xs}	V_{fxs}	K_f	Volts/N	11.351	0.990
F_{ys}	V_{fys}	K_f	Volts/N	11.351	0.990
x	V_x	K_x	Volts/m	775.194	0.999
a_x	V_{ax}	K_a	mV/g	100.000	0.995
-	f	RC	seconds	0.057	1.000

4.5   Summary

The experimental apparatus, procedures and calibration of this research have been discussed in this chapter. The response of the fluid was measured primarily by a sensitive force reaction balance that provided the planar (in the direction of the tank excitation) and the non-planar slosh forces. A spacecraft mode was coupled to the fluid slosh motion using an analog simulation circuit. The experimental apparatus was controlled by a computer which also reduced and stored the measured data.

The extensive set of calibration tests ensured the accuracy of the measured results.

Chapter 5

Experimental Results

This chapter presents the experimental results of the dynamic behavior of fluids in the three tank models studied in this research. The three study models are; a spherical, a square and a rectangular tank. The uncoupled and coupled tests results for each study tank will be presented and discussed separately. Section 5.1 outlines the uncoupled and coupled tests and presents the reader with mechanical linear models of these two tests. The next section (5.2) presents the experimental results for the spherical tank, section 5.3, presents the square tank results and section 5.4, the rectangular tank results.

In section 5.5, a cylindrical tank model, tested by Peterson [1987], is presented. This model was not tested in research but the experimental results obtained by Peterson will be used in Chapter 6 to investigate and verify the analytical model. This section will not repeat or discuss the experimental results obtained by Peterson [1987].

The final section of this chapter (5.5) is a short summary of the experimentally observed dynamic behavior of fluids in spherical, square and rectangular tests.

5.1   Non-Dimensionalization and Data Presentation

This section describes how the experimental results were non-dimensionalized and presented in the subsequent sections. Linear mechanical models of the uncoupled and coupled tests are also presented. These models would describe the dynamic response characteristics if the fluid motion is linear.

5.1.1 Uncoupled Tests

The uncoupled dynamic characteristics of the fluid slosh were determined by measuring the fluid slosh forces while the tank was

sinusoidally excited at various forcing amplitudes and frequencies (Fig. 5.1). In the mechanical linear model of Fig. 5.1, only a portion of the fluid (λm_F) participates in the motion, where (λ) is the mass fraction. The response zero , from eq. A23, occurs at:

$$f = \frac{f_s}{\sqrt{1-\lambda}} \qquad (5.1)$$

The position of the response zeros will be used to verify the slosh mass fractions predicted by the analytical program.

In the uncoupled tests, the response to 5 harmonic excitation levels were studied. As indicated in Table 5.1, the 5 excitation amplitudes form a logarithmic (Log_{10}) series. This table also summarizes the graphic symbols used to plot both the coupled and uncoupled test results. The uncoupled test results are plotted on a logarithmic scale. On a logarithmic scale, linear system responses will be spaced equally for all five excitation levels, but will be spaced differently for nonlinear responses.

Table 5.1   Applied Harmonic Excitation Levels for Uncoupled Tests

Resonance Number	$|F_{ex}|$ (N)	$Log_{10} |F_{ex}|$	Graph Symbol
1	0.264	-0.578	x
2	0.373	-0.428	•
3	0.527	-0.278	+
4	0.746	-0.127	Δ
5	1.057	0.024	◊

The following forces were measured:

F_{xs} The fluid slosh force in the direction of excitation (Planar slosh force).

F_{ys} The fluid slosh force in the nonplanar direction.

The calibration factors given in Chapter 4 were used to transform the measured signals to forces measured in Newton.

Uncoupled Test

Mechanical Model of Linear Fluid Motion
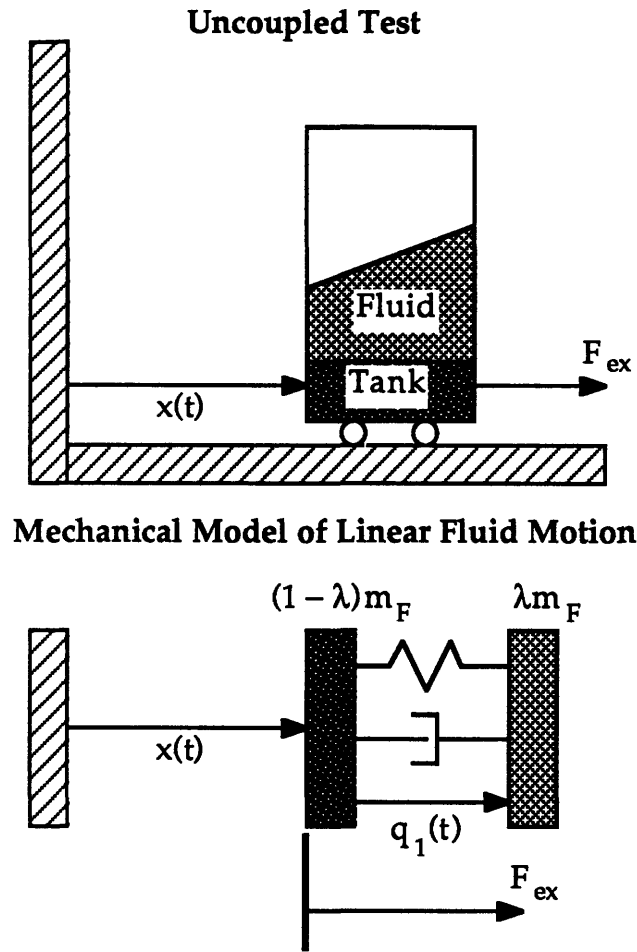
$$(m + m_F)\ddot{x} + \lambda m_F \ddot{q}_1 = F_{ex}$$

$$\lambda m_F \ddot{x} + \lambda m_F \ddot{q}_1 + c_{q_1} \dot{q}_1 + \lambda m_F \omega_s^2 q_1 = 0$$

with

$$F_{xs} = -m_F \ddot{x} - \lambda m_F \ddot{q}_1$$

Figure 5.1   Mechanical Model of Uncoupled Tests

5.1.2 Coupled Tests

In the coupled tests, the compliant actuator was coupled to the fluid tank system to simulate a spacecraft mode. A test matrix with a range of spacecraft mass, damping and stiffness properties was used to determine the effect of these properties on the dynamic behavior of the coupled system. As with the uncoupled tests, the coupled dynamic characteristics of the

Coupled Test
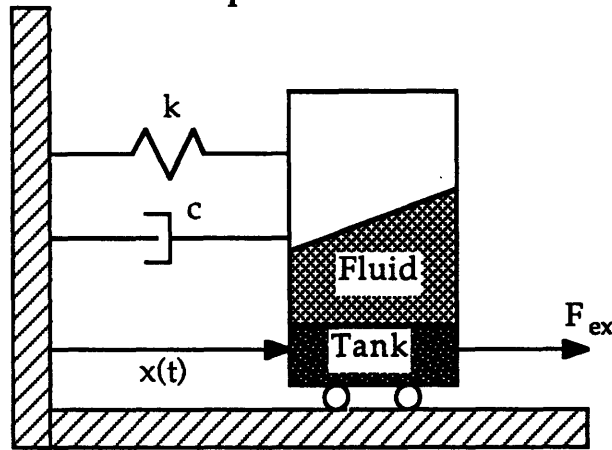
Mechanical Model of Linear Fluid/Spacecraft Motion
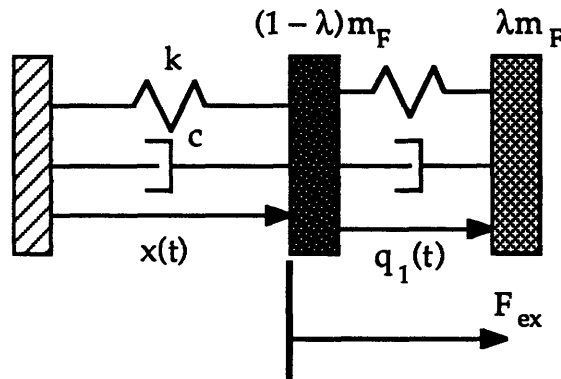
$$(m + m_F)\ddot{x} + \lambda m_F \ddot{q}_1 + c\dot{x} + kx = F_{ex}$$

$$\lambda m_F \ddot{x} + \lambda m_F \ddot{q}_1 + c_{q_1}\dot{q}_1 + \lambda m_F \omega_s^2 q_1 = 0$$

Figure 5.2   Mechanical Model of Coupled Tests

fluid/spacecraft system were determined by measuring some of the system parameters while the tank was sinusoidally excited at various forcing amplitudes and frequencies. The following parameters were measured:

F_{xs} The fluid slosh force in the direction of excitation (Planar slosh force).

F_{ys} The fluid slosh force in the nonplanar direction.

x   The displacement of the spacecraft degree of freedom.

A_x The acceleration of the spacecraft degree of freedom.

In order for the results to be extrapolated to tanks of other sizes, the above mentioned parameters and the input excitation force (F_{ex}) were non-dimensionalized as follows:

Table 5.2   Non-dimensionalization

Parameter	Non-dimensionalized by dividing by:
F_{ex}	kd
F_{xs}	kd
F_{ys}	kd
x	d
a_x	g

Where:

d   =   A characteristic length associated with the tank geometry. In this research d = h, h being the fluid depth.

g   =   Gravity acceleration (g = 9.81 ms^{-2})

k   =   The stiffness of the spacecraft mode, where:

$$k = \frac{(2\pi f_s)^2 m_F}{\mu v^2}$$

(5.2)

with:

$$f_s = 1^{st} \text{ Fluid slosh frequency}$$

(5.3)

$$m_F = \text{Fluid mass} \tag{5.4}$$

$$\mu = \frac{m_F}{m} = \text{Mass ratio} \tag{5.5}$$

where m is the mass of the spacecraft mode.

$$\nu = \frac{f_s}{f_o} = \text{Frequency ratio} \tag{5.6}$$

with fo being the frequency of the spacecraft mode. The non-dimensional excitation force (Ξ_{ex}) is defined by:

$$\Xi_{ex} = \frac{F_{ex}}{kd} \tag{5.7}$$

Important to remember when interpreting the results:
Unfortunately, in the experiments, the force excitation levels were varied for each test to yield acceptable fluid amplitudes. The varying range of force excitation levels makes the comparison of the test results difficult but at the time of the experiments, this was deemed necessary for safety arguments and also to ensure the validity of the experimental results. In the coupled tests, the response to 5 harmonic excitation levels were studied. The excitation was increased from the minimum value to the maximum value in logarithmic (Log_{10}) increments. These minimum and maximum excitation levels will be summarized in the section that discusses the results of the coupled tests performed on the different model tanks.

The fill height in all the tests, except for two of the uncoupled spherical tests, was calculated as follows:

$$h = d_e = 4\frac{\text{Surface Area}}{\text{Circumference}} \tag{5.8}$$

The equivalent diameter (d_e) is a single measure of the tank surface area and surface shape. The equivalent diameter is equal to four times the hydraulic radius, a term often used in fluid mechanics [Daugherty and Franzini, 1977].

134

5.2 Spherical Tank Model

Fig. 5.3 is a drawing of the spherical tank used to investigate the dynamic behavior of a fluid contained in a spherical tank. The tank is a standard chemical spherical glass flask. The inside geometry was determined by pouring water into the flask and recording the volume of fluid added as well as the fluid height. Figure 5.4 depicts the measured results and also the least squares curve that best fitted the results. The spherical radius obtained from this least squares fit was 29.5 mm.
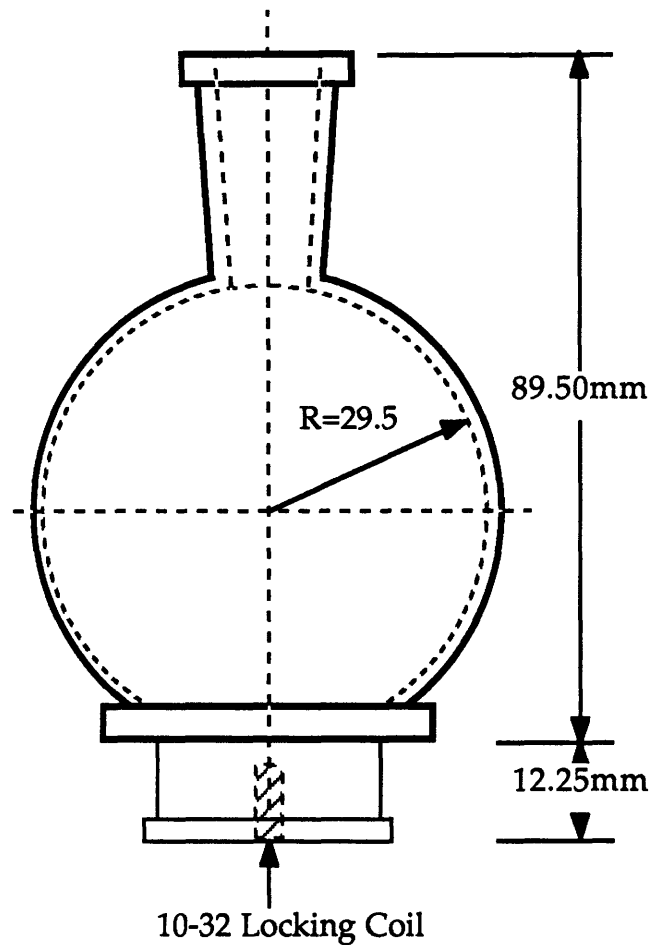
Figure 5.3   Spherical Study Model

The details of the dynamic test, test parameters and test procedures are discussed in chapter 3. The relevant tank parameters are summarized in Table 5.3.

Table 5.3   Spherical Tank Parameters

Parameter	Symbol	Value
Spherical Radius	R	29.50 mm
Fill Height	h	20.60 mm*
Normalization Factor	d	20.60 mm
Bond Number	Bo	117
Empty Mass	m_E	86.62 g
Fluid Mass	m_F	30.00 g*
1st Fluid Slosh Frequency	f_s	3.29 Hz

*   In the uncoupled tests SU2 and SU3 the fluid mass was 50 g and 60 g respectively. The corresponding fluid level heights are 28.10 mm and 31.78 mm. See Table 5.4.
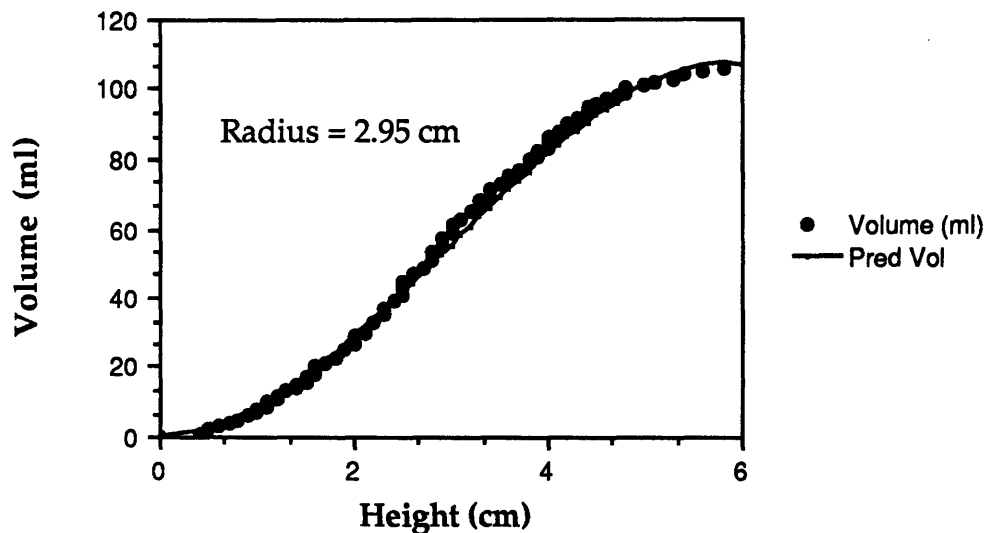
Figure 5.4   Measured and Predicted Fluid Volume versus Fluid Height

5.2.1 Spherical Tank Test Matrix

A series of uncoupled tests were performed to determine the low-amplitude linear characteristics of the fluid and also for comparison with the coupled test results. Each test has a unique test identifier and this identifier is used to identify the experimental results presented in this chapter. Table 5.4 summarizes the uncoupled (fluid alone) test matrix and Table 5.5 the coupled (fluid/spacecraft) test matrix. A 2% photoflo/water solution was used in all these tests except for Test SU4. The excitation frequency ranged from 2 Hz to 5 Hz.

Table 5.4   Spherical Uncoupled Test Matrix

Test Id	Fill Height	Fluid Mass	Fluid	Figures
SU1	20.60	30	2% Photoflo/Water	5.5, 5.6
SU2	28.10	50	2% Photoflo/Water	5.7, 5.8
SU3	31.78	60	2% Photoflo/Water	5.9, 5.10
SW1	20.60	30	Distilled Water	5.11, 5.12

In the uncoupled tests, the fluid/spacecraft system was harmonically excited over a frequency range covering the first fluid slosh mode resonance and in the coupled tests also covering the spacecraft resonance. A total of 5 logarithmically spaced (Log_{10}) force excitation levels were used to determine the dynamic characteristics. The force excitation levels used in the uncoupled tests are summarized in Table 5.1. This table also identifies the graphic symbols used to present the experimental results. In Table 5.6, the minimum force level and maximum force level for the coupled tests are summarized. The intermediate force levels are logarithmically spaced between these minimum and maximum values. Note that the applied force, F_{ex}, is non-dimensionalized by dividing with (kd) to yield the non-dimensional force Ξ_{ex}.

Table 5.5   Spherical Coupled Test Matrix

Test ID	μ	ν	ζ (%)	Figures
SC3	0.091	0.87	0.19	5.13 - 5.14
S12	0.063	0.87	1.94	5.17 - 5.20
S13	0.063	0.87	7.76	5.21 - 5.24
S14	0.160	0.90	8.00	5.25 - 5.28
S15	0.320	0.90	8.00	5.29 - 5.32
S16	0.160	0.85	8.00	5.33 - 5.36
S17	0.160	1.10	8.00	5.37 - 5.40
S18	0.160	0.90	4.00	5.41 - 5.44
S19	0.160	0.95	8.00	5.45 - 5.48

Note: ν = Frequency Ratio = $f_{Slosh}/f_{Spacecraft} = f_s/f_o$

μ = Mass Ratio = $m_{fluid}/m_{spacecraft\ Mode} = m_F/m$

Table 5.6   Minimum and Maximum Non-dimensional Experimentally Applied Harmonic Excitation Levels for the Spherical Tank Coupled Tests

Test ID	$\left|\Xi_{ex_{min}}\right|$	$\left|\Xi_{ex_{max}}\right|$
Graphic Symbol:	x	◊
SC3	0.0060	0.0241
S12	0.0018	0.0167
S13	0.0006	0.0050
S14	0.0075	0.0680
S15	0.0037	0.0340
S16	0.0017	0.0151
S17	0.0045	0.0406
S18	0.0030	0.0272
S19	0.0033	0.0303

5.2.2 Spherical Tank Experimental Results

Paragraph 5.2.2.1 discusses the uncoupled test results and Paragraph 5.2.2.2 the coupled test results.

5.2.2.1   Discussion of the Uncoupled Test Results

The linear eigen-characteristics of the first fluid slosh mode are required for the analytical analysis, described in Chapter 2 (and reported in Chapter 6). The damping ratios were obtained with the half-power-bandwidth method from the lowest force excitation level results and are summarized in Table 5.7.   Figures 5.5 to 5.12 give the results of the uncoupled tests (also see Table 5.4 for a more detailed identification of the figures). The vertical solid line in these figures indicates the position of the resonance peak as predicted by linear theory. Any shift of the resonance peak away from this vertical line represents nonlinear fluid slosh behavior.

Table 5.7   Measured Linear Eigen-characteristics (Spherical Tank)

Test ID	Fill Level (mm)	Slosh Mass Fraction λ	Natural Frequency (Hz)	Damping Ratio (%)
SU1	20.60	0.40	3.29	2.1
SU2	28.10	0.41	3.52	1.9
SU3	31.78	0.38	3.71	1.8
SW1	20.60	0.43	3.33	4.3

The very high damping ratio associated with the first fluid mode of test SW1 (see Fig. 5.11), where water was used as test fluid, disqualifies water as a model test fluid. The damping ratios of the 2% Photoflo/Water solution tests are more typical of space-bound fluids, and this solution was subsequently used in all the model tests. A softening trend (a decrease in the frequency of the first fluid slosh resonance) is apparent in all the uncoupled tests.

5.2.2.2   Discussion of the Coupled Test Results

In the coupled tests, the mass ratios, frequency ratios and damping ratios were varied to determine the effect of these parameters on the coupled behavior of the fluid/spacecraft system. The coupled test results are reported in Figures 5.13 to 5.48 (also see Table 5.5 for a more detailed identification of the figures). As with the uncoupled tests, the vertical solid lines in these figures indicate the positions of the resonance peaks as predicted by linear theory. Any shift of the resonance peaks away from this verticals line represent nonlinear behavior.

Studying Figures 5.25 to 5.28 (Test S14) it can be seen that both the first fluid mode and the spacecraft mode exhibit moderate softening (decrease in resonant frequency with an increase in force excitation amplitude) characteristics and that the damping ratios of these modes are amplitude independent. The nonplanar response is at least one order of magnitude smaller than the planar motion (Fig. 5.26) except for the highest force excitation level where a jump phenomenon occurs and the nonplanar force equals the planar force. This jump phenomenon occurs between the first fluid mode and the simulated spacecraft mode resonant frequencies and is associated with a swirling motion which was experimentally observed. This motion will be discussed in greater detail in Chapter 6. Taking this test (S14, $\mu=0.16$, $\nu=0.90$, $\xi=8.00\%$) as the nominal configuration, the following conclusions can be made on:

The Effect of Mass Ratio: From Fig. 5.23 (Test S13, $\mu=0.063$, $\nu=0.87$) and Fig. 5.31 (Test S15, $\mu=0.32$, $\nu=0.90$), it can be concluded that lower mass fractions result in more nonlinear behavior.

The Effect of Frequency Ratio: From Fig. 5.35 (Test S16, $\mu=0.16$, $\nu=0.85$) and Fig. 5.39 (Test S17, $\mu=0.16$, $\nu=1.1$) it can be seen that configurations with frequencies ratios close to unity are more nonlinear. This is only true for frequency ratios less than unity. For frequency ratios exceeding unity, the filtering effect introduced by the spacecraft mode (the spacecraft mode acts as a second order filter), reduces the amplitude of the first fluid slosh mode and thereby the nonlinear behavior exhibited by that mode.

The Effect of Damping Ratio: Little can be deduced from Fig. 5.43 (Test S18, $\mu=0.16$, $\nu=0.90$, $\xi=4.00\%$). However, one could argue that the

widening (for increased damping ratios) of the spacecraft resonant peak may extend the fluid nonlinear characteristics into the spacecraft dynamics, resulting in the jump phenomenon occurring at lower force excitation levels.

In conclusion, the nonlinear behavior is fluid motion amplitude dependent and any effect that lowers the fluid motion will reduce the nonlinear behavior of the fluid. This observation is of particular importance to control engineers, in that if the amplitude of the fluid motion can be kept below a critical value, the fluid/spacecraft system can be modeled with a linear model.
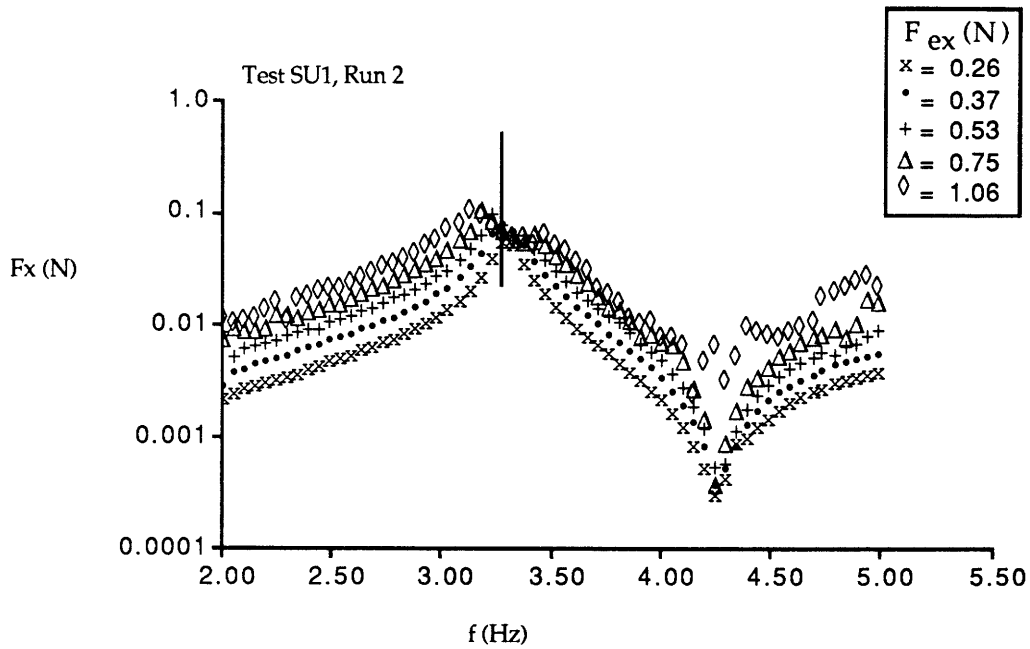
Figure 5.5   Test SU1, Planar Slosh Force (Fx).
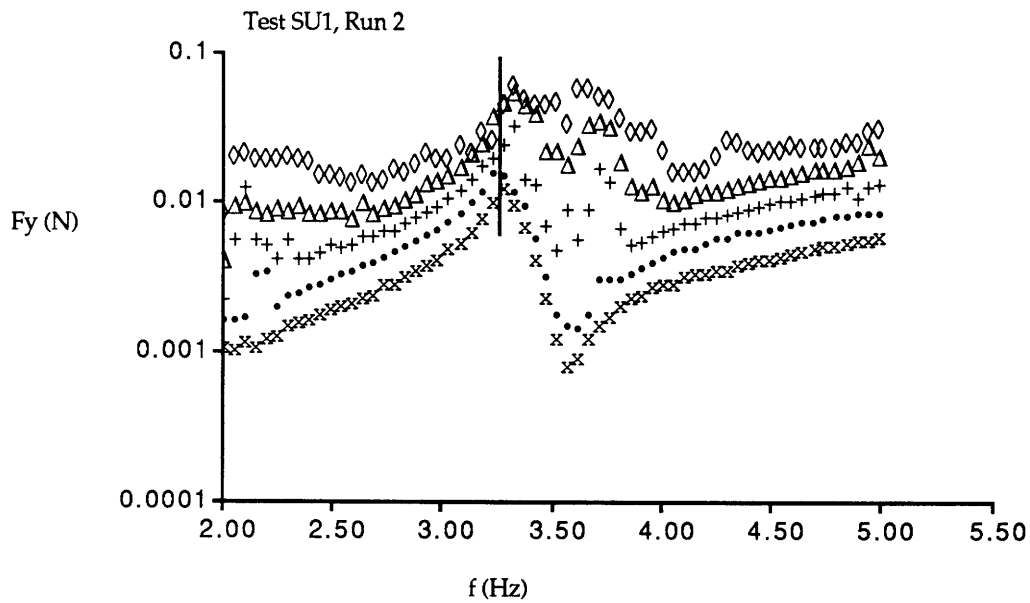
Figure 5.6   Test SU1, Nonplanar Slosh Force (Fy).

(Spherical tank, uncoupled, harmonic excitation, Fluid Mass = 30 g and Fluid = 2% Photoflo/Water Solution)
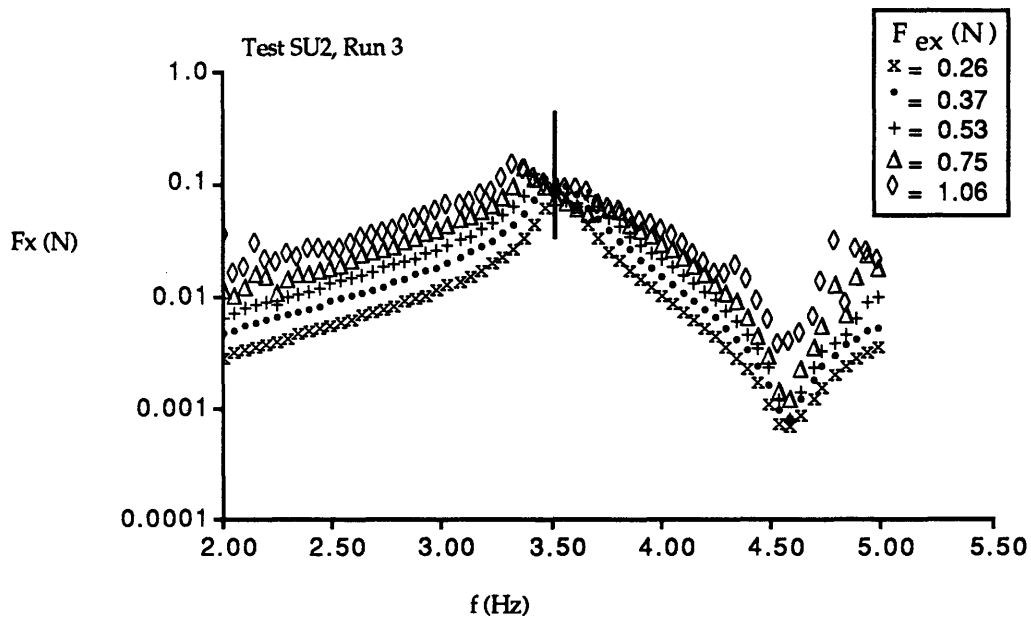
Figure 5.7   Test SU2, Planar Slosh Force (Fx).
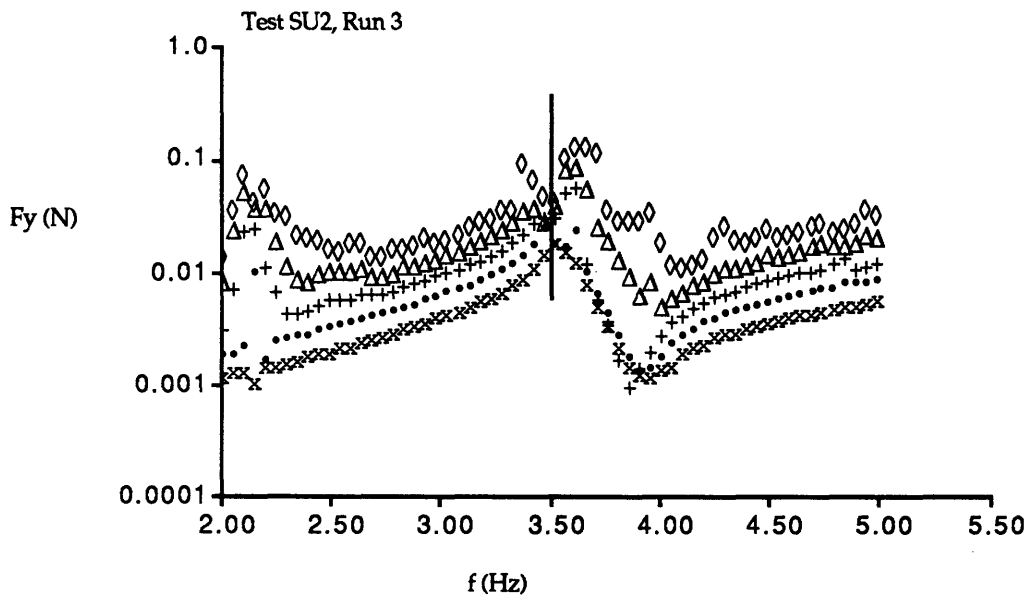
Figure 5.8   Test SU2, Nonplanar Slosh Force (Fy).

(Spherical tank, uncoupled, harmonic excitation, Fluid Mass = 50 g and
Fluid = 2% Photoflo/Water Solution)

143
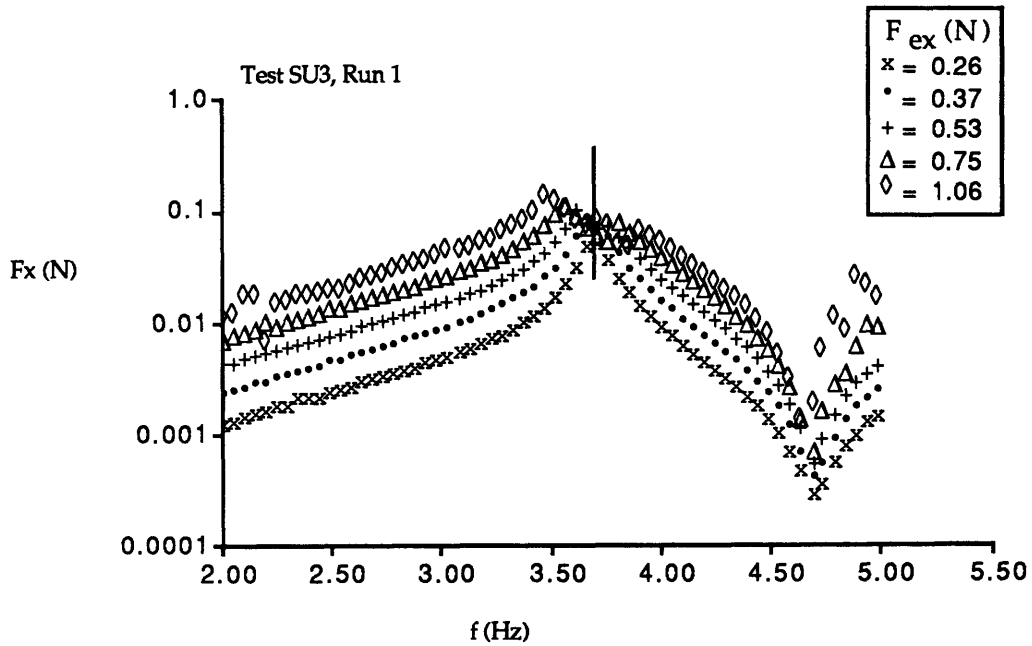
Figure 5.9   Test SU3, Planar Slosh Force (Fx).
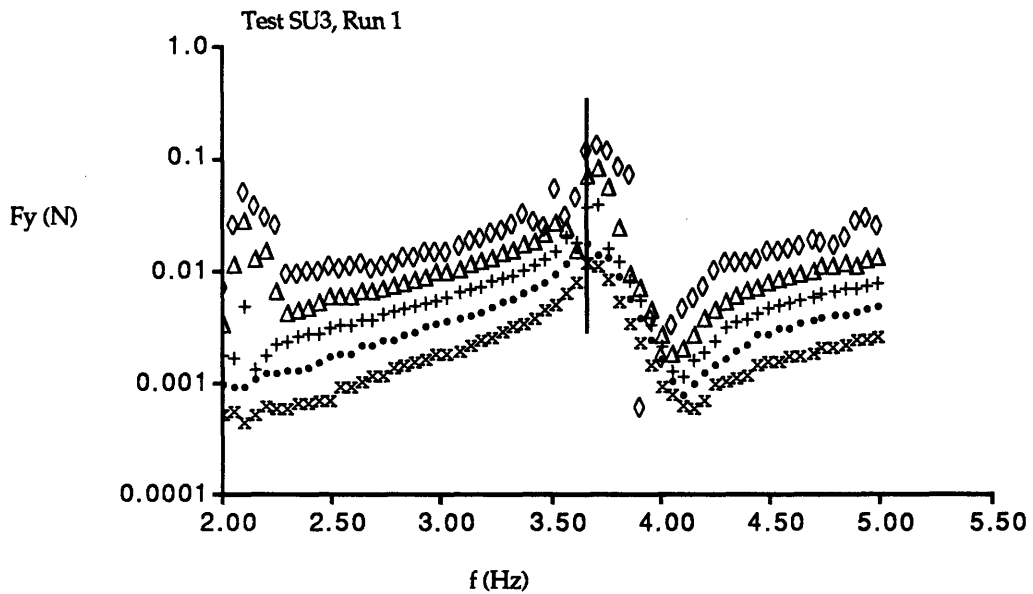
Figure 5.10   Test SU3, Nonplanar Slosh Force (Fy).

(Spherical tank, uncoupled, harmonic excitation, Fluid Mass = 60 g and Fluid = 2% Photoflo/Water Solution)
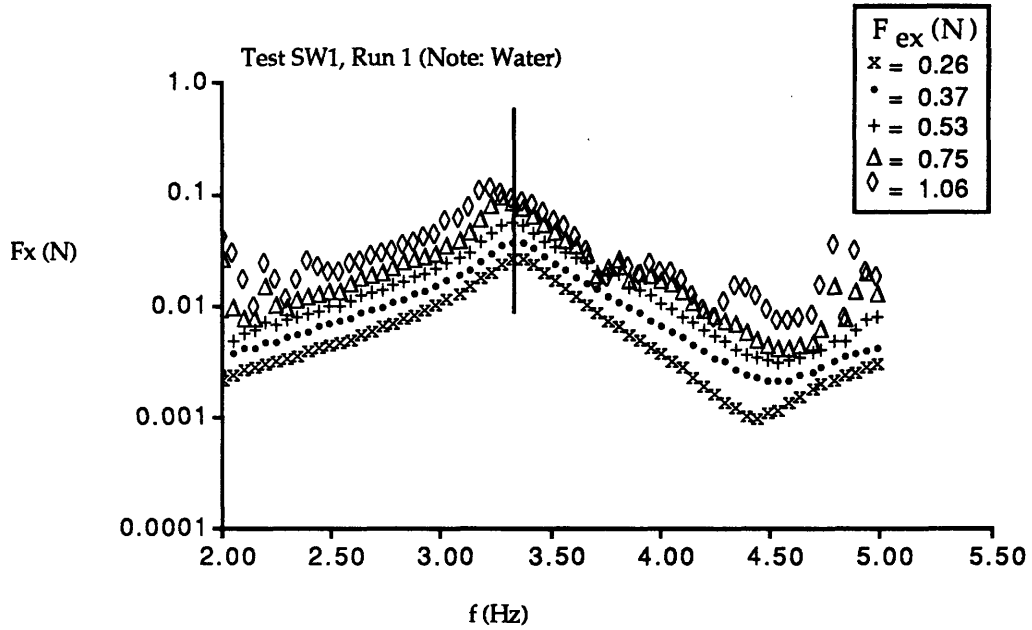
Figure 5.11   Test SW1, Planar Slosh Force (Fx).
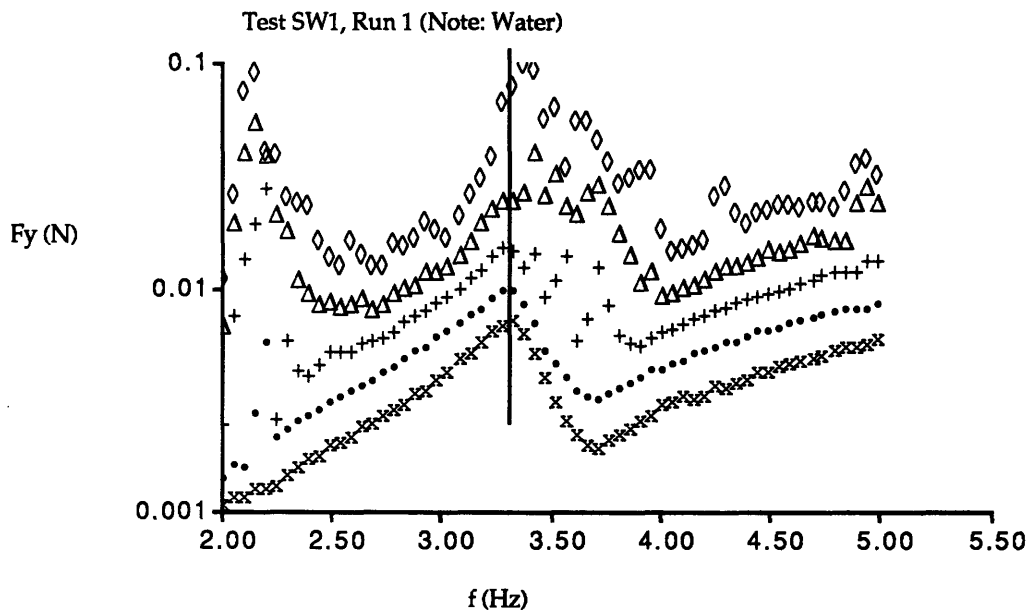
Figure 5.12   Test SW1, Nonplanar Slosh Force (Fy).

(Spherical tank, uncoupled, harmonic excitation, Fluid Mass = 30 g and Fluid = Water)

145

Test SC3, Run 1
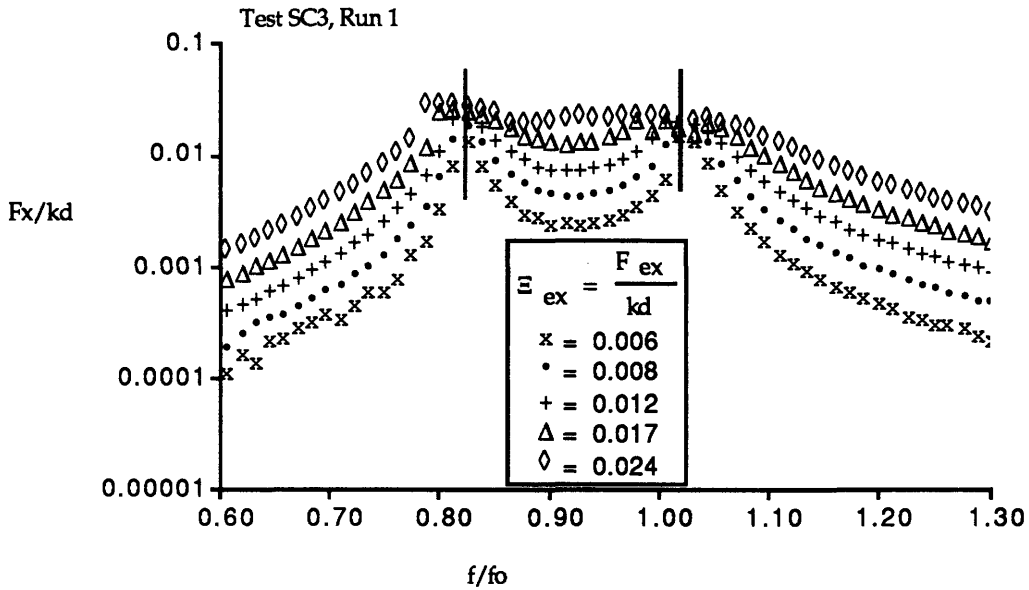
Figure 5.13   Test SC3, Non-dimensional Planar Slosh Force (Fx/kd).

Test SC3, Run 1
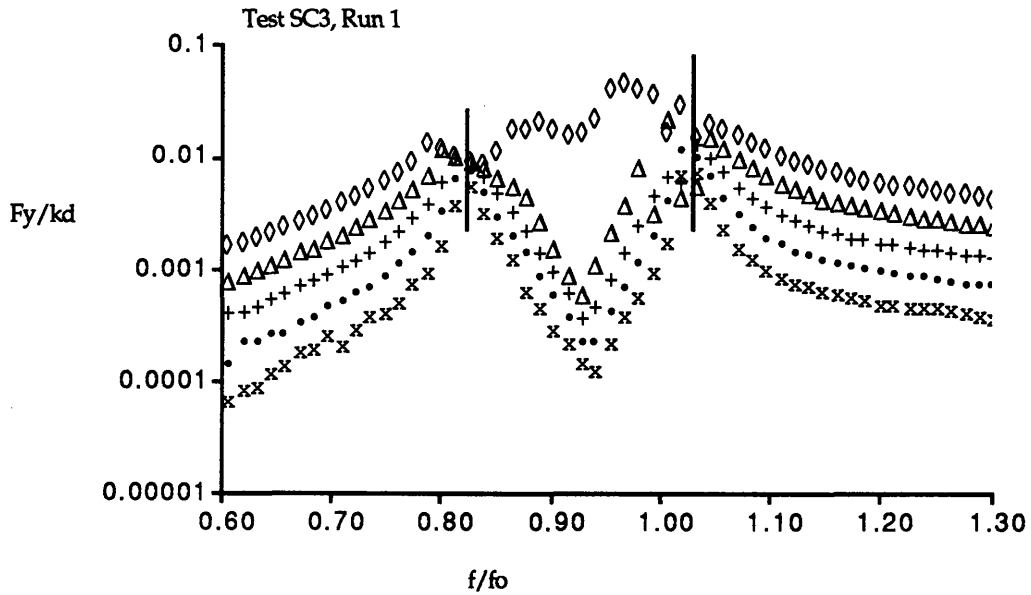
Figure 5.14   Test SC3, Non-dimensional Force (Fy/kd).

(Spherical tank, harmonic excitation, coupled system.
Parameters; $\mu=0.091$, $\nu=0.87$, $\zeta=0.19\%$, Bo=251)
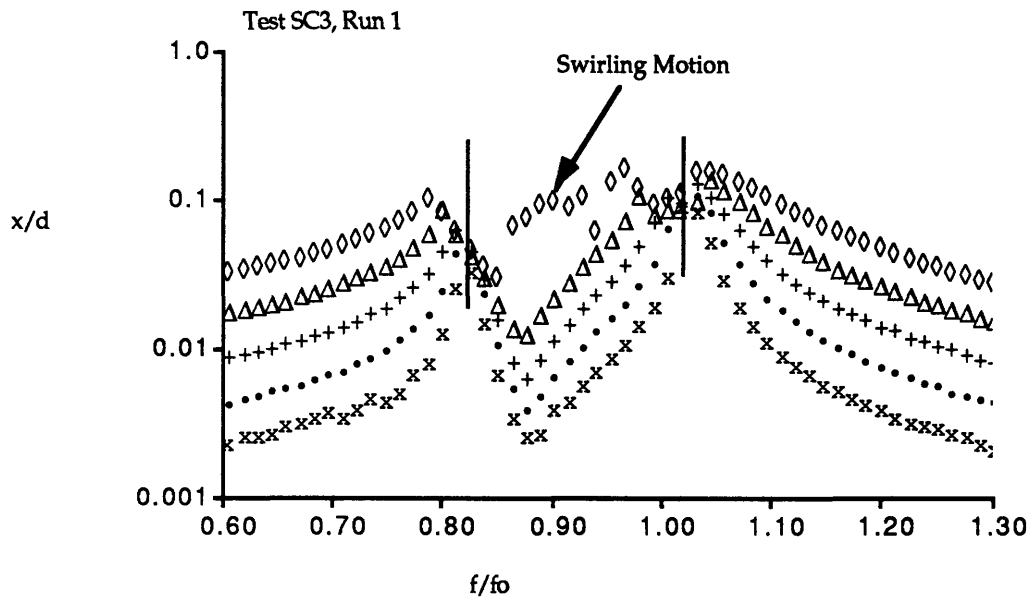
Figure 5.15   Test SC3, Non-dimensional Displacement (x/d).
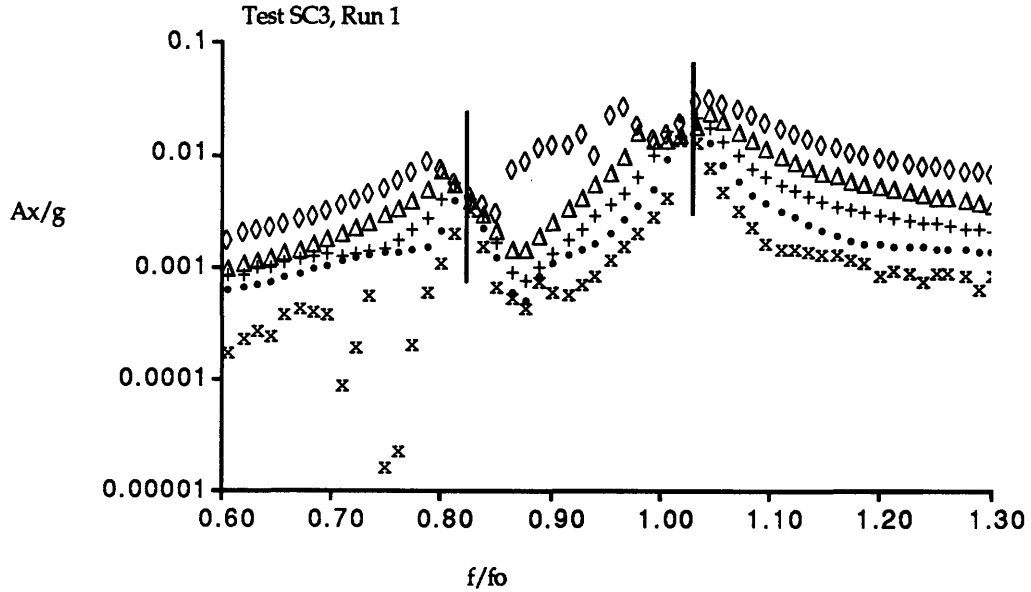
Figure 5.16   Test SC3, Non-dimensional Acceleration (Ax/g).

(Spherical tank, harmonic excitation, coupled system.
Parameters; $\mu=0.091$, $v=0.87$, $\zeta=0.19\%$, $Bo=251$)
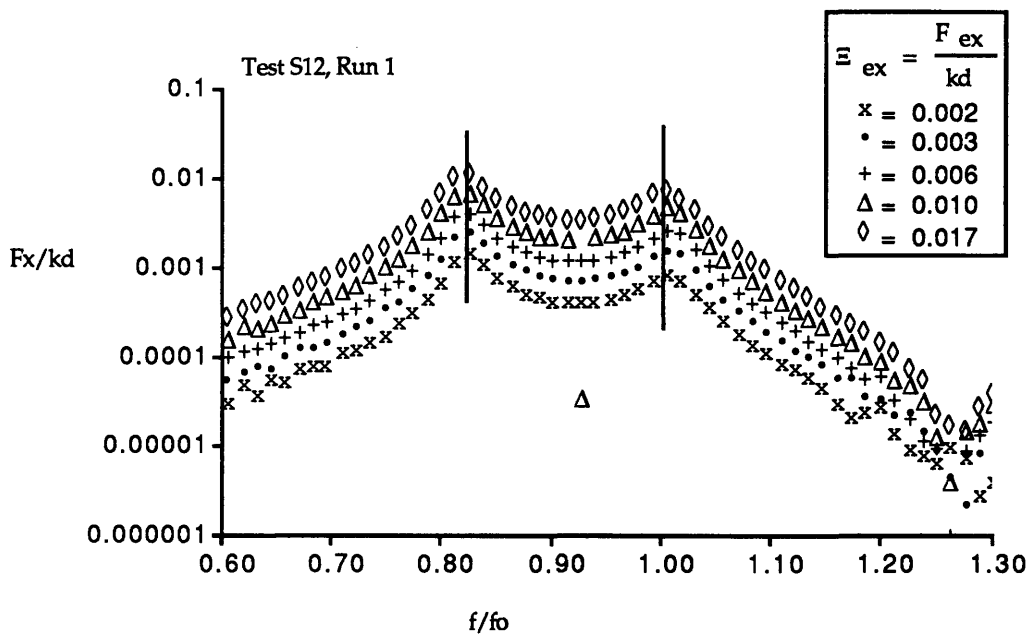
Figure 5.17   Test S12, Non-dimensional Planar Slosh Force (Fx/kd).
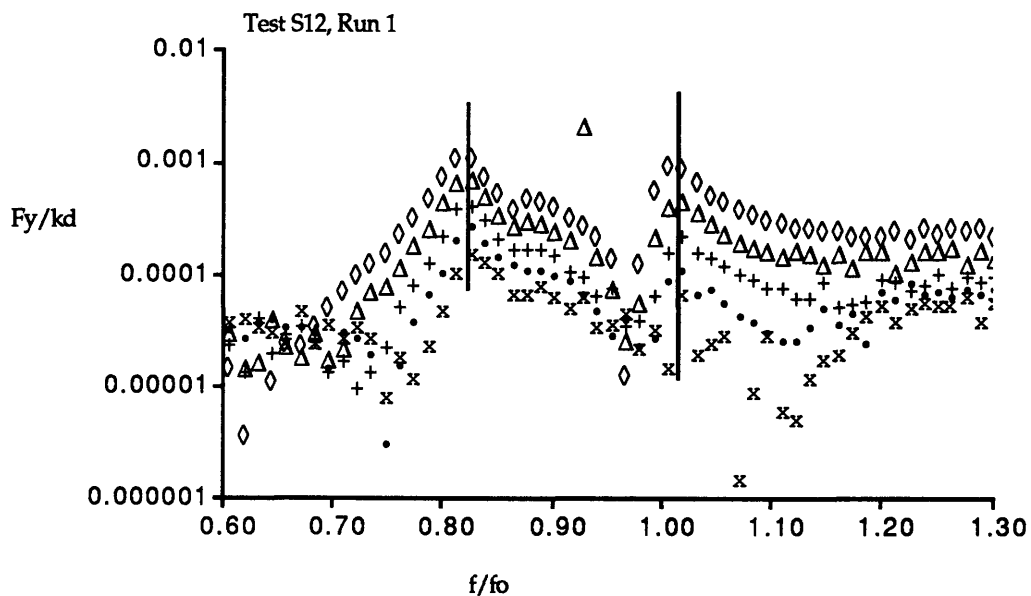
Figure 5.18   Test S12, Non-dimensional Nonplanar Slosh Force (Fy/kd).

(Spherical tank, harmonic excitation, coupled system.
Parameters; Bo=251)

148
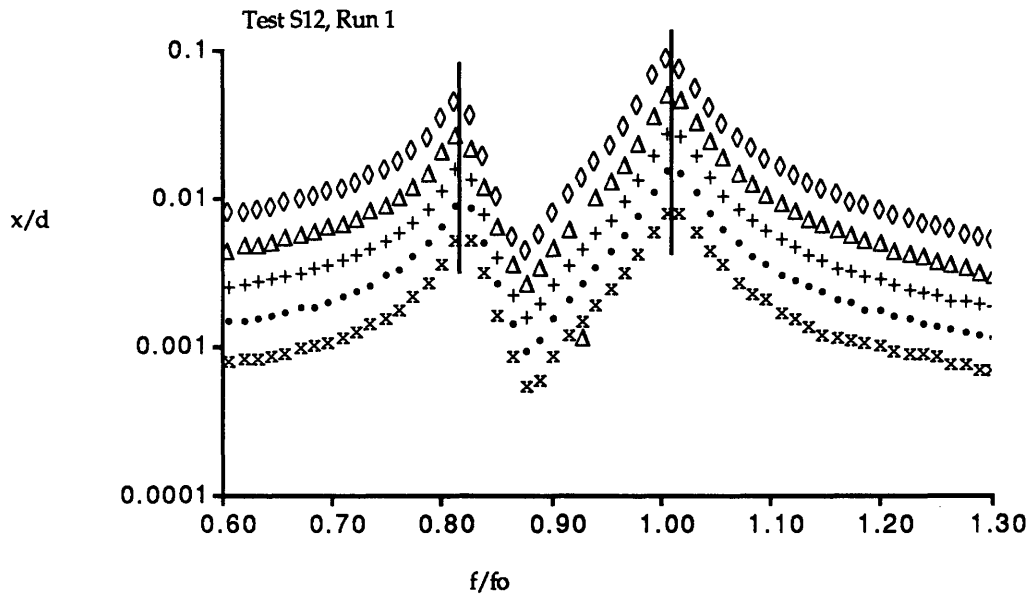
Figure 5.19   **Test S12, Non-dimensional Displacement (x/d).**
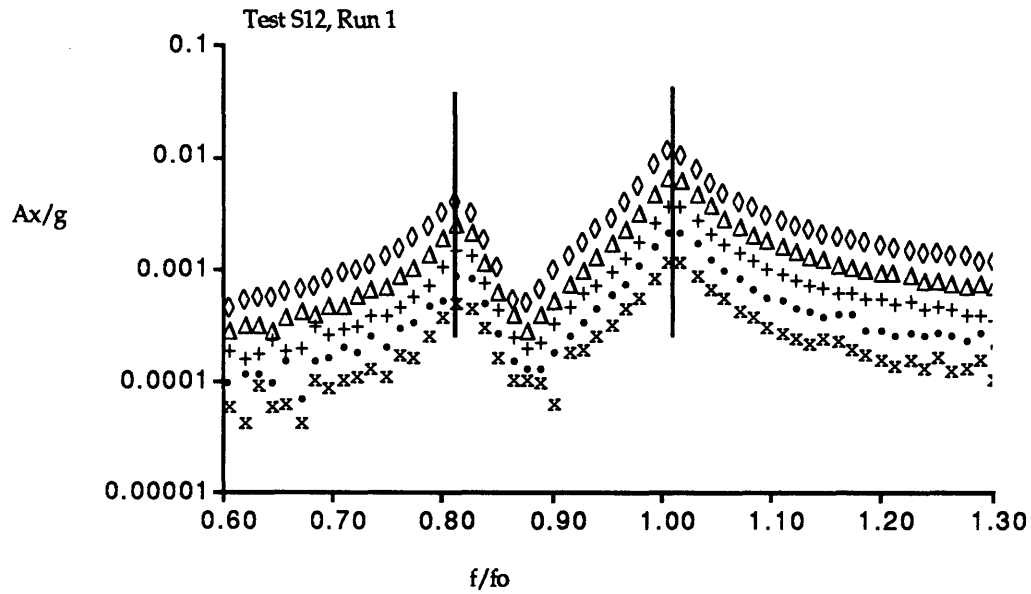
Figure 5.20   **Test S12, Non-dimensional Acceleration (Ax/g).**

(Spherical tank, harmonic excitation, coupled system.
Parameters; μ=0.063, ν=0.87, ζ=1.94%, Bo=251)

149
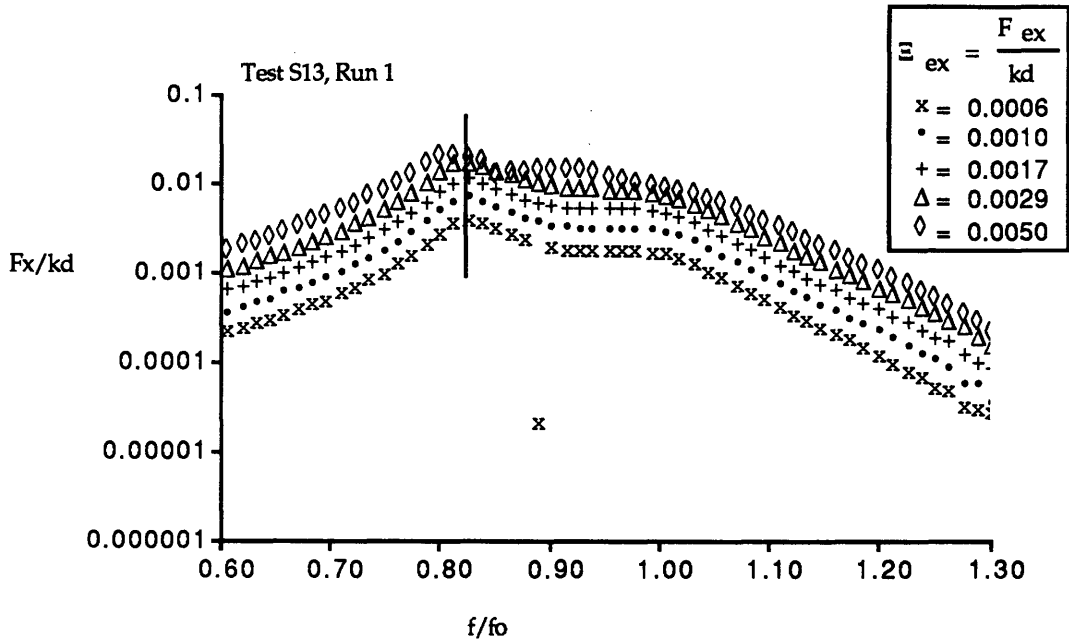
Figure 5.21   Test S13, Non-dimensional Planar Slosh Force (Fx/kd).
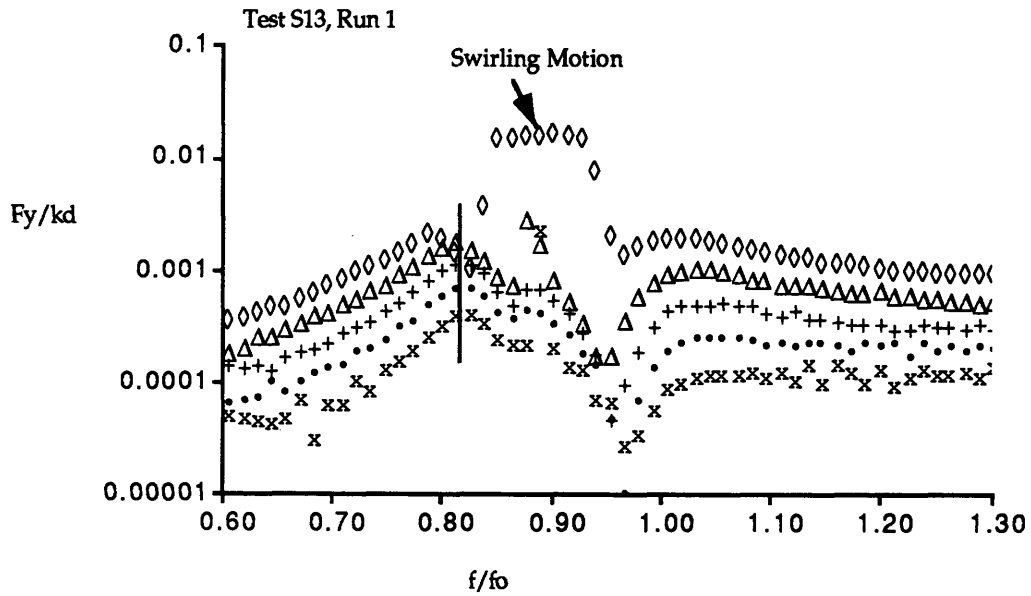
Figure 5.22   Test S13, Non-dimensional Nonplanar Slosh Force (Fy/kd).

(Spherical tank, harmonic excitation, coupled system.
Parameters; μ=0.063, v=0.87, ζ=7.76%, Bo=251)
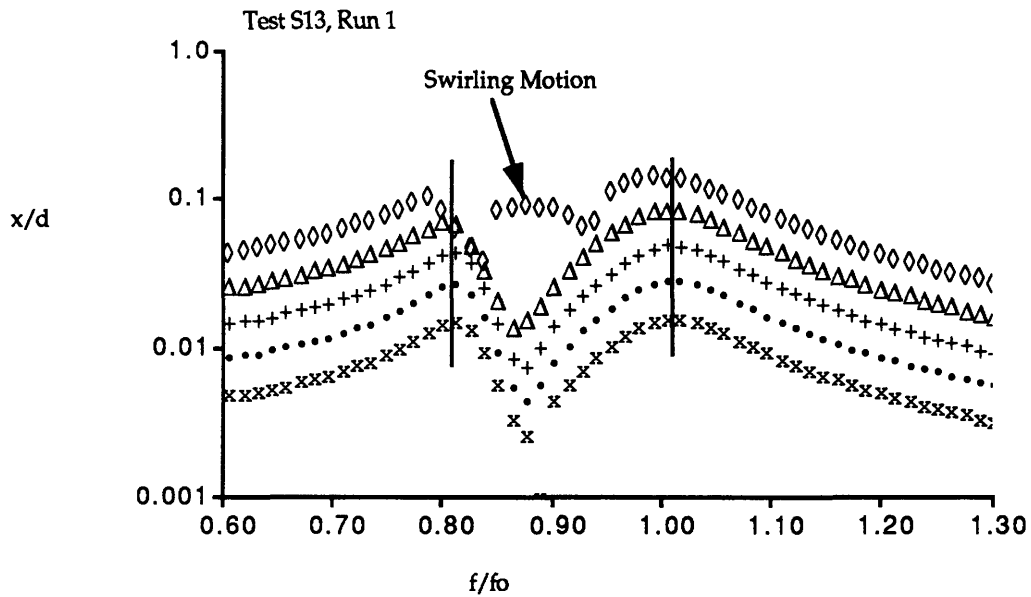
Figure 5.23   Test S13, Non-dimensional Displacement (x/d).
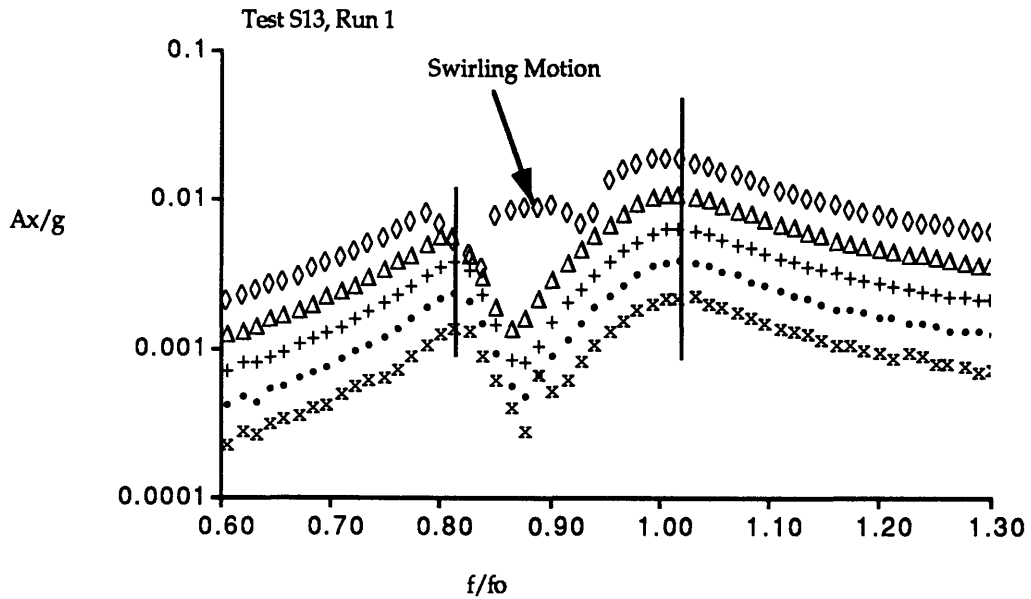
Figure 5.24   Test S13, Non-dimensional Acceleration (Ax/g).

(Spherical tank, harmonic excitation, coupled system.
Parameters; μ=0.063, v=0.87, ζ=7.76%, Bo=251)

Test S14, Run 1

Fx/kd

$$\Xi_{ex} = \frac{F_{ex}}{kd}$$

x = 0.0075
• = 0.0130
+ = 0.0226
Δ = 0.0392
◊ = 0.0680

f/fo
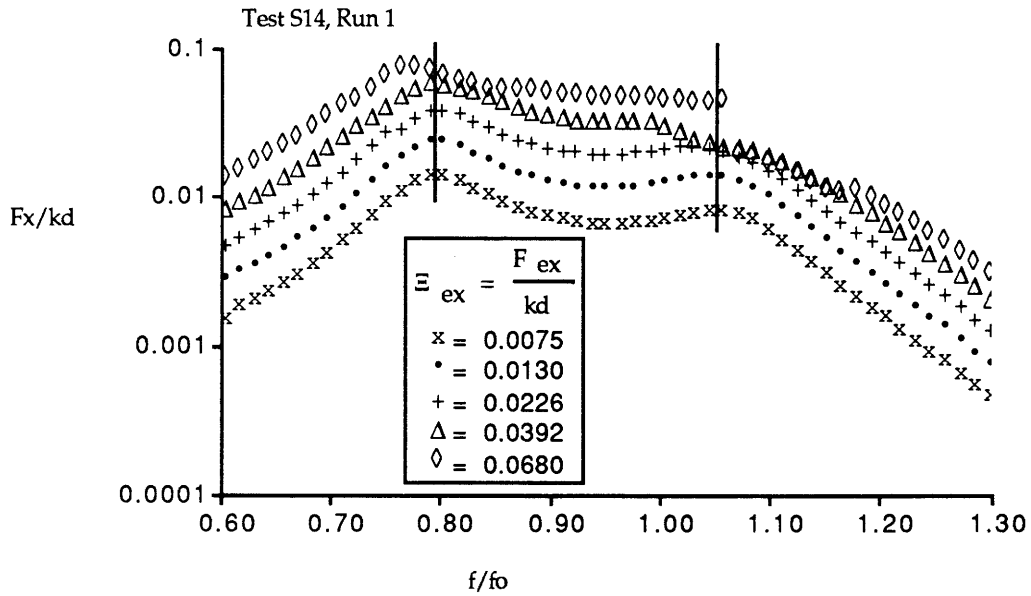
Figure 5.25   Test S14, Non-dimensional Planar Slosh Force (Fx/kd).

Test S14, Run 1

Swirling Motion

Fy/kd

f/fo
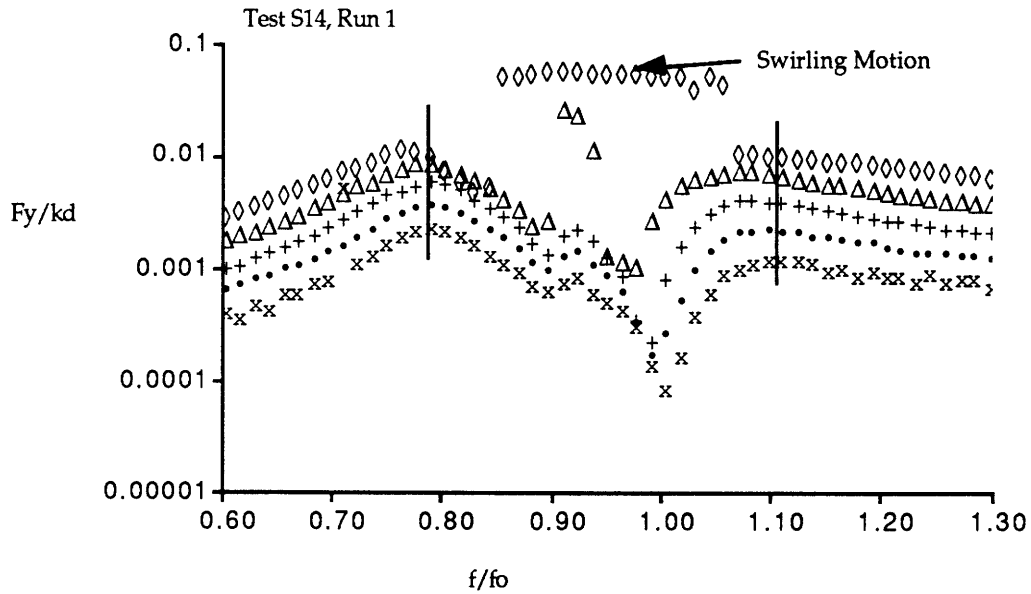
Figure 5.26   Test S14, Non-dimensional Nonplanar Slosh Force (Fy/kd).

(Spherical tank, harmonic excitation, coupled system.
Parameters; μ=0.16, ν=0.90, ζ=8.00%, Bo=251)
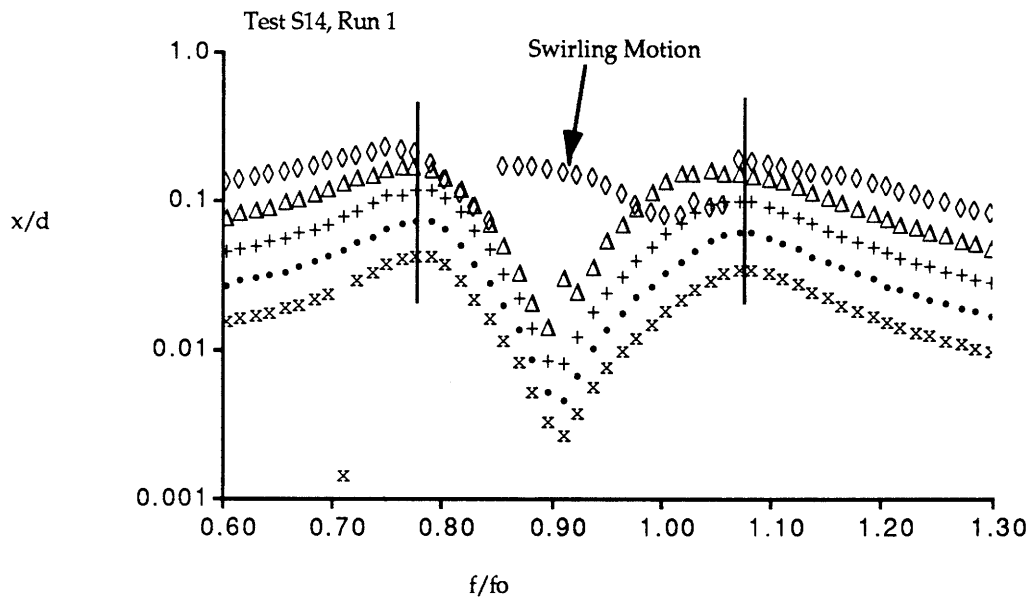
Figure 5.27   Test S14, Non-dimensional Displacement (x/d).
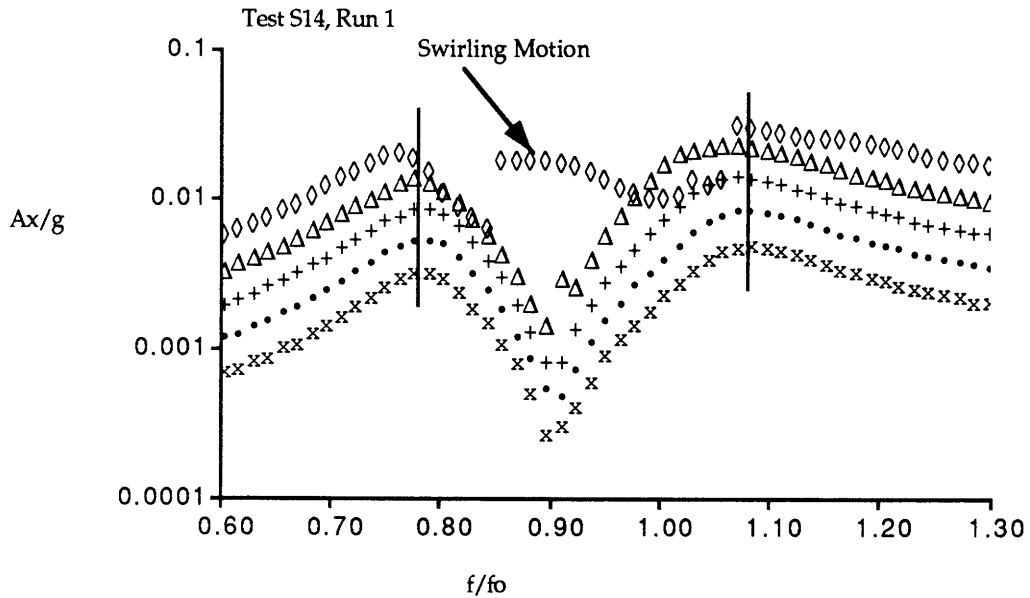
Figure 5.28   Test S14, Non-dimensional Acceleration (Ax/g).

(Spherical tank, harmonic excitation, coupled system.
Parameters; μ=0.16, v=0.90, ζ=8.00%, Bo=251)
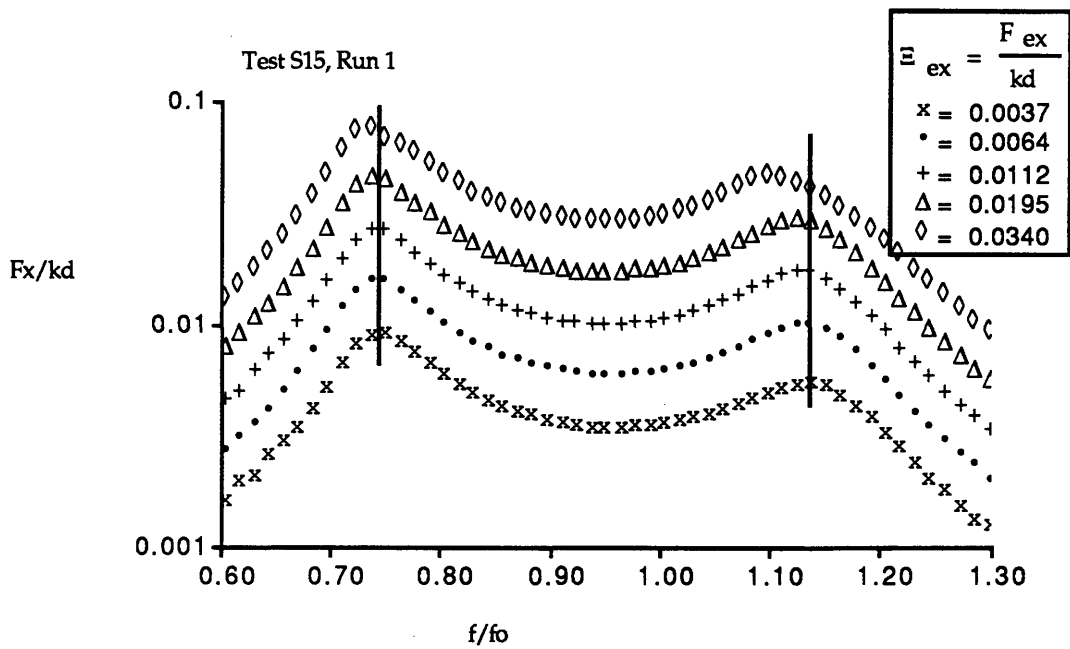
Figure 5.29   Test S15, Non-dimensional Planar Slosh Force (Fx/kd).
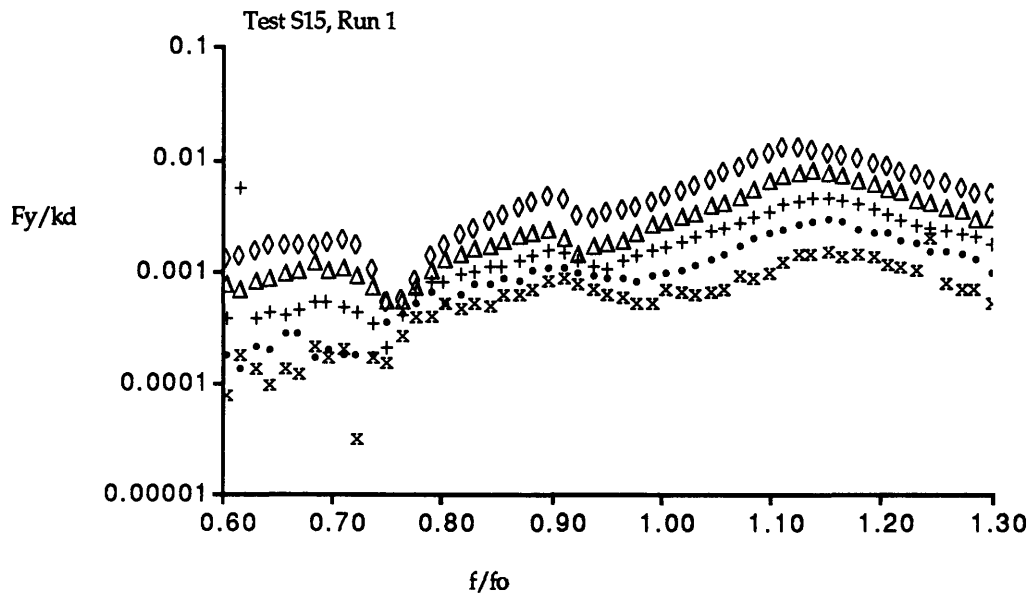
Figure 5.30   Test S15, Non-dimensional Nonplanar Slosh Force (Fy/kd).

(Spherical tank, harmonic excitation, coupled system.
Parameters; μ=0.32, ν=0.90, ζ=8.00%, Bo=251)

154

Test S15, Run 1
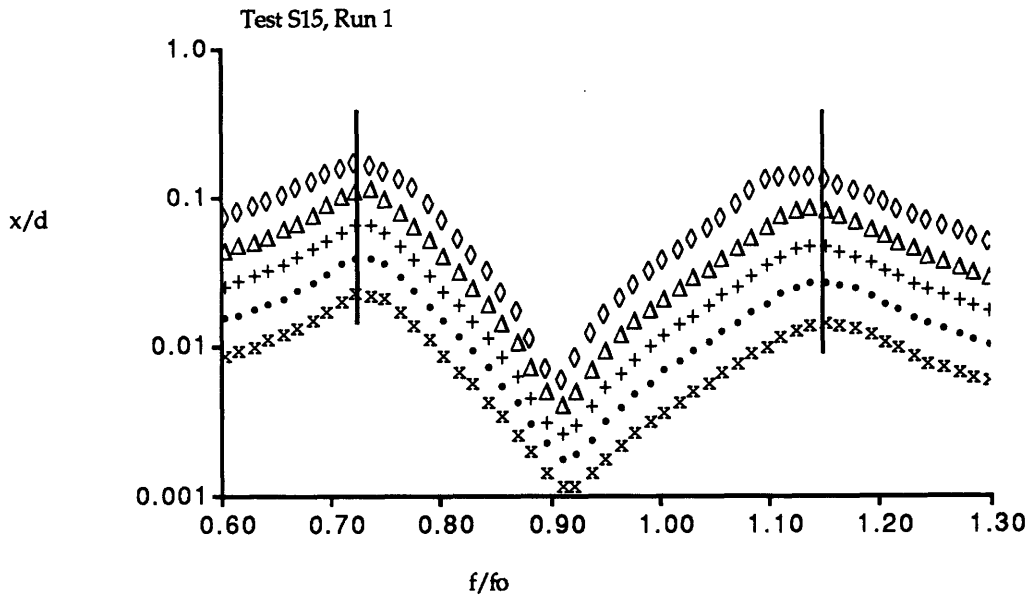
Figure 5.31   Test S15, Non-dimensional Displacement (x/d).

Test S15, Run 1
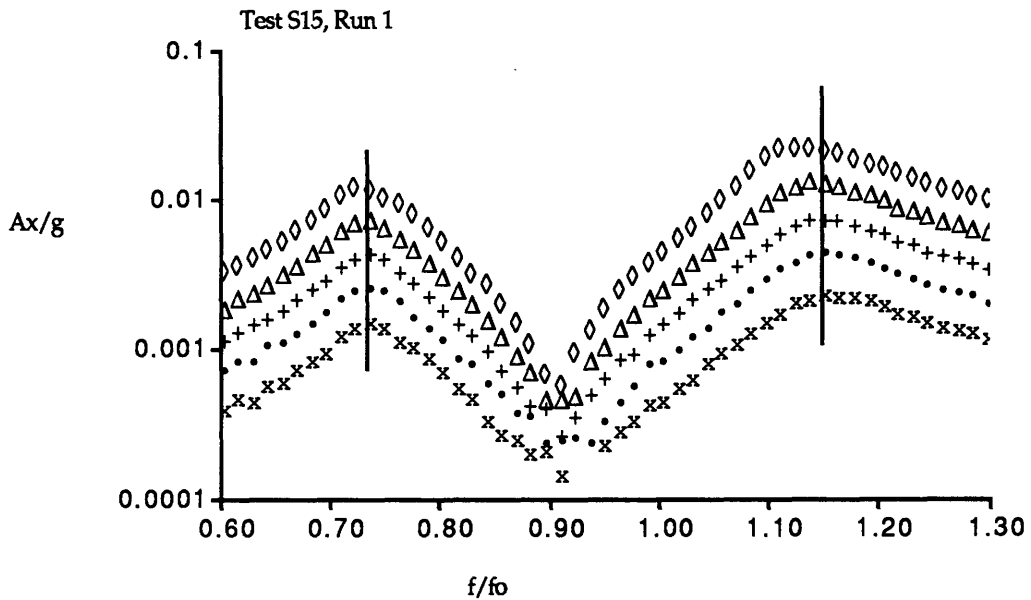
Figure 5.32   Test S15, Non-dimensional Acceleration (Ax/g).

(Spherical tank, harmonic excitation, coupled system.
Parameters; μ=0.32, ν=0.90, ζ=8.00%, Bo=251)

155
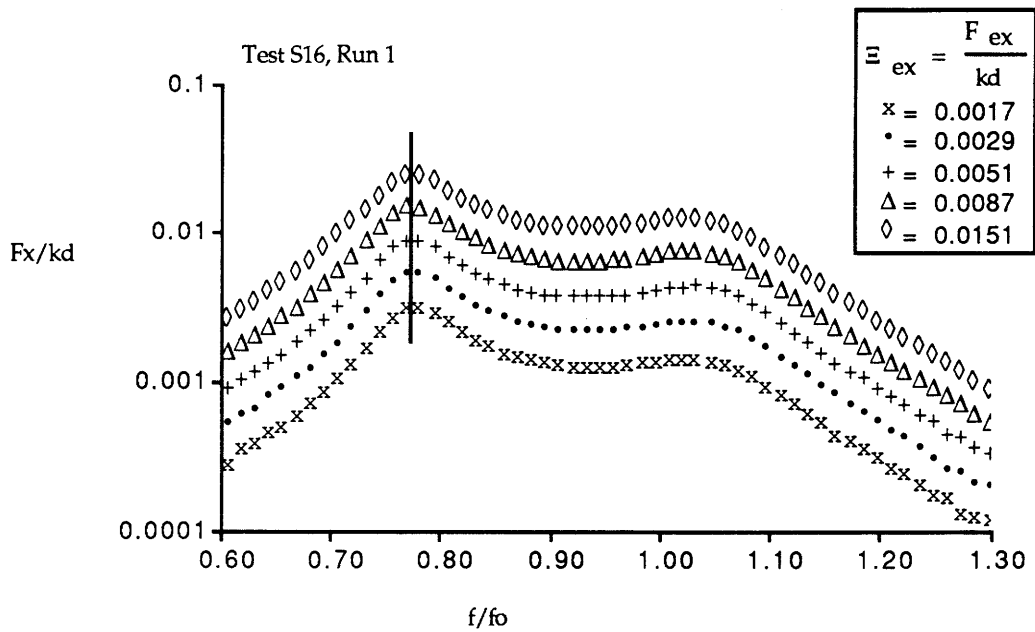
Figure 5.33   **Test S16, Non-dimensional Planar Slosh Force (Fx/kd).**
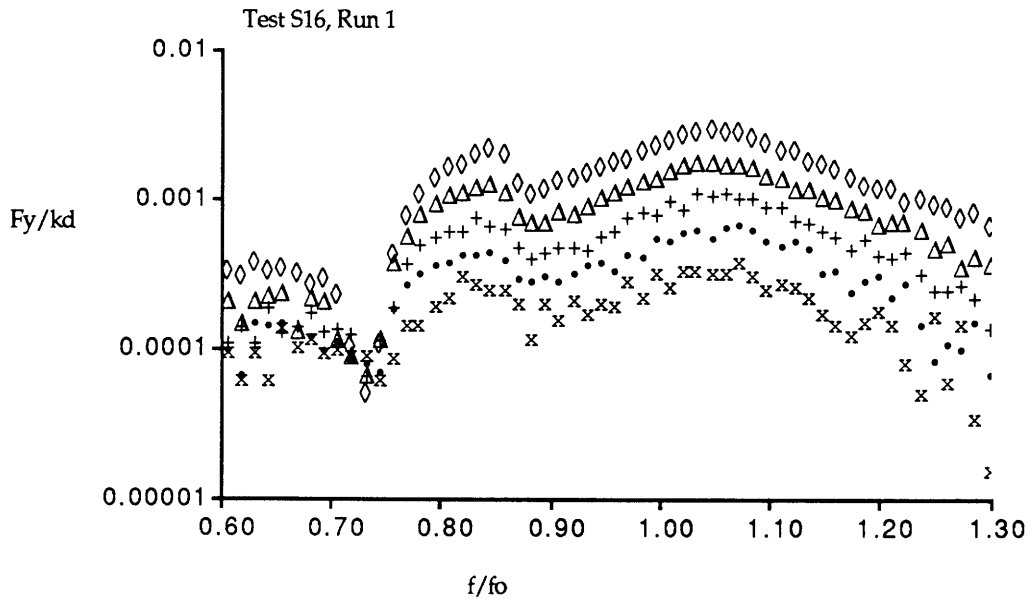
Figure 5.34   **Test S16, Non-dimensional Nonplanar Slosh Force (Fy/kd).**

(Spherical tank, harmonic excitation, coupled system.
Parameters; $\mu=0.16$, $v=0.85$, $\zeta=8.00\%$, $Bo=251$)
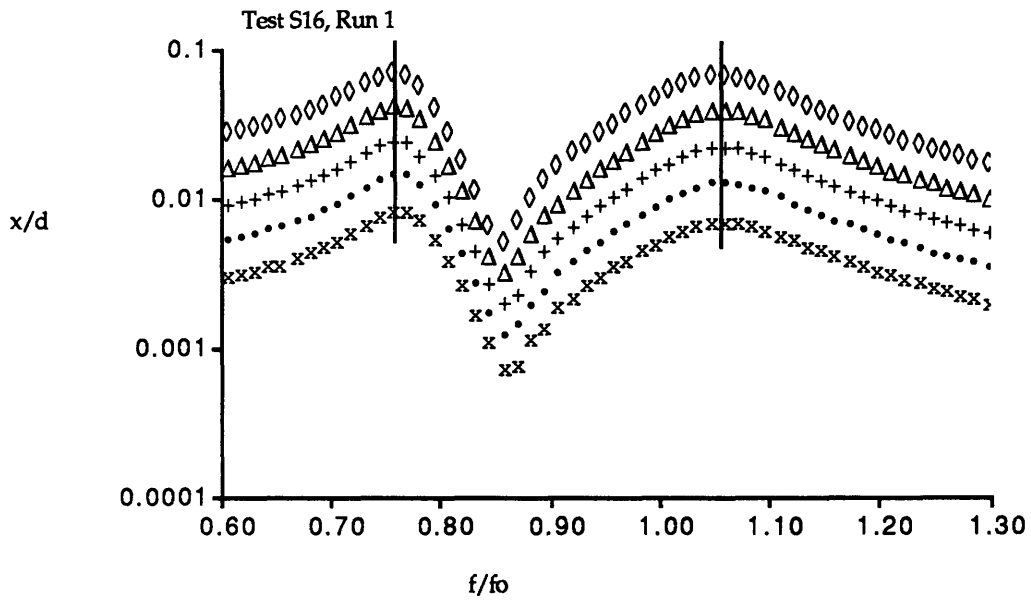
Figure 5.35   Test S16, Non-dimensional Displacement (x/d).
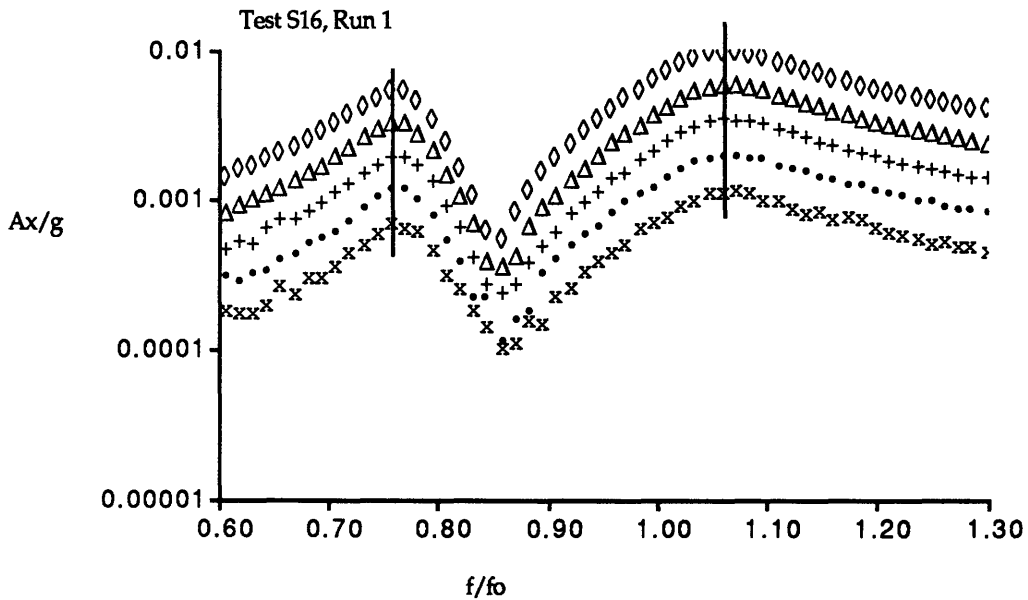
Figure 5.36   Test S16, Non-dimensional Acceleration (Ax/g).

(Spherical tank, harmonic excitation, coupled system.
Parameters; μ=0.16, v=0.85, ζ=8.00%, Bo=251)

157
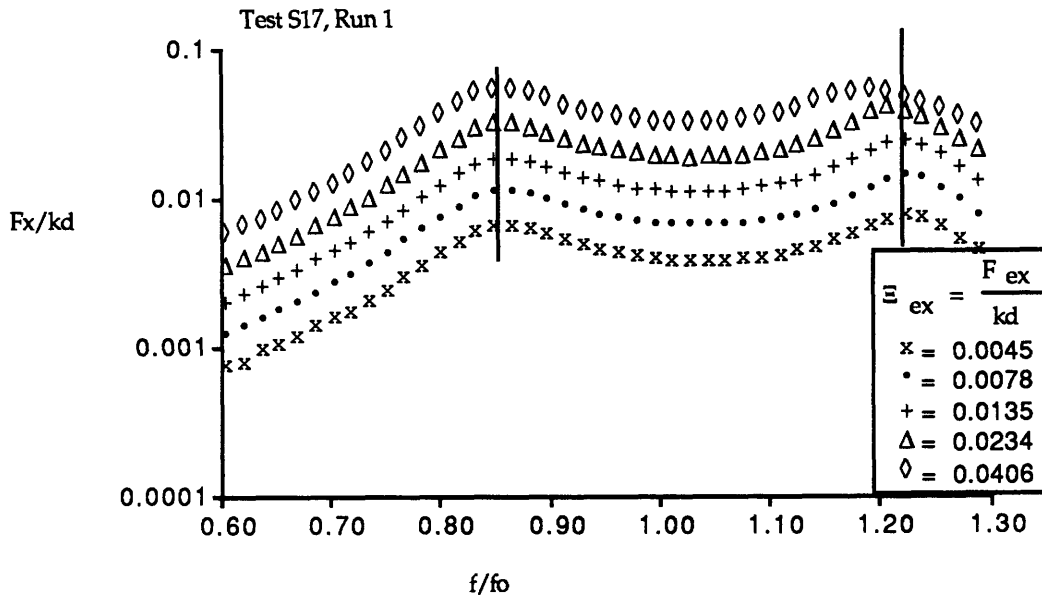
Figure 5.37   Test S17, Non-dimensional Planar Slosh Force (Fx/kd).
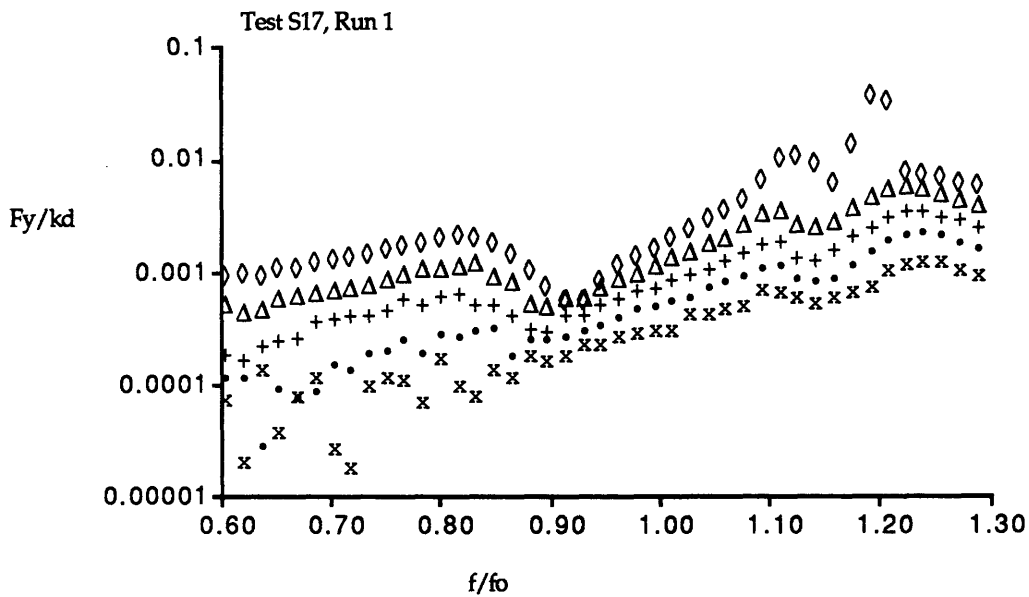
Figure 5.38   Test S17, Non-dimensional Nonplanar Slosh Force (Fy/kd).

(Spherical tank, harmonic excitation, coupled system.
Parameters; μ=0.16, ν=1.10, ζ=8.00%, Bo=251)
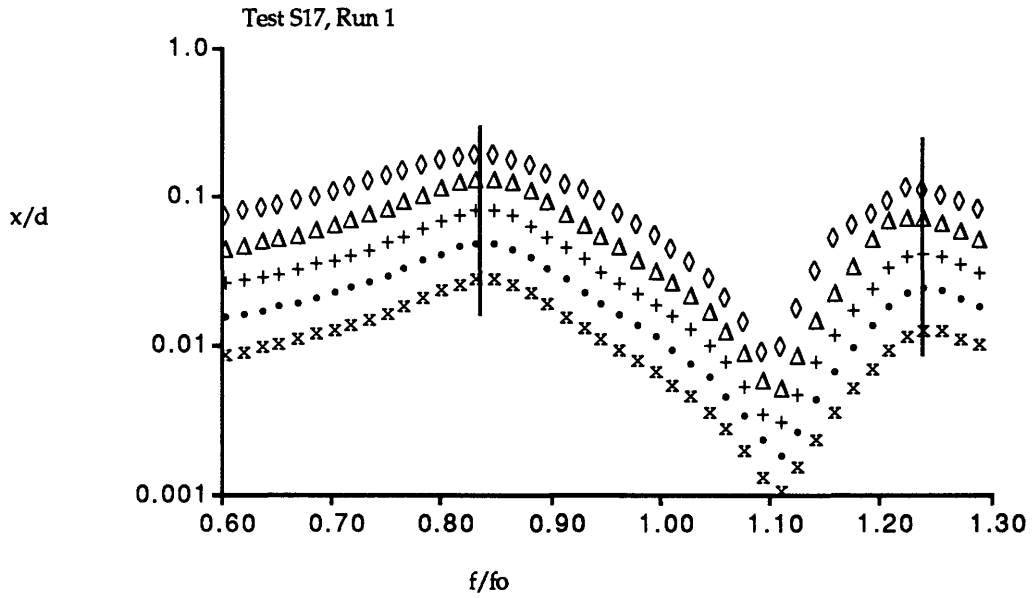
Figure 5.39   Test S17, Non-dimensional Displacement (x/d).
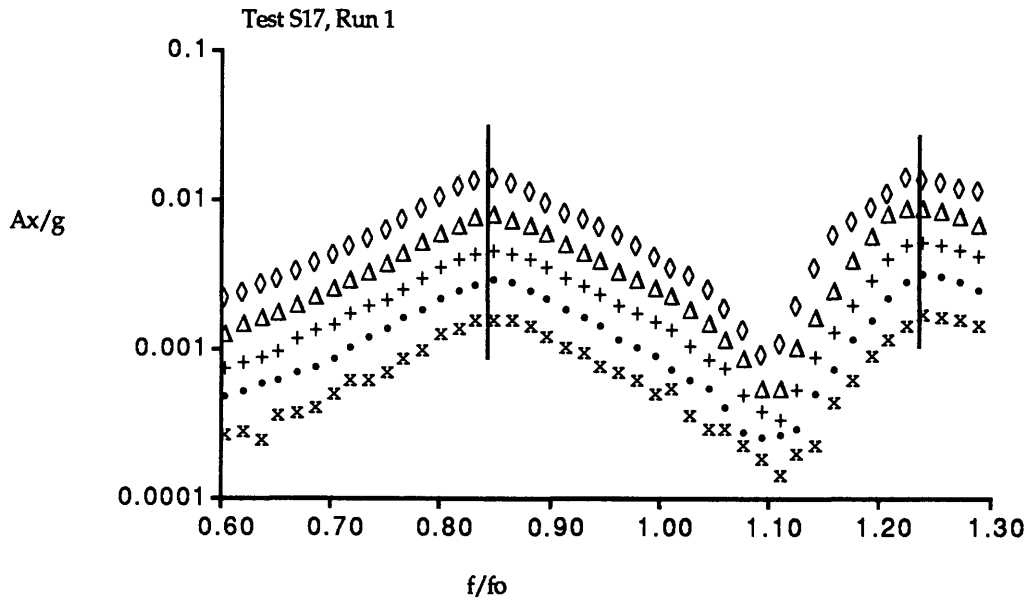
Figure 5.40   Test S17, Non-dimensional Acceleration (Ax/g).

(Spherical tank, harmonic excitation, coupled system.
Parameters; μ=0.16, ν=1.10, ζ=8.00%, Bo=251)
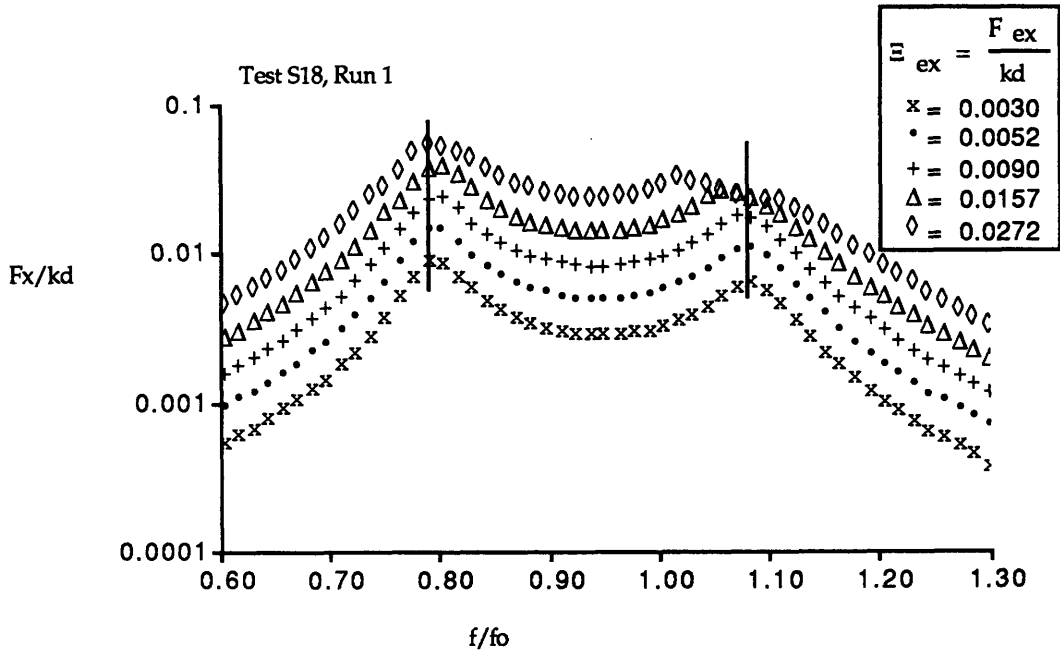
Figure 5.41   Test S18, Non-dimensional Planar Slosh Force (Fx/kd).
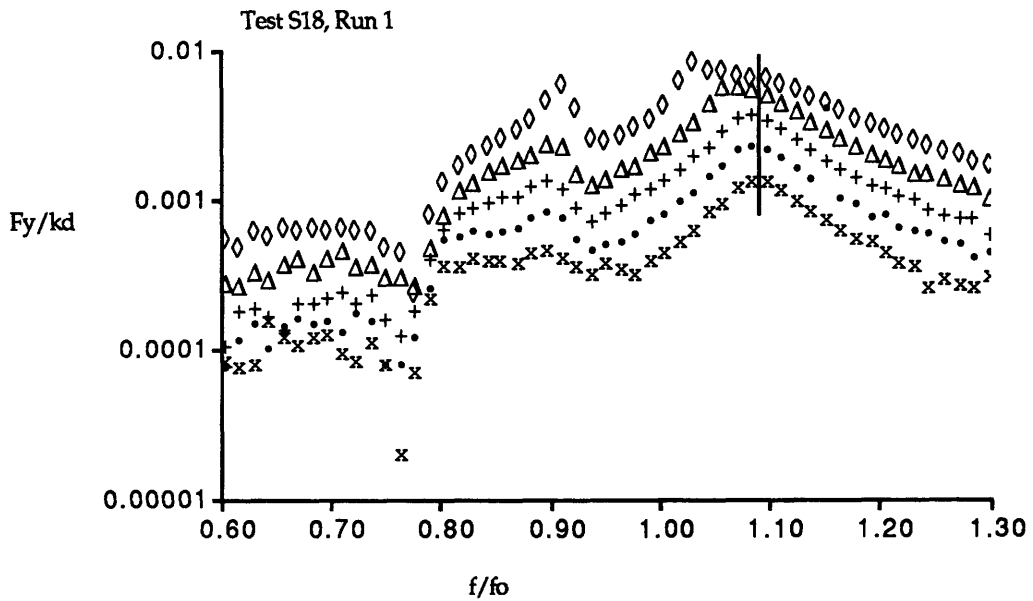
Figure 5.42   Test S18, Non-dimensional Nonplanar Slosh Force (Fy/kd).

(Spherical tank, harmonic excitation, coupled system
Parameters; μ=0.16, ν=0.90, ζ=4.00%, Bo=251)

Figure 5.43   Test S18, Non-dimensional Displacement (x/d).
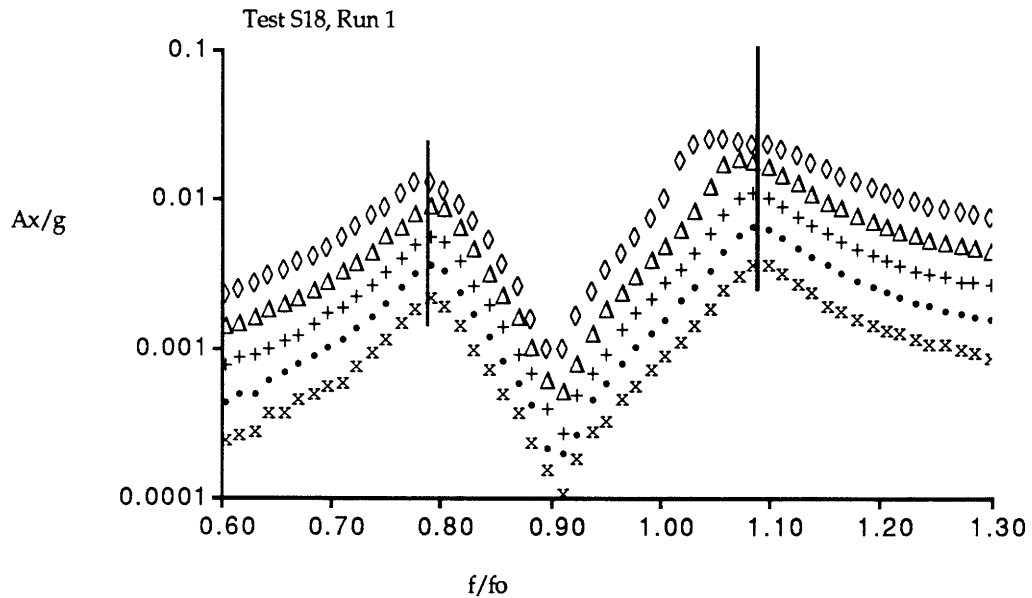
Figure 5.44   Test S18, Non-dimensional Acceleration (Ax/g).

(Spherical tank, harmonic excitation, coupled system.
Parameters; $\mu=0.16$, $\nu=0.90$, $\zeta=4.00\%$, Bo=251)
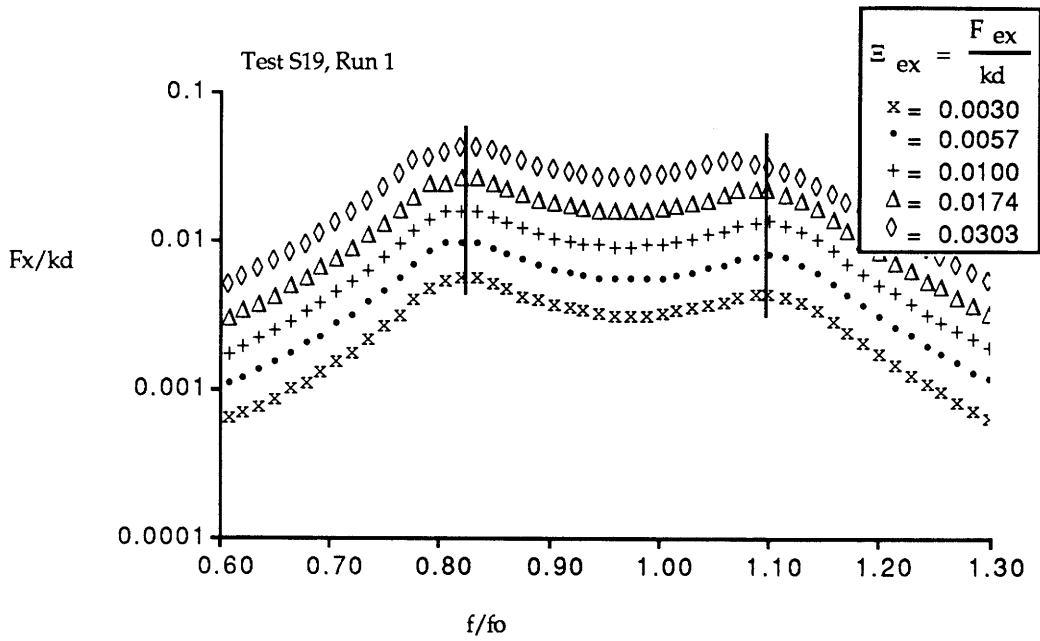
Figure 5.45   Test S19, Non-dimensional Planar Slosh Force (Fx/kd).
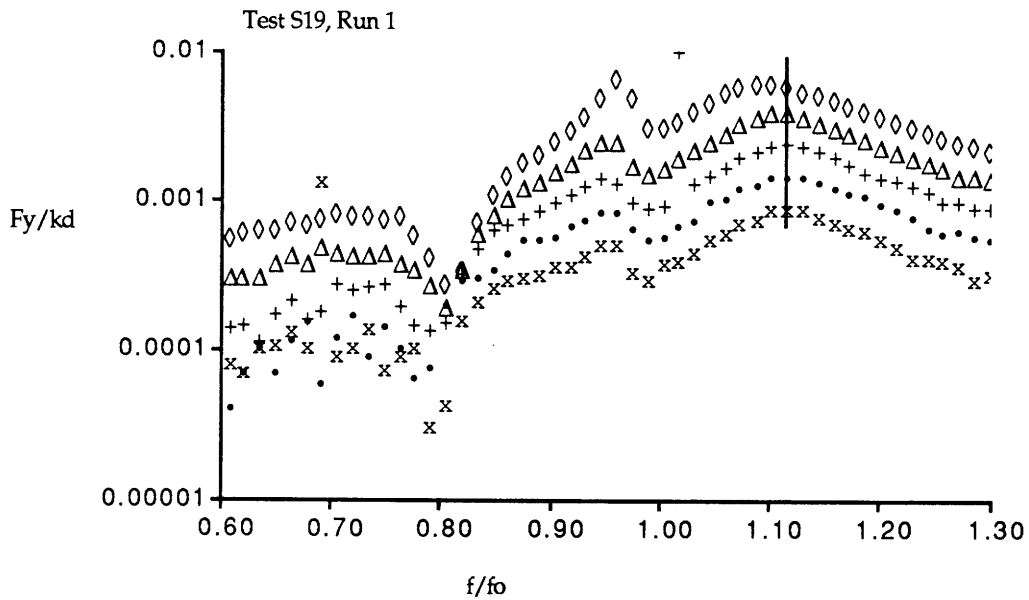
Figure 5.46   Test S19, Non-dimensional Nonplanar Slosh Force (Fy/kd).

(Spherical tank, harmonic excitation, coupled system.
Parameters; $\mu=0.16$, $v=0.95$, $\zeta=8.00\%$, Bo=251)

Test S19, Run 1
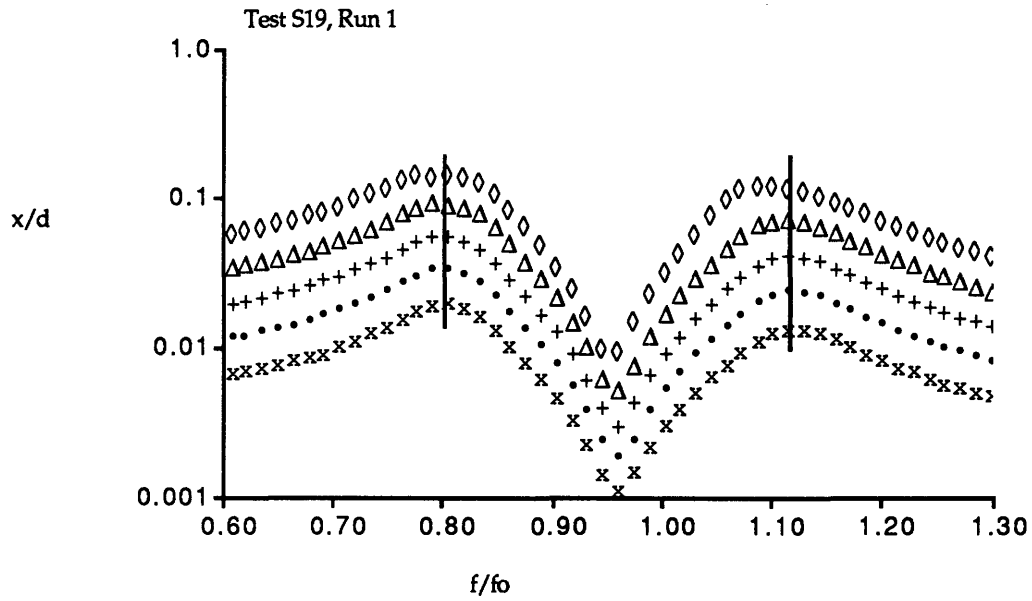
Figure 5.47   Test S19, Non-dimensional Displacement (x/d).

Test S19, Run 1
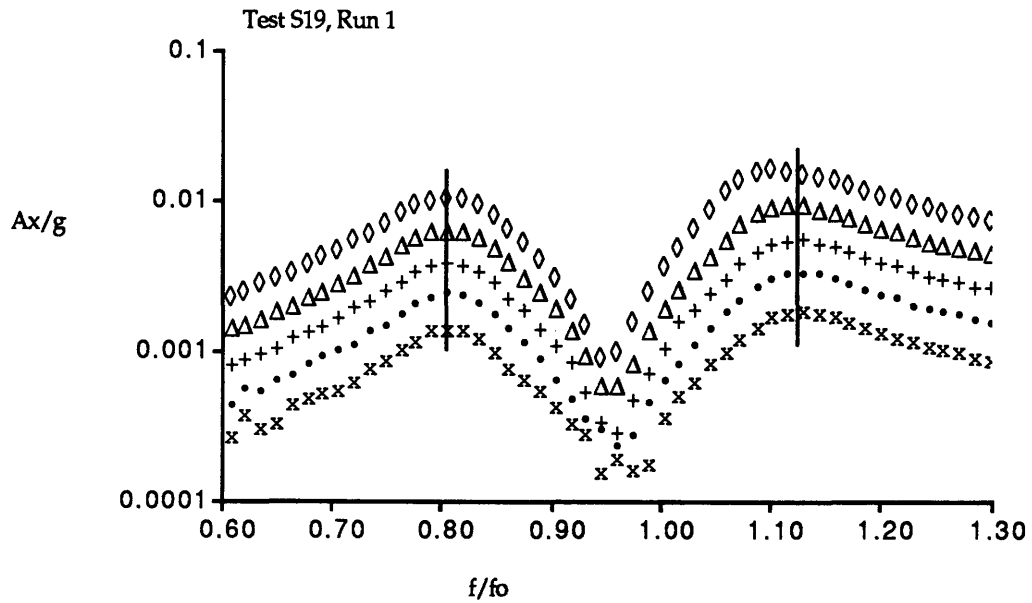
Figure 5.48   Test S19, Non-dimensional Acceleration (Ax/g).

(Spherical tank, harmonic excitation, coupled system.
Parameters; μ=0.16, ν=0.95, ζ=8.00%, Bo=251)

163

5.3 Square Tank Model

Figure 5.49 is a drawing of the square tank used to investigate the dynamic behavior of a fluid contained in a square tank. The details of the dynamic test, test parameters and test procedures are as discussed in chapter 4. The relevant tank parameters are summarized in Table 5.8.

Table 5.8   Square Tank Parameters

Parameter	Abbreviation	Value
Width (Inside)	W	29.64 mm
Tank Height	H	90.00 mm
Fill Height	h	29.64 mm
Normalization Factor	d	29.64 mm
Bond Number	Bo	61
Empty Mass	m_E	85.16 g
Fluid Mass	m_F	26.68 g
1st Fluid Slosh Frequency	f_s	5.09 Hz
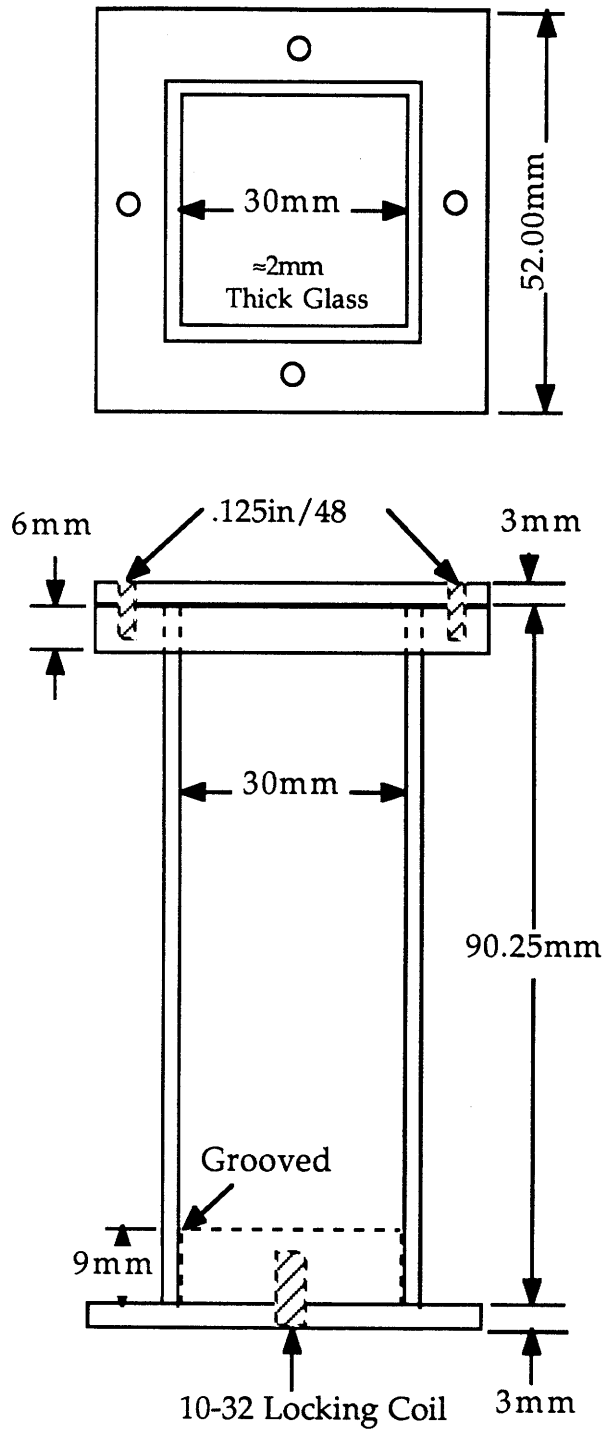
Figure 5.49   Square Study Model

5.3.1 Square Tank Test Matrix

A series of uncoupled tests were performed to determine the low-amplitude linear characteristics of the fluid and for comparison with the coupled test results. The angle between the tank symmetry axis (See Fig. 5.50) was varied to determine the effect of non-planar excitation. Each test has a unique test identifier and this identifier will be used to identify the experimental results presented in this chapter. Table 5.9 summarizes the uncoupled (fluid alone) test matrix and Table 5.10 the coupled (fluid/spacecraft) test matrix. A 2% photoflo/water solution was used in all these tests and the excitation frequency ranged from 3.5 Hz to 6.5 Hz.

Table 5.9 Square Uncoupled Test Matrix

Test ID	Excitation Angle	Figures
VU1	0°	5.51, 5.52
VU2	15°	5.53, 5.54
VU3	30°	5.55, 5.56
VU4	45°	5.57, 5.58
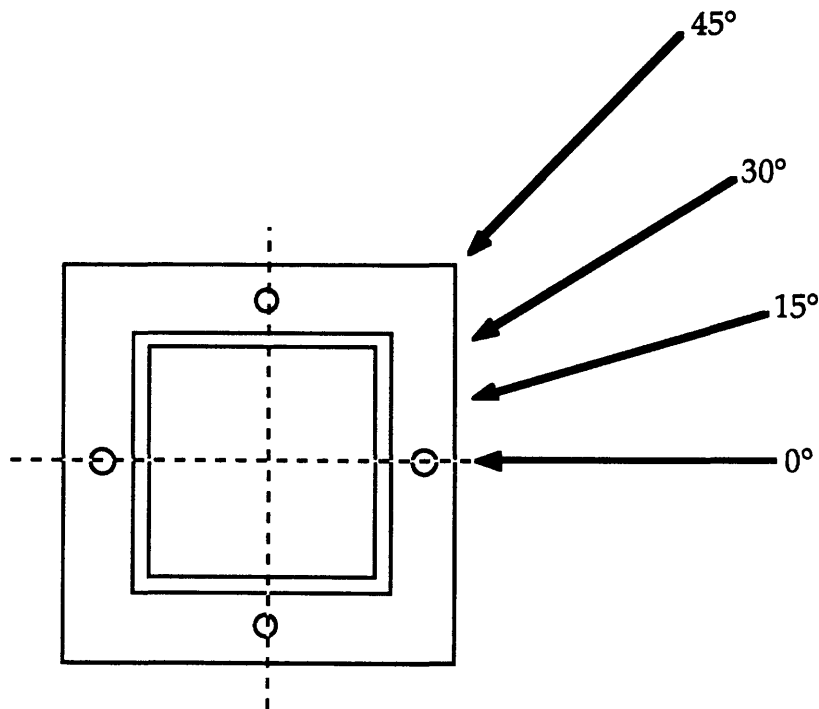
Figure 5.50   Explanation of Excitation Angle

166

Table 5.10   Square Coupled Test Matrix

Test ID	Excitation Angle	μ	ν	$\zeta\,(\%)$	Figures
V16	0°	0.16	0.92	8.00	5.59 - 5.62
V17	0°	0.32	0.92	8.00	5.63 - 5.66
V18*	0°	0.16	0.87	8.00	5.67 - 5.69
V19	0°	0.16	0.92	4.00	5.70 - 5.73
V20	15°	0.16	0.92	8.00	5.74 - 5.77
V21	15°	0.32	0.92	8.00	5.78 - 5.81
V22	30°	0.16	0.92	8.00	5.82 - 5.85
V23	30°	0.32	0.92	8.00	5.86 - 5.89
V24	45°	0.16	0.92	8.00	5.90 - 5.93
V25	45°	0.32	0.92	8.00	5.94 - 5.97

Note: ν = Frequency Ratio = $f_{Slosh}/f_{Spacecraft} = f_s/f_o$

μ = Mass Ratio = $m_{Fluid}/m_{Spacecraft\;Mode} = m_F/m$

ζ = Damping Ratio of Spacecraft Mode

* = Loss of one of the measured signals.

In the uncoupled tests, the fluid/spacecraft system was harmonically excited over a frequency range covering the first fluid slosh mode resonance and in the coupled tests also covering the spacecraft resonance. A total of 5 logarithmically spaced (Log_{10}) force excitation levels were used to determine the dynamic characteristics. The force excitation levels used in the uncoupled tests are summarized in Table 5.1. This table also identifies the graphic symbols used to present the experimental results. In Table 5.11, the minimum force level and maximum force level for the coupled tests are summarized. The intermediate force levels are logarithmically spaced between these minimum and maximum values. Note that the applied force, F_{ex}, is non-dimensionalized by dividing with (kd) to yield the non-dimensional force Ξ_{ex}.

Table 5.11   Minimum and Maximum Non-dimensional Experimentally
Applied Harmonic Excitation Levels for the Square Tank Coupled Tests

Test ID	$\left|\Xi_{ex_{min}}\right|$	$\left|\Xi_{ex_{max}}\right|$
Graphic Symbol:	x	◊
V16	0.0025	0.0231
V17	0.0025	0.0231
V18	0.0014	0.0129
V19	0.0008	0.0069
V20	0.0016	0.0144
V21	0.0013	0.0116
V22	0.0013	0.0116
V23	0.0019	0.0173
V24	0.0013	0.0116
V25	0.0019	0.0173

5.3.2 Square Tank Experimental Results

Section 5.3.2.1 discusses the uncoupled test results and section 5.3.2.2 the coupled test results.

5.3.2.1   Discussion of the Uncoupled Test Results

The linear eigen-characteristics of the first fluid slosh mode, as obtained from the uncoupled tests, are summarized in Table 5.12. The damping ratios were obtained with the half-power-band-width method from the lowest force excitation level results. Figures 5.51 to 5.58 give the results of the uncoupled tests (also see Table 5.9 for a more detailed identification of the figures). The vertical solid line in these figures indicates the position of the resonance peak as predicted by linear theory. Any shift of the resonance peak away from this vertical line represents nonlinear fluid slosh behavior. The direction of excitation is also indicated on each figure.

Table 5.12   Measured Linear Eigen-characteristics (Square Tank, with 2% Photoflo/Water Solution)

Test ID	Excitation Angle	Natural Frequency (Hz)	Damping Ratio (%)	Slosh Mass Fraction λ
VU1	0°	5.09	2.9	0.41
VU2	15°	5.09	3.0	0.41
VU3	30°	5.09	2.9	0.42
VU4	45°	5.09	2.8	0.42

In the uncoupled test results, the fluid slosh mode exhibits a softening tendency (decreasing resonant frequency) with increasing force excitation amplitudes. Above moderate excitation amplitudes, the fluid motion jumps from the expected linear planar motion to a combined planar, nonplanar swirling motion. The regions of swirling motion indicated in the figures are based on experimental observations.

5.3.2.2   Discussion of the Coupled Test Results

In the coupled tests, the mass ratios, frequency ratios and damping ratios were varied to determine the effect of these parameters on the coupled behavior of the fluid/spacecraft system. Figures 5.61 to 5.97 give the results of the coupled tests with the square tank (also see 5.10 for a more detailed identification of the figures). As with the uncoupled tests, the vertical solid lines in these figures indicate the positions of the resonance peaks as predicted by linear theory. Any shift of the resonance peaks away from this verticals line represent nonlinear behavior. The direction of excitation is also indicated on each figure.

Studying the Figures 5.55 to 5.60 (Test V16) it can be seen that both the first fluid mode and the spacecraft mode exhibit softening (decrease in resonant frequency with an increase in force excitation amplitude) trends and that the shape of the resonant peaks are amplitude dependent. At low

169

force excitation amplitudes, the fluid and spacecraft motion exhibit linear planar motion but for moderate force excitation amplitudes, the motion jumped from the expected planar motion to a stable nonplanar swirling motion (as experimentally observed). The swirling motion occurs roughly between the two resonant peaks and the nonplanar reaction slosh force is equal to the planar reaction slosh force in this region. Taking this test (V16 $\mu=0.16$, $v=0.92$, $\xi=8.00\%$) as the nominal configuration, the following conclusions can be made concerning:

The Effect of Mass Ratio: From Fig. 5.65 (Test V17, $\mu=0.32$, $v=0.92$, $\xi=8.00\%$) it can be concluded that, contrary to the results obtained with the spherical tank, higher mass fractions result in more nonlinear fluid behavior. In this figure, for high force excitation amplitudes, the swirling motion completely dominates the dynamics and instead of two resonant peaks, there is only one. This peak occurs roughly between the two linear resonant peaks.

The Effect of Frequency Ratio: The lack of experiments with varying frequency ratios makes a conclusion on the effect of this parameter on the system dynamics difficult. From Fig. 5.68 (Test V18, $\mu=0.16$, $v=0.87$, $\xi=8.00\%$), however, one could conclude that configurations with frequencies ratios close to unity are more nonlinear.

The Effect of Damping Ratio: It is clear from Fig. 5.72 (Test V19, $\mu=0.16$, $v=0.92$, $\xi=4.00\%$) that configurations, with lower spacecraft modal damping ratios, are more nonlinear.

The Effect of Excitation Angle: From Fig. 5.61 (Test V16, Excitation Angle=0°), Fig. 5.76 (Test V20, Excitation Angle=15°), Fig. 5.82 (Test V22, Excitation Angle=30°) and Fig. 5.92 (Test V24, Excitation Angle=45°) it can be concluded that the excitation angle only effects the low force excitation level results. The observed swirling motion, associated with the jump phenomenon, is a combination of the two repeated eigen-modes (the first planar and the first nonplanar fluid slosh modes). This swirling motion dominates above a critical force excitation level and since the motion is already a combination of the two repeated eigen-vectors (the planar and nonplanar modes), the excitation angle has little effect on the dynamics.

In conclusion, the square tank tests indicate that the coupled dynamics of these configurations are very nonlinear. For force excitation amplitudes exceeding a critical value the motion jumps from the linearly

expected planar motion to a very stable nonplanar, swirling motion. The critical force amplitude above which this jump phenomenon occurs is configuration dependent but the indications are that this motion will be very difficult to avoid, complicating any control design.
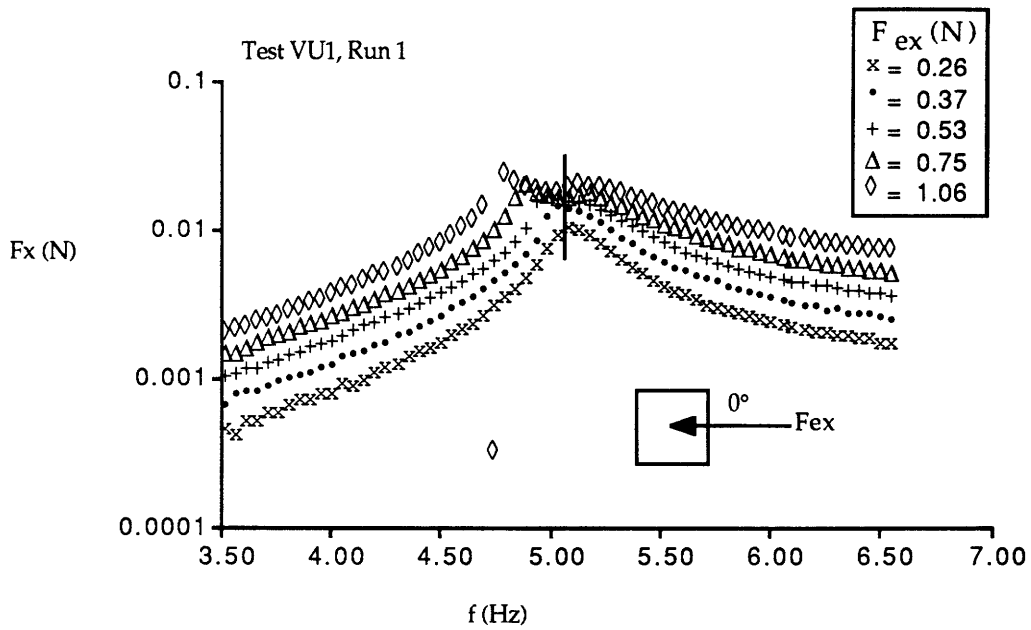
Figure 5.51   Test VU1, Planar Slosh Force (Fx).
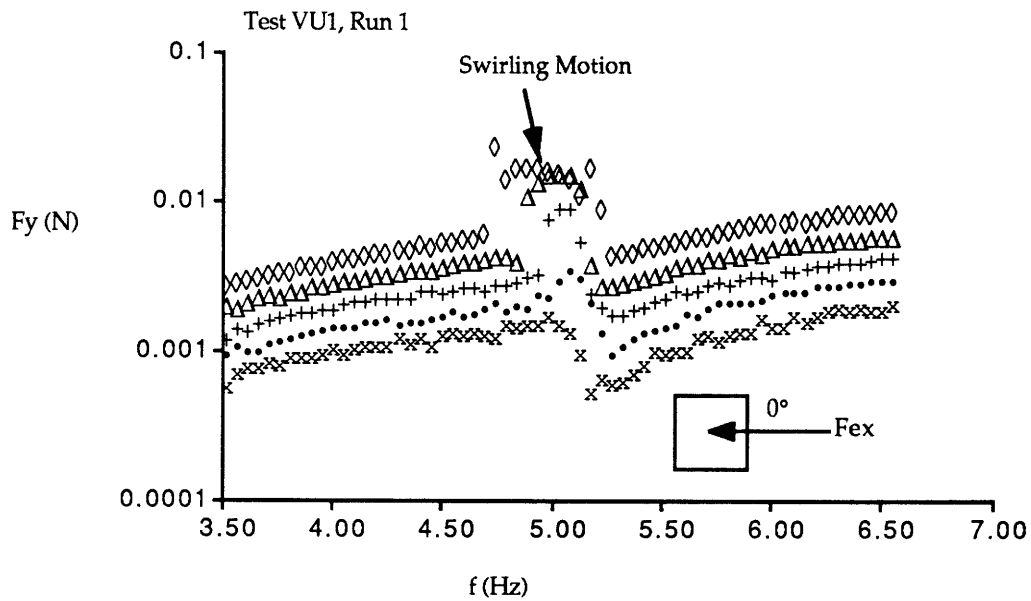
Figure 5.52   Test VU1, Nonplanar Slosh Force (Fy).

(Square tank, uncoupled, harmonic excitation, Excitation angle=0° and
Fluid=2% Photoflo/Water Solution)
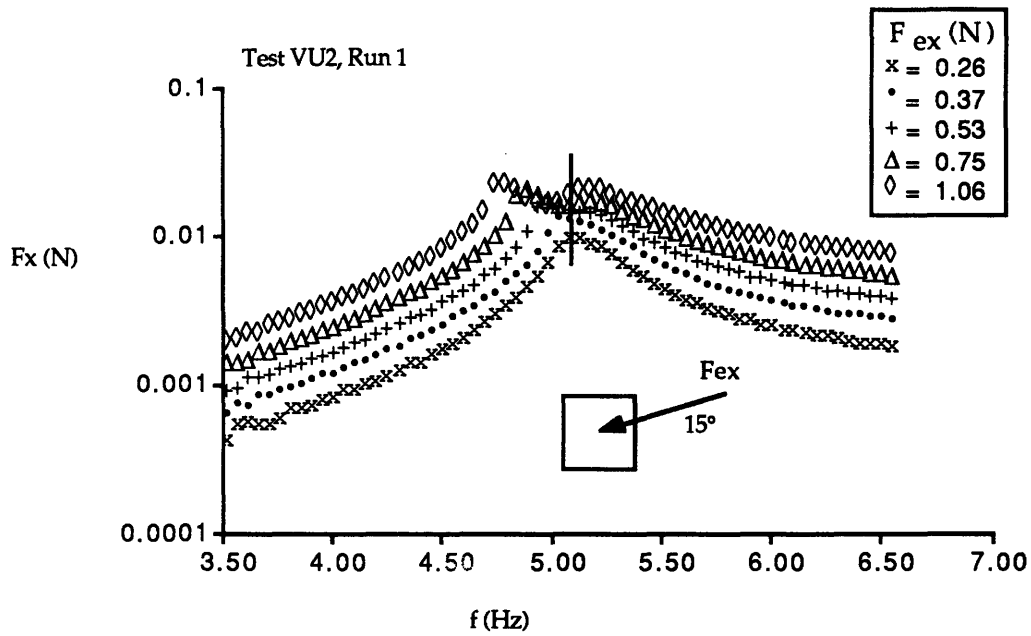
Figure 5.53   Test VU2, Planar Slosh Force (Fx).
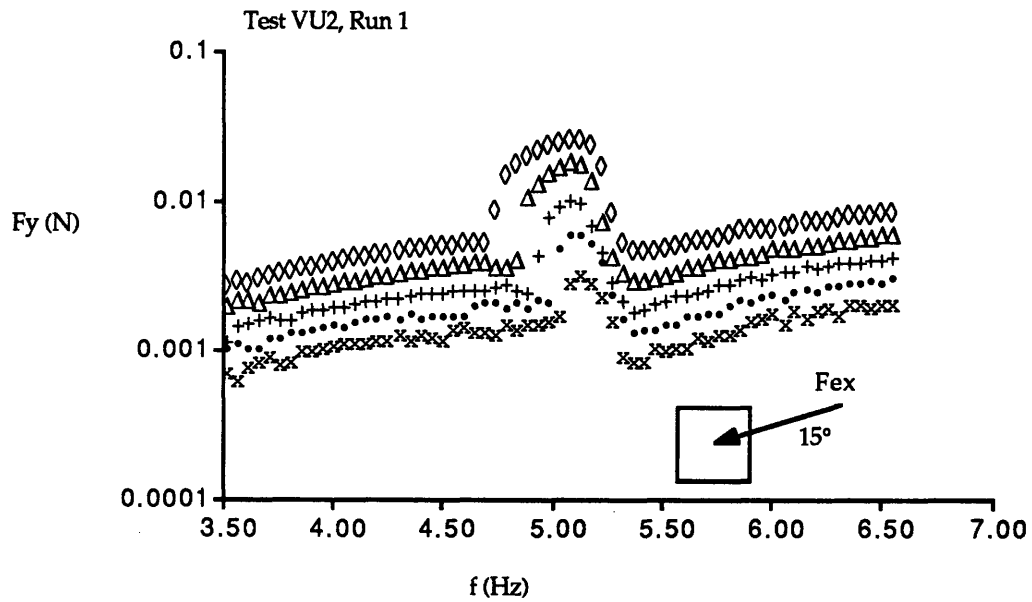
Figure 5.54   Test VU2, Nonplanar Slosh Force (Fy).

(Square tank, uncoupled, harmonic excitation, Excitation angle=15°
and Fluid=2% Photoflo/Water Solution)

173
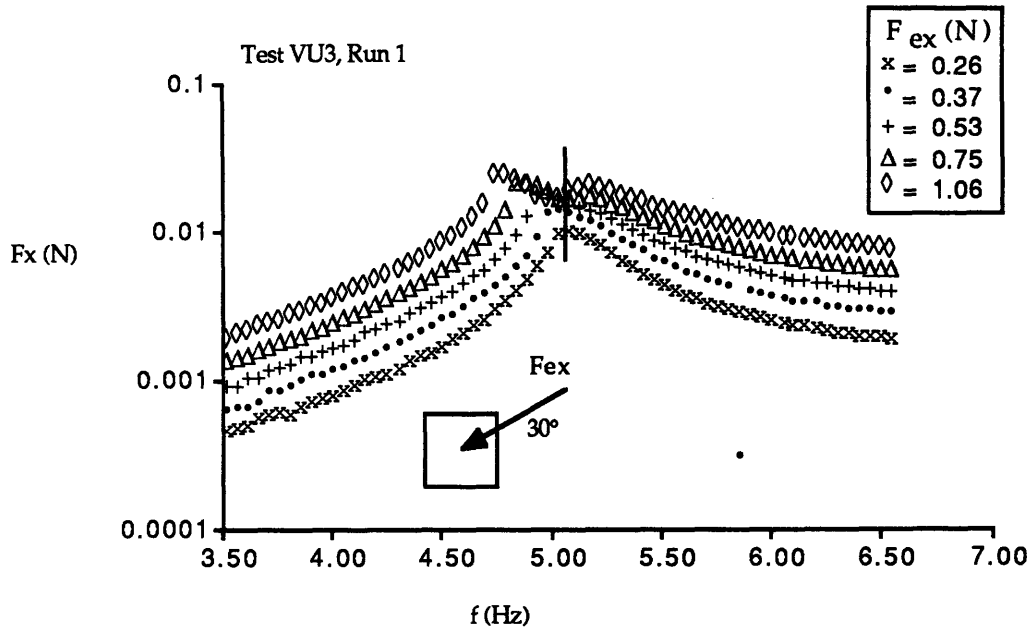
Figure 5.55   Test VU3, Planar Slosh Force (Fx).
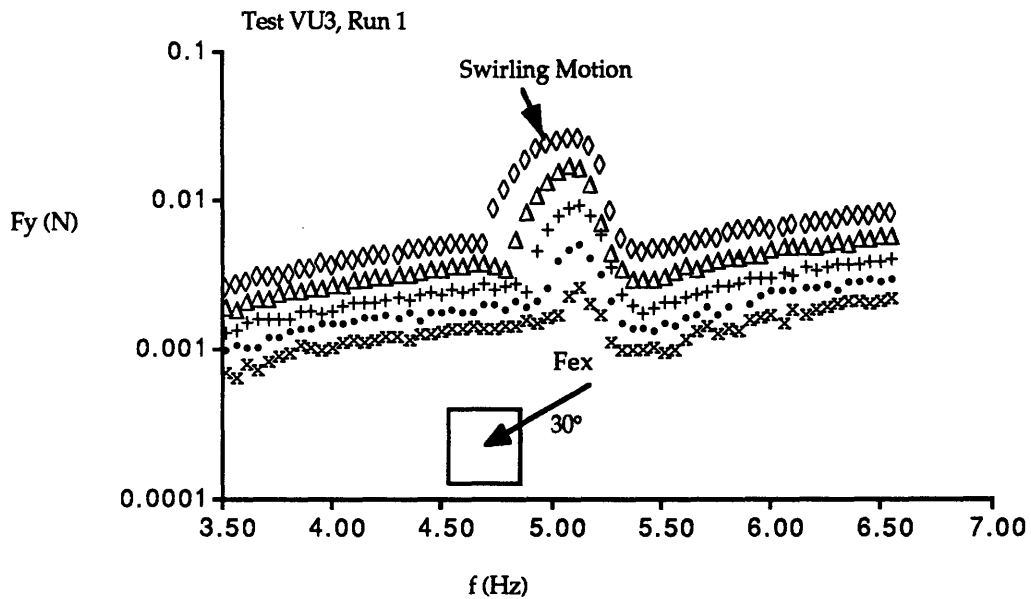
Figure 5.56   Test VU3, Nonplanar Slosh Force (Fy).

(Square tank, uncoupled, harmonic excitation, Excitation angle=30°
and Fluid=2% Photoflo/Water Solution)
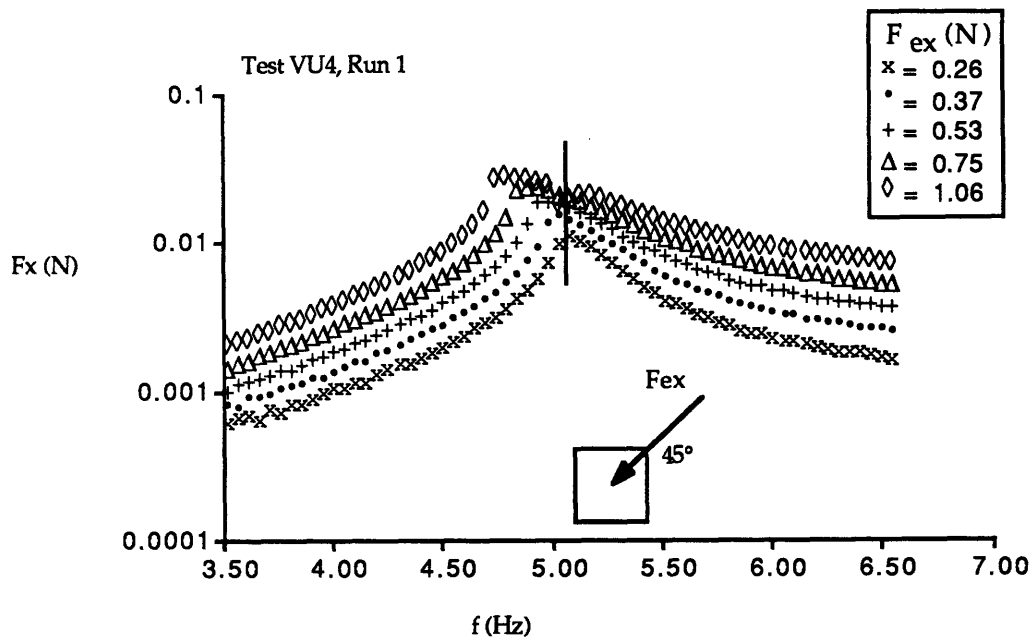
Figure 5.57   Test VU4, Planar Slosh Force (Fx).
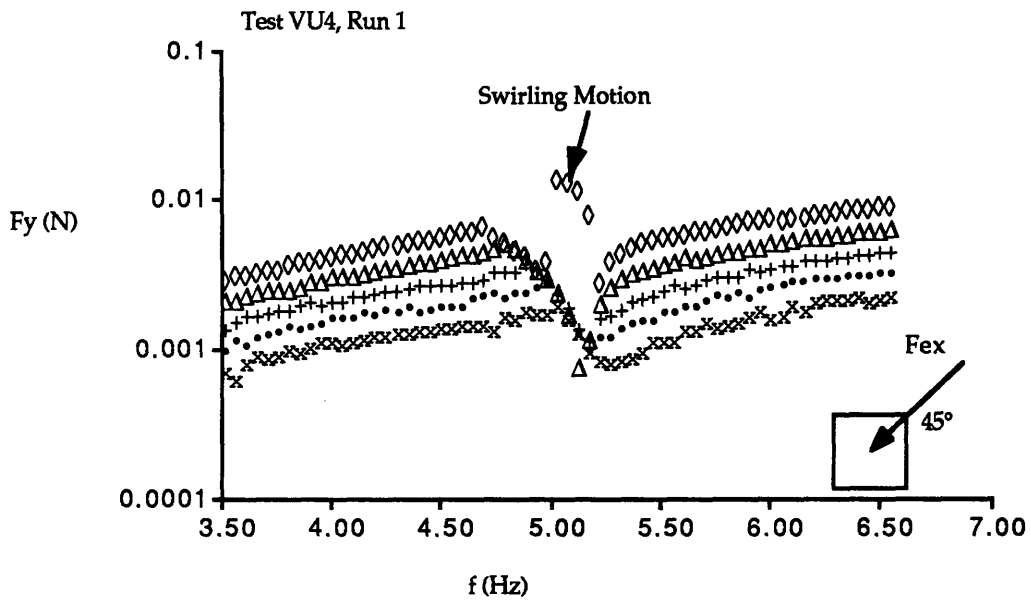
Figure 5.58   Test VU4, Nonplanar Slosh Force (Fy).

(Square tank, uncoupled, harmonic excitation, Excitation angle=90°
and Fluid=2% Photoflo/Water Solution)
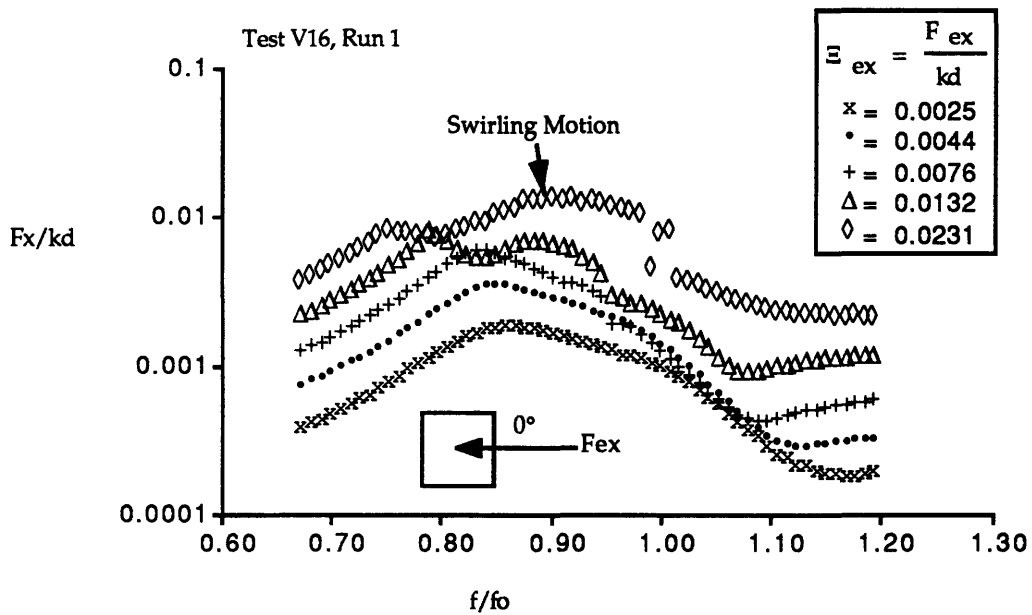
Figure 5.59   Test V16, Non-dimensional Planar Slosh Force (Fx/kd).
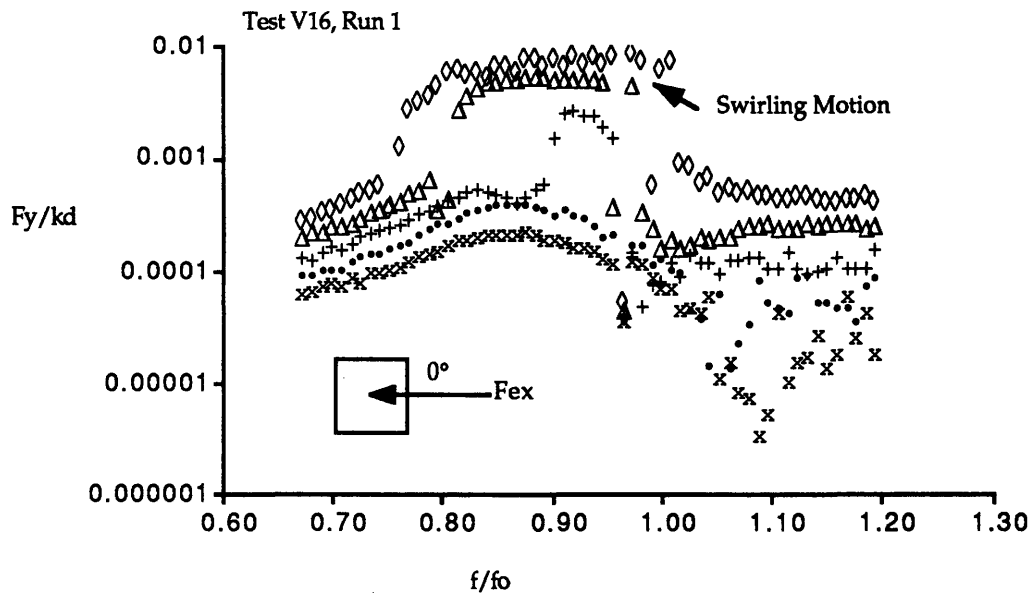
Figure 5.60   Test V16, Non-dimensional Nonplanar Slosh Force (Fy/kd).

(Square tank, coupled, harmonic excitation, Coupled system parameters; μ=0.16, ν=0.92, ζ=8.00%, Bo=61, Excitation angle=0°)

176

Test V16, Run 1

Swirling Motion

x/d

0°
Fex
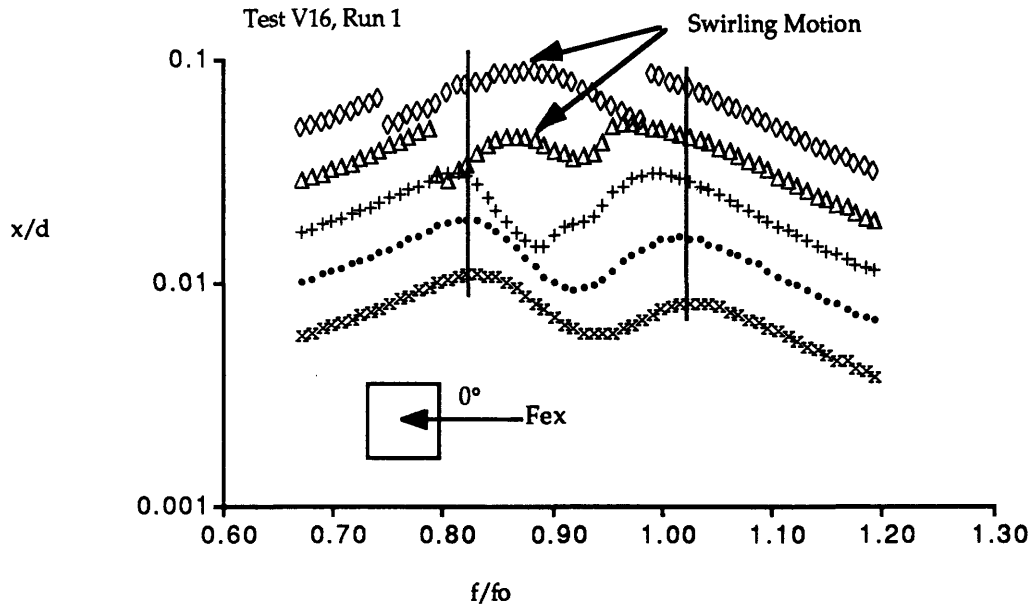
Figure 5.61   Test V16, Non-dimensional Displacement (x/d).

Test V16, Run 1

Swirling Motion

0°
Fex

Ax/g
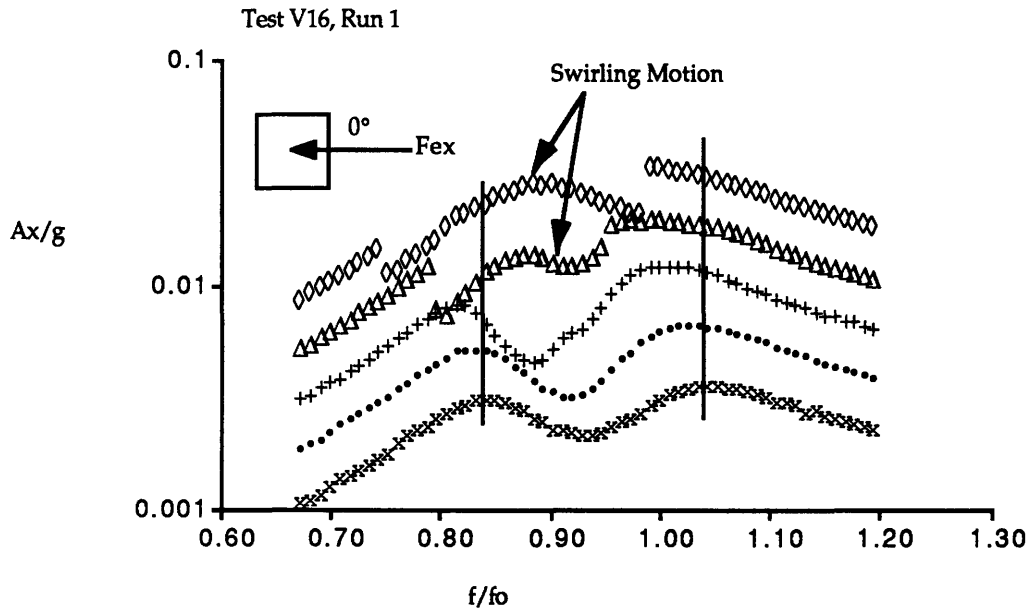
Figure 5.62   Test V16, Non-dimensional Acceleration (Ax/g).

(Square tank, coupled, harmonic excitation, Coupled system
parameters; μ=0.16, v=0.92, ζ=8.00%, Bo=61, Excitation angle=0°)
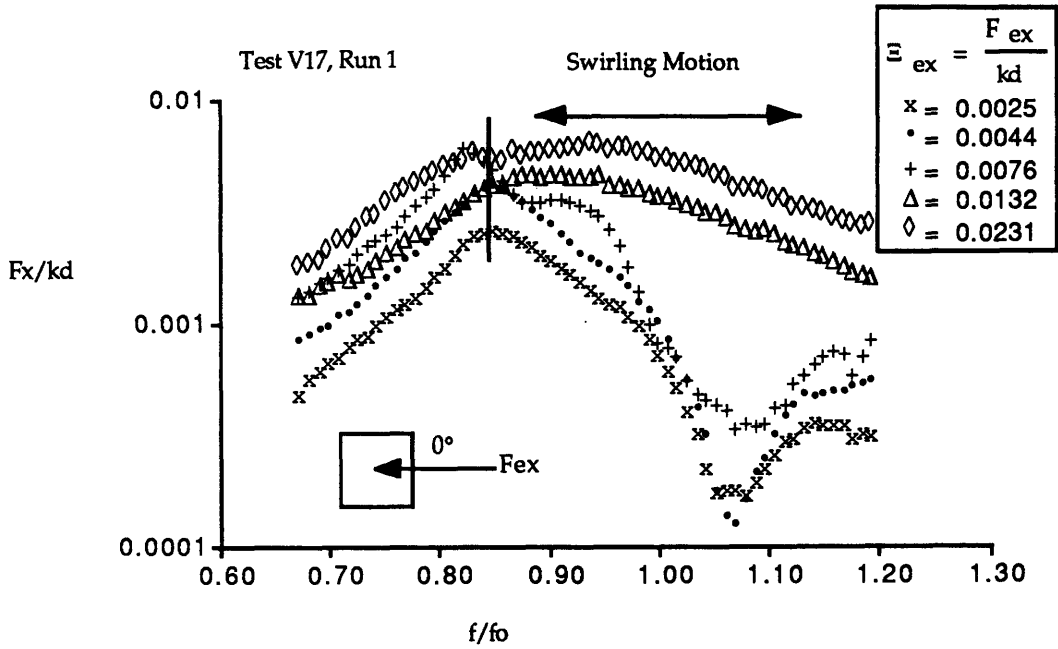
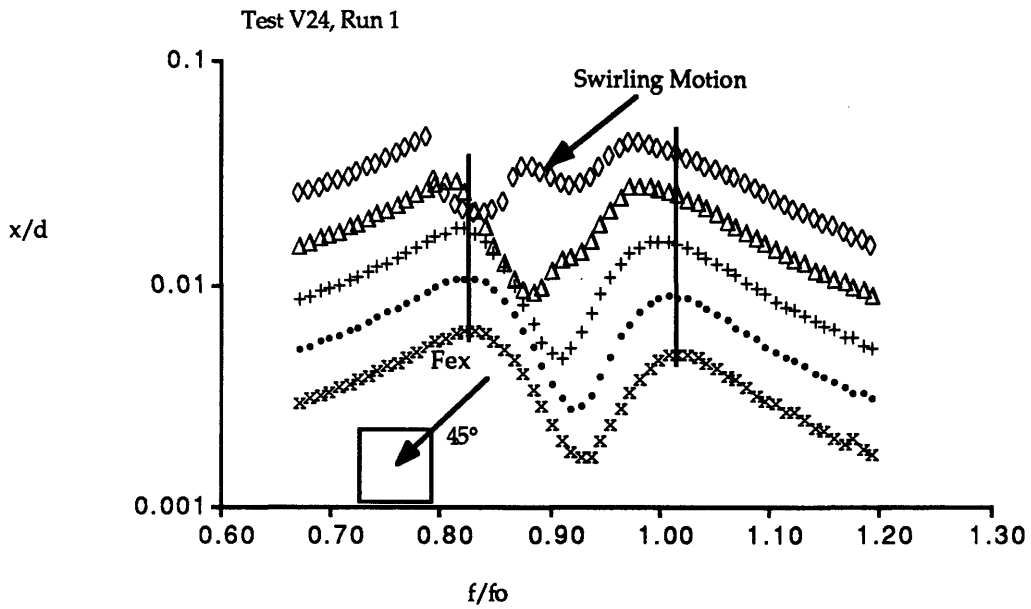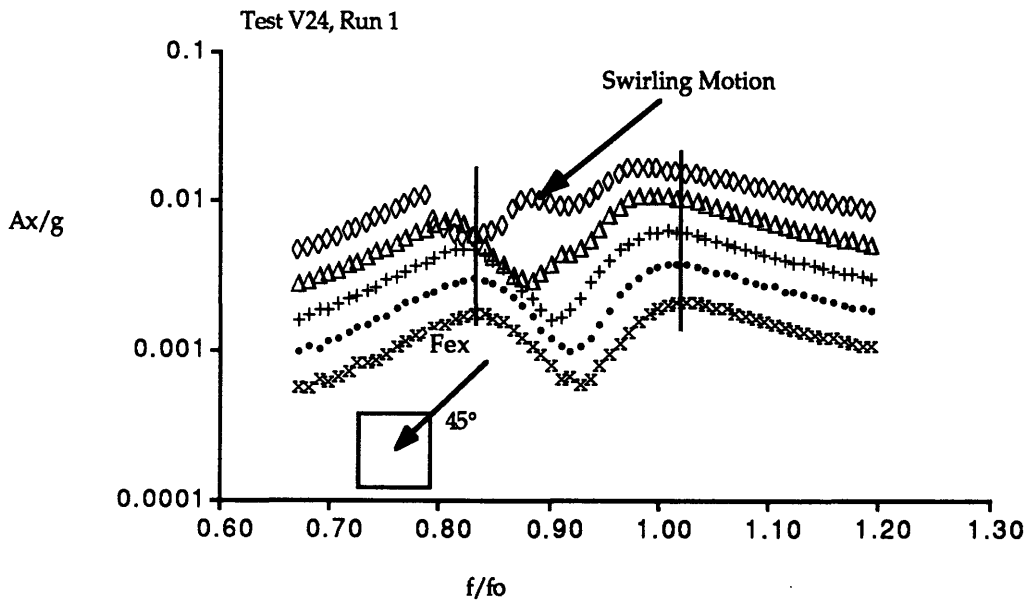**Figure 5.63**   Test V17, Non-dimensional Planar Slosh Force (Fx/kd).
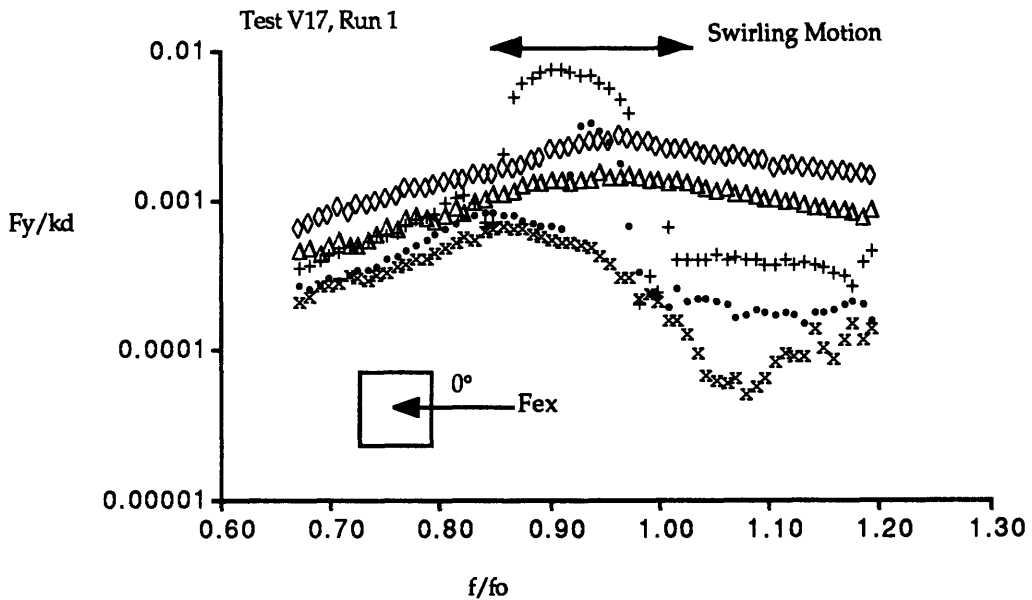
Figure 5.64   Test V17, Non-dimensional Nonplanar Slosh Force (Fy/kd).

(Square tank, coupled, harmonic excitation, Coupled system parameters; μ=0.32, ν=0.92, ζ=8.00%, Bo=61, Excitation angle=0°)
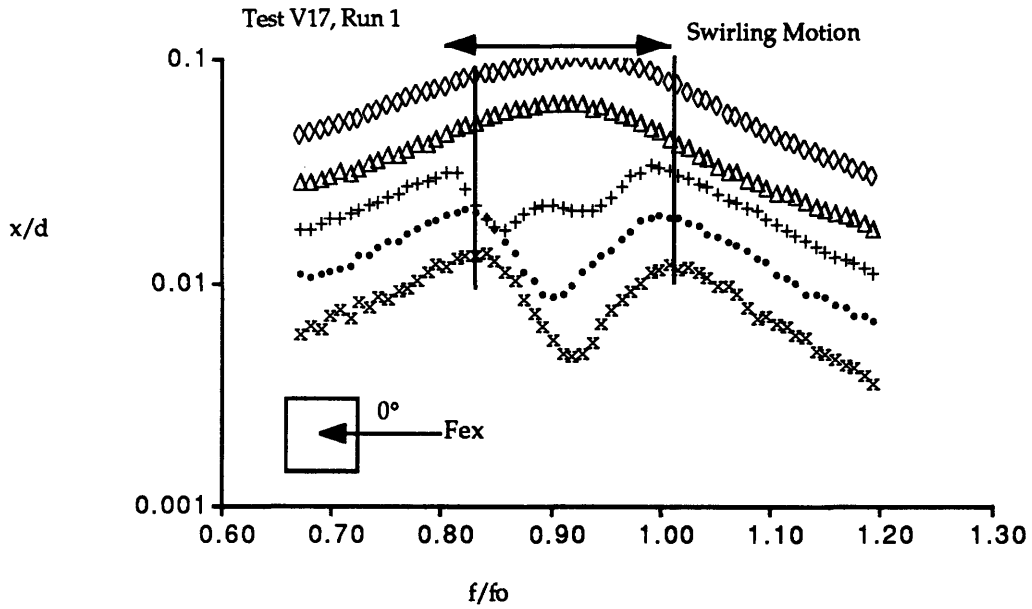
Figure 5.65   Test V17, Non-dimensional Displacement (x/d).
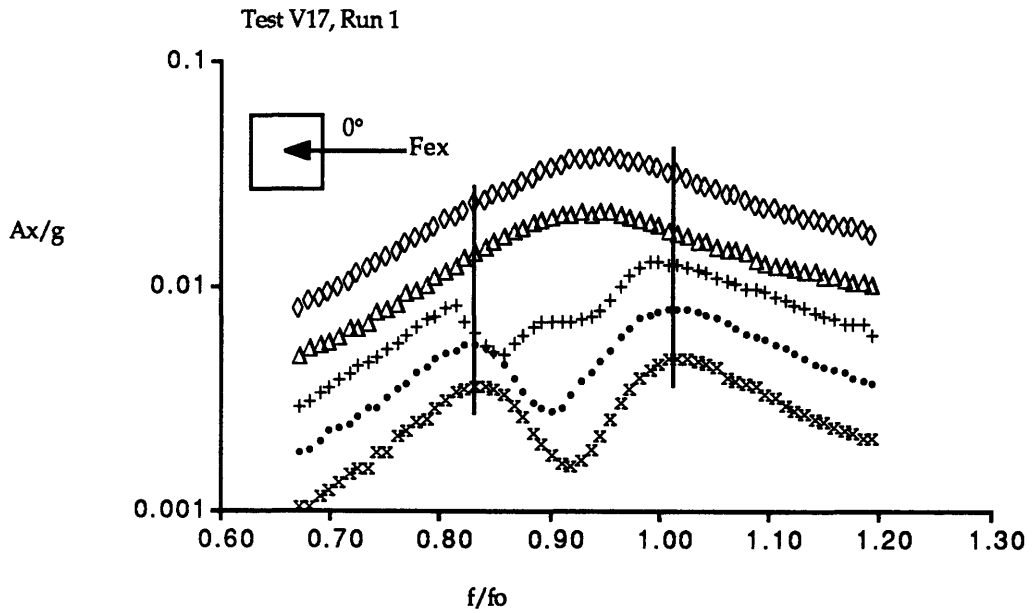
Figure 5.66   Test V17, Non-dimensional Acceleration (Ax/g).

(Square tank, coupled, harmonic excitation, Coupled system parameters; μ=0.32, ν=0.92, ζ=8.00%, Bo=61, Excitation angle=0°)

179
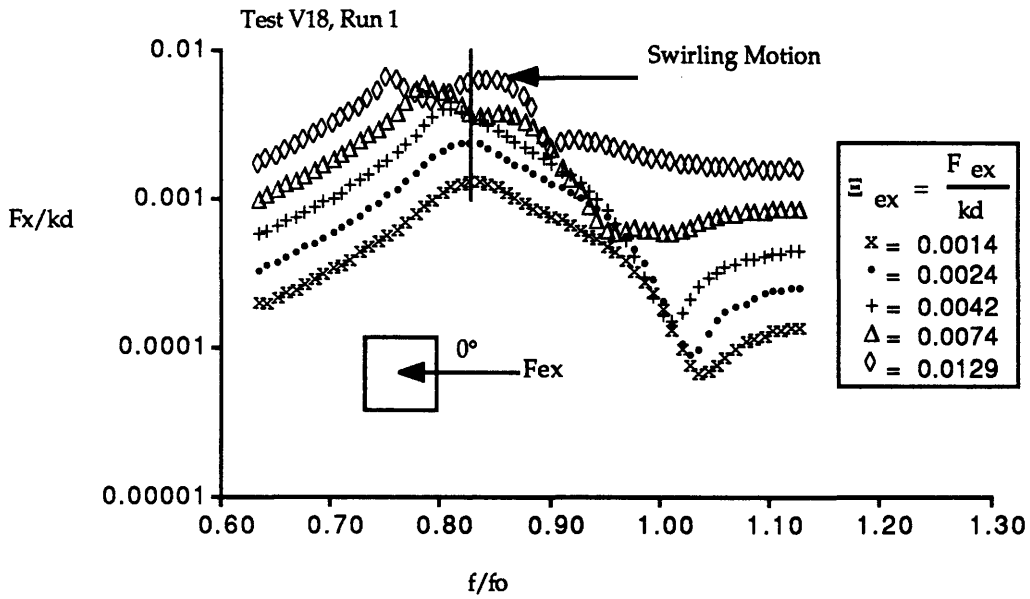
Figure 5.67   Test V18, Non-dimensional Planar Slosh Force (Fx/kd).

(Square tank, coupled, harmonic excitation, Coupled system parameters; $\mu=0.16$, $v=0.87$, $\zeta=8.00\%$, Bo=61, Excitation angle=0°)
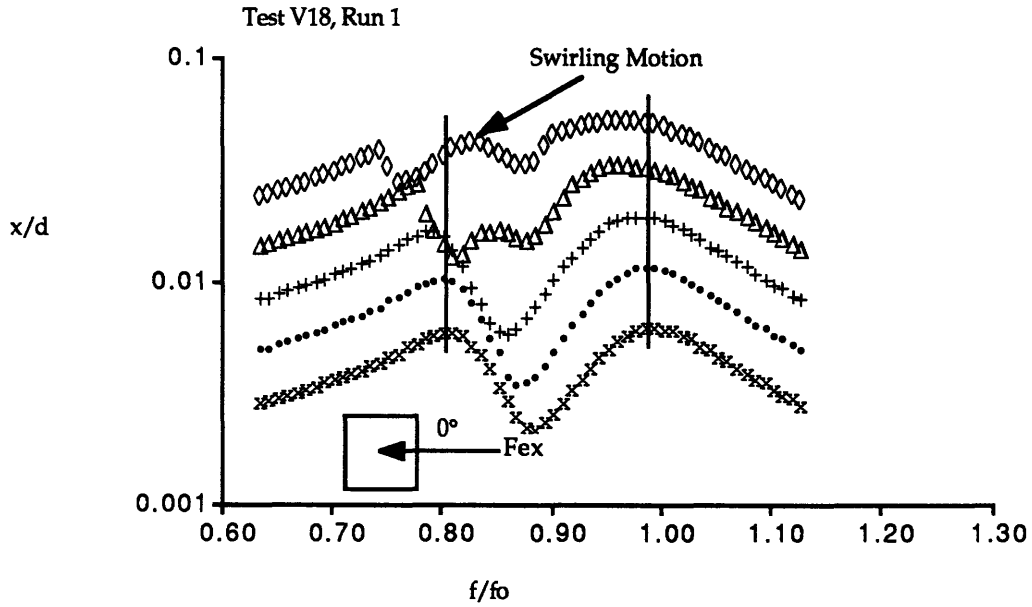
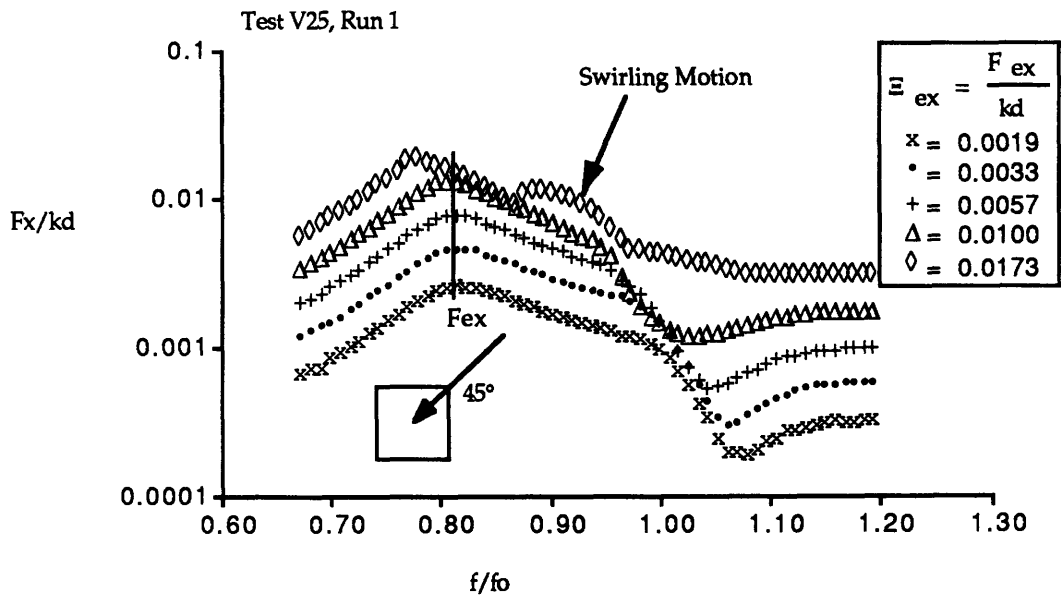**Figure 5.68   Test V18, Non-dimensional Displacement (x/d).**
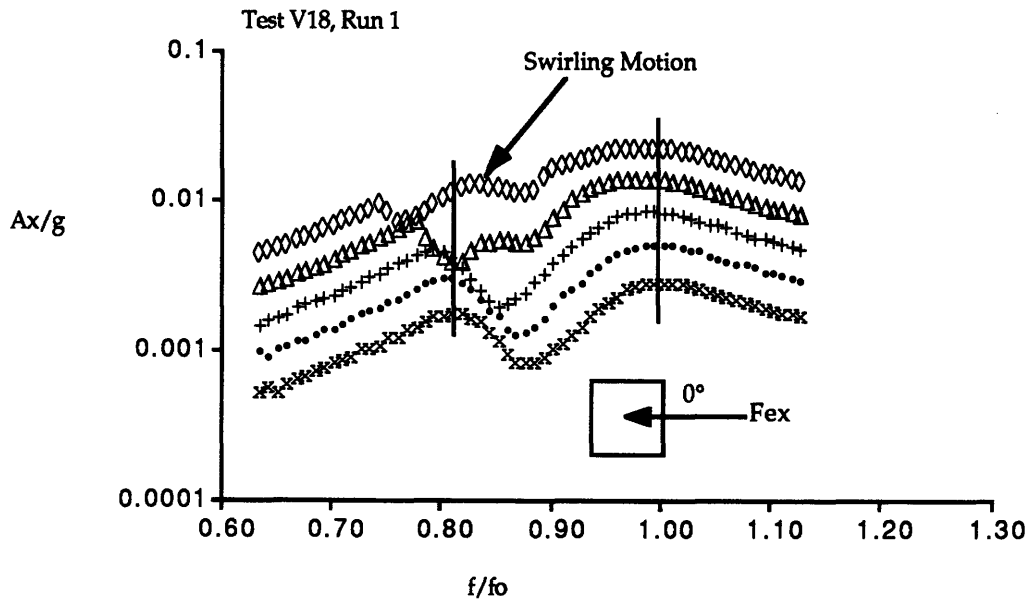
Figure 5.69   Test V18, Non-dimensional Acceleration (Ax/g).

(Square tank, coupled, harmonic excitation, Coupled system parameters; $\mu=0.16$, $v=0.87$, $\zeta=8.00\%$, Bo=61, Excitation angle=0°)
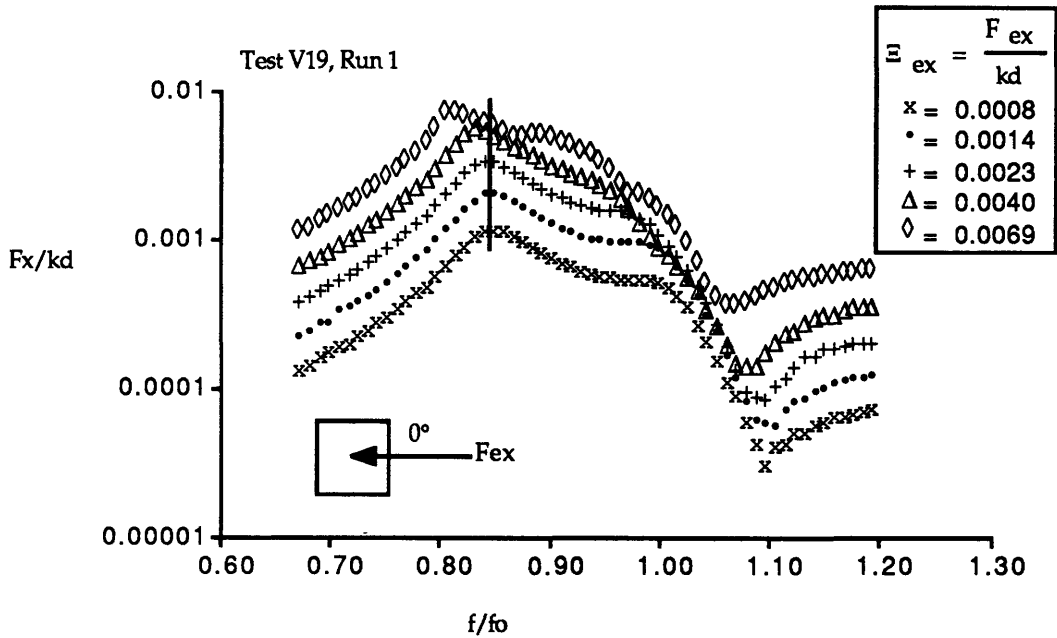
Figure 5.70   Test V19, Non-dimensional Planar Slosh Force (Fx/kd).
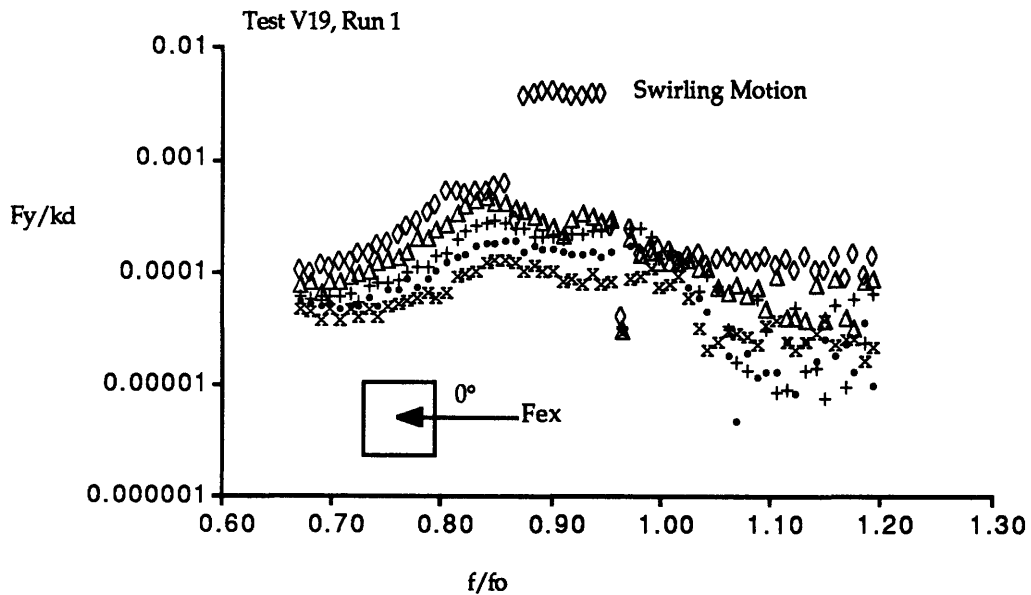
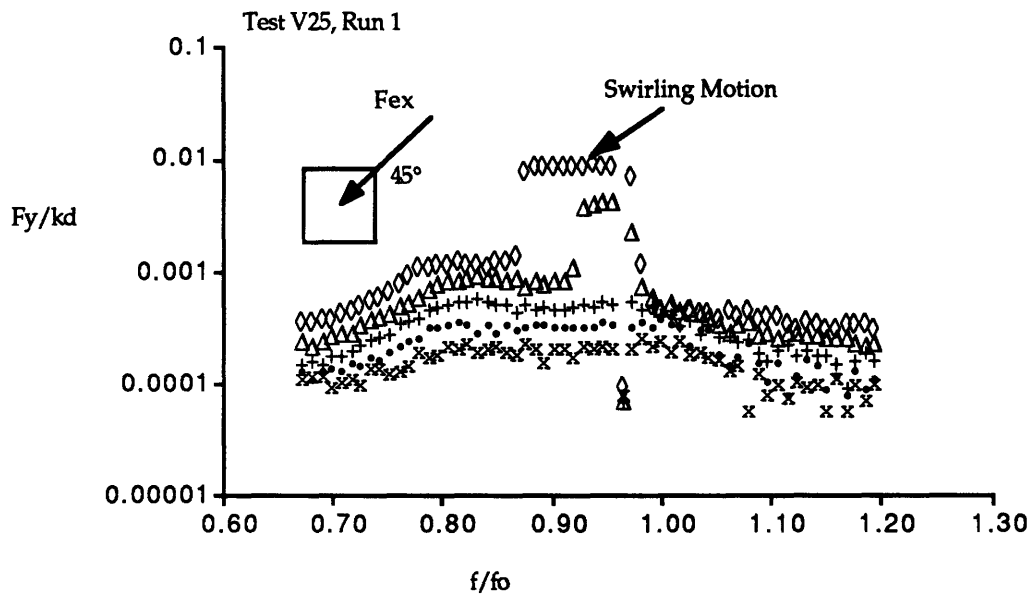**Figure 5.71   Test V19, Non-dimensional Nonplanar Slosh Force (Fy/kd).**

(Square tank, coupled, harmonic excitation, Coupled system parameters; $\mu=0.16$, $v=0.92$, $\zeta=4.00\%$, Bo=61, Excitation angle=0°)
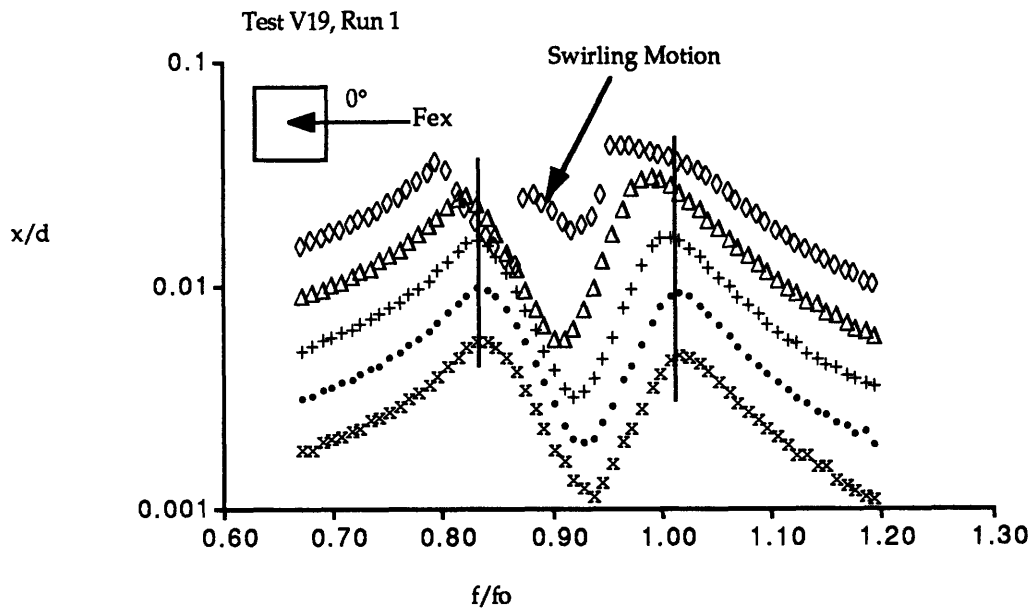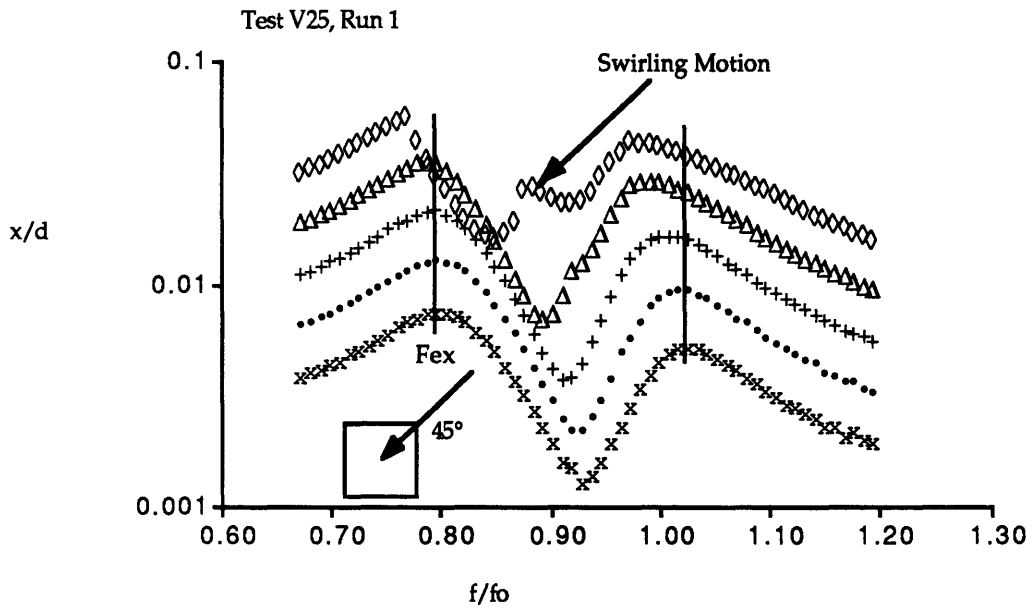
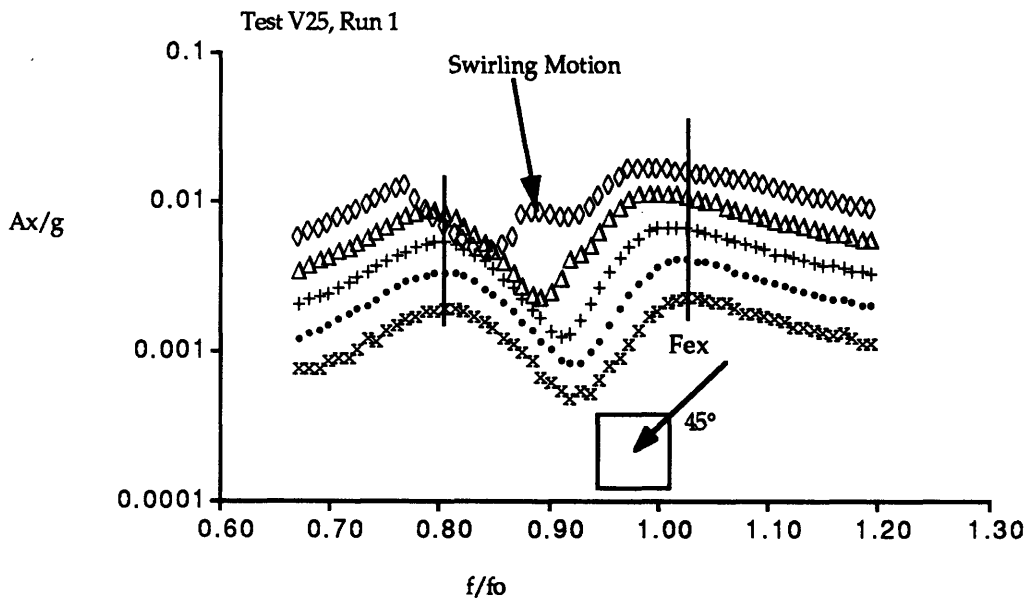**Figure 5.72   Test V19, Non-dimensional Displacement (x/d).**
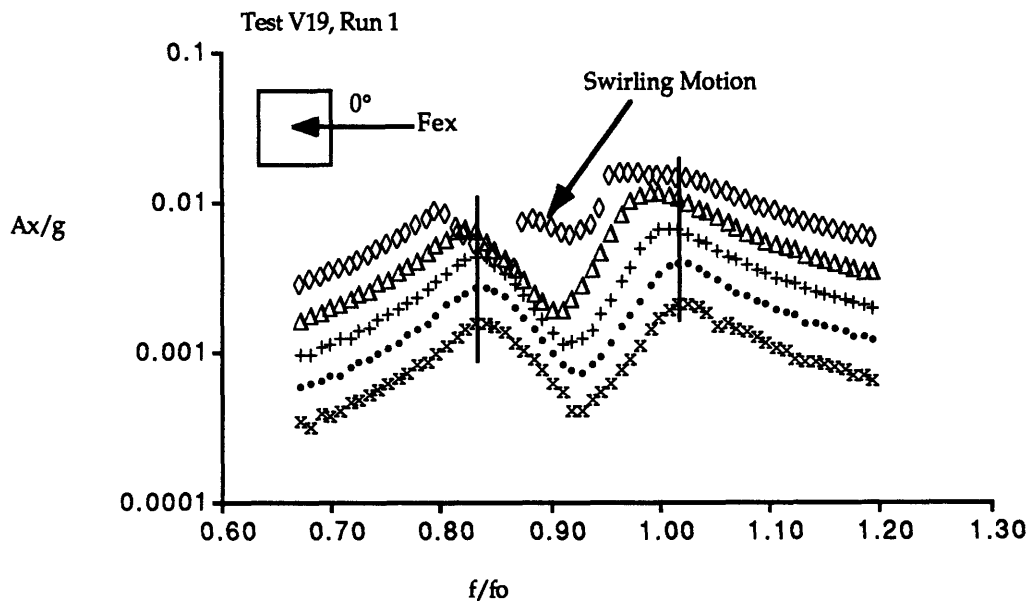
Figure 5.73   Test V19, Non-dimensional Acceleration (Ax/g).

(Square tank, coupled, harmonic excitation, Coupled system parameters; μ=0.16, v=0.92, ζ=4.00%, Bo=61, Excitation angle=0°)

183
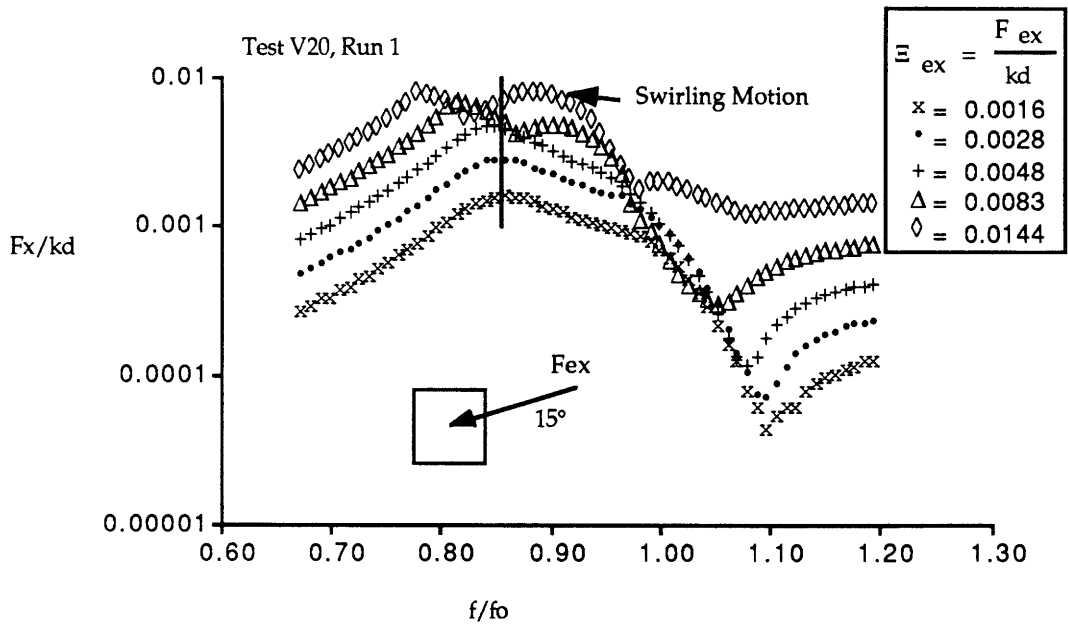
Figure 5.74 Test V20, Non-dimensional Planar Slosh Force (Fx/kd).
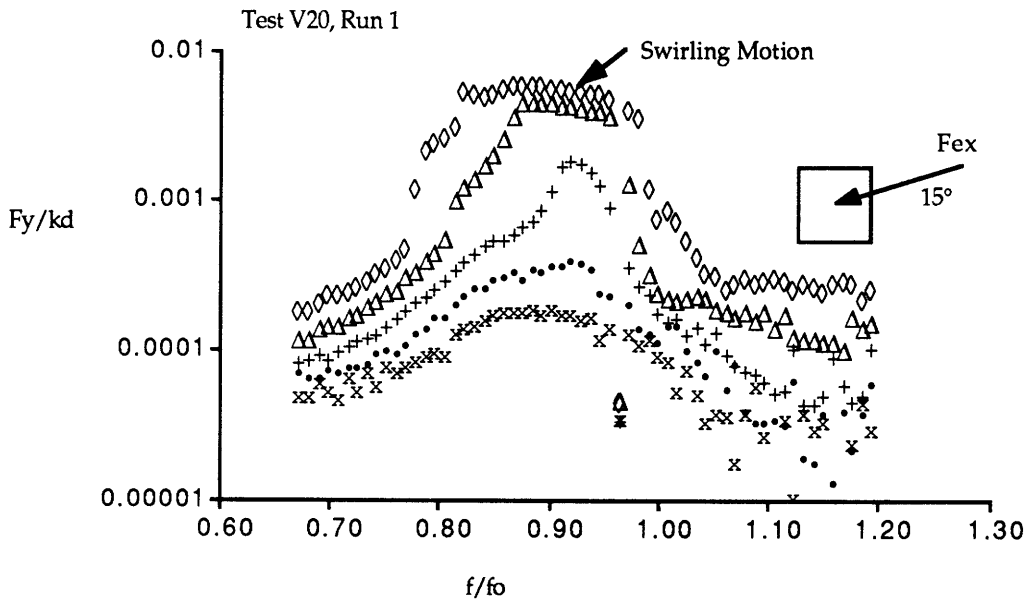
Figure 5.75 Test V20, Non-dimensional Nonplanar Slosh Force (Fy/kd).

(Square tank, coupled, harmonic excitation, Coupled system parameters; μ=0.16, v=0.92, ζ=8.00%, Bo=61, Excitation angle=15°)
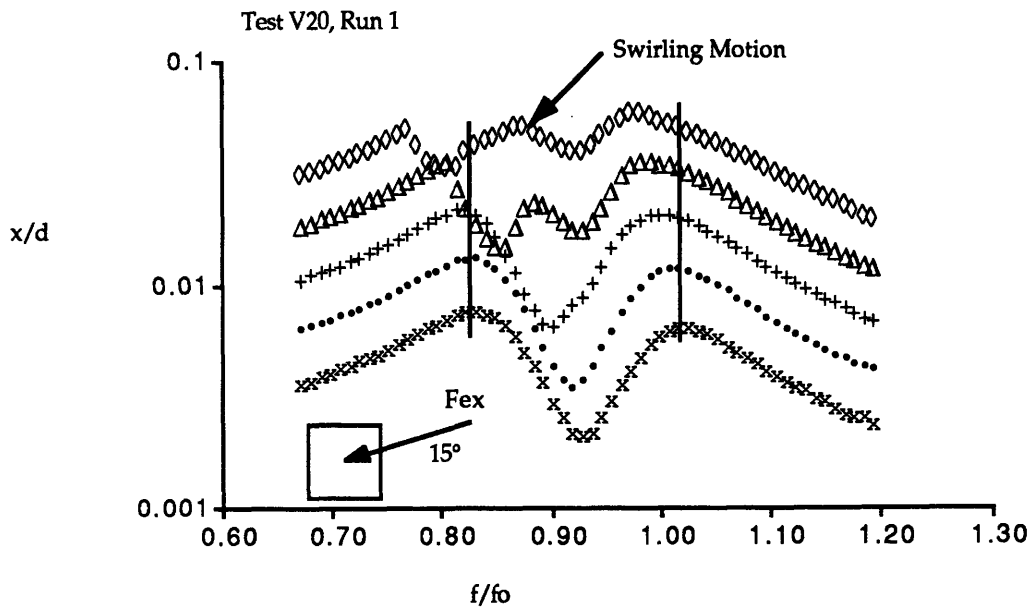
Figure 5.76   Test V20, Non-dimensional Displacement (x/d).
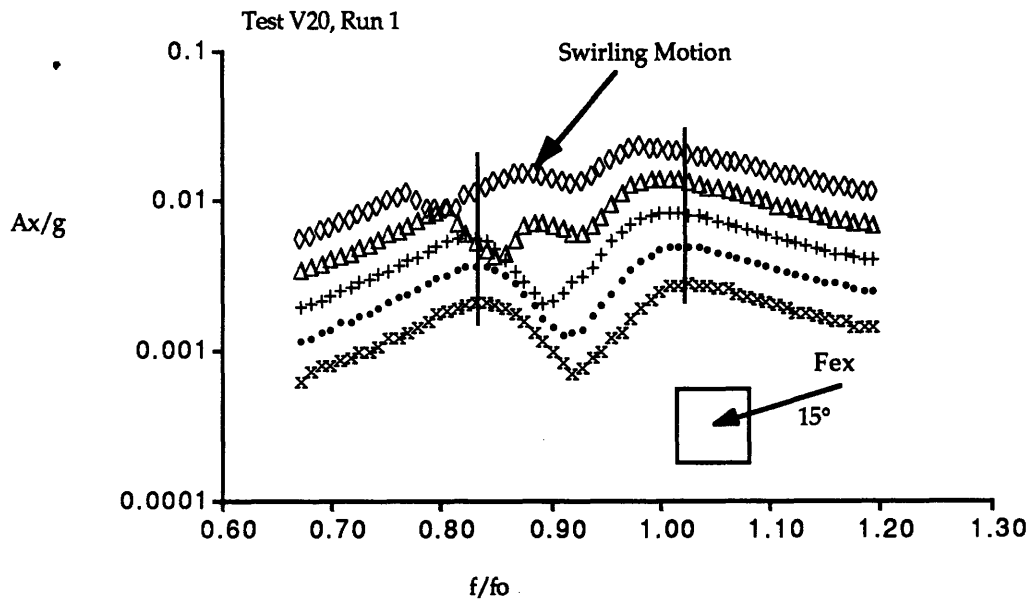
Figure 5.77   Test V20, Non-dimensional Acceleration (Ax/g).

(Square tank, coupled, harmonic excitation, Coupled system parameters; μ=0.16, ν=0.92, ζ=8.00%, Bo=61, Excitation angle=15°)

185
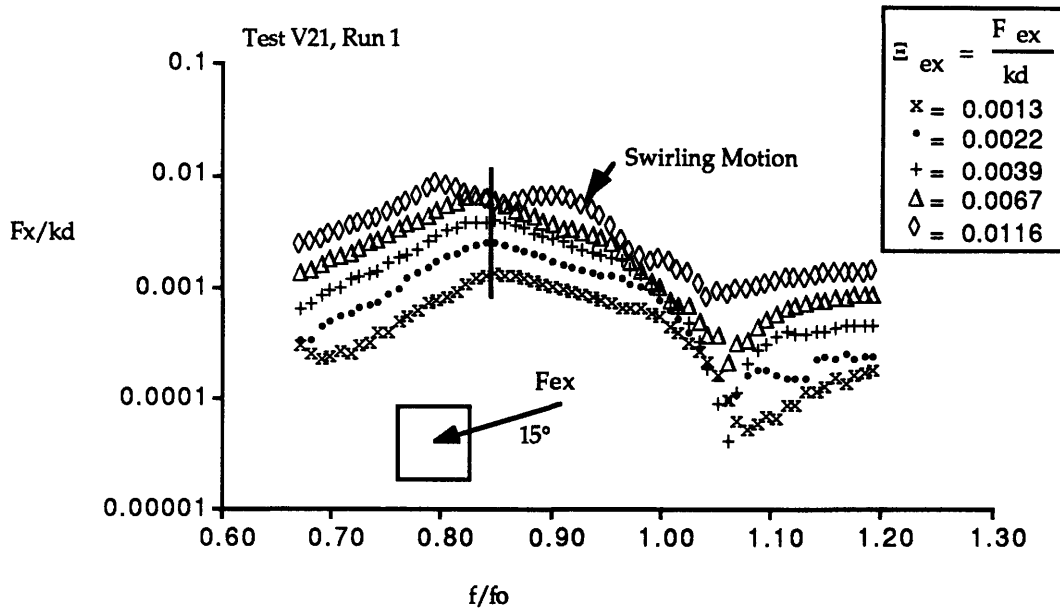
Figure 5.78   Test V21, Non-dimensional Planar Slosh Force (Fx/kd).
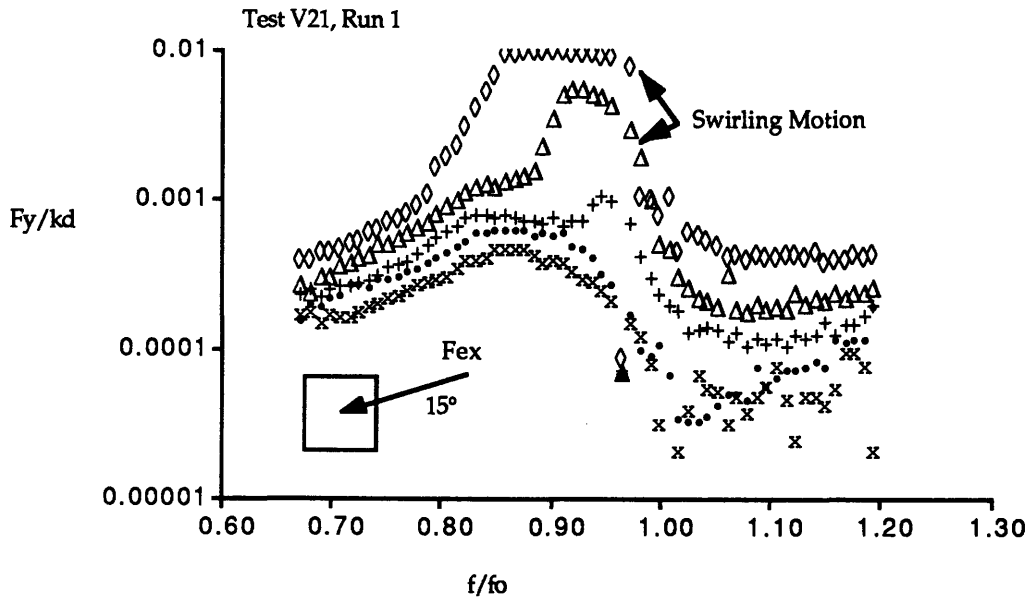
Figure 5.79   Test V21, Non-dimensional Nonplanar Slosh Force (Fy/kd).

(Square tank, coupled, harmonic excitation, Coupled system parameters; μ=0.32, ν=0.92, ζ=8.00%, Bo=61, Excitation angle=15°)

Test V21, Run 1

x/d
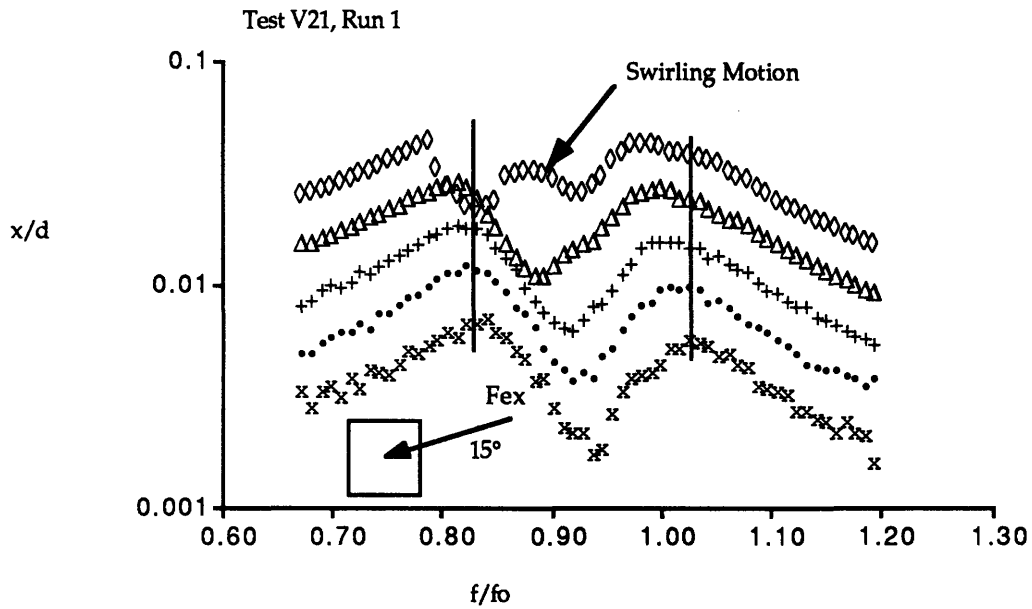
Figure 5.80   Test V21, Non-dimensional Displacement (x/d).

Test V21, Run 1

Ax/g
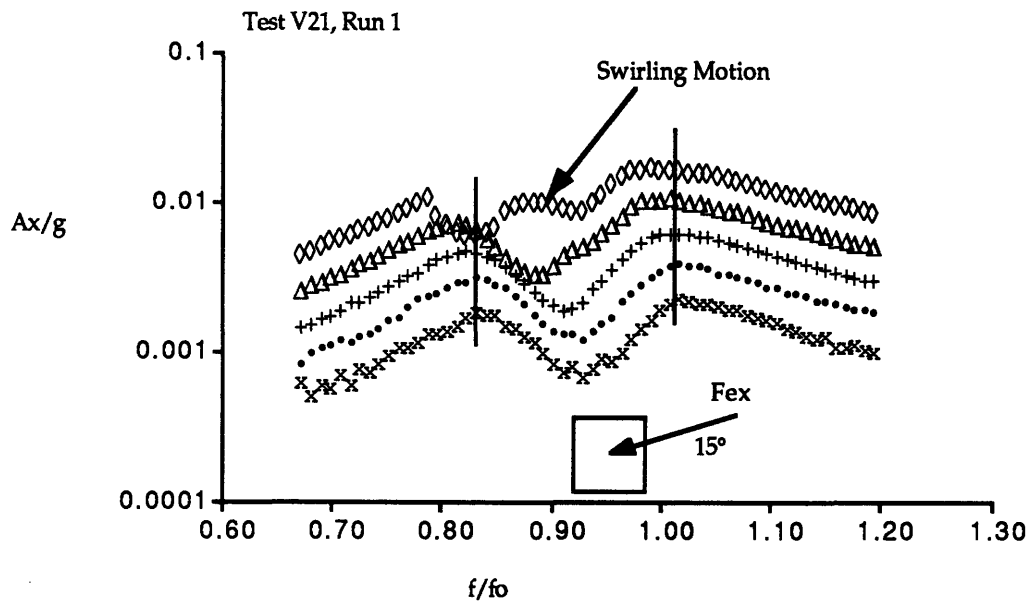
Figure 5.81   Test V21, Non-dimensional Acceleration (Ax/g).

(Square tank, coupled, harmonic excitation, Coupled system parameters; $\mu=0.32$, $\nu=0.92$, $\zeta=8.00\%$, Bo=61, Excitation angle=15°)
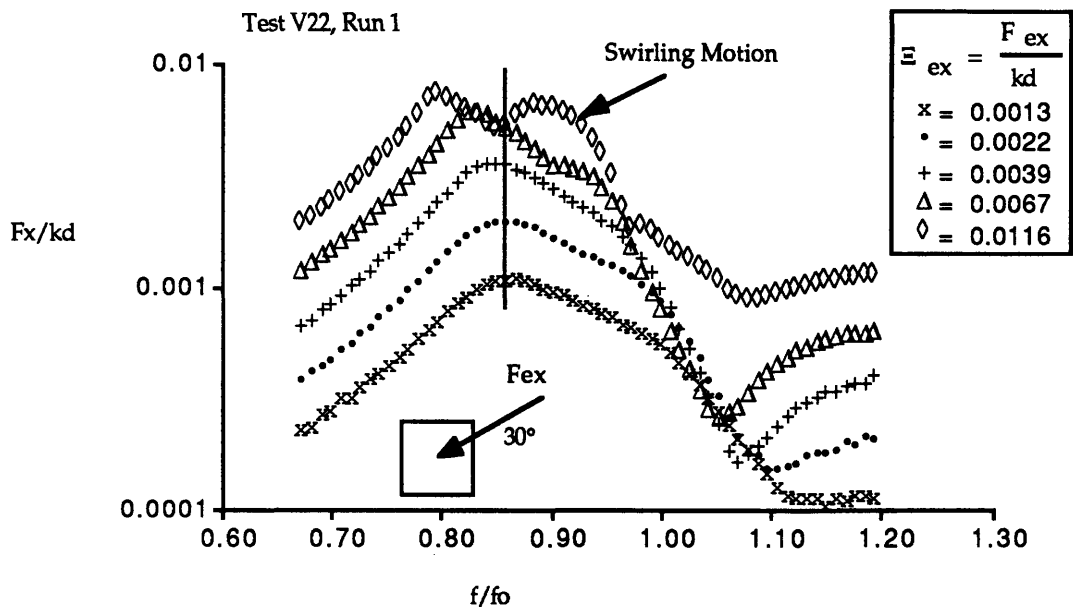
Figure 5.82   Test V22, Non-dimensional Planar Slosh Force (Fx/kd).
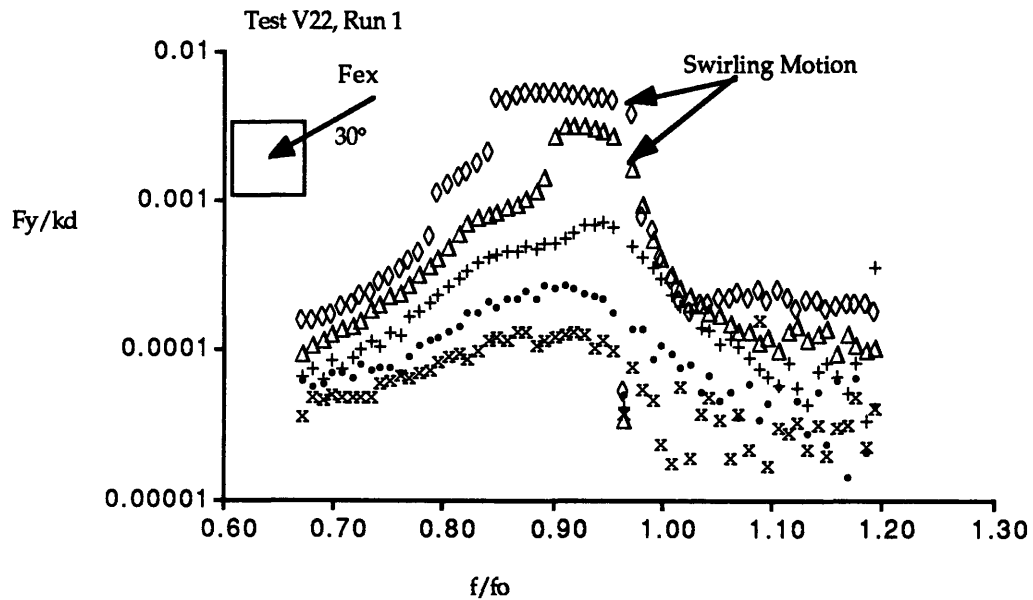
Figure 5.83   Test V22, Non-dimensional Nonplanar Slosh Force (Fy/kd).

(Square tank, coupled, harmonic excitation, Coupled system parameters; μ=0.16, ν=0.92, ζ=8.00%, Bo=61, Excitation angle=30°)
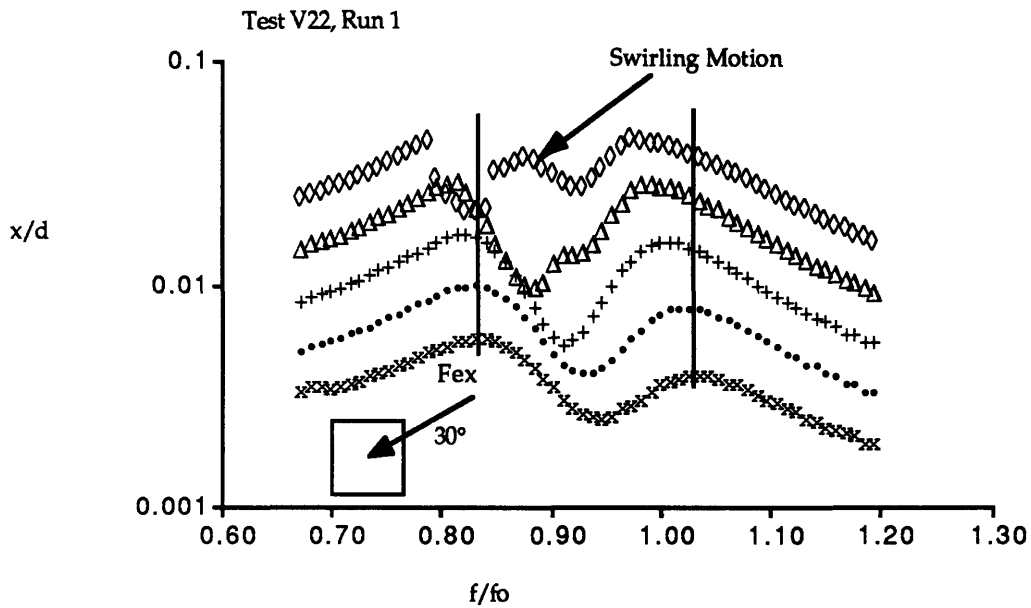
Figure 5.84   Test V22, Non-dimensional Displacement (x/d).
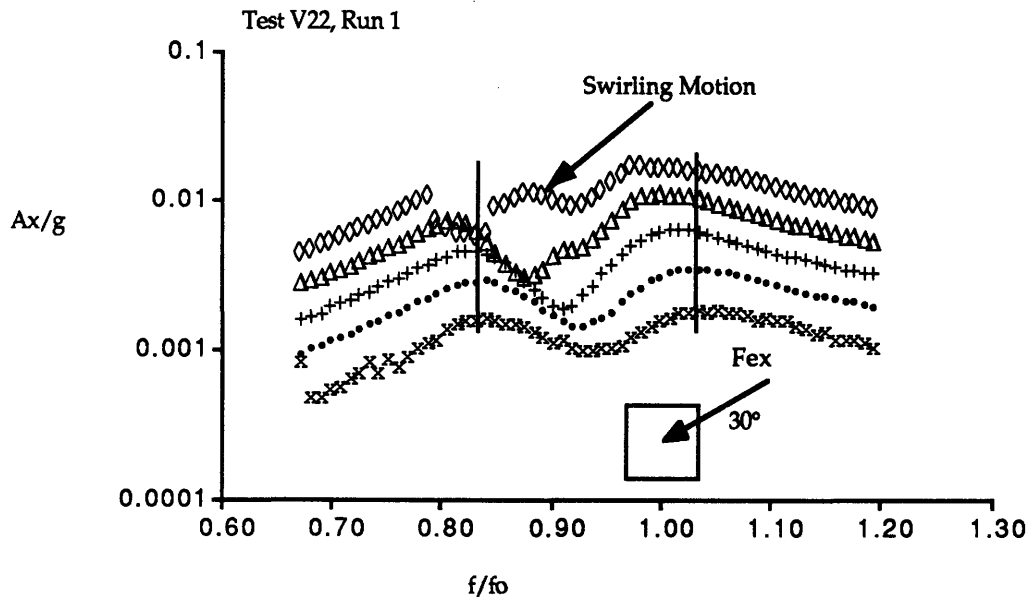
Figure 5.85   Test V22, Non-dimensional Acceleration (Ax/g).

(Square tank, coupled, harmonic excitation, Coupled system parameters; μ=0.16, ν=0.92, ζ=8.00%, Bo=61, Excitation angle=30°)

189
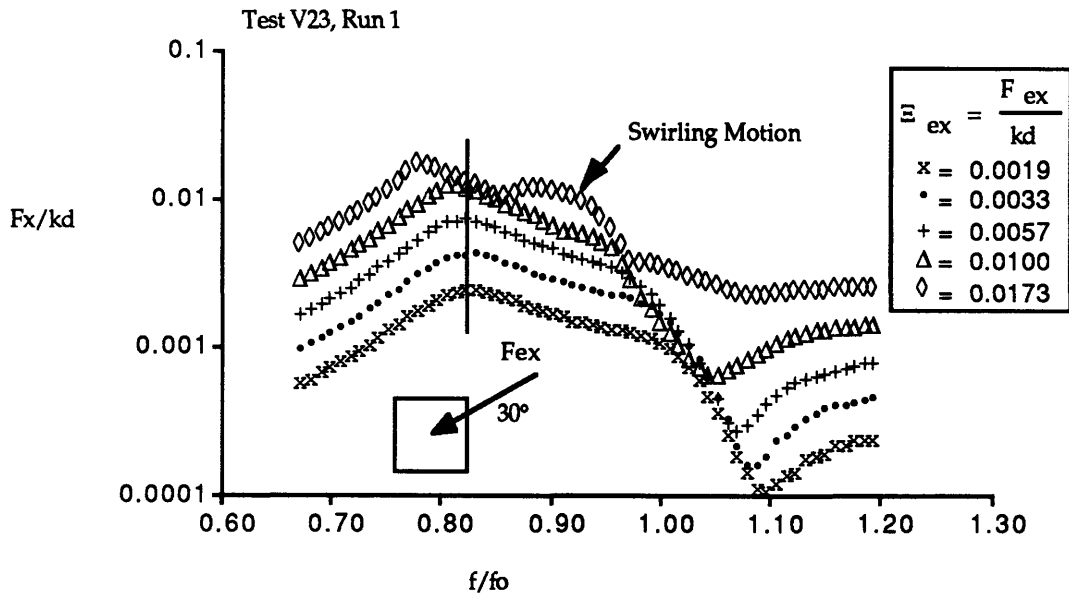
Figure 5.86   Test V23, Non-dimensional Planar Slosh Force (Fx/kd).
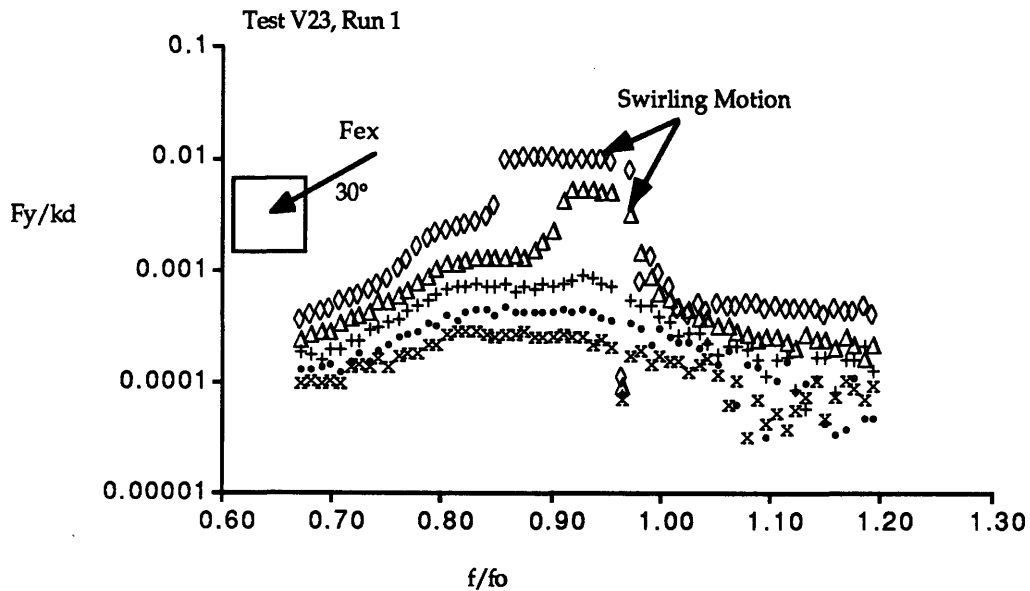
Figure 5.87   Test V23, Non-dimensional Nonplanar Slosh Force (Fy/kd).

(Square tank, coupled, harmonic excitation, Coupled system parameters; $\mu=0.32$, $\nu=0.92$, $\zeta=8.00\%$, Bo=61, Excitation angle=30°)
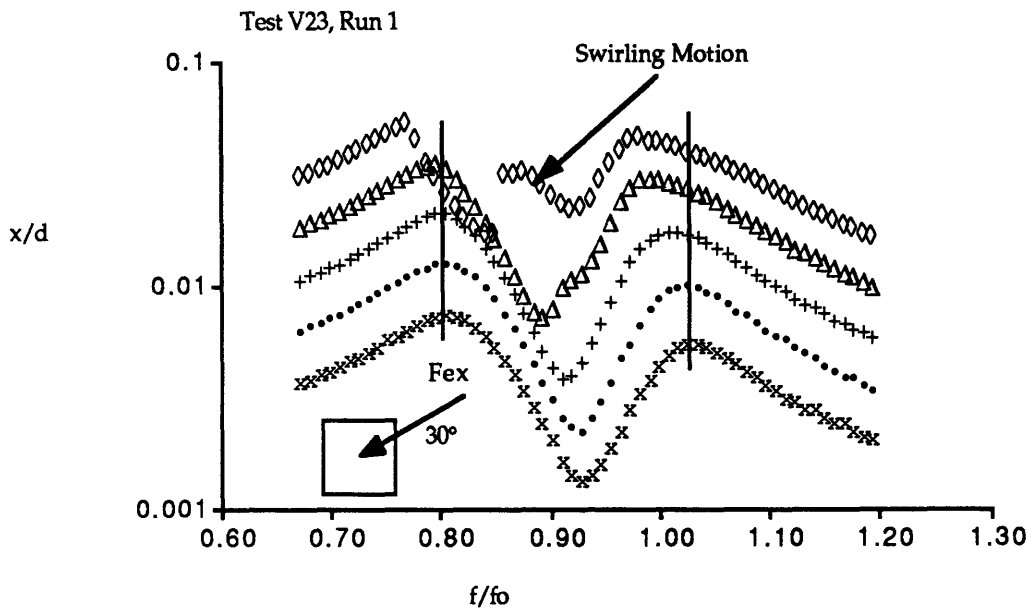
Figure 5.88   Test V23, Non-dimensional Displacement (x/d).
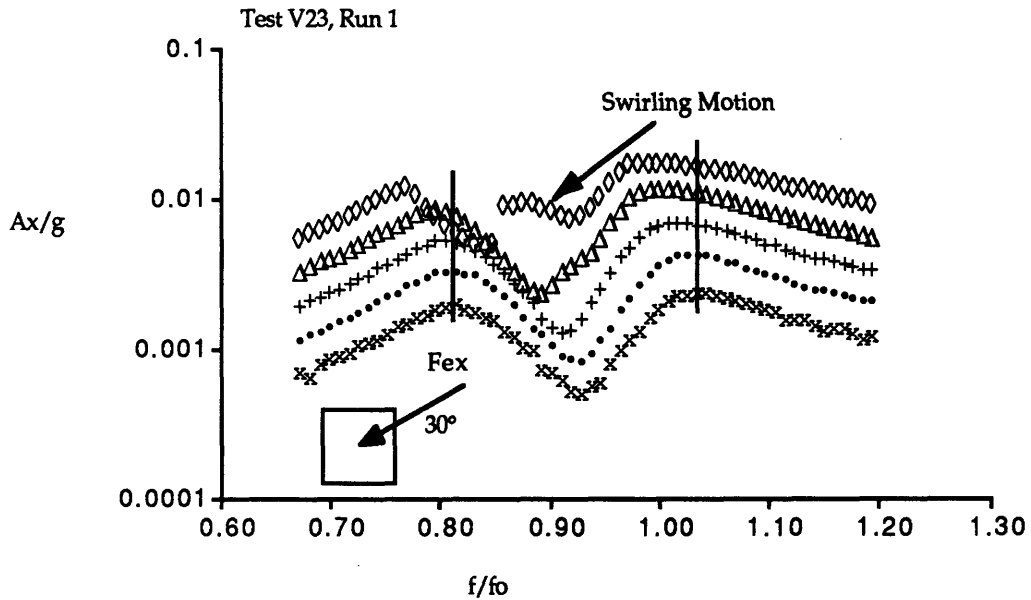
Figure 5.89   Test V23, Non-dimensional Acceleration (Ax/g).

(Square tank, coupled, harmonic excitation, Coupled system parameters; μ=0.32, ν=0.92, ζ=8.00%, Bo=61, Excitation angle=30°)

191
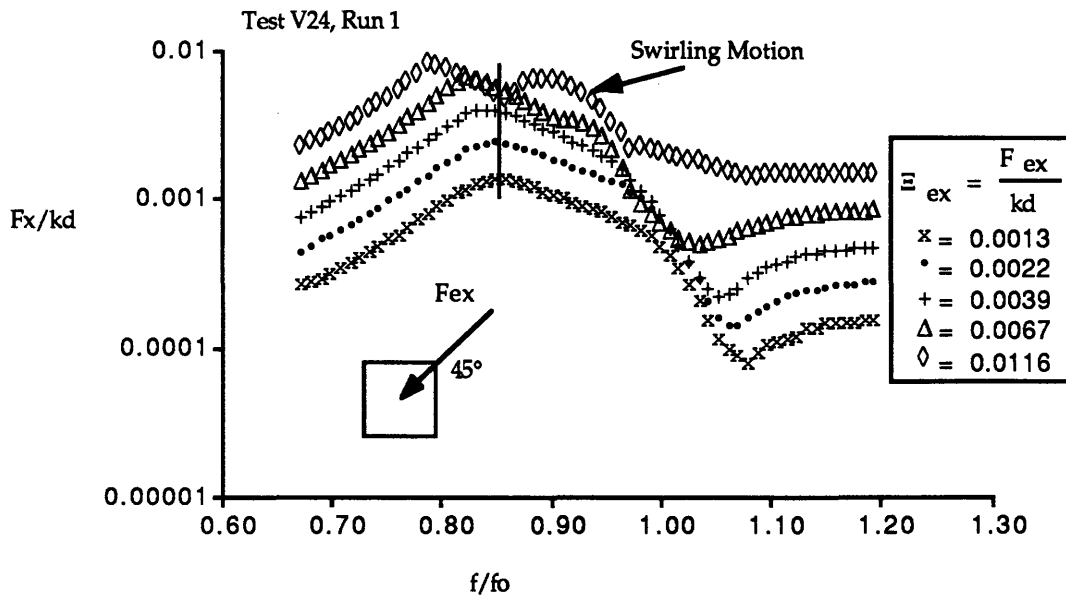
Figure 5.90   Test V24, Non-dimensional Planar Slosh Force (Fx/kd).
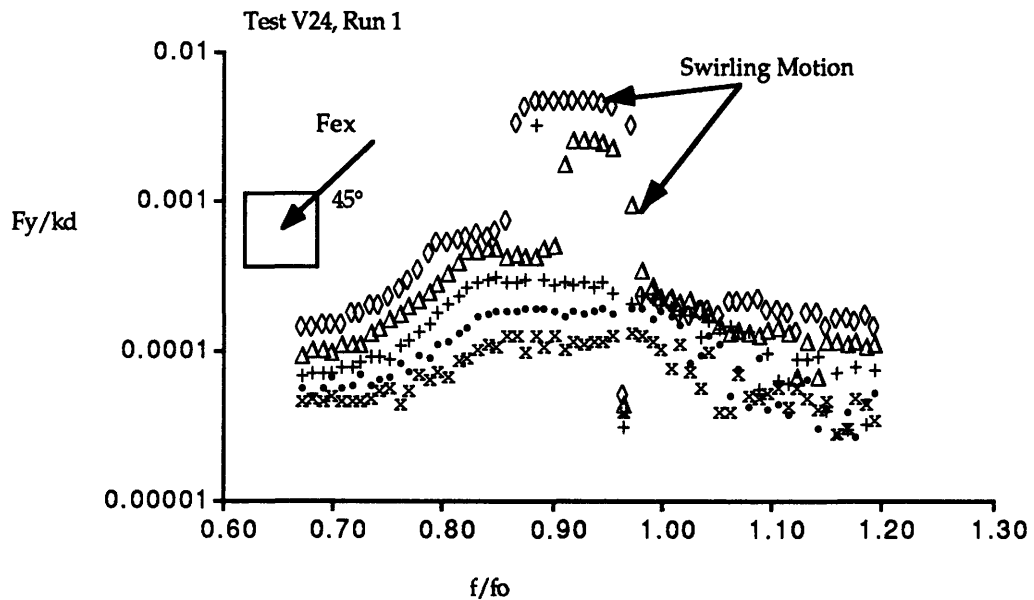
Figure 5.91   Test V24, Non-dimensional Nonplanar Slosh Force (Fy/kd).

(Square tank, coupled, harmonic excitation, Coupled system parameters; μ=0.16, v=0.92, ζ=8.00%, Bo=61, Excitation angle=45°)

Figure 5.92   Test V24, Non-dimensional Displacement (x/d)

Figure 5.93   Test V24, Non-dimensional Acceleration (Ax/g).

(Square tank, coupled, harmonic excitation, Coupled system parameters; μ=0.16, v=0.92, ζ=8.00%, Bo=61, Excitation angle=45°)

Figure 5.94   Test V25, Non-dimensional Planar Slosh Force (Fx/kd).

Figure 5.95   Test V25, Non-dimensional Nonplanar Slosh Force (Fy/kd).

(Square tank, coupled, harmonic excitation, Coupled system parameters; μ=0.32, ν=0.92, ζ=8.00%, Bo=61, Excitation angle=45°)

Figure 5.96   Test V25, Non-dimensional Displacement (x/d).

Figure 5.97   Test V25, Non-dimensional Acceleration (Ax/g).

(Square tank, coupled, harmonic excitation, Coupled system parameters; μ=0.16, ν=0.92, ζ=8.00%, Bo=61, Excitation angle=45°)

5.4 Rectangular Tank Model

Figure 5.98 is a drawing of the rectangular tank used to investigate the dynamic behavior of a fluid contained in a rectangular tank.
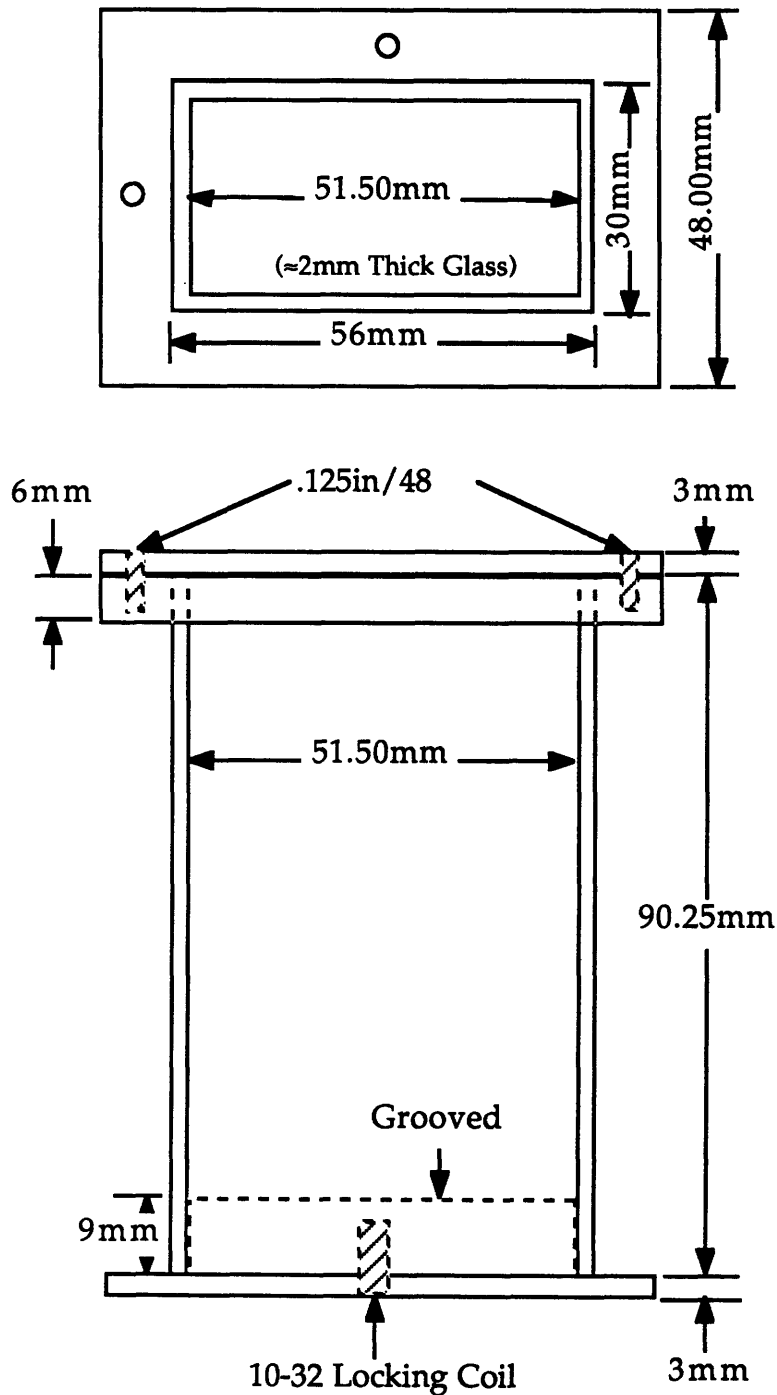
Figure 5.98   Rectangular Study Model

The details of the dynamic test, test parameters and test procedures are as discussed in chapter 3. The relevant tank parameters are summarized in Table 5.13.

Table 5.13   Rectangular Tank Parameters

Parameter	Abbreviation	Value
Width (Inside)	W	25.40 mm
Length (Inside)	L	51.50 mm
Tank Height	H	90.00 mm
Fill Height	h	33.90 mm
Normalization Factor	d	33.90 mm
Bond Number	Bo	78
Empty Mass	m_E	112.33 g
Fluid Mass	m_F	43.70 g
1st Fluid Slosh Frequency	f_s	3.76 Hz
2nd Fluid Slosh Frequency	f_2	5.41 Hz

5.4.1 Rectangular Tank Test Matrix

A series of uncoupled tests were performed to determine the low-amplitude linear characteristics of the fluid and for comparison with the coupled test results. The angle between the tank symmetry axis (See Fig. 5.99) was varied to determine the effect of non-planar excitation. Each test has a unique test identifier and this identifier will be used to identify the experimental results presented in this chapter. Table 5.14 summarizes the uncoupled (fluid alone) test matrix and Table 5.15 the coupled (fluid/spacecraft) test matrix. A 2% photoflo/water solution was used in all these tests and the excitation frequency ranged from 3 Hz to 6 Hz.

197

Table 5.14   Rectangular Uncoupled Test Matrix

Test ID	Excitation Angle	Figures
RU1	0°	5.100, 5.101
RU2	30°	5.102, 5.103
RU3	60°	5.104, 5.105
RU4	90°	5.106, 5.107

F cos (Ωt)

0°

30°

60°

90°
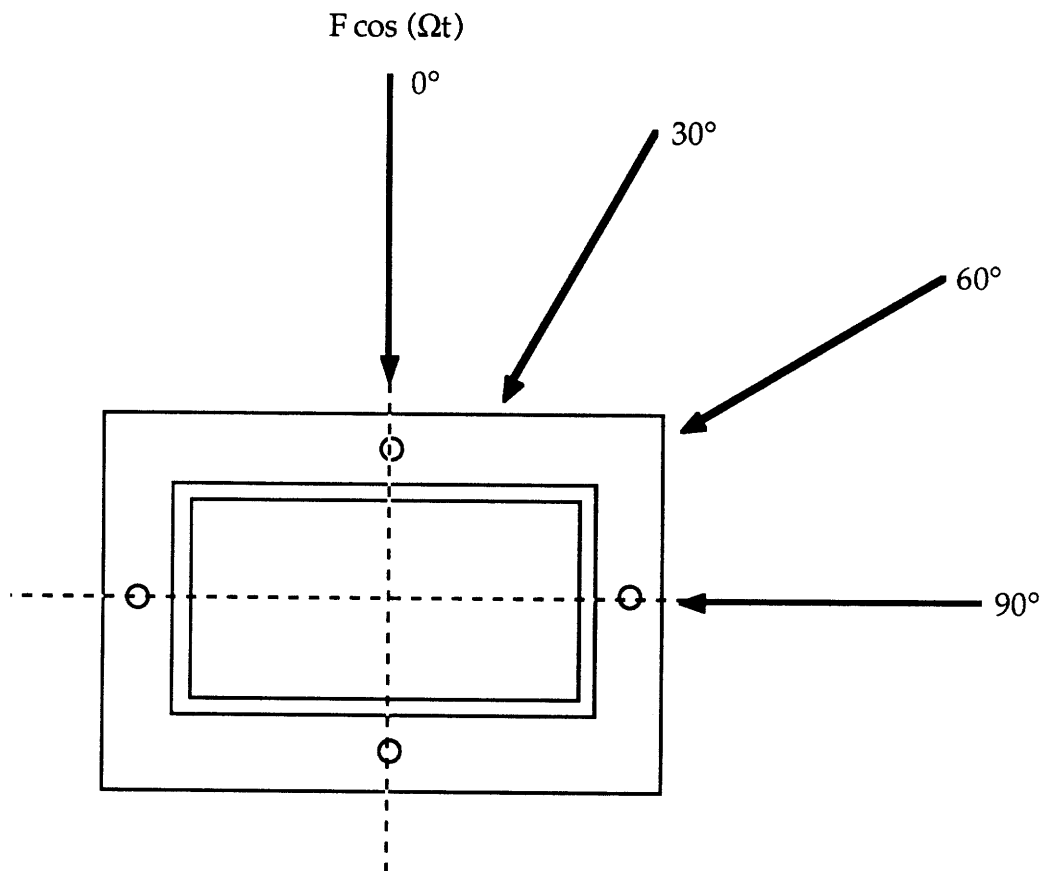
Figure 5.99   Explanation of Excitation Angle

Table 5.15 Rectangular Coupled Test Matrix

Test ID	Excitation Angle	μ	ν	$\zeta\,(\%)$	Figures
R16	90°	0.16	0.90	8.00	5.108 - 5.111
R17	90°	0.32	0.90	8.00	5.112 - 5.115
R18	90°	0.16	0.85	8.00	5.116 - 5.119
R19	90°	0.16	0.90	4.00	5.120 - 5.123
R20	60°	0.16	0.90	8.00	5.124 - 5.127
R21	60°	0.32	0.90	8.00	5.128 - 5.131
R22	30°	0.16	0.90	8.00	5.132 - 5.135
R23	30°	0.32	0.90	8.00	5.136 - 5.139
R24*	0°	0.16	0.90	8.00	5.140 - 5.142
R25	0°	0.32	0.90	8.00	5.143 - 5.146

Note: ν = Frequency Ratio = $f_{Slosh}/f_{Spacecraft}$ = f_s/fo

μ = Mass Ratio = $m_{Fluid}/m_{Spacecraft\ Mode}$ = m_F/m

ξ = Damping Ratio of Spacecraft Mode

* = Loss of one of the measured signals

In the uncoupled tests, the fluid/spacecraft system was harmonically excited over a frequency range covering the first fluid slosh mode resonance and in the coupled tests also covering the spacecraft resonance. A total of 5 logarithmically spaced (Log_{10}) force excitation levels were used to determine the dynamic characteristics. The force excitation levels used in the uncoupled tests are summarized in Table 5.1. This table also identifies the graphic symbols used to present the experimental results. In Table 5.16, the minimum force level and maximum force level for the coupled tests are summarized. The intermediate force levels are logarithmically spaced between these minimum and maximum values. Note that the applied force, F_{ex}, is non-dimensionalized by dividing with (kd) to yield the non-dimensional force Ξ_{ex}.

Table 5.16 Minimum and Maximum Non-dimensional Experimentally Applied Harmonic Excitation Levels for the Rectangular Tank Coupled Tests

Test ID	$\left| \Xi_{\text{ex}_{\min}} \right|$	$\left| \Xi_{\text{ex}_{\max}} \right|$
Graphic Symbol:	x	◊
R16	0.0012	0.0110
R17	0.0019	0.0175
R18	0.0016	0.0147
R19	0.0015	0.0137
R20	0.0021	0.0192
R21	0.0024	0.0219
R22	0.0020	0.0186
R23	0.0024	0.0219
R24	0.0019	0.0175
R25	0.0019	0.0175

5.4.2 Rectangular Tank Experimental Results

Section 5.4.2.1 discusses the uncoupled test results and the following section, section 5.4.2.2, discusses the coupled test results.

5.4.2.1   Discussion of the Uncoupled Test Results

The linear eigen-characteristics of the first fluid mode, from the uncoupled fluid tests, are summarized in Table 5.17 and those for the second fluid mode in Table 5.18. The damping ratios were obtained with the half-power-band-width method from the lowest force excitation level results. Figures 5.100 to 5.107 give the results of the uncoupled tests (also see Table 5.14 for a more detailed identification of the figures). The vertical solid line in these figures indicates the position of the resonance peak as predicted by linear theory. Any shift of the resonance peak away from this

vertical line represents nonlinear fluid slosh behavior. The direction of excitation is also indicated on each figure.

Table 5.17   Measured 1st Mode Linear Eigen-characteristics (Rectangular Tank, with 2% Photoflo/Water Solution)

Test ID	Excitation Angle	Natural Frequency (Hz)	Damping Ratio (%)	Slosh Mass Fraction λ
RU1	0°	-	-	-
RU2	30°	3.76	2.9	0.09
RU3	60°	3.76	2.5	0.24
RU4	90°	3.76	2.5	0.35

Table 5.18   Measured 2nd Mode Linear Eigen-characteristics (Rectangular Tank, with 2% Photoflo/Water Solution)

Test ID	Excitation Angle	Natural Frequency (Hz)	Damping Ratio (%)	Slosh Mass Fraction λ
RU1	0°	5.41	3.1	0.20
RU2	30°	5.42	2.9	0.19
RU3	60°	5.41	3.7	0.10
RU4	90°	-	-	-

In the uncoupled test results, both the first and second fluid slosh modes exhibit a softening tendency with increasing excitation amplitudes. The strength of these nonlinearities are fluid motion amplitude dependent and thus dependent on the excitation angle. The relative amount of energy transferred to these two slosh modes is dependent on the excitation angle. In test RU1, the excitation angle is such that the first slosh mode is not excited and in test RU4 such that the second fluid slosh mode is not excited.

The jump phenomenon observed in the square tanks, where the fluid swirls, was not observed in the rectangular uncoupled tests. The spectral separation of the first two eigen-modes must be seen as the reason for this behavior. For the square tanks the first two modes are repeated planar and nonplanar modes. Energy exchange between these repeated modes is more likely than energy exchange between modes that are spectrally separated.

5.4.2.2   Discussion of the Coupled Test Results

In the coupled tests, the mass ratios, frequency ratios and damping ratios were varied to determine the effect of these parameters on the coupled behavior of the fluid/spacecraft system. Figures 5.108 to 5.146 the results of the coupled tests with the rectangular tank (also see Table 5.15 for a more detailed identification of the figures). As with the uncoupled tests, the vertical solid lines in these figures indicate the positions of the resonance peaks as predicted by linear theory. Any shift of the resonance peaks away from this verticals line represent nonlinear behavior. The direction of excitation is also indicated on each figure.

Studying the Figures 5.110 to 5.113 (Test R16) it can be seen that both the first fluid mode and the spacecraft mode exhibit moderate softening (decrease in resonant frequency with an increase in force excitation amplitude) trends and that the shape of the resonant peaks are slightly amplitude dependent. Using this test (R16 $\mu=0.16$, $v=0.90$, $\xi=8.00\%$) as the nominal configuration, the following conclusions can be made concerning:

The Effect of Mass Ratio: From Fig. 5.114 (Test R17, $\mu=0.32$, $v=0.90$, $\xi=8.00\%$) it can be concluded that, as was observed in the spherical tank results but contrary to the square results, lower mass fractions result in more nonlinear fluid behavior.

The Effect of Frequency Ratio: The lack of experiments with varying frequency ratios makes a conclusion on the effect of this parameter on the system dynamics difficult. From Fig. 5.118 (Test R18, $\mu=0.16$, $v=0.87$, $\xi=8.00\%$), however, one could conclude that configurations with frequencies ratios close to unity are more nonlinear. **Note:** Different force excitation levels were used for tests R16 and R18.

The Effect of Damping Ratio: It is clear from Fig. 5.122 (Test R19, $\mu=0.16$, $\nu=0.92$, $\xi=4.00\%$) that configurations with lower spacecraft modal damping ratios are more nonlinear.

The Effect of Excitation Angle: From Fig. 5.112 (Test R16, Excitation Angle=90°), Fig. 5.126 (Test R20, Excitation Angle=60°), Fig. 5.134 (Test R22, Excitation Angle=30°) and Fig. 5.141 (Test R24, Excitation Angle=0°) it can be concluded that the effect of the excitation angle can be determined from the frequency ratio conclusion. When the excitation angle is such that the first mode is not excited (Test R24, Excitation Angle=0°), the spacecraft mode is linear and the second fluid slosh mode exhibits the same nonlinear behavior observed in the uncoupled tests. For this excitation angle, the frequency ratio between the spacecraft mode and the second fluid slosh mode is greater than unity and the spacecraft mode motion is linear. As the excitation angle increases, the excitation of the first fluid slosh mode increases, yielding a more nonlinear spacecraft mode.
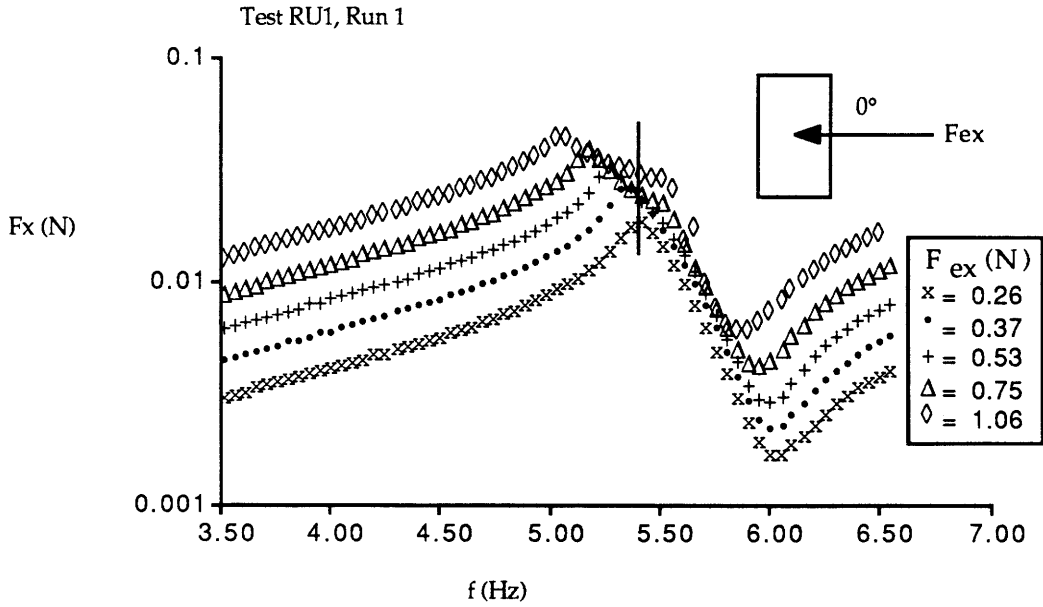
Figure 5.100   Test RU1, Planar Slosh Force (Fx).
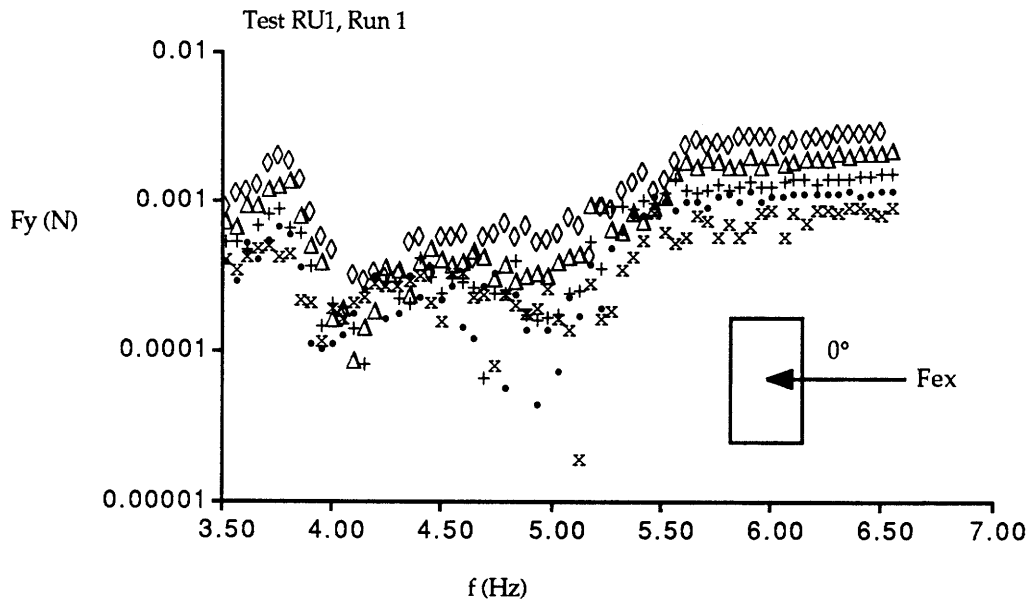
Figure 5.101   Test RU1, Nonplanar Slosh Force (Fy).

(Rectangular tank, uncoupled, harmonic excitation, Excitation angle=0° and Fluid=2% Photoflo/Water Solution)

204
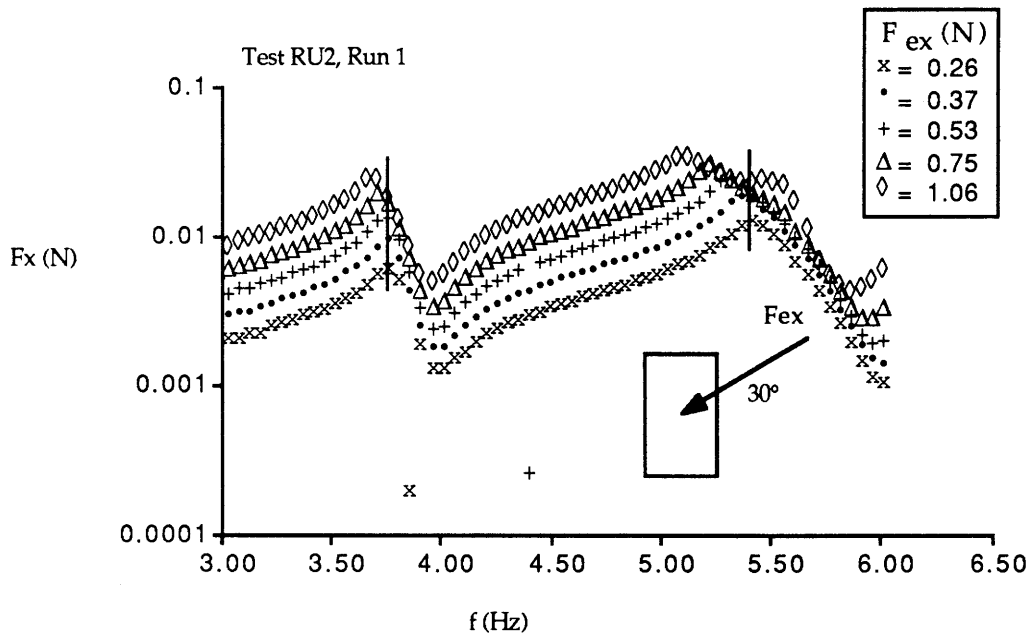
Figure 5.102   Test RU2, Planar Slosh Force (Fx).
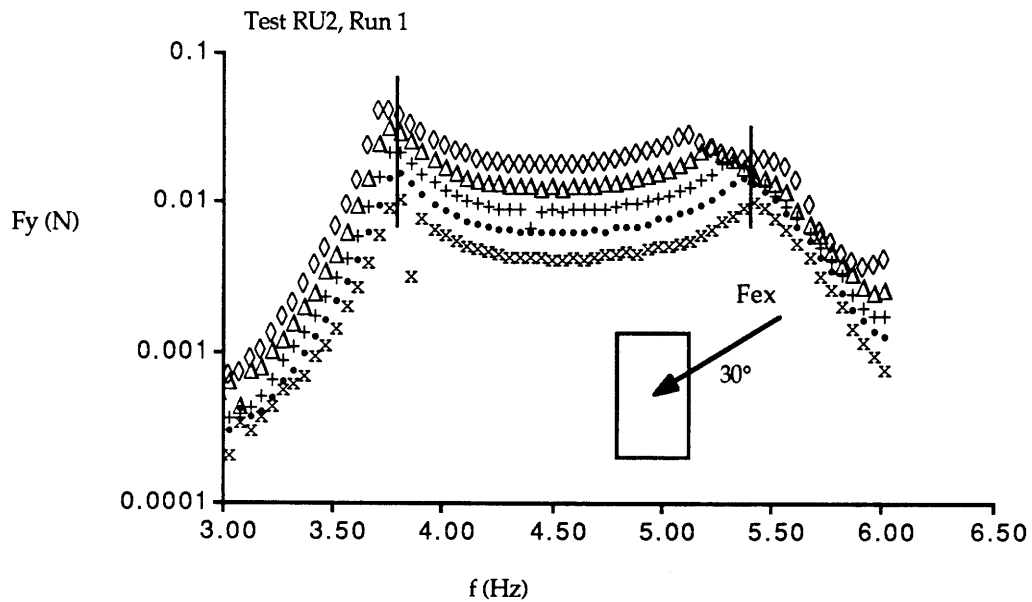
Figure 5.103   Test RU2, Nonplanar Slosh Force (Fy).

(Rectangular tank, uncoupled, harmonic excitation, Excitation angle=30° and Fluid=2% Photoflo/Water Solution)

205
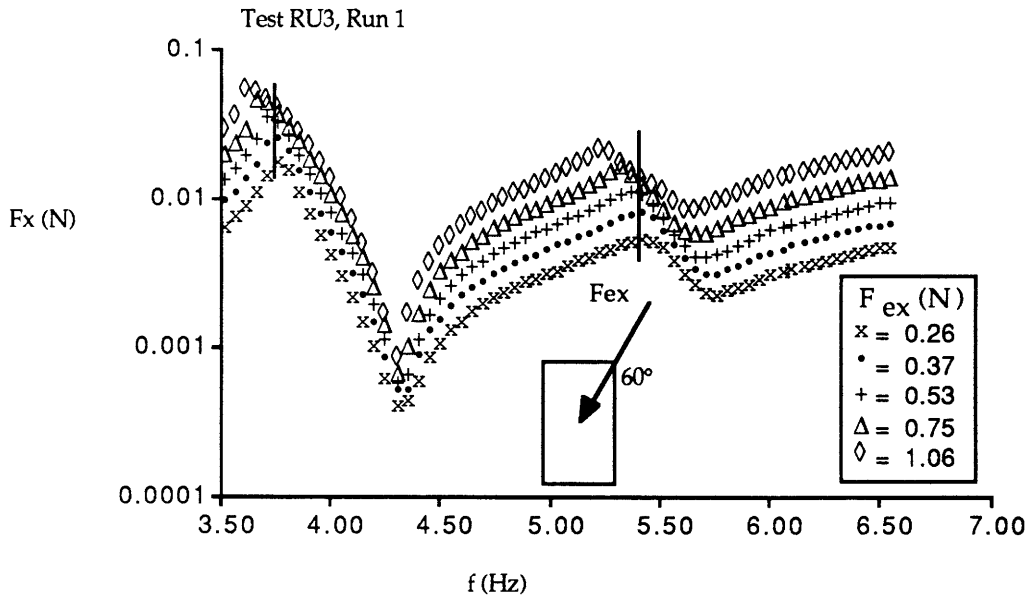
Figure 5.104   Test RU3, Planar Slosh Force (Fx).
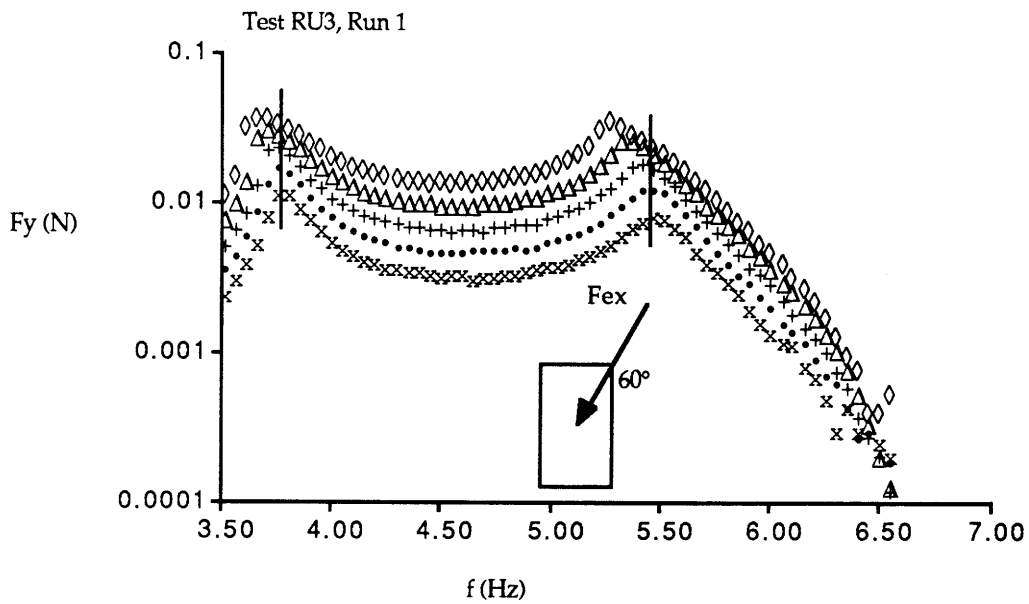
Figure 5.105   Test RU3, Nonplanar Slosh Force (Fy).

(Rectangular tank, uncoupled, harmonic excitation, Excitation angle=60° and Fluid=2% Photoflo/Water Solution)

206
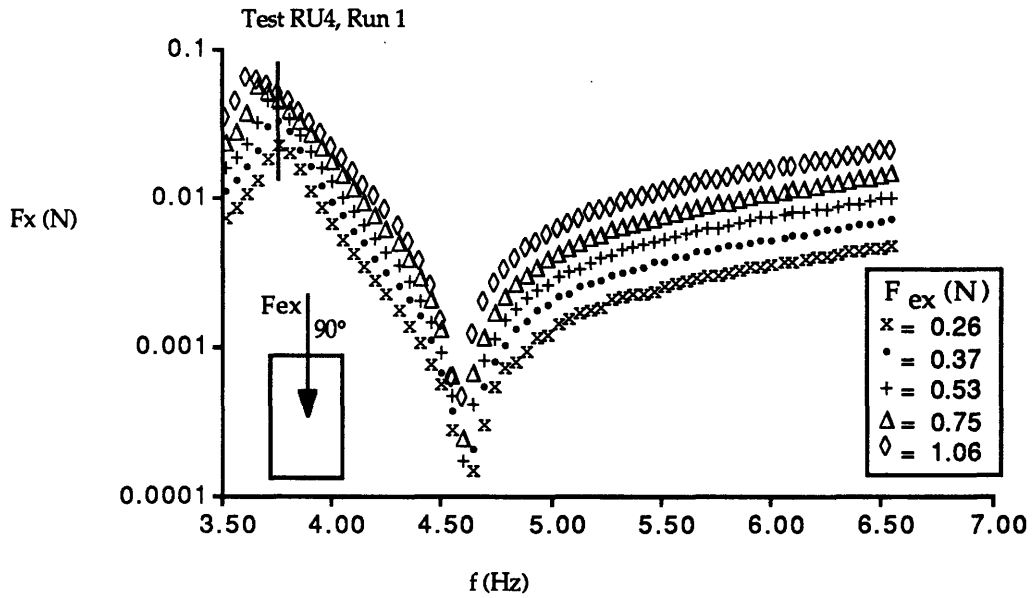
Figure 5.106   Test RU4, Planar Slosh Force (Fx).
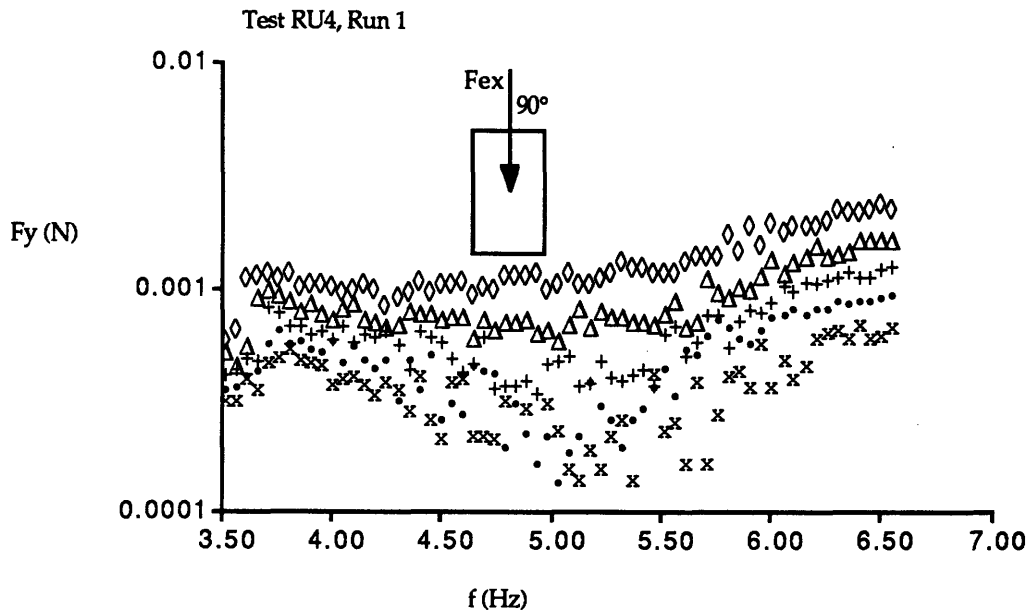
Figure 5.107   Test RU4, Nonplanar Slosh Force (Fy).

(Rectangular tank, uncoupled, harmonic excitation, Excitation angle=90° and Fluid=2% Photoflo/Water Solution)
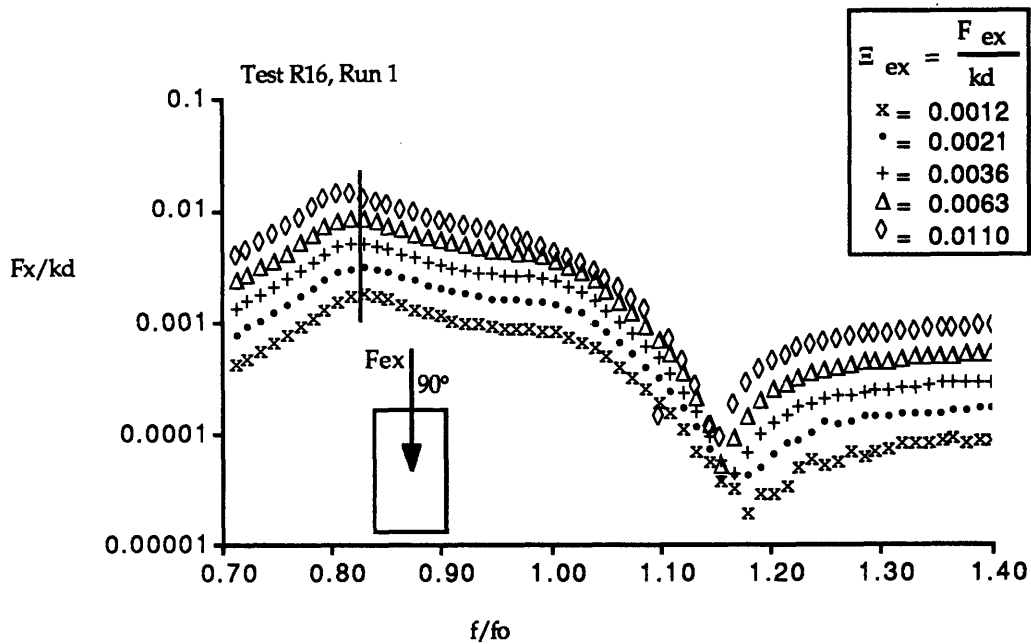
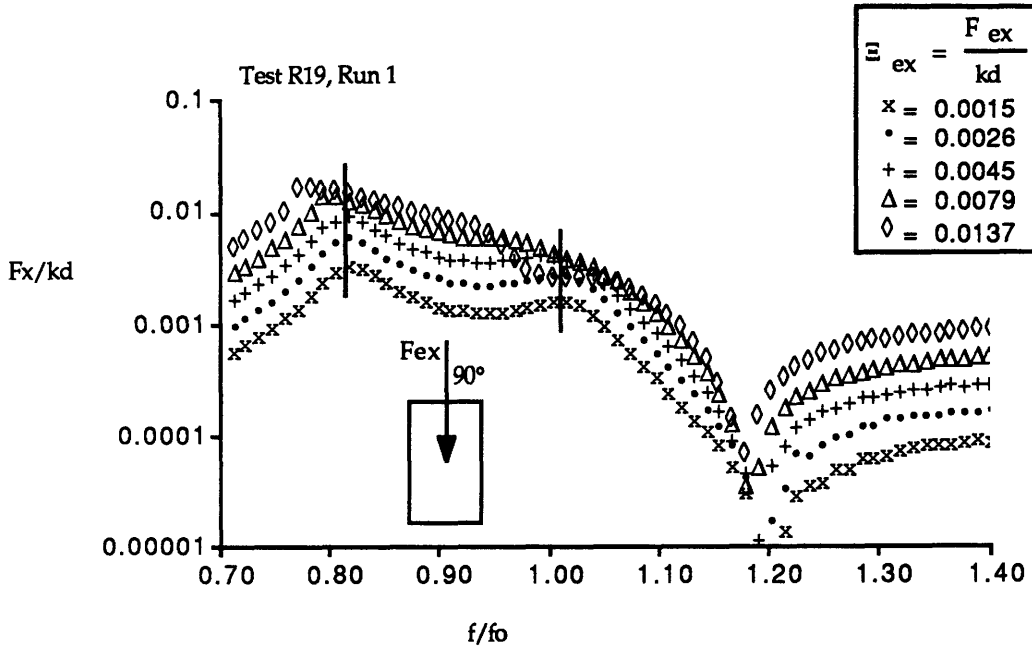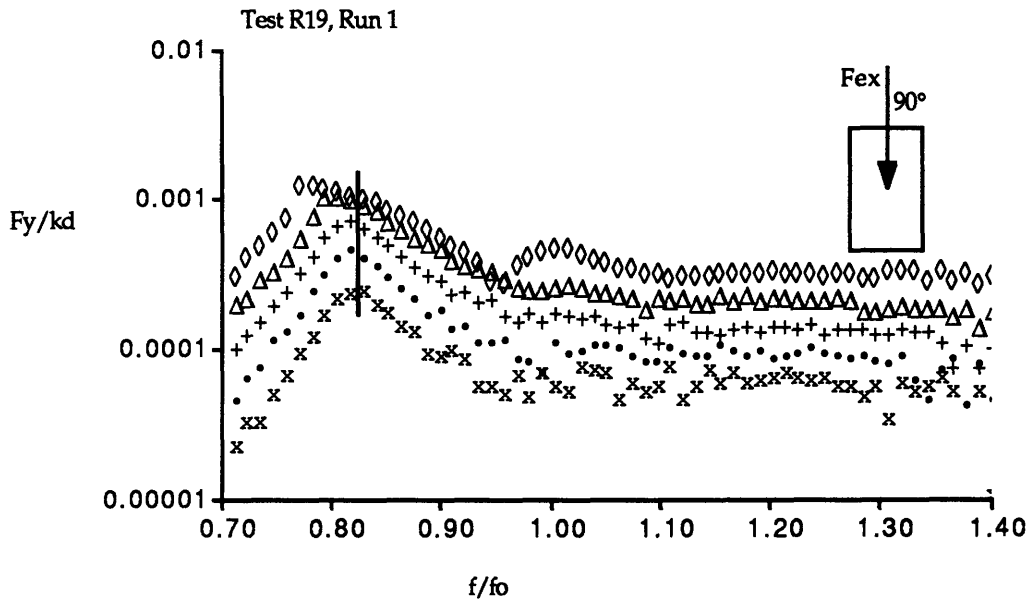**Figure 5.108   Test R16, Non-dimensional Planar Slosh Force (Fx/kd).**
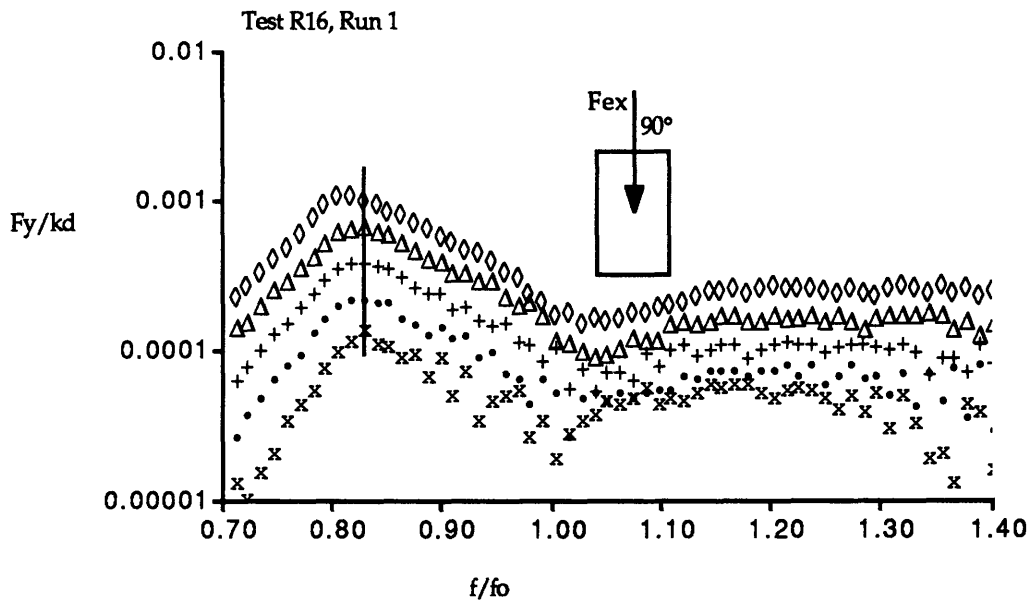
Figure 5.109   Test R16, Non-dimensional Nonplanar Slosh Force (Fy/kd).

(Rectangular tank, coupled, harmonic excitation, Coupled system parameters; $\mu=0.16$, $v=0.90$, $\zeta=8.00\%$, Bo=78, Excitation angle=90°)
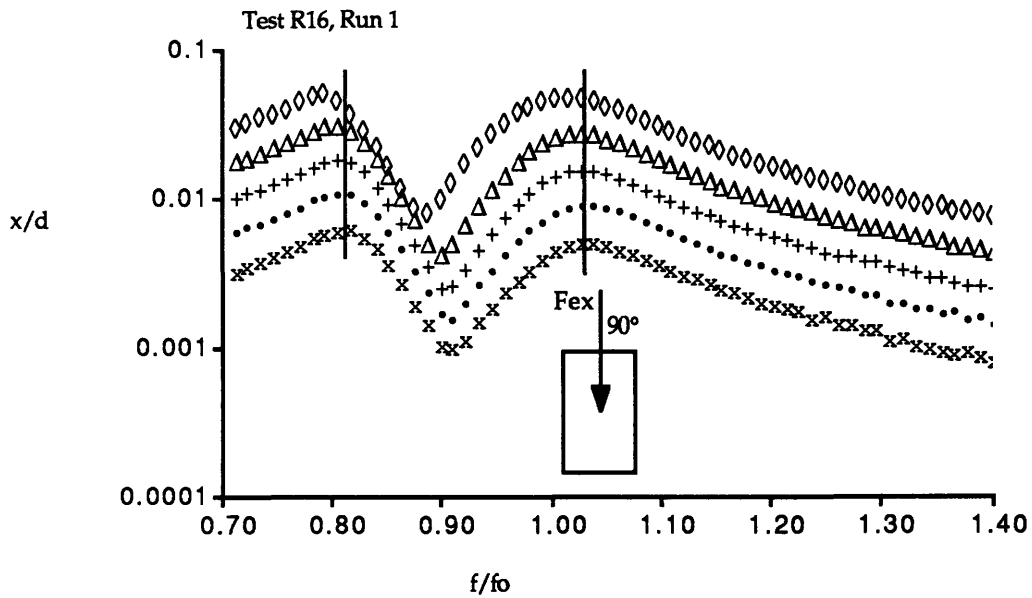
Figure 5.110   Test R16, Non-dimensional Displacement (x/d).
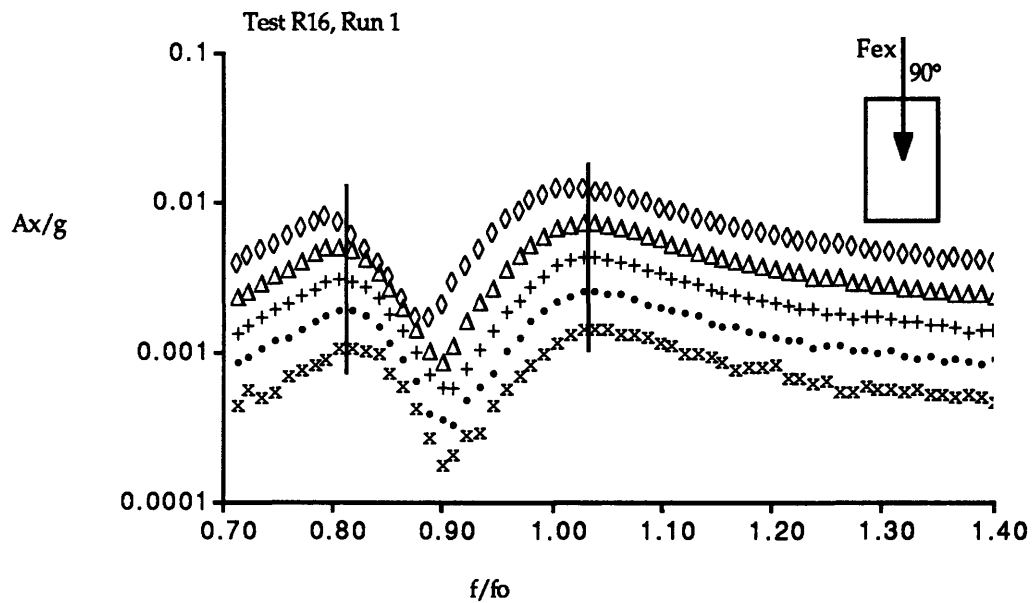
Figure 5.111   Test R16, Non-dimensional Acceleration (Ax/g).

(Rectangular tank, coupled, harmonic excitation, Coupled system parameters; $\mu=0.16$, $v=0.90$, $\zeta=8.00\%$, Bo=78, Excitation angle=90°)
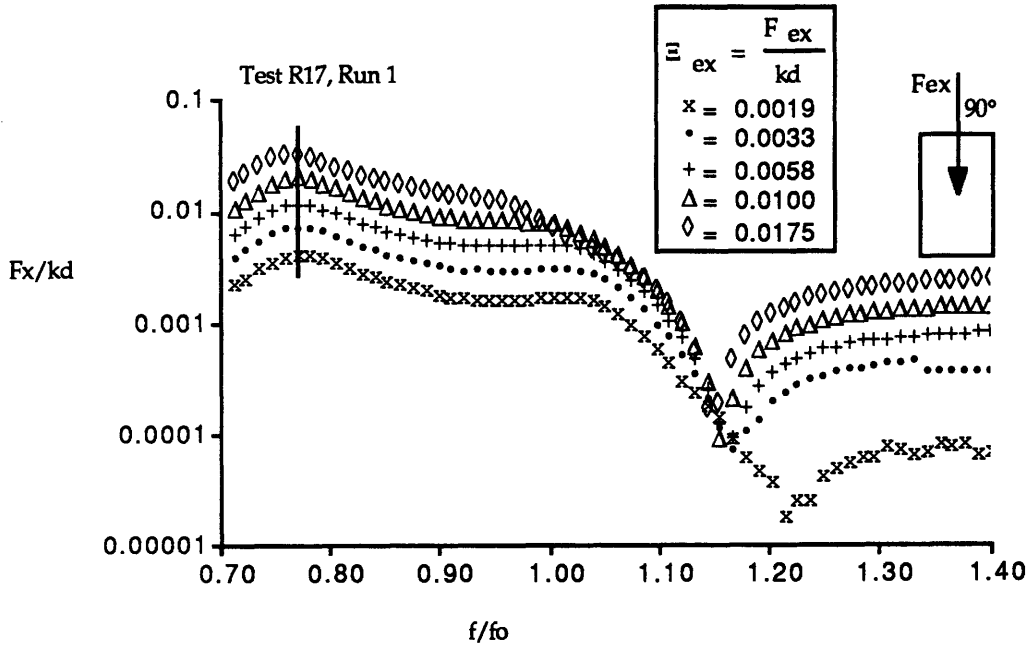
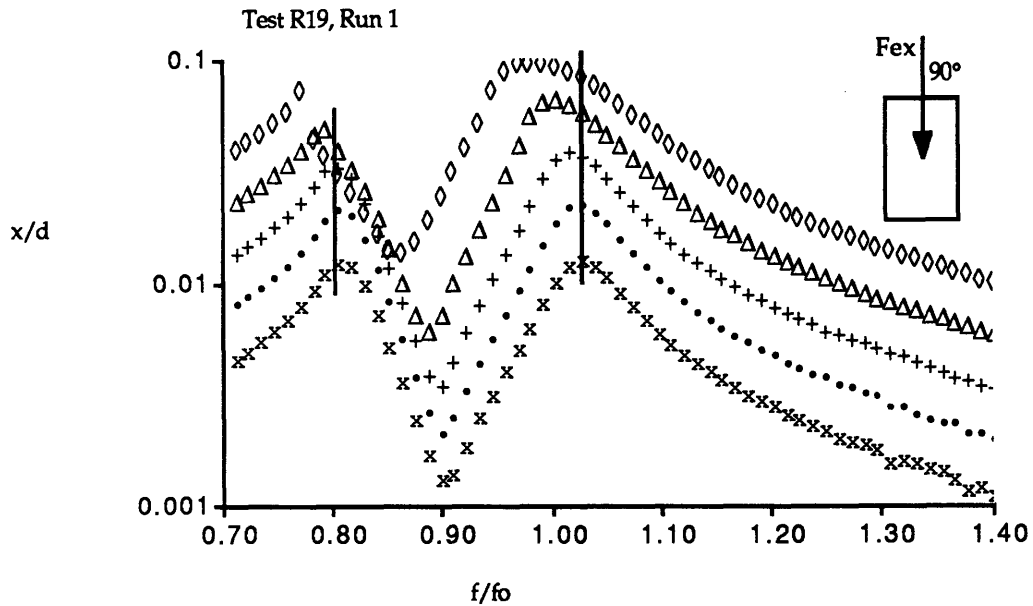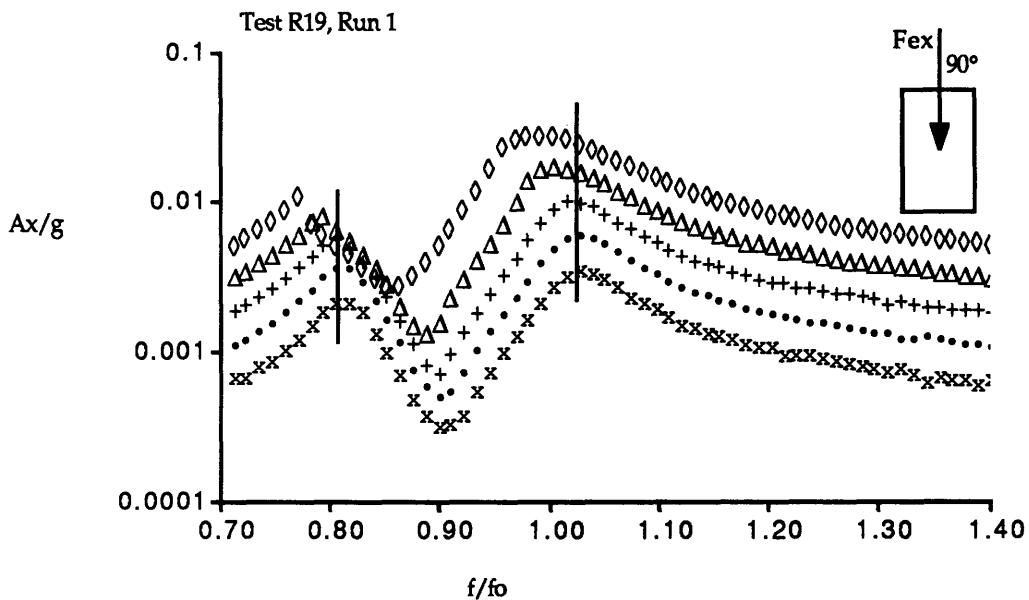**Figure 5.112   Test R17, Non-dimensional Planar Slosh Force (Fx/kd).**
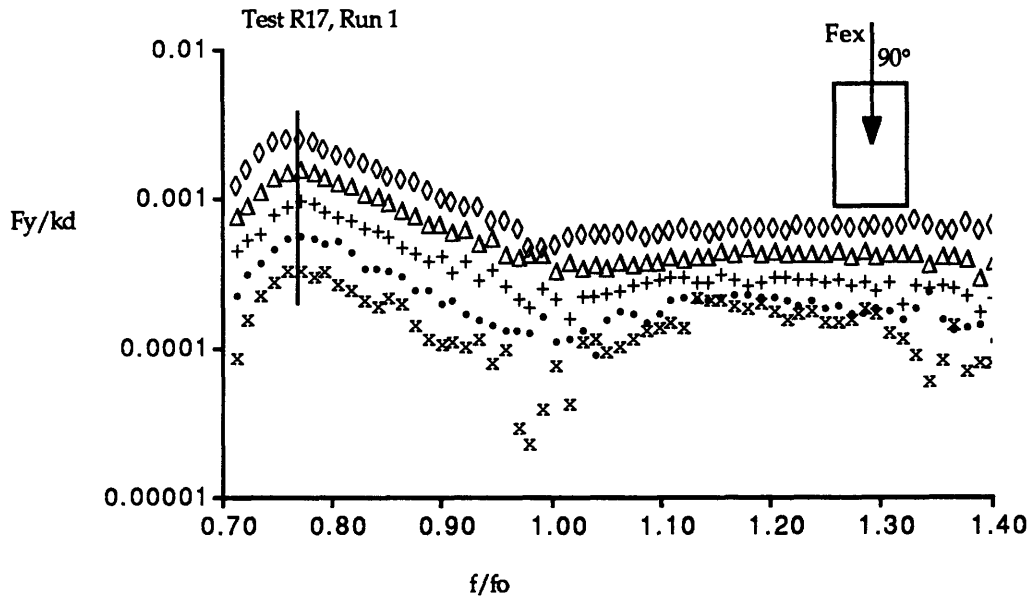
Figure 5.113   Test R17, Non-dimensional Nonplanar Slosh Force (Fy/kd).

(Rectangular tank, coupled, harmonic excitation, Coupled system parameters; $\mu=0.32$, $v=0.90$, $\zeta=8.00\%$, Bo=78, Excitation angle=90°)
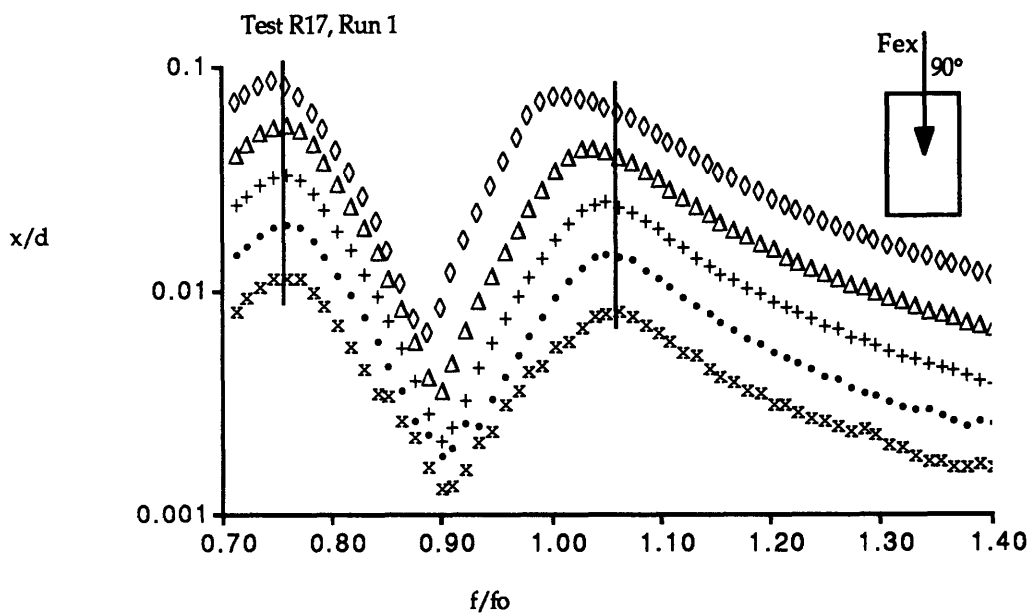
Figure 5.114   Test R17, Non-dimensional Displacement (x/d).
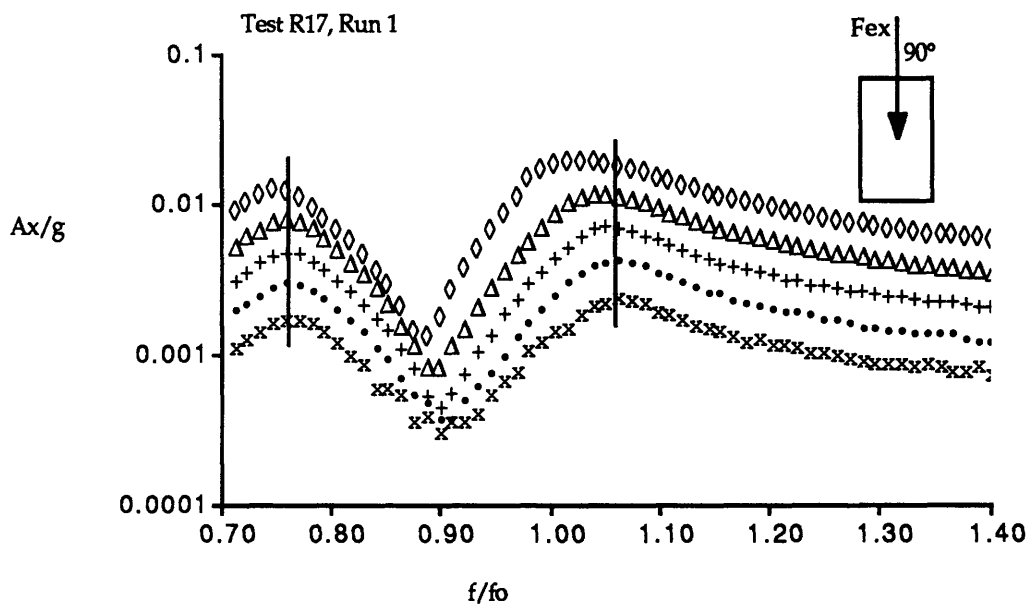
Figure 5.115   Test R17, Non-dimensional Acceleration (Ax/g).

(Rectangular tank, coupled, harmonic excitation, Coupled system parameters; μ=0.32, v=0.90, ζ=8.00%, Bo=78, Excitation angle=90°)
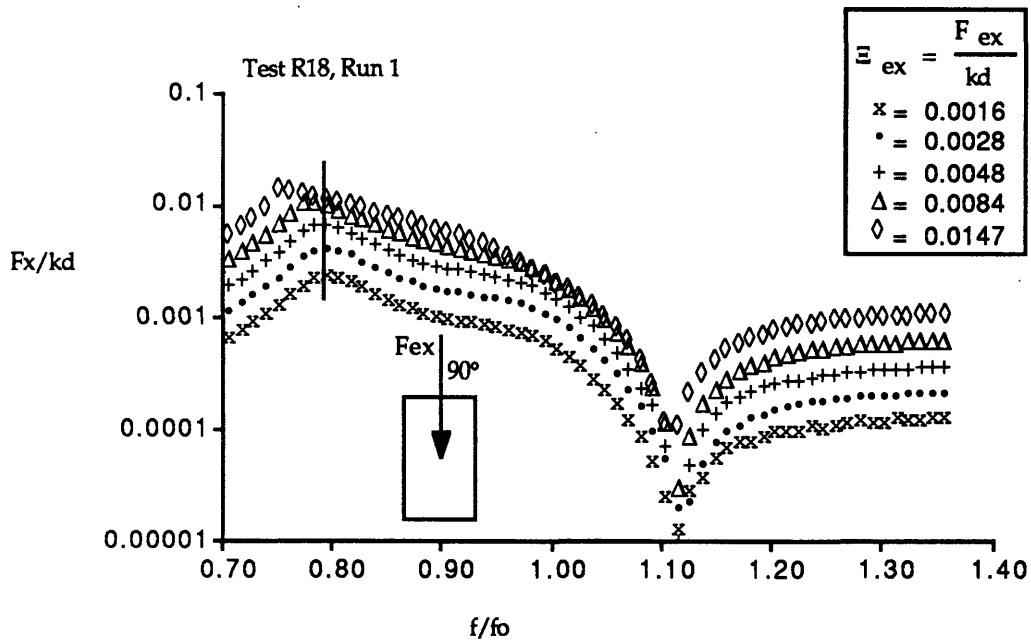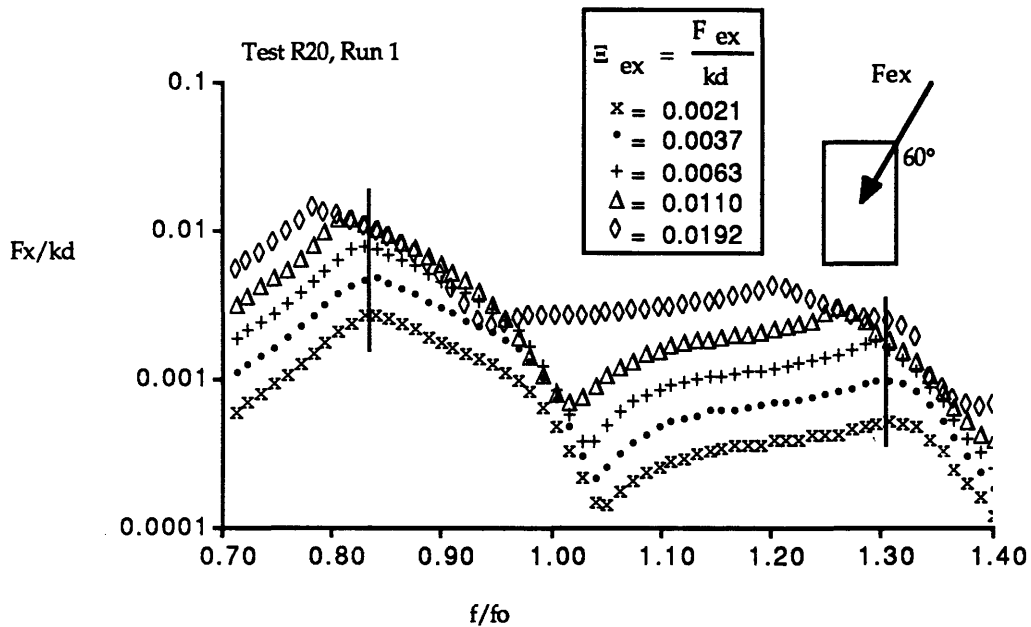
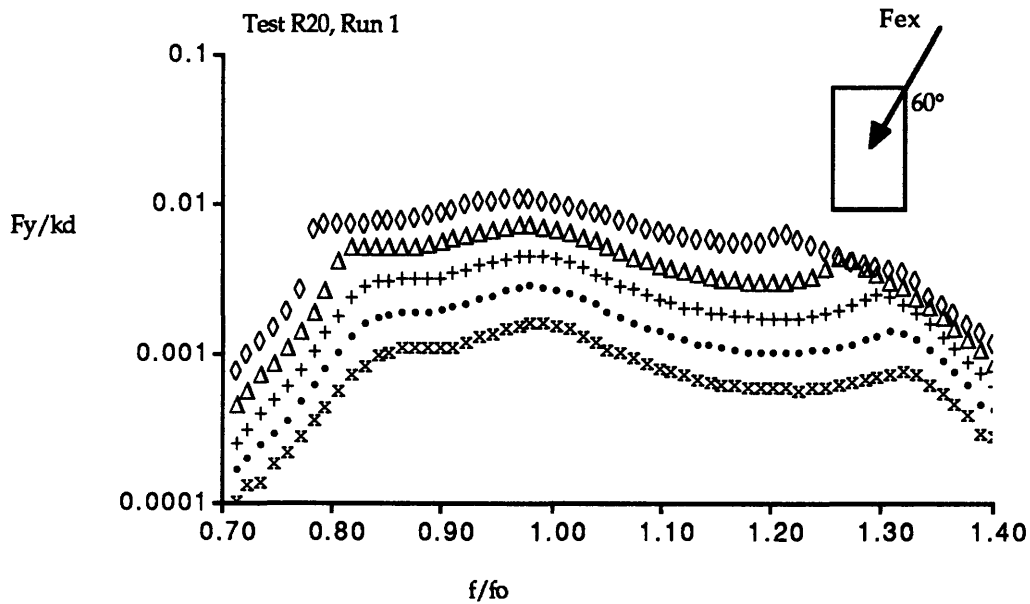**Figure 5.116   Test R18, Non-dimensional Planar Slosh Force (Fx/kd).**
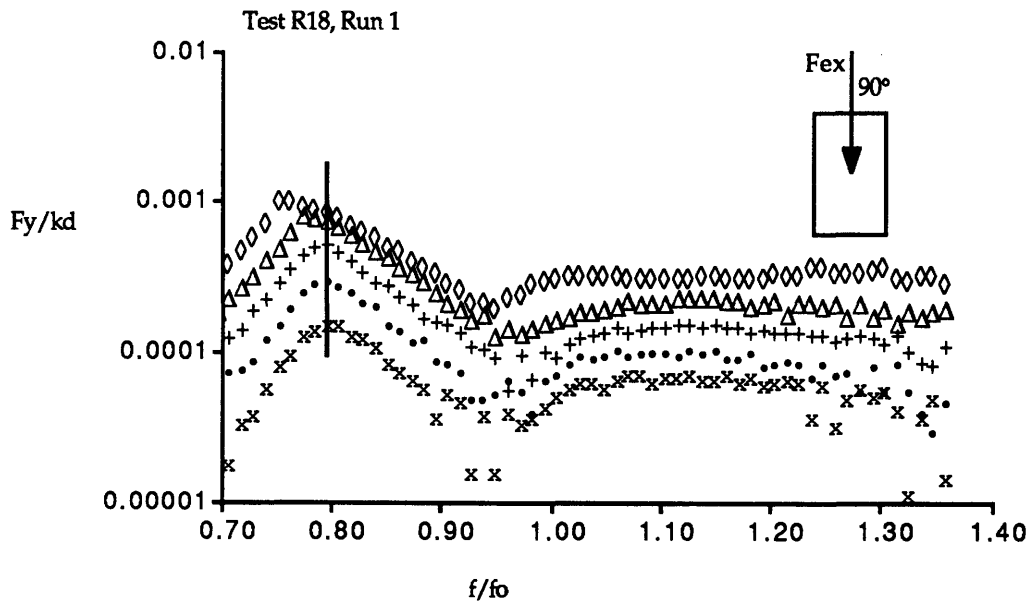
Figure 5.117   Test R18, Non-dimensional Nonplanar Slosh Force (Fy/kd).

(Rectangular tank, coupled, harmonic excitation, Coupled system parameters; $\mu=0.16$, $v=0.85$, $\zeta=8.00\%$, Bo=78, Excitation angle=90°)

Figure 5.118   Test R18, Non-dimensional Displacement (x/d).
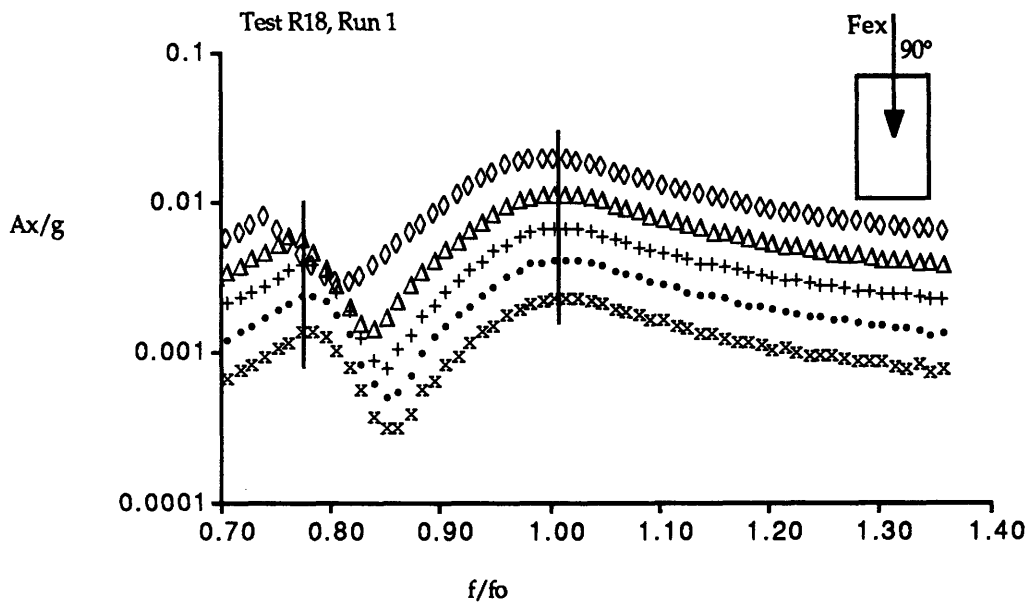
Figure 5.119   Test R18, Non-dimensional Acceleration (Ax/g).

(Rectangular tank, coupled, harmonic excitation, Coupled system parameters; $\mu=0.16$, $\nu=0.85$, $\zeta=8.00\%$, $Bo=78$, Excitation angle=90°)
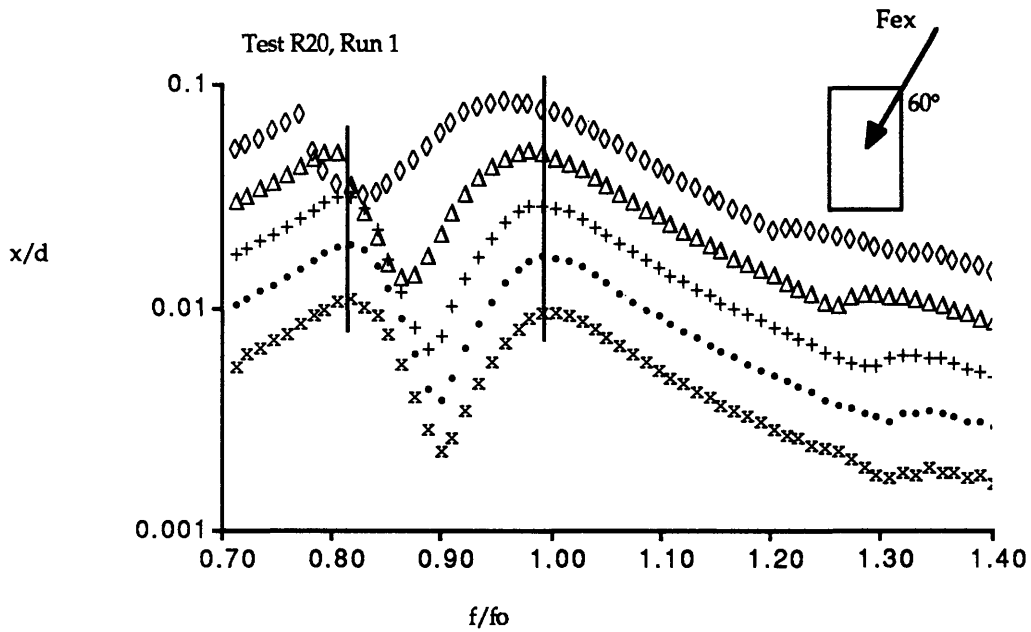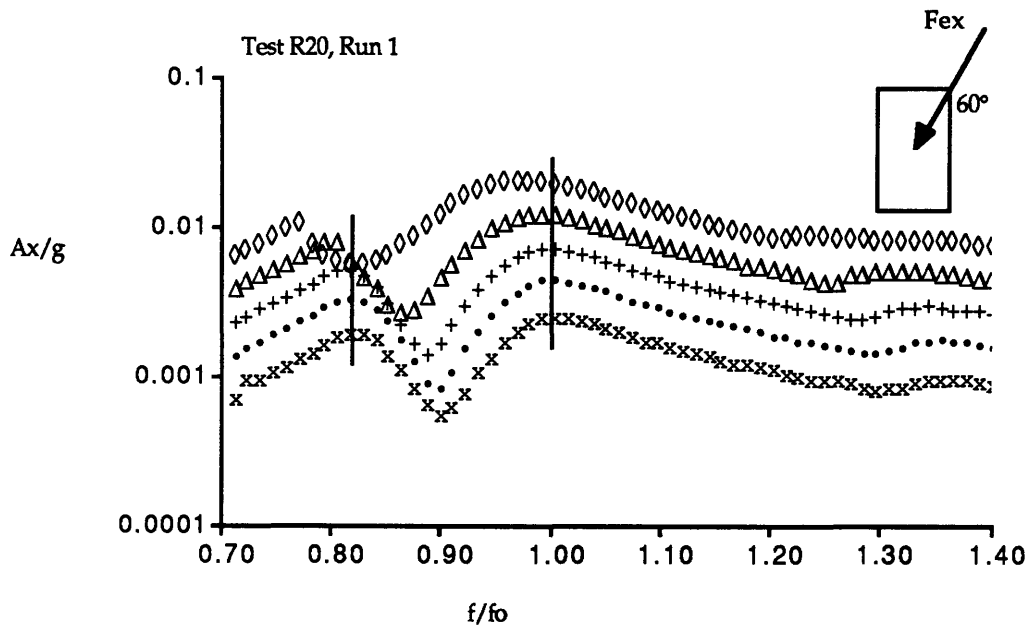
Figure 5.120   Test R19, Non-dimensional Planar Slosh Force (Fx/kd).

Figure 5.121   Test R19, Non-dimensional Nonplanar Slosh Force (Fy/kd).

(Rectangular tank, coupled, harmonic excitation, Coupled system parameters; μ=0.16, v=0.90, ζ=4.00%, Bo=78, Excitation angle=90°)

Figure 5.122   Test R19, Non-dimensional Displacement (x/d).

Figure 5.123   Test R19, Non-dimensional Acceleration (Ax/g).

(Rectangular tank, coupled, harmonic excitation, Coupled system parameters; $\mu=0.16$, $v=0.90$, $\zeta=4.00\%$, Bo=78, Excitation angle=90°)
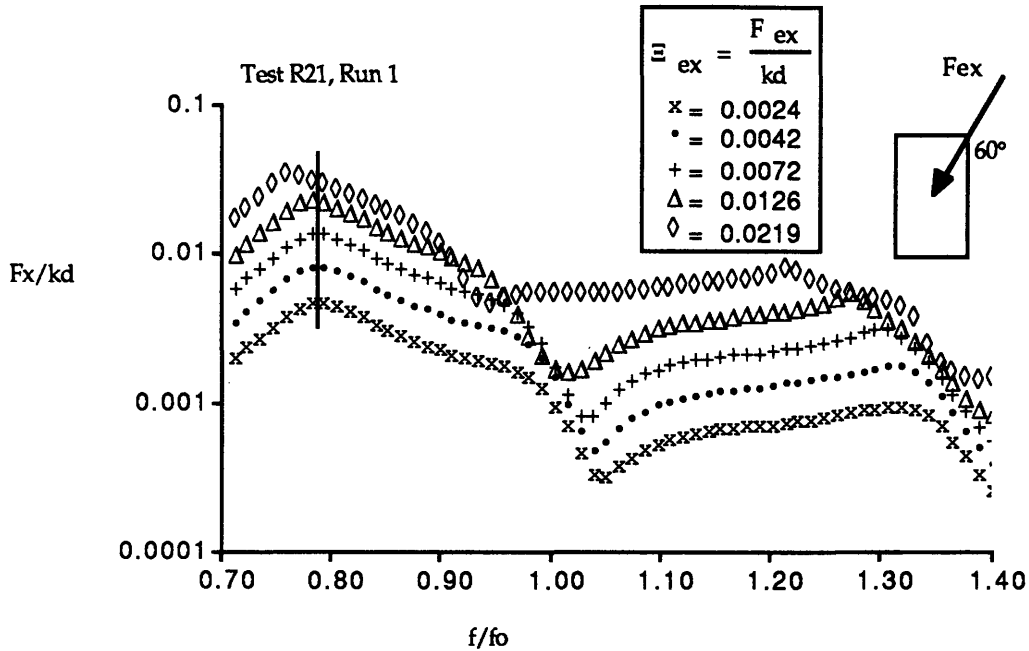
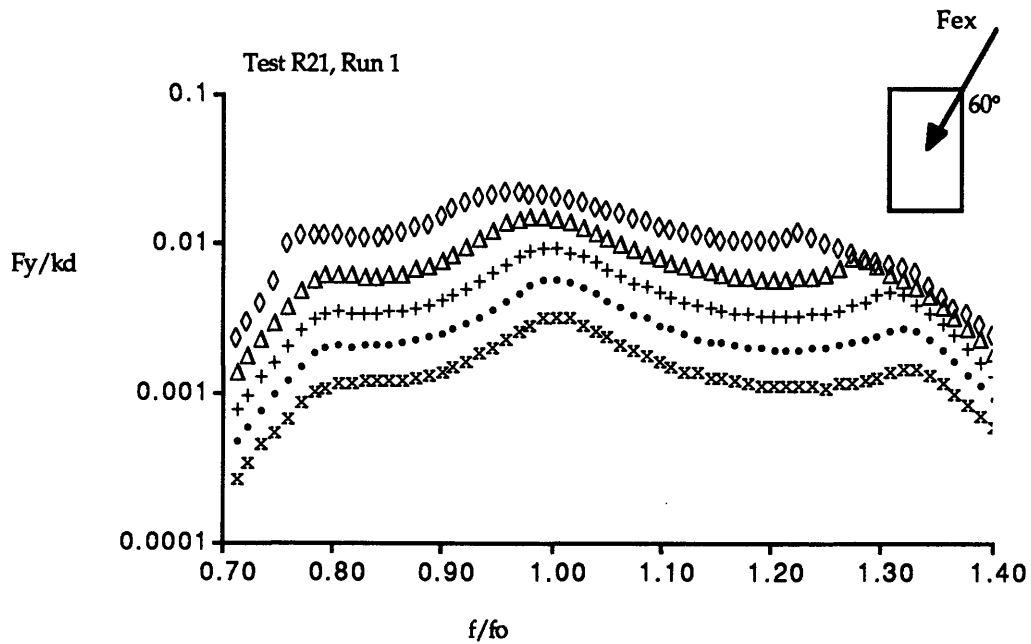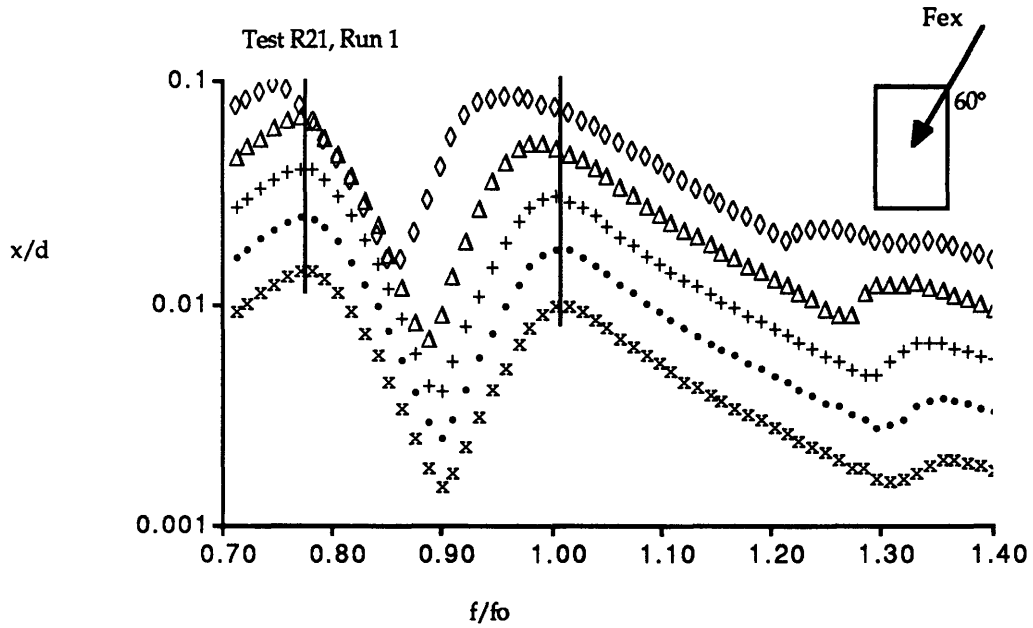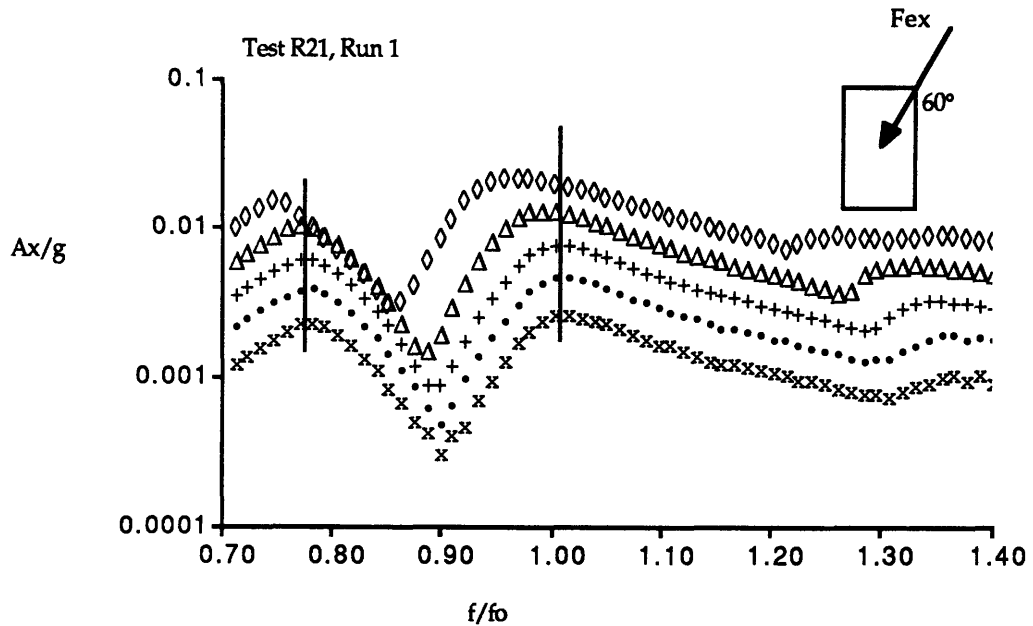**Figure 5.124   Test R20, Non-dimensional Planar Slosh Force (Fx/kd).**

Figure 5.125   Test R20, Non-dimensional Nonplanar Slosh Force (Fy/kd).

(Rectangular tank, coupled, harmonic excitation, Coupled system parameters; μ=0.16, ν=0.90, ζ=8.00%, Bo=78, Excitation angle=60°)

Figure 5.126   **Test R20, Non-dimensional Displacement (x/d).**

Figure 5.127   **Test R20, Non-dimensional Acceleration (Ax/g)**

(Rectangular tank, coupled, harmonic excitation, Coupled system parameters; $\mu=0.16$, $v=0.90$, $\zeta=8.00\%$, Bo=78, Excitation angle=60°)

Figure 5.128   Test R21, Non-dimensional Planar Slosh Force (Fx/kd).

Figure 5.129   Test R21, Non-dimensional Nonplanar Slosh Force (Fy/kd).

(Rectangular tank, coupled, harmonic excitation, Coupled system parameters; μ=0.32, ν=0.90, ζ=8.00%, Bo=78, Excitation angle=60°)

Figure 5.130   Test R21, Non-dimensional Displacement (x/d).

Figure 5.131   Test R21, Non-dimensional Acceleration (Ax/g).

(Rectangular tank, coupled, harmonic excitation, Coupled system parameters; μ=0.32, ν=0.90, ζ=8.00%, Bo=78, Excitation angle=60°)
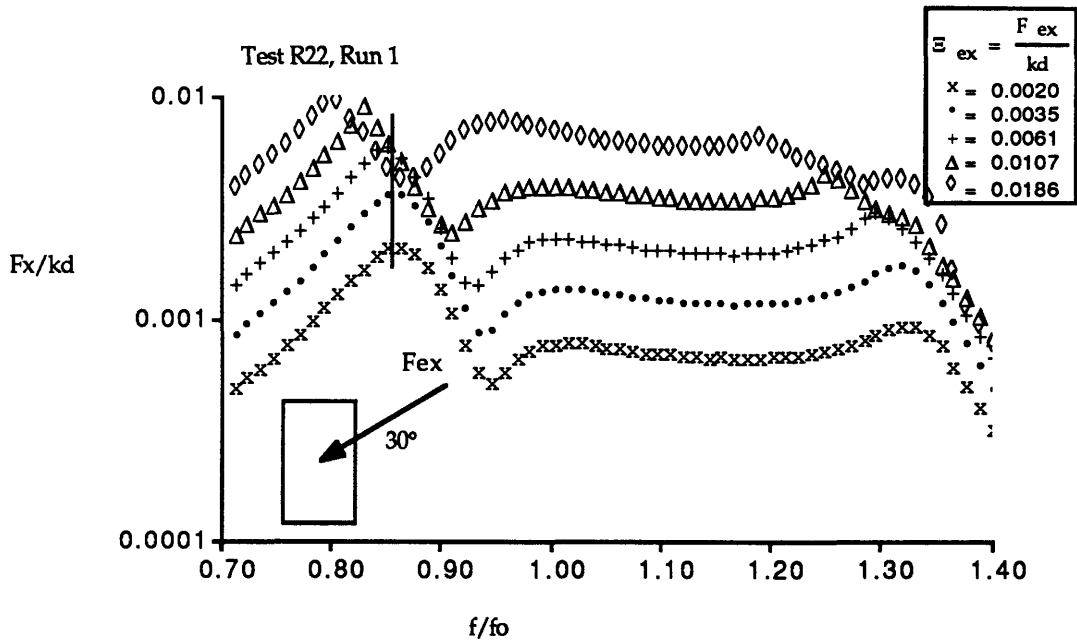
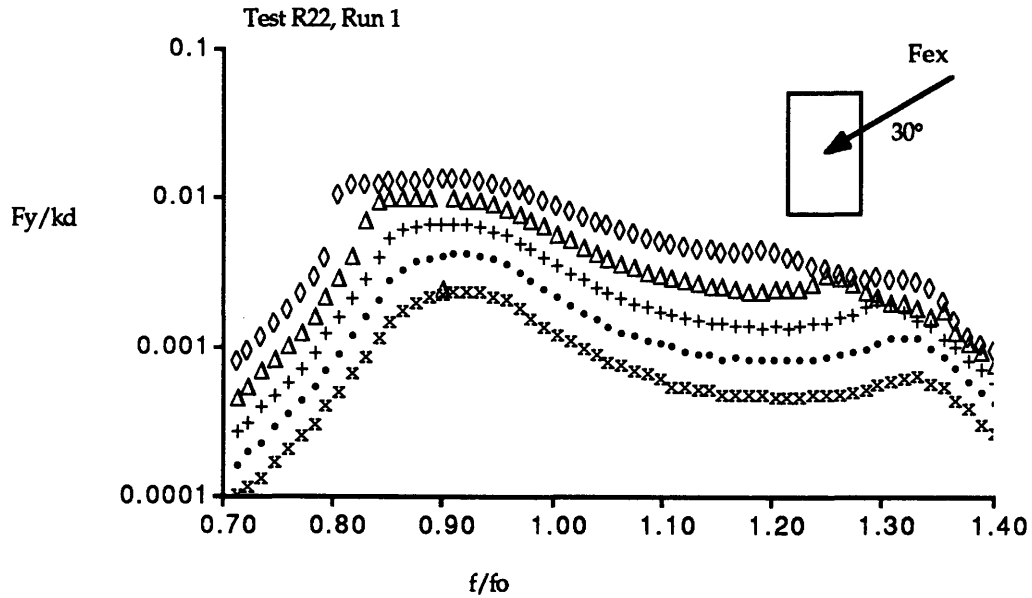**Figure 5.132   Test R22, Non-dimensional Planar Slosh Force (Fx/kd).**

Figure 5.133   Test R22, Non-dimensional Nonplanar Slosh Force (Fy/kd).

(Rectangular tank, coupled, harmonic excitation, Coupled system parameters; $\mu=0.16$, $v=0.90$, $\zeta=8.00\%$, Bo=78, Excitation angle=30°)

Figure 5.134   Test R22, Non-dimensional Displacement (x/d).

Figure 5.135   Test R22, Non-dimensional Acceleration (Ax/g).

(Rectangular tank, coupled, harmonic excitation, Coupled system parameters; μ=0.16, ν=0.90, ζ=8.00%, Bo=78, Excitation angle=30°)

221
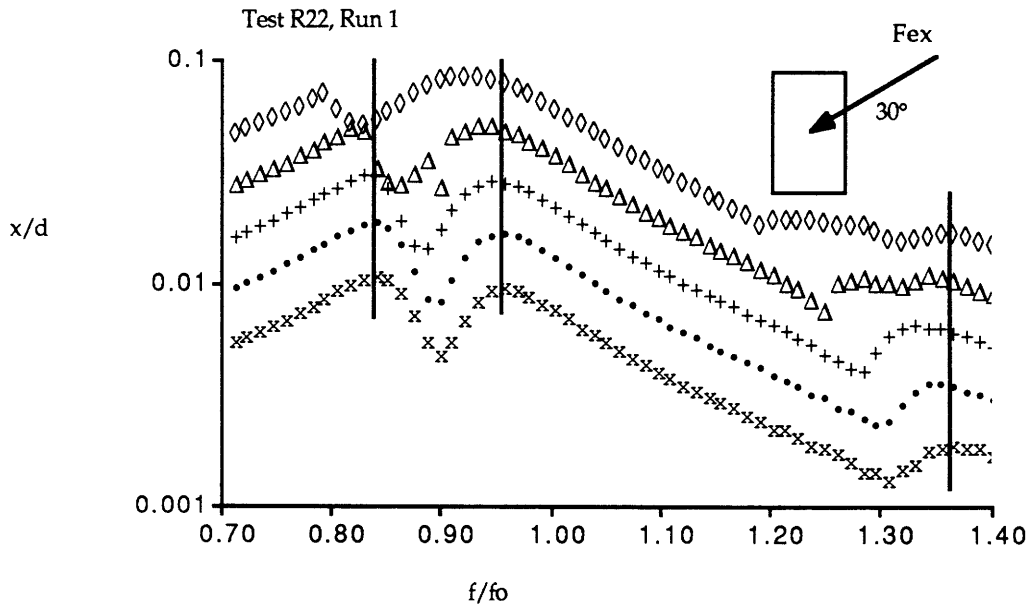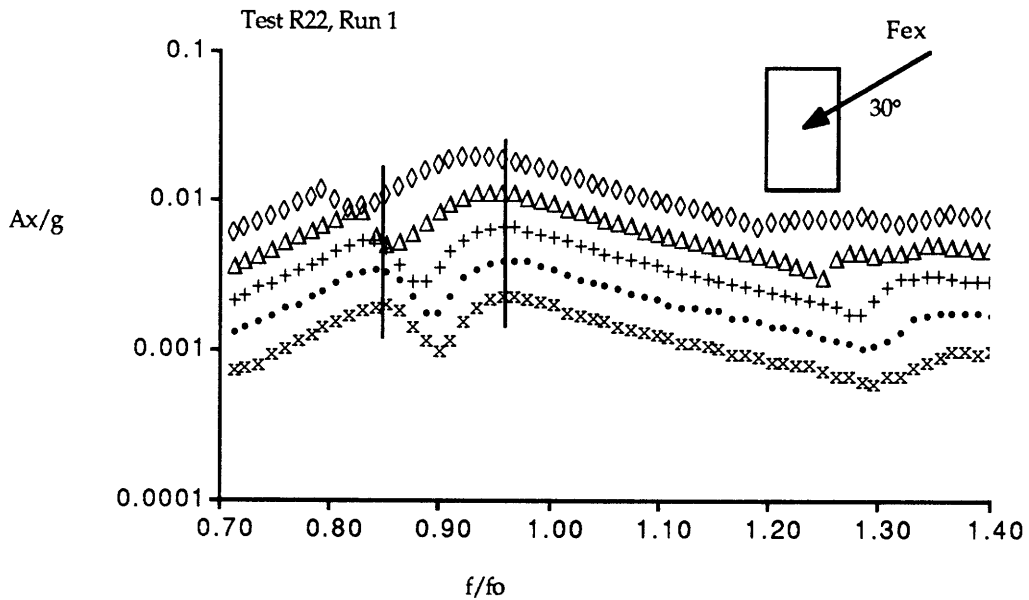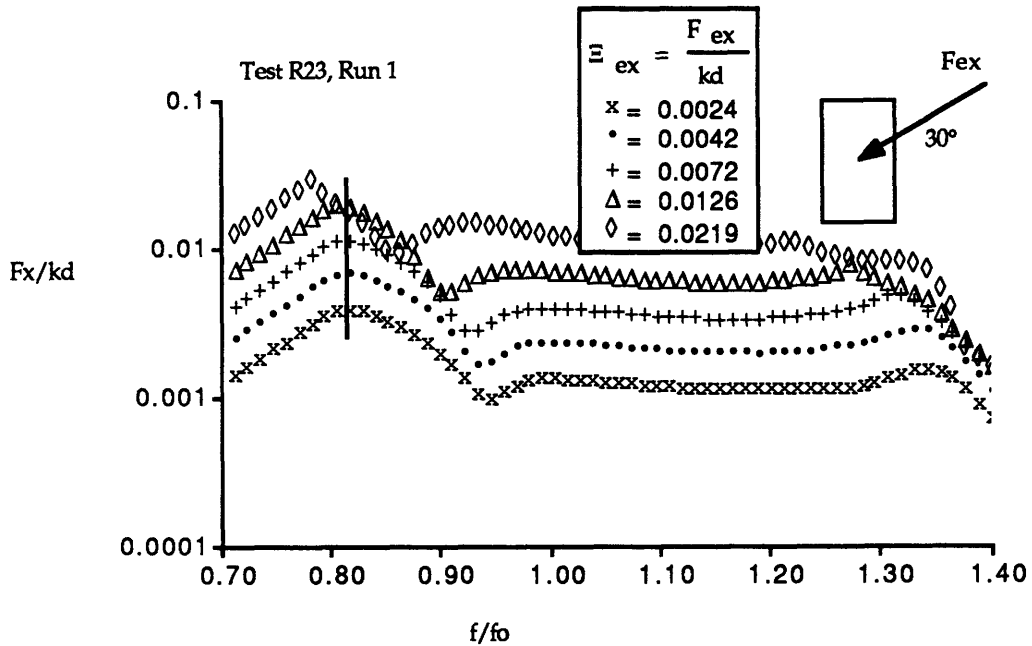
Figure 5.136   Test R23, Non-dimensional Planar Slosh Force (Fx/kd).

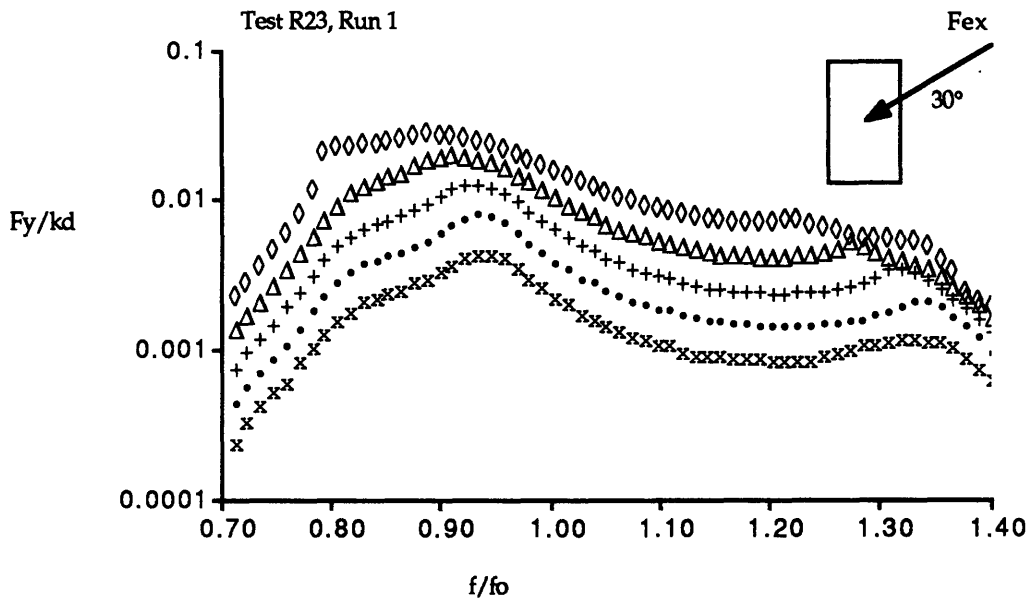**Figure 5.137**   Test R23, Non-dimensional Nonplanar Slosh Force (Fy/kd).

(Rectangular tank, coupled, harmonic excitation, Coupled system parameters; μ=0.32, v=0.90, ζ=8.00%, Bo=78, Excitation angle=30°)

Figure 5.138   Test R23, Non-dimensional Displacement (x/d).

Figure 5.139   Test R23, Non-dimensional Acceleration (Ax/g).

(Rectangular tank, coupled, harmonic excitation, Coupled system parameters; μ=0.32, ν=0.90, ζ=8.00%, Bo=78, Excitation angle=30°)

Figure 5.140   Test R24, Non-dimensional Planar Slosh Force (Fx/kd).

(Rectangular tank, coupled, harmonic excitation, Coupled system parameters; μ=0.16, v=0.90, ζ=8.00%, Bo=78, Excitation angle=0°)

Figure 5.141   Test R24, Non-dimensional Displacement (x/d).

Figure 5.142   Test R24, Non-dimensional Acceleration (Ax/g).

(Rectangular tank, coupled, harmonic excitation, Coupled system parameters; μ=0.16, v=0.90, ζ=8.00%, Bo=78, Excitation angle=0°)
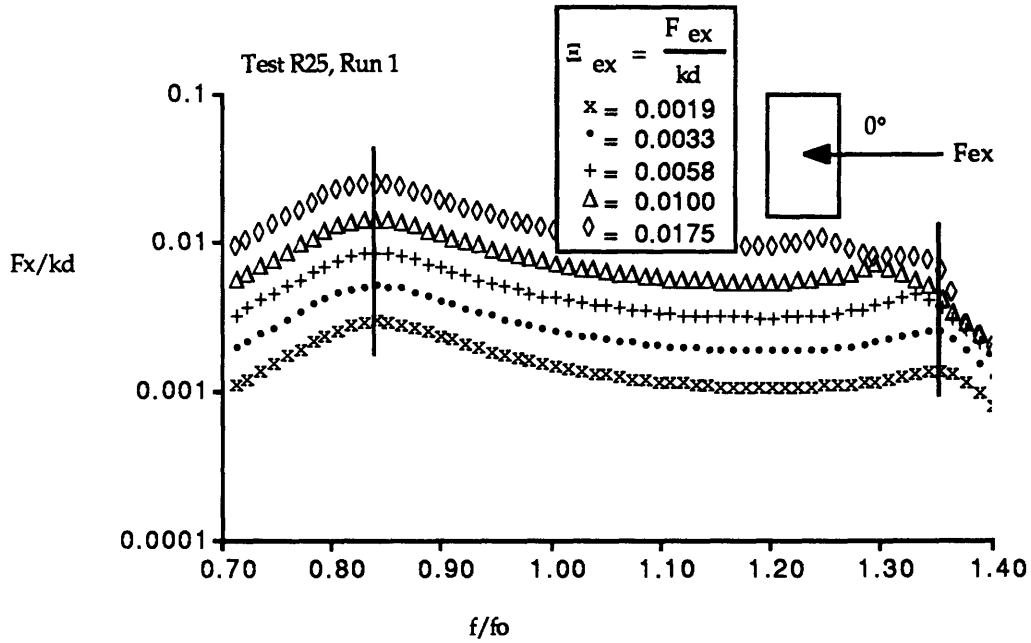
Figure 5.143 **Test R25, Non-dimensional Planar Slosh Force (Fx/kd).**

Figure 5.144 **Test R25, Non-dimensional Nonplanar Slosh Force (Fy/kd).**

(Rectangular tank, coupled, harmonic excitation, Coupled system parameters; $\mu=0.32$, $\nu=0.90$, $\zeta=8.00\%$, Bo=78, Excitation angle=0°)

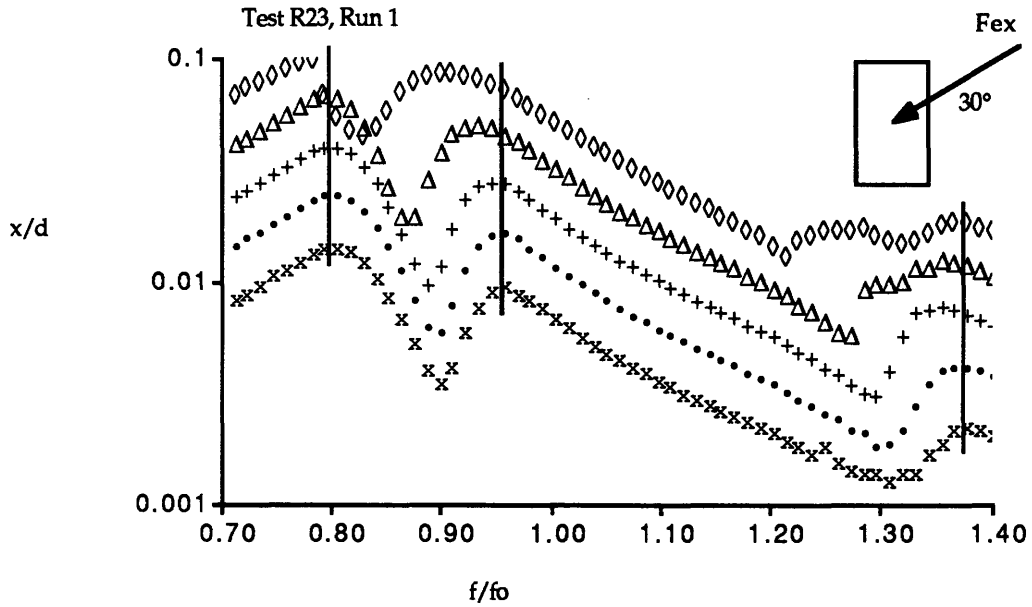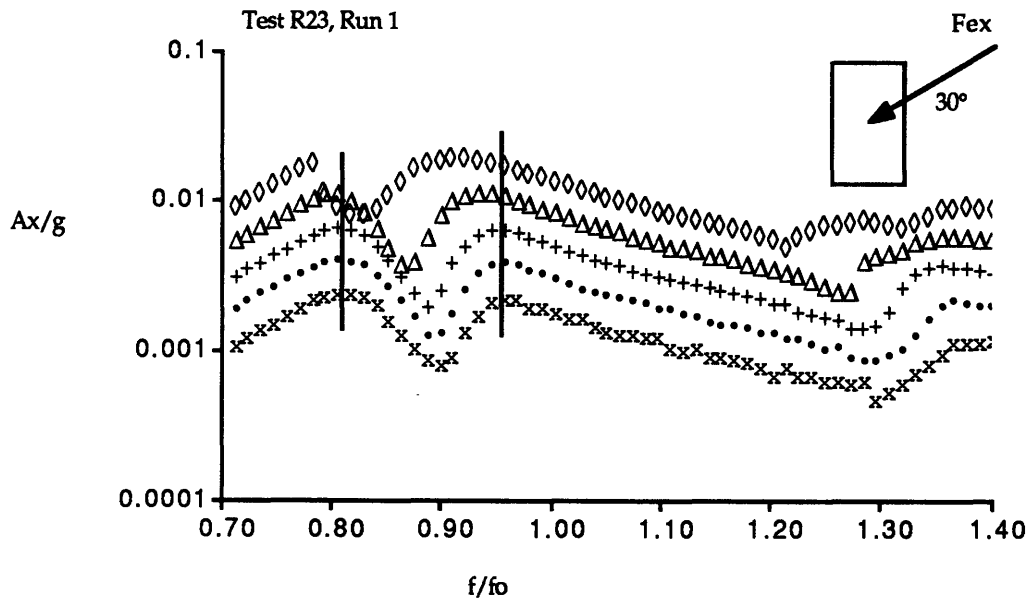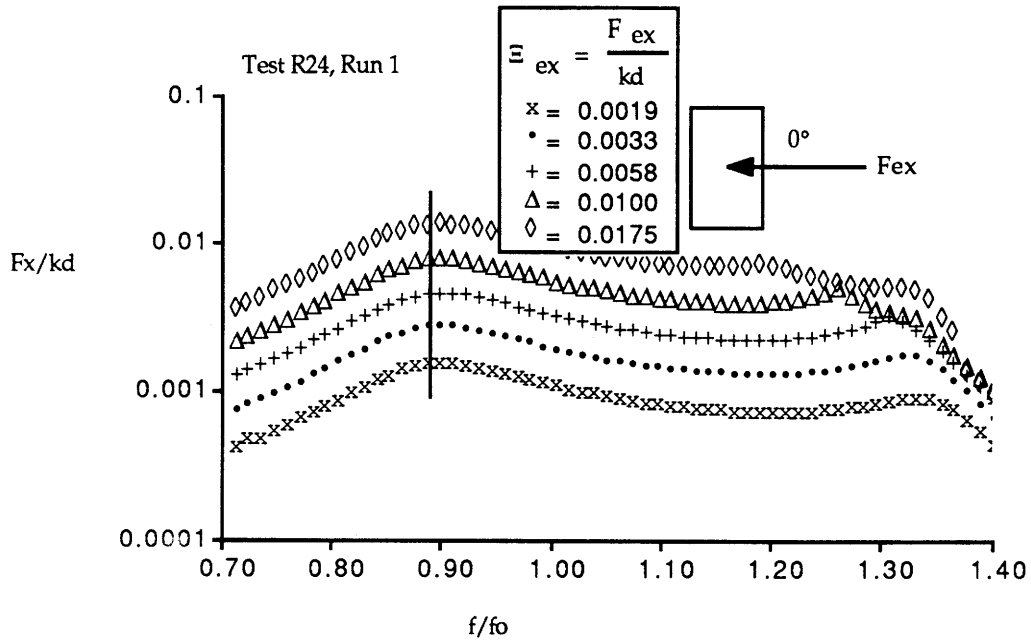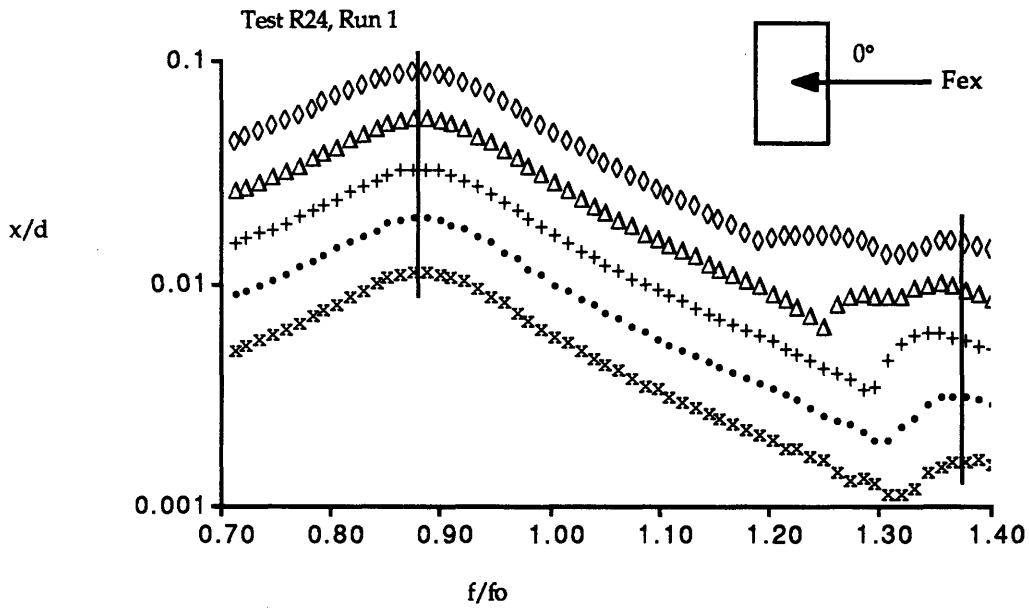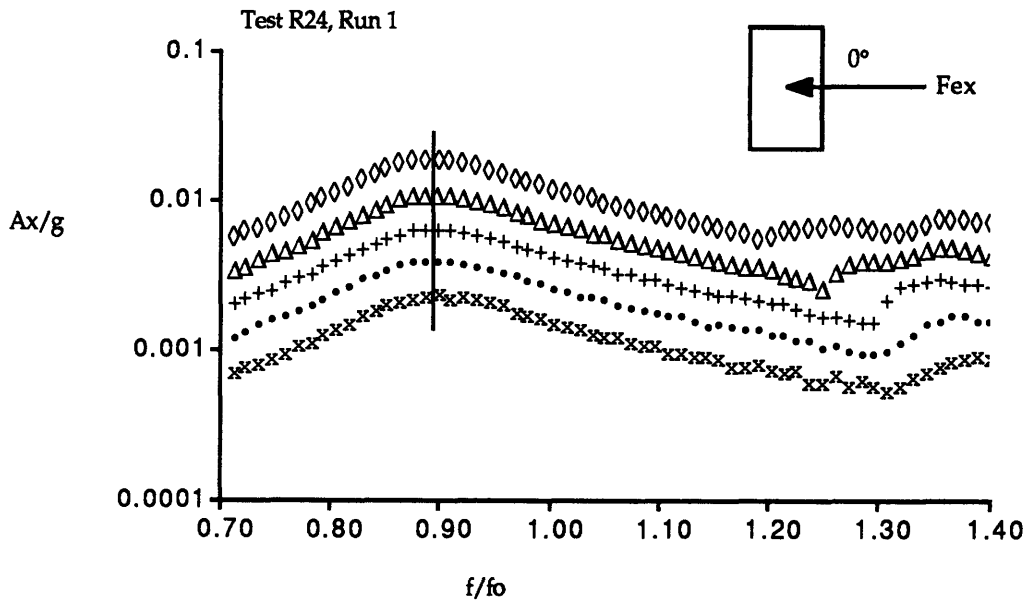**Figure 5.145   Test R25, Non-dimensional Displacement (x/d).**
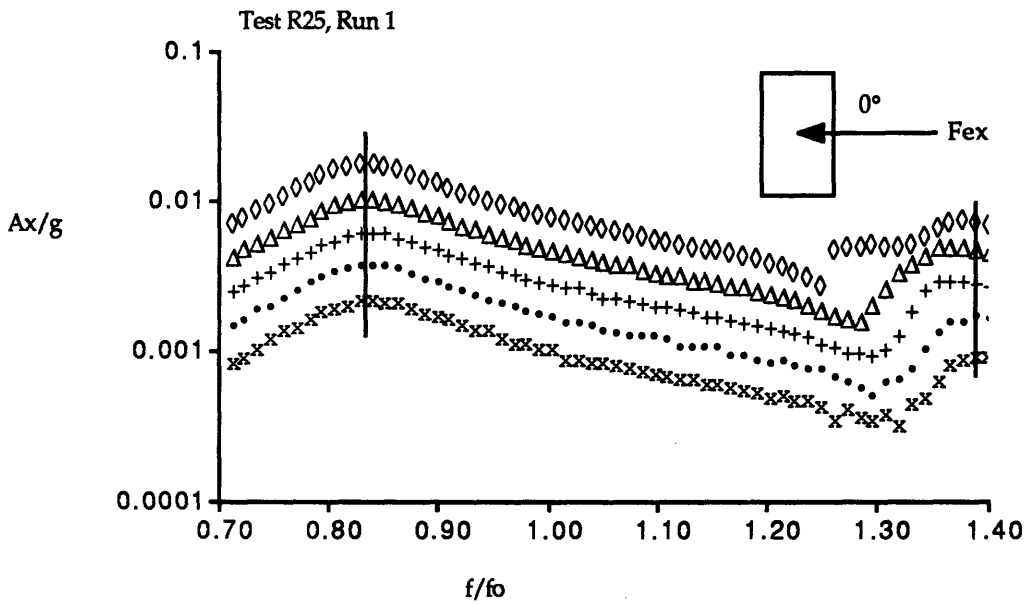
Figure 5.146   Test R25, Non-dimensional Acceleration (Ax/g).

(Rectangular tank, coupled, harmonic excitation, Coupled system parameters; μ=0.32, ν=0.90, ζ=8.00%, Bo=78, Excitation angle=0°)

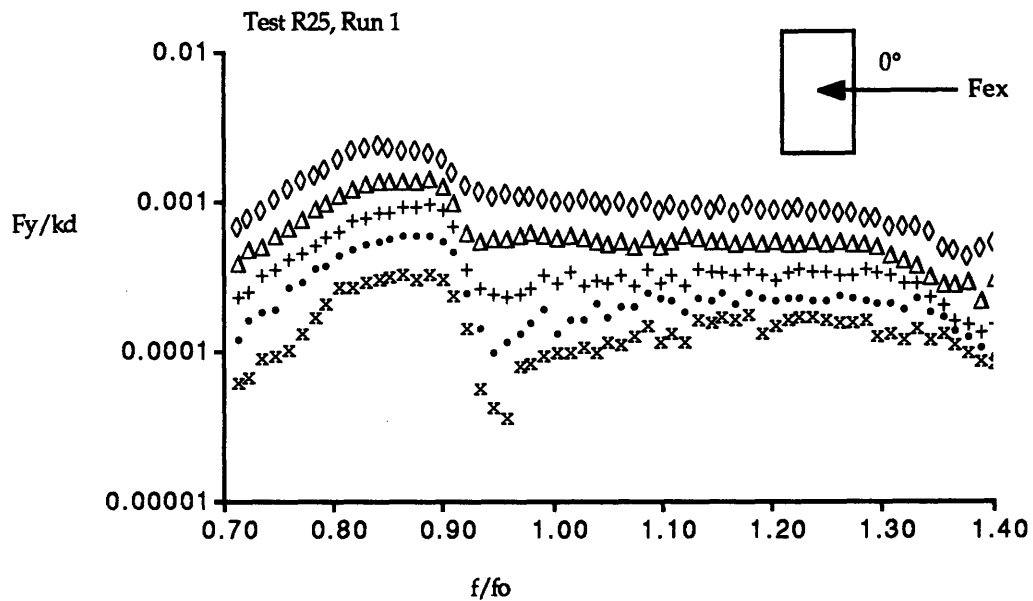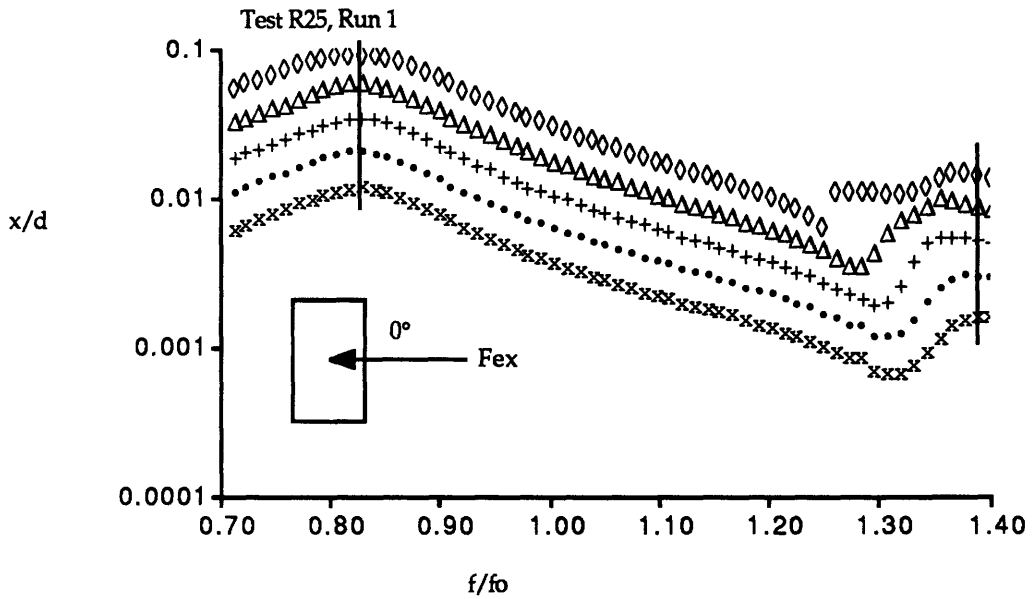## 5.5 Cylindrical Tank Model

The experimental results obtained by Peterson [1987] on the dynamic behavior of fluids in cylindrical tanks were used to developed, investigate and verify the harmonic balance method. The harmonic balance method is used in this research to predict the forced response characteristics from the nonlinear governing differential equations (Appendix B) obtained from the assumed mode model developed in Chapter 2. In order to present the harmonic balance verification results and other solution issues, this section (5.5) presents the cylindrical model used by Peterson and summarizes the configurations used in the verification. The cylindrical tank results will also be used to validate the analytical model. The actual experimental results will not be presented in this section but in Chapter 6 (Section 6.2), the chapter that discusses the harmonic balance method.

Fig. 5.147 depicts the geometry of the cylindrical tank. Three tests (Identification numbers: 420-1, 331-1 and 410-1) were selected from Peterson's work to investigate the harmonic balance method and to verify the analytical model. The relevant parameters of the test articles are tabulated in Table 5.19.

The results presented in Chapter 6 will be identified with the identification numbers 420-1, 331-1 and 410-1. The coupled system parameters for the these three configurations are tabulated in Table 5.20.

228
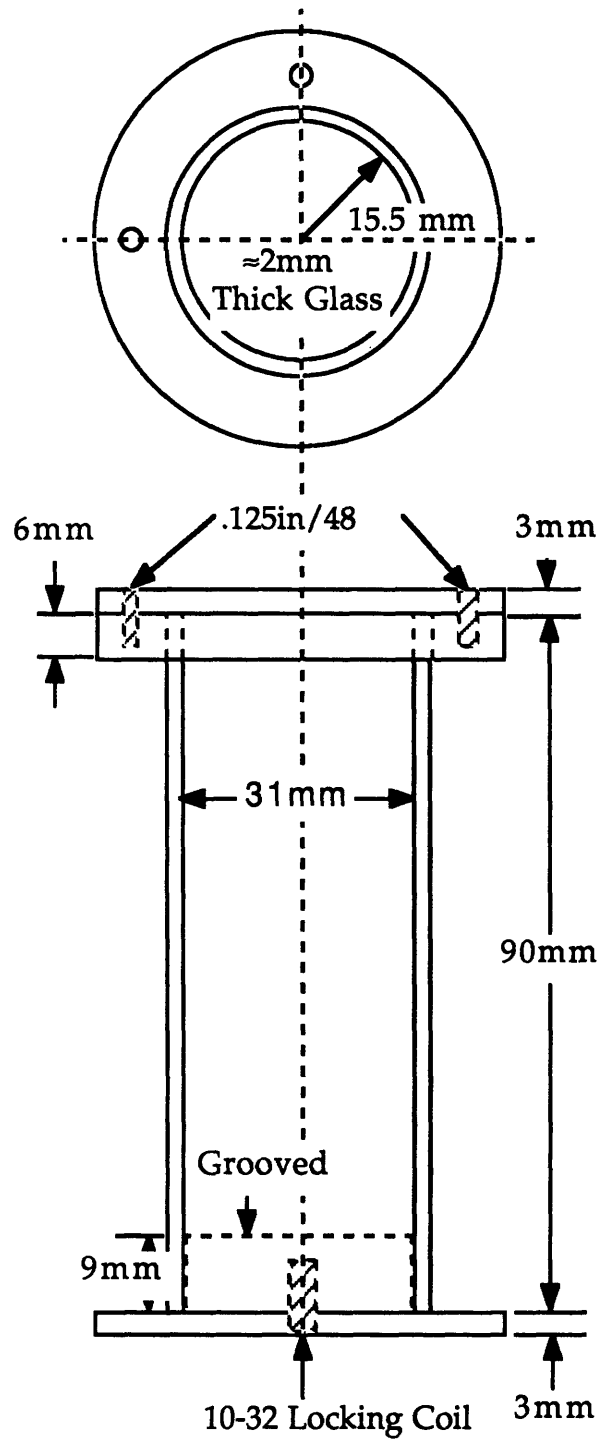
Figure 5.147   Geometry of the 3.1 cm Cylindrical Tank Model.

Note: 4.1 cm Model Tank Geometry is identical to 3.1 cm Model Tank except
for inner diameter and outer diameters.

Table 5.19   Cylindrical Tank Parameters

Parameter	Symbol	Value
Inner Diameter	D	
(420-1 & 410-1)		31.0 mm
(331-1)		41.0 mm
Tank Height	H	90.0 mm
Fill Height	h, d	
& Normalization Factor		
(420-1 & 410-1)		31.0 mm
(331-1)		41.0 mm
Empty Mass	m_E	
(420-1 & 410-1)		339.0 g
(331-1)		379.0 g
Fluid Mass	m_F	
(420-1 & 410-1)		23.40 g
(331-1)		54.10 g
1st Natural Slosh Frequency	f_s	
420-1		5.43 Hz
410-1		5.28 Hz
331-1		6.65 Hz

Table 5.20   Coupled System Parameters

Test ID	Model Fluid	Bond Number	μ	ν	ζ (%)
420-1	Photoflo	66	0.16	0.90	9.3
331-1	Water	58	0.16	0.90	9.8
410-1	Water	33	0.16	0.89	9.1

Note: ν = Frequency Ratio = $f_{Slosh}/f_{Spacecraft}$ = f_s/fo

μ = Mass Ratio = $m_{fluid}/m_{spacecraft\ Mode}$ = m_F/m

ζ = Damping Ratio of Spacecraft Mode

5.6   Summary

All three fluid model tanks exhibit softening behavior. This behavior was observed in both the uncoupled and the coupled tests. In the coupled tests, the simulated spacecraft mode also exhibits this softening behavior. The observed nonlinear behavior was very dependent on the amplitude of the fluid motion and in the axi-symmetric tanks (spherical and square) a jump phenomenon was observed. At the jump, the fluid motion changed from the expected linear planar motion to a combined planar/nonplanar swirling motion. This behavior was not observed in the rectangular model tank where energy exchange between the spectrally separated first and second fluid slosh modes are unlikely.

Chapter 6

Analytical Results

In this chapter the analytical model developed in Chapter 2 will be used to predict the forced response characteristics of the study models considered in this research. The analytical results will be compared with the experimental results of Chapter 5. In addition to the spherical, square and rectangular tanks investigated in Chapter 5, the analytical model will also be used to predict the forced response characteristics of fluids in cylindrical tanks. The predicted results will be compared with experimental results obtained by Peterson [1987]. At the time that the harmonic balance method (Chapter 3) was implemented, only Peterson's experimental results were available to investigate and verify the method. The cylindrical tank results are thus used to discuss the harmonic balance method and serve as additional verification of the analytical model.

This chapter is organized into four parts, the first section (6.1) discusses the issues involved in developing the analytical model. This section outlines how the linear eigen-mode shapes were calculated with the finite difference method developed in Chapter 2 and the calculation of the coefficients of the nonlinear analytical model. The results include the equilibrium free surface shapes for the tank models, verification of eigen-routines and the linear mode shapes used in the assumed mode analytical model.

In the next section (6.2) the harmonic balance method is used to predict the forced response characteristics of fluids in a selected cylindrical tank configuration. This section uses the cylindrical tank experimental results of Peterson [1987] to investigate issues such as, the use of numerically determined mode shapes as assumed modes, model truncation, the value of the Newton-Raphson method and Inverse Solution technique as nonlinear equation solvers and the dependence of these methods on the initial guess at the modal amplitudes.

In section 6.3, the analytical models (developed in section 6.1) are used to predict the forced response characteristics of a few selected model tank configurations that were experimentally investigated. The analytical predictions are compared with the corresponding experimental results to

232

determine the validity and limitations of the analytical model. The final section (6.4) summarizes the results presented in this chapter.

6.1 Analytical Modeling Issues

The analytical model developed in Chapter 2 requires a set of assumed mode shapes. The conclusion in Chapter 2 was that the eigen-mode shapes of the linearized model form a good set of assumed modes. Using the linear eigen-mode shapes will ensure that at least the linear dynamics are correctly modeled. Given a set of assumed mode shapes, the coefficients of the nonlinear governing differential equations can then be calculated.

In order to correctly model Bond number effects, the analytical model requires that the equilibrium free surface shape must be used to define the fluid surface geometry. In the first sub-section (6.1.1) of this section, the equilibrium free surface shapes, as calculated with the method developed in Chapter 2, will be presented for the four tank models.

In the next sub-section (6.1.2) the finite difference method, with which the linear eigen-mode shapes will be calculated, is verified. In general the method is verified by comparing the eigen-characteristics, obtained with this method, with theoretically known values. Sub-section 6.1.3 discusses the inclusion of contact angle hysteresis effects and in 6.1.4 the analytical models developed for the different tank models are discussed.

6.1.1 Equilibrium Free Surface

The Bond number effects are modeled by using the equilibrium free surface to define the fluid equilibrium free surface geometry. The Bond number relates the relative importance of capillary forces to gravitation (acceleration) forces. The equilibrium free surface changes from a flat free surface at infinite Bond number to a spherical shape at very low Bond numbers. The capillary energy associated with the free surface motion is correctly modeled if the equilibrium free surface is included in the fluid geometry.

233

As discussed in section 2.3.1, the equilibrium free surface is calculated by expressing the time independent energy terms as a variational problem (eq. 2.72). A finite difference approximation of the resultant nonlinear governing differential equation (eq. 2.77) is used to solve for the equilibrium free surface as a function of the fluid Bond number. This program was verified by repeating a few example cases presented in Myshkis [Myshkis, et al, 1987] and repeating the cylindrical tank equilibrium free surface results obtained by Peterson [1987]. The slope of the equilibrium free surface shape at the wall must satisfy the required liquid-vapor-wall contact angle. Based on experimentally observed values, a 10° contact angle (α) was used for cases where a 2% Photoflo/water solution was used as a model fluid and a 60° contact angle was assumed for the cases in which water was used as model fluid. In Chapter 5 the relevant Bond numbers are presented; Table 5.3 (Spherical tank), Table 5.8 (Square tank), Table 5.13 (Rectangular tank) and Table 5.20 (Cylindrical tanks).

Using the symmetry of the model tanks, the determination of the equilibrium free surface is significantly simplified. In the cylindrical and spherical tank cases the shape is completely defined by the shape in the radial direction. Figure 2.8 presents the equilibrium free surface shapes for the cylindrical tank cases (See section 5.4 for a description of the cylindrical tank models) and Fig. 6.1 depicts the predicted equilibrium free surface shapes for the spherical tank model. In the square and rectangular cases only one quarter of the tanks was modeled. In Fig. 6.2 (Square tank) and Fig. 6.3 (Rectangular tank), the thick solid lines indicate the axes of symmetry. In all the predictions, a non-uniformly spaced mesh was used. As can be seen in the figures, a finer mesh was used near the wall where the equilibrium free surface is changing rapidly.

Free Surface Shape for Spherical Tank
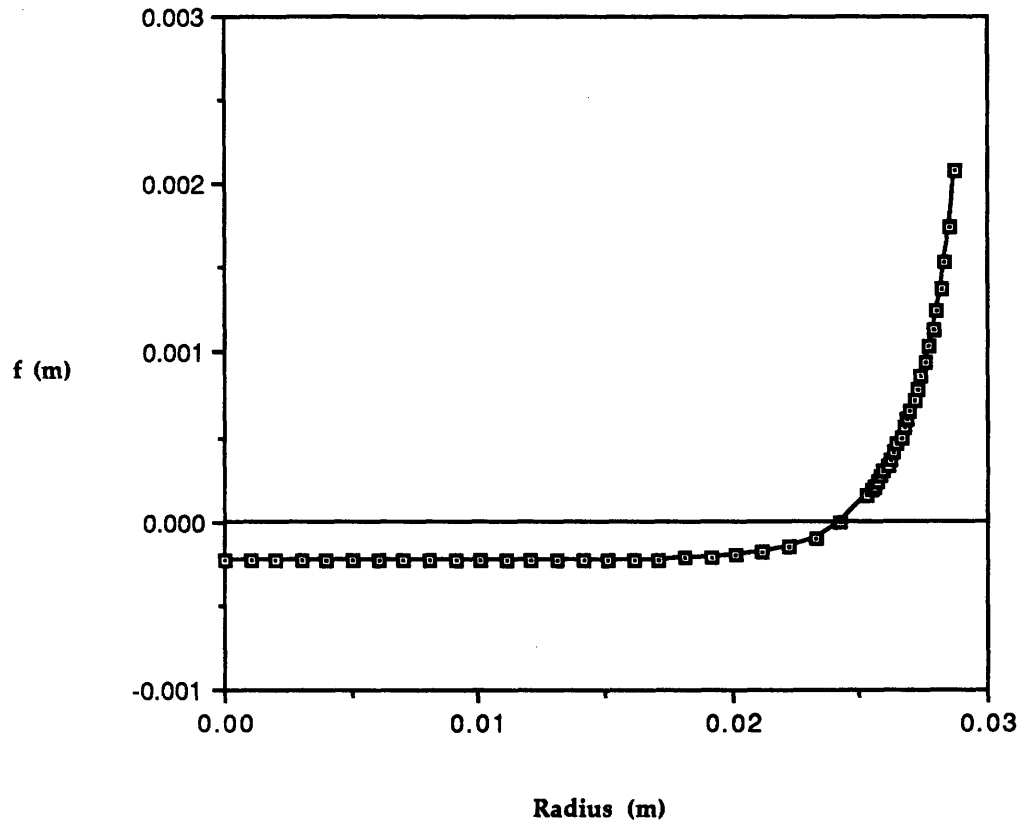
Figure 6.1   Fluid Free Surface Shape for the Spherical Tank (Bo = 117).

Square Tank: Bo = 61.31, Alpha = 10.0°
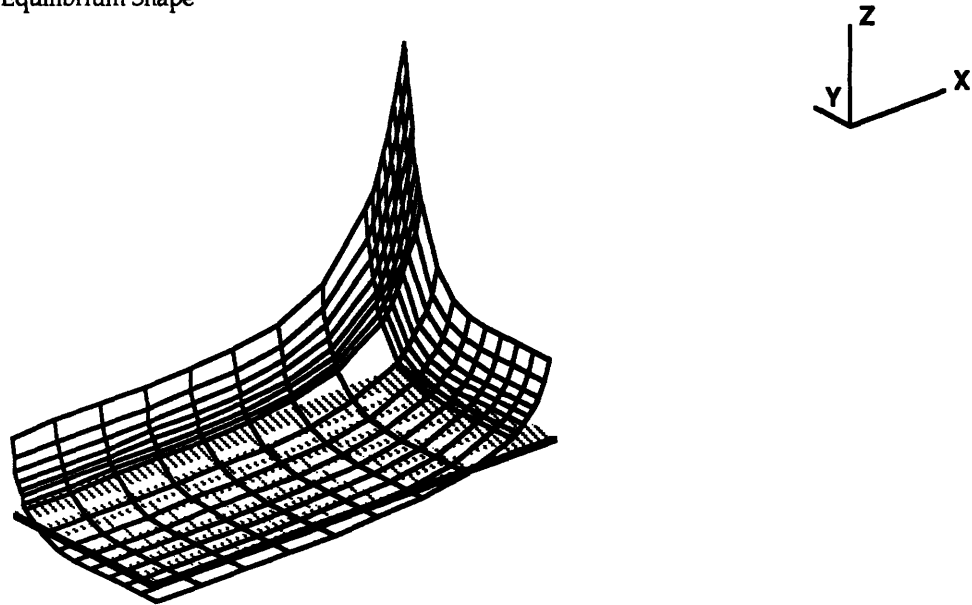
Equilibrium Shape

Figure 6.2   **Equilibrium Fluid Free Surface Shape for the Square Tank.**

The dashed lines are the finite difference mesh and the thick solid lines are the axes of symmetry.

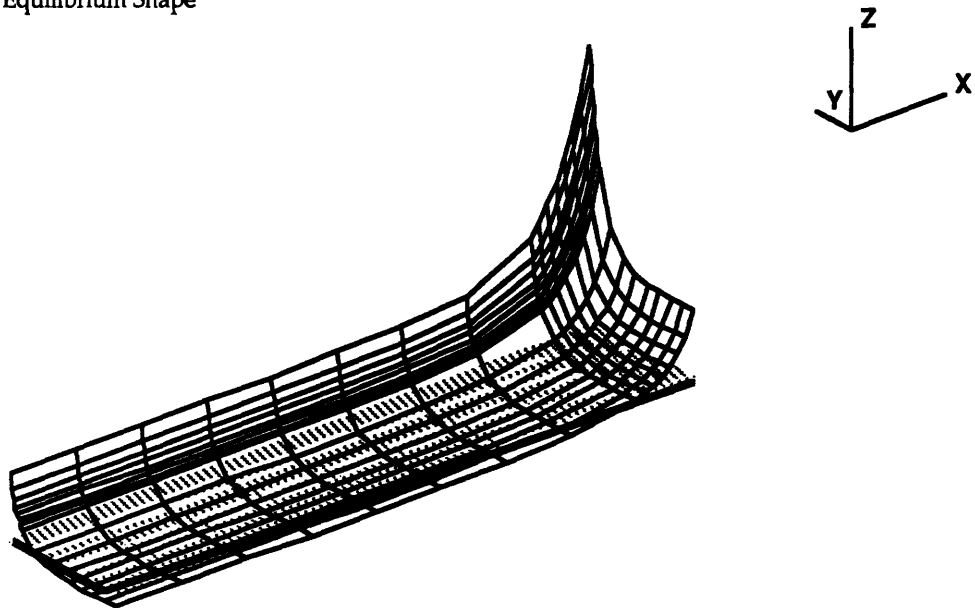Rectangular Tank: Bo = 78.1, Alpha = 10.0°

Equilibrium Shape

Figure 6.3   **Equilibrium Fluid Free Surface Shape for the Rectangular Tank.**

The dashed lines are the finite difference mesh and the thick solid lines are the axes of symmetry.

6.1.2 Calculation of the Linear Eigen-Mode Shapes

In this section, the program that calculates the linear eigen-mode shapes, used in the assumed mode analytical model, is verified. Thorough verification of this program was required to ensure a good set of assumed modes for the analytical model and that the analytical model accurately models the linear fluid behavior. The finite difference model used to model the linear eigen-characteristics is discussed in section 2.3.2. Given that this program uses different coordinate systems for the different tank geometries, the program will be verified for each model tank. Since theoretical solutions only exist for flat free surface cases, a flat free surface was assumed in all the verification cases. This allows the predicted eigen-frequencies to be compared with the values predicted by linear theory. Although the mode shapes could be verified by checking the orthogonality between the predicted and theoretical mode shapes, only the eigen-frequencies were compared.

Calculation of the Linear Eigen-characteristics of Fluids in Cylindrical Tanks: For the cylindrical tanks, a cylindrical coordinate system was used to calculate the small deflection (motion) eigen-mode shapes. The program was verified by calculating the eigen-characteristics for a 3.1 cm diameter cylindrical tank, containing a fluid with a flat free surface, and comparing the results with theory [Blevins, 1987]. For a cylindrical tank, the linear (small motion) eigen-mode shapes are Bessel functions in the radial direction and sinusoids in the azimuth direction. These exact mode shapes are obtained from the linear governing differential equations, by separation of time and spatial variables and application of the boundary conditions. In order to compare the finite difference results with the exact solution, it contact angle hysteresis effects were ignored. The fill height equaled the tank diameter and the comparison is summarized in Table 6.1.

Table 6.1 Comparison of Predicted and Theoretical Eigen-Frequencies for a Cylindrical Tank (Diameter=Fill height=3.1 cm)

Mode Number	Natural Frequency (Hz)		Difference
	Finite Difference	Exact	(%)
1	0.00	0.00	0.0
2	5.42	5.43	0.2
3	5.42	5.43	0.2
4	6.99	7.00	0.1
5	6.99	7.00	0.1
6	7.95	7.84	1.4
7	8.18	8.21	0.4
8	8.18	8.21	0.4
9	9.16	9.25	1.0
10	9.16	9.25	1.0

Based on these results, it can be concluded that the finite difference program will yield reliable mode shapes for a cylindrical geometry.

Calculation of the Linear Eigen-characteristics of Fluids in Spherical Tanks: For the spherical tank a cartesian mesh was used, and the boundary conditions, that are not aligned with the spherical boundaries, were imposed with shape functions (as discussed in Chapter 2, sub-section 2.3.2). This program differs from those used to predict the linear eigen-characteristics in cylindrical and rectangular tanks, in that the mesh is not aligned with the fluid boundaries. In the cylindrical and rectangular cases, a simple curvilinear coordinate system can be found that is aligned with all the fluid boundaries. In the spherical container problem this is not possible since the equilibrium free surface in the spherical container is not aligned with any of the spherical coordinates. Given the special implementation of the boundary conditions, a thorough verification of the program was required. The program was verified in two ways:

(a) By predicting, with the cartesian mesh spherical finite difference (FD) program, the eigen-characteristics of a fluid, with an equilibrium flat

free surface, contained in a spherical tank and comparing the results with an analytical solution that uses Legendre assumed functions in a Ritz approach [Moiseev and Petrov, 1966].

Figure 6.4 depicts the results of the first verification case. The x-axis in the figure is the fluid height non-dimensionalized with the spherical radius. The y-axis is a multiplier (λ), such that the first fluid frequency is given by:

$$f_s = \frac{1}{2\pi}\left(\frac{\lambda g}{r}\right)^{\frac{1}{2}}$$

(6.3)

Where r is the spherical radius and g the gravity acceleration constant.

Verification of Spherical Finite Difference Program
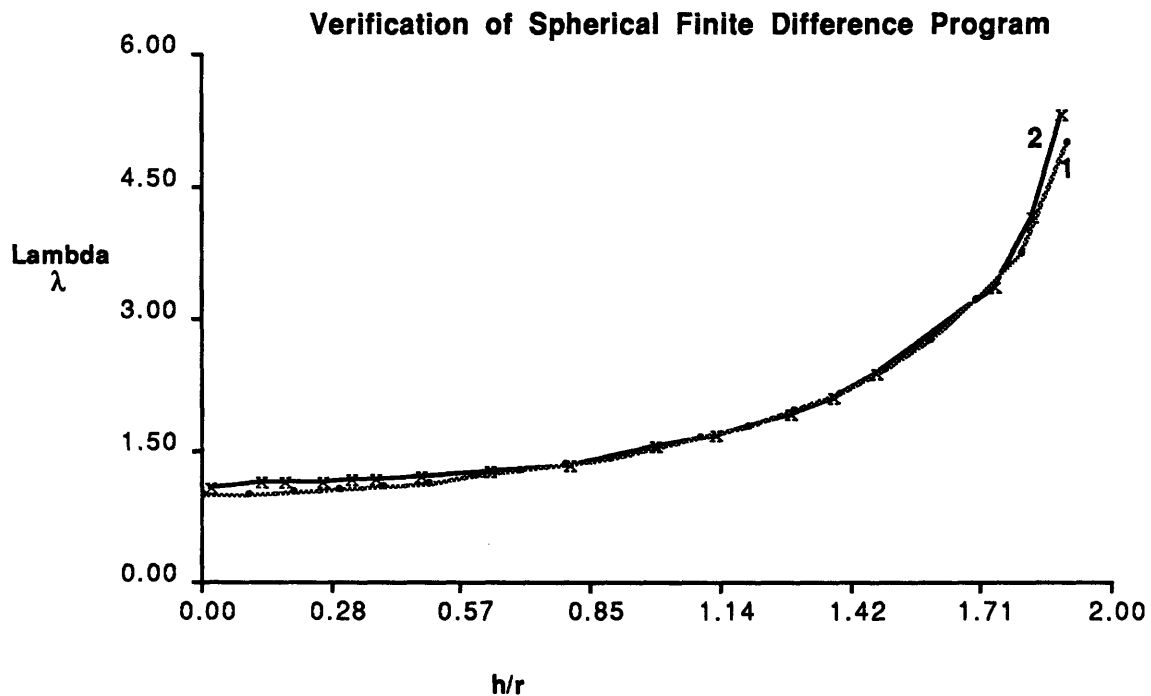
Figure 6.4   Comparison of the Normalized Frequency for Spherical Geometry

Note: 1.   h is the fluid depth and r the spherical radius.
        2.   Curve 1 is the analytically predicted result from [Moiseev and Petrov] and curve 2 is the results as obtained with the spherical finite difference program.

(b) The program was also verified by, using this cartesian mesh finite difference program to predict the eigen-characteristics of the cylindrical tank verification example (a fluid, with a flat free surface, contained in the 3.1 cm diameter cylindrical tank) and to compare the results with the exact solution presented in Table 6.1 (See Table 6.2). The fill height was equal to the tank diameter and a total of 197 surface nodes were used in finite difference mesh. The mesh had 10 mesh levels in the fluid depth direction. The mode shapes were also checked to verify that the predicted modal order is correct.

Table 6.2   **Comparison of Predicted and Theoretical Eigen-Frequencies for a Cylindrical Tank, using a Cartesian Mesh**

Mode Number	Theory Frequency (Hz)	Spherical FD Program Frequency (Hz)	Difference (%)
1	0.00	0.00	0.0
2	5.43	5.48	0.9
3	5.43	5.48	0.9
4	7.00	7.11*	1.6
5	7.00	7.12*	1.6
6	7.84	8.13	3.7
7	8.21	8.44	2.8
8	8.21	8.44	2.8
9	9.25	9.61*	3.9
10	9.25	9.63*	4.1

*   Frequencies should be equal but differ because of non-axi-symmetric grid. See discussion below.

Fig. 6.4 and Table 6.3 indicate that the spherical finite difference program can reliably predict the linear eigen-characteristics of fluids contained in spherical containers and that boundary conditions which are not aligned with a mesh grid can be imposed using the shape function approach discussed in Chapter 2. The cartesian grid used results in a non-axi-symmetric model of the fluid (See Fig. 6.5). This leads to modes that
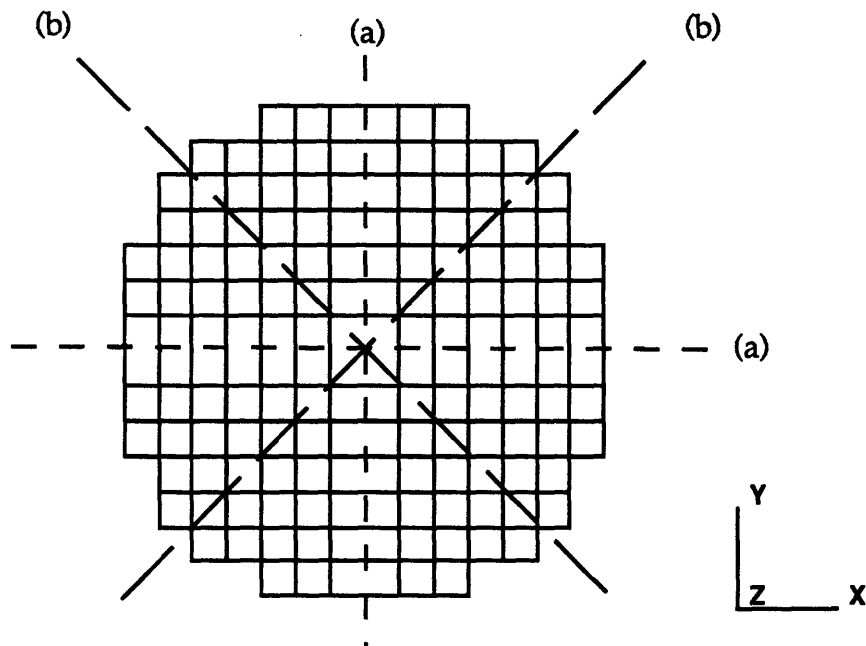
Figure 6.5   Non-axi-symmetric mesh for the axi-symmetric cylindrical test problem.

Mode with nodal lines (a) will be slightly different from Mode with nodal lines (b).

should have equal frequencies actually have slightly different frequencies. The difference between frequencies will decrease as the mesh size decreases.

Calculation of the Linear Eigen-characteristics of Fluids in Square and Rectangular Tanks: One program was used to predict the eigen-characteristics of fluids in both the square and rectangular tanks. The finite difference (FD) program used a cartesian mesh that was aligned with the tank walls. The program was verified by predicting the linear eigen-characteristics of a fluid (flat equilibrium free surface) contained in a rectangular tank and comparing the results with theory [Blevins, 1987] (See Table 6.3). The theoretical solution is obtained by solving the linear (small motion) governing differential equations exactly. The dimensions of the container equaled those of the rectangular model tank used in the experimental studies, a surface area of 3 cm by 3 cm and a fill height of 3 cm (see section 5.3).

Table 6.3   Verification of the Square and Rectangular Finite Difference Program

Mode Number	Finite Difference Program Frequency (Hz)	Theory Frequency (Hz)	Difference (%)
1	0.00	0.00	0.00
2	3.84	3.83	0.3
3	5.56	5.50	1.1
4	5.61	5.54	1.3
5	5.94	5.85	1.5
6	6.72	6.57	2.3
7	6.88	6.74	2.1
8	7.66	7.41	3.4
9	8.05	7.84	2.4
10	8.20	7.96	3.2

Similar results were obtained for a square tank. Table 6.3 shows that the finite difference program can reliably predict the linear eigen-characteristics of fluids contained in square and rectangular tanks.

One final point must be made on the calculation of the linear eigen-mode shapes used in the assumed mode analytical model. In order to obtain the best possible set of mode shapes, the equilibrium free surface shape was included in the finite difference mesh describing fluid geometry. In the cylindrical and spherical tank models, this was easily achieved by linear interpolation of the equilibrium free surface shape to obtain the shape at the finite difference mesh nodes. The interpolation was required since the mesh used in the calculation of the equilibrium free surface shapes was different from the one used in the determination of the eigen-characteristics. In the square and rectangular models, a more complex two-dimensional spline fit to the equilibrium free surface was used to obtain the free surface shape at the mesh nodes of the eigen-characteristics program.

6.1.3 Contact Angle Hysteresis Effects

Except for two cylindrical cases where water was used, a 2% Photoflo/water solution was used as a model fluid. This solution has almost no contact angle hysteresis. Water however, has significant contact angle hysteresis, so much so that the fluid slosh frequencies are significantly higher for tanks with water as model fluid compared to tanks with the Photoflo solution as model fluid. This behavior is a linear effect and true for low amplitude (linear) vibrations. The first order effect of contact angle hysteresis is thus to increase the eigen-frequencies and modify the eigen-mode shapes. Satterlee and Reynolds [1967] showed that the linear effect of contact angle hysteresis can be included in the linear model (and thus in the eigen-finite difference program) as an inhomogeneous boundary condition. The boundary condition is, from Chapter 2:

$$\frac{\partial}{\partial n_{cs}}\left(\frac{\partial \Phi}{\partial n_{fs}}\right) = \frac{\Gamma \lambda^2}{gd}\Phi\Big|_{\text{on contact surface}} \tag{2.100}$$

In the finite difference program, the hysteresis constant (Γ) was set to yield the experimentally observed eigen-frequencies. The hysteresis constants that yielded the correct linear eigen-frequencies are presented in Table 6.4. This table also summarizes the experimentally observed linear eigen-characteristics of the cylindrical tank cases. See section 5.4 for more detail on the cylindrical test cases.

Note that an analytical model based on eigen-mode shapes that was calculated without including contact angle hysteresis effects, would fail to correctly predict the linear forced response characteristics.

Table 6.4   Model Parameters

Test ID	Fluid	f_s (Hz)	ζ_{q1} (%)	Γ
420-1	2% Photoflo/Water	5.43	3.49	0.00
331-1	Water	5.28	4.20	-3.40
410-1	Water	6.65	4.64	-5.95

6.1.4 Analytical Models

The previous sub-sections discussed the calculation of the equilibrium free surface, the verification of the program that will be used to calculate the linear eigen-mode shapes and the inclusion of contact angle hysteresis effects in the linear model. At this point it can be assumed that a representative set of assumed mode shapes (the linear eigen-mode shapes) is available for the analytical model. The assumed mode shapes are used to calculate the coefficients in the nonlinear governing differential equations (Appendix A and B). Section 6.1.4.1 will discuss which modes were included in the analytical model and present some of the assumed mode shapes in detail. Section 6.4.1.2 discusses the modeling of fluid dissipation effects.

6.1.4.1   Assumed Mode Shape Selection

In Chapter 2 (2.1.5) it was noted that the best approach in an assumed mode model is to progressively increase the number of modes used in order to determine convergence. Truncation of the assumed set however, is possible at two points in the analysis process. In Chapter 2, the kinematic boundary condition is satisfied in a "least squares sense" by expressing the flow potential generalized coordinates in terms of the free surface generalized coordinates (eq. 2.36).

$$P_m = \sum_{n=1}^{N} l_{mn}^{(0)} \dot{q}_n + \sum_{n=1}^{N}\sum_{r=1}^{N} l_{mnr}^{(1)} \dot{q}_n q_r + \sum_{n=1}^{N}\sum_{r=1}^{N}\sum_{s=1}^{N} l_{mnrs}^{(2)} \dot{q}_n q_r q_s \qquad (2.36)$$

The wavelength matrices (*l*) are a summation of matrices and the linear correction to the wavelength matrix, for example, is given by:
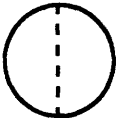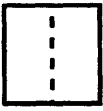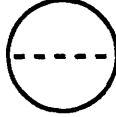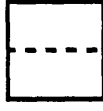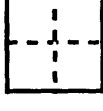
$$l^{(1)}_{mnr} = \sum_{i=1}^{N} k^{(0)^{-1}}_{mi} \left[d^{(1)}_{nir} - \sum_{j=1}^{N}\sum_{k=1}^{N} k^{(1)}_{ijr} k^{(0)^{-1}}_{jk} d^{(0)}_{nk} \right] \tag{2.34}$$

The accuracy of these wavelength matrices will depend on the number of modes used. Thus, in order to obtain the best possible *"least squares"* match between the fluid flow potential and free surface generalized coordinates, many modes can be used to calculate the wavelength matrices,s but the nonlinear governing differential equations can be truncated after this step to retain only the first (M) modes. The two truncation points are thus; (a) the number of modes used in the calculation of the wavelength matrices and (b) the number of modes retained in the nonlinear governing differential equations. The second truncation can be justified on the grounds of modal separation.

In this research, the set of modes, used to calculate the wavelength matrices, was obtained by progressively increasing the number of modes, while tracking the change in the nonlinear coefficients. The number of modes included were truncated as soon as additional modes failed to change the coefficients by more than 5%. Section 6.2 of this chapter will discuss the truncation of the model on the grounds of spectral separation of the modes.

The same type of assumed mode shapes (modal numbers and description) were used in the cylindrical, spherical and square tank models. In Appendix A and B two models are developed, a planar and nonplanar model. The planar model includes the spacecraft degree-of-freedom and the first three planar/axi-symmetric fluid slosh modes. In the nonplanar model, two nonplanar slosh modes are added to the planar model. The modes used in these models, for the axi-symmetric tanks, are summarized in Table 6.5 (Also see Table B1).

Table 6.5   Fluid Modes used in Planar and Nonplanar Models

Mode Description	Node Lines *Circular Tanks*	*Square Tank*	Degree-of-Freedom in Analytical Model	Planar Model	Nonplanar Model
x-Translation			x	√	√
Primary, Planar			q_1	√	√
Primary, Nonplanar			q_2	-	√
Axi-symmetric			q_3	√	√
Secondary, Planar			q_4	√	√
Secondary, Nonplanar			q_5	-	√

Cylindrical Tanks: The finite difference mesh used to calculate the eigen-characteristics of the cylindrical tanks had a total of 384 surface nodes (32 in the angular direction and 12 in the radial direction) and 10 mesh levels in the fluid depth direction. Fig. 6.6 to Fig. 6.10 presents the mode shapes for the model tank in which a 2% Photoflo/Water solution was used as a model fluid (Test 420-1). In these figures, the dotted mesh is the undeformed equilibrium free surface. Studying these figures yields a better understanding of the nomenclature used in Table 6.5. The figures are only the mode shape at the fluid surface. The mode shapes are required as a function of fluid depth in order to calculate the wavenumber (k) matrices (see 2.1.6) in the assumed mode model. The finite difference program does

calculate the mode shapes as a function of fluid depth but for clarity the mode shapes are not displayed for the whole fluid volume.

Fig. 6.11 and Fig. 6.12 depict the primary planar slosh modes of Test 331-1 and Test 410-1 in which water was used as model fluid. These two figures illustrate how the eigen-mode shapes are modified by the effect of contact angle hysteresis and must be contrasted with Fig. 6.6 which depicts the primary planar slosh mode of Test 420-1. In Test 420-1, a 2% Photoflo/water solution which has no contact angle hysteresis, was used as a model fluid.

Cylindrical Tank, ID: 420-1

Mode No 2   Frequency =   5.431 Hz

Figure 6.6   Cylindrical Test 420-1. Assumed Mode Shape for the q_1 Degree-of-Freedom of the Analytical Model.

Cylindrical Tank, ID: 420-1

Mode No 3   Frequency =   5.431 Hz

Z
Y
X

**Figure 6.7   Cylindrical Test 420-1. Assumed Mode Shape for the q_2
Degree-of-Freedom of the Analytical Model.**

Cylindrical Tank, ID: 420-1

Mode No 6   Frequency =   8.014 Hz

Z
Y
X

**Figure 6.8   Cylindrical Test 420-1. Assumed Mode Shape for the q_3
Degree-of-Freedom of the Analytical Model.**

Cylindrical Tank, ID: 420-1

Mode No 4   Frequency =   7.106 Hz

Figure 6.9   Cylindrical Test 420-1. Assumed Mode Shape for the q_4 Degree-of-   Freedom.

Cylindrical Tank, ID: 420-1

Mode No 5   Frequency =   7.106 Hz

Figure 6.10   Cylindrical Test 420-1. Assumed Mode Shape for the q_5 Degree-of-Freedom of the Analytical Model.

Cylindrical Tank, ID: 331-1
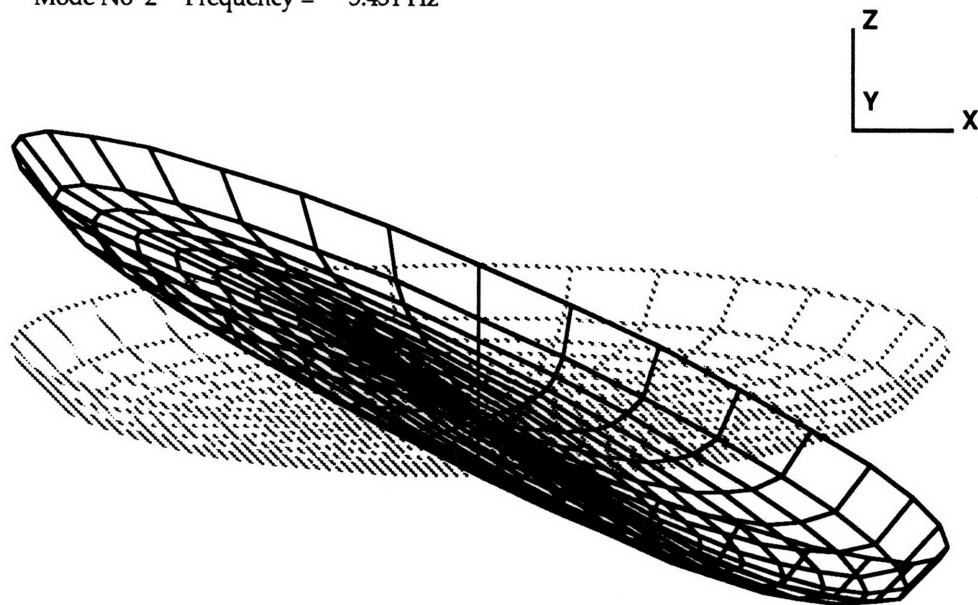
Mode No 2   Frequency =   5.346 Hz
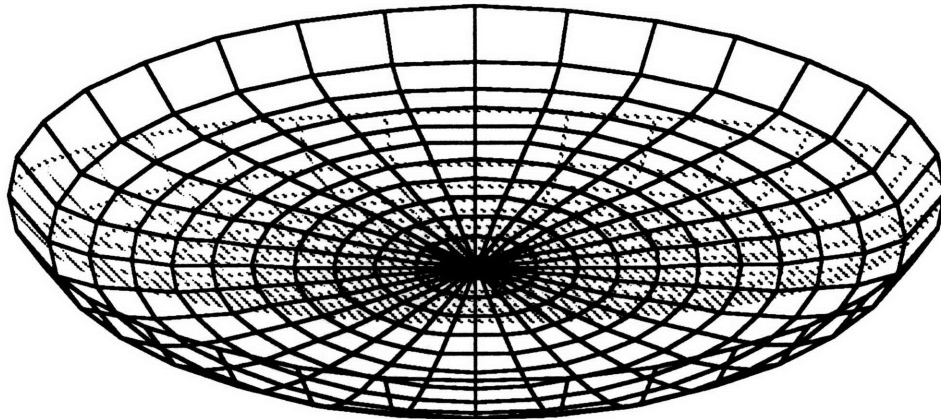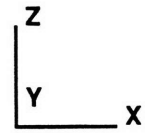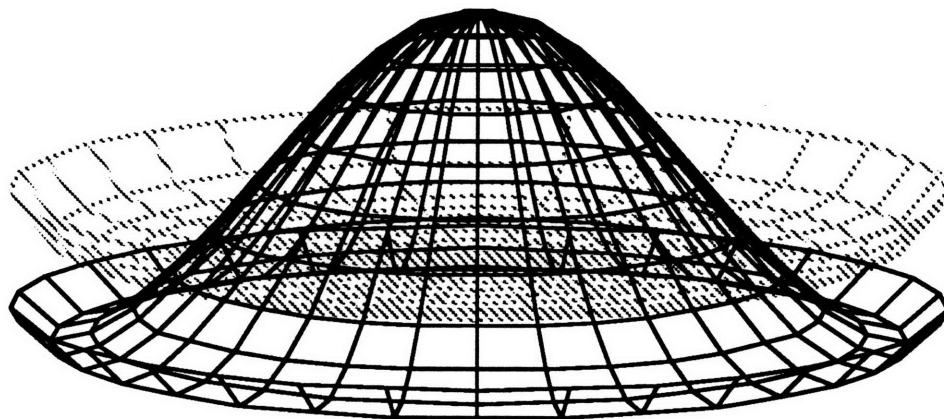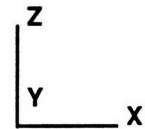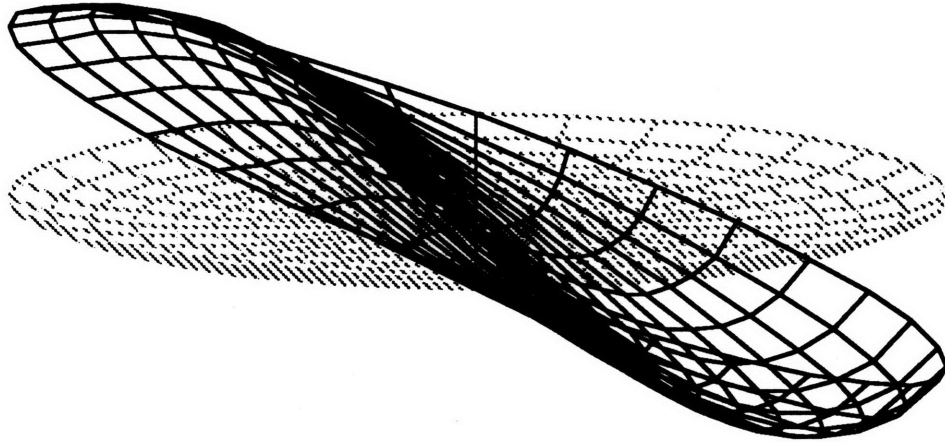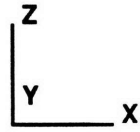

Figure 6.11   Cylindrical Test 331-1. Assumed Mode Shape for the q_1 Degree-of-Freedom of the Analytical Model.

Cylindrical Tank, ID: 410-1

Mode No 2   Frequency =   6.587 Hz
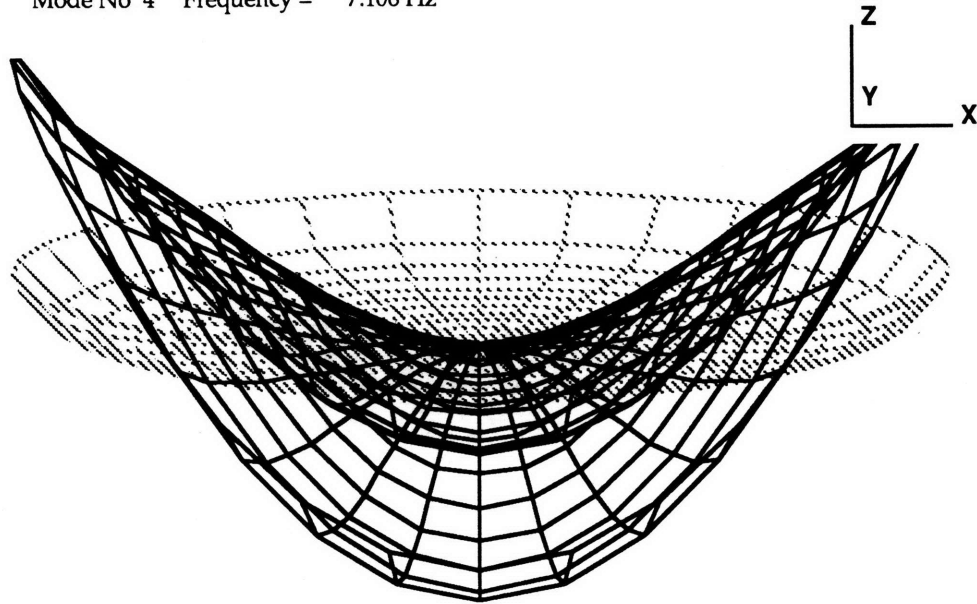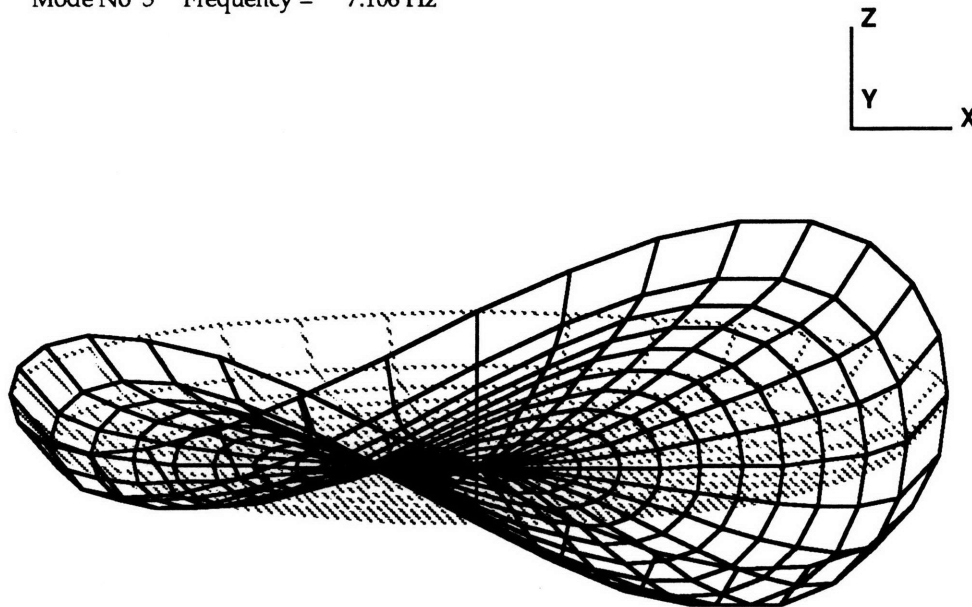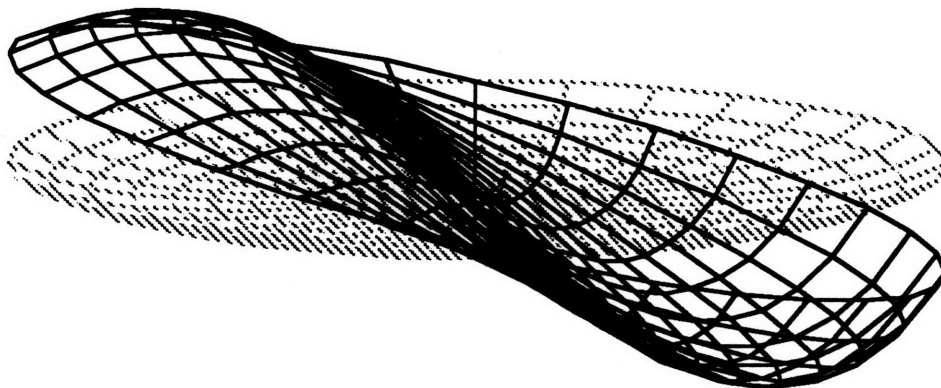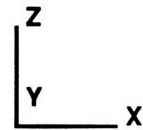

Figure 6.12   Cylindrical Test 410-1. Assumed Mode Shape for the q_1 Degree-of-Freedom of the Analytical Model.

250

Spherical Tank: Given that the assumed mode model is only valid for tanks with straight and parallel walls (see section 2.1.6), an analytical model for the spherical tank was developed that assumed straight walls for the spherical tank. This assumption is clearly not valid but Fig. 6.13 shows this assumption can be justified for moderate fluid amplitudes. Fig. 6.13 shows the change in projected fluid surface area for a range of fluid heights. In this figure it was assumed that the motion is only the first fluid slosh mode. As expected, the error is a function of the fill height. Given that the non-dimensional fill height used in the spherical tests (Chapter 5) was 35%, the error is less than 10% for non-dimensional fluid amplitudes less than 15%.

For the spherical tank, a total of 317 surface nodes and 10 mesh levels in the fluid depth direction were used. Fig. 6.14 and 6.15 are examples of the spherical tank eigen-modes. Also clear from these figures is the cartesian grid used in the spherical tank model.
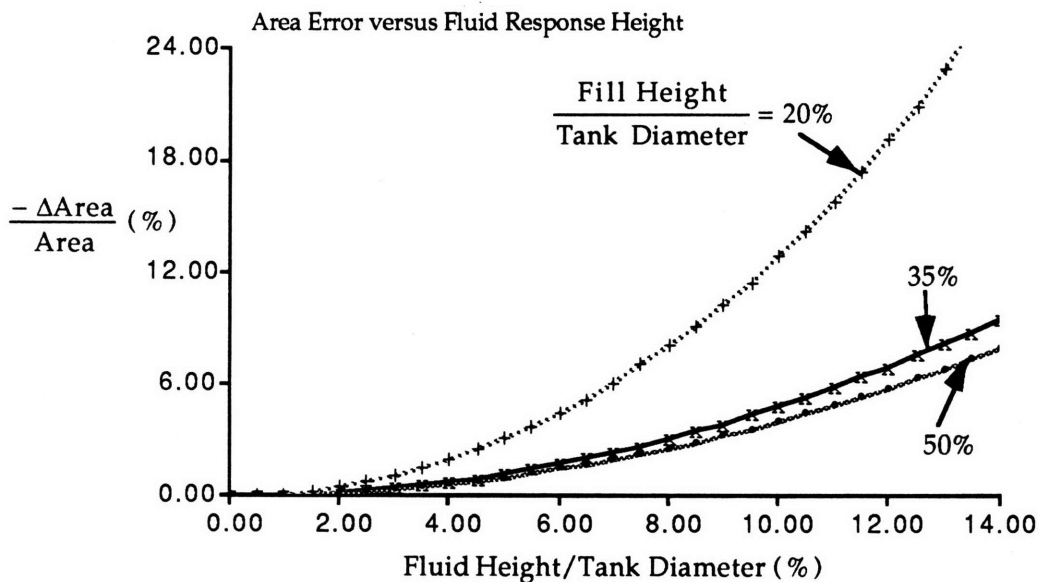
Figure 6.13   Change in Projected Fluid Surface Area versus 1st Fluid Slosh Mode Amplitude.

(Spherical Tank. Given fluid height, the area is the fluid surface area projected on the horizontal (e_1, e_2) plane.)

Spherical Tank

Mode No 3   Frequency =   3.400 Hz
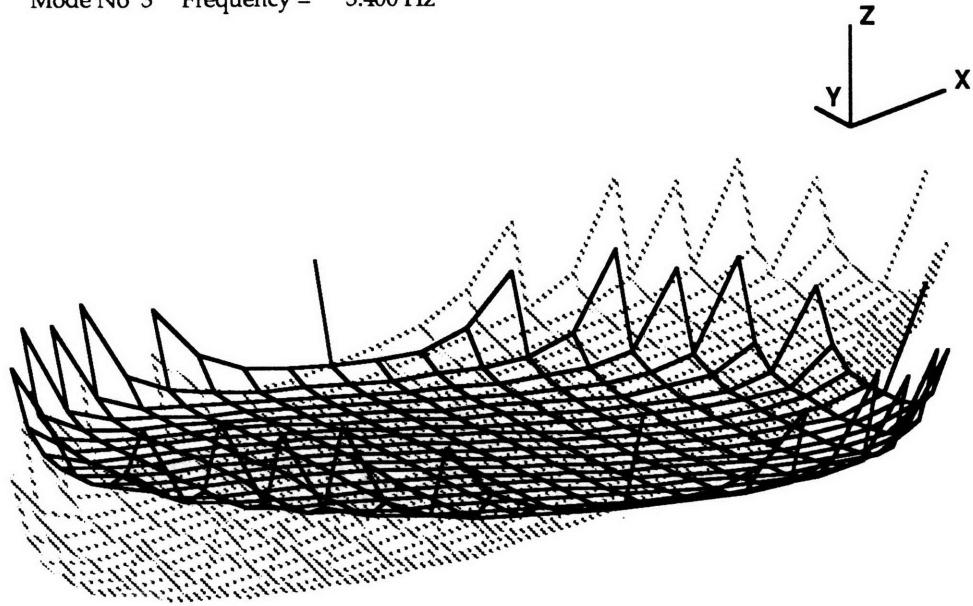
Figure 6.14   Spherical Tank. Assumed Mode Shape for the q_1 Degree-of-Freedom.

Spherical Tank

Mode No 6   Frequency =   5.568 Hz
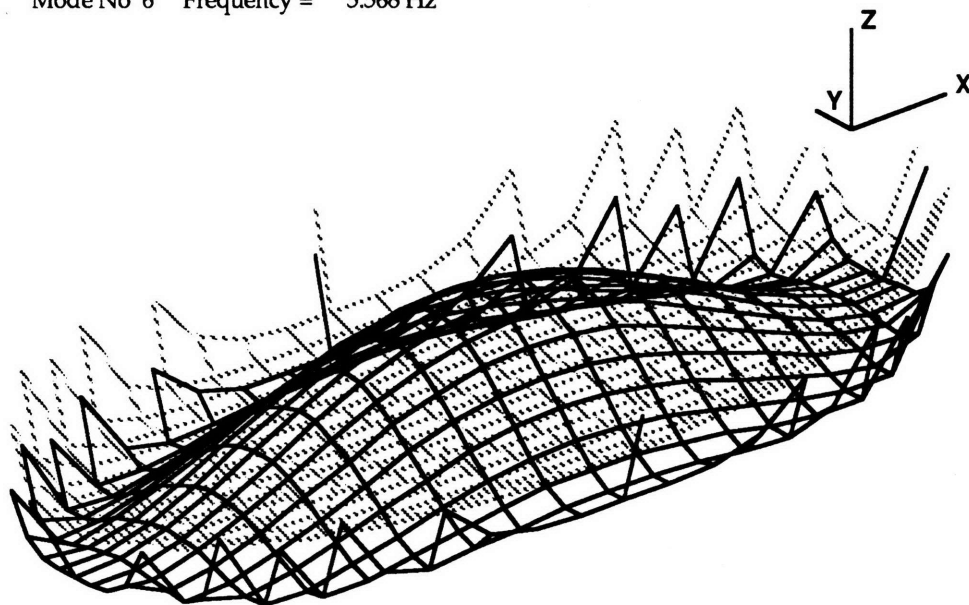
Figure 6.15   Spherical Tank. Assumed Mode Shape for the q_3 Degree-of-Freedom.

Square Tank: In the square tank case, a total of 361 surface nodes (19 x 19) and 10 mesh levels in the fluid depth direction were used. Fig. 6.16 to 6.18 are examples of the square tank eigen-modes.

Square Tank

Mode No 2   Frequency =   5.188 Hz
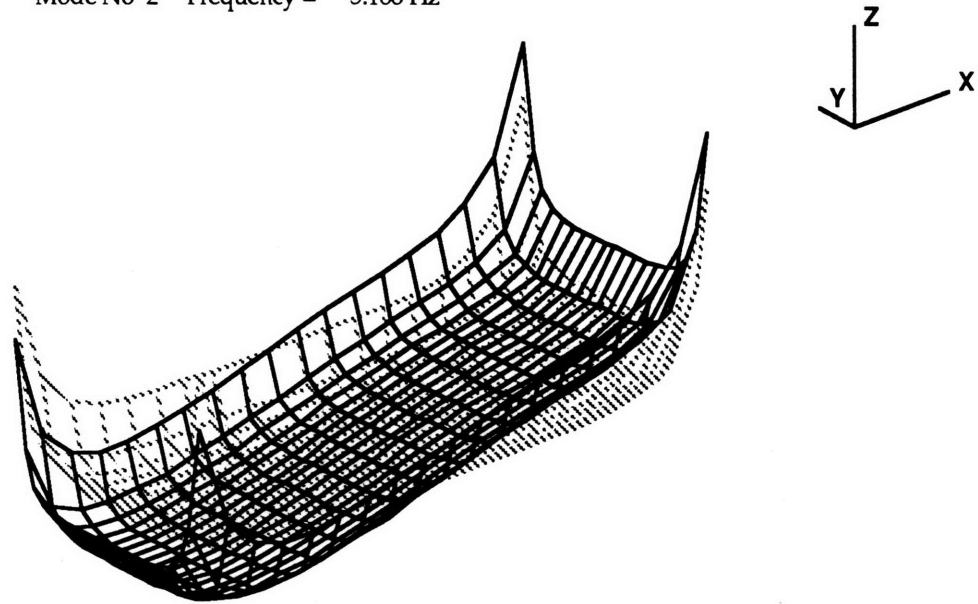
Figure 6.16   Square Tank. Assumed Mode Shape for the q_1 Degree of Freedom.

Square Tank

Mode No 6   Frequency =   7.499 Hz
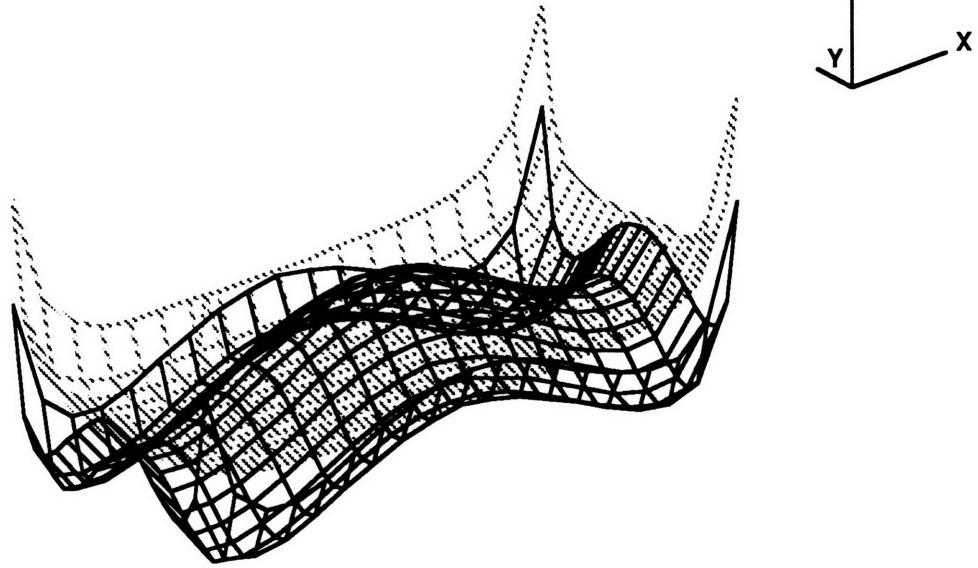
Figure 6.17   Square Tank. Assumed Mode Shape for the q_3 Degree of
                   Freedom.

Square Tank

Mode No 4   Frequency =   6.267 Hz
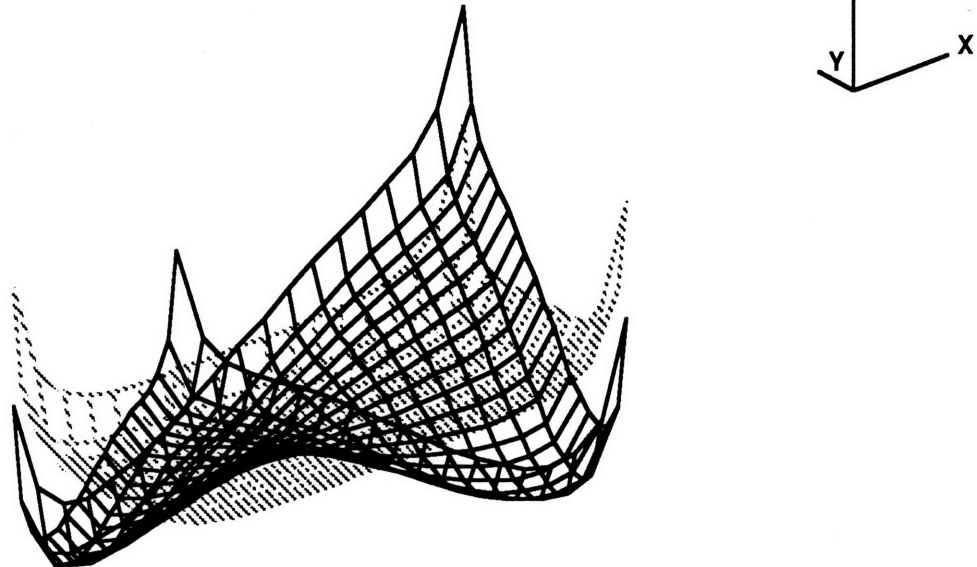
Figure 6.18   Square Tank. Assumed Mode Shape for the q_5 Degree of
                   Freedom.

Rectangular Tank: The same mesh used in the square tank case, was used for the rectangular tank. The rectangular tank however, does not have the repeated eigen-values of the axi-symmetric tanks (Cylindrical, spherical and square) and a different set of assumed mode shapes was used for the rectangular model. The mode shapes used are summarized in Table 6.6 along with the corresponding figure numbers. In Table 6.6, the long side refers to the long side of the rectangular tank, and the short side to the short side of the tank.

Table 6.6   Fluid Modes used in Rectangular Tank Model

Mode Description	Nodal Lines	Degree-of-Freedom used in Analytical Model	Figure
x-Translation Mode		x	
1st Axi-symmetric Mode (Long Side)		q_1	6.19
1st Axi-symmetric Mode (Short Side)		q_2	6.20
1st Skew Symmetric		q_3	6.21
1st Symmetric Mode (Long Side)		q_4	6.22
1st Symmetric Mode (Short Side)		q_5	6.23

Rectangular Tank

Mode No 4   Frequency =   5.673 Hz
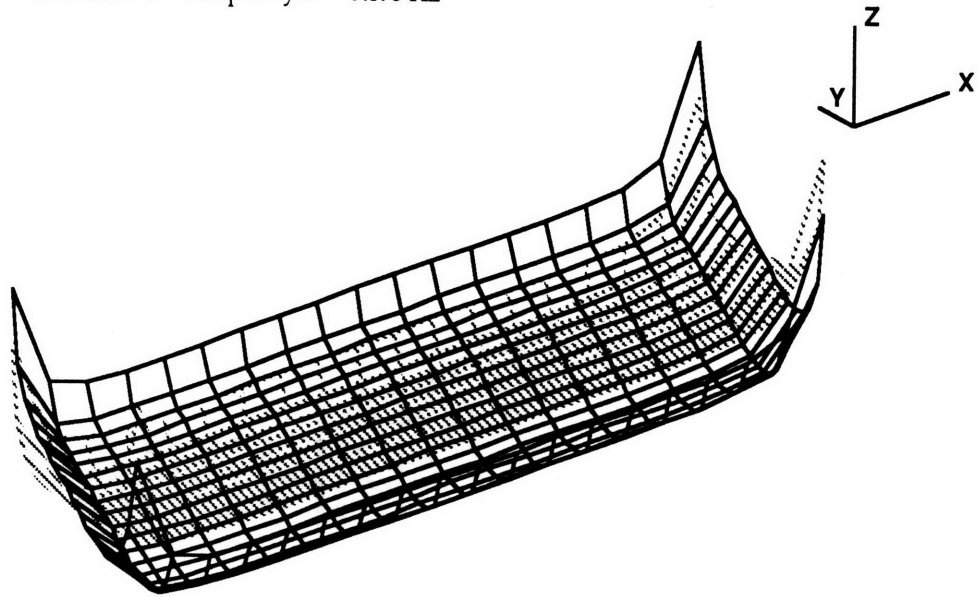
Figure 6.20   Rectangular Tank.   Assumed Mode Shape for the q_2 Degree-of-Freedom.

Rectangular Tank

Mode No 3   Frequency =   5.656 Hz
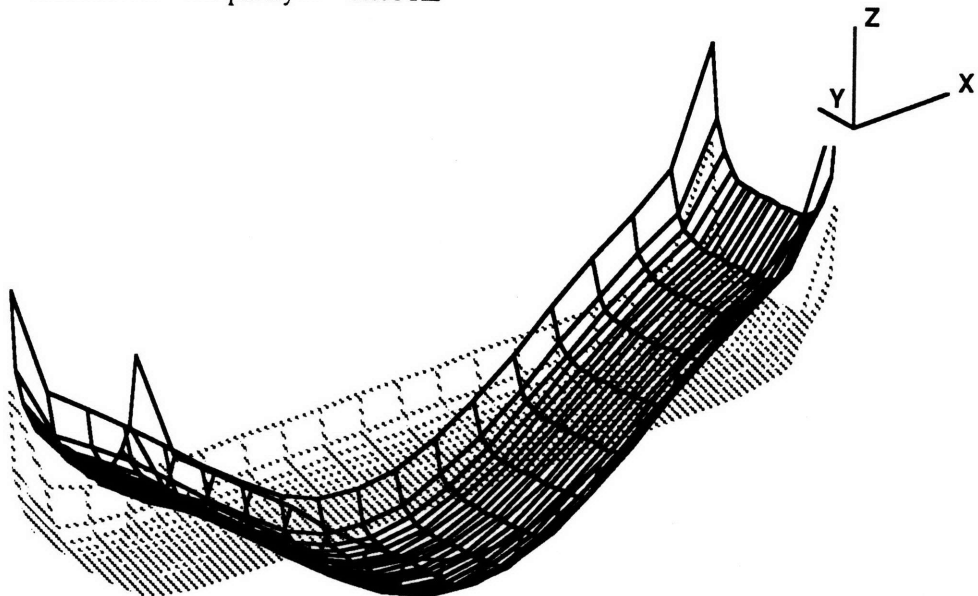
Figure 6.21   Rectangular Tank.   Assumed Mode Shape for the q_3 Degree-of-Freedom.

Rectangular Tank

Mode No 10   Frequency =   8.290 Hz
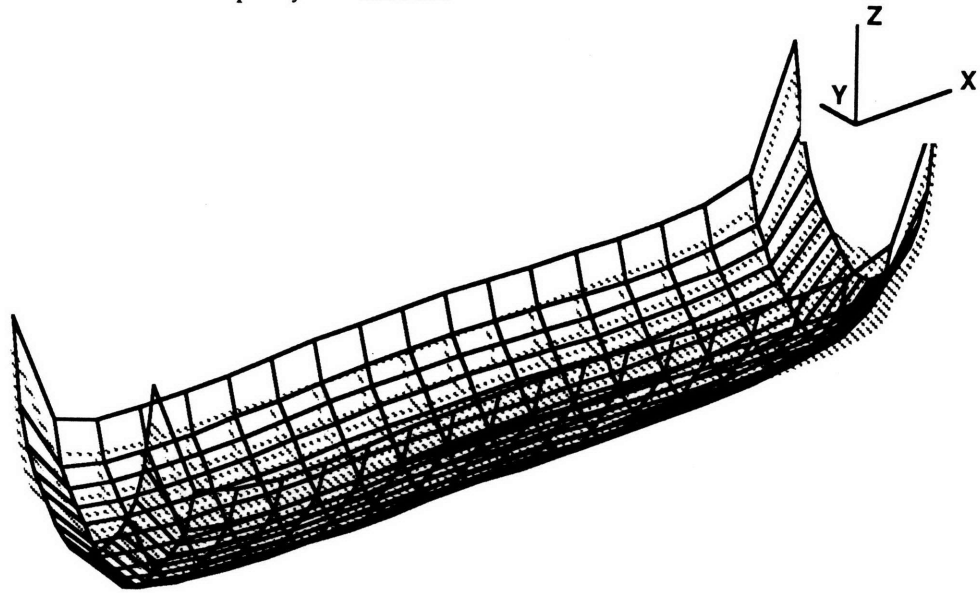
Figure 6.22   Rectangular Tank. Assumed Mode Shape for the q_4 Degree-of-Freedom.

Rectangular Tank

Mode No 5   Frequency =   6.047 Hz
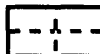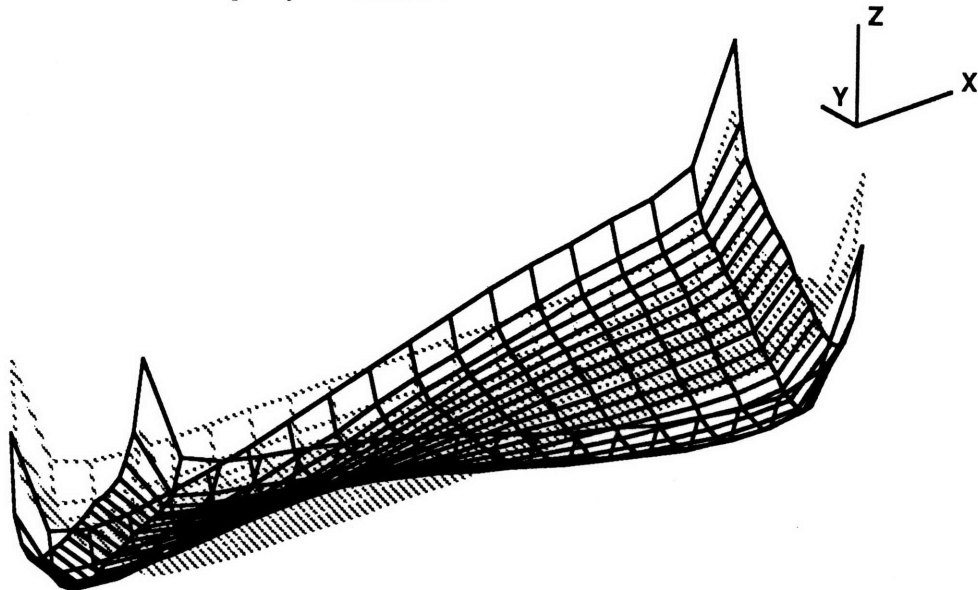

Figure 6.23   Rectangular Tank. Assumed Mode Shape for the q_5 Degree-of-Freedom.

6.1.4.2   Fluid Dissipation Effects

All the coefficients in the analytical model can be calculated from a knowledge of the fluid geometry (including boundary conditions), fluid type and acceleration field, except for the fluid damping coefficients. Modeling of the viscous boundary layer dissipation effects is extremely difficult. For small motions, this effect can be sufficiently modeled by a small, linear viscous damping term. The experimentally observed fluid damping ratios in the uncoupled fluid slosh tests were used as an estimate of the resulting modal damping terms.

6.2   Forced Response Characteristics

In this section, the Harmonic Balance method will be used to predict the forced response characteristics of one of the cylindrical tank cases (Test 410-1). In test 410-1 water which has significant contact angle hysteresis, was used as a model fluid. At the time that the Harmonic Balance method was implemented, only the cylindrical tank experimental results (obtained by Peterson [1987]) were available. The verification and investigation of the method were thus performed by comparing the forced response characteristics of the fluid contained in the cylindrical tank, as predicted by the Harmonic Balance method, with the cylindrical tank experimental results.

The following implementation questions will be addressed in sub-section 6.2.1:

- Can the Harmonic Balance method be used to predict the forced response characteristics using the nonlinear governing differential equations obtained from the assumed mode model developed in Chapter 2. How does the Harmonic Balance results compare with the Multiple-Time-Scales method used by Peterson [1987].

- Can this method predict jump phenomena and find multiple solutions (roots).

- How dependent is the Newton-Raphson solver on the initial guess.

- Which non-linear equation solver is the best? Inverse solution versus Newton-Raphson.

In order to determine whether the assumed mode model can be made more general by the use of numerically determined mode shapes, the question posed is: What is the loss in accuracy when such mode shapes are used instead of theoretical mode shapes? This question is addressed, in the next sub-section (6.2.2), by comparing the results obtained with an analytical model based on theoretical mode shapes with the results obtained with a model based on numerically determined mode shapes. Model truncation, based on spectral separation of the modes is also discussed in this section. Finally sub-section 6.2.2 shows that the analytical model, if slightly perturbed, can predict the swirling motion observed in the experiments.

6.2.1 Implementation Issues

In order to simplify the analysis, all the results presented in this sub-section are based on a truncated planar model of the cylindrical tank. The planar model summarized in Table 6.5 was further truncated to retain only the spacecraft x-translation mode and the first primary planar fluid slosh mode. This truncation will be justified in section 6.2.2. The coefficients of the planar model were obtained by exact integration of theoretical mode shapes [Blevins, 1987]. A FORTRAN program, named DCONS (Dynamic Characteristics of Non-linear Systems) was developed which implemented the Harmonic Balance method, as described in Chapter 3. An entry subroutine to DCONS read the coefficients of the nonlinear governing differential equations from a data file and also calculated the Fourier integration coefficients (See eqs 3.30). Given an initial guess for the modal amplitudes, DCONS iteratively solved for the modal amplitudes using one of two solution techniques: the Inverse solution technique and the Newton-Raphson method (See Chapter 3). A subroutine evaluated the Fourier

coefficients (eqs 3.17), using the integration coefficients calculated by the entry subroutine, during the iterative solution procedure.

The following paragraphs will address the implementation issues outlined in the introduction of this section (6.2).

Verification of the Harmonic Balance method: In Fig. 6.24 the results are shown for the case in which the Harmonic Balance method was used to predict the forced response characteristics for the cylindrical tank (Test 410-1). The Newton-Raphson solver was used to solve for the modal amplitudes, and the initial guess for each forcing frequency and amplitude was taken to be the solution at the previous forcing frequency. In this prediction, the forcing frequency was increased from the minimum ($f/fo = 0.6$) to the maximum value ($f/fo = 1.3$). At the minimum forcing frequency, the initial guess was taken to be the modal amplitudes predicted by the linearized model. The forcing level was increased in logarithmic (Log_{10}) steps to match the forcing levels used in the experiments. In the figures, the solid lines are the Harmonic Balance predictions, the curved vertical lines, the Multiple-Time-Scales (MTS) method predictions and the symbols are the experimental results.

The results show that the analytical model combined with Harmonic Balance method can be used to predict the forced response characteristics of fluids in cylindrical tanks. The predicted shift in resonant peaks by the Harmonic balance method is as good as the Multiple-Time-Scales prediction but the ability of the Harmonic Balance method to predict the amplitude dependent dissipation rates is a significant improvement over the MTS method. As will be seen in the following paragraph, multiple solutions exist at the higher excitation level and that these solutions can be found if different initial guesses are used in the nonlinear equation solvers.

Test 410-1. Non-dimensional Tank Displacement (x/d).

Test 410-1. Non-dimensional Planar Slosh Force (Fx/kd).
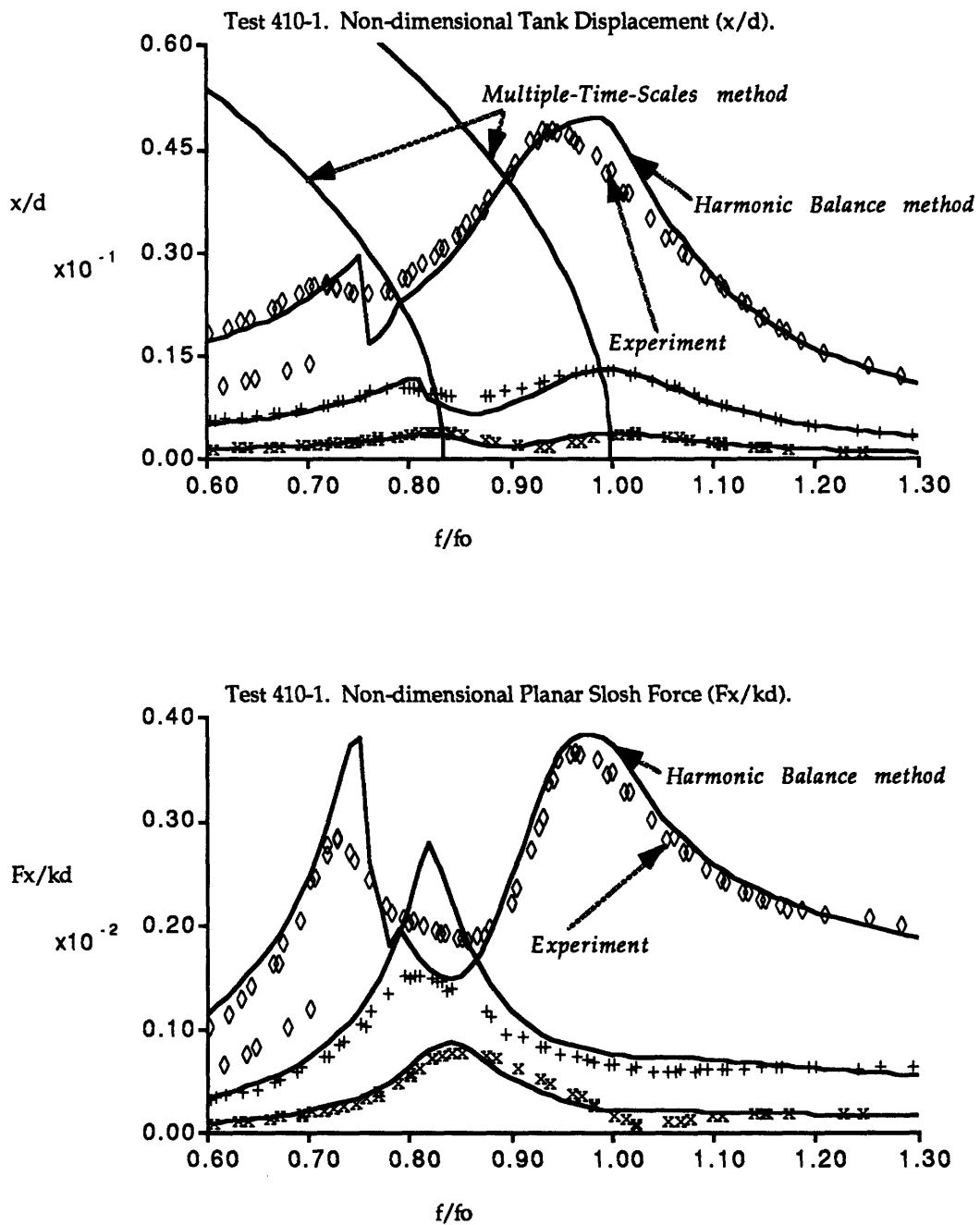
Figure 6.24   Comparison between Analytical and Experimental Results. "Increasing" Excitation Frequency.

(Cylindrical tank, Test 410-1, Bo=33, d=3.1 cm. Coupled system parameters: μ=0.16, ν=0.89 and ζ=9.1%)

261

Multiple Solutions and Jump Phenomena: In Fig. 6.24 the forcing frequency was increased from low to high. The initial guess at each new forcing frequency was thus based on the solution at a lower frequency. In Fig. 6.25, the forcing frequency was decreased from the maximum (f/fo = 1.3) to the minimum (f/fo = 0.6). The initial guess used in the Newton-Raphson solver was thus the solution at the preceding higher frequency. This figure shows that the solver can find multiple roots, given different initial conditions. In particular, the ability of the Newton-Raphson solver to predict the jump at the first resonance peak in Fig. 6.24, is satisfactory proof that the method can handle jump phenomena.

The ability of the model to correctly predict the multiple solution in the region marked (a) supports the conclusion that the analytical model combined with the Harmonic Balance method can predict the forced response characteristics of fluids. The planar slosh force prediction however, indicates that the response is not correctly modeled in this region by this simplified truncated model.

Test 410-1. Non-dimensional Tank Displacement (x/d).

Test 410-1. Non-dimensional Planar Slosh Force (Fx/kd).
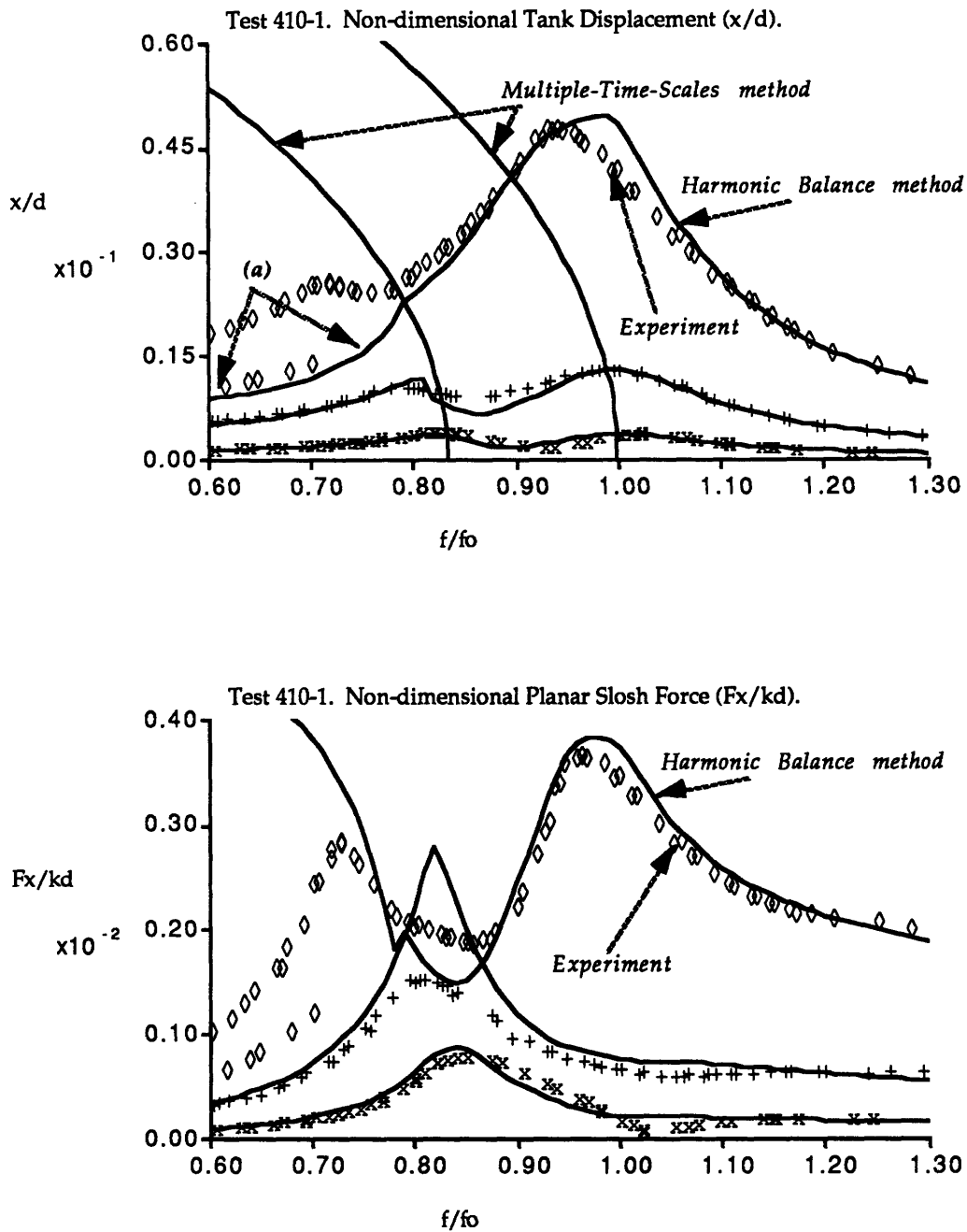
Figure 6.25   Comparison between Analytical and Experimental Results. "Decreasing" Excitation Frequency.

(Cylindrical tank, Test 410-1, Bo=33, d=3.1 cm. Solid lines=Harmonic balance method, Symbols=Experiment. Coupled system parameters: μ=0.16, ν=0.89 and ζ=9.1%)

263

**Dependence on Initial Guess:** It is well known that almost all nonlinear equation solvers are very dependent on the initial guess. In order to determine this dependence and to determine whether it would be possible to converge on different solutions by using different initial guesses, the solution to the linearized equations was used as an initial guess (Fig. 6.26). Studying this figure, one must conclude that the Newton-Raphson method is dependent on the initial guess and that in order to obtain a reliable prediction, the best initial guess must be used. In this research, the best initial guess is the solution at a previous forcing frequency. Finely spaced forcing frequencies will yield better initial guesses and improve the convergence of the Newton-Raphson method.

**Newton-Raphson versus Inverse Solution Technique:** The Inverse Solution technique does not require the Jacobian to be evaluated during each iteration, making the method much faster than the Newton-Raphson method per iteration loop. In Fig. 6.27 however, it is shown that the Inverse Iteration method fails to converge at the higher excitation levels. The method also took more iterations to converge at moderate excitation levels compared to the Newton-Raphson method. Given this result, the Newton-Raphson method was used for the remainder of the analytical predictions. However, the speed of the Inverse Iteration method, suggests that the best approach is to use this method at low forcing amplitudes and to switch to the Newton-Raphson method at higher forcing levels, when convergence of the Inverse Iteration method begins to fail.

Test 410-1. Non-dimensional Tank Displacement (x/d).
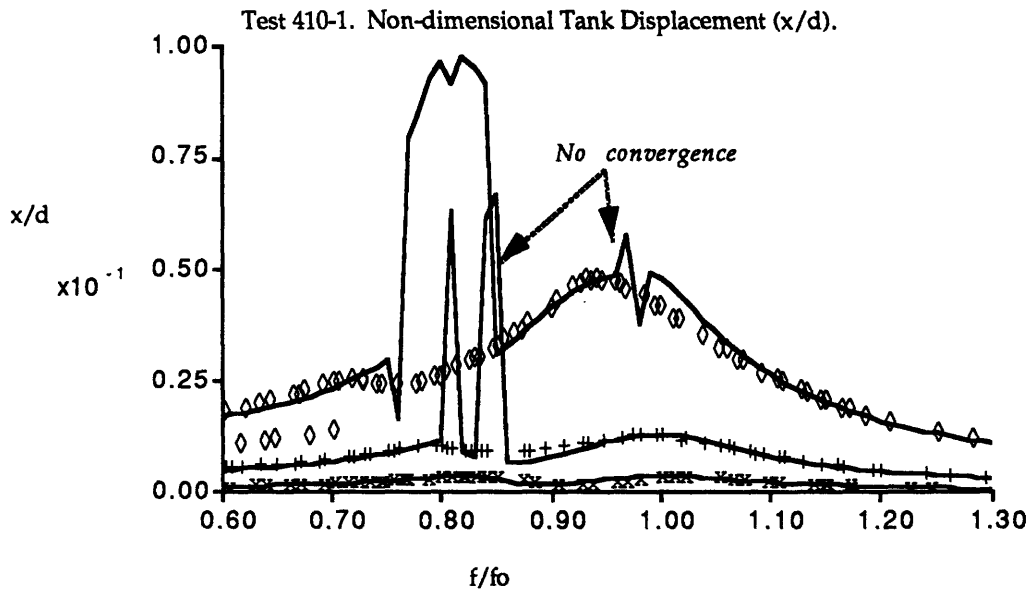
Figure 6.26   Dependence on Initial Guess. Prediction Obtained using
Linear Solution as an Initial Guess.

Test 410-1. Non-dimensional Tank Displacement (x/d).
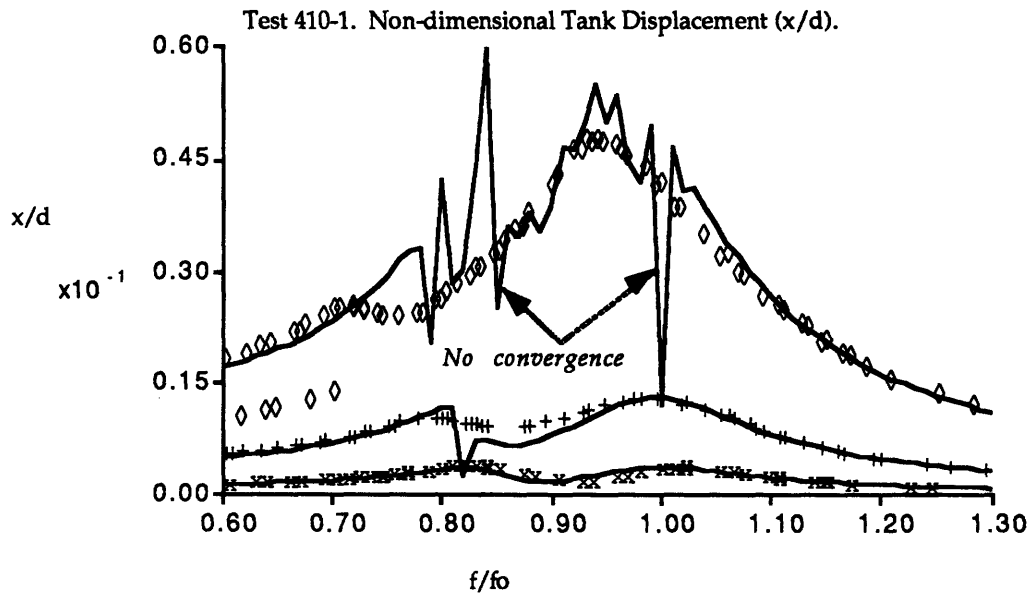
Figure 6.27   Evaluation of the Inverse Solution Technique.

(Cylindrical tank, Test 410-1, Bo=33, d=3.1 cm. Solid lines=Harmonic
balance method, Symbols=Experiment. Coupled system parameters:
$\mu=0.16$, $v=0.89$ and $\zeta=9.1\%$)

265

6.2.2 Modeling Issues

In this section certain modeling issues will be discussed. In the first part model truncation is investigated, in the second, the use of numerically determined mode shapes is justified. This section also shows that the analytical model, if perturbed, can predict the swirling motion that was experimentally observed by Peterson [1987]. In the final part, for completeness, the frequency and damping ratio shifts are predicted for the cylindrical test article (Test 410-1).

Model Truncation: The modal truncation of the analytical model is possible at two stages of the modeling process, as described in sub-section 6.1.4.1. As explained in this section, the number of modes used in the analysis can be truncated before and after the wavelength matrices are calculated. In this research, the number of modes used in the calculation of the wavelength matrices were determined by checking the convergence of the matrix entries as the mode number was increased. In theory it is possible to retain all the modes used to calculate the wavelength matrices but in practice this is undesirable. Including more modes in the analysis significantly increases the solution time of the Newton-Raphson solver. Thus, although it was possible to use many modes in the calculation of the wavelength matrices only the modes indicated in Tables 6.5 and 6.6 were retained in the governing differential equations.

Given that the cylindrical model used to predict the forced response characteristics in the previous section included two secondary modes, the question is whether spectral separation of the modes can be used to truncate the model further so that only the spacecraft x-translation and first planar fluid slosh modes are retained. Fig. 6.28 compares the results obtained with the truncated two mode model with results obtained with the planar model of Table 6.5. The two models are identical except for the failure of the 4 mode model to converge in the region between the resonant peaks and the different solution predicted by the 4 mode model in region (a). The failure of the more complex model to converge is expected and the different solution in region (a) can be explained either by the fact that the 4 mode model does have an additional solution in that region or by the fact that given a different model, the Newton-Raphson solver converged on a

266

Test 410-1. Non-dimensional Tank Displacement (Fx/kd).
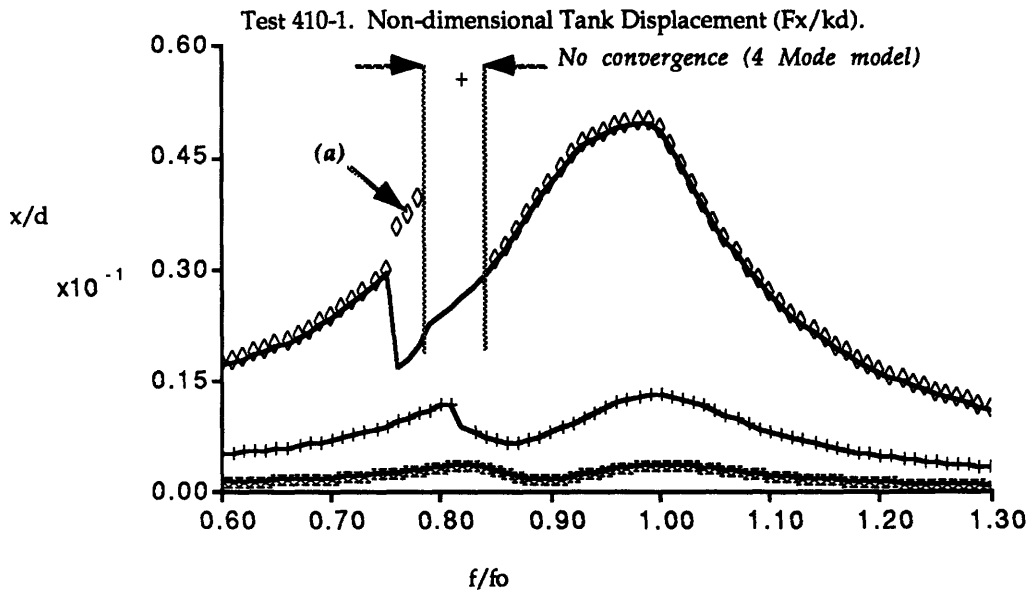
Figure 6.28   Model Truncation. 2 Mode Model versus 4 Mode Model.

(Cylindrical tank, Test 410-1, Bo=33, d=3.1 cm. Solid lines=2 Mode Model, Symbols=4 Mode Model. Coupled system parameters: μ=0.16, v=0.89 and ζ=9.1%)

different solution. Based on these results, it can be concluded that model truncation, based on modal separation, can be justified.

Numerically Determined Mode Shapes: The coefficients of the planar model used to predict the analytical results up to this point were calculated by exact integration of the theoretical mode shapes for a cylindrical tank. In order to make the analytical method applicable to more general problems, the use of numerically determined mode shapes is desirable. Given that the calculation of the coefficients of the nonlinear governing differential equations require first and second order derivatives of the mode shapes as well as integration over the volume and free surface area, the question posed is: what is the loss in accuracy if numerically determined mode shapes are used? Errors are introduced by (a) numerical integration of the mode shapes and (b) by the use of numerically determined mode shapes. Although not presented, it was determined that the errors introduced by numerical integration of the mode shapes are insignificant.

In Fig. 6.29, the coefficients of the planar (see Table 6.5) model were obtained by numerical integration of the numerically determined mode

shapes (see section 6.1.4). It can be concluded that the model based on the numerical integration of the numerically determined mode shapes (to calculate the coefficients) is different from the one obtained by the exact integration of the theoretical mode shapes. A true measure of the validity of the numerical model is to compare the results with the experiment (Fig. 6.30). Comparing these figures with those of Fig. 6.24, it can be concluded that the theoretical mode shapes yields a better prediction of the planar slosh force but that the numerical mode shapes better predicts the tank displacement near the first resonance peak.

Two reasons exist for the differences between the two models. There are the errors introduced by using numerically determined mode shapes and there is the fact that the numerical mode shapes were obtained by including the equilibrium free surface in the fluid geometry. The theoretical mode shapes assumed a flat free surface.

Although the model based on the numerically determined mode shapes is not identical to the model based on the theoretical mode shapes, the results of Fig. 6.30 indicate that the "numerical" model will yield adequate predictions of the forced response characteristics of fluids in cylindrical containers. Section 6.3 addresses the question whether this conclusion can be extended to tanks of other geometry.

Test 410-1. Non-dimensional Tank Displacement (x/d).

Model based on numerically determined mode shapes

Model based on theoretical mode shapes

x/d

x10⁻¹

f/fo

Test 410-1. Non-dimensional Planar Slosh Force (Fx/kd).

Model based on theoretical mode shapes

Fx/kd

x10⁻²

Model based on numerically determined mode shapes

f/fo
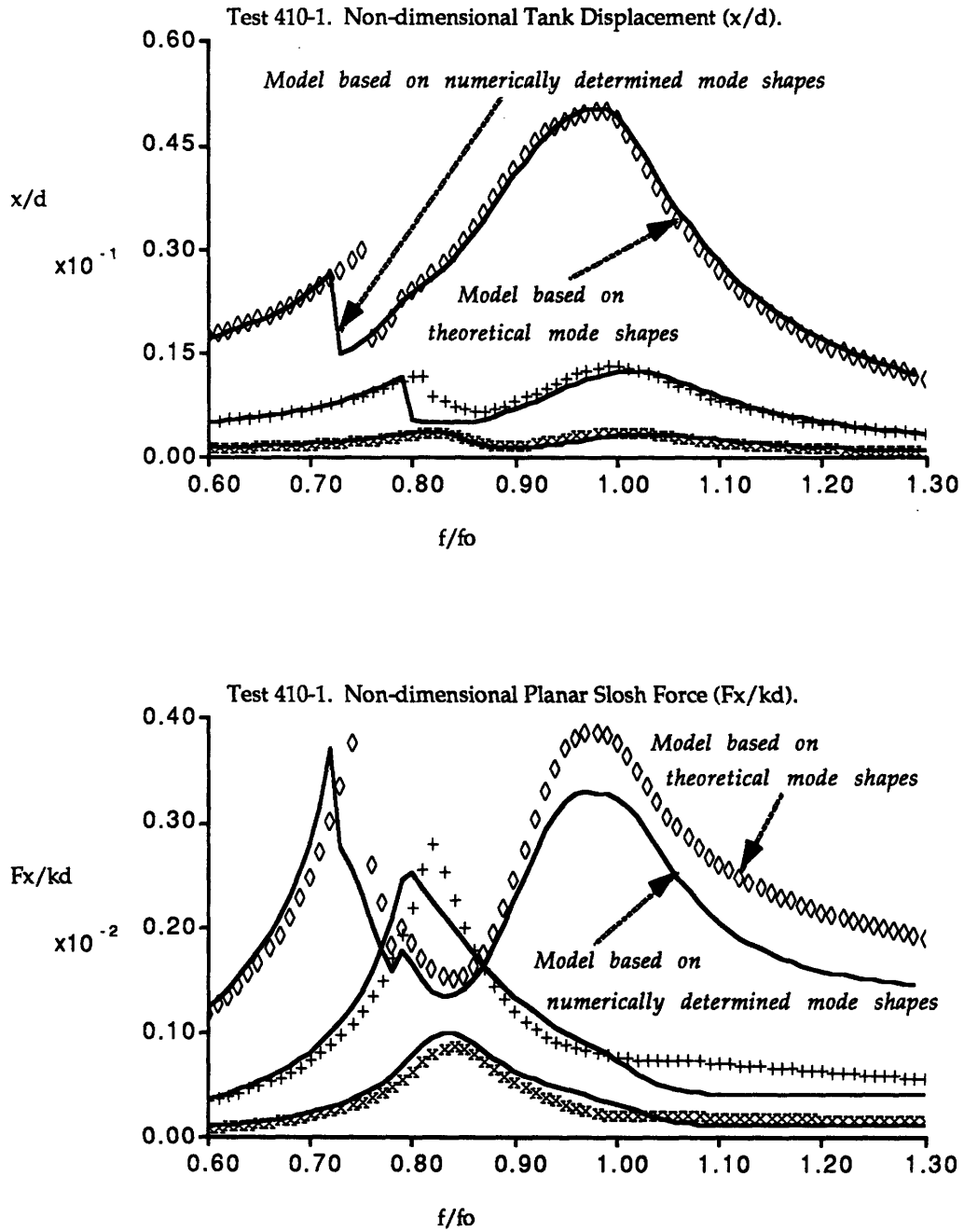
Figure 6.29   **Comparison of Models Based on Theoretical and Numerically Determined Mode Shapes.**

(Cylindrical tank, Test 410-1, Bo=33, d=3.1 cm. Solid lines=Nonplanar model based on numerically determined mode shapes, Symbols=Planar model based on theoretical mode shapes. Coupled system parameters: μ=0.16, v=0.89 and ζ=9.1%)

269

Test 410-1. Non-dimensional Tank Displacement (x/d).

Test 410-1. Non-dimensional Planar Slosh Force (Fx/kd).
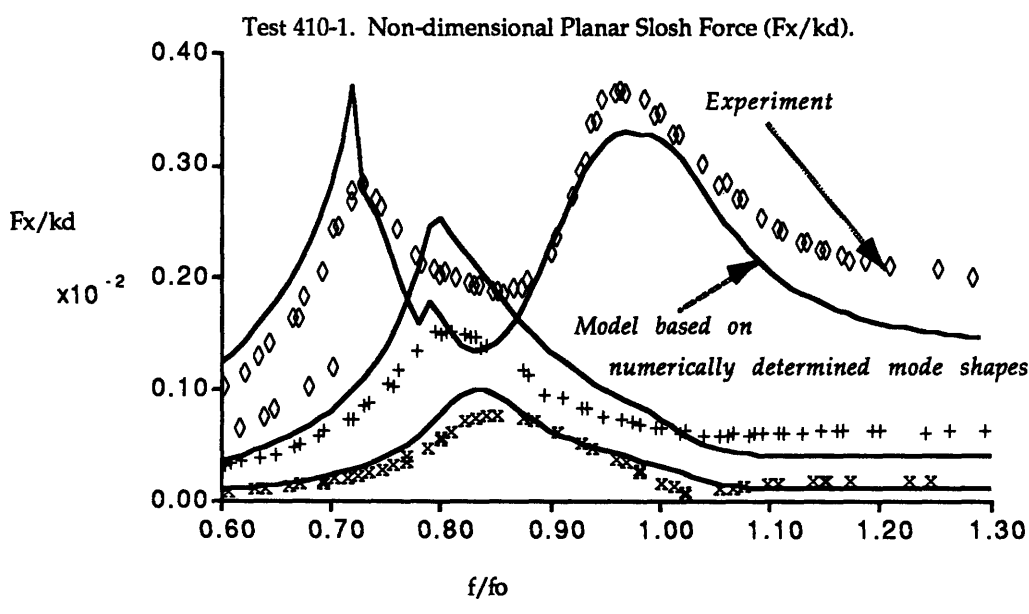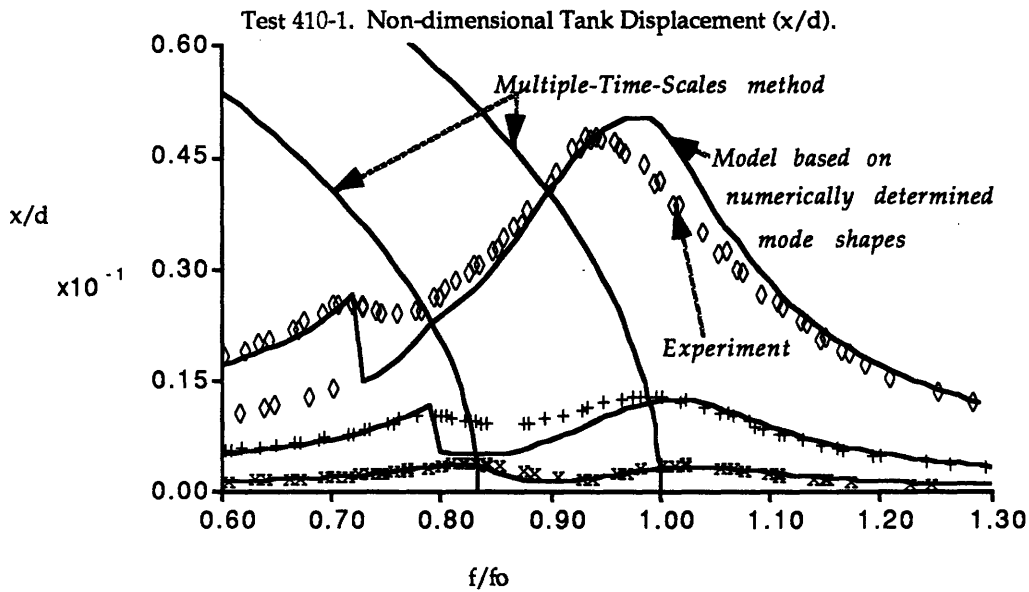
Figure 6.30   **Comparison between Analytical and Experimental Results.   Nonplanar model based on Numerically Determined Mode Shapes.   "Increasing" Excitation Frequency.**

(Cylindrical tank, Test 410-1, Bo=33, d=3.1 cm.   Coupled system parameters: μ=0.16, ν=0.89 and ζ=9.1%.   Solid lines=Nonplanar model based on numerically determined mode shapes, Symbols=Experiment)

270

Swirling Motion: Peterson [1987] observed that the fluid motion in cylindrical tanks jumps from the expected planar motion to a combined planar/nonplanar swirling motion. The nonplanar model discussed in the previous paragraph failed to predict this response but when a small mass coupling term between the spacecraft degree-of-freedom and the nonplanar slosh mode was added to the non-homogeneous governing differential equations, this swirling motion was predicted. The coupling term added was 2% of the mass coupling between the spacecraft mode and the planar slosh mode and was added in the corresponding spacecraft/nonplanar primary slosh mass matrix entries. The possible existence of such a coupling term can be explained by either (a) unmodeled nonplanar characteristics of the excitation system or (b) small perturbations in the geometry of the tank that would couple the planar and nonplanar modes. The results of the perturbed analysis are depicted in Fig. 6.31 and 6.32. Fig. 6.31 depicts the first planar and nonplanar slosh mode amplitudes. The fluid motion jumps, near the first resonance, from a pure planar motion to a motion that has equal planar and nonplanar fluid motion amplitudes.

In Fig. 6.32, the fluid motion, amplified for clarity by a factor of 2, at a forcing frequency (Ω/fo = 0.73) and at the highest forcing amplitude is plotted (see Fig. 6.31). Each picture represents the fluid shape at different phase angles. The phase angle between the two repeated eigen-values (first planar and first nonplanar modes) is roughly 90° and the motion closely resembles the swirling motion observed in the experiments.

Prediction of the swirling motion with the nonplanar model based on the numerically calculated mode shapes is one of the major successes of this research. A planar model cannot predict this motion. As shown in this section, the response is very sensitive to small nonplanar inputs and at moderate excitation levels, a small nonplanar input can result in significant planar/nonplanar (swirling) motion. It is believed that the electro-mechanical shaker is not perfectly rigid in the nonplanar direction and that in order to correctly model the swirling motion, an accurate model of this shaker nonplanar degree-of-freedom will be required.

Test 410-1. Planar Fluid Slosh Mode (q1/d).

Test 410-1. Nonplanar Fluid Slosh Mode (q2/d).
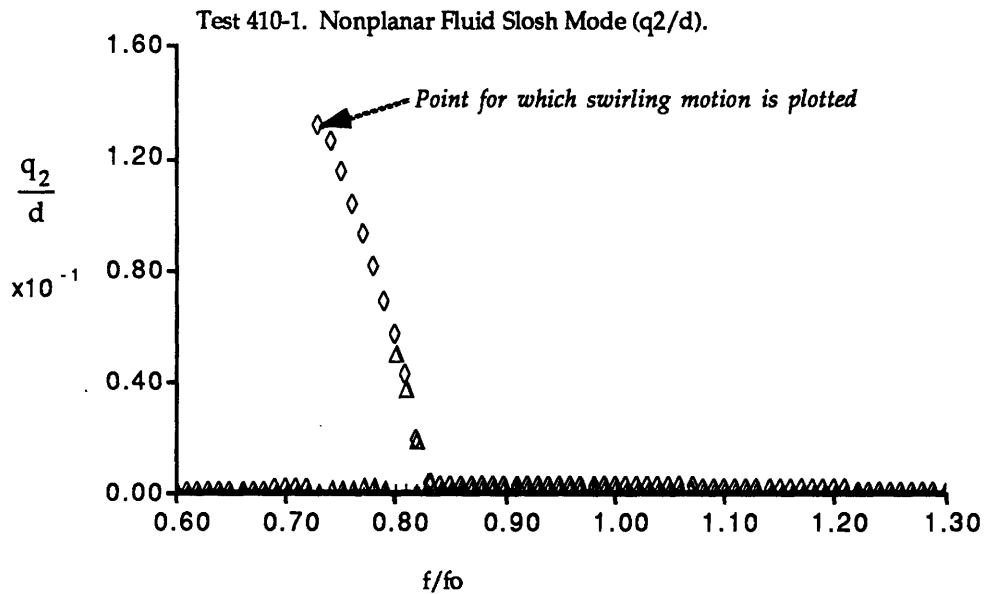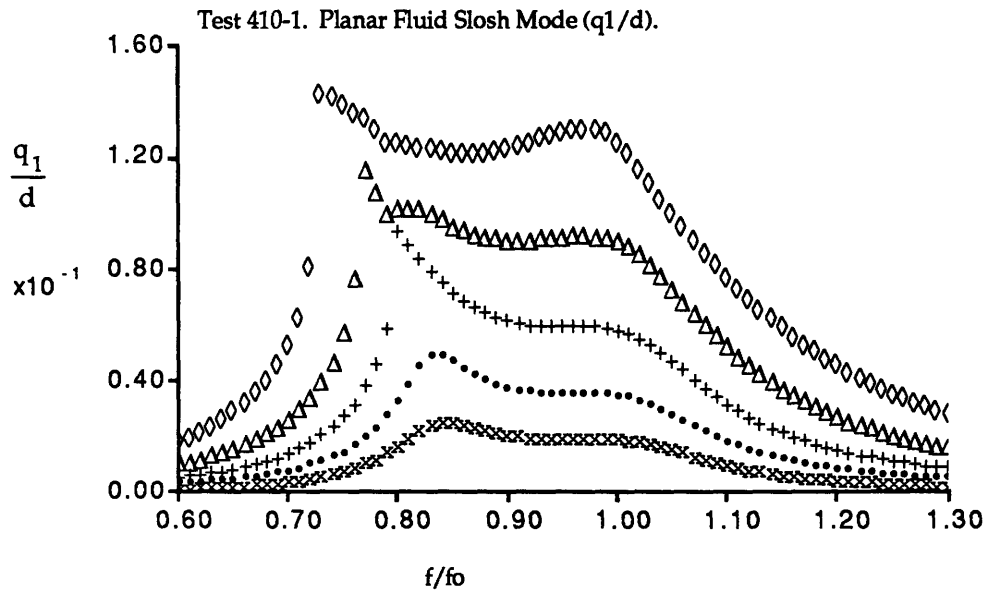
Figure 6.31   Jump Phenomenon Resulting in Swirling Motion.
Note: "Increasing" Excitation Frequency.

(Cylindrical tank, Test 410-1, Bo=33, d=3.1 cm. Coupled system
parameters: μ=0.16, v=0.89 and ζ=9.1%. Solid lines=Nonplanar model
based on numerically determined mode shapes, Symbols=Experiment)

272

CYLINDRICAL TANK: 410–1   FINITE DIFFERENCE MODES

FORCING AT: 0.730 f/fo AND AMPLITUDE: 0.010
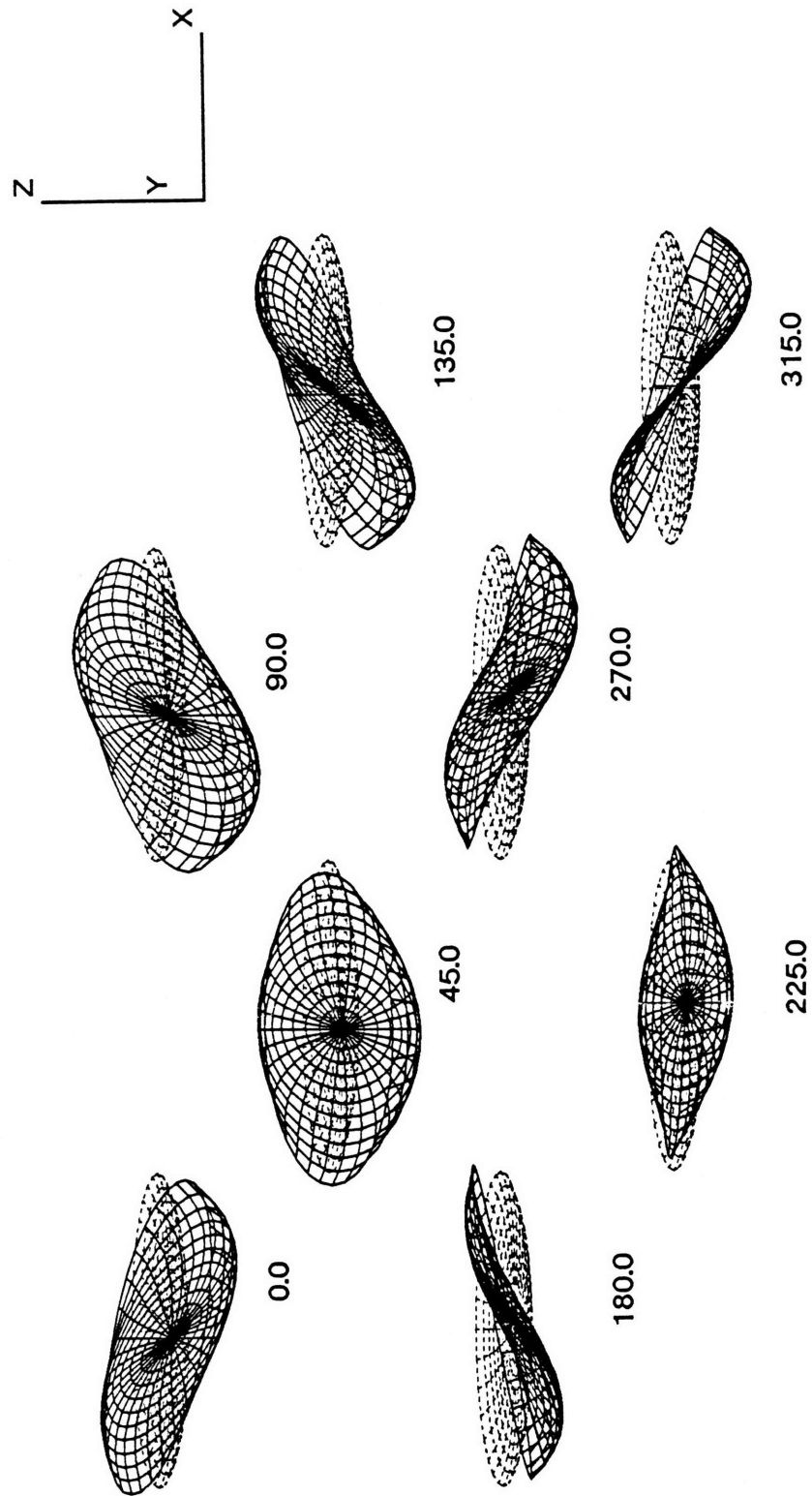
Figure 6.32   Cylindrical Test 410-1.   Predicted Swirling Motion near First Resonant Peak.

Shift in Model Frequencies and Damping Ratios: Given the modal

amplitudes predicted by the analytical model, the equivalent linear modal
frequencies and damping ratios can be inferred (See section 3.3.5). The
importance and meaning of these amplitude and frequency dependent
frequencies and damping ratios are that a linear system with these eigen-
characteristics will yield the same forced response characteristics as the
nonlinear fluid/spacecraft system at the given forcing amplitude and
frequency. These values can be used by a control engineer as tolerance limits
for his control design.

In order to complete the analysis of Test 410-1, the shifts in linear
frequencies and damping ratios are presented. Fig. 6.33 and Fig. 6.34 depict
the shift in model frequencies and damping ratios of the first two coupled
modes. These graphs predict frequency shifts as high as 20% for the fluid
slosh (coupled) mode and 7% for the spacecraft mode. The maximum
predicted shift in damping ratio is 45% for the fluid slosh mode and 12% for
the spacecraft mode. The numbers in the graphs indicate the corresponding
experimental forcing levels (Chapter 5).

Test 410-1. Shift in Planar Slosh Mode's Frequency.

$\dfrac{\Delta f_{\text{Planar Slosh}}}{f_{\text{Planar Slosh}}}$

(%)

-0.00

-6.00

-12.00

-18.00

-24.00

0.60   0.70   0.80   0.90   1.00   1.10   1.20   1.30

f/fo

Test 410-1. Shift in Spacecraft Mode's Frequency.

$\dfrac{\Delta f_{\text{Spacecraft}}}{f_{\text{Spacecraft}}}$

0.00

-2.00

-4.00

-6.00

-8.00

0.60   0.70   0.80   0.90   1.00   1.10   1.20   1.30

f/fo
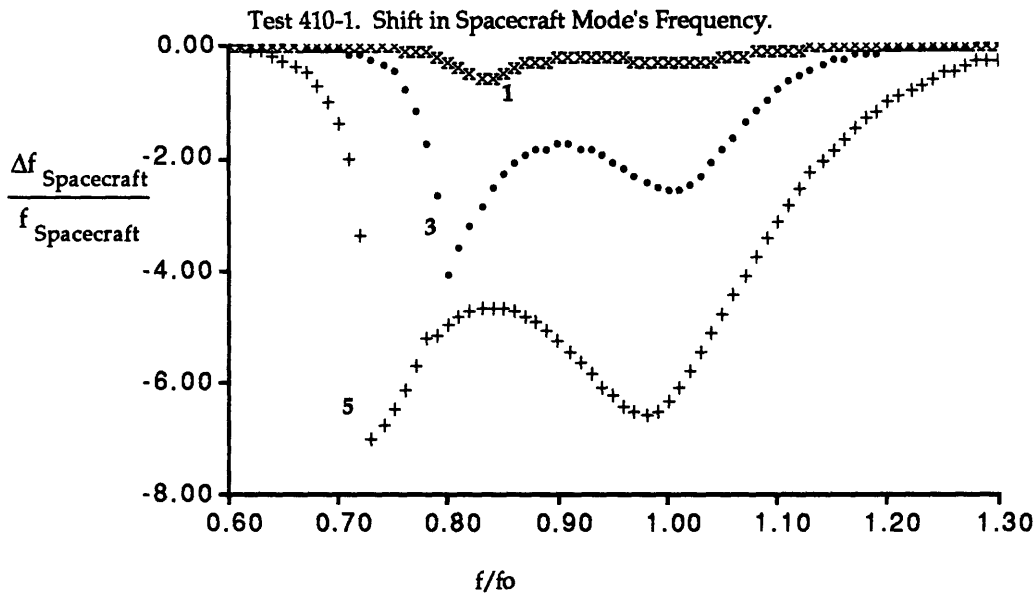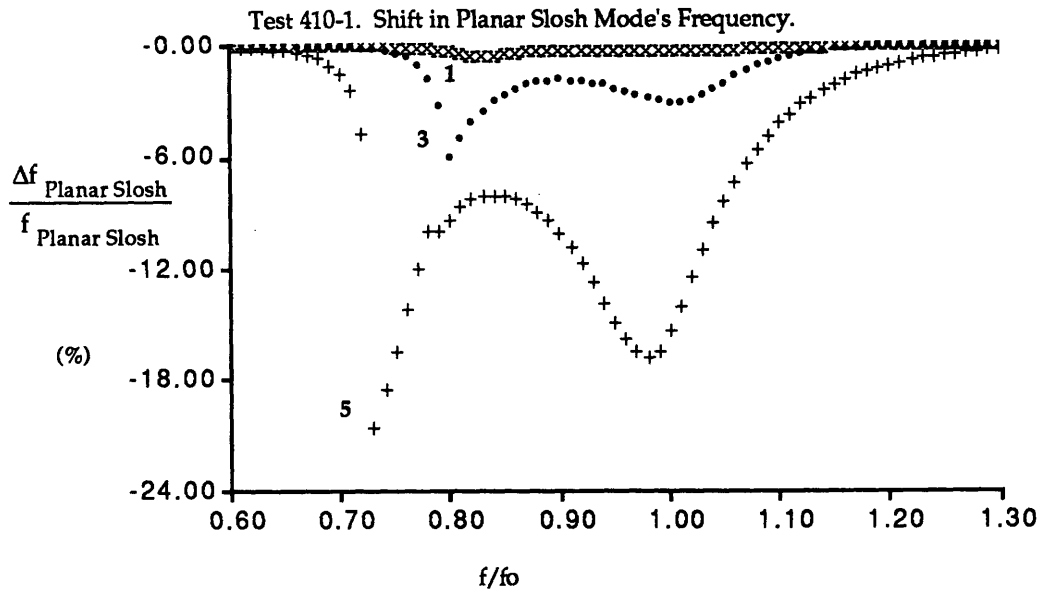
Figure 6.33   Cylindrical Tank, Test 410-1. Predicted Shift in Coupled Frequencies.

(Cylindrical   tank,   Test   410-1,   Bo=33,   d=3.1   cm.
Numbers=Corresponding experimental excitation level. Note: Results
are eigen-characteristics of coupled fluid/spacecraft system: μ=0.16,
v=0.89 and ζ=9.1%.)

275

Test 410-1. Shift in Planar Slosh Mode's Damping Ratio.

$$\frac{\Delta \zeta_{\text{Planar Slosh}}}{\zeta_{\text{Planar Slosh}}}$$

(%)

Test 410-1. Shift in Spacecraft Mode's Damping Ratio.

$$\frac{\Delta \zeta_{\text{Spacecraft}}}{\zeta_{\text{Spacecraft}}} \; (\%)$$
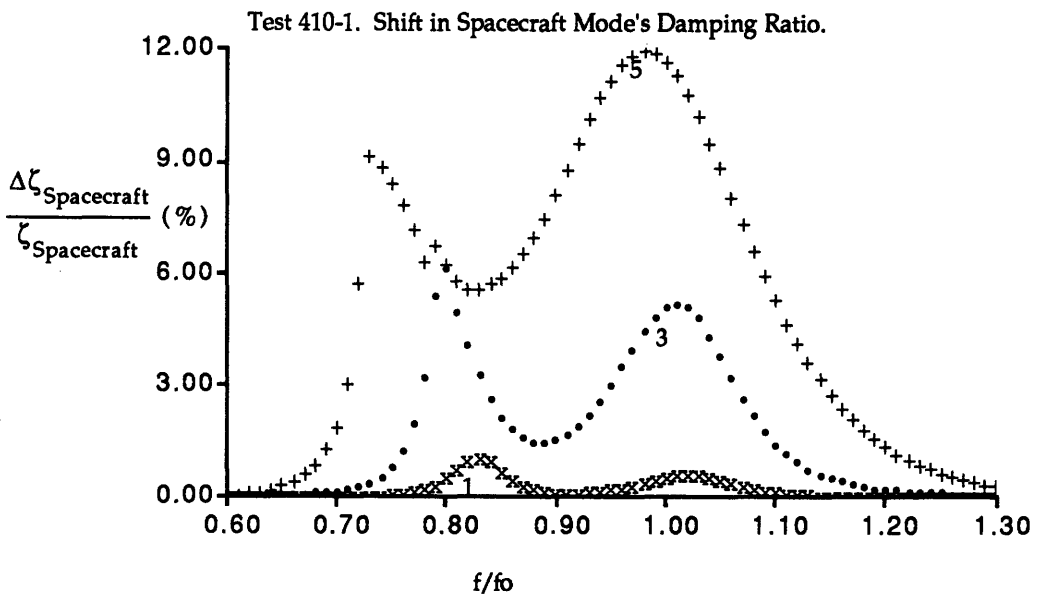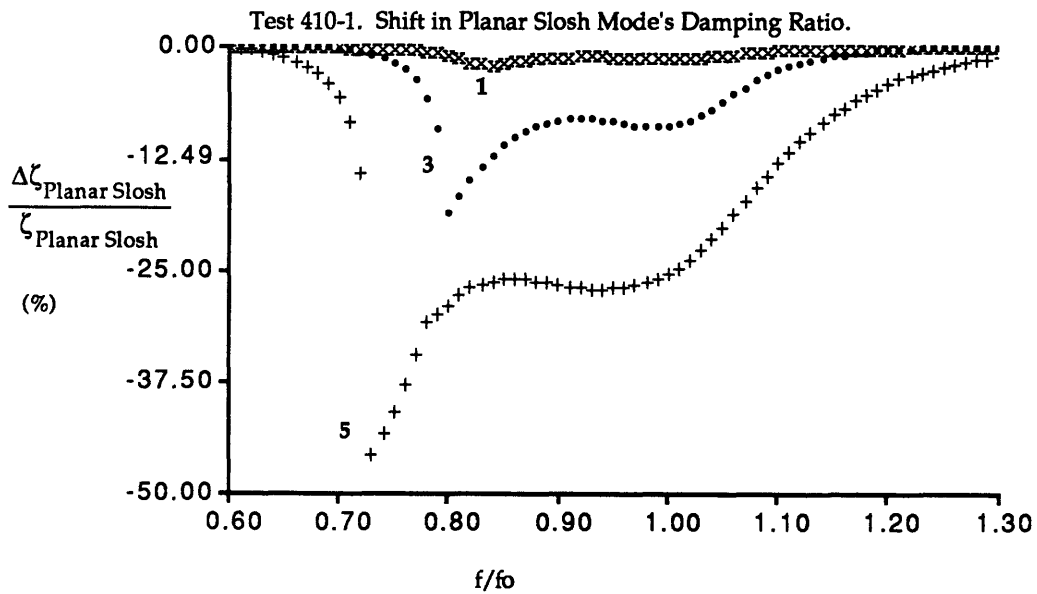
Figure 6.34 **Cylindrical Tank, Test 410-1. Predicted Shift in Coupled Damping Ratios.**

(Cylindrical tank, Test 410-1, Bo=33, d=3.1 cm. Numbers=Corresponding experimental excitation level. Note: Results are eigen-characteristics of coupled fluid/spacecraft system: μ=0.16, ν=0.89 and ζ=9.1%.)

276

6.2.3 Summary

In section 6.2, it has been shown that the analytical model combined with the Harmonic Balance method can be used to predict the forced response characteristics of coupled fluid systems. Given the results in section 6.2.1, the rest of the analytical predictions will be performed with: (a) the Newton-Raphson solver, (b) using the solution at the previous forcing frequency as the initial guess and (c) a nonplanar analytical model based on numerically determined mode shapes. The next section (6.3) will compare the analytical results of a few selected cases with the experimental results.

In Section 6.2, model truncation has been justified on the grounds of modal spectral separation and it was shown that with a small perturbation of the analytical model, the experimentally observed swirling motion can be predicted.

6.3   Comparison of Analytical and Experimental Results

In this section, the analytical models (section 6.1) will be used to predict the forced response characteristics of a few selected cases. In section 6.3.1, two more cylindrical cases are presented (Test 420-1 and Test 331-1), section 6.3.2 compares the analytical results of spherical test S14 with the experimental results presented in Chapter 5. In section 6.3.3, the predicted forced response characteristics for a square tank case (V16) is compared with experimental results and in section 6.3.4 two rectangular cases (R16 and R20) are studied.

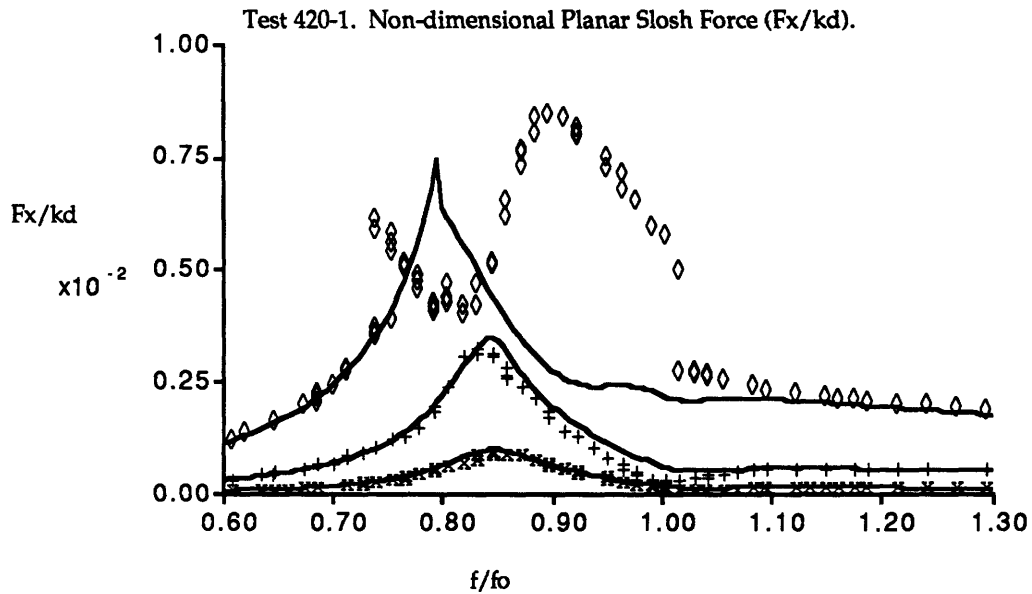### 6.3.1 Cylindrical Model Tanks

Using the mode shapes obtained from the finite difference program (Section 6.1), the coefficients of the nonlinear governing differential equations were numerically calculated. The Harmonic Balance method was used to predict the results presented in Fig. 6.35 to 6.36 (Test 420-1) and Fig. 6.37 to 6.38 (Test 331-1). In Test 420-1 a 3.1 cm diameter cylindrical tank was

used with a 2% Photoflo/water solution as modeling fluid. This test can be compared with the results of Test 410-1, in which the same tank geometry was used but water as modeling fluid. Test 331-1 examined the coupled fluid behavior of water in a 4.1 cm diameter cylindrical tank.

By comparing the analytical results with the experimental results, one can conclude that the analytical model does a credible job for low to moderate excitation amplitudes. At the highest excitation amplitude, the correlation is more complex. For example, examining the planar slosh force prediction for Test 331-1 as an example (see Fig. 6.38), the analytical model predicts (at high excitation levels) the response correctly in region (a) if the increasing excitation frequency result is used. In region (b) the prediction is correct if decreasing excitation frequency result is used and in region (d), either one of the results can be used. The model fail to predict the response in region (c), where the motion jumps from the linearly predicted planar motion to the exotic planar/nonplanar swirling motion.

Except for the prediction of the swirling motion, one can conclude that the nonlinear cylindrical model, based on the numerically calculated mode shapes, can be used to predict the forced response characteristics of coupled fluid/spacecraft systems. The unmodeled nonplanar characteristics of the excitation system (no matter how small) is believed to be one of the major reasons why the nonplanar model fails to accurately predict the motion between the first and second resonant peaks.

Note on Chaotic Motion: A second reason explaining the failure of the nonplanar model in the region between the first and second resonant peaks, is the possibility of chaotic behavior. Given that two solutions exist in this region, it is possible that the motion jumps from one to the other and that the experimentally measured results are actually an average of the two motions. The motion will be dependent on the initial conditions, which can be seen as random and the measured results will be an average of the chaotic motion.

Test 420-1. Non-dimensional Tank Displacement (x/d).

Test 420-1. Non-dimensional Planar Slosh Force (Fx/kd).
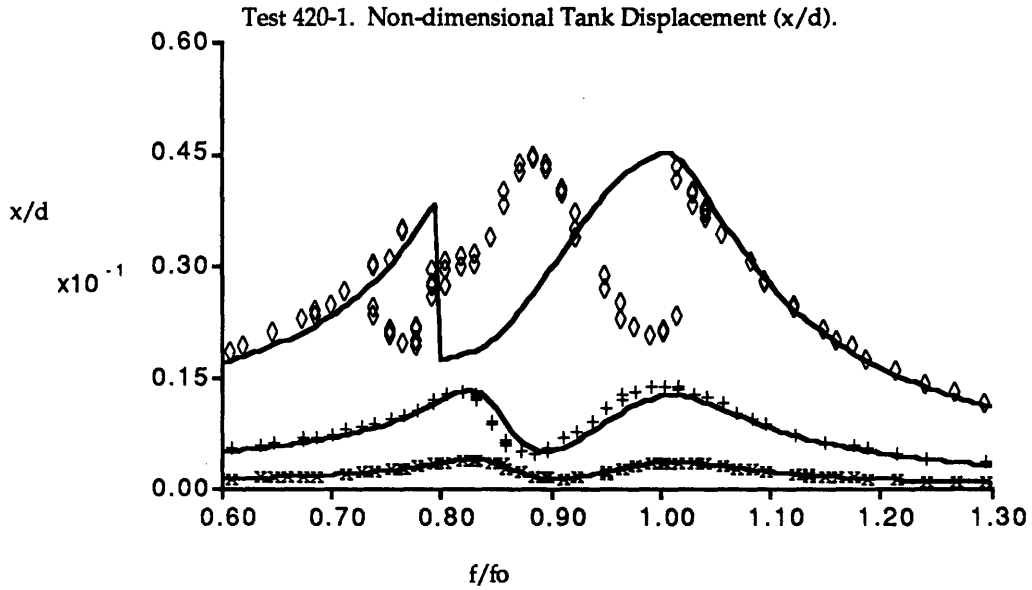
Figure 6.35   Comparison between Analytical and Experimental Results. "Increasing" Excitation Frequency.

(Cylindrical tank, Test 420-1, Bo=66, d=3.1 cm. Solid lines=Harmonic balance method, Symbols=Experiment. Coupled system parameters: μ=0.16, ν=0.90 and ζ=9.3%. Model fluid=2% Photoflo/Water solution.)

Test 420-1. Non-dimensional Tank Displacement (x/d).

Test 420-1. Non-dimensional Planar Slosh Force (Fx/kd).
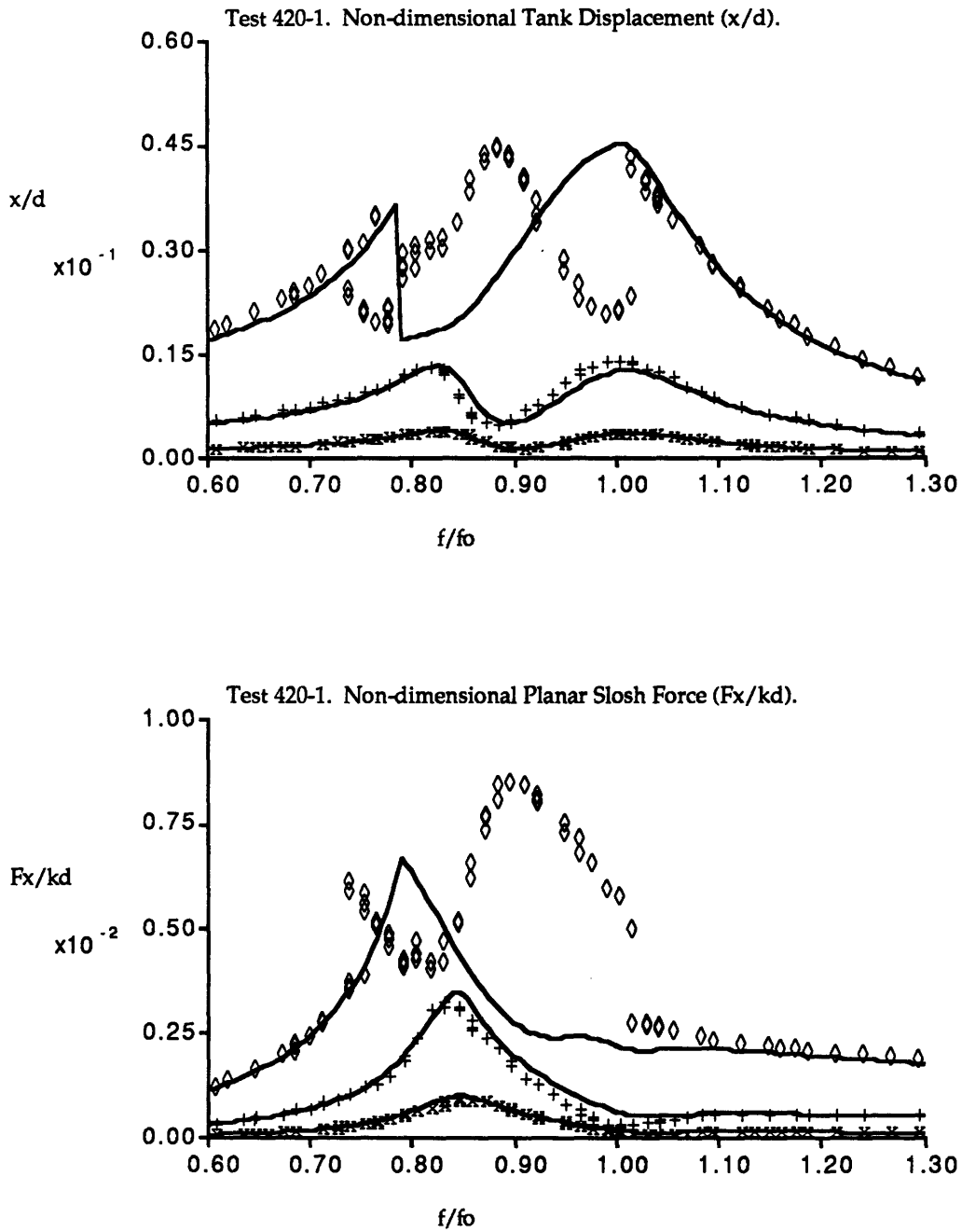
Figure 6.36   Comparison between Analytical and Experimental Results. "Decreasing" Excitation Frequency.

(Cylindrical tank, Test 420-1, Bo=66, d=3.1 cm. Solid lines=Harmonic balance method, Symbols=Experiment. Coupled system parameters: μ=0.16, ν=0.90 and ζ=9.3%. Model fluid=2% Photoflo/Water solution.)

Test 331-1. Non-dimensional Tank Displacement (x/d).

Test 331-1. Non-dimensional Planar Slosh Force (Fx/kd).

Figure 6.37   Comparison between Analytical and Experimental
               Results. "Increasing" Excitation Frequency.

(Cylindrical tank, Test 331-1, Bo=58, d=4.1 cm. Solid lines=Harmonic
balance method, Symbols=Experiment. Coupled system parameters:
μ=0.16, v=0.90 and ζ=9.8%. Model Fluid=Water.)

Test 331-1. Non-dimensional Tank Displacement (x/d).

Test 331-1. Non-dimensional Planar Slosh Force (Fx/kd).

Figure 6.38   Comparison between Analytical and Experimental Results. "Decreasing" Excitation Frequency.

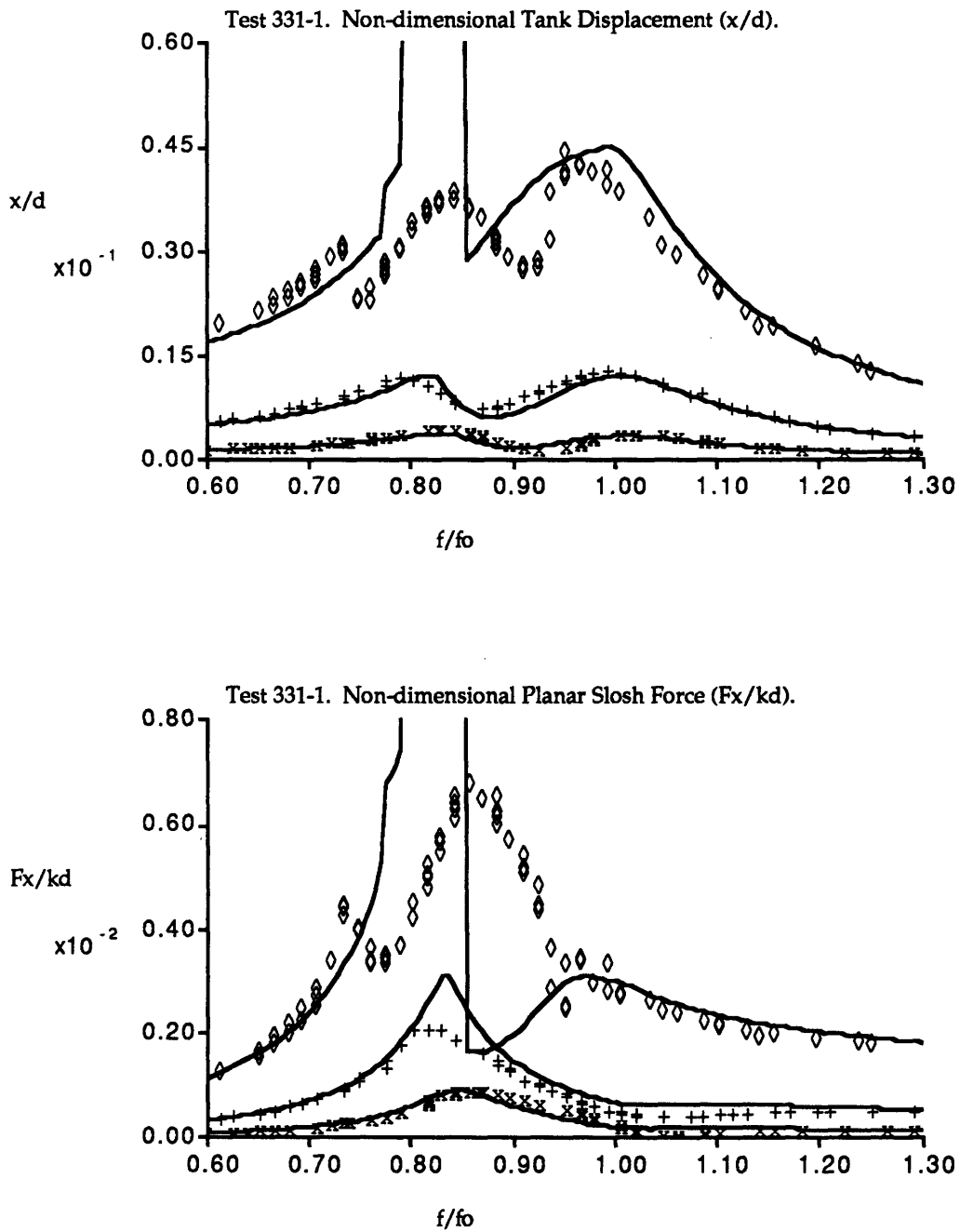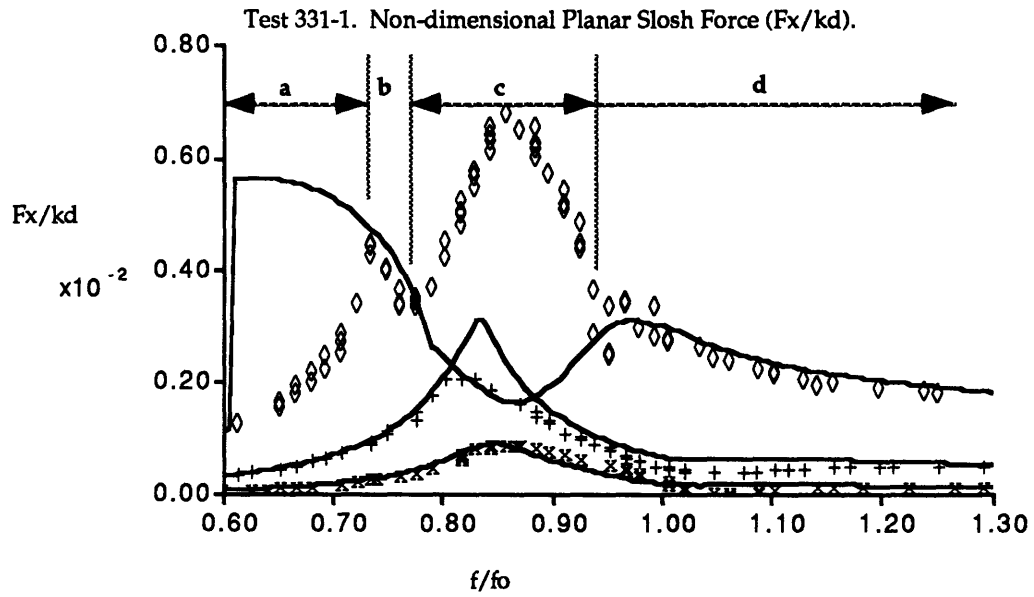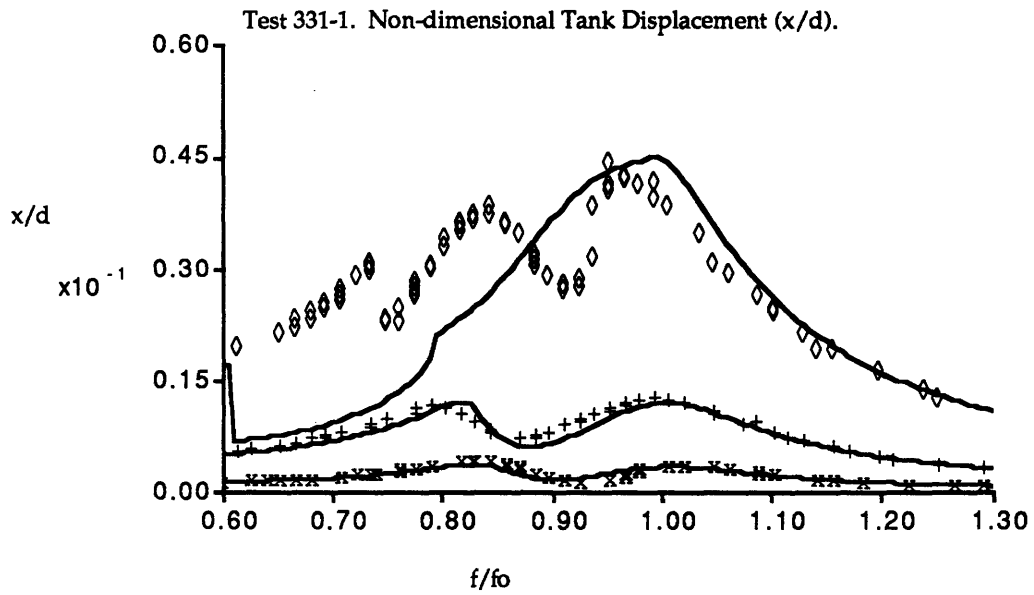(Cylindrical tank, Test 331-1, Bo=58, d=4.1 cm. Solid lines=Harmonic balance method, Symbols=Experiment. Coupled system parameters: μ=0.16, v=0.90 and ζ=9.8%. Model fluid=Water.)

6.3.2 Spherical Model Tank

In this section the spherical model will be used to predict the forced response characteristics of the S14 spherical experimental test. The results will indicate how well the analytical model will be able to model tank geometries with non-straight or non-parallel walls.

The response in figures 6.39 were calculated using an increasing excitation frequency, and figures 6.40 by using a decreasing excitation frequency. Note that only the results of three of the experimental force excitation levels (levels 1, 3 and 5) are retained in these figures. As with the cylindrical predictions, 2% of the planar coupling term (between spacecraft displacement and planar slosh mode) was added to the nonplanar equations, thus coupling the spacecraft mode with the nonplanar slosh mode. The results indicate a small mismatch in the resonance peak of the spacecraft mode. The model predicts swirl motion (Fig. 6.41) but not at the same excitation frequencies as experimentally observed. Extending the predicted curve (highest excitation frequency), one may conclude that the model may predict swirl motion at the experimentally observed excitation frequencies if the Newton-Raphson solver was able to find all the roots of the nonlinear equations. Even though the slosh amplitudes are as high as 30% of the tank diameter, the slosh force predictions are surprisingly accurate.

In figures 6.42 and 6.43, the predicted changes in the coupled resonant equivalent linear frequencies and damping ratios for the first two modes are plotted. These graphs predict frequency shifts as high as 16% for the coupled fluid planar slosh mode and 7% for the spacecraft mode. The maximum predicted shift in damping ratio is 60% for the fluid planar slosh mode and 18% for the spacecraft mode.

The analytical predictions obtained with spherical model, indicates that the straight and parallel model assumptions can be relaxed and the analytical model developed may be used for more complex tank geometries. The applicability will be decided by the change in surface area and boundary conditions as a function of fluid height (of which Fig. 6.13 is an example).

Test S14. Non-dimensional Tank Displacement (x/d).

Test S14. Non-dimensional Planar Slosh Force(Fx/kd).

Figure 6.39   Comparison between Analytical and Experimental Results. "Increasing" Excitation Frequency.

(Spherical Tank, Test S14, Bo=117.   Solid lines=Harmonic balance method, Symbols=Experiment.   Coupled system parameters: μ=0.16, ν=0.90 and ζ=8.0%.   Model fluid=2% Photoflo/Water solution.)
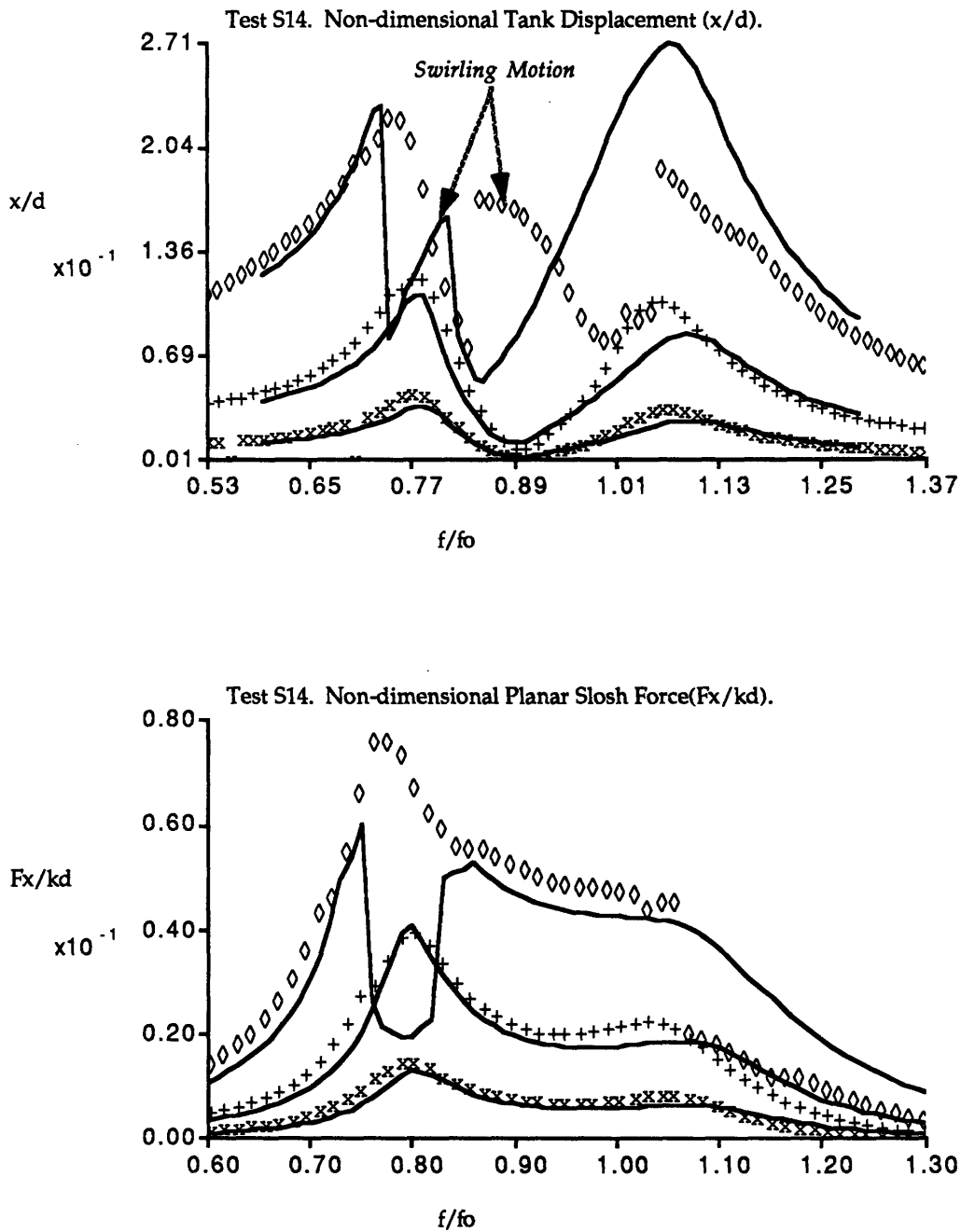
Test S14. Non-dimensional Tank Displacement (x/d).

Test S14. Non-dimensional Planar Slosh Force (Fx/kd).

Figure 6.40   Comparison between Analytical and Experimental
Results. "Decreasing" Excitation Frequency.

(Spherical Tank, Test S14, Bo=117.   Solid lines=Harmonic balance
method, Symbols=Experiment.   Coupled system parameters: μ=0.16,
ν=0.90 and ζ=8.0%.   Model fluid=2% Photoflo/Water solution.)
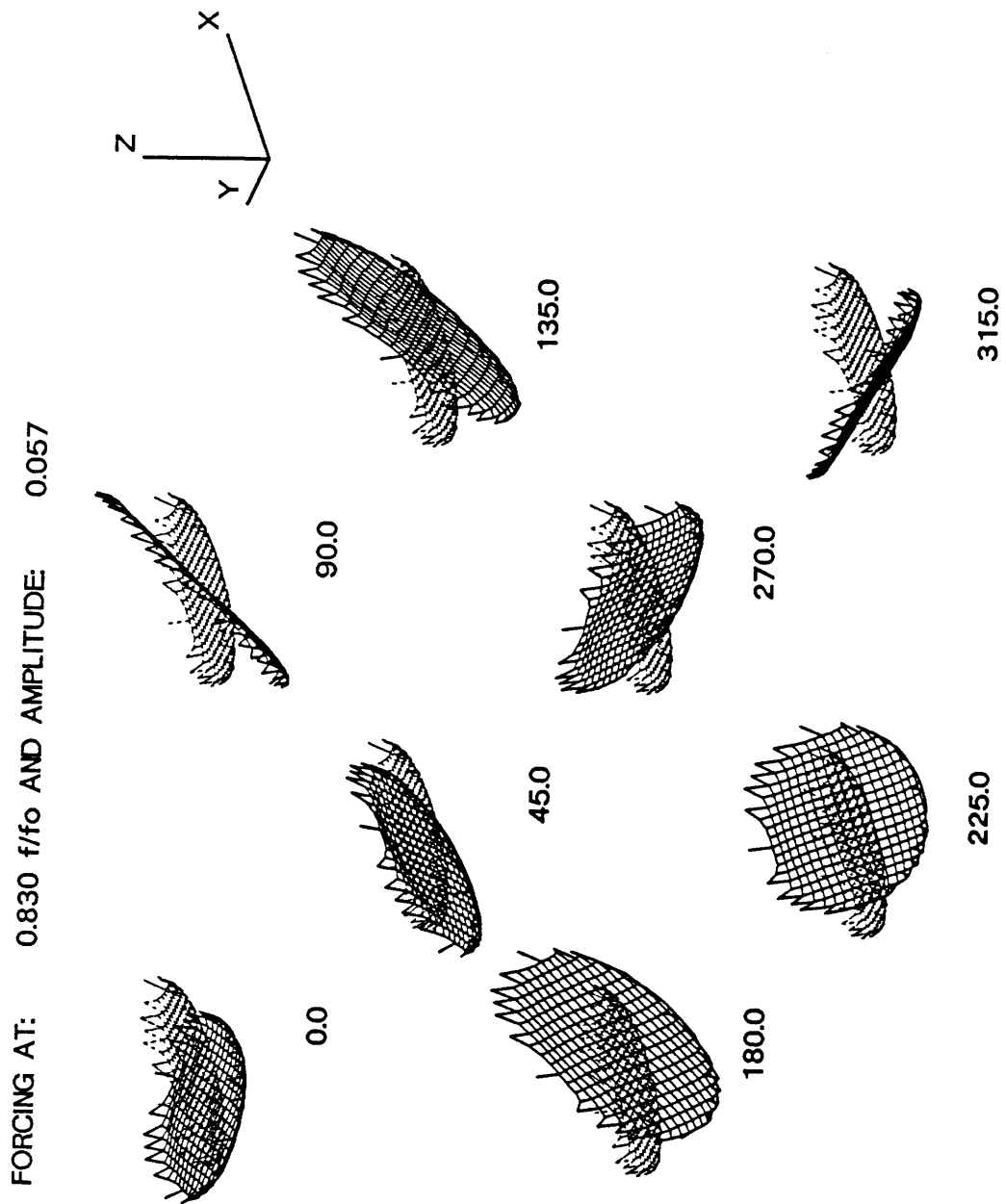
Figure 6.41   Spherical Test S14. Predicted Swirling Motion near First
Resonant Peak.
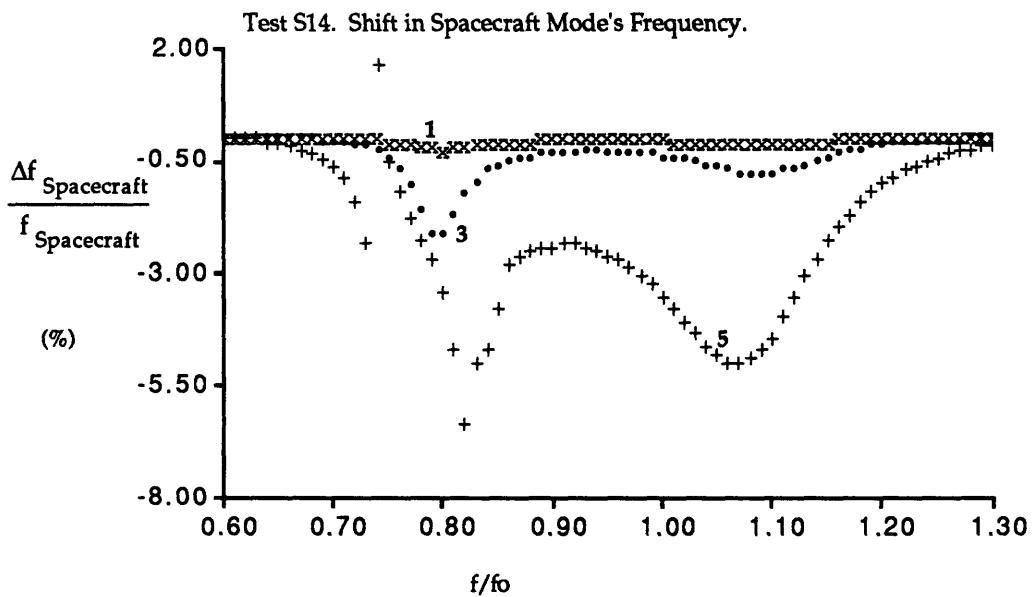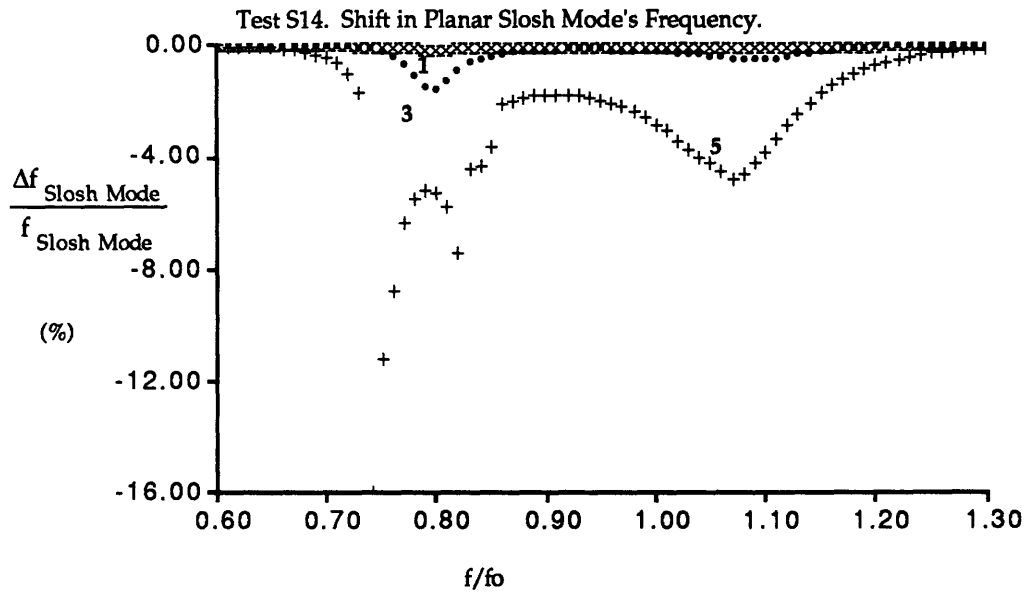
Figure 6.42   Spherical Tank, Test S14.   Predicted Shift in Coupled Frequencies.

(Spherical Tank, Test S14, Bo=117.   **Note:** Results are eigen-characteristics of coupled fluid/spacecraft system: μ=0.16, ν=0.90 and ζ=8.0%.   Model fluid=2% Photoflo/Water solution.   Numbers= Corresponding experimental excitation level.)

287
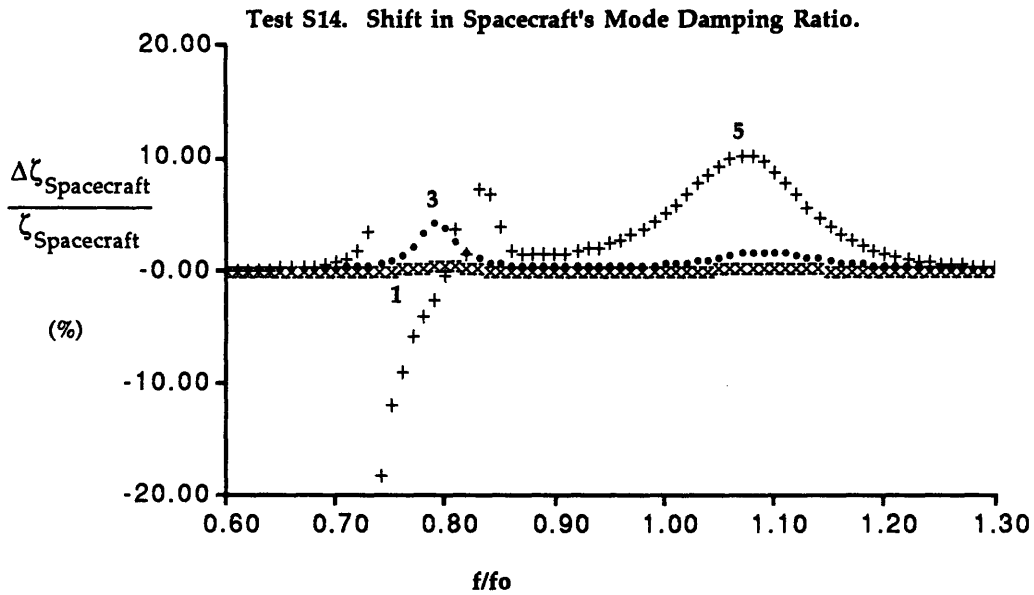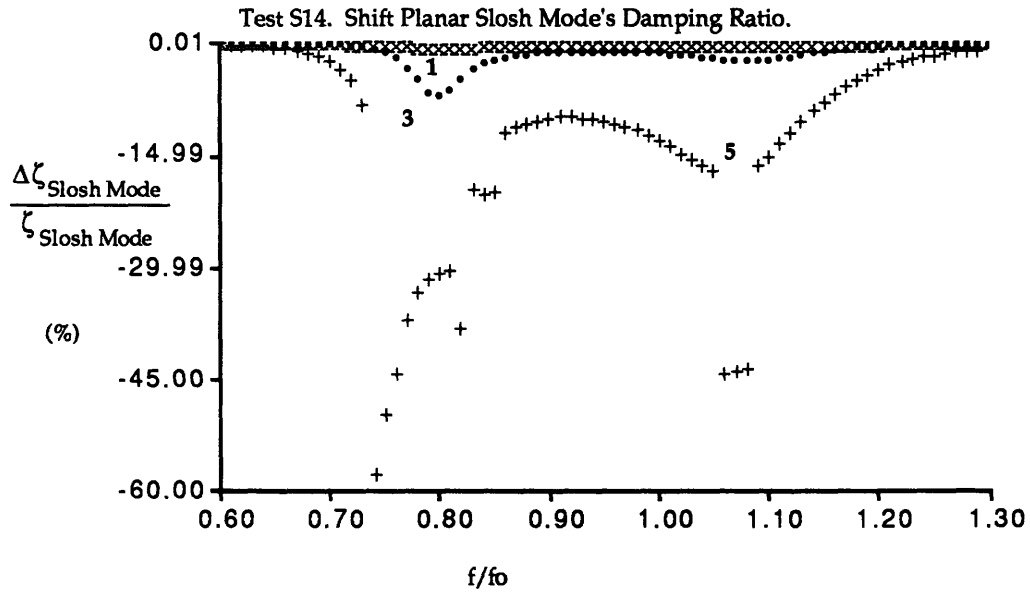
Figure 6.43   Spherical Tank, Test S14. Predicted Shift in Coupled
Damping Ratios.

(Spherical tank, Test S14, Bo=117. Note: Results are eigen-
characteristics of coupled fluid/spacecraft system: μ=0.16, ν=0.90 and
ζ=8.0%. Model fluid=2% Photoflo/Water solution. Numbers=
Corresponding experimental excitation level.)

288

6.3.3 Square Model Tank

The applicability of the analytical model to square tank geometries was investigated by predicting the forced response characteristics of a square experimental test (V16). In this test the direction of the excitation was parallel to one of the tank sides. The ability to handle different excitation angles is investigated in the next section (6.3.4). The coefficients of the nonlinear governing differential equations (Appendix B) were obtained by numerical integration of the mode shapes obtained with finite difference program (see section 6.1.4).

The results are depicted in Fig.s 6.44 and 6.45. The results obtained with the square model are disappointing. The model does predict the shift in the coupled fluid mode's frequency but fails in the region of the spacecraft mode resonance. The major reason for this failure, is the very strong swirling motion behavior observed in the experiments. Even for moderate excitation amplitudes, the motion jumps from the expected planar motion to a very stable swirling motion. The analytical model can predict this swirling motion, as shown in Fig. 46 but a more detailed model of the nonplanar excitation system degree-of-freedom will be required to correctly model this behavior.

In Fig. 6.47 and 6.48, the predicted changes in the coupled resonant (eigen) frequencies and damping ratios for the first two modes are plotted. These graphs predict frequency shifts as high as 24% for the fluid slosh mode and 8% for the spacecraft mode. The maximum predicted shift in damping ratio is 60% for the fluid slosh mode and 24% for the spacecraft mode.
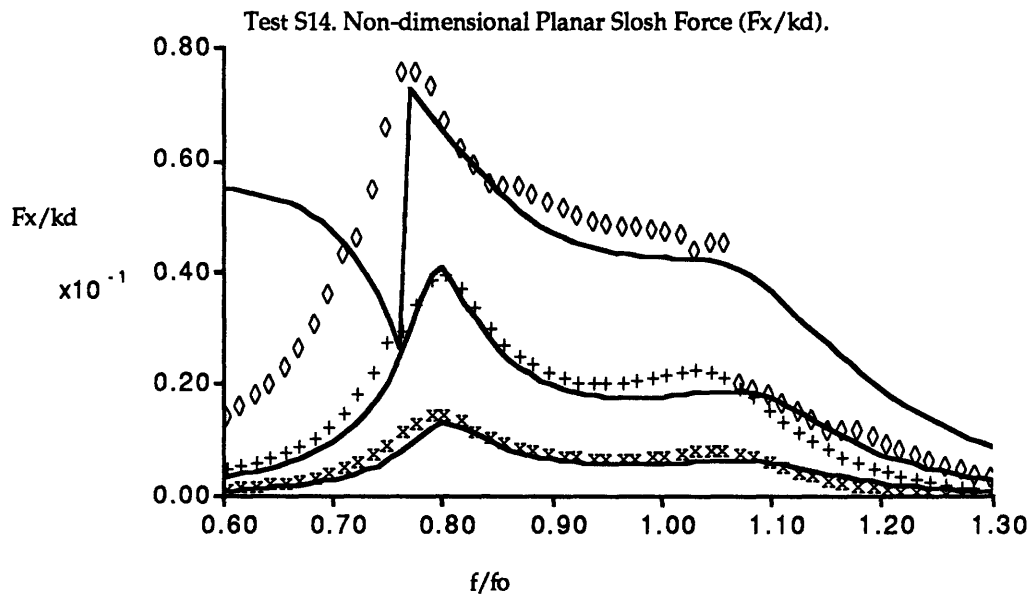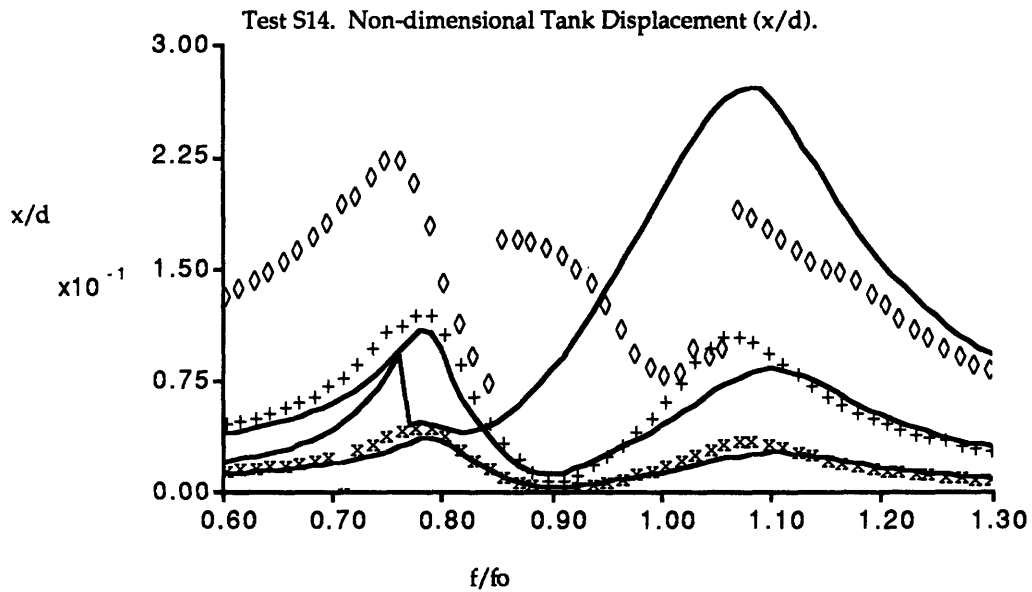
Test V16. Non-dimensional Tank Displacement (x/d).

Test V16. Non-dimensional Tank Displacement (x/d).

Figure 6.44 **Comparison between Analytical and Experimental Results. "Increasing" Excitation Frequency.**

(Square tank, Test V16, Bo=61. Solid lines=Harmonic balance method, Symbols=Experiment. Excitation angle=0°. Coupled system parameters: μ=0.16, ν=0.90 and ζ=8.0%. Model fluid=2% Photoflo/Water solution.)

Test V16. Non-dimensional Tank Displacement (x/d).

Test V16. Non-dimensional Planar Slosh Force (Fx/kd).
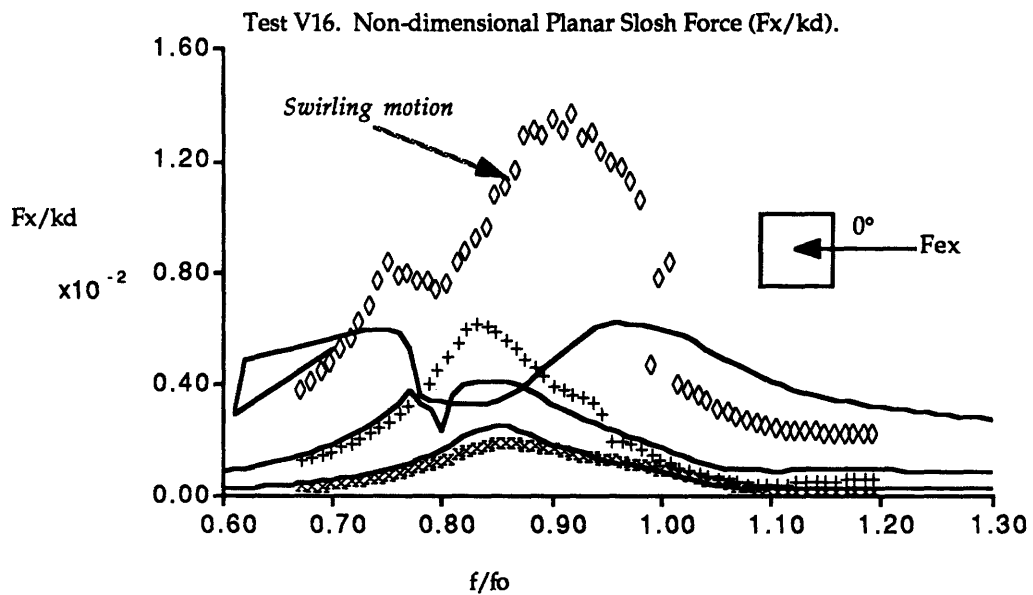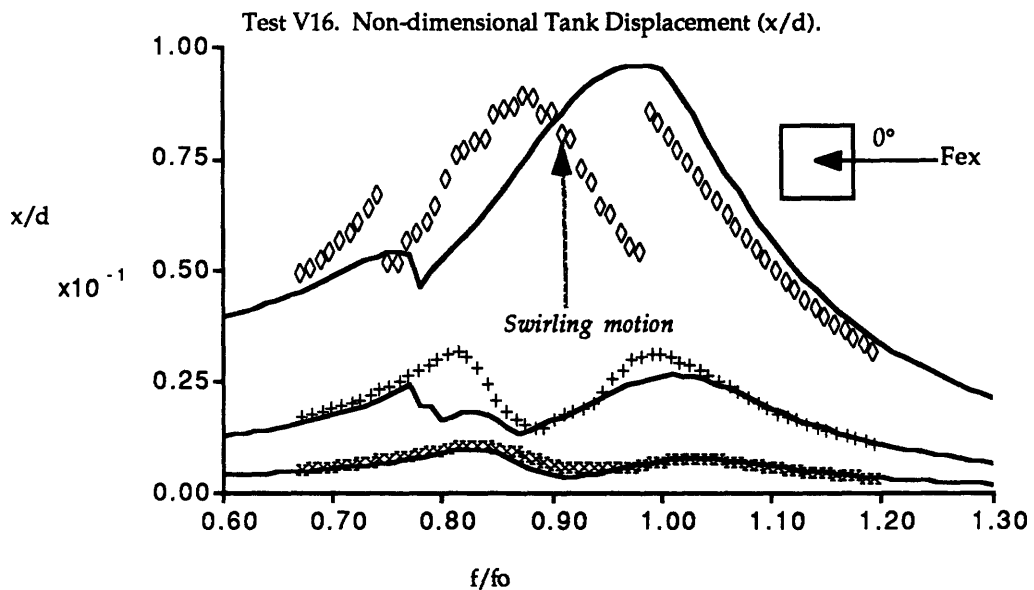
Figure 6.45   Comparison between Analytical and Experimental Results. "Decreasing" Excitation Frequency.

(Square tank, Test V16, Bo=61. Solid lines=Harmonic balance method, Symbols=Experiment.   Excitation angle=0°. Coupled system parameters: μ=0.16, ν=0.90 and ζ=8.0%.   Model fluid=2% Photoflo/Water solution.)

291

Figure 6.46   Square Test V16.   Predicted Swirling Motion near First
Resonant Peak.

Figure 6.47   Square Tank, Test V16.   Predicted Shift in Coupled Frequencies.

(Square tank, Test V16, Bo=61. Excitation angle=0°. Note: Results are eigen-characteristics of coupled fluid/spacecraft system: μ=0.16, v=0.90 and ζ=8.0%.   Model fluid=2% Photoflo/Water solution. Numbers= Corresponding experimental excitation level.)

293
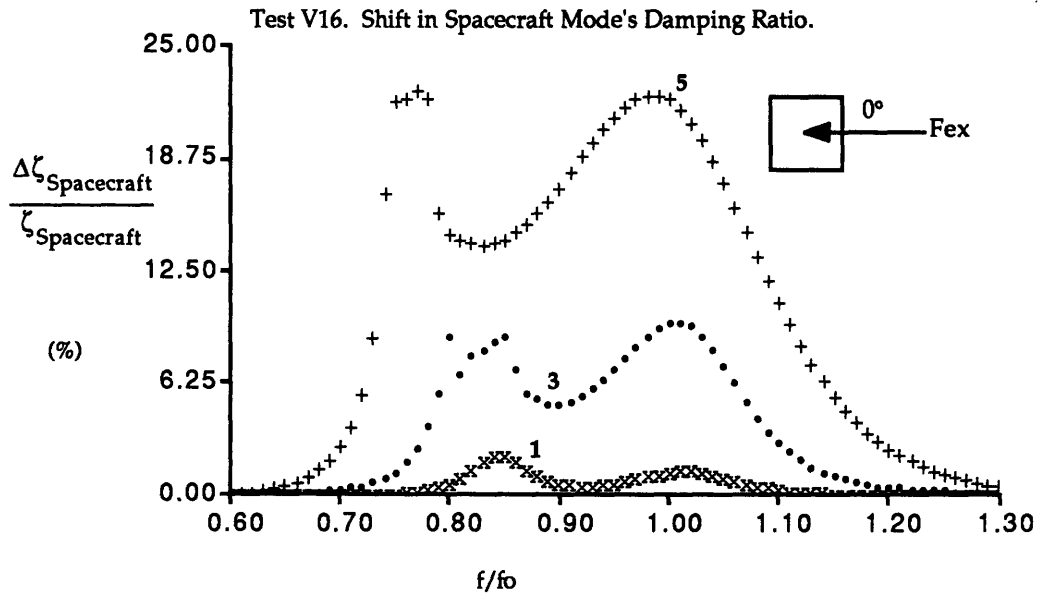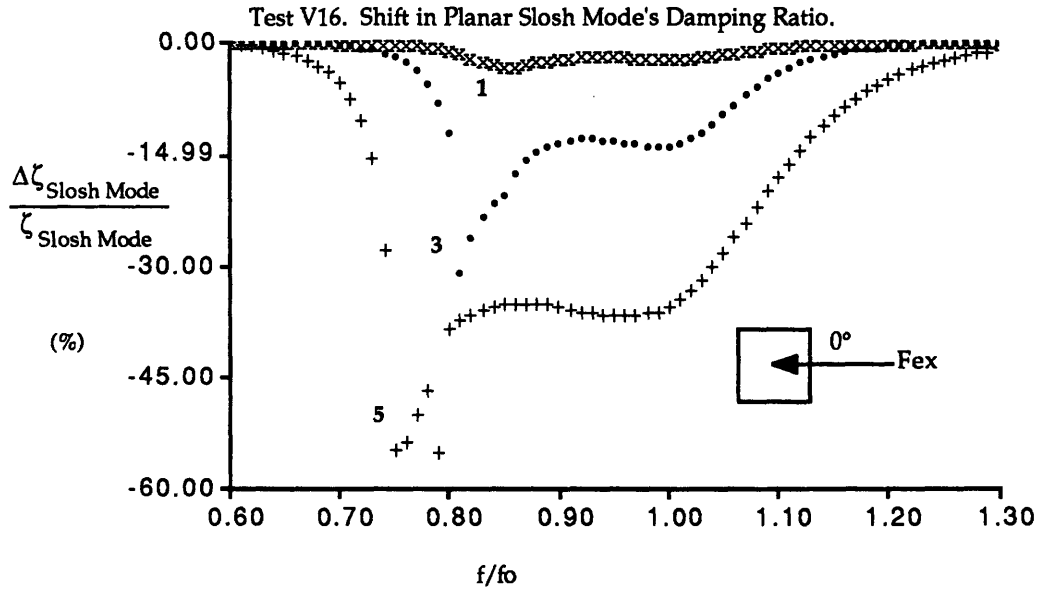
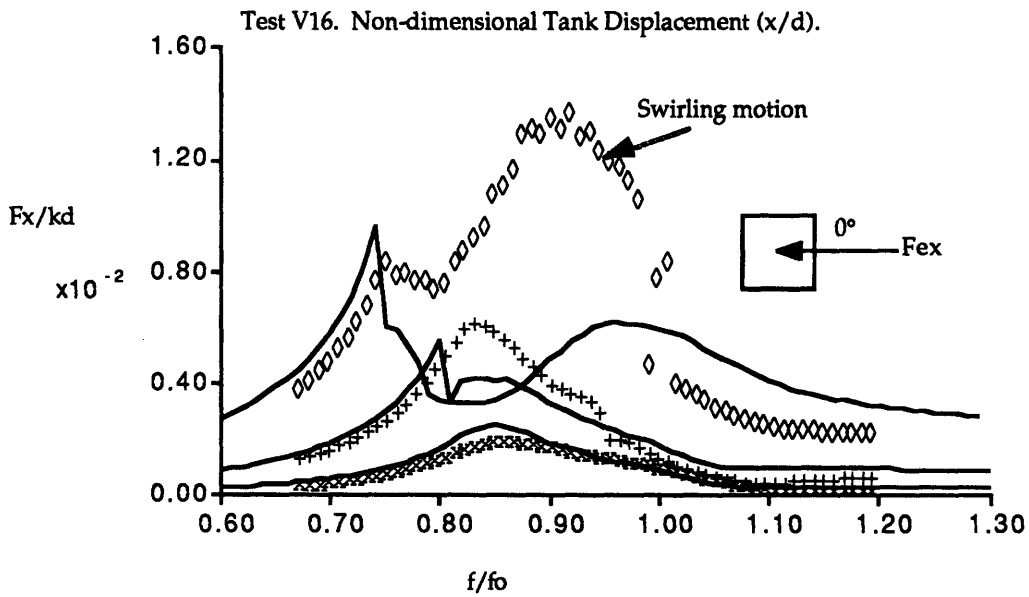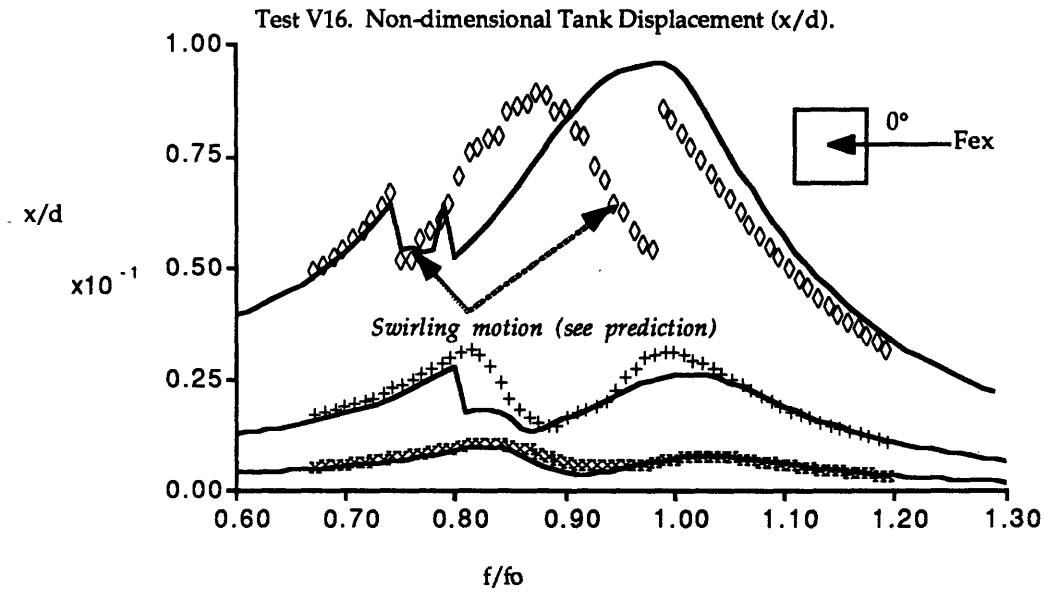**Figure 6.48** **Square Tank, Test V16. Predicted Shift in Coupled Damping Ratios.**

(Square tank, Test V16, Bo=61. Excitation angle=0°. Note: Results are eigen-characteristics of coupled fluid/spacecraft system: μ=0.16, ν=0.90 and ζ=8.0%. Model fluid=2% Photoflo/Water solution. Numbers= Corresponding experimental excitation level.)

6.3.4 Rectangular Model Tank

The ability of the model to predict the forced response characteristics of fluids systems that do not have repeated eigen-modes is studied in this section. The analytical model is used to predict the forced response characteristics of Test R16. In test R16 (see Chapter 5), the direction of excitation is aligned with the long side of the rectangular tank. In predicting the behavior of Test R20, the ability of the analytical model to analyze the characteristics of tanks in which the excitation is not aligned with one of the principle axis, is investigated. In this test, the direction of excitation was aligned at a 60° angle with the short side's axis.

Test R16: The results of the analysis are depicted in Fig. 6.49 (increasing excitation frequency) and Fig. 6.50 (decreasing excitation frequency). The results depicted in these figures clearly illustrate the power of the analytical model to predict the forced response characteristics of tanks which do not have repeated eigen-modes. Tanks without repeated eigen-modes are unlikely to exhibit the swirling motion so frequently observed in tanks with repeated eigen-modes. Energy exchange between spectrally separated modes is less likely than energy exchange between the repeated planar and nonplanar slosh modes of the axi-symmetric tanks.

In Fig. 6.51 and Fig. 6.52, the predicted changes in the coupled resonant (eigen) frequencies and damping ratios for the first two modes are plotted for Test R16. Frequency shifts as high as 11% for the fluid slosh (coupled) mode and 6% for the spacecraft mode are predicted. The maximum predicted shift in damping ratio is 47% for the fluid slosh mode and 15% for the spacecraft mode.

Test R16. Non-dimensional Tank Displacement (x/d).

Test R16. Non-dimensional Planar Slosh Force (Fx/kd).

Figure 6.49   Comparison between Analytical and Experimental Results. "Increasing" Excitation Frequency.

(Rectangular tank, Test R16, Bo=78. Solid lines=Harmonic balance method, Symbols=Experiment. Excitation angle=90°. Coupled system parameters: μ=0.16, ν=0.90 and ζ=8.0%. Model fluid=2% Photoflo/Water solution.)

Test R16. Non-dimensional Tank Displacement (x/d).

Test R16. Non-dimensional Planar Slosh Force (Fx/kd).
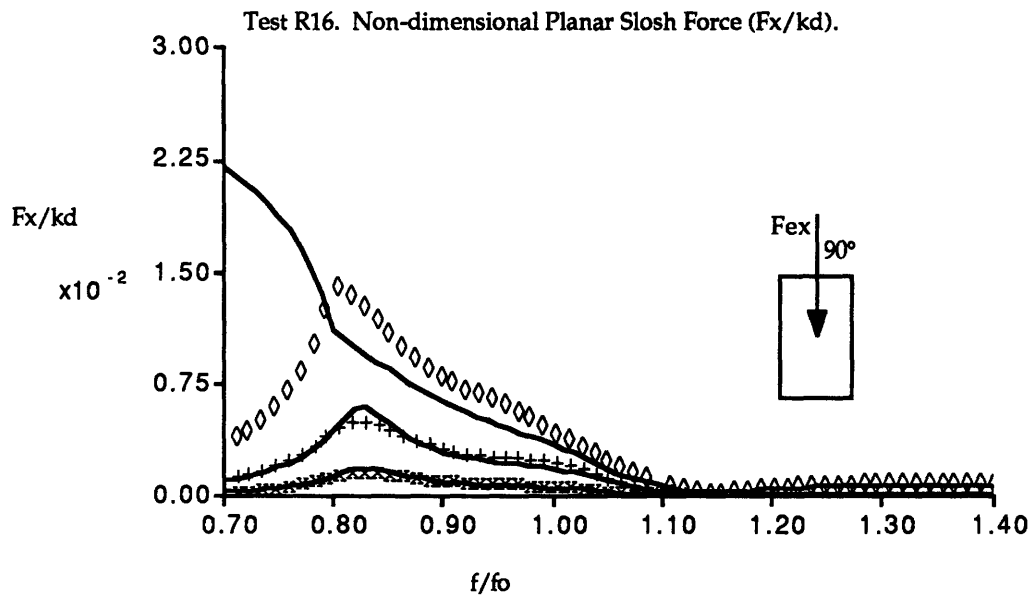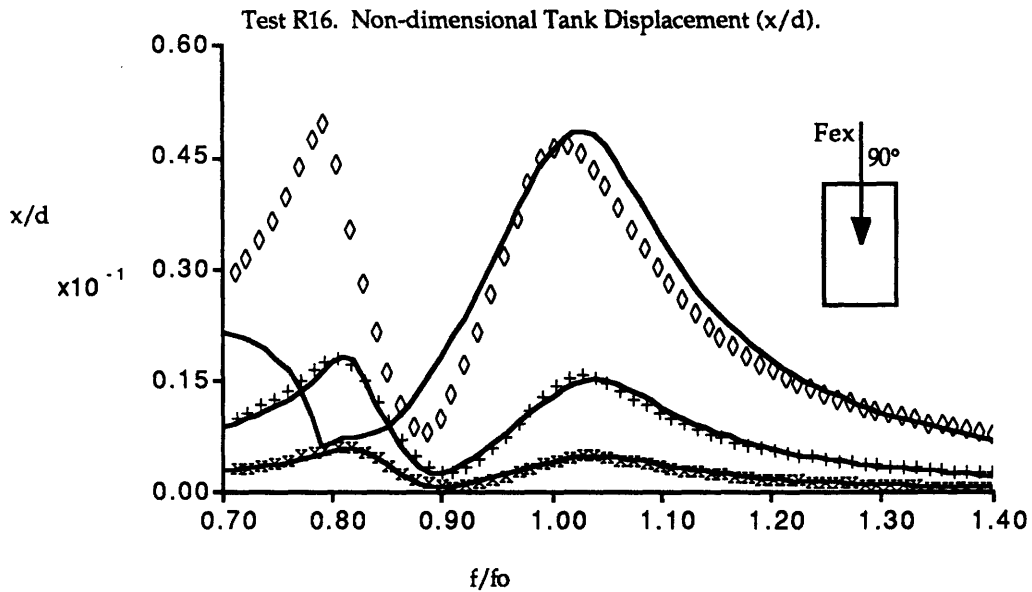
Figure 6.50 **Comparison between Analytical and Experimental Results. "Decreasing" Excitation Frequency.**

(Rectangular tank, Test R16, Bo=78. Solid lines=Harmonic balance method, Symbols=Experiment. Excitation angle=90°. Coupled system parameters: μ=0.16, ν=0.90 and ζ=8.0%. Model fluid=2% Photoflo/Water solution.)
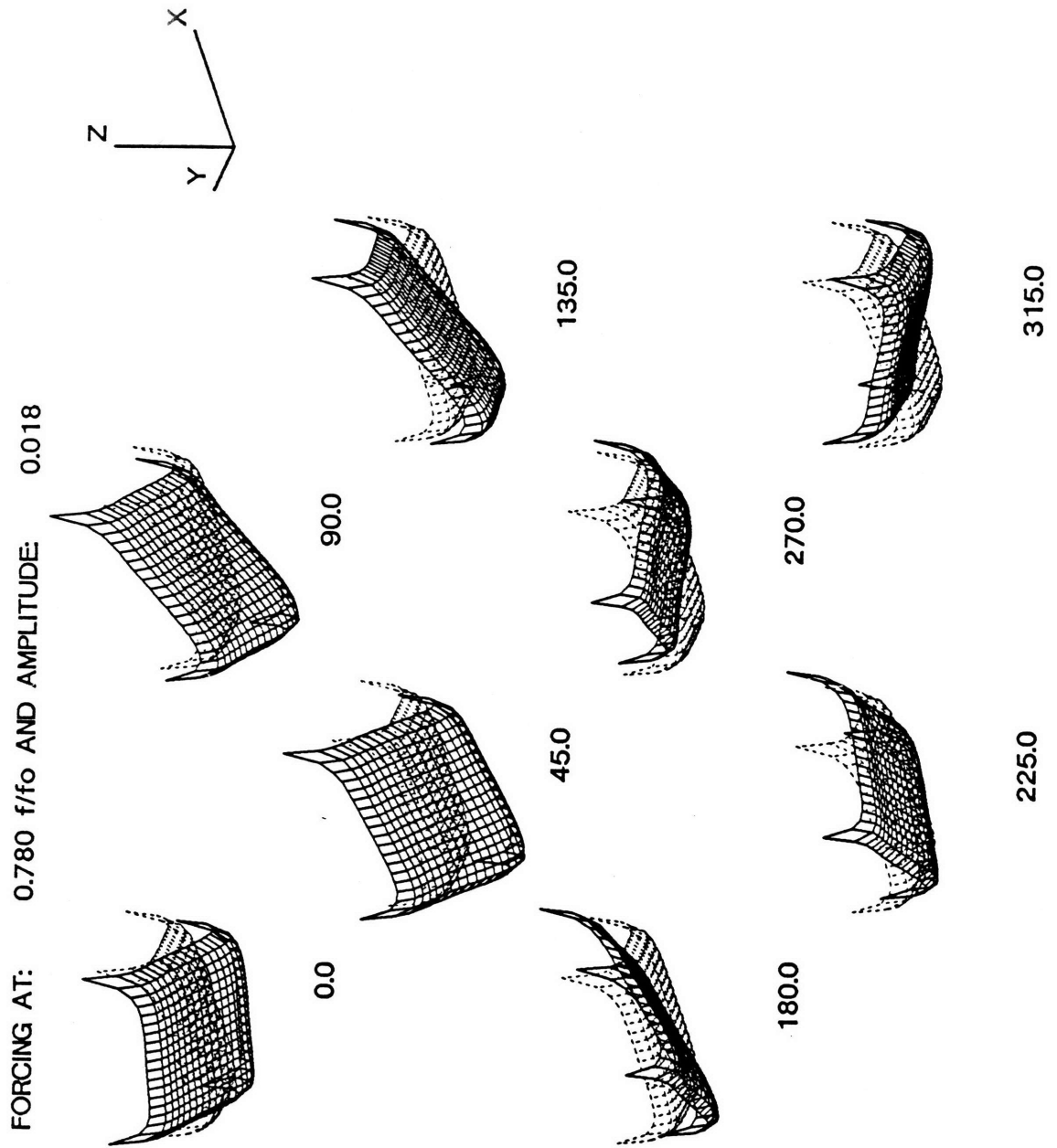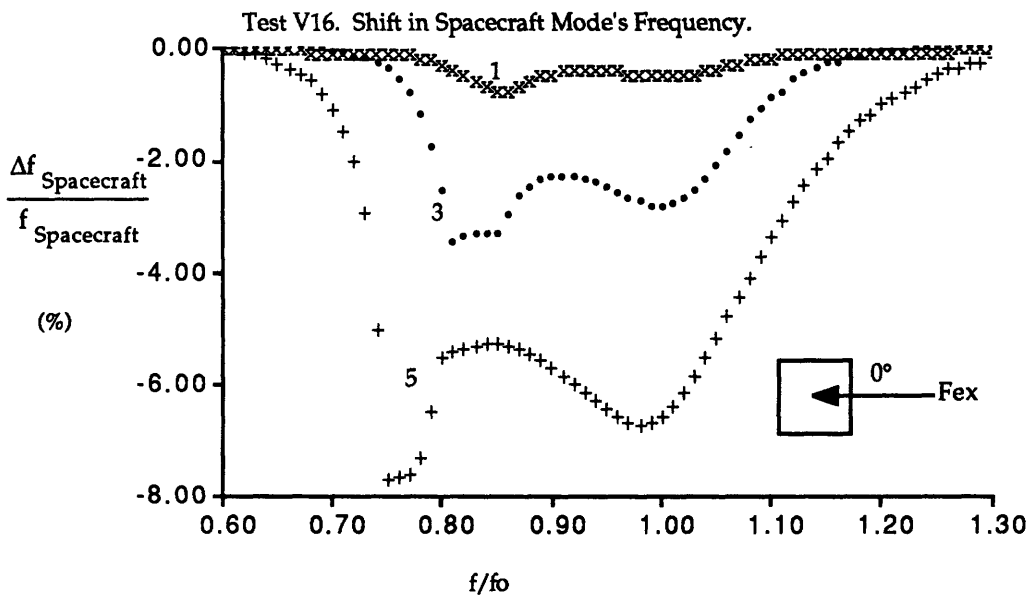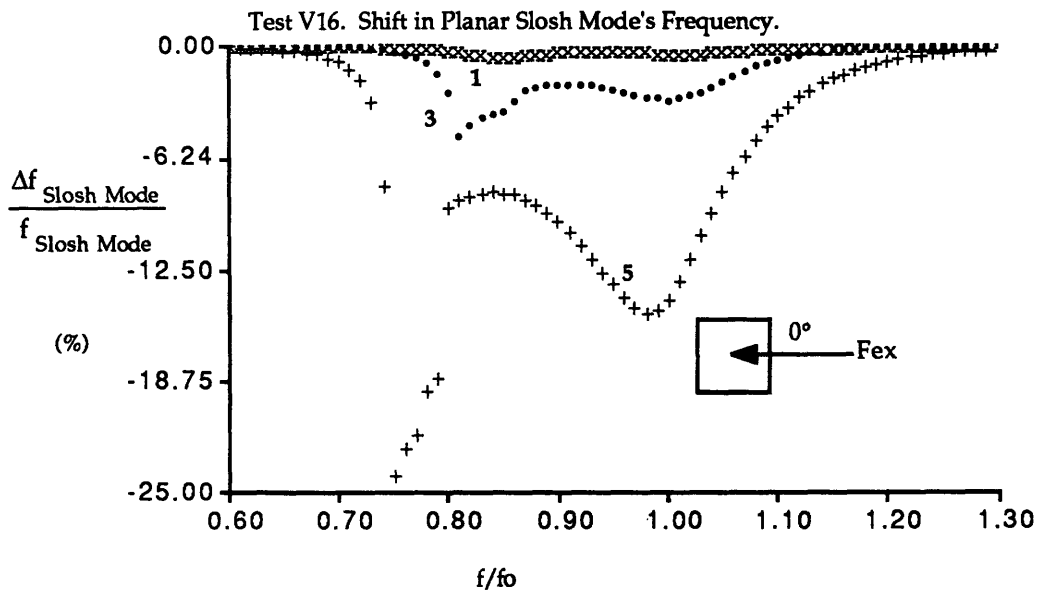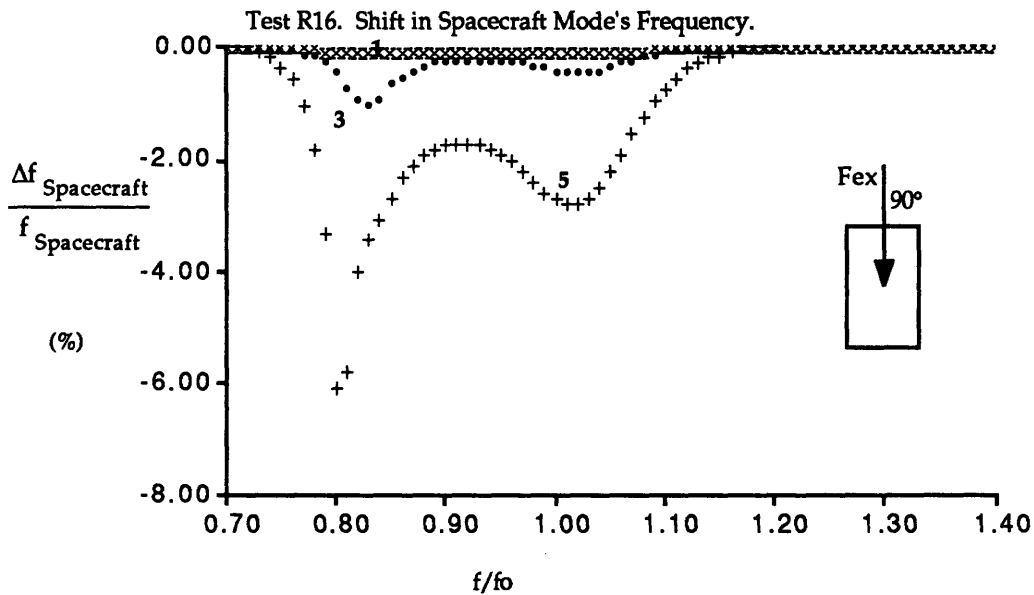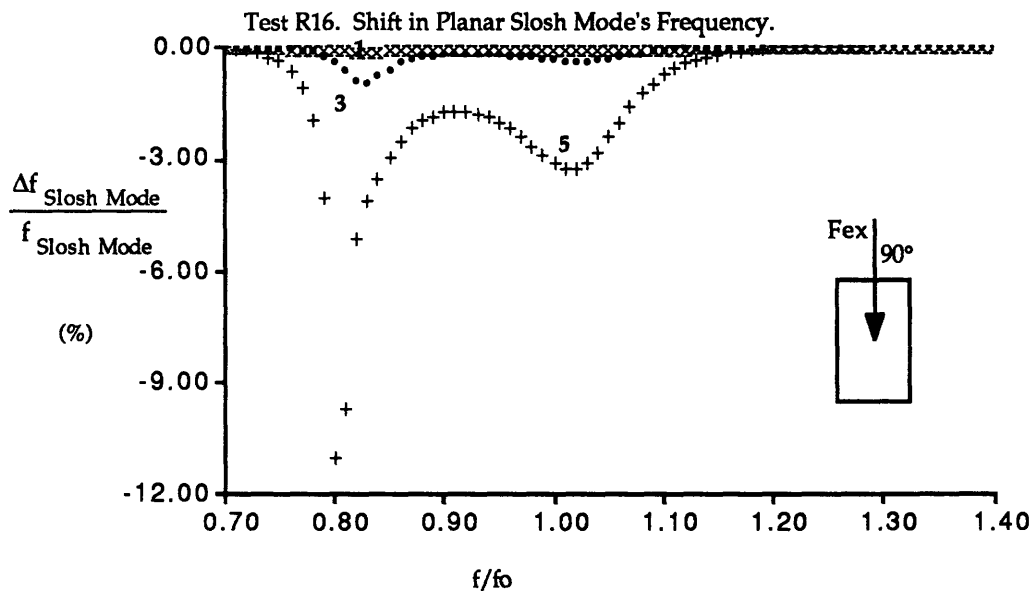
Figure 6.51   Rectangular Tank, Test R16.   Predicted Shift in Coupled Frequencies.

(Rectangular tank, Test R16, Bo=78.   Excitation angle=90°.   **Note:** Results are eigen-characteristics of coupled fluid/spacecraft system: μ=0.16, ν=0.90 and ζ=8.0%.   Model fluid=2% Photoflo/Water solution. Numbers= Corresponding experimental excitation level.)

Test R16. Shift in Planar Slosh Mode's Damping Ratio.

Test R16. Shift in Spacecraft Mode's Damping Ratio.
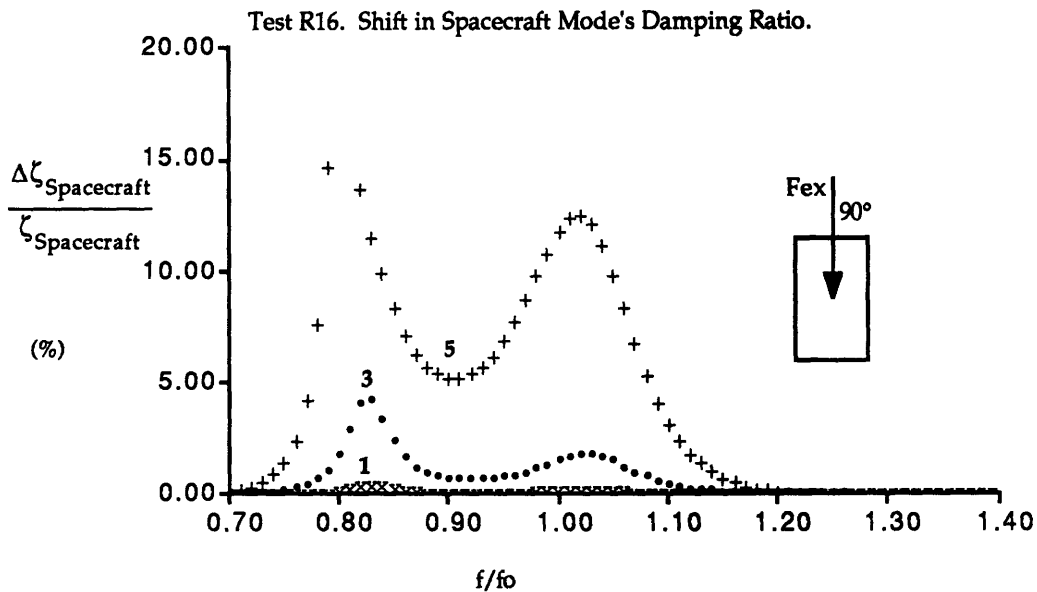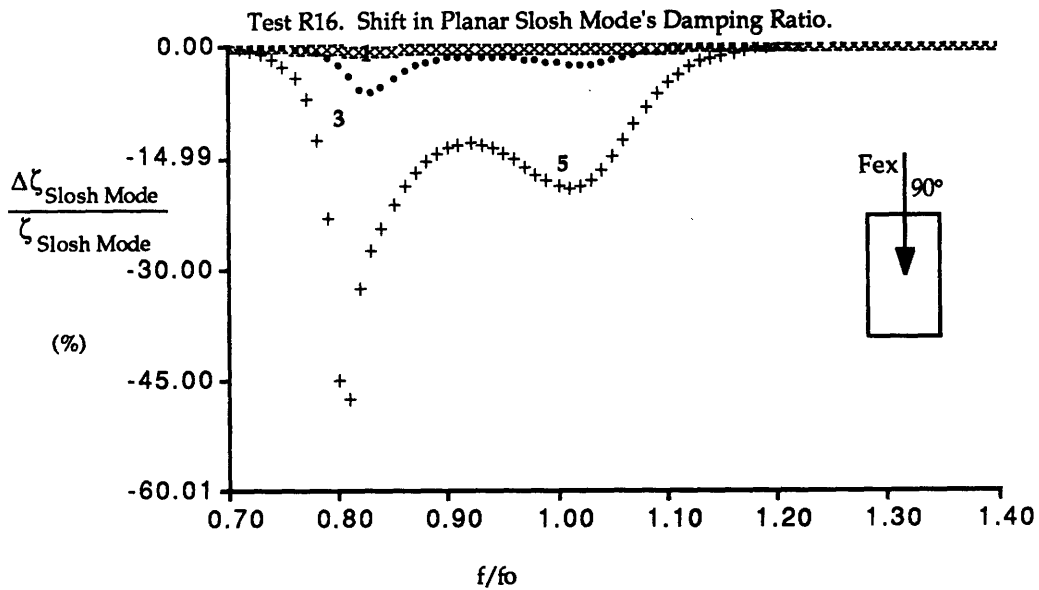
Figure 6.52   Rectangular Tank, Test R16. Predicted Shift in Coupled Damping Ratios.
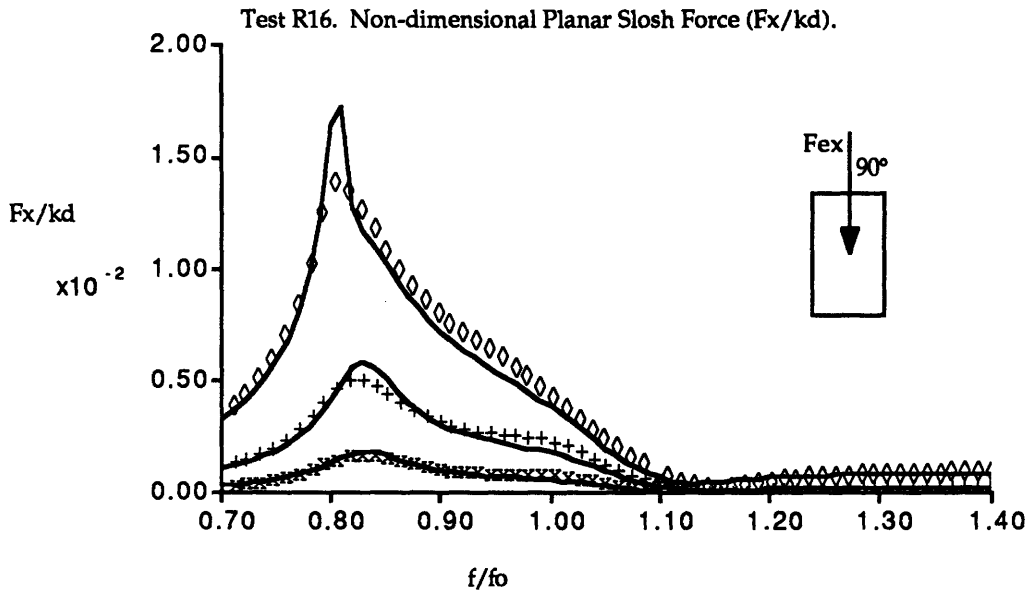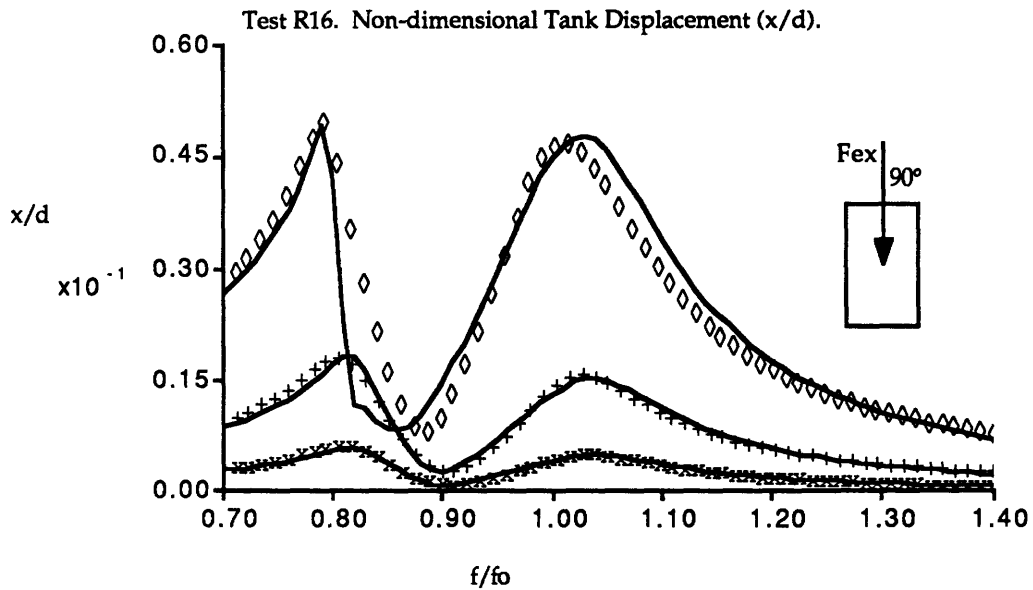
(Rectangular tank, Test R16, Bo=78. Excitation angle=90°. Note: Results are eigen-characteristics of coupled fluid/spacecraft system: μ=0.16, v=0.90 and ζ=8.0%. Model fluid=2% Photoflo/Water solution. Numbers= Corresponding experimental excitation level.)

Test R20: The results for test R20 are depicted in Fig. 6.53 (increasing excitation frequency) and in Fig. 6.54 (decreasing excitation frequency). The results for test confirm the conclusion of the previous section, namely; the analytical model yields good results for systems which do not have repeated eigen-modes. The failure of this model for non-dimensional frequencies above the unity ($f/fo > 1.2$), can be attributed to the number of modes included in the analytical model. In the analytical model only one secondary mode was added for each of the first slosh modes in the long side and short side directions of the rectangular tank. Inclusion of more modes may enable the model to correctly predict the higher forcing frequency behavior. The different results obtained, near the lowest resonance peak, for increasing and decreasing excitation frequencies, indicate that the fluid behavior in this tank also have multiple solutions.

Note that the nomenclature in this test case can be misleading. Planar slosh force means, the slosh force measured in the direction of excitation.

The maximum frequency shift for Test R20, from Fig. 6.55, is 10% for both the coupled fluid slosh mode and the coupled spacecraft mode. The maximum shift in damping ratios (Fig. 56) for this case is; 50% for the fluid slosh mode and 40% for the spacecraft mode.

Test R20. Non-dimensional Tank Displacement (x/d).

Test R20. Non-dimensional Planar Slosh Force (Fx/kd).
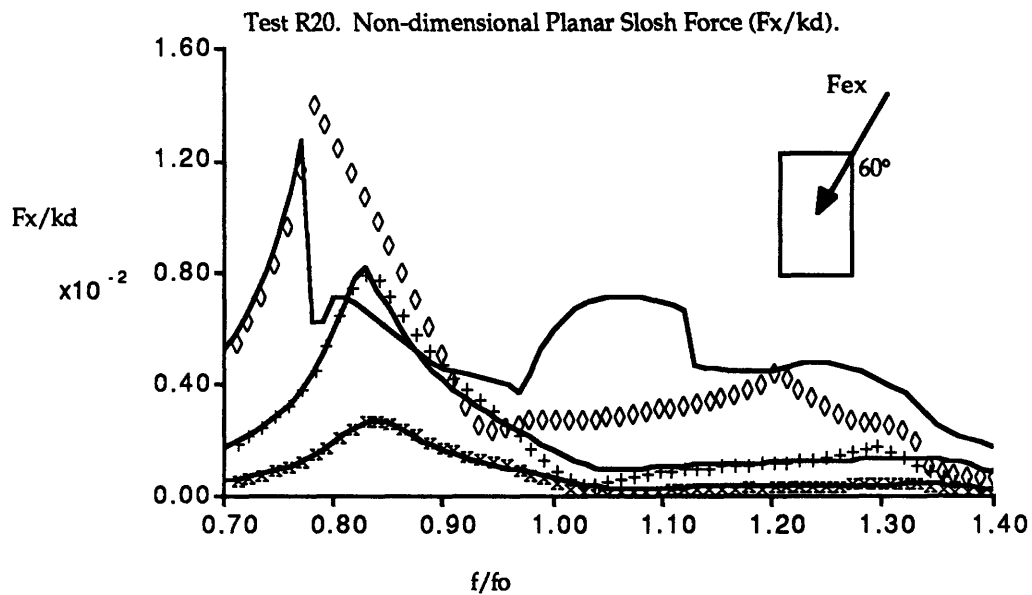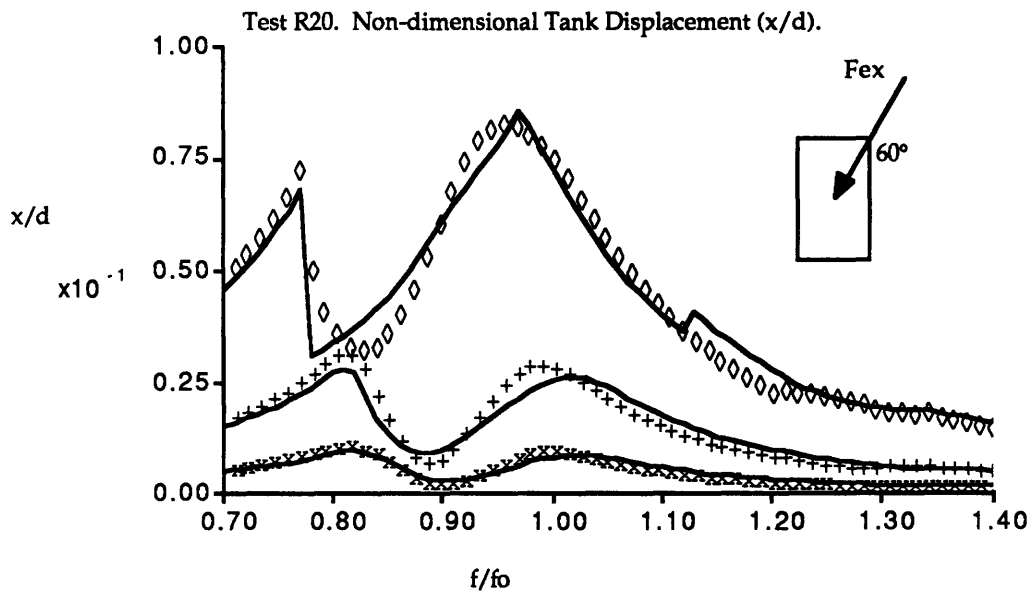
Figure 6.53   Comparison between Analytical and Experimental Results. "Increasing" Excitation Frequency.

(Rectangular tank, Test R20, Bo=78. Solid lines=Harmonic balance method, Symbols=Experiment. Excitation angle=60°. Coupled system parameters: μ=0.16, ν=0.90 and ζ=8.0%.   Model fluid=2% Photoflo/Water solution.)

301

Test R20. Non-dimensional Tank Displacement (x/d).

Test R20. Non-dimensional Planar Slosh Force (Fx/kd).
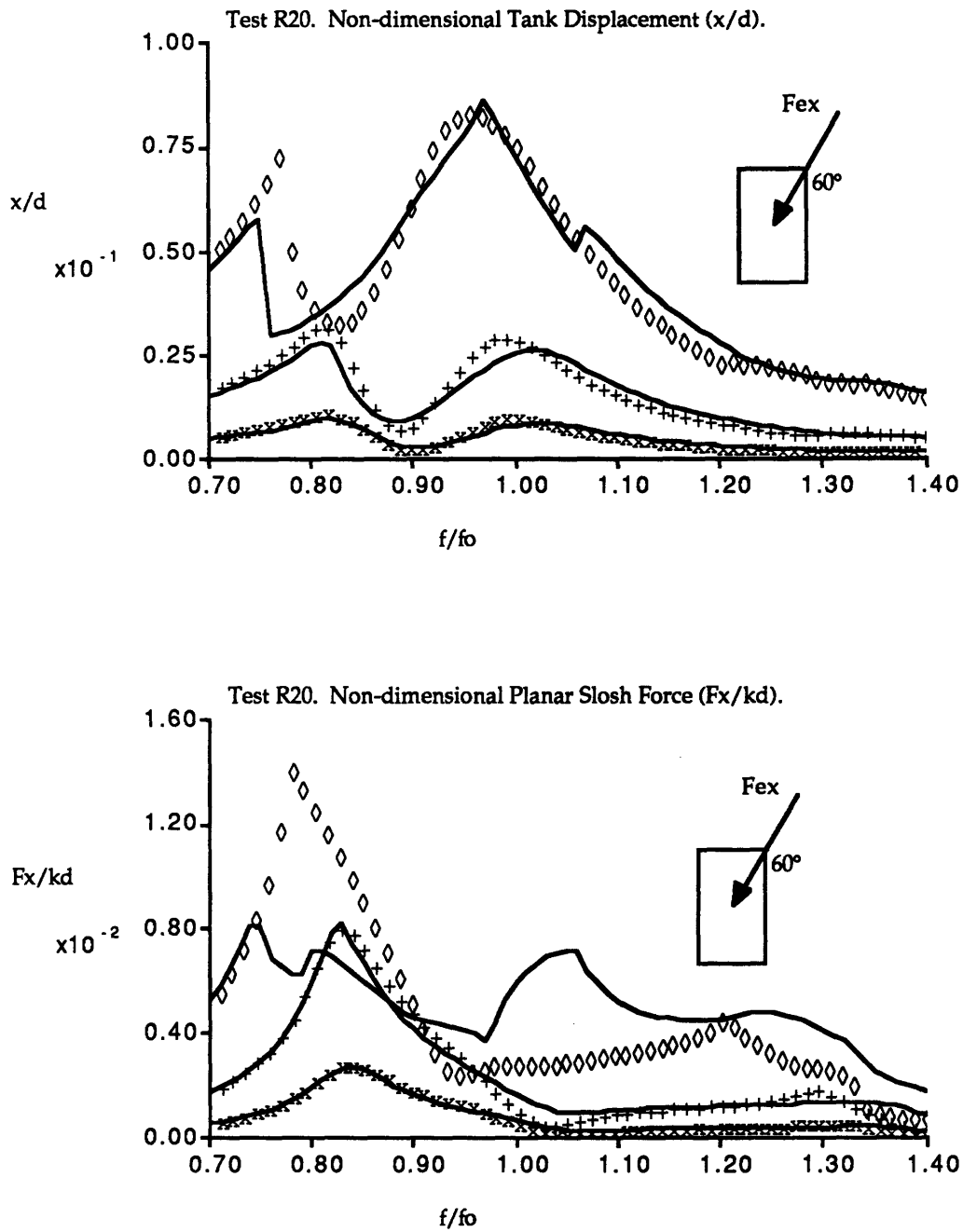
Figure 6.54 **Comparison between Analytical and Experimental Results. "Decreasing" Excitation Frequency.**

(Rectangular tank, Test R20, Bo=78. Solid lines=Harmonic balance method, Symbols=Experiment. Excitation angle=60°. Coupled system parameters: μ=0.16, v=0.90 and ζ=8.0%. Model fluid=2% Photoflo/Water solution.)

302

Test R20. Shift in Lowest Fluid Slosh Mode's Frequency.

Test R20. Shift in Spacecraft Mode's Frequency.
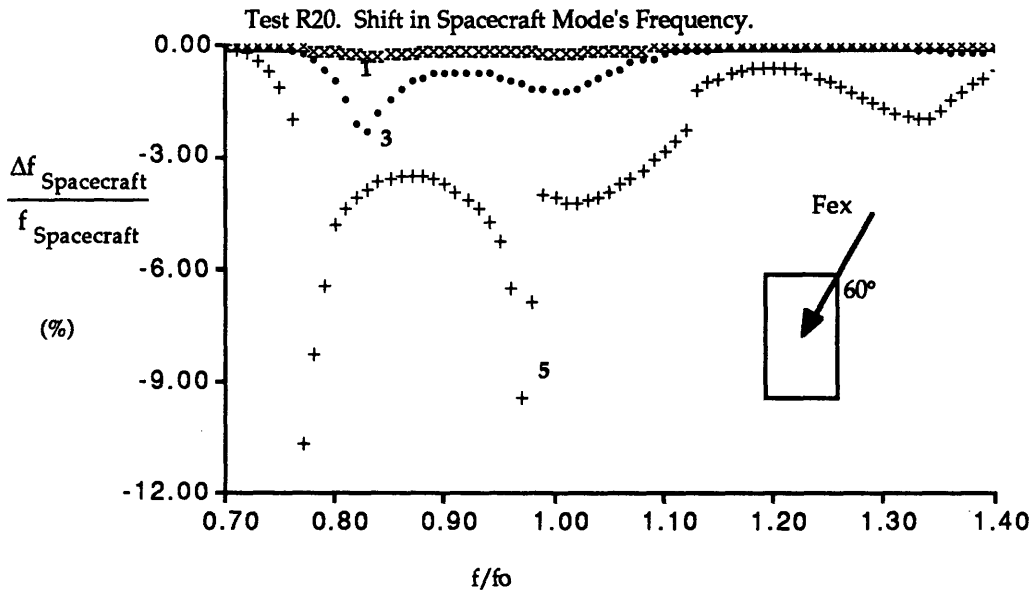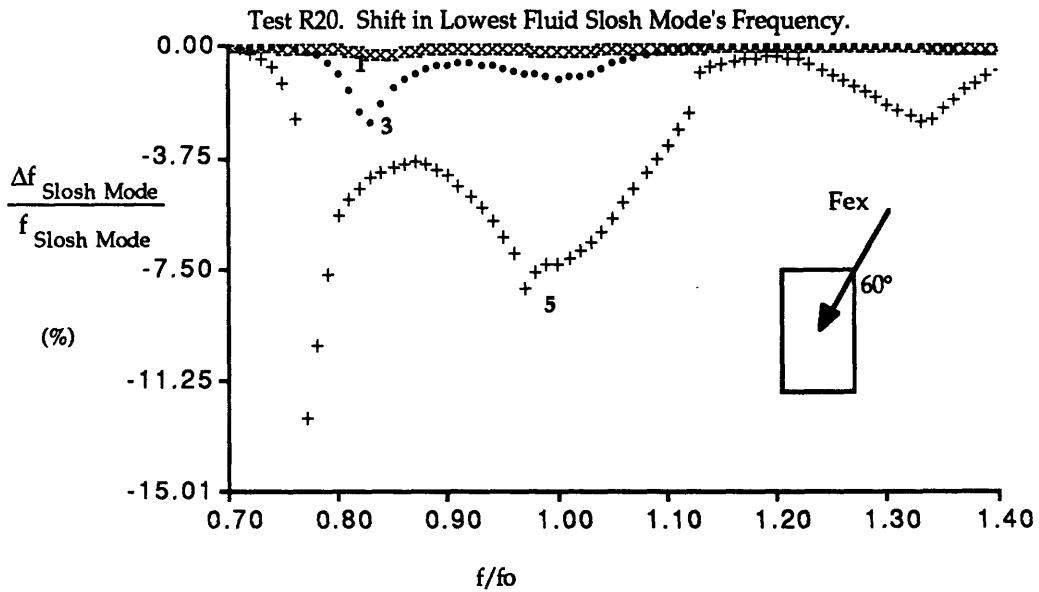
Figure 6.55   Rectangular Tank, Test R20. Predicted Shift in Coupled Frequencies.

(Rectangular tank, Test R20, Bo=78. Excitation angle=60°. Note: Results are eigen-characteristics of coupled fluid/spacecraft system: μ=0.16, v=0.90 and ζ=8.0%. Model fluid=2% Photoflo/Water solution. Numbers= Corresponding experimental excitation level.)
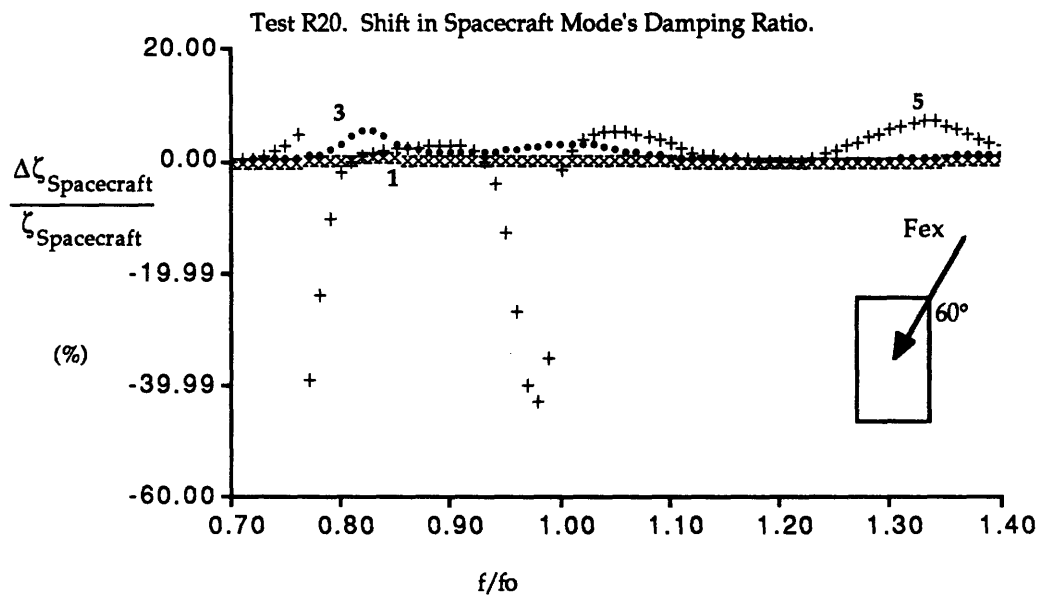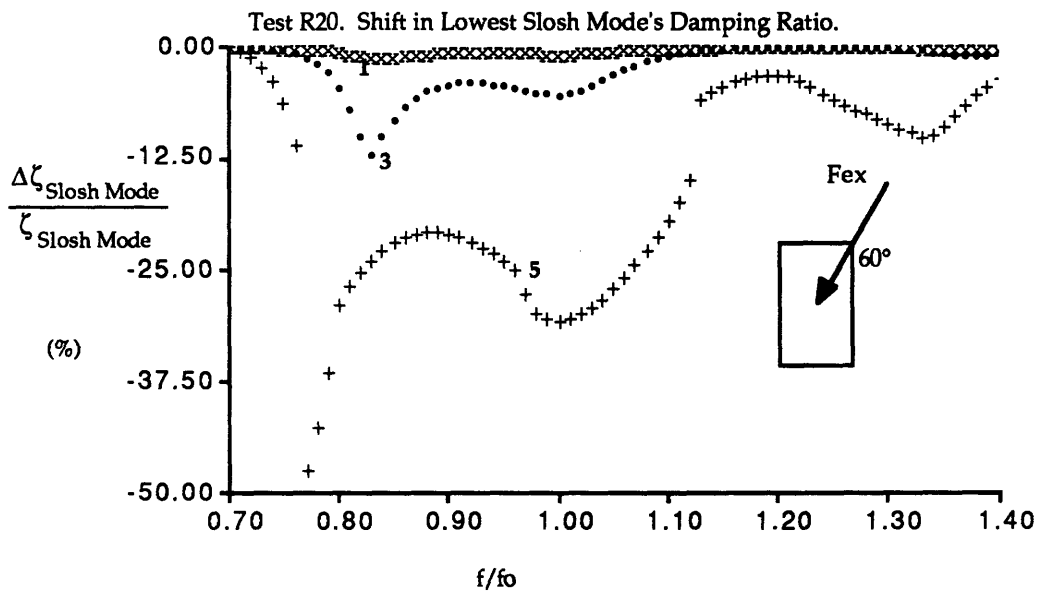
Figure 6.56   Rectangular Tank, Test R20. Predicted Shift in Coupled Damping Ratios.

(Rectangular tank, Test R20, Bo=78. Excitation angle=60°. Note: Results are eigen-characteristics of coupled fluid/spacecraft system: μ=0.16, ν=0.90 and ζ=8.0%. Model fluid=2% Photoflo/Water solution. Numbers= Corresponding experimental excitation level.)

6.4 Summary

The results presented in this chapter shows that the analytical model, developed in Chapter 2, can be used to predict the nonlinear forced response characteristics of fluids in cylindrical, spherical and rectangular (square) tanks. The conclusion is also that the harmonic balance method, combined with the Newton-Raphson solver, can be used to determine the modal amplitudes associated with the harmonic term and that numerically determined eigen-mode shapes can be used as assumed modes without a significant loss in accuracy.

The nonlinear model of the coupled fluid/spacecraft system consistently predicts the experimentally observed shift in eigen-frequencies but failed to predict the correct shape of the forced response curves in the region where the system exhibits swirling motions. A better identification and model of the nonplanar characteristics of the excitation system will be required to correctly model the fluid response in this region. It is also possible that the measured response is the "average" of more than one stable state and it will be necessary to find all the solutions of the nonlinear system, to correctly predict the forced response characteristics.

Chapter 7

Conclusions and Recommendations

This chapter first presents a brief summary of the work accomplished along with the conclusions that can be drawn from the experimental and analytical results. Finally possible future research directions are presented.

7.1　Summary

This research studied the nonlinear dynamics of spacecraft interacting with contained fluids. A general nonplanar model describing the fluid/spacecraft dynamics was developed and verified by comparing analytical with experimental results. The analytical and experimental results contributed to a general understanding of the complex behavior of fluid/spacecraft dynamic systems.

The nonlinear model of the fluid/spacecraft system, developed in this research, is accurate to third order in terms of the fluid motion amplitudes. In a assumed mode approach, the kinematic free surface boundary condition, posed as a variational problem, provided the relationship between the assumed free surface generalized coordinates and the fluid flow potential coordinates. Given the generalized coordinate description of the fluid, linear and nonlinear capillary forces, along with the standard energy terms, are included in the fluid Lagrangian. The method is valid for tanks with straight and parallel walls but the spherical tank analytical results, presented in this document, showed that this method can be extended to tanks of more complex geometry.

The nonlinear set of equations obtained by applying Lagrange's principle to the fluid Lagrangian, was solved for the forced response characteristics by numerical implementation of the harmonic balance method. The nonlinear time independent equations provided by this method was solved using an Inverse Iteration technique as well as a Newton-Raphson solver.

Three scaled fluid tank models, spherical, square and rectangular, were experimentally tested to determine the nonlinear characteristics of

fluids contained in these types of tanks. The tanks were scaled to yield Bond numbers representative of actual spacecraft fluid tanks. Both uncoupled (tank alone) and coupled forced planar excitation tests were performed. In the coupled tests, the fluid slosh force was fed to an analog simulation of a spacecraft control mode, thus coupling the fluid and spacecraft dynamics. The effects of system mass ratio, frequency ratio and damping ratio on the nonlinear coupled behavior was investigated.

The analytical model was verified by comparing analytical with experimental results for a few selected test cases. In addition to the three tank models mentioned in the previous paragraph, the experimental cylindrical tank results obtained by Peterson [1987] were also used in the verification process.

7.2 Conclusions

The following important conclusions, supported by both the analytical and experimental results, give insight as to the nonlinear dynamics of coupled fluid/spacecraft systems:

- The coupled system, contrary to the linear modal superposition result, exhibits strong nonlinear behavior for both the fluid slosh mode and the spacecraft mode.

- All the fluid model tanks exhibit softening behavior. This behavior was observed in both the uncoupled and the coupled tests. In the coupled tests, the simulated spacecraft mode also exhibited this softening behavior.

- The observed nonlinear behavior was very dependent on the amplitude of the fluid motion. Defining the equivalent diameter (four times the surface area divided by the surface circumference) as the characteristic dimension, it was found that wave heights > 5% of the equivalent diameter show noticeable nonlinear behavior. Vibrations exceeding 10-15% of the equivalent diameter showed multi-valued responses (characterized by a jump phenomenon).

- In the axi-symmetric tanks (cylindrical, spherical and square) a jump phenomenon was observed. At the jump the fluid motion changed from the expected linear planar motion to a combined planar/nonplanar swirling motion. This behavior was not observed in the rectangular model tank where energy exchange between the spectrally separated first and second fluid slosh modes is unlikely.

- The complete nonplanar model developed in this research can predict the nonlinear forced response behavior and the experimentally observed swirling motion. However, a better model of the nonplanar characteristics of the excitation system will be required to accurately predict the forced response characteristics when swirling occurs.

- Convective (kinematic) nonlinearities are important for all Bond numbers and capillary nonlinear effects must be included for Bond numbers as high as 60.

- For all the study models, the nonlinearities were the strongest for frequency ratios between 0.8 and 1.0, as well as for those coupled systems with lighter mass fractions. The nonlinearities were also stronger for light damping of the spacecraft mode.

In addition to these specific conclusions on the fluid behavior , the analytical results also showed that a linear model is only accurate for very low fluid motion amplitudes and that the nonplanar model developed in this research can predict all the important nonlinear characteristics. The research also demonstrated that numerically determined linear eigen-modes can be used in the assumed mode model without a significant loss of accuracy. The Harmonic balance method, combined with the Newton-Raphson solver, yields forced characteristics close to the measured results. The ability of the Harmonic balance method to predict the shape of the forced response curves is a significant improvement over the multiple time scales method used by Peterson [1987].

Although this research did not attempt to identify Bond number effects on the fluid dynamic characteristics, it is important to note that a decrease in Bond numbers will increase the nonlinear characteristics of the fluid/spacecraft system. Two factors contribute to this effect, the first being

that as the Bond number decreases, the nonlinear capillary forces increases. The second is that as the Bond number decreases, the secondary modes, essential to the fluid dynamics, are closer to the critical coupled system frequencies, thus strongly effecting the motion. This conclusion may require more assumed modes to be included for low Bond numbers cases. Considering the size of the Bond number-dependent nonlinear coefficients , it can be concluded that Bond number effects must be included for Bond numbers as high as 60. This conclusion is supported by the work of Satterlee and Reynolds [1966]. They concluded that if Bond number effects are ignored in cylindrical tanks, for Bond numbers less than 60, the error in the fluid slosh frequencies will exceed 5%. Note that the Bond number of the study models, considered in this research, ranged from 33 to 117.

The nonplanar model of the coupled fluid/spacecraft system consistently predicts the experimentally observed shift in eigen-frequencies but failed to predict the correct shape of the forced response curves in the region where the system exhibits swirling motions. Although the nonplanar model can predict swirling motion, a better model of the nonplanar characteristics of the excitation system will be required to correctly model the fluid response in this region. It is also possible that the response is the "average" of chaotic motion and it will be necessary to find all the solutions of the nonlinear system in order to correctly predict the forced response characteristics.

This research suggests the following guidelines to avoid nonlinear response in a fluid/spacecraft coupled system, namely;

- Avoid the linear coupled eigen-frequencies close to unity and if possible place the spacecraft mode before the first fluid slosh mode. The spacecraft mode will act as a second order filter that will reduce the fluid slosh amplitude and thus the nonlinear behavior of the system.

- Avoid containers with repeated eigen-modes. These tanks exhibit very dominant and stable swirling motions. The repeated modes can be separated by either changing the tank geometry or by installing baffles [Abramson, 1966].

- Avoid low mass fractions for which the excitation of the spacecraft mode more efficiently resonates the fluid.

- Design optimal controllers with severe penalties on the fluid motion degree-of-freedom. This may degrade performance but would avoid nonlinear behavior of the system.

The experimental results of this research contributes to the already vast database available on the subject of fluid sloshing and the nonlinear, nonplanar analytical model developed can serve as a valuable prediction tool for structural and control engineers. The method can not only predict the forced response characteristics of fluid/spacecraft systems, but can also be used to design and verify control designs.

7.3   Recommendations

The results of this research suggest several future research directions. The first problem to be addressed is to improve the solution of the nonlinear system equations obtained from the Harmonic balance method. The continuation method [Ricther and DeCarlo, 1983] may find all the solutions and thereby predict the multi-valued response observed at higher excitation levels. Implementation of this method will require careful manipulation of the nonlinear equations but the results may justify the effort.

The Harmonic balance method used in this research, yields only the harmonic response amplitudes of the harmonically forced system. This method cannot predict super- or sub-harmonic resonances. The describing function method or the least squares fitting technique, both of which were discussed in this research, may be used to characterize these responses. The least squares fitting technique may succeed in predicting transient behavior which is of importance in control applications.

The analytical method developed in this research is formulated to facilitate the use of numerically determined eigen-mode shapes. The value of the analytical method can be demonstrated by applying the method to tanks with internal baffles or to tanks of more complex geometry. The effect of internal baffles can be included by using the linear eigen-modes of the baffled tank. The power of this method can also be enhanced by expanding the theory to account for flexible containers. An additional set of

generalized coordinates, describing the flexible motion of the tank walls, can be related to the fluid surface motion set of generalized coordinates by applying the wall boundary conditions. The present experimental setup and flexible container can be used to verify such a model.

References

Abramson, H. N., Chu, W. and Garza, L.R., "Liquid Sloshing in Spherical Tanks," *AIAA Journal,* Vol. 1, No. 2, pp. 384-389, Feb. 1963.

Abramson, H. N., ed., *"Liquid Sloshing in Spherical Tanks,"* NASA-SP106, 1966.

Agrawal, B. N. and James, P., "Energy dissipation due to liquid slosh in spinning spacecraft," *Dynamics and Control of Large Flexible Spacecraft Symposium,* 439-452, 1981.

Agrawal, B.N., "Interaction between Liquid Propellant Slosh Modes and Attitude Control in a Dual-spin Spacecraft," Proceedings of the 28 th Structures, Structural Dynamics and Materials Conference, Monterey, CA, pp. 774-780, AIAA Paper 87-0928, 1987.

Anderson, D.A., Tannehill, J.C., and Pletcher, R.H., *Computational Fluid Mechanics and Heat Transfer,* McGraw-Hill Book Company, Washington, 1984.

Arfken, G., *Mathematical Methods for Physicists,* Academic Press, New York, 1970.

Arnold, V.I., *Geometrical Methods in the Theory of Ordinary Differential Equations,* Springer-Verlag, Berlin, 1983.

Berry, R.L., Demchak, L.J., Tegart, J.R. and Craig, M.K., "An Analytical Tool for Simulating Large Amplitude Propellant Slosh," Proceedings of the 22 th Structures, Structural Dynamics and Materials Conference, Atlanta, GA, pp. 55-61, AIAA Paper 81-0500, 1981.

Balindra, T., Ang, K.K., Paramasivam, P. and Lee, S.L., "Free Vibration Analysis of Cylindrical Liquid Storage Tanks," *Int. J. Mech. Sci.,* Vol. 24, No. 1, pp. 47-59, 1982.

Bauer, H.F. and Eidel, W., "Non-linear Hydroelastic Vibrations in Rectangular Containers," *Journal of Sound and Vibration,* 1988, 125(1), pp. 93-114.

Blevins, R.D., *Formulas for Natural Frequency and Mode Shape*, Robert E. Krieger Publishing Company, Florida, 1987.

Chu, W., "Fuel Sloshing in a Spherical Tank Filled to an Arbitrary Depth," *AIAA Journal*, Vol. 2, No. 11, pp. 1972-1979, Nov. 1964.

Daugherty, R.L., and Franzini, J.B., *Fluid Mechanics with Engineering Applications*, Mcgraw-Hill, London, 1977.

Hildebrand, F. B., *Advanced Calculus for Applications*. Prentice-Hall, Englewood Cliffs, New Jersey, 1976.

Hildebrand, F. B., *Methods of Applied Mathematics*, Prentice-Hall, Englewood Cliffs, New Jersey, 1965.

Hutton, R. E., "An investigation of resonant, nonlinear, nonplanar free surface oscillations of a fluid," NASA TN D-1870, 1963.

Hughes, P.C., *Spacecraft Attitude Dynamics* , John Wiley and Sons, New York, 1986.

Ibrahim, R.A., and Barr, A.D.S., 1975a, "Autoparametric resonance in a structure containing a liquid, Part I: Two Mode Interaction", *Journal of Sound and Vibration*, Vol. 42, No. 2, pp. 159-179, 1975.

Ibrahim, R.A., and Barr, A.D.S., 1975b, "Autoparametric resonance in a structure containing a liquid, Part II: Three Mode Interaction", *Journal of Sound and Vibration*, Vol. 42, No. 2, pp. 181-200, 1975.

Ibrahim, R.A., and Heinrich, R.T., "Experimental Investigation of Liquid Sloshing under Parametric Random Excitation," Proceedings of the 28 th Structures, Structural Dynamics and Materials Conference, Monterey, CA, AIAA Paper 87-0712, 1987.

Kanan, D.D., "A Model for Nonlinear Rotary Slosh in Propellant Tanks," *Journal of Spacecraft*, Vol. 24, No. 2, pp. 169-177, 1987.

Kaplan, M.H., *Modern Spacecraft Dynamics and Control*, John Wiley and Sons, New York, 1976.

Keller, H.B., Rabinowitz, P.H., (ed.), *"Applications of Bifurcation Theory - Numerical Solution of Bifurcation and Nonlinear Eigenvalue Problems,"* Academic, pp. 359, 1977.

Komatsu, K., "Non-linear Sloshing Analysis of Liquid in Tanks with Arbitrary Geometries," *Int. Journal of Non-linear Mechanics*, Vol. 22, No. 3, pp. 193-207, 1987.

Kozlov, L.F. and Nikitina, G.D., "Possibility of Using Quasistationary Models in Calculating Free Oscillations of Fluids," Institute of Hydromechanics, Academy of Sciences of the Ukranian SSR, Kiev. (translated from *Prikladnaya Mekhanika* vol 15, no 12, pp. 95–100), 1979.

Kuttler, J.R., and Sigillito, V.G., "Sloshing of Liquids in Cylindrical Tanks," *AIAA Journal*, Vol. 22, Feb. 1984, pp. 309-311..

Lapidus, L., and Pinder, G.F., *Numerical Solution of Partial Differential Equations in Science and Engineering*, John Wiley and Sons, New York, 1982.

Limarchenko, O. S., "Variational formulation of the problem on the motion of a tank with fluid," *Dopov. Akad. Nauk Ukrsr. Ser. A (USSR)* no. 10, pp. 903–907. in Ukranian, 1978a.

Limarchenko, O. S., "Direct method for solution of nonlinear dynamics problems for a tank with fluid," *Dopov. Akad. Nauk Ukrsr. Ser. A (USSR)* no. 11, pp. 999–1002. in Ukranian, 1978b.

Limarchenko, O. S., "Variational–method investigation of problems of nonlinear dynamics of a reservoir with a liquid," *Soviet Applied Mechanics* (translated from *Prikladnaya Mekhanika* vol 16, no 1, pp. 99–105), 1980.

Limarchenko, O. S., "Effect of Capillarity on the Dynamics of a Container–Liquid System," *Soviet Applied Mechanics* (translated from *Prikladnaya Mekhanika* vol 17, no 6, pp. 124–128), 1981.

Limarchenko, O. S., "Direct method of solving problems on the combined spatial motions of a body–fluid system," *Soviet Applied Mechanics* (translated from *Prikladnaya Mekhanika* vol 19, no 8, pp. 77–84), 1983a.

Limarchenko, O. S., "Application of a variational method to the solution of nonlinear problems of the dynamics of combined motions of a tank with fluid," *Soviet Applied Mechanics* (translated from *Prikladnaya Mekhanika* vol 19, no 11, pp. 100–104), 1983b.

Luke, J. C., "A variational principle for a fluid with a free surface," *J.Fluid Mechanics*, Vol. 27:2 pp. 395-397, 1967.

Miles, John W., "Internally resonant surface waves in a circular cylinder," *J.Fluid Mech.*, Vol. 149 pp. 1-14, 1984a.

Miles, John W., "Resonantly forced surface waves in a circular cylinder," *J.Fluid Mech.*, Vol. 149 pp. 15-31, 1984b.

Miles, John W., "Resonant, nonplanar motion of a stretched string," *J. Acoust. Soc. Am.*, Vol. 75:5 pp. 1505-1510, 1984c.

Miles, John W., "Resonant motion of a spherical pendulum" *Physica*, Vol. 11D, no 3, pp. 309-323, 1984d.

Miles, John W., "Parametrically Excited Solitary Waves," *Journal of Fluid Mechanics*, Vol. 148, pp. 451-460, 1984e.

Miles, John W., "Nonlinear surface waves in closed basins," *J.Fluid Mech.*, Vol. 75, part 3, pp. 419-448, 1976.

Miles, John W., "Surface-wave damping in closed basins," *Proc. Roy. Soc. Lon. A*, Vol. 297, pp. 459-475, 1967.

Miles, John W., "Stability of forced oscillations of a spherical pendulum," *Quart. Appl. Math*, Vol. 20, pp. 21-32, 1962.

Moiseev, N.N. and Petrov, A.A., "The Calculation of Free Oscillations of a Liquid in a Motionless Container," Advances in Applied Mathematics, Vol. 9, 1966.

Myshkis, A.D., Babskii, V.G., Kopachevskii, N.D., Slobozhanin, L.A. and Tyuptsov, L.A., *Low-Gravity Fluid Mechanics*, Springer-Verlag, New York, 1987.

Nakayama, T. and Washizu, K., "Nonlinear Analysis of Liquid Motion in a Container Subjected to Forced Pitching Oscillations," *Int. Journal for Numerical Methods in Engineering,* Vol. 15, pp. 1207-1220, 1980.

Nakayama, T. and Washizu, K., "The Boundary Element Method Applied to the Analysis of Two-dimensional Nonlinear Sloshing Problems," *Int. Journal for Numerical Methods in Engineering,* Vol. 17, pp. 1631-1646, 1981.

Nayfeh, A.H., *Introduction to Perturbation Techniques,* John Wiley and Sons, New York, 1981.

Nayfeh, A.H. and Mook, D. T., *Nonlinear Oscillations,* John Wiley and Sons, New York, 1979.

Peterson, L.D., Crawley E.F. and Hansman, R.J., "The Nonlinear Coupled Dynamics of Fluids and Spacecraft in Low Gravity," MIT Space Systems Laboratory Report, No. SSL 22-87, 1988.

Press, W.J., Flannery, B.P., Teukolsky, S.A. and Vetterling, W.T., *Numerical Recipes - The Art of Scientific Computing,* Cambridge University Press, 1987.

Rayleigh, Lord, "Deep water waves, progressive or stationary, to the third order of approximation," *Proc. Roy. Soc. Lon. A,* Vol 91, pp. 345-353, 1915.

Reynolds, W. C., Saad, M. A. and Satterlee, H. M., "Capillary Hydrostatics and Hydrodynamics at Low g," TR LG-3, Mechanical Engineering Department, Stanford University, 1964.

Reynolds, W.C. and Satterlee, H.M., "Liquid Propellant Behavior at Low and 0-G," in Abramson, 1966.

Richter, S.L. and DeCarlo, R.A., "Continuation Method: Theory and Application," *IEEE Transaction on Automatic Control,* Vol. AC-28, No. 6, June 1983.

Salzman, J.A. and Masica, W.J., "An Experimental Investigation of the Frequency and Viscous Damping of Liquids during Weightlessness", NASA TND-5058, 1969.

Satterlee, H.M. and Reynolds, W.C., "The Dynamics of the Free Liquid Surface in Cylindrical Containers Under Strong Capillary and Weak Gravity Conditions," Stanford University TR-LG-2, 1964.

Sayar, B.A., and Baumgarten, J.R., "Pendulum Analogy for Nonlinear Fluid Oscillations in Spherical Containers," *Journal of Applied Mechanics*, Vol. 48, pp. 769-772, 1981.

Schilling, U., and Siekmann, J., "Numerical Calculation of the Natural Frequencies of a Sloshing Liquid in Axial Symmetrical Tanks under Strong Capillary and Weak Gravity Conditions," *Israel Journal of Technology*, Vol. 19, pp. 44-50, 1981.

Simmons, G.F., *Differential Equations- with Applications and Historical Notes*, McGraw Hill, 1972.

Stavrindis, C., "Evaluation of Techniques for Determination of Loads due to Fluid-Structure Interaction --- Spacecraft Structures," Final Report, Erno Raumfahrtechnik G.M.B.H., NTIS HC A11/MF A01, June 1985.

Tegart, J.R., Berry, R.L. and Craig, M.K., "Measurement of Forces due to Liquid Motion in Propellant Tanks," Proceedings of the 22 th Structures, Structural Dynamics and Materials Conference, Atlanta, GA, p. 295-302, AIAA Paper 81-0566, 1981.

Whitham, G.B., "Non-linear Dispersion of Water Waves," *Journal of Fluid Mechanics*, Vol. 27, part 2, pp. 399-412, 1967.

Yeh, G.C.K., "Free and Forced Oscillations of a Liquid in a Ax-Symmetric Tank at Low-Gravity Environments," *Journal of Applied Mechanics*, Vol. 34, No. 1, pp. 23-28, March 1967.

Yu, B. Nash, W.A., and Kirchhoff, "A Nonlinear Analysis of Sloshing in Circular Cylindrical Tanks by Perturbation Method," Special Volume on Fluid/Structure Vibrations and Liquid Sloshing, ASME Pressure Vessels and Pipes Conference San Diego, June 1987.

Appendix A

Nonlinear Fluid/Spacecraft Equations of Motion

This appendix gives the nonlinear equations of motion obtained by applying Lagrange's Principle (eq. 2.101) to the Fluid Lagragian developed in Chapter 2. In the last section of this chapter, the equations of motion are non-dimensionalized by appropriate scaling. Appendix B gives the nonlinear matrixes (non-dimensionalized) for a truncated planar and a nonplanar model.

A1.0 Nonlinear Equations of Motion

The governing equations obtained by applying Lagrange's Principle to the Fluid Lagrangian are:

Equation 1:

$$(m + m_F)\ddot{x} + m_{xq}\ddot{q}_1 + c_x\dot{x} + k_x x = F_{ex} \tag{A1}$$

Equation 2:

$$(m + m_F)\ddot{y} + m_{yq}\ddot{q}_2 + c_y\dot{y} + k_y y = F_{ey} \tag{A2}$$

Equation 3:

$$m_{xq}\ddot{x} + \frac{\rho}{2}\sum_{m=1}^{N}\left(a_{m1}^{(0)} + a_{1m}^{(0)}\right)\ddot{q}_m + c_{q_1}\dot{q}_1 +$$

$$\frac{\rho}{2}\left(\sum_{m=1}^{N}\sum_{n=1}^{N}\left(a_{1mn}^{(1)} + a_{m1n}^{(1)}\right)\ddot{q}_m q_n + \left(a_{1mn}^{(1)} + a_{m1n}^{(1)} - a_{mn1}^{(1)}\right)\dot{q}_m\dot{q}_n\right) +$$

$$\frac{\rho}{2}\left(\sum_{m=1}^{N}\sum_{n=1}^{N}\sum_{r=1}^{N}\left(a_{1mnr}^{(2)} + a_{m1nr}^{(2)}\right)\left[\ddot{q}_m q_n q_r + \dot{q}_m q_n \dot{q}_r\right]\right) +$$

$$\frac{\rho}{2}\left(\sum_{m=1}^{N}\sum_{n=1}^{N}\sum_{r=1}^{N}\left(a_{1mnr}^{(2)} + a_{m1nr}^{(2)} - a_{mn1r}^{(2)} - a_{mnr1}^{(2)}\right)\dot{q}_m\dot{q}_n q_r\right) +$$

$$\rho g \sum_{m=1}^{N}\iint_S \xi_1\xi_m q_m \, dS +$$

$$\sigma\sum_{m=1}^{N}\left(S_{m1}^{(2)} + S_{1m}^{(2)}\right)q_m + \sigma\sum_{m=1}^{N}\sum_{n=1}^{N}\left(S_{1mn}^{(3)} + S_{m1n}^{(3)} + S_{mn1}^{(3)}\right)q_m q_n +$$

$$+ \sigma\sum_{m=1}^{N}\sum_{n=1}^{N}\sum_{r=1}^{N}\left(S_{1mnr}^{(4)} + S_{m1nr}^{(4)} + S_{mn1r}^{(4)} + S_{mnr1}^{(4)}\right)q_m q_n q_r = 0$$

$$(A3)$$

Equation 4:

$$m_{yq}\ddot{y} + \frac{\rho}{2}\sum_{m=1}^{N}\left(a_{m2}^{(0)} + a_{2m}^{(0)}\right)\ddot{q}_m + c_{q_2}\dot{q}_2 +$$

$$\frac{\rho}{2}\left(\sum_{m=1}^{N}\sum_{n=1}^{N}\left(a_{2mn}^{(1)} + a_{m2n}^{(1)}\right)\ddot{q}_m q_n + \left(a_{2mn}^{(1)} + a_{m2n}^{(1)} - a_{mn2}^{(1)}\right)\dot{q}_m\dot{q}_n\right) +$$

$$\frac{\rho}{2}\left(\sum_{m=1}^{N}\sum_{n=1}^{N}\sum_{r=1}^{N}\left(a_{2mnr}^{(2)} + a_{m2nr}^{(2)}\right)\left[\ddot{q}_m q_n q_r + \dot{q}_m q_n \dot{q}_r\right]\right) +$$

$$\frac{\rho}{2}\left(\sum_{m=1}^{N}\sum_{n=1}^{N}\sum_{r=1}^{N}\left(a_{2mnr}^{(2)} + a_{m2nr}^{(2)} - a_{mn2r}^{(2)} - a_{mnr2}^{(2)}\right)\dot{q}_m\dot{q}_n q_r\right) +$$

$$\rho g \sum_{m=1}^{N}\iint_S \xi_2\xi_m q_m \, dS +$$

$$\sigma\sum_{m=1}^{N}\left(S_{m2}^{(2)} + S_{2m}^{(2)}\right)q_m + \sigma\sum_{m=1}^{N}\sum_{n=1}^{N}\left(S_{2mn}^{(3)} + S_{m2n}^{(3)} + S_{mn2}^{(3)}\right)q_m q_n +$$

$$+ \sigma\sum_{m=1}^{N}\sum_{n=1}^{N}\sum_{r=1}^{N}\left(S_{2mnr}^{(4)} + S_{m2nr}^{(4)} + S_{mn2r}^{(4)} + S_{mnr2}^{(4)}\right)q_m q_n q_r = 0$$

$$(A4)$$

Equation 5, etc: (Valid for i=3, 4, 5,...)

$$\frac{\rho}{2} \sum_{m=1}^{N} \left(a_{mi}^{(0)} + a_{im}^{(0)} \right) \ddot{q}_m + c_{q_i} \dot{q}_i +$$

$$\frac{\rho}{2} \left(\sum_{m=1}^{N} \sum_{n=1}^{N} \left(a_{imn}^{(1)} + a_{min}^{(1)} \right) \ddot{q}_m q_n + \left(a_{imn}^{(1)} + a_{min}^{(1)} - a_{mni}^{(1)} \right) \dot{q}_m \dot{q}_n \right) +$$

$$\frac{\rho}{2} \left(\sum_{m=1}^{N} \sum_{n=1}^{N} \sum_{r=1}^{N} \left(a_{imnr}^{(2)} + a_{min\,r}^{(2)} \right) [\ddot{q}_m q_n q_r + \dot{q}_m q_n \dot{q}_r] \right) +$$

$$\frac{\rho}{2} \left(\sum_{m=1}^{N} \sum_{n=1}^{N} \sum_{r=1}^{N} \left(a_{imnr}^{(2)} + a_{min\,r}^{(2)} - a_{mnir}^{(2)} - a_{mnri}^{(2)} \right) \dot{q}_m \dot{q}_n q_r \right) +$$

$$\rho g \sum_{m=1}^{N} \iint_{S} \xi_i \xi_m q_m \, dS +$$

$$\sigma \sum_{m=1}^{N} \left(S_{mi}^{(2)} + S_{im}^{(2)} \right) q_m + \sigma \sum_{m=1}^{N} \sum_{n=1}^{N} \left(S_{imn}^{(3)} + S_{min}^{(3)} + S_{mni}^{(3)} \right) q_m q_n +$$

$$+ \sigma \sum_{m=1}^{N} \sum_{n=1}^{N} \sum_{r=1}^{N} \left(S_{imnr}^{(4)} + S_{min\,r}^{(4)} + S_{mnir}^{(4)} + S_{mnri}^{(4)} \right) q_m q_n q_r = 0 \tag{A5}$$

where m_{xq} is given by:

$$m_{xq} = \rho \iint_{S} \left(x \xi_1 \right) dS \tag{A6}$$

and m_{yq}:

$$m_{yq} = \rho \iint_{S} \left(y \xi_2 \right) dS \tag{A7}$$

Eq. 2.106 is valid for all q_i's (except q_1, q_2) included in the modal series expansion. The coefficients in eq.'s A1 to A5 can be evaluated numerically given the linear eigen-characteristics of the fluid and the equilibrium fluid free surface shape.

In eq.'s A1 to A5 linear viscous damping was added for each of the system generalized coordinates while other nonlinear viscous and contact angle forces were ignored.

320

A2.0 Model Truncation and Simplification

In this research, the spacecraft mode's frequency will be set to be close to the lowest slosh mode natural frequency. The fluid response is expected to be dominated by the low frequency fluid slosh modes. The theoretical and experimental work of Hutton [1964] for nonlinear slosh at high Bond numbers, has shown that the nonlinear motion of the primary modes are strongly coupled to the motion of the 'secondary' slosh modes. In general, if the amplitude of the primary slosh modes is of order ε, (ε a small number), the amplitude of the secondary modes is of order ε^2. There may also be an infinite number of higher order modes which are coupled to the primary modes but Miles [1976, 1984a and 1984b] has shown that the three lowest frequency modes contribute at least ten times as much as the remaining secondary modes to the fluid Lagrangian.

In this research, given the relative amplitudes of the primary and secondary modes, ε and ε^2 respectively, all coefficients in eq.'s A1 to A5 that are multiplied by ε^3 and higher were set to zero. The number of assumed modes were determined by starting out with the first ten linear modes, as determined with the finite difference program, and then, while keeping track of the change in the nonlinear coefficients, the number of assumed modes were reduced. The modes retained were those that significantly contributed to the nonlinear coefficients. It must be noted that the retained modes are tank geometry specific as shown in Chapter 6. For all the study models, however, only three secondary modes were found to be needed.

Note also that eq.'s A1 to A6 can be simplified if the orthogonality of the mode shapes are used and if the symmetry of some of the coefficients are taken into account. For tanks of arbitrary geometry, most of eq.'s A1 to A5 coefficients will be non-zero but for the study models considered in this research, eq's A1 can be significantly simplified. Using orthogonality, truncating the model to retain only three secondary modes and setting terms of ε_3 and higher equal to zero, the following set of governing differential equations describes the coupled nonlinear fluid/spacecraft motion.

Equation 1:

$$\left(m + m_F\right)\ddot{x} + m_{xq_1}\ddot{q}_1 + m_{xq_2}\ddot{q}_2 + c_x\dot{x} + k_x x = F_{ex} \tag{A8}$$

Equation 2:

$$m_{xq_1}\ddot{x} + \rho a_{11}^{(0)}\ddot{q}_1 + c_{q_1}\dot{q}_1 + \left[\rho g G_{11} + 2\sigma S_{11}^{(2)}\right]q_1 +$$

$$\rho a_{113}^{(1)}\ddot{q}_1 q_3 + \rho a_{311}^{(1)}\ddot{q}_3 q_1 + \rho a_{114}^{(1)}\ddot{q}_1 q_4 +$$

$$\rho a_{411}^{(1)}\ddot{q}_4 q_1 + \rho a_{125}^{(1)}\ddot{q}_2 q_5 + \rho a_{512}^{(1)}\ddot{q}_5 q_2 +$$

$$\rho a_{113}^{(1)}\dot{q}_1 \dot{q}_3 + \rho a_{114}^{(1)}\dot{q}_1 \dot{q}_4 + \rho\left[a_{125}^{(1)} + a_{512}^{(1)} - a_{521}^{(1)}\right]\dot{q}_2 \dot{q}_5 +$$

$$\rho\left[a_{2121}^{(2)} + a_{2112}^{(2)}\right]\ddot{q}_2 q_1 q_2 + 2\rho a_{2211}^{(2)}\dot{q}_1 q_2 \dot{q}_2 +$$

$$\rho\left[a_{2121}^{(2)} + a_{2112}^{(2)} - a_{2211}^{(2)}\right]q_1 \dot{q}_2^2 + \rho a_{2211}^{(2)}\ddot{q}_1 q_2^2 +$$

$$\rho a_{1111}^{(2)}\ddot{q}_1 q_1^2 + \rho a_{1111}^{(2)}\dot{q}_1^2 q_1 +$$

$$\sigma\left[2S_{311}^{(3)} + 4S_{113}^{(3)}\right]q_1 q_3 + \sigma\left[2S_{411}^{(3)} + 4S_{114}^{(3)}\right]q_1 q_4 +$$

$$\sigma\left[2S_{521}^{(3)} + 4S_{125}^{(3)}\right]q_2 q_5 + \sigma\left[4S_{2211}^{(4)} + 8S_{2121}^{(4)}\right]q_1 q_2^2 +$$

$$4\sigma S_{1111}^{(4)}q_1^3 = 0 \tag{A9}$$

Equation 3:

$$m_{xq_2}\ddot{x} + \rho a_{22}^{(0)}\ddot{q}_2 + c_{q_2}\dot{q}_2 + \left[\rho g G_{22} + 2\sigma S_{22}^{(2)}\right]q_2 +$$

$$\rho a_{223}^{(1)}\ddot{q}_2 q_3 + \rho a_{322}^{(1)}\ddot{q}_3 q_2 + \rho a_{224}^{(1)}\ddot{q}_2 q_4 +$$

$$\rho a_{422}^{(1)}\ddot{q}_4 q_2 + \rho a_{125}^{(1)}\ddot{q}_1 q_5 + \rho a_{521}^{(1)}\ddot{q}_5 q_1 +$$

$$\rho a_{223}^{(1)}\dot{q}_2 \dot{q}_3 + \rho a_{224}^{(1)}\dot{q}_2 \dot{q}_4 + \rho\left[a_{125}^{(1)} + a_{521}^{(1)} - a_{512}^{(1)}\right]\dot{q}_1 \dot{q}_5 +$$

$$\rho\left[a_{2121}^{(2)} + a_{2112}^{(2)}\right]\ddot{q}_1 q_1 q_2 + 2\rho a_{2211}^{(2)}\dot{q}_1 q_1 \dot{q}_2 +$$

$$\rho\left[a_{2121}^{(2)} + a_{2112}^{(2)} - a_{2211}^{(2)}\right]\dot{q}_1^2 q_2 + \rho a_{2211}^{(2)}q_1^2\ddot{q}_2 +$$

$$\rho a_{2222}^{(2)}\ddot{q}_2 q_2^2 + \rho a_{2222}^{(2)}\dot{q}_2^2 q_2 +$$

$$\sigma\left[2S_{322}^{(3)} + 4S_{223}^{(3)}\right]q_2 q_3 + \sigma\left[2S_{422}^{(3)} + 4S_{224}^{(3)}\right]q_2 q_4 +$$

$$\sigma\left[2S_{521}^{(3)} + 4S_{125}^{(3)}\right]q_1 q_5 + \sigma\left[4S_{2211}^{(4)} + 8S_{2121}^{(4)}\right]q_1^2 q_2 +$$

$$4\sigma S_{2222}^{(4)} q_2^3 = 0 \qquad (A10)$$

Equation 4:

$$\rho a_{33}^{(0)}\ddot{q}_3 + c_{q_3}\dot{q}_3 + \left[\rho g G_{33} + 2\sigma S_{33}^{(2)}\right]q_3 +$$

$$\rho a_{311}^{(1)}\ddot{q}_1 q_1 + \rho\left[a_{311}^{(1)} - \frac{1}{2}a_{113}^{(1)}\right]\dot{q}_1^2 + \rho a_{322}^{(1)}\ddot{q}_2 q_2 +$$

$$\rho\left[a_{322}^{(1)} - \frac{1}{2}a_{223}^{(1)}\right]\dot{q}_2^2 + \sigma\left[2S_{113}^{(3)} + S_{311}^{(3)}\right]q_1^2 +$$

$$\sigma\left[2S_{223}^{(3)} + S_{322}^{(3)}\right]q_2^2 = 0 \qquad (A11)$$

Equation 5:

$$\rho a_{44}^{(0)}\ddot{q}_4 + c_{q_4}\dot{q}_4 + \left[\rho g G_{44} + 2\sigma S_{44}^{(2)}\right]q_4 +$$

$$\rho a_{411}^{(1)}\ddot{q}_1 q_1 + \rho\left[a_{411}^{(1)} - \frac{1}{2}a_{114}^{(1)}\right]\dot{q}_1^2 + \rho a_{422}^{(1)}\ddot{q}_2 q_2 +$$

$$\rho\left[a_{422}^{(1)} - \frac{1}{2}a_{224}^{(1)}\right]\dot{q}_2^2 + \sigma\left[2S_{114}^{(3)} + S_{411}^{(3)}\right]q_1^2 +$$

$$\sigma\left[2S_{224}^{(3)} + S_{422}^{(3)}\right]q_2^2 = 0 \qquad (A12)$$

Equation 6:

$$\rho a^{(0)}_{55}\ddot{q}_5 + c_{q_5}\dot{q}_5 + \left[\rho g G_{55} + 2\sigma S^{(2)}_{55}\right]q_5 +$$

$$\rho a^{(1)}_{512}\ddot{q}_1 q_2 + \rho a^{(1)}_{521} q_1 \ddot{q}_2 +$$

$$\rho\left[a^{(1)}_{521} + a^{(1)}_{512} - a^{(1)}_{125}\right]\dot{q}_1\dot{q}_2 + \sigma\left[4S^{(3)}_{125} + 2S^{(3)}_{521}\right]q_1 q_2 = 0 \qquad \text{(A13)}$$

where G_{mm} is given by:

$$G_{mm} = \iint_{S_F}\xi^2_m dS_F \qquad \text{(A14)}$$

Note that q_1 is the planar, (x-direction), primary fluid slosh mode and q_2 the nonplanar, (y-direction), primary fluid slosh mode.

A3.0 Non-dimensionalization

Equations A8 to A13 were non-dimensionalized to reveal the inherent scaling in system dynamics. The unit of time was selected to be the inverse of the spacecraft mode's natural frequency, ω^{-1}. The unit of displacement was the fluid height $h = d$. Using these non-dimensionalizing parameters, the following relationships are obtained;

$$x \Rightarrow dx \qquad \dot{x} \Rightarrow \omega d\dot{x} \qquad \ddot{x} \Rightarrow \omega^2 d\ddot{x}$$

$$q_n \Rightarrow dq_n \qquad \dot{q}_n \Rightarrow \omega d\dot{q}_n \qquad \ddot{q}_n \Rightarrow \omega^2 d\ddot{q}_n \qquad \text{(A15)}$$

The spacecraft mode is scaled by dividing with $m\omega^2 d$ and the fluid slosh modes by $\rho S a^{(0)}_{11}\omega^2 d$. Using these transformations, the truncated, nonlinear, nonplanar equations of motions are:

Equation 1:

$$\left(1 + \mu\right)\ddot{x} + \mu_{xq_1}\ddot{q}_1 + \mu_{xq_2}\ddot{q}_2 + 2\zeta_x\dot{x} + x = \Xi_{ex} \tag{A16}$$

Equation 2:

$$\lambda_{xq_1}\left[\frac{\mu}{\mu_{xq_1}}\right]\ddot{x} + \ddot{q}_1 + 2\zeta_1\nu\dot{q}_1 + \nu^2 q_1 +$$

$$\alpha_{113}\ddot{q}_1 q_3 + \alpha_{311}\ddot{q}_3 q_1 + \alpha_{114}\ddot{q}_1 q_4 + \alpha_{411}\ddot{q}_4 q_1 +$$

$$\alpha_{125}\ddot{q}_2 q_5 + \alpha_{512}\ddot{q}_5 q_2 + \alpha_{113}\dot{q}_1\dot{q}_3 + \alpha_{114}\dot{q}_1\dot{q}_4 +$$

$$\left[\alpha_{125} + \alpha_{512} - \alpha_{521}\right]\dot{q}_2\dot{q}_5 + \left[\alpha_{2121} + \alpha_{2112}\right]\ddot{q}_2 q_1 q_2 +$$

$$2\alpha_{2211}\dot{q}_1 q_2\dot{q}_2 + \left[\alpha_{2121} + \alpha_{2112} - \alpha_{2211}\right]q_1\dot{q}_2^2 +$$

$$\alpha_{2211}\ddot{q}q_2^2 + \alpha_{1111}\ddot{q}_1 q_1^2 + \alpha_{1111}\dot{q}_1^2 q_1 +$$

$$\nu^2\beta_{113}q_1 q_3 + \nu^2\beta_{114}q_1 q_4 + \nu^2\beta_{125}q_2 q_5 +$$

$$\nu^2\beta_{2121}q_1 q_2^2 + \nu^2\beta_{1111}q_1^3 = 0 \tag{A17}$$

Equation 3:

$$\lambda_{xq_2}\left[\frac{\mu}{\mu_{xq_2}}\right]\ddot{x} + \mu_{22}\ddot{q}_2 + 2\mu_{22}\zeta_2\nu_2\dot{q}_2 + \mu_{22}\nu_2^2 q_2 +$$

$$\alpha_{223}\ddot{q}_2 q_3 + \alpha_{322}\ddot{q}_3 q_2 + \alpha_{224}\ddot{q}_2 q_4 + \alpha_{422}\ddot{q}_4 q_2 +$$

$$\left[\alpha_{125} + \alpha_{521} - \alpha_{512}\right]\ddot{q}_1 q_5 + \alpha_{521}\ddot{q}_5 q_1 + \alpha_{223}\dot{q}_2\dot{q}_3 +$$

$$\alpha_{224}\dot{q}_2\dot{q}_4 + \alpha_{125}\dot{q}_1\dot{q}_5 + \left[\alpha_{2121} + \alpha_{2112}\right]\ddot{q}_1 q_1 q_2 +$$

$$2\alpha_{2211}\dot{q}_1 q_1\dot{q}_2 + \left[\alpha_{2121} + \alpha_{2112} - \alpha_{2211}\right]\dot{q}_1^2 q_2 +$$

$$\alpha_{2211}q_1^2\ddot{q}_2 + \alpha_{2222}\ddot{q}_2 q_2^2 + \alpha_{2222}\dot{q}_2^2 q_2 +$$

$$\nu^2\beta_{223}q_2 q_3 + \nu^2\beta_{224}q_2 q_4 + \nu^2\beta_{125}q_1 q_5 +$$

$$\nu^2\beta_{2121}q_1^2 q_2 + \nu^2\beta_{2222}q_2^3 = 0 \tag{A18}$$

Equation 4:

$$\mu_{33}\left[\ddot{q}_3 + 2\zeta_{q_3}\nu_3\dot{q}_3 + \nu_3^2 q_3\right] + \alpha_{311}\ddot{q}_1 q_1 +$$

$$\left[\alpha_{311} - \frac{1}{2}\alpha_{113}\right]\dot{q}_1^2 + \alpha_{322}\ddot{q}_2 q_2 + \left[\alpha_{322} - \frac{1}{2}\alpha_{223}\right]\dot{q}_2^2 +$$

$$\frac{1}{2}\beta_{113}\,q_1^2 + \frac{1}{2}\beta_{223}\,q_2^2 = 0 \tag{A19}$$

Equation 5:

$$\mu_{44}\left[\ddot{q}_4 + 2\zeta_{q_4}\nu_4\dot{q}_4 + \nu_4^2 q_4\right] + \alpha_{411}\ddot{q}_1 q_1 +$$

$$\left[\alpha_{411} - \frac{1}{2}\alpha_{114}\right]\dot{q}_1^2 + \alpha_{422}\ddot{q}_2 q_2 + \left[\alpha_{422} - \frac{1}{2}\alpha_{224}\right]\dot{q}_2^2 +$$

$$\frac{1}{2}\beta_{114}\,q_1^2 + \frac{1}{2}\beta_{224}\,q_2^2 = 0 \tag{A20}$$

Equation 6:

$$\mu_{55}\left[\ddot{q}_5 + 2\zeta_{q_5}\nu_5\dot{q}_5 + \nu_5^2 q_5\right] + \alpha_{512}\ddot{q}_1 q_2 + \alpha_{521}q_1\ddot{q}_2 +$$

$$\left[\alpha_{521} + \alpha_{512} - \alpha_{125}\right]\dot{q}_1\dot{q}_2 + \beta_{125}\,q_1 q_2 = 0 \tag{A21}$$

Where:

$$\mu_{xq_1} = \frac{m_{xq_1}}{m} \qquad \mu_{yq_2} = \frac{m_{yq_2}}{m} \qquad \lambda_{xq_i} = \left[\frac{\mu_{xq_i}}{\mu}\right]^2 \frac{V}{a_{11}^{(0)}}$$

$$\mu = \frac{m_F}{m} \qquad \mu_{mm} = \frac{a_{mm}^{(0)}}{a_{11}^{(0)}} \quad \text{valid for } m > 1$$

$$\nu^2 = \frac{\dfrac{1}{\omega^2}\dfrac{g}{a}\left[G_{11} + \dfrac{2S_{11}^{(2)}}{Bo}\right]}{a_{11}^{(0)}} = \frac{\omega_s^2}{\omega^2} \qquad \nu_m^2 = \nu^2\left[\frac{a_{11}^{(0)}}{a_{mm}^{(0)}}\right]\left[\frac{G_{mm}Bo + 2S_{mm}^{(2)}}{G_{11}Bo + 2S_{11}^{(2)}}\right]$$

$$\text{valid for } m > 1.$$

$$\alpha_{mnr} = \frac{d}{a}\frac{a_{mnr}^{(1)}}{a_{mn}^{(0)}} \qquad \alpha_{mnrs} = \left(\frac{d}{a}\right)^2\frac{a_{mnrs}^{(2)}}{a_{mn}^{(0)}}$$

$$\beta_{113} = \frac{\frac{d}{a}\left[2S_{311}^{(3)} + 4S_{113}^{(3)}\right]}{\left[G_{11}Bo + 2S_{11}^{(2)}\right]} \qquad \beta_{114} = \frac{\frac{d}{a}\left[2S_{411}^{(3)} + 4S_{114}^{(3)}\right]}{\left[G_{11}Bo + 2S_{11}^{(2)}\right]}$$

$$\beta_{223} = \frac{\frac{d}{a}\left[2S_{322}^{(3)} + 4S_{223}^{(3)}\right]}{\left[G_{11}Bo + 2S_{11}^{(2)}\right]} \qquad \beta_{224} = \frac{\frac{d}{a}\left[2S_{422}^{(3)} + 4S_{224}^{(3)}\right]}{\left[G_{11}Bo + 2S_{11}^{(2)}\right]}$$

$$\beta_{125} = \frac{\frac{d}{a}\left[2S_{521}^{(3)} + 4S_{125}^{(3)}\right]}{\left[G_{11}Bo + 2S_{11}^{(2)}\right]} \qquad \beta_{2121} = \frac{\left(\frac{d}{a}\right)^2\left[4S_{2112}^{(4)} + 8S_{2121}^{(4)}\right]}{\left[G_{11}Bo + 2S_{11}^{(2)}\right]}$$

$$\beta_{1111} = \frac{\left(\frac{d}{a}\right)^2 4S_{1111}^{(4)}}{\left[G_{11}Bo + 2S_{11}^{(2)}\right]} \qquad \beta_{2222} = \frac{\left(\frac{d}{a}\right)^2 4S_{2222}^{(4)}}{\left[G_{11}Bo + 2S_{11}^{(2)}\right]}$$

$$(A22)$$

The slosh mass fractions λ_{xq_i} is important in that, for forced harmonic excitation, the coupled system has response zeros at the following forcing frequencies.

$$f_i = \frac{f_{s_i}}{\sqrt{1 - \lambda_{xq_i}}}$$

$$(A23)$$

A4.0 Summary

Eq.'s A17 to A21 can be written in equivalent matrix form, facilitating implementation of the harmonic balance solution technique discussed in Chapter 3. Appendix B gives these matrices for the full nonplanar model (eq.'s A17 to A21) and a planar model, where the nonplanar degrees of freedom were set to zero.

Appendix B

Planar and Nonplanar Models

This appendix provides the planar and nonplanar matrices as obtained from the theoretical model of Chapter 2 and Appendix A. These matrices are valid for all the study models considered in this research but may not be valid for other tank geometries. The models (planar or nonplanar) for tanks of other geometries may have other non-zero coefficients than those of this appendix. Table B1 summarizes the modes included in the planar and nonplanar models used in this research.

Table B1   Fluid Modes used in Planar and Nonplanar Models

Mode Description	Mode Number used in Analytical Model	Planar Model	Nonplanar Model
x-Translation	x	√	√
Primary, Planar	q_1	√	√
Primary, Nonplanar	q_2	-	√
Secondary, Axi-symmetric	q_3	√	√
Secondary, Planar	q_4	√	√
Secondary, Nonplanar	q_5	-	√

B1.0 Planar Model

Using the mode shapes identified in Table B1, the following planar model was obtained from eq.s 2.117 to 2.122:

Planar "**Mass**" Matrix:

$$
\begin{bmatrix}
[1+\mu] & \mu_{xq_1} & 0 & 0 \\
\lambda_{xq_1}\left[\dfrac{\mu}{\mu_{xq_1}}\right] & \left\{\dfrac{1+\alpha_{113}q_3+\alpha_{114}q_4}{\alpha_{1111}q_1^2}\right\} & \alpha_{311}q_1 & \alpha_{411}q_1 \\
0 & \alpha_{311}q_1 & \mu_{33} & 0 \\
0 & \alpha_{411}q_1 & 0 & \mu_{44}
\end{bmatrix}
\qquad\text{(B1)}
$$

Planar **"Damping"** Matrix:

$$
\begin{bmatrix}
2\zeta_x & 0 & 0 & 0 \\[2ex]
0 & \left\{ \begin{array}{c} 2\zeta_{q_1}\nu + \alpha_{113}\dot{q}_3 + \alpha_{114}\dot{q}_4 + \\ \alpha_{1111}q_1\dot{q}_1 \end{array} \right\} & 0 & 0 \\[3ex]
0 & \left[\alpha_{311} - \dfrac{1}{2}\alpha_{113}\right]\dot{q}_1 & 2\mu_{33}\zeta_{q_3}\nu_3 & 0 \\[2ex]
0 & \left[\alpha_{411} - \dfrac{1}{2}\alpha_{114}\right]\dot{q}_1 & 0 & 2\mu_{44}\zeta_{q_4}\nu_4
\end{bmatrix}
\tag{B2}
$$

Planar **"Stiffness"** Matrix:

$$
\begin{bmatrix}
1 & 0 & 0 & 0 \\[2ex]
0 & \left\{ \begin{array}{c} \nu^2 + \nu^2\beta_{113}q_3 + \\ \nu^2\beta_{114}q_4 + \nu^2\beta_{1111}q_1^2 \end{array} \right\} & 0 & 0 \\[3ex]
0 & \dfrac{1}{2}\nu^2\beta_{113}q_1 & \mu_{33}\nu_3^2 & 0 \\[2ex]
0 & \dfrac{1}{2}\nu^2\beta_{114}q_1 & 0 & \mu_{44}\nu_4^2
\end{bmatrix}
\tag{B3}
$$

Note these matrices are multiplied with:

The **Mass** matrix with:

$$\begin{Bmatrix} \ddot{x} \\ \ddot{q}_1 \\ \ddot{q}_3 \\ \ddot{q}_4 \end{Bmatrix}$$

the **Damping** matrix with:

$$\begin{Bmatrix} \dot{x} \\ \dot{q}_1 \\ \dot{q}_3 \\ \dot{q}_4 \end{Bmatrix}$$

and the **Stiffness** matrix with:

$$\begin{Bmatrix} x \\ q_1 \\ q_3 \\ q_4 \end{Bmatrix}$$

(B4)

B2.0 Nonplanar Model

Using the mode shapes of Table B1 (for nonplanar model), the following nonplanar model was obtained (from eq.s 2.117 to 2.122):

Nonplanar "**Mass**" Matrix:

$$
\begin{bmatrix}
[1+\mu] & \mu_{xq_1} & \mu_{xq_2} & 0 & 0 & 0 \\[2mm]
\lambda_{xq_1}\left[\dfrac{\mu}{\mu_{xq_1}}\right] & \left\{\begin{array}{l} 1+\alpha_{113}q_3+\alpha_{114}q_4 \\ \alpha_{1111}q_1^2+\alpha_{2211}q_2^2 \end{array}\right\} & \left\{\begin{array}{l} \alpha_{125}q_5+ \\ [\alpha_{2121}+\alpha_{2112}]q_1q_2 \end{array}\right\} & \alpha_{311}q_1 & \alpha_{411}q_1 & \alpha_{512}q_2 \\[4mm]
\lambda_{xq_2}\left[\dfrac{\mu}{\mu_{xq_2}}\right] & \left\{\begin{array}{l} \alpha_{125}q_5+ \\ [\alpha_{2121}+\alpha_{2112}]q_1q_2 \end{array}\right\} & \left\{\begin{array}{l} \mu_{22}+\alpha_{223}q_3+\alpha_{224}q_4+ \\ \alpha_{2211}q_1^2+\alpha_{2222}q_2^2 \end{array}\right\} & \alpha_{322}q_2 & \alpha_{422}q_2 & \alpha_{521}q_1 \\[4mm]
0 & \alpha_{311}q_1 & \alpha_{322}q_2 & \mu_{33} & 0 & 0 \\[2mm]
0 & \alpha_{411}q_1 & \alpha_{422}q_2 & 0 & \mu_{44} & 0 \\[2mm]
0 & \alpha_{512}q_2 & \alpha_{521}q_1 & 0 & 0 & \mu_{55}
\end{bmatrix} \quad \text{(B5)}
$$

Nonplanar "**Damping**" Matrix:

$$
\begin{bmatrix}
2\zeta_x & 0 & 0 & 0 & 0 & 0 \\[2ex]
0 & \left\{\begin{array}{l} 2\zeta_{q_1}\nu + \alpha_{113}\dot{q}_3 + \alpha_{114}\dot{q}_4 + \\ 2\alpha_{2211}q_2\dot{q}_2 + \alpha_{1111}q_1\dot{q}_1 \end{array}\right\} & \left\{\begin{array}{l} [\alpha_{125} + \alpha_{512} - \alpha_{521}]\dot{q}_5 + \\ [\alpha_{2121} + \alpha_{2112} - \alpha_{2211}]q_1\dot{q}_2 \end{array}\right\} & 0 & 0 & 0 \\[3ex]
0 & \left\{\begin{array}{l} [\alpha_{125} + \alpha_{521} - \alpha_{512}]\dot{q}_5 \\ {[\alpha_{2121} + \alpha_{2112} - \alpha_{2211}]q_2\dot{q}_1} \end{array}\right\} & \left\{\begin{array}{l} 2\zeta_{q_2}\mu_{22}\nu_2 + \alpha_{223}\dot{q}_3 + \alpha_{224}\dot{q}_4 + \\ 2\alpha_{2211}q_1\dot{q}_1 + \alpha_{2222}q_2\dot{q}_2 \end{array}\right\} & 0 & 0 & 0 \\[3ex]
0 & \left[\alpha_{311} - \dfrac{1}{2}\alpha_{113}\right]\dot{q}_1 & \left[\alpha_{322} - \dfrac{1}{2}\alpha_{223}\right]\dot{q}_2 & 2\mu_{33}\zeta_{q_3}\nu_3 & 0 & 0 \\[2ex]
0 & \left[\alpha_{411} - \dfrac{1}{2}\alpha_{114}\right]\dot{q}_1 & \left[\alpha_{422} - \dfrac{1}{2}\alpha_{224}\right]\dot{q}_2 & 0 & 2\mu_{44}\zeta_{q_4}\nu_4 & 0 \\[2ex]
0 & \left[\alpha_{512} - \dfrac{1}{2}\alpha_{125}\right]\dot{q}_2 & \left[\alpha_{521} - \dfrac{1}{2}\alpha_{125}\right]\dot{q}_1 & 0 & 0 & 2\mu_{55}\zeta_{q_5}\nu_5
\end{bmatrix}
$$

(B6)

Nonplanar "**Stiffness**" Matrix:

$$
\begin{bmatrix}
1 & 0 & 0 & 0 & 0 & 0 \\[2ex]
0 & \left\{\begin{array}{c} \nu^2 + \nu^2\beta_{113}q_3 + \\ \nu^2\beta_{114}q_4 + \nu^2\beta_{2121}q_2^2 + \\ \nu^2\beta_{1111}q_1^2 \end{array}\right\} & \nu^2\beta_{125}q_5 & 0 & 0 & 0 \\[4ex]
0 & \nu^2\beta_{125}q_5 & \left\{\begin{array}{c} \mu_{22}\nu_2^2 + \nu^2\beta_{223}q_3 + \\ \nu^2\beta_{224}q_4 + \nu^2\beta_{2121}q_1^2 + \\ \nu^2\beta_{2222}q_2^2 \end{array}\right\} & 0 & 0 & 0 \\[4ex]
0 & \dfrac{1}{2}\nu^2\beta_{113}q_1 & \dfrac{1}{2}\nu^2\beta_{223}q_2 & \mu_{33}\nu_3^2 & 0 & 0 \\[2ex]
0 & \dfrac{1}{2}\nu^2\beta_{114}q_1 & \dfrac{1}{2}\nu^2\beta_{224}q_2 & 0 & \mu_{44}\nu_4^2 & 0 \\[2ex]
0 & \dfrac{1}{2}\nu^2\beta_{125}q_2 & \dfrac{1}{2}\nu^2\beta_{125}q_1 & 0 & 0 & \mu_{55}\nu_5^2
\end{bmatrix} \quad \text{(B7)}
$$